Development of a Nanostructured Thin Film Device and Optics System for Protein Detection

by

Hillary M. Sweet

A thesis submitted in partial fulfillment of the requirements for the degree of

Doctor of Philosophy

in

Materials Engineering

Department of Chemical and Materials Engineering and Biomedical Engineering
University of Alberta

Abstract

Although various medical diagnostics exist to test biologics for biomarkers, diseases, or proteins of interest; there is currently no point-of-care platform test that is quick, inexpensive, and easy to use. The aim of this work was to further develop a stand-alone, point-of-care medical diagnostic based on thin film visible interference. The use of different anodization parameters (i.e. electrolyte, voltage, length of time) created devices with drastically different structures and properties. Analyzing the reflections and interference off these surfaces demonstrated that the surface porosity influences the reflectance and in turn the optimal viewing conditions. Highly porous films formed in oxalic and sulfuric acids generated optimal interference colours when viewed through a *p*-polarizing filter, whereas less porous films created in phosphoric acid generated optimal interference colours when *s*-polarized. The device structure proved to be highly tunable during the anodization process. Varying the sputtered aluminum thickness changed the length of anodization, and ultimately the refractive index of the resulting alumina layer. Current density provided a viable method to monitor and regulate the oxidation process. X-ray photoelectron spectroscopy and secondary ion mass spectroscopy analysis of devices oxidized in phosphoric acid at 5 and 8 V potentials showed that the phosphate integration from phosphoric acid was equal at these potentials, as well as the nitrogen to aluminum ratio on the surface of both with protein exposure. Secondary ion mass spectroscopy was used to detect CN^- ions from the proteins, and monitored the signal strength and depth, showing greater protein penetration in the 5 V samples compared to the 8 V samples. Furthermore, surface analysis techniques showed the importance of consistent storage and handling of devices, as it can lead to a noticeable difference in the surface chemistry. Tunability was further explored using phosphoric acid and a constant potential of 8 V. The importance of tantalum oxide generation and thickness was demonstrated, as without this layer, low interference colours result. Furthermore, without the tantala layer

ellipsometry models contain large standard error and prevent accurate alumina parameters from being obtained. With the adsorption of an antigen and subsequently antibody pair the optimal changes in optical path lengths were observed using colour coordinates from the surface interference generated. Changes in the deposition energy during tantalum layer formation created different tantalum phases, α-Ta and β-Ta. These layers possessed different optical constants and interference colours, while also impacting the resulting alumina thicknesses in the anodized device. In some instances, devices created on α-Ta showed delamination during the oxidation process. Various vitamin K-dependent proteins were exposed to the alumina device surface in solutions of constant molarity, yet the size of the molecule was the main factor contributing to the limit of detection. The addition of calcium and magnesium ions to prothrombin solutions showed drastic increases in the optical path length, and colour shift, that were though to result from changes to the protein structure and potentially the binding efficiency. Radiolabelled prothrombin studies showed that ~0.2 mg/ml prothrombin solutions were required to form a monolayer on the surface in 15 minutes. Furthermore, binary solutions of prothrombin and competing proteins were analyzed as well as subsequent wash solutions, some of which demonstrated prothrombin removal. Comparing the visible colour shifts resulting on the device surface to radiolabelled data, it was found that 34 to 38% prothrombin surface coverage was required to generate a detectable colour shift, and the base colour of the device was deemed highly relevant to the sensitivity of protein detection. Detection of an antigen-antibody prototype of prothrombin and anti-prothrombin showed colour quantification is possible with this device. The limit of detection and analytical sensitivity were determined from this work for the antigen-antibody complex. Overall, the thin film interference device showed quantification with colour, and detection after 15 minutes of exposure, which demonstrates its potential as a point-of-care diagnostic in a variety of applications.

Acknowledgements

First and foremost, I would like to thank my supervisors Dr. Robert Burrell and Dr. Todd McMullen. Thank you for asking questions, sharing your knowledge, and for believing in me more than I believed in myself. The personal growth I achieved over the duration of my graduate studies would not have been possible without both of your guidance. Gratitude to my supervisory committee members Dr. Hasan Uladag, Dr. Larry Unsworth, and Dr. Gregory Shultz for their valuable input and time.

To Matthew Nickel, the countless discussions surrounding the diagnostic and other areas of interest were invaluable. It has been the utmost pleasure to work with you, and I could not have handpicked a better teammate. To students whom I had the opportunity to work with and supervise over my graduate degree, I thank you all for your hard work. Sally Fung (summer 2015), Freya Hik (Dean's Research Award projects: fall 2016 & fall 2016 to winter 2017), Gavin Melligan (summer 2016), Kyle Moxham (summer 2016 and summer 2017), Josh Tutak (summer 2016 to fall 2016), Aryn Ketsa (summer 2017), and Mackenzie Baert (CME 458: winter 2018).

I would like to acknowledge the Natural Sciences and Engineering Research Council for the funding received through their Postgraduate Scholarship-Doctorate Program.

Last but not least, I would like to thank my family and friends for their never-ending love. To my parents, Diane and Steve, and my siblings, Ben and Hanna, I am so thankful to have you all for support and as a source of inspiration. To my partner, Kurt, your patience and encouragement during the completion of this work has been appreciated more than words can describe. You all mean the world to me.

Table of Contents

Abstract ii

Acknowledgements iv

Table of Contents v

List of Tables xix

List of Figures xxvii

List of Symbols and Abbreviations xlvii

Chapter 1 – Purpose and Scope 1

1.1 Motivation 1

1.2 Aims & Objectives 2

1.3 Scope of Thesis 3

Chapter 2 – Introduction and Literature Review 6

2.1 Introduction – Review of Diagnostic Tests 6

2.1.1 Summary 11

2.2 Background of Device Colour Generation 12

2.2.1 Thin Film Interference 12

2.2.1.1 Waves at an Interface 13

2.2.1.2 Optical Path Length (OPL) 14

2.2.1.3 Constructive or Destructive Interference 17

2.2.1.4 Fresnel Coefficients 17

2.2.2 Sputtering of Thin Films 18

2.2.3 Electrochemical Oxidation 19

2.2.3.1 History 19

2.2.3.2 Pore Formation 20

2.2.3.3 Alumina Surfaces 22

2.2.3.4 Alumina Refractive Index 24

2.2.4 Protein Detection on Thin Film Surfaces 24

2.2.4.1 Aluminum Oxide Thin Film Sensors 25

2.2.4.2 Protein Immobilization on Alumina 27

2.2.5 Optics 31

2.2.5.1 Colour Sensitivity 31

2.2.5.2 Human Vision 32

2.2.5.3 Methods for Colour Detection 33

2.2.5.4 Chromaticity Diagrams 34

2.2.5.5 Illumination Controls 36

2.2.5.6 Light Polarization 37

Chapter 3 – General Materials and Methods 40

3.1 Introduction 40

3.2 Device Preparation 40

3.2.1 University of Alberta Nano Fabrication and Characterization Facility (nanoFAB) 40

3.2.1.1 Piranha 40

3.2.1.2 Sputtering....41

3.2.2 Northern Alberta Institute of Technology (NAIT) Fabrication Facility....44

3.2.2.1 Sputtering....44

3.2.3 Wafer Cleaving....45

3.2.4 Electrochemical Oxidation....46

3.3 Protein Exposure and Adsorption....49

3.4 Custom Optics Viewing System....50

3.5 Calculating Sensitivities....51

3.6 Analytical Techniques....52

3.6.1 Profilometry....52

3.6.2 Scanning Electron Microscopy....52

3.6.3 Ellipsometry....53

3.6.4 X-ray Diffraction....54

3.6.5 Spectrophotometer....54

3.6.6 X-ray Photoelectron Spectroscopy....54

3.6.7 Secondary Ion Mass Spectroscopy....55

3.6.8 Statistics....55

Chapter 4 – The Effect of Anodization Parameters and Aluminum Deposition on the Device Structure and Operation....56

4.1 Introduction....56

4.2 Materials and Methods 59
4.2.1 Electrolyte Type and Concentration 59
4.2.2 Current Density 59
4.2.3 Sputtered Aluminum Thickness 60
4.2.3.1 Part A – Aluminum Deposition in Constant Power Mode 60
4.2.3.2 Part B – Aluminum Deposition in Constant Current Mode 60
4.2.4 Analysis 60
4.3 Results 61
4.3.1 Electrolyte Type and Concentration 61
4.3.2 Applied Potential 72
4.3.3 Current Density 76
4.3.4 Sputtered Aluminum 78
4.3.4.1 Part A – Aluminum Deposition in Constant Power Mode 78
4.3.4.2 Part B – Aluminum Deposition in Constant Current Mode 80
4.3.4.3 Comparison of Aluminum Deposition Modes 82
4.4 Discussion 82
4.4.1 Temperature 83
4.4.2 Electrolyte Type and Concentration 84
4.4.2.1 Tantalum Films 84
4.4.2.2 Aluminum/Tantalum Films 85
4.4.2.3 Birefringence 92

4.4.2.4 Hydration 93
4.4.3 Applied Potential 94
4.4.4 Current Density 96
4.4.5 Sputtered Aluminum Thickness 97
4.5 Future Work 99
4.6 Conclusions 99
4.6.1 Electrolyte Type and Concentrations 100
4.6.2 Applied Potential 100
4.6.3 Current Density 100
4.6.4 Sputtered Aluminum Thickness 101
Chapter 5 – Adsorption of Prothrombin and Anti-prothrombin Layers onto Porous Anodic Alumina: an XPS and SIMS Investigation 102
5.1 Introduction 102
5.2 Materials and Methods 103
5.2.1 Device Preparation 103
5.2.2 Adsorption of Biologics 104
5.2.3 Analysis 104
5.2.3.1 SEM 104
5.2.3.2 Ellipsometry 104
5.2.3.3 XPS 104
5.2.3.4 SIMS 105

5.2.3.5 Statistical Analysis 106
5.3 Results 106
5.3.1 XPS 107
5.3.1.1 Phosphorous Content 107
5.3.1.2 Surface Behavior Diagrams 108
5.3.1.3 Nitrogen Content 109
5.3.2 SIMS 109
5.3.2.1 Surface Ions 111
5.3.2.2 Protein Depth 112
5.4 Discussion 114
5.4.1 XPS 114
5.4.1.1 Phosphorous Content 114
5.4.1.2 Surface Behavior Diagrams 114
5.4.1.3 Nitrogen Content 115
5.4.2 SIMS 116
5.4.2.1 Surface Ions and Surface Hydration 116
5.4.2.2 Protein Depth Penetration 117
5.5 Future Work 118
5.6 Conclusions 119
Chapter 6 – Point-of-Care Detection Platform Using Tunable Anodic Alumina Surfaces 121

6.1 Introduction....121
6.2 Materials and Methods....123
6.2.1 Thin Film Deposition....123
6.2.2 Thin Film Oxidation....124
6.2.3 SEM....125
6.2.4 Ellipsometry....125
6.2.5 Adsorption of Biologics....125
6.2.6 Visible Interference Colour Detection....126
6.2.7 Statistical Analysis....127
6.3 Results....127
6.3.1 Aluminum Thin Film Deposition and Oxidation....127
6.3.2 Variable Angle Spectroscopic Ellipsometry....129
6.3.3 Alumina Etch Rates and Tantala Growth Rates....134
6.3.4 Visible Interference Colour Detection....136
6.4 Discussion....137
6.5 Conclusions....141
Chapter 7 – The Impact of Layers at the Tantalum and Aluminum Interface....143
7.1 Introduction....143
7.1.1 Interstitial native and anodic oxide layers....143
7.1.2 Tantalum Oxide Reduction with Adjacent Aluminum Deposition....144
7.1.3 Characteristic Properties of Sputtered Thin Films....146

7.2 Materials and Methods 149
7.2.1 Device Preparation 149
7.2.2 Analysis 150
7.2.2.1 SEM 150
7.2.2.2 Time Calculation of Barrier Oxide Formation 150
7.2.2.3 Ellipsometry 151
7.2.2.4 EDS 151
7.2.2.5 Sensitivity Analysis with Protein Adsorption 151
7.3 Results 152
7.3.1 As Sputtered Tantalum and Anodic Tantala Films 152
7.3.1.1 SEM with EBSD 153
7.3.1.2 XRD 153
7.3.1.3 Surface Colour 154
7.3.2 Standard Anodization of Aluminum on α and Mixed α-β Tantalum Structures 156
7.3.3 Primary and Standard Anodization on Mixed α-β Tantalum Films 161
7.3.4 Primary and Standard Anodization on α Tantalum Film 168
7.3.4.1 NAIT Tantalum Surfaces 169
7.3.4.2 Analysis of Film Failure 170
7.4 Discussion 177

7.4.1 As Sputtered Tantalum and Anodic Tantala Films 177

7.4.1.1 SEM with EBSD 178

7.4.1.2 XRD 179

7.4.1.3 Surface Colour 180

7.4.2 Standard Anodization of Aluminum on α and Mixed α-β Tantalum Structures 182

7.4.3 Primary and Standard Anodization Processes on Mixed α-β Tantalum Films 183

7.4.4 Primary and Standard Anodization Processes on α Tantalum Films 185

7.5 Future Work 189

7.6 Conclusions 190

Chapter 8 – Detection of Vitamin K-dependent Proteins 192

8.1 Introduction 192

8.1.1 Vitamin K-dependent Proteins 193

8.1.2 Gla Domain Metal Ion Binding Sites 195

8.2 Materials and Method 197

8.2.1 Device Preparation 197

8.2.2 Protein Modelling 198

8.2.3 Protein Adsorption 199

Part A – Detection of Vitamin K-dependent Proteins 199

8.2.3.1 Prothrombin Loss in Ordinary Micro-centrifuge Tubes 199

8.2.3.2 Sensitivity of Vitamin K-dependent Proteins 200

8.2.3.3 Time Dependence of Vitamin K-dependent Proteins..... 201

Part B – Detection of Prothrombin with Metal Ions in Solution 201

8.2.3.4 Binding of Prothrombin from Solutions Containing Metal Ions 201

8.2.3.5 The Effect of Metal Ions and Chelators in Solution..... 202

8.2.4 Characterization 202

8.2.5 Liquid Chromatography Mass Spectrometry..... 202

8.3 Results 203

8.3.1 Protein Modelling 203

8.3.2 Protein Adsorption to Alumina..... 207

Part A – Detection of Vitamin K-dependent Proteins..... 207

8.3.2.1 Prothrombin Loss in Ordinary Tubes..... 207

8.3.2.2 Sensitivity of Vitamin K-dependent Proteins 208

8.3.2.3 Time Dependence of Vitamin K-dependent Proteins..... 210

Part B – Detection of Prothrombin with Metal Ions in Solution 212

8.3.2.4 Binding of Prothrombin from Solutions Containing Metal Ions 212

8.3.2.5 The Effect of Metal Ions and Chelators in Solution..... 216

8.3.3 Liquid Chromatography Mass Spectrometry..... 217

8.4 Discussion..... 220

8.4.1 Protein Modelling 220

8.4.2 Protein Adsorption to Alumina 221

Part A – Detection of Vitamin K-dependent Proteins 221

8.4.2.1 Prothrombin Loss in Ordinary Tubes 221

8.4.2.2 Sensitivity of Vitamin K-dependent Proteins 223

8.4.2.3 Time Dependence of Vitamin K-dependent Proteins 224

Part B – Detection of Prothrombin with Metal Ions in Solution 225

8.4.2.4 Binding Effects of Prothrombin Solutions Containing Metal Ions 225

8.4.2.5 The Effect of Metal Ions and Chelators in Solution 228

8.4.3 Liquid Chromatography Mass Spectrometry 229

8.5 Future Work 231

8.6 Conclusions 232

Chapter 9 – Prothrombin Surface Density and the Effect of Wash Solutions on the Alumina/Tantala Device 234

9.1 Introduction 234

9.2 Materials and Method 235

9.2.1 Device Preparation 235

9.2.1.1 Gold Conjugated Anti-prothrombin 235

9.2.1.2 Radiolabelled Prothrombin 236

9.2.2 Anti-prothrombin Gold Conjugation 236

9.2.3 Prothrombin Radiolabelling Materials 237
9.2.3.1 NOTA Conjugation 238
9.2.3.2 ^{64}Cu Labeling 238
9.2.4 Protein Adsorption 239
9.2.4.1 Gold Conjugated Anti-prothrombin 239
9.2.4.2 Radiolabelled Prothrombin 239
9.2.4.3 Radioactivity Variation 240
9.2.4.4 Adsorption Isotherm 240
9.2.4.5 Time Variation 240
9.2.4.6 Protein Competition 240
9.2.4.7 Wash-out of Radioactivity 240
9.2.5 Protein Analysis 241
9.2.6 Surface Analysis 241
9.3 Results 242
9.3.1 Gold Conjugated Anti-prothrombin 242
9.3.2 Characterization of Prepared Devices 245
9.3.3 Prothrombin Radiolabelling 246
9.3.4 Adsorption of Radiolabelled Prothrombin 247
9.3.4.1 Radioactivity Variation 247
9.3.4.2 Adsorption Isotherm 248
9.3.4.3 Time Variation 251

9.3.4.4 Protein Competition 252

9.3.4.5 Wash-out of Radioactivity 255

9.3.5 Quantification of Immobilized Prothrombin with Colour Coordinates 258

9.3.5.1 Alumina Thickness of ~95 nm 258

9.3.5.2 Alumina Thickness of ~100 nm 265

9.4 Discussion 269

9.4.1 Gold Nanoparticle Conjugation 269

9.4.2 Radiolabelled Prothrombin 271

9.4.2.1 Protein Labelling 271

9.4.2.2 Radioactivity Variation 271

9.4.2.3 Adsorption Isotherm 271

9.4.2.4 Time Variation 274

9.4.2.5 Protein Competition 275

9.4.2.6 Wash-out of Radioactivity 276

9.4.3 Quantification of Immobilized Prothrombin with Colour Coordinates 278

9.5 Future Work 282

9.6 Conclusions 283

Chapter 10 – Anti-Prothrombin Sensitivity on a Prothrombin-Coated Multilayer Device 285

10.1 Introduction 285

10.2 Methods 287

10.2.1 Theoretical Calculations for Anti-Prothrombin Limit of Detection 287

10.2.2 Device Preparation 287

10.2.3 Prothrombin Immobilization and Complex Formation 288

10.2.4 Analysis 288

10.3 Results 288

10.4 Discussion 294

10.5 Future Work 296

10.6 Conclusions 296

Bibliography 298

Appendix 1 – SOPs ..... Error! Bookmark not defined.

1.1 Piranha Cleaning SOP 358

1.2 Bob Sputtering System SOP 362

1.3 Floyd Sputtering System SOP 366

1.4 NAIT Sputtering System SOP 370

1.5 Spectrophotometer SOP 376

Appendix 2 – Alpha Step IQ Profilometer SOP 382

Appendix 3 – XPS Spectra 385

List of Tables

Table 2.1. Analysis of current protein diagnostic tests based on low (+), medium (++) and high (+++) rankings. 11

Table 4.1. Summary of average current density (J) and time values for critical oxidation points. Devices were formed in 0.4 M and 1.0 M solutions of phosphoric, sulfuric, and oxalic acid electrolytes at 8 V. 62

Table 4.2. Parameters measured from SEM images for samples anodized in 0.4 M and 1.0 M of phosphoric, sulfuric, and oxalic acid electrolytes at 8 V. 65

Table 4.3. Parameters measured from ellipsometry for samples anodized in 0.4 M and 1.0 M of phosphoric, sulfuric, and oxalic acid electrolytes at 8 V. 66

Table 4.4. Fresnel equations were used to calculate the reflectivity of horizontally and vertically polarized light off the anodic tantala and tantalum surface and varying angles of incidence. 69

Table 4.5. Ellipsometry measured values of anodic tantala layers formed in electrolytes at 8 V. 69

Table 4.6. A comparison of the reflectivity values obtained with experimental (spectrophotometer) and theoretical (Fresnel equation) techniques. 72

Table 4.7. Parameters measured from SEM topographic images for samples anodized in 0.4 M phosphoric acid electrolyte at applied potentials of 2, 5, 8, and 10 V. 74

Table 4.8. Summary of ellipsometry analysis for multilayer devices created with anodization in 0.4 M phosphoric acid electrolyte at 2, 5, 8, and 10 V. 75

Table 4.9. Average temperature and anodization length across intra and inter wafer sets. 77

Table 4.10. Average temperature and anodization length in intra and inter wafer sets. 78

Table 4.11. Anodization parameters of slides with aluminum sputtered in constant power mode. 78

Table 4.12. Multilayer devices created with different aluminum thicknesses, under constant power, lead to changes in the resulting alumina film parameters following anodization. 78

Table 4.13. Statistical analysis showed the effect of alumina thickness on refractive index of the alumina layer sputtered in constant power mode. (Tukey's HSD test, $F(5,12)=7.413$, $p=.002$. 79

Table 4.14. Anodization parameters of slides with aluminum sputtered in constant current mode. 80

Table 4.15. Multilayer devices created with different aluminum thicknesses, under constant current, lead to changes in the resulting alumina film parameters following anodization. 80

Table 4.16. Statistical analysis comparing the effect of alumina thickness on refractive index of the alumina layer sputtered in constant current mode. (Tukey's HSD test, $F(5,12)=52.797$, $p=.000$)..... 81

Table 4.17. Statistical analysis comparing the effect of the aluminum sputtering mode on refractive index of the alumina layer. Selected slides were close in alumina thicknesses. 82

Table 4.18. A comparison of wall thickness values obtained in low voltage work in different electrolyte conditions..... 88

Table 4.19. Calculations using Fresnel equations to determine the R_s and R_p to balance the intensity off the alumina and tantalum layers. Highlighted boxes show conditions for optimal colour generation. 89

Table 4.20. Fresnel reflectivity values corrected to account for alumina surface porosities of ~55 and 20% for $\eta=1.35$ and $\eta=1.58$ respectively. Nearly balanced reflectance off the alumina and tantala layers are highlighted for R_s and R_p. 90

Table 5.1. Ellipsometry and SEM data on the device structures formed with anodization at 5 and 8 V in 0.4 M phosphoric acid. 106

Table 5.2. Summary of average P (2s)/Al (2p) ratios for unanodized, 5 V, and 8 V samples with exposure to no protein, prothrombin for 15 minutes, and prothrombin followed by anti-prothrombin for 15 minutes each. (n=3)..... 108

Table 5.3. Summary of average N (1s)/Al (2p) ratios for unanodized, 5 V, and 8 V samples with exposure to no protein, prothrombin for 15 minutes, and prothrombin followed by anti-prothrombin for 15 minutes each. (n=3)..... 109

Table 6.1. Statistical analysis comparing the effect of anodization stage on the alumina layer refractive index. (n=3) 130

Table 6.2. Statistical analysis comparing the effect of alumina thickness on the alumina layer refractive index at 370 nm anodized to stage b. (Welch's t-test, F(5,5.35)=57.65, p=.000) (n=3) 132

Table 6.3. Statistical analysis comparing the effect of the measurement technique (SEM or variable angle spectroscopic ellipsometry (VASE)) used to obtain the alumina thicknesses with anodization to stage a and b. Separate tests were carried out for each of the four different initial aluminum films. (n=3)..... 134

Table 6.4. Visible colours and Yxy coordinates from the surface of anodized slides prior to and following protein immobilization. Three different initial aluminum thicknesses were deposited and anodized at 8 V in 0.4 M phosphoric acid until stage a, b, and c. 137

Table 7.1. Elemental data and standard deviations (SD) from as sputtered and anodized tantalum layers. Elements found were carbon (C), tantalum (Ta), oxygen (O), and nitrogen (N). (n=3, except nanoFAB as sputtered n=2) 153

Table 7.2. XRD peaks identified in tantalum slides deposited in nanoFAB and NAIT magnetron sputter systems, and corresponding peak information. 154

Table 7.3. Reflectivity values at 550 nm are shown for tantalum films deposited in the nanoFAB or NAIT systems. Tantalum films were analyzed in as sputtered and anodized states. Anodization was carried out at 6 V in 0.4 M phosphoric acid. 156

Table 7.4. Ellipsometry generated thicknesses and optical constants for tantalum coatings deposited in nanoFAB and NAIT systems and anodized in 0.4 M phosphoric acid at 8 V. As sputtered and anodized tantalum films were analyzed to generate tantalum and tantalum oxide layer data. 156

Table 7.5. Ellipsometry generated thickness and optical constant values obtained from devices containing aluminum and tantalum coatings, deposited in nanoFAB and NAIT systems, anodized following the standard process at 8 V..... 157

Table 7.6. Measurements of alumina thicknesses and surface porosity values from SEM images of aluminum and tantalum coatings, deposited in nanoFAB and NAIT systems, anodized following the standard process at 8 V..... 157

Table 7.7. RGB coordinates and differences in colour between prothrombin-coated surfaced exposed to anti-prothrombin solutions (ΔE*) at varying concentrations. 160

Table 7.8. Yxy chromaticity coordinates were transformed from RGB colour coordinates to plot coordinates on the CIE chart. 160

Table 7.9. Average time required to form the barrier oxide layer during the standard oxidation process in 0.4 M phosphoric acid electrolyte. The difference between oxide formation time for slides with only the standard anodization versus slides with primary and standard anodization were compared at the respective voltages used for the standard anodization process (4, 6, or 8 V). 162

Table 7.10. Ellipsometry data for slides formed with the standard anodization process or primary and standard anodization processes. The standard anodization was carried out at 4, 6, and 8 V on devices with an initial aluminum thickness of 99 nm..... 163

Table 7.11. Measurements of alumina thicknesses and surface porosity values from SEM images of aluminum and tantalum coatings, deposited in the nanoFAB system, anodized

following the primary and 8 V standard processes for test samples or with the standard process at 8 V for control samples. 164

Table 7.12. RGB coordinates and differences in colour between prothrombin-coated surfaced exposed to anti-prothrombin solutions (ΔE*) at varying concentrations. 167

Table 7.13. Yxy chromaticity coordinates were transformed from RGB colour coordinates in order to plot coordinates on the CIE chart. 167

Table 7.14. Elemental point analysis data collected from the locations depicted in Figure 7.24. Elemental compositions of the porous alumina and the to-be-determined (TBD) locations are shown with standard deviations. 172

Table 7.15. Deposition parameters used for tantalum deposition in the nanoFAB and NAIT sputter systems. 178

Table 8.1. A comparison of vitamin K-dependent proteins involved in the coagulation cascade. Blank spaces indicate parameters that are not present in some proteins and * represents a value that was not present in the literature. 194

Table 8.2. Outlines the prothrombin concentrations, moles present in 20μl spots, and the number of times this quantity can cover the nominal surface area within a 1 cm diameter spot with short and long side molecule binding. The effective alumina surface area has a porosity of ~50% of the nominal are, not taking into account surface roughness. 200

Table 8.3. Concentrations of various metal ion solutions applied to the alumina surface with other constituents, typically prothrombin. 201

Table 8.4. The initial concentration and molarity of prothrombin in solution were used along with a maximum adsorption value of 570 ng/cm^2 and the centrifuge tube internal surface area of 8.8 cm^2 to determine the moles adsorbed and the final concentration exposed. 208

Table 8.5. Protein molecular weight and radius of gyration values were used to calculate diffusion coefficients in water at 21°C and the length of time for diffusion from the surface of a 20 µl spot to the alumina surface. 211

Table 8.6. Shows the calculated net charges and mass-to-charge ratios for the vitamin k-dependent proteins of interest. 211

Table 8.7. Average peak intensity of prothrombin control solutions and prothrombin solutions exposed to the alumina surface as a percentage of the maximum control peak intensity (bold). Average percentages and standard deviations were achieved from solutions of 0.035, 0.05, and 0.1 mg/ml. Standard deviations (SD) and coefficient of variations (CV) were shown for peak percentage values of control and exposed solutions. 219

Table 8.8. Gla residue density of vitamin K-dependent linker molecule. 221

Table 9.1. Parameters of the bare anodic multilayer slides that were exposed to radiolabelled or original prothrombin solutions. 246

Table 9.2. Parameters determined with fitting LF and GAB equations to the adsorption isotherm data. Adsorption data was collected using varying prothrombin concentrations exposed to the surface for 15 minutes 249

Table 9.3. Ellipsometry values with radiolabelled and original prothrombin solutions exposed to slide surfaces. It was assumed that alumina and prothrombin have the same refractive index for data generation. 249

Table 9.4. The thickness increase and change in mean standard error (MSE) from the base device with various radiolabelled prothrombin and original prothrombin solutions exposed. 250

Table 9.5. Results of statistical analyzes on the effect of radiolabelled vs the original prothrombin solution exposed to slides on the change in thickness measured. Statistically significant results are in italics. 251

Table 9.6. Results of statistical analyzes on the effect of varying the test on the surface density with 0.1 and 1 mg/ml prothrombin solutions exposed to the surface for 15 minutes. Statistically significant results are in italics. 252

Table 9.7. Post hoc test results on the effect of human serum albumin to prothrombin ratios in solutions exposed to the surface on the amount of radioactive prothrombin that binds. (n=3) 254

Table 9.8. Results of statistical analyzes on the effect of varying the exposed prothrombin solution on the radioactivity that remains bound after exposing wash solutions of human serum albumin and FBS. Statistically significant results are in italics..... 255

Table 9.9. The radioactivity remaining on surfaces coated with 0.1 mg/ml prothrombin solutions and subsequently exposed to varying wash solutions for 1 and 12 hours. 258

Table 9.10. Yxy colour coordinates of the bare surfaces for slides with a 95 nm alumina layer. Coordinates were collected from four points around the exterior of each protein spot. (n=3 for average of set, 10 spots per set)..... 260

Table 9.11. Yxy colour coordinates for slides with 95 nm alumina layers with immobilized protein layers created by placing ten prothrombin concentrations on the surface for 15 minutes. Coordinates were collected from five points within each protein spot for each set. (n=3 for average of sets)..... 261

Table 9.12. Results of the statistical analysis of the effect of exposed prothrombin concentration on the average chromaticity coordinates collected from surface images. The base alumina layer was 95 nm. Statistically significant results are in italics. (n=3 spots, 5 locations within each spot)..... 262

Table 9.13. Results of the statistical analysis on the effect of exposed prothrombin concentration on set 1 chromaticity coordinates collected from the surface images. The base alumina layer was 95 nm. Statistically significant results are in italics and differences that became significant when analyzing the set 1 coordinates are in bold. (n=5 locations within one spot)..... 264

Table 9.14. Yxy colour coordinates of the bare surfaces for sides with ~100 nm alumina layers. Coordinates were collected from four points around the exterior of each protein spot. (n=3 for average of set, 6 spots per set) 265

Table 9.15. Yxy colour coordinates for slides with 100 nm alumina layers with immobilized protein layers created by placing six prothrombin concentrations on the surface for 15 minutes. Coordinates were collected from five points within each protein spot for each set. (n=3 for average of sets).....266

Table 9.16. Results of the statistical analysis of the effect of exposed prothrombin concentration on the average chromaticity coordinates collected from images of the device surface. The base alumina layer was 100 nm. Statistically significant results are in italics. (n=3 spots, 5 locations within each spot).....267

Table 9.17. Results of the statistical analysis on the effect of exposed prothrombin concentration on set 1 chromaticity coordinates collected from surface images. The base alumina layer was 100 nm. Statistically significant results are in italics and differences that became significant when analyzing set 1 coordinates are in bold. (n=5 locations within one spot).....268

Table 10.1. Parameters of various slides observed and measured with ellipsometry after device preparation. 289

Table 10.2. Results of the statistical analysis on the effect of exposed anti-prothrombin molar concentrations on chromaticity coordinates collected from the surface images. The base alumina layer was 97 nm and was coated with a monolayer of prothrombin. Statistically significant results are in italics. (n=3) (A) Shows the limit of detection by eye and using colour coordinates and (B) shows the analytical sensitivity determined from analyzing the colour coordinates.....291

List of Figures

Figure 1.1. Flow diagram for the work completed in the thesis. 5

Figure 2.1. Changes in the optical path length of light passing through gasoline on wet pavement results in optical path differences and visible interference colours (A). [76] A cross-section of the gasoline layer is shown, with thickness labelled as t, to comprehend how changes to the physical path length influence the optical path difference (B). 12

Figure 2.2. Depicts the paths of incident light through the multilayer device that contribute to the formation of interference colours on the bare device surface. 15

Figure 2.3. Depicts the changes in refracted and reflected light as the protein and oxide interface. When light is refracted at the interface the system in unable to generate visible interference, as wavelengths do not travel the required minimum path length through the protein layer. 16

Figure 2.4. Reflectance off the porous alumina layer, adsorbed prothrombin layer, and adsorbed anti-prothrombin layer shows an increase in the optical path length. 16

Figure 2.5. Demonstrates the effects of constructive and destructive wavelength interference. 17

Figure 2.6. Structure of highly ordered porous anodic alumina showing important dimensions of the porous oxide as well as the barrier alumina film at the oxide and metal interface during formation. Image taken from work by Sulka. [107] 21

Figure 2.7. Lewis acid and base sites on the alumina surface.[117] 23

Figure 2.8. The alumina surface structure and charge that results with the formation in solutions with varying pH.[120] 24

Figure 2.9. Possible surface structures with carbonate adsorbed to the alumina surface include: (a) monodentate, (b) bidentate, and (c) bridging-bidentate. Oxygen atoms that correspond to the metal ions (M) are labelled with I and those from the carboxylic acid are labelled II.[166] 28

Figure 2.10. Shows carboxylic acid binding to hydroxyl groups on the alumina surface through an esterification reaction.[173] 29

Figure 2.11. The structure of (A) prothrombin depicting fragment 1, fragment 2, and thrombin[181] with dimensions from Lim et. al. [182] The Gla domain is shown in red, kringle-1 in orange, kringle-2 in yellow, and the protease domain in blue. Structures of (B) glutamic acid and the post translational gamma-carboxyglutamic acid residues show available carboxyl groups that lead to immobilization on the positively charged alumina surface. 30

Figure 2.12. A revised version of the Michel-Lévy interference colour chart showing path difference in nanometers along the horizontal axis and colour orders from first to fifth.[188] 31

Figure 2.13. CIE 1931 colour diagrams show MacAdam ellipses (left) and Sandström et al. work on colour diagram (right). Both charts demonstrate the ability of the human eye to distinguish different colours.[82,190].....32

Figure 2.14. CIE 1931 chromaticity diagrams with (A) coordinates x and y along axes and regions attributed to specific colours that can be perceived by the human eye from work by Gage. [212] The chromaticity diagram (B) shows the colours that can be defined using RGB coordinates or transformations of these coordinates from work by Ito et al. [213] Other colour gamuts were shown for an organic light emitting diode (OLED) and the National Television System Committee (NTSC) standard. 35

Figure 2.15. The colour shift from reddish to bluish white light that occurs with changing the CCT from 1500 K to infinity, mapped on a CIE plot. [192] 37

Figure 2.16. Depicts the orientation of s-polarized and p-polarized light wave planes with regards to the plane of incidence and surface under analysis.[77].....38

Figure 2.17. Reflectance at an interface comprised of materials with η_1=1 (upper layer of air) and η_2=1.5 (lower layer of glass) for light at one wavelength polarized in the plan of

incidence (horizontal or s-pol), normal to the plane of incidence (vertical or p-pol), or unpolarized. The left image was taken from Hecht. [78] 39

Figure 3.1. Magnetron sputter-up system (Bob) used for the deposition of tantalum onto silicon wafers at the nanoFAB. 41

Figure 3.2. Circles show the positions of four 100 mm diameter wafers on the sputter-up platen in the Bob system. 42

Figure 3.3. Magnetron sputter-down system (Floyd) used for the deposition of aluminum onto wafers previously coated with tantalum. 43

Figure 3.4. The six-platen shelf holder that is loaded into the Floyd load-lock with substrates prior to deposition. The image contains top (left) and side views (right)..... 44

Figure 3.5. NAIT magnetron sputter system used for the deposition of tantalum onto wafers. 45

Figure 3.6. Draft of the cleaving tool designed for fracturing wafers along lines parallel and perpendicular to the flat notch along the inner diameter of the tool to create devices of a consistent size. 46

Figure 3.7. The electrochemical cell used for anodization of individual slides. The beaker contains electrolyte, a stir bar, a thermometer, a calomel reference electrode, and the anode and cathode held parallel and 4 cm apart by the 3D printed holder. 47

Figure 3.8. Current density as a function of time with (A) critical stages labelled as a, b, and c and (B) current density trends with oxidation generating a porous oxide film and a barrier oxide film. 48

Figure 3.9. Schematic of the 1 cm diameter circles outlined on an anodized slide..... 50

Figure 4.1. Current density as a function of time during anodization in 0.4 M and 1.0 M solutions of (a) phosphoric (Phos), (b) sulfuric (Sul), and (c) oxalic (Ox) acid electrolytes at 8 V. 62

Figure 4.2. SEM images of alumina surfaces anodized in 0.4 M and 1.0 M solutions of phosphoric (Phos), sulfuric (Sul), and oxalic (Ox) acid electrolytes at 8 V. Scale bars show 100 nm at different magnifications. 63

Figure 4.3. SEM images 45° from the sample surfaces anodized in 0.4 M and 1.0 M solutions of phosphoric (Phos), sulfuric (Sul), and oxalic (Ox) acid electrolytes at 8 V. Scale bars show 100 nm at different magnifications. 64

Figure 4.4. Changes in feature sizes with anodization in different electrolyte compositions... 65

Figure 4.5. Variability in the (a) tantala and alumina thicknesses, (b) percent alumina at each surface, and (c) alumina layer refractive indices of samples anodized in 0.4 M and 1.0 M solutions of phosphoric (Phos), sulfuric (Sul), and oxalic (Ox) acid electrolytes at 8 V. 67

Figure 4.6. Anodic tantala on tantalum formed in each electrolyte composition at 8 V. Surfaces were viewed with horizontal and vertical polarization at (a) ~75º and (b) ~5º from normal..... 68

Figure 4.7. Spectrophotometric data from the surface of tantalum oxide films formed at 8 V in 0.4 and 1.0 M phosphoric (Phos), sulfuric (Sul), and oxalic (Ox) acid electrolytes. Reflections were captured at 45º from normal to the surface. (n=2)..... 69

Figure 4.8. Samples anodized in different electrolyte solutions at 8 V viewed through a polarizing filter for horizontal and vertical polarization at ~75° from normal. 70

Figure 4.9. Reflectivity data with horizontal, vertical, and no polarization for device surfaces prepared with anodization at 8 V in 0.4 and 1.0 M solutions of phosphoric (Phos), sulfuric (Sul), and oxalic (Ox) electrolytes. Reflections were captured at 45º from normal to the surface. 71

Figure 4.10. Theoretical R_s and R_p values are shown for alumina/tantala/tantalum and tantala/tantalum (labelled Ta only) devices. The refractive indices of the alumina and

tantala films created in phosphoric, sulfuric, and oxalic electrolytes were used in the equations. Fresnel equations were used and a viewing angle of 45°. 72

Figure 4.11. Current density as a function of time for samples anodized at 2, 5, 8, and 10 V. 73

Figure 4.12. SEM images of alumina surfaces anodized in 0.4 M phosphoric acid at 2, 5, 8, and 10 V. Scale bars show 100 nm at different magnifications. 73

Figure 4.13. SEM images 45° from the sample surfaces anodized in 0.4 M phosphoric acid at 2, 5, 8, and 10 V. Scale bars show 100 nm at different magnifications. 74

Figure 4.14. Variability in feature sizes with different applied potentials during anodization in 0.4 M phosphoric acid. (n=2) 75

Figure 4.15. The tantala thickness, percent alumina and refractive indices over the visible spectrum resulting from samples anodized in 0.4 M phosphoric at applied potentials of 2, 5, 8, and 10 V. 76

Figure 4.16. Device surfaces after anodization in 0.4 M phosphoric acid electrolyte at 2, 5, 8, and 10 V. 76

Figure 4.17. Average current density plots for aluminum thicknesses of 109.2, 114.0, and 117.5 nm collected from the anodization of intra (n=3) and inter (n=3) wafer sets. (n=9) 77

Figure 4.18. Individual current density plots for aluminum thicknesses of 109.2, 114.0, and 117.5 nm collected from the anodization of inter (left) and intra (right) wafer slides. (n=3) 77

Figure 4.19. Refractive indices resulting with different alumina thicknesses. The mean category letter above points indicates significant differences and correlates with Table 4.13. (n=3) 79

Figure 4.20. Colour shifts of slides with increasing alumina thicknesses from left to right. Spot rows from top to bottom show (i) prothrombin (II), (ii) II and anti-II, and (iii) anti-II. Slide labels 1_a to 6_a correspond with table information. 79

Figure 4.21. Refractive indices resulting at different alumina thicknesses. Means with a different letter above points indicate a significant difference. The mean category letter indicates significant differences and correlates with Table 4.16. (n=3)..... 81

Figure 4.22. Anodized slides comprised of different alumina thicknesses overlying the tantalum oxide and tantalum layers. Alumina increases from left to right: 76, 84, 93, 100, 109, and 117 nm. Slide labels 1_b to 6_b correspond with table information..... 82

Figure 5.1. Pore diameter distributions following oxidation at (A) 5 V and (B) 8 V respectively. Anodization procedures both were carried out in 0.4 M phosphoric acid. 107

Figure 5.2. The 5 V (black +) and 8 V (red circle) anodized sample data plotted on tertiary surface chemistry diagrams from (A) wafer 1 and (B) wafer 2. (n=3 for each diagram) 108

Figure 5.3. Typical ToF-SIMS depth profile of a typical unanodized control sample exposed to prothrombin for 15 minutes. Insert shows the first 120 seconds of the same scan magnified. 110

Figure 5.4. ToF-SIMS depth profile of a sample anodized at 5 V with no subsequent protein exposure. Insert shows the isolated and magnified CN^- ion curve..... 110

Figure 5.5. ToF-SIMS depth profile with regimes and important points labelled. Insert shows the first 120 seconds of the same scan magnified. The sample was anodized at 5 V and exposed to prothrombin for 15 minutes..... 111

Figure 5.6. ToF-SIMS depth profile of a sample anodized at 5 V and exposed to prothrombin for 15 minutes. The CN, H, OH, and CNO curves have been isolated to demonstrate their comparable trend. 112

Figure 5.7. ToF-SIMS depth profiles of a typical sample anodized at (A) 5 V with exposure to prothrombin for 15 minutes and a typical sample anodized at (B) 8 V and exposed to prothrombin for 15 minutes. Inserts show the first 120 seconds of their respective scans magnified. 113

Figure 6.1. Shows a typical anodization current density versus time plot with critical stages labelled (top) along with cross-sections of the devices at these stages (bottom). Formation consists of (1) as sputtered, (2) after anodization at 8 V in 0.4 M phosphoric acid until the end of pore formation - stage a, and (3) oxidation until the majority of tantala formed or a period of 900 seconds - stage b/stage c. 124

Figure 6.2. SEM images of porous alumina surfaces from four initial aluminum thicknesses. Anodization was conducted at 8 V in 0.4 M phosphoric acid until stage a, b, and c.... 128

Figure 6.3. Mean pore diameters at the alumina surface from four sputtered aluminum thicknesses. 128

Figure 6.4. Frequency of pore diameter resulting from devices with four initial aluminum thicknesses following anodization at 8 V in 0.4 M phosphoric acid. Plots are shown from top to bottom for anodization to stage a, b, and c respectively. 129

Figure 6.5. Optical constants in the xy plane for devices with different initial aluminum thicknesses anodized until stage b or c are shown at wavelengths of 370 and 700 nm. Extinction coefficients were zero. 130

Figure 6.6. Optical constants in the xy plane for devices with initial aluminum thicknesses from ~20 to 150 nm, anodized until stage b are shown at wavelengths of 370 and 700 nm. Letters shown above markers categorizes statistically significant mean values. Extinction coefficients were zero. 131

Figure 6.7. Alumina and tantala thicknesses following anodization at 8 V in 0.4 M stirred phosphoric acid until stage a, b, and c. Sputtered aluminum thicknesses were 78, 95, 115, and 149 nm. 132

Figure 6.8. A comparison of alumina thicknesses with oxidation to stage a and b of formation, measured with ellipsometry and SEM techniques. Separate tests were carried out for each of the four initial aluminum thicknesses. Letters shown above bars categorizes statistically significant means. 133

Figure 6.9. Alumina surface pore diameter etch rates (A) and tantala growth rates (B) at each stage of anodization. Rates are shown for all initial aluminum thicknesses and anodized at 8 V in 0.4 M phosphoric acid until stage a, b, and c. Rates were shown from the start of oxidation to stage a, from stage a to stage b, and from stage b to stage c. 135

Figure 6.10. Interference colours of films after protein exposure. Initial aluminum thicknesses are shown to the left of images and stages of oxidation as well as the protein solution exposed are shown at the bottom of the image. Solutions consist of prothrombin (P) and anti-prothrombin (AP). The images were taken at 75 degrees from normal. 136

Figure 7.1. The Ellingham diagram outlines the stability of various metal oxides with respect to temperature. Image from Sato et al. [7] with modifications to highlight the tantalum (purple) and aluminum (green) reaction lines. 145

Figure 7.2. The device structure following the standard anodization in 0.4 M phosphoric acid at 8 V, regardless of whether a native tantalum oxide layer was present at the interface of the tantalum and aluminum layers prior to anodization. 146

Figure 7.3. Depicts the thermal and intrinsic stresses contributing to the total stress in a sputtered coating. Image from Thornton and Hoffman. [9] 147

Figure 7.4. Thornton's structure zone diagram[10] outlines the influence of substrate temperature and argon pressure on the structure of sputtered coatings deposited in a cylindrical magnetron system. With the substrate temperature, T (K), and the melting point of the deposited material, Tm (K). 148

Figure 7.5. Device structure after sputtering tantalum and aluminum thin films on a silicon wafer in two separate sputter systems with exposure to atmosphere between or primary anodization of the tantalum before aluminum deposition. 150

Figure 7.6. SEM images at 0° (upper right) and 45° from the tantalum surfaces were captured of films deposited in the nanoFAB system (A) as sputtered and (B) anodized films, and tantalum surfaces deposited in the NAIT system (C) as sputtered and (D) anodized films. Anodized films were obtained by oxidation in 0.4 M phosphoric acid at 6 V under

potentiostatic conditions. All topographic and cross-sectional images have the same scales as those shown on (C) lower left images. 152

Figure 7.7. Roughness of the sputtered tantalum layers in as sputtered multilayer devices containing tantalum from nanoFAB (left) and NAIT (right) sputter systems with subsequent aluminum films deposited in the nanoFAB system. The scale bar is pertinent to both images. 153

Figure 7.8. Tantalum peaks present in the XRD scans of films sputtered in the nanoFAB (left) and NAIT (right) deposition systems. Crystallite orientations in nanoFAB and NAIT as sputtered films correspond with mixed alpha- beta (α-β) tantalum and α-Ta, respectively. 154

Figure 7.9. Tantalum thin films on silicon wafers sputtered in nanoFAB and NAIT sputter systems viewed at a high angle of incidence (top) and perpendicular to the surface (bottom). Slides from left to right contain: tantalum deposited in the nanoFAB system anodized at 6 V and 8 V, and tantalum deposited in the NAIT system anodized at 6 V and 8 V. Anodization was carried out in 0.4 M phosphoric acid. 155

Figure 7.10. Reflectivity off tantalum surfaces over the visible spectrum at 5° from the surface normal. Samples were tantalum as sputtered from nanoFAB and NAIT systems and anodized tantalum samples at 6 V under potentiostatic condition in 0.4 M phosphoric acid. The error is shown in black for each sample. (n=2)..... 155

Figure 7.11. Slides consisting of identical aluminum thicknesses on tantalum layers from nanoFAB and NAIT systems, anodized to stage b in 0.4 M phosphoric acid at 8 V. Images show the surfaces captured at 75° from normal. From left to right: nanoFAB and NAIT tantalum with 99 nm aluminum followed by nanoFAB and NAIT tantalum with 104 nm of aluminum..... 158

Figure 7.12. Shows the visible surface colours resulting with exposing 28 picomoles of prothrombin (20 µl at 0.1 mg/ml) and subsequently 2, 3.3 and 6.7 picomoles of anti-prothrombin (20 µl at 0.015, 0.025, and 0.050 mg/ml) to the control slide surfaces

formed on nanoFAB and NAIT tantalum. Images were taken using the custom optics system. (n=1)..... 159

Figure 7.13. Colour plots showing the colours resulting with 0.1 mg/ml prothrombin (outlined shape) and subsequently 0.015, 0.025, and 0.050 mg/ml anti-prothrombin (from top right to bottom left). Plots compare colours on control slides with NAIT tantalum and nanoFAB tantalum layers. 161

Figure 7.14. Current density plots show anodization curves from initial aluminum thicknesses of 99±11.2 nm (A) and 104±9.2 nm (B) that represent the trends shown in each set of triplicates. Curves were generated for the standard anodization process. Test samples had the primary anodization of tantalum at 6 V prior to aluminum deposition, followed by the standard anodization process. Control samples had one standard anodization process. Current density curves for test (primary and standard anodization) and control (standard anodization) samples were generated from oxidation of devices with identical aluminum thicknesses at voltages of 4, 6, and 8 V in 0.4 M phosphoric acid electrolyte. 162

Figure 7.15. Topographic and cross-sectional images of a slide formed with the standard anodization process (left) and a slide formed with primary and standard anodization processes (right). The standard anodization was carried out at 8 V and the initial aluminum thicknesses for both slides were 99 nm. All scale bars show 100 nm. 163

Figure 7.16. SIMS scans of control (left) and test (right) samples formed with the standard anodization processes completed at 8 V. 164

Figure 7.17. Images show slides in order of (left to right): 4 V test, 4 V control, 6 V test, 6 V control, 8 V test, and 8 V control. The test samples were prepared by primary anodization of the tantalum layer at 6 V and subsequently, aluminum deposition and the standard anodization process at 4, 6, or 8 V. The anodization of control samples, containing aluminum and tantalum, were carried out at 4, 6, or 8 V. 165

Figure 7.18. Shows the visible surface colours resulting with exposing 28 picomoles of prothrombin (20 µl at 0.1 mg/ml) and subsequently 2, 3.3 and 6.7 picomoles of anti-

prothrombin (20 µl at 0.015, 0.025, and 0.050 mg/ml) to the control and test slide surfaces formed on nanoFAB tantalum. Images were taken using the custom optics system. (n=1)..... 166

Figure 7.19. Colour plots showing the colours resulting with 0.1 mg/ml prothrombin (outlined shape) and subsequently 0.015, 0.025, and 0.050 mg/ml anti-prothrombin (from right to left). Plots compare colours on control and test slides with nanoFAB tantalum layers. 168

Figure 7.20. Current density curves for samples that lead to areas of delamination following the standard anodization process. The legend provides sample information on which anodization processes were carried out with the applied voltages..... 169

Figure 7.21. Images of slides showing delamination captured at incident angles of (A) 0° and (B) 75°. Samples were prepared with primary (Pri.) anodization at 6V followed by standard (Std.) anodization at 6 or 8 V, or standard (Std.) anodization at 8 V. Anodization processes used are labelled above the corresponding slides. These films correspond with current density plots shown in the figure above..... 169

Figure 7.22. Wafers viewed in a bright box to examine tantalum coatings deposited in the NAIT sputter system..... 170

Figure 7.23. A sample with delamination after primary anodization at 6 V, aluminum deposition, and standard anodization at 6 V. The image shows porous alumina on the left of both images and removal of this layer on the right..... 171

Figure 7.24. EDS map scan and sites used for point analysis on the alumina (left side) and a region where delamination occurred (left side). Individual elements were mapped for tantalum (Ta), aluminum (Al), and oxygen (O), which are shown alongside the SEM map scan..... 172

Figure 7.25. A sample with delamination shows a larger field of view and allows for the observation of failure lines. The device had tantalum and aluminum thin films with exposure to atmosphere between sputtering and the standard oxidation process was

complete at 8 V in 0.4 M phosphoric acid electrolyte. Bright regions are alumina and darker regions are tantalum. 173

Figure 7.26. Delamination that resulted during the standard oxidation process, completed at 8 V in 0.4 M phosphoric acid electrolyte. “Worm-tracks” are visible where delamination and rolling of the porous alumina layer results. Bright regions are alumina and darker regions are tantalum. 174

Figure 7.27. Delamination of the alumina layer shown at 45° from normal to the surface. The sample contains tantalum and aluminum thin films, exposed to atmosphere between film depositions, and the standard oxidation process was complete at 8 V in 0.4 M phosphoric acid electrolyte. Bottom images at a higher field of view show from left to right: complete alumina delamination, the transition point where there is both no alumina and alumina, and the alumina layer. 174

Figure 7.28. SEM images of the top area of an anodized sample showing delamination. Images in the left column start at (A) the electrolyte line and (B and C) move down towards an area with less delamination. The right column shows select areas at an increased field-of-view. 175

Figure 7.29. SEM with EDS map scans of the top portion of an anodized sample showing delamination. Images from top to bottom show the non-uniform region at the electrolyte line and move towards the area where porous alumina remains. 176

Figure 8.1. Depicts the structural domains of vitamin K-dependent proteins prothrombin (PT), factor IX (FIX), factor X (FX), factor VII (FVII), protein C (PC), protein S (PS), matrix Gla protein (MGP), and bone Gla protein (BGP). The legend identifies protein components. Proteolytic cleavage sites are shown with thin arrows when cleaving occurs to create the mature protein structure, and cleavage sites are indicated by thick arrows when linked to enzymatic activation. Images from Furie and Furie (1988).[2] ... 192

Figure 8.2. An image from the literature[5] depicts prothrombin activation with cleavage at Arg320 (R320 in FASTA sequence) and Arg271 (R271) which leads to fragment 12 (F12) and thrombin (IIa). F12 contains the Gla and both kringle domains (Gla-K1-K2).

Further cleavage at Arg155 (R155) separates F12 into fragment 1 (F1) and fragment 2 (F2). It is possible to remove the Gla domain with cleaving at Tyr43 (Y43). Other components of prothrombin can be found in the literature.[6,7] 193

Figure 8.3. Images from Ohkubo and Tajkhorshid (2008) provide a detailed outline of the Gla domain of vitamin K-dependent proteins. [46] (A) Shows the typical structure of vitamin K-dependent proteins. (B) The Gla domain structure of FVIIa with the backbone of the structure shown as tubing and the Ca^{2+} ions as numbered spheres. (C) The first 46 amino groups of the Gla domain sequence have γ-carboxyglutamic acid groups depicted as gamma (γ) and the bound Ca^{2+} are positioned under the residue(s) that bind them to the Gla domain. 196

Figure 8.4. The 3D structure of prothrombin generated using I-TASSER. The 10 Gla residues (red) are located at sites 49, 50, 57, 59, 62, 63, 68, 69, 72, 75 on the protein (excluding signal peptide and propeptide sites: 6, 7, 14, 16, 19, 20, 25, 26, 29, and 32). 204

Figure 8.5. A 3D structure of prothrombin (left) and surface charge map (right) in same orientation. The 10 Gla residues form an 8.3 nm^3 carboxyglutamic domain at the base of the structure where binding to the alumina substrate occurs. 204

Figure 8.6. The 3D structure of human coagulation factor IX generated using I-TASSER. The 12 Gla residues (red) are located at sites 53, 54, 61, 63, 66, 67, 72, 73, 76, 79, 82, and 86 on the protein (excluding signal peptide and propeptide sites: 7, 8, 15, 17, 20, 21, 26, 27, 30, 33, 36, and 40). Additional metal binding sites (purple) are 47, 48, 93, 94, 96, 110, 111, 281, 283, 286, 288, and 291 (excluding signal peptide and propeptide sites: 1, 2, 47, 48, 50, 64, 65, 235, 237, 240, 242, and 245). 205

Figure 8.7. The 3D structure of human coagulation factor IX (left) and surface charge map (right) in same orientation. The 12 Gla residues form an 17 nm^3 carboxyglutamic domain at the base of the structure where binding to the alumina substrate occurs. 205

Figure 8.8. The 3D structure of protein S generated using I-TASSER. The 11 Gla residues are located at sites 47, 48, 55, 57, 60, 61, 66, 67, 70, 73, and 77 (excluding signal peptide and propeptide sites: 6, 7, 14, 16, 19, 20, 25, 26, 29, 32, and 36). [30] 206

Figure 8.9. A 3D structure of protein S (left) and surface charge map (right) in the same orientation. The 11 Gla residues form a 12.3 nm^3 carboxyglutamic domain at the base of the structure where binding to the alumina substrate occurs. 206

Figure 8.10. The alumina surface after prothrombin exposure. Spots on (A) show concentrations from left to right of 0.001, 0.01, 0.1, and 1 mg/ml and (B) shows concentrations from left to right of 0.03, 0.06, 0.08, and 0.1 mg/ml. 207

Figure 8.11. The dimensions of polypropylene micro-centrifuge tubes used for mixing and storing proteins. 207

Figure 8.12. Prothrombin, factor IX, and protein S solutions exposed and adsorbed to the device surface are shown from top to bottom. Spots on each slide show molar concentrations from left to right of 0.1, 0.2, 0.3, 0.5, 0.7, 1.1, and 1.4 μM..... 209

Figure 8.13. Colour shifts resulting when 2 picomoles of prothrombin, factor IX, and protein S solutions are in contact with the surface for periods of 45, 50, and 55 minutes. 212

Figure 8.14. Alumina surface with exposure to (left to right) Ca and EDTA, prothrombin with Ca, prothrombin with Ca and EDTA, prothrombin control, and prothrombin with EDTA. All solutions of prothrombin were at concentrations of 0.1 mg/ml with constituents of 1 mM Ca and 1 mM EDTA. 212

Figure 8.15. Colour shifts (left to right) from solutions of: prothrombin and 1 mM Mg, prothrombin and 5 mM Mg, prothrombin control, prothrombin and 1 mM Ca, prothrombin and 2.5 mM Ca, prothrombin and 10 mM Ca. All solutions contain a final prothrombin concentration of 0.1 mg/ml. 213

Figure 8.16. Colour shifts (left to right) from solutions of: prothrombin and 5/2.5 mM Mg/Ca, prothrombin and 5/10 mM Mg/Ca, prothrombin control, prothrombin and 1/1 mM Mg/Ca, prothrombin and 1/2.5 mM Mg/Ca, prothrombin and 1/10 mM Mg/Ca. All solutions contain a final prothrombin concentration of 0.1 mg/ml. 213

Figure 8.17. Colour coordinates shown on each plot show the average surface coordinates (solid black) and the prothrombin control solution (black outline). Plots from left to

right show prothrombin with Ca ions (blue), prothrombin with Mg ions (green), and Ca/Mg ions (purple). The marker outlines provide information on the ion concentration in the protein solutions with white indicating the lowest, grey the middle value (if one exists), and black the largest. Solutions containing both Ca and Mg ions show coordinate averages of the lowest and highest Mg ions with all Ca concentrations. 214

Figure 8.18. Anti-prothrombin visual detection sensitivity with exposed cumulative concentrations from left to right of no anti-prothrombin solution, 2, 3, 7, and 13 picomoles (20 μl of 0.015, 0.025, 0.05, and 0.1 mg/ml). Solutions were exposed to surfaces initially coated with 28 picomoles prothrombin solutions containing various amounts of Ca or Mg ions for 30 minutes. 215

Figure 8.19. Anti-prothrombin visual detection sensitivity with exposed cumulative concentrations from left to right of no anti-prothrombin solution, 2, 3, 7, and 13 picomoles (20 μl of 0.015, 0.025, 0.05, and 0.1 mg/ml). Solutions were exposed to device surfaces coated with 28 picomoles of prothrombin solutions with 1 mM Ca and 1mM Mg ions for 30 minutes.....216

Figure 8.20. The alumina surface exposed to (left to right) Mg/Ca ions in solution, prothrombin with Mg/Ca ions, prothrombin control, and prothrombin followed by Mg/Ca ion solution. All prothrombin solutions were at 0.1 mg/ml, Mg ion solutions were at 1 mM, and Ca ion solutions were at 2.5 mM. 217

Figure 8.21. An overlay of the low mass regions (counts vs mass-to-charge) obtained from LCMS where the polymer is detectable. The prothrombin initial solution (orange) and the solution after exposure to the alumina surface for 15 minutes before examination (black) are shown to outline differences between the two.....217

Figure 8.22. Deconvoluted plots show the 3 sets of peaks in a prothrombin control solution (top) and the solution after exposure to the alumina surface (bottom) with an initial concentration of 0.1 mg/ml. Set 1 was in the 72100 amu range, set 2 was in the 72400 amu range, and set 3 was in the 73100 amu range. 218

Figure 8.23. Deconvoluted plots show peaks from set 2 for the initial prothrombin solution (red) and the prothrombin solution exposed to the porous alumina surface for 15 minutes (black). The initial prothrombin concentrations were (A) 0.1, (B) 0.05, and (C) 0.035 mg/ml for plots shown. The main peaks are labelled 1 to 6. 219

Figure 9.1. SEM in-lens image (left) and EBSD image (right) of the bare anodic alumina surface. 242

Figure 9.2. SEM in-lens image (left) and EBSD image (right) of the anodic alumina surface exposed to a prothrombin solution at 1 mg/ml for 15 minutes. 243

Figure 9.3. SEM in-lens image (left) and EBSD image (right) of the anodic alumina exposed to a prothrombin solution at 1 mg/ml for 15 minutes and following an anti-prothrombin solution with gold conjugated antibodies at ~0.6 mg/ml for 1.5 hours. A greater magnification was used for images shown in the bottom row to locate the gold nanoparticles. Gold nanoparticles are outlined with circles and bright specks are outlined with squares. 244

Figure 9.4. SEM in-lens image (left) and EBSD image (right) of the anodic alumina exposed to a gold conjugated anti-prothrombin solution at ~0.6 mg/ml for 1.5 hours. Gold nanoparticles are outlined with circles and bright specs are outlined with squares. 245

Figure 9.5. Prepared bare anodic slides used for radiolabel tests. 245

Figure 9.6. LCMS scan of prothrombin modified with a chelator, NOTA, bound to the protein for radiolabelling. 246

Figure 9.7. The resulting bands from an SDS-PAGE of the labelled prothrombin solution. . 247

Figure 9.8. Prothrombin surface density with exposed solutions of 2, 4, 9, 11, and 12% modified prothrombin in a ~0.1 mg/ml prothrombin solution. Plot (A) shows the slope and intercept with standard deviations and plot (B) shows 2σ standard error lines from the mean. 248

Figure 9.9. The adsorption isotherm for modified prothrombin on the alumina surface for 15 minutes shown as a standard (A) and log (B) plot. 248

Figure 9.10. The effect of varying prothrombin incubation time on the resulting surface density. Total prothrombin concentrations of 0.1 and 1 mg/ml were used. 252

Figure 9.11. Prothrombin surface density that results with ~0.01 mg/ml labelled prothrombin in solution with human serum albumin (HSA) or prothrombin added to achieve the total protein concentration. 253

Figure 9.12. The effect of human serum albumin and FBS wash solutions for 1 hours on prothrombin activity. Prothrombin was immobilized from 0.02 and 0.1 mg/ml solutions for 30 minutes..... 255

Figure 9.13. The effect of prothrombin wash solution at 5 mg/ml for 1 hour on prothrombin activity. Prothrombin was immobilized from 0.1 and 1 mg/ml solutions for 30 minutes. 256

Figure 9.14. The effect of prothrombin wash solution at 5 mg/ml and HS wash solution at physiological concentrations for 1 hour and 12 hours on prothrombin activity. Prothrombin was immobilized from a 0.1 mg/ml solution for 30 minutes..... 256

Figure 9.15. The resulting band from an SDS-PAGE of the HS wash solution after exposure to the prothrombin-coated surface shows a complex mixture of protein and fragments. . 257

Figure 9.16. Prothrombin radioactivity change with different wash solutions after forming a monolayer of prothrombin on the surface. Wash solutions were human serum albumin at 5 mg/ml, prothrombin at 5 mg/ml, FBS, and HS for 1 hour..... 258

Figure 9.17. Images of surfaces exposed to labelled (bottom) and original prothrombin solutions (top). The exposed prothrombin concentrations are shown under the corresponding images and the resulting surface densities above..... 259

Figure 9.18. Images captured of the slide surfaces after original prothrombin solutions were exposed to the surface. The exposed prothrombin concentrations are shown under the corresponding image and the resulting surface densities above. 260

Figure 9.19. Average chromaticity coordinates and standard deviations are shown on the CIE chart for 95 nm alumina layers exposed to various prothrombin concentrations. With increasing exposed concentration and colour order the trajectory moves from the tan/orange region toward the purple region. Increasing concentrations of 0.003, 0.005, 0.01, 0.015, 0.025, 0.035, 0.05, 0.1, 0.5, and 1.0 mg/ml are mapped however the lowest six concentrations are difficult to separate on the plot (upper right markers). The white marker shows the average bare surface coordinates.....263

Figure 9.20. Images of the surfaces after prothrombin solutions were exposed to the surface. Exposed prothrombin concentrations are shown under the corresponding images. 265

Figure 9.21. Average chromaticity coordinates and standard deviations are shown on the CIE chart for 100 nm alumina layers exposed to various prothrombin concentrations. With increasing exposed concentration and colour order the trajectory moves from the tan/orange region toward the purple region. Increasing concentrations of 0.015, 0.025, 0.035, 0.050, 0.08, and 0.1 mg/ml are mapped however the two highest concentration markers are difficult to separate on the plot. The white marker shows the average bare surface coordinates. 267

Figure 9.22. Electron penetration distance into Al, Cu, and Au samples calculated using the Bethe expression computed by Rao-Sahib and Wittry (1972) and modified expressions extended by Joy and Luo (1989). [38].....269

Figure 10.1. Anti-prothrombin solutions of different molar concentrations were exposed to spots previously coated with prothrombin (II) solutions (20 μl at 1.4 μM). Solutions were exposed to the surface for 15 minutes. Slides (A) and (B) are from the same wafer and prothrombin control spots are shown on each. 289

Figure 10.2. Average chromaticity coordinates and standard deviations are shown on the CIE chart for 97 nm alumina layers coated with a monolayer of prothrombin and

subsequently exposed to various anti-prothrombin solutions. Increasing molar concentrations between 0.02 and 1.33 μM are mapped from right to left on the plot (black markers). The white marker shows the average prothrombin-coated surface coordinates from all slides. 290

Figure 10.3. Visible interference colours resulting on prothrombin-coated slides 20 μl at 1.4 μM with alumina thicknesses from top to bottom of 102, 108, and 124 nm with subsequent anti-prothrombin solution incubation on the surface at concentrations (from left to right) of II control only, 0.03, 0.05, 0.08, and 0.067 μM..... 293

Figure 10.4. Visible surface colours on slides with 102, 108, and 124 nm alumina film thicknesses exposed to prothrombin (II) solutions (20 μl at 1.4 μM) and varying anti-prothrombin molar concentrations (20 μl volumes for μM solutions labelled above). Protein solutions were exposed for 15 minutes in all cases. 293

Figure A3.1. Low resolution spectra of an unanodized aluminum surface. 385

Figure A3.2. Unanodized aluminum surface exposed to prothrombin. 385

Figure A3.3. Unanodized aluminum surface exposed to prothrombin and anti-prothrombin solutions. 386

Figure A3.4. As prepared surface created with an applied anodic potential of 5 V. 386

Figure A3.5. Surface exposed to prothrombin solution created with an applied anodic potential of 5 V. 387

Figure A3.6. Surface exposed to prothrombin and anti-prothrombin solutions created with an applied anodic potential of 5 V. 387

Figure A3.7. As prepared surface created with an applied anodic potential of 8 V. 388

Figure A3.8. Surface exposed to prothrombin solution created with an applied anodic potential of 8 V. 388

Figure A3.9. Surfaces exposed to prothrombin and anti-prothrombin solutions created with an applied anodic potential of 8 V. 389

List of Symbols and Abbreviations

Abbreviation	Definition
2D	two dimensional
3D	three dimensional
A	absorbance
A_p	area of each pore
ANOVA	analysis of variance
BCA	bicinchonic acid protein assay
BET	Brunauer-Emmett-Teller
BSA	bovine serum albumin
c	velocity of light in a vacuum
C_p	cross-sectional area of pores
CCD	charge-coupled device
CCT	correlated colour temperature
CFU	colony forming units
CIE	International Commission on Illumination or Commission Internationale de I'Eclairage
Da	Dalton
DC	direct current
EBSD	electron backscattered detector
EDTA	ethylenediaminetetraacetic acid
EDX	energy dispersive X-ray
EIA	enzyme immunoassay
ELISA	enzyme-linked immunosorbent assay
EMA	effective medium approximation
ESCA	electron spectroscopy for chemical analysis
f	frequency
f	femto (10^{-15})
FBS	fetal bovine serum

FESEM	field emission scanning electron microscopy
GAB	Guggenheim-Anderson-de Boer
HEPES	4-(2-hydroxyethyl)-1-piperazineethanesulfonic acid
HPLC	high-performance liquid chromatography
HS	human serum
HSA	human serum albumin
HSL	hue, saturations, and lightness values
I	intensity
IgG	Immunoglobulin G
ICPMS	Inductively coupled plasma mass spectrometry
II	Prothrombin or Factor II
IR	infrared
IPA	isopropyl alcohol
K	extinction coefficient or imaginary refractive index
LED	light-emitting diode
LF	Langmuir-Freundlich
LFA	lateral flow assay
LoC	lab-on-a-chip
LCMS	liquid chromatography mass spectrometry
m	milli (10^{-3})
MEMS	micro-electro-mechanical systems
n	nano (10^{-9})
N_l	number of pores along length of device
N_p	number of pores on device surface
N_w	number of pores along width of device
NaCl	sodium chloride
$NaHCO_3$	sodium bicarbonate
NaOAc	sodium acetate
NAIT	Northern Alberta Institute of Technology
nanoFAB	nano fabrication and characterization facility
NEMS	nano-electro-mechanical systems

OPD	optical path difference
OPL	optical path length
p	pico (10^{-12})
p-	light with electric field oscillating vertical (parallel) to the plane of incidence
p-SCN-Bn-NOTA	2-*S*-(4-isothiocyanatobenzyl)-1,4,7-triazacyclononane-1,4,7-t riacetic acid
PoC	point-of-care
PC	personal computer
PBS	phosphate-buffered saline
PCR	polymerase chain reaction
PDGFR-α	platelet-derived growth factor receptor alpha
PEG	polyethylene glycol
PFU	plaque forming units
PVD	physical vapour deposition
R or r	reflectivity
RGB	red-green-blue
rpm	revolutions per minute
RIU	refractive index units
s-	light with electric field oscillating horizontal (perpendicular) to the plane of incidence
SD	standard deviation
SDS	sodium dodecyl sulphate
SDS-PAGE	sodium dodecyl sulphate-polyacrylamide gel electrophoresis
SEM	scanning electron microscope
SIMS	secondary ion mass spectroscopy
SOP	standard operating procedure
SP	surface plasmon
SPR	surface plasmon resonance

T or t	transmittance
TBS	tris-buffered saline
TFA	trifluoroacetic acid
TLC	thin layer chromatography
ToF	time-of-flight
UV	ultraviolet
VIS	visible
XPS	X-ray photoelectron spectroscopy
XRD	X-ray diffraction
XRF	X-ray fluorescence spectroscopy
w/w	weight per weight
w/v	weight per volume
v/v	volume per volume
α	alpha
β	beta
μ	micro (10^{-6})
η	real refractive index
$\bar{\eta}$	complex refractive index
λ	wavelength
ϕ	angle of incidence
Ψ	psi
Δ	delta
γ	gamma
ν	velocity
θ_i	angle of incidence
θ_r	angle of reflectance

Chapter 1 – Purpose and Scope

1.1 Motivation

Laboratory testing in healthcare systems is a massive enterprise and the backbone of patient care. Biomarker assessments for disease processes, whether to diagnose a new disease or follow a chronic condition, include everything from heart disease to malignancy. These assessments are typically performed in specialized settings where a laboratory process is required to analyze and quantify the protein biomarker linked to a particular disease state. Initial steps consist of collecting the tissue (e.g. solid organ or blood), saliva, urine, fecal, or exudate sample and transportation to a designated lab facility for processing. Upon sample arrival, standard diagnostic tests are used to detect and possibly quantify specific proteins. These tests include; enzyme immunoassay (EIA), high-performance liquid chromatography (HPLC), and polymerase chain reaction (PCR). It is not until after testing that results are obtained, and a diagnosis reached. Ultimately this delays prognosis and treatment while simultaneously creating significant expenses for test conduction along with sample transportation and handling.

To date, a small fraction of the tests used provide rapid results. When testing for infectious disease, front line healthcare worker must send samples to centralized facilities with expensive equipment and trained personnel to determine if patients are a risk to themselves or others. A point-of-care (PoC) test is a realistic alternative to lab testing and would provide immediate information to determine precautionary measures, diagnosis, and/or patient treatment. Such a test must be economical and prompt with the required specificity and sensitivity to generate data for protein detection. A device of this sort has the ability to revolutionize the medical field, as these are breakthrough characteristics not yet possible in any single diagnostic device.

One approach for a PoC test is the utilization of thin film interference for the visible detection of biologics. It would ensure nearly instantaneous results and, in some applications, would work to shift detection into the hands of the user (e.g. patient or surgeon). While there are many obvious applications for infectious diseases, there are some fundamental applications within other fields as well. One application could be to direct therapy during surgery when the decision to complete a more aggressive surgical procedure could be guided

by the presence of biomarkers. In some cases, the most invasive surgery is completed, followed by a pathological analysis that decides further therapy. One example of this is the detection of platelet-derived growth factor receptor alpha (PDGFR-α), a biomarker linked to metastatic papillary thyroid cancer. [1,2] In this situation, a positive or negative result is required to diagnose the presence or development of metastatic cancer. During surgery a homogenized tissue sample would be placed on the device containing an immobilized antibody layer specific to PDGFR-α, to detect if the biomarker is present in 15 minutes while the patient is still on the operating table. The sue of a highly sensitive test means a negative result would have a high likelihood of ruling out disease. [3-5] A negative test result indicates a less invasive procedure can be completed. [1] As it currently stands patients and surgeons have to apply their best estimates of when to do a more aggressive surgery, which increases the risk substantially. As a result, nearly 2/3 of all node dissections for thyroid cancer surgery were likely unnecessary and many patients were at risk of a permanently hoarse voice or calcium supplementation without any benefit. [6]

This example in the surgical setting is just one facet of a test that can be applied to many acute or chronic diseases where monitoring is ongoing such as; heart disease, [1,2] cancer, [3,4] and infectious diseases.[5-8] A positive or negative result may be the desired outcome, however there is a foreseeable benefit in the quantification of these results. The thin film diagnostic will be examined in conjunction with the thin film optics to work towards a complete system that allows for accurate observation of the visible interference contrast on the device surface.

1.2 Aims & Objectives

The purpose of this thesis is to further develop a stand-alone, functional point-of-care medical diagnostic based on thin film interference. The device must be economical, rapid, and with required specificity and sensitivity to generate visible interference colours for protein detection. The focus will be placed on quantitative measures of proteins on thin film diagnostic devices with a view to establish the broad applications that are possible for protein biomarkers from many different disease sites. The primary goals of this work include:

1. Manufacturing a reproducible thin film slide with optimized characteristics allowing protein complexes to adsorb to the surface and produce interference colours in the first and second order range;

2. Determine the surface-prothrombin (II) interactions to determine binding orientation, surface density, and depth of protein penetration into the porous alumina surface during adsorption onto the surface;
3. Establish if immobilized protein on the device surface can be quantified based on the visible interference colour.

This thesis builds upon the work patented by Burrell et al., [9] on a thin film platform that consists of a porous aluminum oxide (alumina), tantalum oxide (tantala), and tantalum on a substrate. The tunable multilayer structure shows visible interference colours that change with protein immobilization on the surface for detection. Additional colour contrast results upon exposure to successive antibody layers with an optimal substrate microstructure. The aim is to improve understanding in the area of thin film visible interference detection and further develop the point-of-care diagnostic. This device has the potential to shift the entire paradigm of testing. Implementing a simple, inexpensive, and robust point-of-care platform into the health care system or rural settings would be revolutionary, providing users the power to diagnose illness and guide early interventions.

1.3 Scope of Thesis

This study commences with an introduction and detailed literature review (Chapter 2) examining current diagnostics, concepts of thin film technology, thin film deposition, electrochemical oxidation, protein binding, optics and its use for visual protein detection. The subsequent chapter (Chapter 3) provides general materials and methods for aspects of this work, and the following chapter (Chapter 4) discusses the effects of altering anodization parameters and sputtered aluminum thickness on the resulting device. Chapter 5 analyzes differences in the surface structure of samples anodized at 5 and 8 V before and after protein immobilization, as well as protein penetration into the pores. Next, the device is characterized and the tunability optimized (Chapter 6). Chapter 7 describes the impact of layers at the tantalum and aluminum interface, followed by the sensitivity of vitamin K-dependent proteins immobilized on the device surface and the effect of metal ions in prothrombin solutions prior to device exposure (Chapter 8). Chapter 9 addresses how changing the amount of prothrombin exposed to the device surface effects the resulting surface density and colour shifts measured

with radiolabelling. The removal of prothrombin with subsequent wash solutions placed on the surface was quantified using the radiolabel. Lastly, Chapter 10 shows the colour shifts on a prothrombin-coated surface with subsequent anti-prothrombin solutions exposed and complex formation. A study flow guide for the thesis is shown in Figure 1.1.

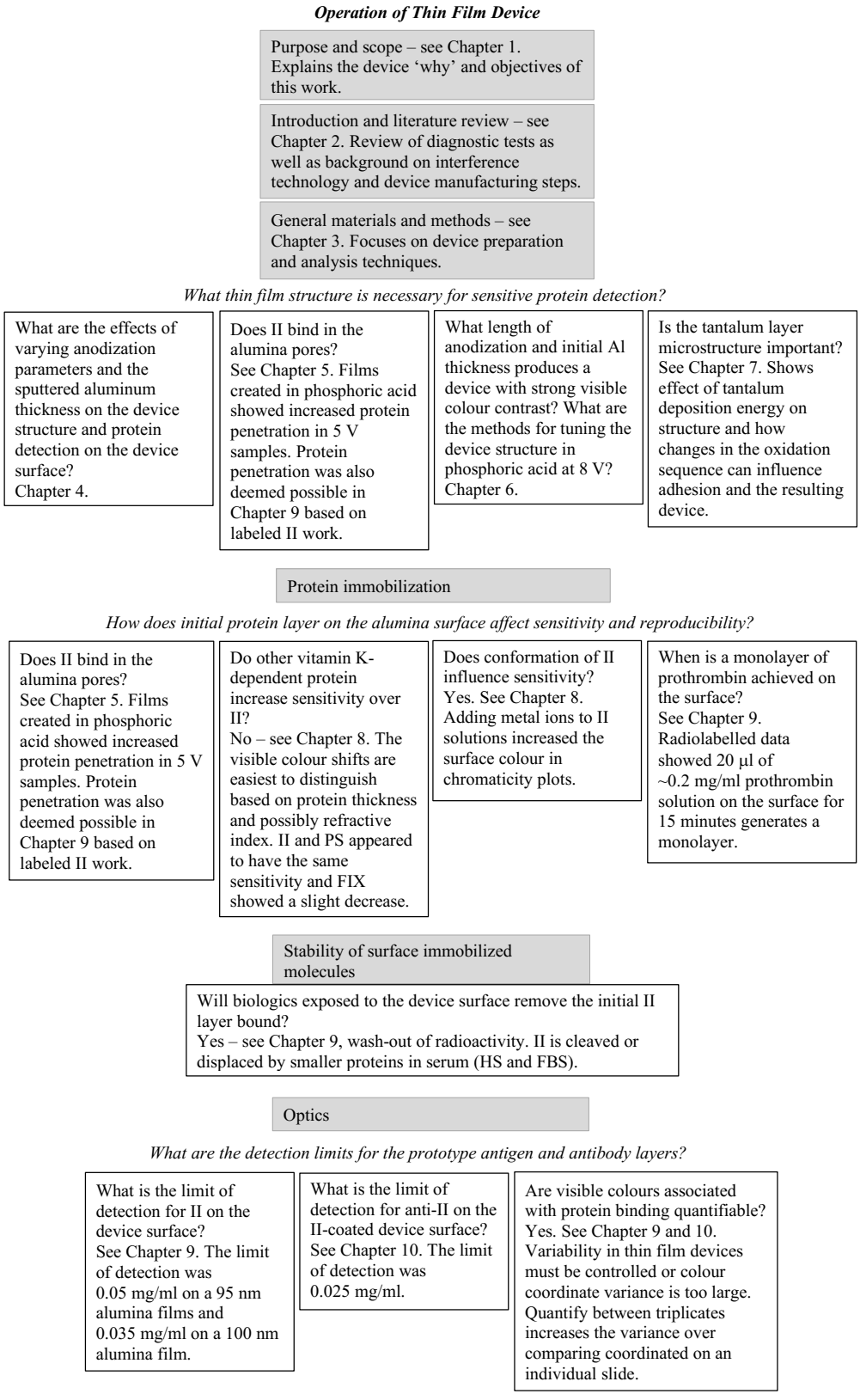

Figure 1.1. Flow diagram for the work completed in the thesis.

Chapter 2 – Introduction and Literature Review

2.1 Introduction – Review of Diagnostic Tests

The majority of commercial protein detection tests occur in a centralized lab setting with costly detection systems and an overlying infrastructure required to transport specimens. Consequently, current methodologies are expensive, unable to achieve prompt detection, and limit the location of completion. EIAs, HPLC, and PCR are technologies for standard diagnostic tests run in health care facilities. [1] Widely used EIAs are ELISAs. ELISAs were developed in 1971[2] and have since been one of the main techniques used for detecting and quantifying antibodies and antigens, as tests are relatively easy to use and commercially available. [3] The four main ELISA setups are indirect, direct, sandwich, and competitive. [4,5] These methods have different analytes, but each format has similarities. In all cases detection occurs through binding an enzyme-linked antibody and incubating with a substrate to commence a measurable reaction. Various detection mechanisms exist (i.e. chemiluminescence, enhanced chemiluminescent, fluorescence, etc.) and influence the constituents used. For example, colorimetric detection occurs after binding a biotinylated antibody conjugated to streptavidin-horseradish peroxidase and adding the hydrogen peroxide substrate containing tetramethyl benzene. [4-6] These assays are lengthy with blocking, washing, and incubation steps and have shown low amounts of active antibodies after immobilization (2 to 8%).[7,8] Furthermore, ELISA, HPLC, and PCR testing methods all require expensive equipment and trained personnel for completion and data interpretation

Although the majority of current testing is conducted in a hospital or laboratory setting, there has been extensive research towards the development of a point-of-care device that is inexpensive, sensitive, specific, portable, quick, and easy to use. [9,10] A device of this sort would shift testing into the hands of the patient and meet the needs of people in undeveloped countries or regions, who have limited access to healthcare facilities and labs. [10] The commercialization of point-of-care tests has shown promise in the field; however, further development is needed. Of the companies investigated by Holland and Kiechle in 2005[11] there are 4 that remain; Cepheid, [12] IQ^{uum} – acquired by Roche in 2014, [13] Nanosphere – acquired by Luminex Corp in 2016, [14] and Lumora – acquired by ERBA in 2015. [15] Cepheid and Roche tests operate using PCR technology in real-time, Luminex Corp uses gold nanoparticles

xMAP® bead technology to deliver multiplex assays for proteins and nucleic acids, [16,17] and Lumora uses bioluminescence for nucleic acid amplification and detection. [11] In a study by Chin et al. additional companies detecting small molecules, proteins, cells, and nucleic acids were evaluated.[18]

Commercial devices that show the closest resemblance to the ideal point-of-care test are lateral flow assays (LFAs). The first identified LFA was introduced in 1987[19] and this technique currently remains one of the most common point-of-care tests, along with glucose meters. [20] LFAs are commercially available tests (i.e. pregnancy test, streptococcus, flu, and HIV) [18] that are ideal for diagnosis when analyte levels are high, no samples preparation is necessary, and a qualitative result is acceptable. [21] LFAs have a simple and quick test procedure as well as a long shelf life, requiring no refrigeration. [22] The down side of these tests is that multiplexing is difficult on LFAs and sensitivity is typically low (in the μM to mM range). [18,20,22] Although sensitivity can be increased with amplification, this increases complexity. [18,22] Tetracore® is a company with commercial LFA test strips used for detecting 10 different proteins and readers that attach to cell phones and tablets. [23] Detection was demonstrated with laboratory grown orthopoxvirus. [24] In addition, phone based detection was used with LFAs from ThyroChek (Cliawaived Inc., San Diego, CA) to measure thyroid stimulating hormone levels. [25,26] An overview of LFA applications in research settings can be found in the literature.[27]

Alternate test platforms, such as microfluidics, continue to be studied but are restricted by the extensive research and development required in these areas to reach commercialization. Furthermore, readers are typically required for these tests, which increases the already high-test cost. For healthcare professionals this is not a limiting factor, but for individual users this prevents easy adoption. Categories of microfluidics include micro-electro-mechanical systems (MEMS), nano-electro-mechanical systems (NEMS), lab-on-a-chip (LoC), and PCR based technology. MEMS and NEMS are integrated devices containing electrical and mechanical components in the micro (μ) and nano (n) meter scale. With electronics controlling and mechanics acting as sensors and actuators, the system as a whole can react based on its external environment. Cantilevers and beams are used as mechanical sensing components and strive to detect minute changes in mass causing quantifiable nanoscale deflections. [28,29] Further, microsystems capable of operating in aqueous environments are known as LoC.

These devices contain micro channels connected to form a complete system of desired features. Detection methods consist of optical, electrochemical, and mass spectrometry, but additional development is necessary. [30] There have been few commercial products using LoC to date, as cheaper manufacturing methods are necessary to replace micromachining and lithography. [18] A Dianax prototype claims the test will use a finger prick of blood and LoC technology combined with MEMS. [31] It is intended that the processed data will be relayed using a smartphone, PC, or another user interface.

Commercial microfluidic tests based on PCR technology were produced by Cepheid (Sunnyvale, CA) and IQ^{uum} (Allston, MA) for the detection of nucleic acids. [11] Gene Xpert® was the initial reader created by Cepheid and many iterations have been released since, with the latest being the GeneXpert® Omni assay (see Systems section on website). [12] These diagnostics, now sold by Roche, can perform 80 immunoassays[32] for healthcare related inflections, infectious diseases, and sexually transmitted diseases (see Clinical IVD Tests section on website). [12] Disposable microfluidic cartridges are required for different tests costing ~$40 each and the bench top reader costs between ~$24000 and $80000, based on online listings. The initial investment for the reader prevents the average person from using this test. The disadvantages of GeneXpert® are high cost and limited multiplexing capability.[33]

Furthermore, the handheld Abbott i-Stat device (founded in 1983 and acquired by Abbott in 2004) [18] uses microfluidic cartridges for the electrochemical detection of specific molecular markers to determine results on 25 parameters (i.e. blood gases, electrolytes, haemostasis, cardiac markers, among others) in minutes. [21,34] For each test a different cartridge is required and a few drops of blood. The i-Stat has proven to be faster than bench top tests and the central laboratory, [35] explaining their adoption in some hospitals. [21] However, amplification is generally required, and non-specific interactions can generate background. Furthermore, the detection technique is sensitive to variations in temperature, pH, ionic concentrations, and electrode surface conditions. [21] The reader requires an initial investment between $2000 and $6000, and the disposable cartridges for different molecular tests, range from $200 to $500 each, based on online listings.

Alternatively, microfluidic paper-based analytical devices allow for a colorimetric result in less than 15 minutes with a small volume of blood, while demonstrating, ease of use, and

inexpensive materials yet, there are no commercial devices using this technology, and reproducibility as well as mass production are problematic.[33]

Generally, in microfluidic devices, it is crucial to ensure protein receptor sites remain active and are not denatured during fabrication or packaging to allow for proper detection.[36] Additionally, further research on interactions at the micro level and how it differs from the macro scale are crucial to understanding the operations and properties of miniaturized devices.[37] The length of time necessary for most microfluidic tests results in weak consumer demand, as users experience little decrease in turnaround time with the processing required.[36,38,39]

Surface plasmon resonance (SPR) was introduced in 1968 as a potential optical detection technique for studying the interactions between molecules.[40] Within the same year the concept of surface plasmon (SP) excitation was demonstrated,[41,42] and by 1983 SPR was successfully applied for gas detection and biosensing.[43] Today research continues on this label free technology that provides information on molecular interactions such as: binding, kinetics, affinity, specificity, and concentration.[44] The overall performance of an SPR sensor is dependent on the optical performance and the surface functionalization for molecule recognition. Multiple surface functionalization techniques are presented in the literature to immobilize the receptor proteins on the sensor to detect the analyte.[45] The refractive index resolution of the system is on the order of 10^{-5} refractive index units (RIU) (in Biosuplar 6 system).[46] RIU is a ratio of the change in sensor output to the change in refractive index of the dielectric medium. The refractive index near the metal and dielectric interface changes with analyte binding from solution and alters one of the measured properties proportionally to the analyte mass bound.[45] Specialization of SPR sensors for immunoassays has led to biocompatible sensors.[45,47] Recent progress demonstrates an SPR imaging platform integrated with a smartphone reader.[48] The sensor successfully detected mouse IgG antibodies, using a receptor of rabbit anti-mouse IgG, with nanomolar sensitivity.[48] The assay was successful with the completion of multiple calibration, alignment, initiation, and connection steps, demonstrating that the device operations are far from user-friendly. Additional studies exist where a smartphone aids in SPR sensing,[46,49-52]all showing complex operations. To operate SPR trained personnel and optics systems are necessary, at the very least, and oftentimes further requirements include expensive equipment along with reagents and software to obtain results. Additional challenges for the majority of SPR sensors in the commercial sector

include miniaturization, and portability, among other limitations of improving sensitivity and specificity. [44,45]

Although less common, thin film sensors have shown optical detection. Thin film interference technology was used and allowed for visible colour shifts through changes in the OPL of light, a product of the refractive index and physical path length. The use of thin films interference for visual detection was demonstrated as early as the 1930's. Langmuir and Schaefer[53] first reported the adsorption of proteins from a solution through the production of light interference. The device consisted of a reflective substrate, and a single film of barium stearate along with an antibody layer that created light interference. Succeeding this, Rothen and Landsteiner[54] developed a device using a similar technique comprised of different materials. However, both experienced limitations with regards to colour contrast and low viewing angles, also known as glancing. Furthermore, the use of various thin film tests to detect antigen-antibody complexes using visible interference colour was an occurrence proven by many. [55-59] The problem of glancing angle was overcome in these works but the interference signal remained weak, as a result of mismatched refractive indices between the surface layer and the polymer layer of the device. The patent filed by Burrell et al. [60] explored a new method for reducing background noise, while also working towards solving the issues of time and sensitivity. Introducing a porous surface layer allows the structure to be tailored to match the optical properties of the protein layer, working to eradicate background interference at the protein-surface interface. This thin film device has been able to detect proteins in periods as short as 5 minutes. [61]

Thermo BioStar produced a commercial application that uses thin film detection technology combined with ELISA amplification to transduce visible colour changes, called SILAS™. [62,63] The SILAS™ platform uses an antigen detection assay to bind antigens in solution, increasing the optical thickness, to produce colour contrast. Subsequent addition of a conjugated antibody increased the visible signal making the assay more sensitive. One test detects snake venom and users can quantify 27 different levels of venom concentrations. The initial film is gold and with detection and amplification, via horseradish peroxidase and tetramethylbenzidine, a purplish-blue precipitate forms. Although amplification makes the device more sensitive, the time interval between the precipitation step and capturing an image for quantification is crucial, as the precipitate will continue to form and colour intensity will

increase with time. [64,65] This governs strict user rules for the device to ensure accurate results and is an issue preventing self-testing, as a trained user is necessary.

A point-of-care test with visual detection of antigen-antibody complexes would provide insight on diagnosis and treatment for a range of infectious diseases and immune responses.

2.1.1 Summary

Improvements have been achieved, however, there is currently no affordable, simple test that can be used as a platform for detecting multiple analytes. Table 2.1 summarizes details of the protein diagnostic tests outlined above.

Table 2.1. Analysis of current protein diagnostic tests based on low (+), medium (++) and high (+++) rankings.

Test	Cost	Sensitive	Portable	Rapid	Simple to use	Multiplex	Quantitative	Refs.
EIA (i.e. ELISA)	+++	+++	+	+	+	+	+++	1-4
HPLC	+++	+++	+	+	+	+++	+++	3,5,6
PCR	+++	+++	+	++	+	+	+++	7
LFA	+	+	+++	+++	+++	+	+	8-10
Microfluidics (i.e. MEMS, NEMS, LoC, and PCR technology)	++ ++ ++	++ ++ ++	++ ++ ++	++ +++ +++	+ +++ +++	+ ++ ++	++ ++ +++	9,11-14 26,27 9,15-17
SPR	++	++	+	++	+	++	+++	18-21
Thin film interference	+	++	+++	+++	++	+++	++	22-25

The ideal point-of-care diagnostic should be inexpensive, have a high sensitivity and specificity, be portable, provide rapid results, demonstrate ease of use, and be capable of multiplexing. [33] In addition to these, the World Health Organization criteria for the diagnosis of sexually transmitted diseases in limited resource settings included that minimal or no equipment be required, and that the test is deliverable to the end-user. [74] This thesis is based on the premise that there may be substantial benefits to a thin film diagnostic in terms of cost, simplicity of use, and diversity of application. This work will delve further into the optimization and comprehension of the thin film interference technology patented by Burrell et al. [60] A test of this sort has the potential to operate as a point-of-care platform, but improved knowledge and understanding of the device is required. The impact of manufacturing methods and conditions of use may improve device operation or provide information on which properties are necessary for stable protein adsorption, detection, and colour generation.

Visible detection without amplification eliminates the need for standing laboratories or established infrastructure to obtain test results. A point-of-care test using thin film technology has the potential to transform standard laboratory testing, with its initial use where lack of time and centralized laboratory facilities prohibit other testing regimes.

2.2 Background of Device Colour Generation

2.2.1 Thin Film Interference

The introduction of colour in nature can be due to thin layers creating interference patterns (e.g. insect wings, peacock feathers, minerals, etc.). At each thin film interface when the optical constants change, a combination of reflected and refracted light results. Material properties can be altered to generate the desired combination of reflected light in a multilayered system that leads to strong interference colours. Mimicking the same structures in nature, commercial applications have been developed for anti-reflection and high-reflection coatings, and filters (Fabry-Pérot interferometer) that either prevent or create interference. [75]

A phenomenon that aids in understanding the generation of interference colours is gasoline on wet pavement shown in Figure 2.1. Changes in gasoline thickness alter the path length of light traveling through the fuel layer and in turn the path difference of the reflections off the water and gasoline surfaces that combine to generate interference.

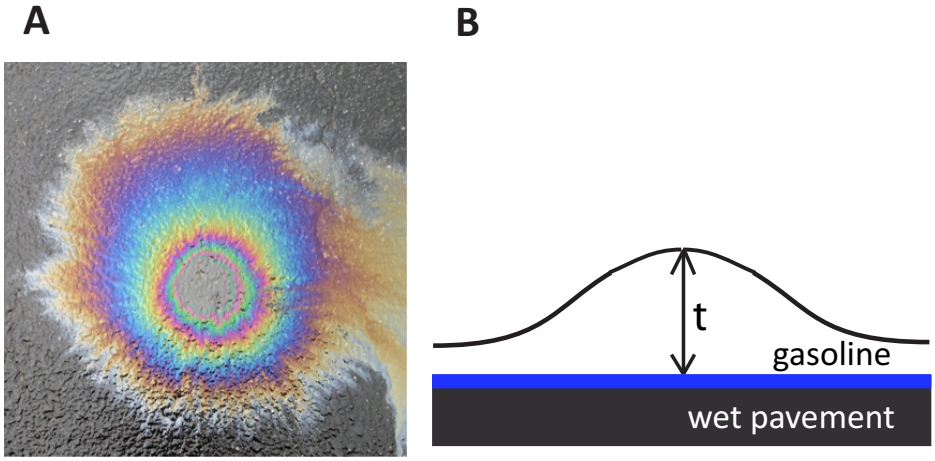

Figure 2.1. Changes in the optical path length of light passing through gasoline on wet pavement results in optical path differences and visible interference colours (A). [76] A cross-section of the gasoline layer is shown, with

thickness labelled as t, to comprehend how changes to the physical path length influence the optical path difference (B).

In addition to the thickness, the formation of distinguishable colours by the unaided eye is largely related to the thin films refractive index, which describes how light interacts with a material. This number consists of a real and imaginary portion, known as η and k, respectively (see Equation 2-1). These can be determined using psi (Ψ) and delta (Δ) values obtained from ellipsometry or by measuring parameters of a material that are impacted by the refractive index, such as the angle of light that has contacted the medium.[77]

$$\bar{\eta} = \eta + ik \qquad \text{Equation 2-1}$$

$$\eta = \frac{c}{v_{phase}} \qquad \text{Equation 2-2}$$

The refractive index is defined as $\bar{\eta}$, the real refractive index is η, and the imaginary part is signalled by ik with k known as the extinction coefficient that shows energy lost within the layer. The velocity of light in a vacuum is c, phase velocity in the material is v_{phase}. The refractive index of a material varies slightly with respect to the incident light wavelength and results in dispersion, the splitting of incident light that results from wavelengths refracting at different angles. As light travels through the thin film device from one medium to another the wave frequency stays the same; however, the speed changes relative to the refractive index as demonstrated in the following equations. [78]

$$v = \lambda f \qquad \text{Equation 2-3}$$

$$v = c/\eta \qquad \text{Equation 2-4}$$

In the equations above v is velocity in a substance, λ is wavelength, f is frequency, c is the velocity of light in a vacuum and η is the real refractive index value. [78,79]

2.2.1.1 Waves at an Interface

Light moving from one medium to another is reflected (R), refracted or transmitted (T), scattered (S) or absorbed (A). [80] The angle of incident light is equal to the angle of reflected light, based on the Law of Reflection shown below.

$$\theta_i = \theta_r \qquad \text{Equation 2-5}$$

The angle of incidence is θ_i and the angle of reflectance is θ_r. The angle of transmitted light depends on the change in refractive indices between the two mediums at the interface. The higher the refractive index of the medium light passes into, the smaller the transmission angle measured from the normal and vice versa. The transmission angle can be determined using Snell's Law shown below.[78]

$$\eta sin\theta_i = \eta_1 sin\theta_t \qquad \text{Equation 2-6}$$

Sine of the angle of incidence is $sin\theta_i$ and sine of the angle of transmission is $sin\theta_t$, and the refractive index of the thin film layers is represented by η with the appropriate subscript. Subscripts correspond with Figure 2.2 and aid in identifying the layers light is leaving and entering.

2.2.1.2 Optical Path Length (OPL)

Light that is refracted at the surface interface and travels through the medium, and is subsequently reflected and exits the medium, determines the physical path length through the film. The OPL is a product of the material's refractive index and physical path length, which describes the distance light in a thin film would have travelled with the same amount of time in the air. Differences between the OPL of reflections, also known as OPD, at each interface (R, R1, and R2 in Figure 2.2) are crucial to the formation of distinct colours by the unaided eye. Figure 2.2 outlines the thin film layers within this device that contribute to the total interference.

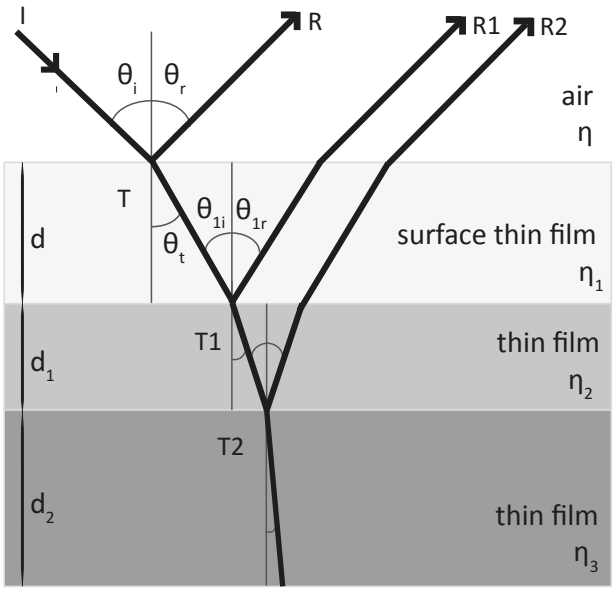

Figure 2.2. Depicts the paths of incident light through the multilayer device that contribute to the formation of interference colours on the bare device surface.

The interference of reflected wavelengths in a system is controlled by the distance light travels through each medium, also known as the optical path length. Geometry is used to determine the distance light travels through a medium and the change in wavelength as light travels from air into a new medium must also be accounted for by the refractive index. If there is a change in film thickness (e.g. adsorption of a protein monolayer), a colour alteration can be observed due to the change in OPL of R1 and R2, leading to an OPD. The OPL and the OPD through the surface thin film in Figure 2.2 can be calculated using Equations below.

$$OPL_{surface\ thin\ film} = 2d\eta_1/cos\theta_{1i} \quad \text{Equation 2-7}$$

$$OPL_{air} = 2d\eta \cdot tan\theta_{1i} \cdot cos\,(90° - \theta_i) \quad \text{Equation 2-8}$$

$$OPD = OPL_{surface\ thin\ film} - OPL_{air} \quad \text{Equation 2-9}$$

The distance travelled through the surface thin film is d, the angle of incident light contacting the air and thin film interface is θ_i and the refractive index of each layer is represented by η. Subscripts were used to identify subsequent angles and properties for each layer. From Equation 2-7 and Equation 2-8, it is apparent that the OPL changes with respect to the viewing angle of the device, as this alters the distance light travels through the films. Using Equation 2-7, refractive index, incidence angle, and desired OPL the required film thickness for a system to generate interference at some wavelength can be determined. The

creation of difference visible colours on oxide films changing the layer thickness, and OPL, has been investigated. [81,82] This concept is fundamental to the operations of this thin film device as a protein layer of ~10 nm is not large enough to generate a path difference and visible interference shift when reflections combine. However, by tuning the surface refractive index (e.g. alumina) to match that of the protein layer, the required minimum OPL is achieved. Without matching the refractive indices of these two layers the refracted light would not travel the required path length within the protein layer before contacting the alumina layer and being reflected, and no interference in the visible range would occur.
Figure 2.3 demonstrates this concept.

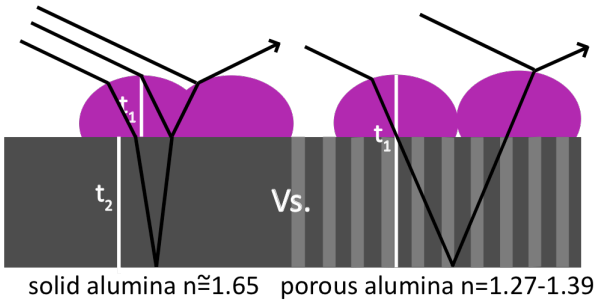

Figure 2.3. Depicts the changes in refracted and reflected light as the protein and oxide interface. When light is refracted at the interface the system in unable to generate visible interference, as wavelengths do not travel the required minimum path length through the protein layer.

Matching the refractive indices of the protein layer and the alumina layer will eliminate undesirable scattering of light at this interface and allow for sensitive detection of changes in the OPL of light reflected at the alumina-tantalum interface. With tuning the surface layer, changes in thickness with adsorbing antigen and antibody layers generated different colour shifts. The change in path length with adsorbed protein layers is demonstrated in Figure 2.4.

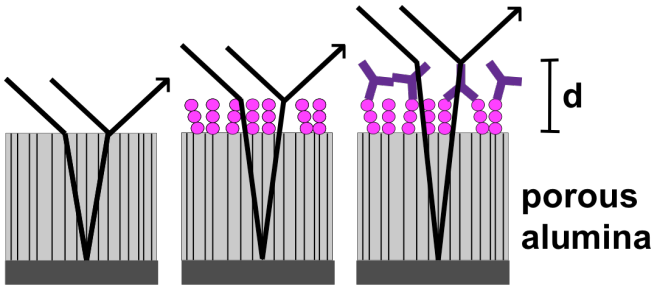

Figure 2.4. Reflectance off the porous alumina layer, adsorbed prothrombin layer, and adsorbed anti-prothrombin layer shows an increase in the optical path length.

2.2.1.3 Constructive or Destructive Interference

Depending on the thin film thicknesses the resulting OPL changes and when reflections recombine so does the wavelengths. The interference enhances or diminishes wavelengths of light known as constructive or destructive interference respectively (see Figure 2.5). One can determine whether entirely constructive or destructive interference will occur if the optical constants of the mediums of either side of the interface are known, and if the OPL is a multiple of half or the full wavelength.[79,83]

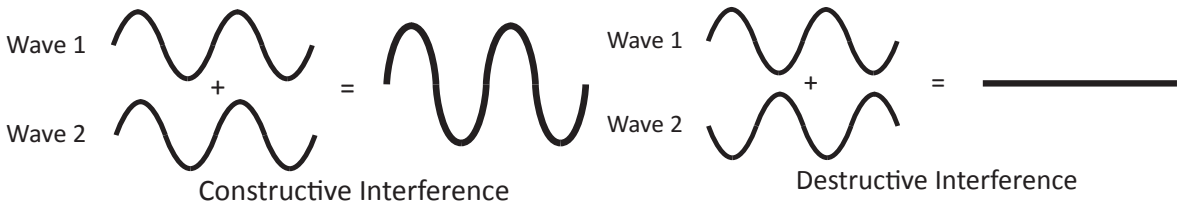

Figure 2.5. Demonstrates the effects of constructive and destructive wavelength interference.

In theory, to produce visible interference colours, the wavelength refracted into the thin film must have an OPL that is at least half the wavelength of light before being reflected at an interface and exiting the device surface.

2.2.1.4 Fresnel Coefficients

To generate strong interference colours the intensity of reflected light at interfaces must be balanced. If the reflected intensities are unequal, then one reflection will overpower the other and weak interference colours results. Fresnel equations described the relationship between incident, reflected, and transmitted light at an interface. [78] In this work, equations were used to determine the theoretical reflection intensity at each interface based on the angle of incidence and differences in the optical constants of layers adjacent to the interface. In these equations the polarization state are also taken into account. Simplified equations for the reflectance and transmittance of *s*-polarized light (perpendicular to the plane of incidence) and *p*-polarized light (parallel to the plane of incidence) are shown. [78]

$$r_{s-pol} = -\frac{\sin(\theta_i - \theta_t)}{\sin(\theta_i + \theta_t)} \qquad \text{Equation 2-10}$$

$$r_{p-pol} = \frac{\tan(\theta_i - \theta_t)}{\tan(\theta_i + \theta_t)} \qquad \text{Equation 2-11}$$

$$t_{s-pol} = \frac{2\,sin\theta_t\,cos\theta_i}{\sin(\theta_i+\theta_t)} \quad \text{Equation 2-12}$$

$$t_{p-pol} = \frac{2\,sin\theta_t\,cos\theta_i}{\sin(\theta_i+\theta_t)\cos(\theta_i-\theta_t)} \quad \text{Equation 2-13}$$

Where amplitude coefficients of r and t denote reflectance and transmittance and the polarization states are *s*-polarized and *p*-polarized. Assuming no absorption, transmittance and reflectance can be calculated as the ratio of light intensity to the incidence light intensity. Equations can be found in the literature. [78] The quantity of light reflected is dependent on the transparency of the adjacent mediums at the boundary. Furthermore, if light is moving into a medium with a higher refraction index the reflected *p*-polarized light rays experience a phase shift of π radians or 180°. If light travels into a medium with a lower refractive index the reflected light rays are in phase, and no phase shift occurs. [78,79] This information is crucial when determining the optimal thickness of each medium to ensure interference.

2.2.2 Sputtering of Thin Films

The myriad of applications for thin films in society ranges from the electronic and semiconductor industry to the medical industry. Some of the original uses were decorative; however, breakthrough technologies include light emitting diodes, hard coatings for cutting tools, and energy generation (i.e. solar cells and batteries). [84,85] Procedures for creating thin film layers are primarily categorized as physical or chemical. Examples of physical deposition are molecular beam epitaxy, pulsed laser deposition, and physical vapour deposition (PVD), with subsets of evaporation and sputtering. Chemical deposition techniques include; Langmuir-Blodgett, spin coating, chemical vapour deposition, and atomic layer deposition. Of these methods, a subset of PVD, direct current (DC) planar magnetron sputtering, was selected for the deposition of metallic thin films with relatively high deposition rates, high-purity films, strong adhesion to a substrate, and excellent uniformity. [86]

The precision and uniformity of the aluminum film thickness is essential to the operations of the thin film device because it contributes to the resulting interference colours. Following device preparation, notable colour shifts occur for thickness increases of 2.7 nm after binding a monolayer film of stearic acid to the surface, [60] and 2 nm in work binding nucleic acid sequences. [87] The tantalum thickness uniformity is less important, as this material is only required to be optically thick to absorb a significant portion of the incident light. To

ensure a high consistency, sputtering parameters of power density, base pressure, argon pressure, argon flow rate, and working distance, were regulated. Controlling the deposition parameters aims to create thin films with a high degree of reproducibility and low variances.

The magnetron sputtering operates by bombarding the cathode surface (i.e. target) with energetic ions to eject atoms or molecules from a target. The collisions generate the release of target material for deposition onto the anode and substrate. With ion bombardment, the emission of secondary electrons from the target also results. In planar magnetron sputtering an applied magnetic field is used to trap charged particles (electrons) within field lines above the sputter target surface.[88] Thereby, increasing the number of collisions with electrons and the inert gas (e.g. argon) allowing for higher rates of ionization, cathode bombardment, and ejected material from the target.[88] As a result, greater deposition rates are attainable in a chamber with a lower gas pressure. Low pressures are required to ensure high-energy ions reach the target and to decrease the number of target atom collisions after ejection from the cathode, also known as increasing the mean free path. Depending on the operating parameters of the system, the deposited film characteristics can vary significantly.[86,89]

2.2.3 Electrochemical Oxidation

2.2.3.1 History

As early as the 1950's, anodization processes were documented for altering the structure and properties of aluminum prior to use. Commercial use included the aircraft industry, which created aluminum oxide surfaces of specific morphology for improve adhesive bonding. Three employed anodization processes include the forestry products laboratory process,[90] the Boeing phosphoric acid process,[91] and the chromic acid process that is similar to the Bell chromic acid process.[92] Later work showed improved adhesion when the Boeing process was carried out following the forestry products laboratory process in phosphoric acid at 10 V for 25 minutes, creating a whisker surface with low order and high etching. The resulting film was ~100 nm thick with an underlying ordered hexagonal base structure ~400 nm thick.[93]

In 1995 Masuda and Fukuda showed further development of an anodic process to grow highly uniform honeycomb structures.[94] Since then numerous applications have utilized properties of these anodic alumina structures for templates to grow nanostructures,[95-98]

corrosion resistant surface layers, and biosensing where high surface area to volume ratios can improve detection sensitivity. [99,100]

An alternate method of oxidation includes heating materials to elevated temperatures. [101] However; the selected method of electrochemical oxidation benefits the reproducibility and adaptability of this device design. Following porous alumina formation, the current moves into the underlying tantalum layer and generates a tantala barrier layer. The resulting thickness of this layer is proportional to the applied potential, and while reaching the maximum thickness causes the current density to decline and approach zero. [102,103] The formation of this tantala barrier layer acts as a process control and helps to ensure consistent interference colours. By achieving reproducible tantala thicknesses, the colour generated by the tantala layer is consistent and has the same contribution to the device surface colour. [104,105] The underlying tantalum metal remains optically thick and absorbs a portion of the light, producing a reflection in the visible spectrum of 40 to 60%, depending on the wavelength and angle of incidence. [104] Absorption by the tantalum layer reduces the amount of reflected light from within the multilayer device, allowing the light emitted from the device surface and light reflected at the alumina surface to combine at nearly equal intensities.

2.2.3.2 Pore Formation

The alumina surface can be highly tuned to achieve optimal conditions for the intended application. [106-108] Important factors include; cathode to anode size ratio, stirring of electrolyte during process, the distance of separation, the volume of electrolyte, concentration and type of electrolyte solution, applied potential, the length of oxidation, temperature, and pre and post anodization treatments. An ordered porous alumina structure is shown in Figure 2.6. Labelled features will be useful in future chapters for characterizing the resulting films.

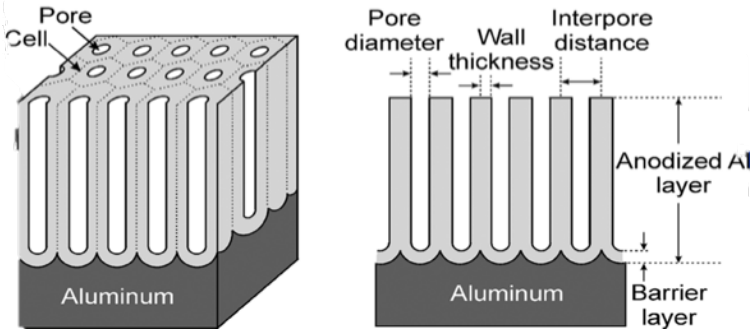

Figure 2.6. Structure of highly ordered porous anodic alumina showing important dimensions of the porous oxide as well as the barrier alumina film at the oxide and metal interface during formation. Image taken from work by Sulka. [107]

Anodic aluminum oxide growth occurs from ionic migration (i.e. Al^{3+}, O^{2-}, and OH^-) through existing films and creates an oxide layer at the interface. When the film being oxidized is insoluble in the electrolyte, anodic barrier layers form. In barrier oxide films the metal ions released through dissolution are not consumed by migration into the film. Integration of these ions into new films can still take place depending on the precipitation and deposition that results. [109] Work by Hunter and Fowle showed that barrier layers contain two different compositions. [110] Electrolytes known to form barrier layers are neutral boric acid, electrolytes with borates, and several organic solutions such as citric and malic acids. [111] Anodization to create a barrier film shows a rapid decline in current density as the oxide layer increased thickness barrier layer. However, because the dissolution of metal ions into solution is minimal, the barrier oxide continues to increase in thickness at a rate proportional to the applied voltage and limits the current. The current density reaches zero when the current can no longer penetrate the barrier layer.

When the film being oxidized is soluble in the electrolyte, a porous alumina layer forms. Anodic porous films are not pure oxide, but typically incorporate anion species from the electrolyte. The integration of different molecules influences the chemical, physical, and optical properties that result. Stability of the surface alumina film can be tailored to achieve an inert device. Anodization in different electrolytes incorporates ions present in solution. Phosphoric, sulfuric, and oxalic electrolyte solutions are known to generate porous alumina films[111] containing ~7.6, 11.1, and 2.4 wt.% of anions from the respective solution. [109] These

values can fluctuate depending on the electrolyte concentration among other system parameters. When using an acidic electrolyte the resulting porous anodic alumina is hydrated and has a positively charged surface. [106,112] The surface chemistry is important when immobilizing groups from polymers and proteins directly to the surface, or when using linkers to binding specific molecule sites.[106]

Positive and negative ions in the electrolyte accelerate towards the anode and cathode with an applied potential. Positive hydrogen ions move towards the cathode and upon gaining an electron are converted to hydrogen gas, whereas the negative species move towards the anode and convert aluminum to a porous aluminum oxide film. The following reactions occur and lead to the formation (Equation 2-14) and dissolution (Equations 2-15 and 2-16) of the oxide layer, respectively. [113,114] Changes in the electrochemical process generate different alumina films, as different rates of formation and dissolution result.

$$2Al^{3+} + 3O^{2-} \rightarrow Al_2O_3 \qquad \text{Equation 2-14}$$

$$Al_2O_3 + 6H^{+} \rightarrow 2Al^{3+}(aq) + 3H_2O \qquad \text{Equation 2-15}$$

$$2OH^{-} + Al_2O_3 \rightarrow 2AlO_2^{-} + H_2O \qquad \text{Equation 2-16}$$

During porous anodization an initial decrease in current density results as with the growth of a resistant oxide barrier layer, the same as in the beginning of the barrier oxide formation. With continued oxidation of this layer the oxide thickness increases and propagation of individual paths through the oxide film form, specifically along high-energy grain boundaries. These micro cracks are precursors to pore formation in the oxide layer and have completely formed when the resistance is reduced, causing an increase in current density. At this point, the barrier film begins to breakdown and the formation of a porous layer begins. In some cases, the current density reaches a local maximum after which it decreases slightly and plateaus. At this current density plateau, an equilibrium has been reached between O^{2-} and OH^{-} integration into the oxide film and metal ion dissolution.

2.2.3.3 Alumina Surfaces

Exposed aluminum ions in an aqueous environment, attract water molecules or OH^{-} ions towards the surface and achieve surface hydroxyl groups. The alumina surface can contain between a few tenths and 5% water, depending on the temperature and vapour pressure of the

surrounding environment. [112] Water molecules can be physisorbed or chemisorbed as an undissociated or dissociated molecule. [115] Undissociated water molecules are adsorbed to the alumina through strong hydrogen bonds. At increased temperatures hydroxyls form on the alumina surface and are then expelled as water molecules with increased temperatures.[112]

Water chemisorption is thought to be a reaction between the aluminum ion, termed the Lewis acid (electron acceptor), and the hydroxyl ion, termed the Lewis base (electron donor). [112,116] The gradual dehydration of the alumina was shown to form oxygen bridges between two aluminum ions, creating active Lewis sites (see Figure 2.7). [117] The aluminum oxide activity speaks to the ability of the material to catalyze reactions. Active sites develop alongside the dehydroxylation process and are related to the defect structure of the alumina. Alumina films that are fully dehydroxylated or well-ordered are not active. [116] Work by Flockhart et al. showed that active alumina can act as a Lewis acid or base, leading to oxidation and reduction reactions. [118]

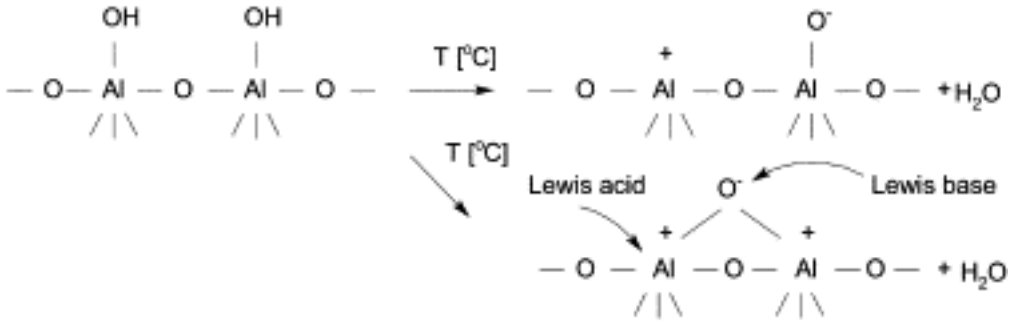

Figure 2.7. Lewis acid and base sites on the alumina surface.[117]

In work by Mardilovich et al. it was suggested that aluminum ions bonded with two terminal hydroxyl groups have increased activity. These ions are found on the edges and corners of the alumina particles.[119]

Hydroxyl groups on the alumina surface have an amphoteric nature. [112] The change in the surface alumina structure and charge depends on the electrolyte pH. An acidic pH, lower than the point of zero charge, generates a positively charged surface, and a basic pH leads to a negatively charged alumina surface. [120] Neutral alumina surfaces were formed in solutions with a pH in the range of 7 to 10. [112,121]

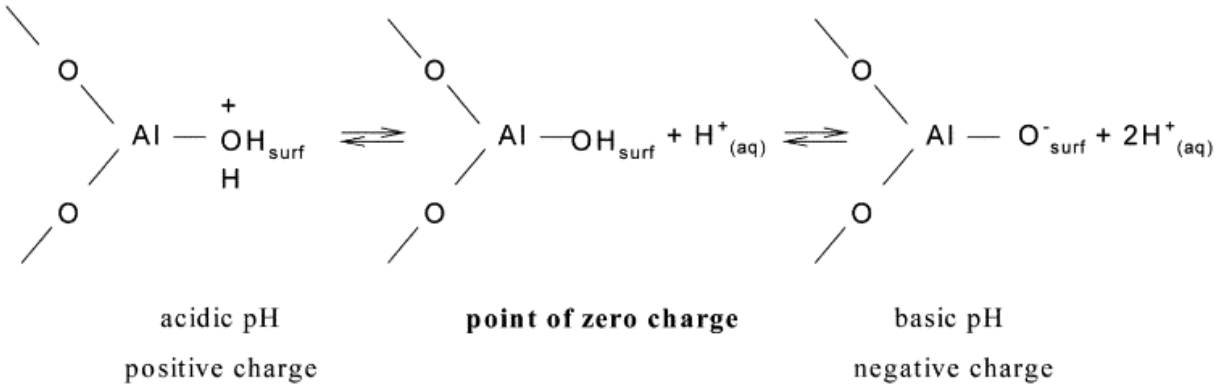

Figure 2.8. The alumina surface structure and charge that results with the formation in solutions with varying pH.[120]

The zeta potential was zero in 0.1 and 0.01 M NaCl solutions with a pH of 4.5 and 4.0, respectively. [121] Adsorption of electrolyte species creates a net charge on the alumina surface.[112]

2.2.3.4 Alumina Refractive Index

Various refractive indices can be found for aluminum oxide barrier layers. The manufacturing techniques such as deposition and oxidation influence the material's refractive indices. Commonly applied alumina refractive index values in the visible spectrum (~370 to 700 nm) are between 1.76 and 1.79. However, these values are for aluminum oxide in the form of sapphire. [122] Alternately, amorphous alumina waveguides created through pulsed laser deposition showed a refractive index of 1.67 at 633 nm. [123] Alumina films created with atomic layer deposition showed refractive indices of 1.66 at 370 nm and 1.64 at 700 nm. [124] Lastly, alumina deposited by radio frequency sputtering showed a higher refractive index of 1.70, where the films measured have a relative density of 98% to that of an amorphous anodic alumina. [125] For this work the anodic alumina barrier layer is assumed to have refractive indices between 1.65 and 1.70.

2.2.4 Protein Detection on Thin Film Surfaces

Numerous techniques are used for the detection of biological molecules on thin films including ellipsometry, electrochemical, visual, and radioisotopic methods. [126] Among these, visual contrast distinguishable by the unaided eye allows for the simplest detection.

Specifically, test processes that do not require an amplification step or expensive detection equipment.

Medical diagnostics and the use of thin films as a detection platform for biological molecules began in the early 1900's. Langmuir and Schaefer[53] first reported the adsorption of proteins from a solution through the production of light interference. The device consisted of a reflective substrate, and a single film of barium stearate along with an antibody layer that created light interference. Succeeding this, Rothen and Landsteiner[54] developed a device using a similar technique that was comprised of different materials, however both experienced limitations with regards to colour contrast and glancing angles (high viewing angles from the surface normal). The roadblock of glancing angle was overcome in the 1970's through patents published by Giaever (1974, 1975, and 1976) that reduced the substrate reflection. [55-57] His first patent used a method to produce voids in a thin film where adsorption of large biological particles to the antibody-coated substrate had occurred. Subsequent variations utilized varying surfaces, such as indium and gold, to detect antibodies and very low concentrations, but the synthesis of these devices was complex and difficult to reproduce. The problem of glancing angles was overcome, but contrast of the interference colours remained weak as a result of failing to match the surface layer refractive index to the protein refractive index.

The patent by Burrell et al. [60] demonstrated an increase in sensitivity by utilizing a porous alumina surface layer that allowed the refractive index to be tuned to closely match the protein layer. This decreased scatter and increased the interference signal.

2.2.4.1 Aluminum Oxide Thin Film Sensors

Porous alumina membranes have been used in numerous biological applications[127] such as sensors, [128,129] protein separation, [130,131] and drug delivery. [132] Typically alumina surface used in biological applications undergo modifications to increase biocompatibility and chemical stability. [113] In prior work, the use of porous aluminum oxide thin films has been applied for sensing applications. Several report using electrochemical techniques (i.e. impedance spectroscopy, capacitance, ionic conductivity, etc.) to immobilize specific antibodies in the alumina pores and measure changes in the alumina membrane with analyte adsorption and have demonstrated sensing capabilities. The detection of parathyroid hormone-like hormone secretions in cultured human cells using anodic aluminum oxide membranes

was demonstrated, with a limit of detection between 60 and 100 ng/ml. [133] Immobilized strains of *Escherichia coli* and *Staphylococcus aureus* were measured, with a detection limit of 10^2 colony forming units (CFU)/ml. [134] The antigen, atrazine, showed detection in the fg/ml (part-per-trillion) range. With platinum electrodes on either side of the alumina membrane, 20 µl of Dengue 2 and 3 viruses were exposed for 30 minutes, and proved a limit of detection of 0.23 plaque forming units (PFU)/ml and 0.71 PFU/ml, respectively. [135] Another few studies detecting Dengue virus 2 showed limit of detections of 1 PFU/ml. [136,137] A capacitance sensor detected polychlorinated biphenyls on alumina; with a limit of detection of 80 nM[138] and lastly, a novel logic gate sensor detected Pb^{2+} with a detection limit of 0.1 nM. [139] These tests did not generate a visible colour shift on the surface, but used other mechanism of detection.

A similar process for immobilizing DNA probes has been used on functionalized porous alumina membranes. Electrochemical detection of the corresponding DNA was successful for measuring changes in analyte. Detecting complementary DNA demonstrated limit of detections of 12.5 nM in PBS, [140] 9.55 pM for Dengue virus RNA detection in 45 minutes, [141] and 1 pM for Dengue virus. [142] With a similar process, a single strange 21mer DNA sequence from *Legionella pneumophila* showed a detection limit of 0.31 pM. [143] Amplification techniques for DNA detection with magnetic nanoparticles created a sensor with a limit of detection of 3 nM for histamine detection, [144] and gold labelled nanoparticle tags labelled with single strand DNA to conduct a sandwich assay showed 1 pM. [145] A multitude of other sensing applications using an alumina membrane were demonstrated. [112,146-153] These sensors for DNA detection were defined by electrochemical detection mechanisms showing no visible colour shift.

A multitude of other sensing applications using alumina membranes were demonstrated. [146-153] These included sensors that bind lipids within the alumina pore and measure differences in the electrochemical signal with exposure to non-ionic detergent, to determine the alteration of lipid membranes. [146] Immobilization of enzymes within alumina pores was used to demonstrate 100% activity was retained in comparison to free enzymes. [147] A piezoelectric response was measurable for urea detection as low as 0.05 µM. [148] One application demonstrated a microchip that completed a number of steps including PCR on an alumina membrane, [149] while another used alumina as the foundation for a MEMS gas sensor. [150] In

addition, alumina membranes were used for filtration and growth by incubating bacteria, media, and antibiotics on the surface showing optical detection with an imaging unit, providing 1 hour antibiotic screening. [151] In another study the membrane was used to test the effect of an anti-cancer drug on epithelial cancer cells. [152] The method of optical polarimetry showed phase retardation shifts in the alumina membranes and demonstrated changes with immobilizing bioreceptors and subsequently the analyte on the pore wall. [153] The LOD was 225 pM using <100 μl volume solutions and <1 hour of incubation time.

Although less common, several alumina sensors have utilized optical detection techniques. In addition to work already mention using thin film alumina for sensing, [60,61] visual detection by eye and reflectance were also used to identify colour shifts with covalently binding a molecule for trinitrotoluene binding in the mM range. [154] In another study, surface colour shifts were demonstrated with single and double BSA layer adsorption on an alumina film.[155]

2.2.4.2 Protein Immobilization on Alumina

Furthermore, the alumina surface is critical to protein stability on the device surface. Different applications of alumina have proven immobilization of substances from aqueous solutions. Combining studies, the alumina adsorptive force for anions in water are; $OH^- > PO_4^{3-} > SO_3^- > SO_4^{2-} > HCO_2^- > NO_2^- > NO_3^- > S^{2-}$.[156,157] The formate group (HCO_2^-) in this sequence is analogous to the carboxyl groups in aspartic acid and glutamic acid groups that exist in solutions where the hydroxyl group is deprotonated. This is advantageous for immobilizing proteins with a large number of carboxyl groups. As a result, the surface alumina thin film has been found to securely bind vitamin-K dependent proteins. The vitamin K-dependent proteins contain a GLA domain with a high density of carboxyl groups. These structures eliminate the need for any surface modifications and creates a bridging molecule of a consistent thickness. The stable layer can be built upon to create a detection system for specific antigens or antibodies. Other linking methods between biological molecules and anodic alumina surfaces include organophosphates[158,159] and amino silanes. [160,161]

Small organic molecules adsorb to oxide surfaces when functional groups (i.e. carboxylic, phenolic-OH, or amino groups) replace the hydroxyl groups. [162] The adsorption of carboxylic acid onto aluminum oxide is stronger than other organic compounds. [112] For

polyelectrolytes with multiple functional groups, the driving force for adsorption is electrostatic attraction. [163] Two models have been proposed for binding of the carboxylic group to the alumina, bridging[164] and chelating[165] models.

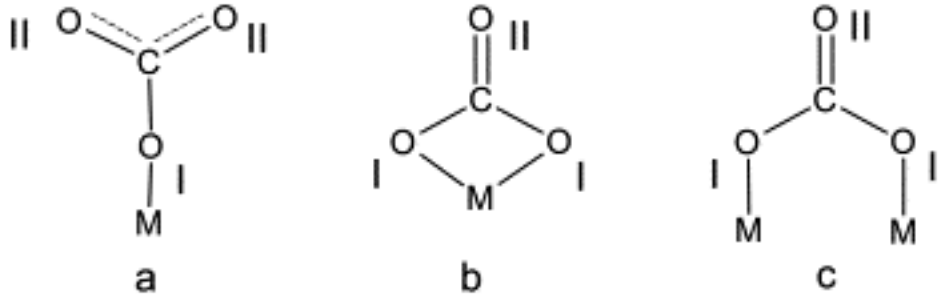

Figure 2.9. Possible surface structures with carbonate adsorbed to the alumina surface include: (a) monodentate, (b) bidentate, and (c) bridging-bidentate. Oxygen atoms that correspond to the metal ions (M) are labelled with I and those from the carboxylic acid are labelled II.[166]

Work by Wijnja et al. found that monodentate structure was present on gamma alumina at a pH between 5.2 and 7.2. [166] Further work supporting the chemisorption of carboxylic acids on alumina was found. [164,167,168] The C–O bonds of the carboxylate (COO^-) become equal when the double bond is lost and the carboxylate adsorbs to the alumina surface through two aluminum ions. [169-171] Bidentate bridging was noticed between the compounds and oxide layers. The amount of surface hydroxyls showed a correlation to the number of carboxylic acid molecules adsorbed.[167]

In addition, studies showed the use of chelation or monodentate formation for carboxylate binding to alumina. [172,173] Coordination through bridging ligation was evident in past works exposing phosphonic acid, formic, and acetic acid to alumina surfaces. [174,175] In the study by Karaman et al., carboxylic acids demonstrated binding to the hydroxyl groups on the alumina surface through the formation of esters. [173] Various surface hydrophobicity and stability resulted.

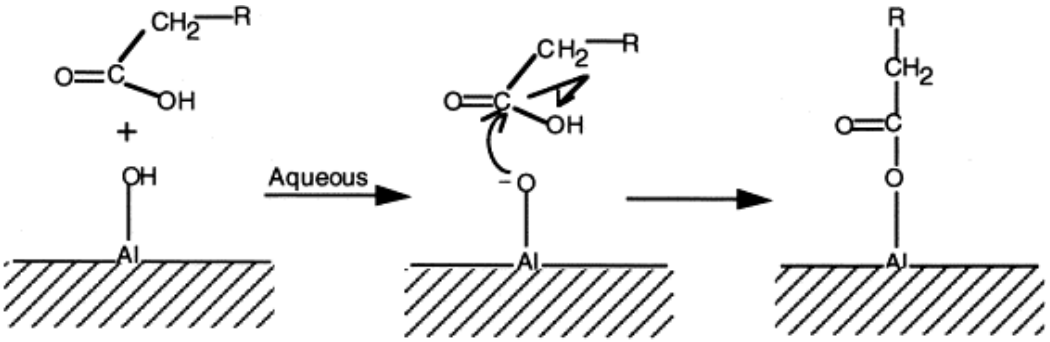

Figure 2.10. Shows carboxylic acid binding to hydroxyl groups on the alumina surface through an esterification reaction.[173]

X-ray crystallography demonstrated the ability of the carboxylate molecules to function as a bridging ligand for variable aluminum atom separation distances. Carboxylate groups have bridged aluminum atom spacing between 3.1 and 5.4 Å. [176,177] Hydrated, and partially hydrated, alumina surfaces containing aluminum atoms with ~3.7 Å of separation lead to stable bridging and no reorganization of the aluminum atoms is required.[177]

Prothrombin, or coagulation factor II, is a vitamin K-dependent protein involved in the blood coagulation cascade. There are ten carboxyglutamic acid residues in the first 33 amino acids of fragment 1 that are used in the body to bind the molecule to lipid membranes. [178] Carboxyl groups are a readily available constituent of gamma-carboxyglutamic acid residues, making this protein an excellent native linker to the alumina film. These multifunctional anionic groups improve the adsorption onto alumina[112,179,180] and govern the orientation of binding. The molecular weight of prothrombin is ~72 kDa, and the three-domain protein consists of a Gla domain and kringle-1 that make up fragment 1, kringle-2 which makes up fragment 2, and the serine protease domain that makes up thrombin (see Figure 2.11).

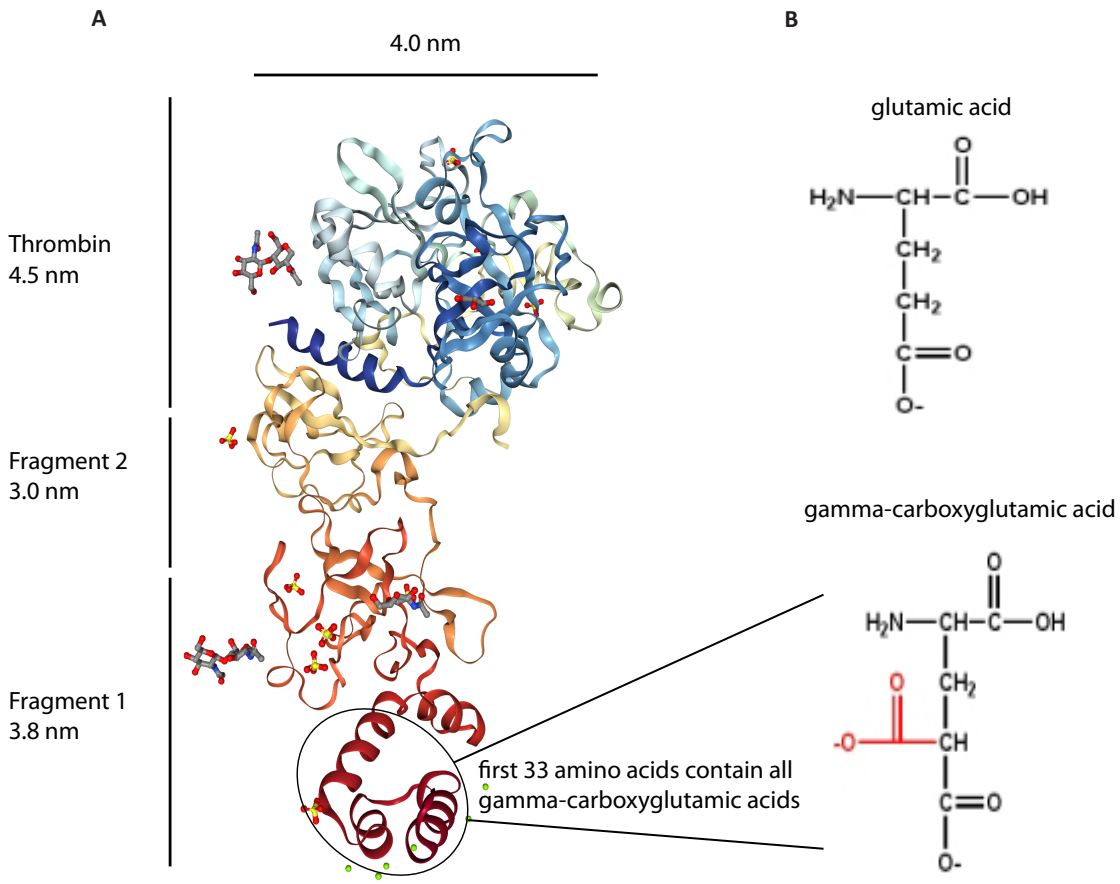

Figure 2.11. The structure of (A) prothrombin depicting fragment 1, fragment 2, and thrombin[181] with dimensions from Lim et. al. [182] The Gla domain is shown in red, kringle-1 in orange, kringle-2 in yellow, and the protease domain in blue. Structures of (B) glutamic acid and the post translational gamma-carboxyglutamic acid residues show available carboxyl groups that lead to immobilization on the positively charged alumina surface.

In past literature, alumina surfaces have demonstrated protein degradation with exposure to the surface[112,183,184] as well as the loss of biological activity. [185,186] Prothrombin not only contains a high-density charge region, but the structure of the protein positions the charged region at the short side of the molecule. Hence, with stable binding of the prothrombin Gla domain to the alumina surface, the molecule naturally positions the remaining portion of the protein off the alumina surface. Therefore, the structure of prothrombin makes it an ideal bridging molecule, as it ensures a stable protein monolayer while preventing the unbound protein region from sitting on the alumina surface.

To construct a specific detection test, the receptor protein would be immobilized to the initial protein layer. Detection would result by exposing a biologic solution and if the target

antigens or antibodies were present, binding to the receptor protein would increase the path length and lead to a visual colour shift. The immobilization process generates a platform diagnostic device with stable binding of the receptor proteins on the surface, adaptable to a variety of detection applications.

2.2.5 Optics

2.2.5.1 Colour Sensitivity

Work by Chu et al. demonstrates the increasing colour orders with anodic alumina thickness increasing from 240 to 7000 nm. Changes in the pore size with pore widening were also shown to influence the colour order by altering the optical constants. [187] The production of visible interference colours ranges from first order to an infinite number, with first and second colours providing the highest visual intensity, as shown in Figure 2.12.

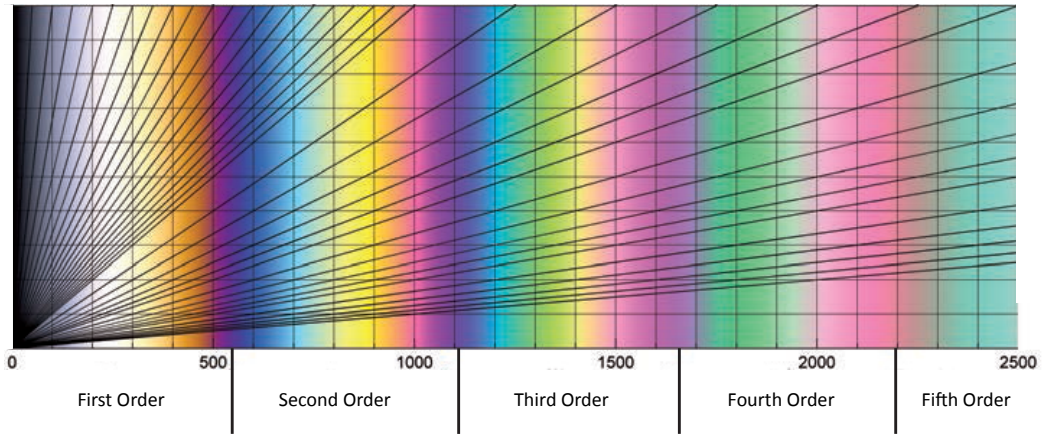

Figure 2.12. A revised version of the Michel-Lévy interference colour chart showing path difference in nanometers along the horizontal axis and colour orders from first to fifth.[188]

In the first and second orders, colour reductions are minute and can only affect one particular wavelength. First order shows the greatest sensitivity, with red showing optimal colour shifts with thickness changes. An increase in wavelength moves towards cyan or a decrease in wavelength moves to tan. Colours generated above the third order are diffuse because a greater number of wavelengths are interfering. [188,189] Visible colours can be evaluated by mapping chromaticity coordinates on an International Commission on Illumination or Commission Internationale de I'Eclairage (CIE) plot. The CIE 1931 plot is not visually uniform, and therefore equally spaced coordinates in the CIE plot are not perceived to

be equally different. This concept is demonstrated by MacAdam ellipses and colour shifts associated with 2 nm thickness changes in Figure 2.13. [82,190]

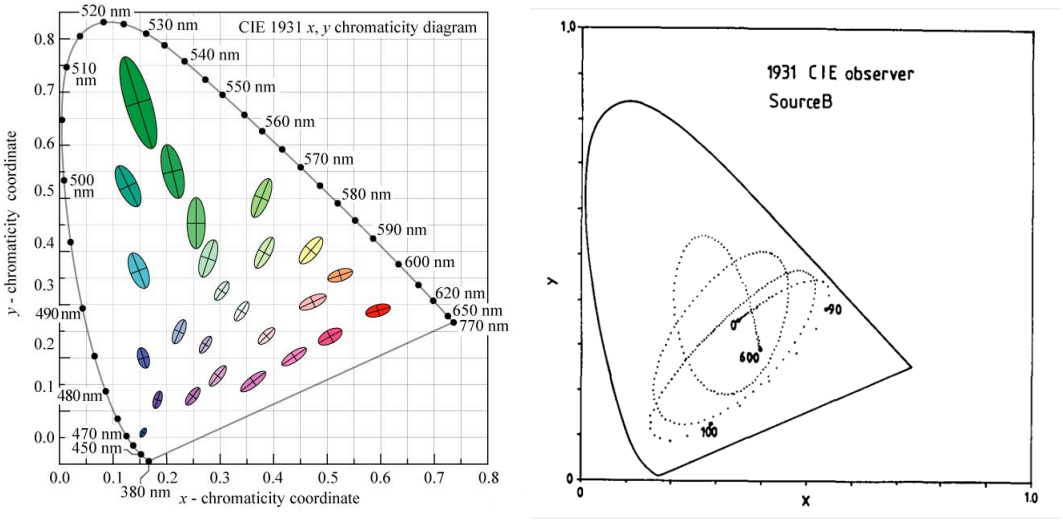

Figure 2.13. CIE 1931 colour diagrams show MacAdam ellipses (left) and Sandström et al. work on colour diagram (right). Both charts demonstrate the ability of the human eye to distinguish different colours.[82,190]

Work by MacAdam and Sandström demonstrate how far apart colours must be in various directions before the human eye can perceive a difference. This is critical to ensure the most sensitive colour region is used for detection by eye so shifts resulting with protein binding are visible. There is no coincidence that the first and second order interference regions of the CIE colour diagram show the highest colour sensitivity.

2.2.5.2 Human Vision

For this work, the detection source is important for interpreting the visible surface colour or wavelengths. The visible (VIS) region makes up a small portion of the electromagnetic spectrum, ranging from violet to red (370 to 700 nm). Beyond the violet end of the spectrum is the ultraviolent (UV) region with shorter wavelengths and higher frequencies. The infrared (IR) region exists at longer wavelengths with lower frequencies. [191] The visible colour perceived by the human eye differs from a phone camera, and a spectrophotometer. The human eye gathers signals from the light that enters the retina through two types of photoreceptors, cones and rods. Red, green, and blue cones exist and give us the ability to see colour, whereas the rods measure low intensity light and allow us to see grey scale in low lighting conditions. [78,192,193] Colour cones in the human eye are sensitive to the

three wavelength regions. Changes in the intensity of each peak allow our eyes to perceive different colours. Blue cones are sensitive to wavelengths between 380 and 550 nm and green cones detect wavelengths between 430 and 670 nm. Lastly, red cones are sensitive to wavelengths between 500 and 700 nm with a secondary detection region between 400 and 480 nm. Interference colour contrast is detectable by the human eye; however, for colour identification an optical method that creates an accurate and reproducible system should be used.

2.2.5.3 Methods for Colour Detection

For the detection of protein adsorbed onto an alumina surface there are a number of different methods that have been utilized. Sensing applications can be detected electrically, [93,94] optically, or by integrating methods. Optical sensing uses techniques of fluorescent emission, [194,195] interference, [129,196,197] surface-plasmon excitations, [198] surface enhanced Raman spectroscopy, and optical waveguide coupling.

Applications in nature commonly analyze colours to establish trends in ecology. Flower colours were quantified using a spectrometer, light source, constant angle, and white standard. [199] The collected colour data was mapped in a colour space based on the photoreceptors of hummingbirds and bees. Differences were calculated based on the distance between points to provide an indication of the perceived colour shift. [199,200] In fieldwork it is often hard to use spectrometry for analysis but the capture of images and digital processing[201] is more easily applied in biological studies to quantify and analyze colour patterns. [202-206]

A study by Tapia-McClung et al. modelled the relative colour and distribution of colour on the abdomen of orb web spiders using tools for digital processing. [207] The spiders were place in a box on a blue background and images were captured from 15 cm above with constant camera and light source. Software algorithms were used for processing data from the images and Lab colour coordinates were applied and allowed a Euclidean distance to be calculated that corresponds with the perceived colour shift. [207]

In another study, a comparison of the orange spots on guppies was carried out with images captured to determine correlations among populations. [208] Within the image a black background was used, an orange patch for reference, and an illumination source. Colour

coordinates of hue, saturation, and lightness values (HSL) were used as well as HSL values normalized using the orange reference to account for differences between imaging conditions.

In work comparing scrotal colour among monkey populations RAW images were captured to avoid processing and chromaticity diagrams were used to give a visual representation for variation in the perceived hue. [209] Differences in the RGB values were also calculated for analysis.

In nature, difficulties stem from controlling parameters (i.e. lighting, angles, and position of the object of interest, etc.) and reproducibility. [210] Controls for colour measurements were typically used to ensure reproducible angles and illumination. Various methods have demonstrated using a calibration standard in images to provide a permanent reference. [211] An ideal standard should have relatively equal reflectance across the spectrum of interest and be highly diffuse or Lambertian. [201] A Lambertian standard, with a very low surface roughness, achieves approximately equal reflectance at every direction and angle, which is beneficial to account for slight variation in the setup. White Lambertian surfaces are typically made of Spectralon, barium sulphate, or magnesium oxide coatings. However, other white materials (e.g. cotton cloth, paper, or Teflon tape) can be used, the surfaces just require calibration. [210] Measuring reflectance with a constant geometry or of a Lambertian or mirrored surface does not provide a true reflectance; however, it allows for the data to be compared to previous work. [210] For exact colour identification values some calibration and analysis is necessary. [201]

A consistent experimental setup is required to measure reflectance of complex objects to reduce error. The angle and azimuth of incidence light and the detector should be accounted for. The four-dimensional bidirectional reflectance distribution function accounts for the vertical and horizontal angles of incident light and of the detector. [210]

2.2.5.4 Chromaticity Diagrams

Coordinate systems commonly used for colour identification and mapping include red-green-blue (RGB), Yxy, XYZ, L*a*b*, and HSL among others. Colours are separated into chromaticity and luminance components. Chromaticity is based on two independent parameters of hue and saturation and is irrelevant to luminance. Figure 2.5 (A) shows the CIE colour diagram that can be used to map x and y chromaticity coordinates along with the

labelled colours for each region. Figure 2.5 (B) shows the chromaticity area where RGB (Adobe and s) coordinates can be mapped on the CIE chart, as the outermost line includes all colours visible by eye.

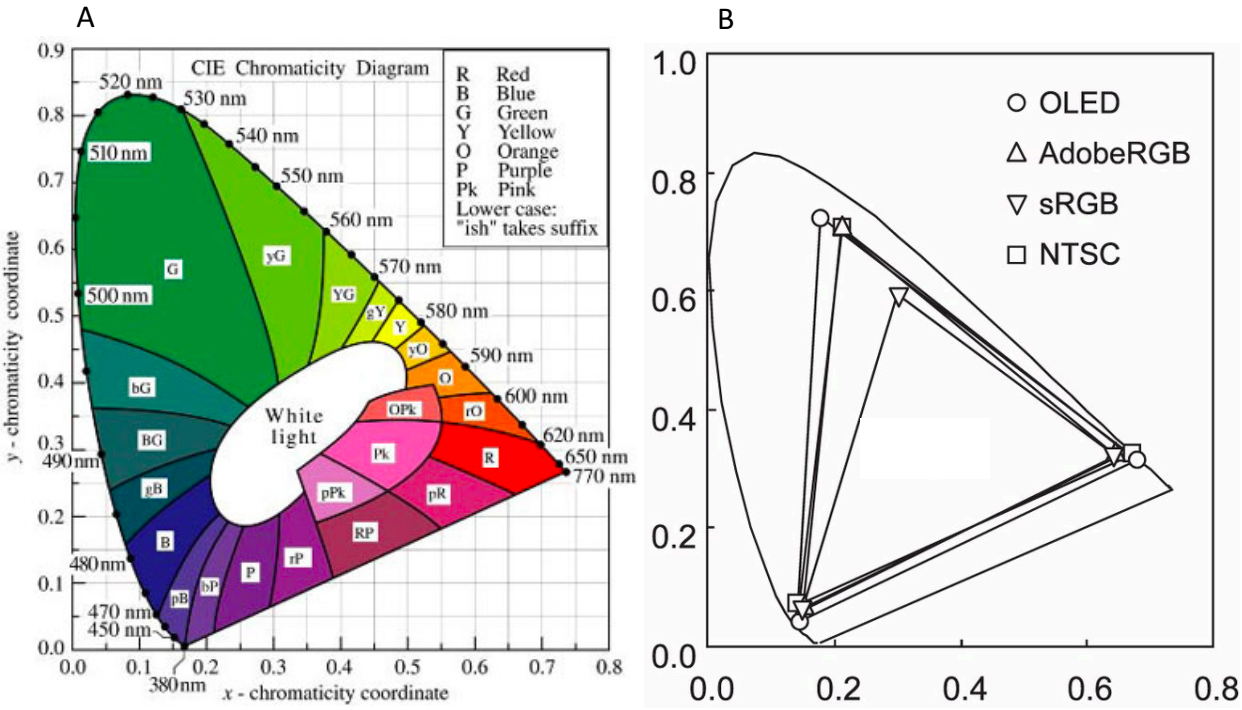

Figure 2.14. CIE 1931 chromaticity diagrams with (A) coordinates x and y along axes and regions attributed to specific colours that can be perceived by the human eye from work by Gage. [212] *The chromaticity diagram (B) shows the colours that can be defined using RGB coordinates or transformations of these coordinates from work by Ito et al.* [213] *Other colour gamuts were shown for an organic light emitting diode (OLED) and the National Television System Committee (NTSC) standard.*

The white central region of the CIE colour chart is a neutral reference characterized by chromaticity, with the colour defined about this point. Hue, or colour, is the angular component and purity, or saturation, is the radial component. Although colour detection under highly reproducible and sensitive conditions is ideal, if colour shifts are below the visible detection limit and are not apparent by eye, more sensitive methods for detection exist.

Spectrometry, spectrophotometric, and other photon counting detectors allow for the analysis of shifts in reflected wavelengths. Spectrophotometers can provide analysis with full spectrum measurements on reflectance properties, beyond what is detectable by the human eye. A broad range of applications exists for identifying colour shifts with a spectrophotometer such as in the food industry, [214,215] for material assessment, [216,217] and for

confirming the presence of nanoparticle labels.[218,219] Furthermore, for low levels of light intensity, photodiodes[220,221] and photomultipliers[222-224] can be used to measure the number of photons.

2.2.5.5 Illumination Controls

For colour measurements lighting is critical as the luminance and colour of the light source effects the measured colour. Natural and artificial light sources show variability in colour. In some studies, natural lighting was used, as the samples of interest were animals in their natural habitat, and in others artificial lighting sources were used, in combination or individually, to improve illumination or consistency. With differences in lighting, objects cannot be accurately compared unless the change in illumination is accounted for.[201] Including a calibration standard in the frame when collecting the images, allows for normalization of images based on a uniform reflectance level off the standard. Normalization of the region of interest with a standard used in each image captured ensures changes in illumination and other potentially influential parameters are accounted for. This includes changes in the correlated colour temperature (CCT) and intensity. Controlling the incident light source and the experimental set up are additional methods that allow objects to be compared under nearly identical conditions. The effect of CCT on the light colour, and ultimately the object of interest, is shown in Figure 2.15.

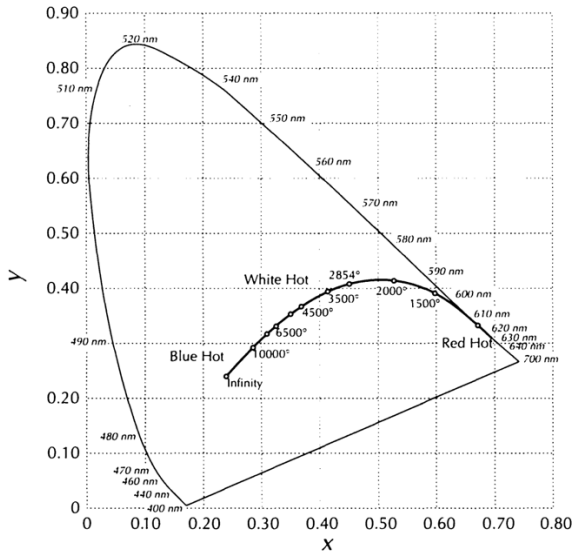

Figure 2.15. The colour shift from reddish to bluish white light that occurs with changing the CCT from 1500 K to infinity, mapped on a CIE plot. [192]

With increasing the light source CCT from 1500 to 10000 K the perceived white light shifts from warm to cool with undertones of orange to blue, respectively. Differences in wavelengths do not appear equally bright even with equal power or intensity settings, as the human eye detects red, green, and blue light with difference sensitivities. [193]

2.2.5.6 Light Polarization

Prior studies using thin film interference colours have identified that improved contrast and decreased glare are important aspects of visualizing the colour change on the thin film diagnostic. One method to control and alter the glare and reflection is through the use of a polarization filter. Unpolarized light travels equally on any axis whereas polarized light is mainly in one axis. Polarized light contains only p or s-polarized light depending on the plane of polarization and can be achieved with a polarizing filter that cancels the electric field in one direction. When the electric field component is oscillating parallel to the plane of incidence light is classified as p-polarized (vertically polarized) and when perpendicular as s-polarized (horizontally polarized). The orientation of polarization refers to the planes made by the direction of light propagation and a vector perpendicular to the reflecting thin film surface, also known as the plane of incidence shown in Figure 2.16.[225]

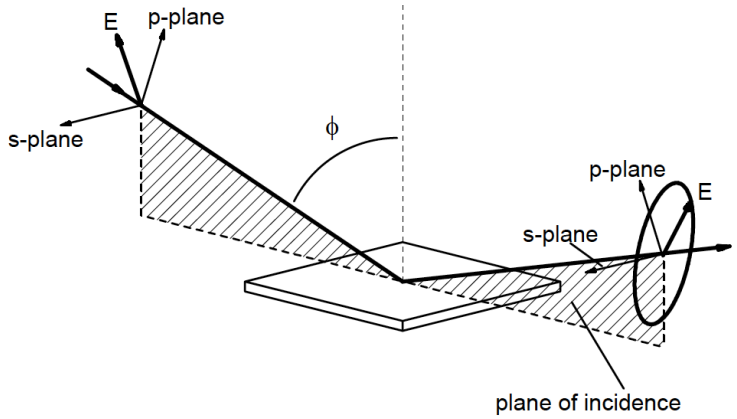

Figure 2.16. Depicts the orientation of s-polarized and p-polarized light wave planes with regards to the plane of incidence and surface under analysis.[77]

Incoming electromagnetic waves are shown by the electric field, E, which is the component affected by the polarizer. In past work visible interference created by thin films has been viewed at large angles of incidence (ϕ). The plane of polarization for viewing the device surface colours will be selected to capitalize on the interference and produce the strongest colour change. Alternative methods or finding to improve the colour contrast may be discovered during experimental testing that assist further with the visual detection process.

An application of Fresnel equations is shown through the polarization of light that occurs with reflectance at an interface. Figure 2.17 shows the reflected light for each polarization state with increasing angles of incidence.

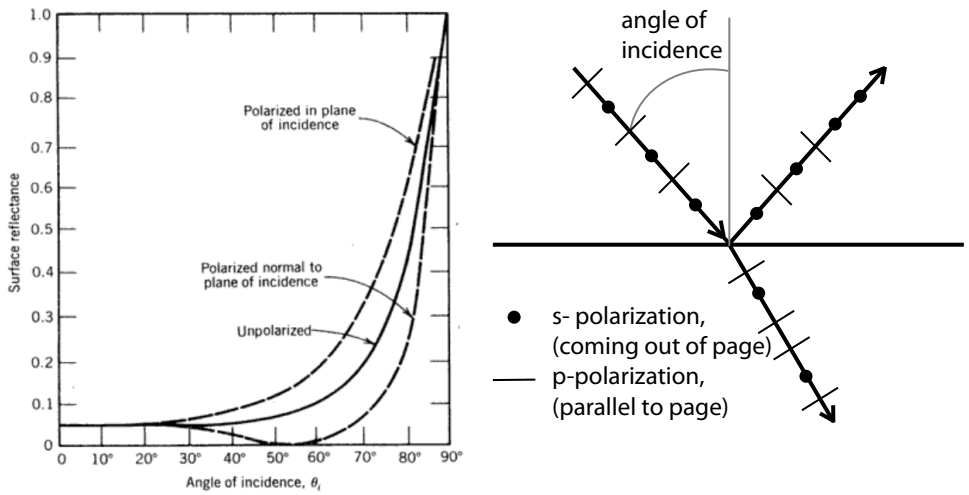

Figure 2.17. Reflectance at an interface comprised of materials with η_1=1 (upper layer of air) and η_2=1.5 (lower layer of glass) for light at one wavelength polarized in the plan of incidence (horizontal or s-pol), normal to the plane of incidence (vertical or p-pol), or unpolarized. The left image was taken from Hecht. [78]

The reflectivity at an interface changes based on the materials optical constants as well as the angle of incidence.

Chapter 3 – General Materials and Methods

3.1 Introduction

Thin film devices consisted of sputtered aluminum and tantalum films that were anodized to form a multilayer point-of-care test operating through visible thin film interference. In most tests, immobilization and sensitivity were analyzed by the resulting visible colour shifts after exposing protein solutions to the alumina surface. Additional analysis techniques were used to increase device knowledge and determine the effects of various parameters on the resulting device. Details of characterization techniques that are introduced include; profilometry, scanning electron microscopy (SEM), ellipsometry, X-ray diffraction (XRD), spectrophotometry, X-ray photoelectron spectroscopy (XPS), and secondary ion mass spectroscopy (SIMS).

3.2 Device Preparation

3.2.1 University of Alberta Nano Fabrication and Characterization Facility (nanoFAB)

The University of Alberta nano fabrication and characterization facility (class 10k and 100k clean rooms) and two sputtering systems were utilized for constructing the multilayer device. Materials used were unprocessed test grade silicon wafer substrates 100 mm in diameter with (100) crystal plane configuration (University Wafer, South Boston, MA). Additionally, hydrogen peroxide (H_2O_2) and sulfuric acid (H_2SO_4) for piranha solution (J.T. Baker, Center Valley, PA), and aluminum and tantalum 7.62 cm (3") sputtering targets of 99.9995% and 99.95% purity respectively (Kurt J. Lesker Company, Jefferson Hills, PA) were used. All other chemicals required were purchased from Thermo Fisher Scientific Inc. (Massachusetts, USA) unless otherwise stated. Standard operating procedures (SOPs) were followed when available (see **Error! Reference source not found.**).

3.2.1.1 Piranha

In initial work Piranha solutions were used to clean wafer substrates in the nanoFAB clean room (class 10k) prior to sputtering. This treatment process removes organics through oxidation to carbon dioxide. The procedure is provided in the Appendix (see section 1.1 Piranha Cleaning SOP). Any tools used throughout the cleaning process were cleaned using

isopropyl alcohol (IPA) to remove particulates. When a piranha clean was complete the subsequent depositions were done within 24 hours. The procedure led to strong adhesion.

3.2.1.2 Sputtering

PVD was used to sputter thin films of tantalum and aluminum on the bare silicon wafer substrates. Specifically, DC magnetron sputtering systems Bob and Floyd (Kurt J. Lesker Company, Jefferson Hills, PA) were used for deposition. The planar magnetron sputtering system Bob (see Figure 3.1) was used for deposition of an optically thick tantalum film (~200 nm) on wafer substrates. A tantalum 7.62 cm (3") sputtering target of 99.95% purity (Kurt J. Lesker Company, Jefferson Hills, PA) was used.

Figure 3.1. Magnetron sputter-up system (Bob) used for the deposition of tantalum onto silicon wafers at the nanoFAB.

The Bob system is manually operated and has one rotating platen at the top of the chamber. The operations protocol is provided in the Appendix (see 1.2 Bob Sputtering System SOP). Specific deposition parameters are as follows. The tantalum target was loaded in gun 2 for consistency. A base pressure of low 10^{-6} Torr was achieved and argon gas was pumped into the chamber to attain a working gas pressure of 7 mTorr with a flow rate of 10.1 sccm. A power density of 6.6 W/cm^2 was applied in constant power mode with a substrate rotation of 20 rpm and a working distance of 12 cm. In this sputter-up system the samples were secured

to a circular platen 40 cm in diameter, shown in Figure 3.2. The desired tantalum thickness of ~200 nm was reached after 24 minutes with a deposition rate of ~8.3 nm/min.

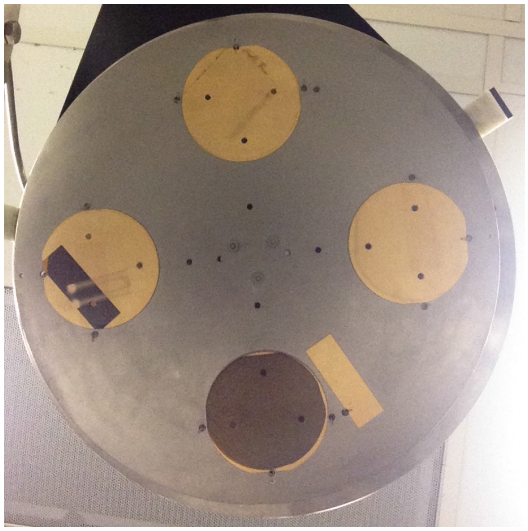

Figure 3.2. Circles show the positions of four 100 mm diameter wafers on the sputter-up platen in the Bob system.

Thickness deviation occurs from the outer edge of the platen towards the center. To maximize device uniformity, wafers were positioned with the flat notch closest to the outer edge and parallel to the outer circumference of the circular sample holder. Aligning substrates in this manner ensures gradients in the tantalum layer that result from the variance in this sputtering system, are consistent from one wafer to the next and are positioned along the length of devices once cleaved. Wafers were stored in the cleanroom until the aluminum deposition was completed to prevent the introduction of surface contaminants.

The second planar magnetron sputtering system Floyd (see Figure 3.3) was used to deposit the overlying aluminum thin film ranging from 20 to 200 nm with a lower tolerance. An aluminum 7.62 cm (3") sputtering target of 99.9995% purity (Kurt J. Lesker Company, Jefferson Hills, PA) was used.

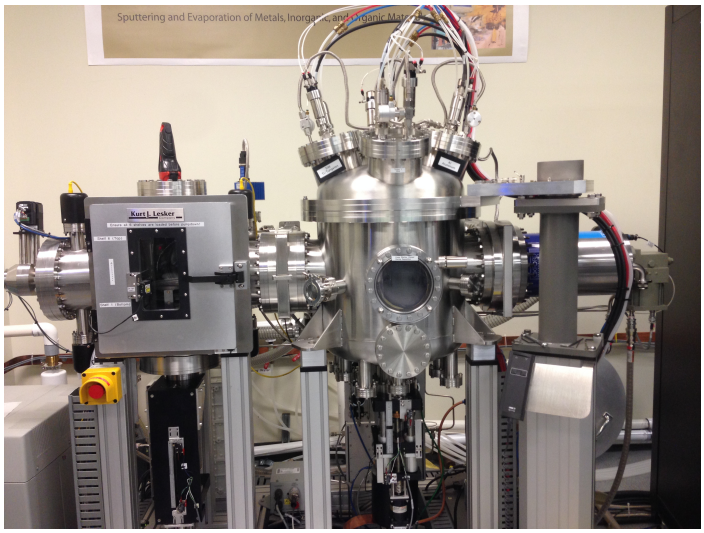

Figure 3.3. Magnetron sputter-down system (Floyd) used for the deposition of aluminum onto wafers previously coated with tantalum.

This system operation is semi-automated using eKLipse software (Kurt J. Lesker Company, Jefferson Hills, PA). The SOP for the system is provided in the Appendix (see 1.3 Floyd Sputtering System SOP). Typically, this system is operated in constant power mode. A base pressure of low 10^{-7} to high 10^{-8} Torr was reached in the process chamber and argon gas pressure was set to 7 mTorr with a flow rate of 55 sccm. A power density of 6.6 W/cm^2 was applied in constant power mode, a substrate rotation of 20 rpm, and a working distance of 12.5 cm with the target positioned at a 15° angle from the platen. To operate the system under constant current mode the operation parameters were similar to those listed above, however, an external power supply was required and an increase in the number of manual operations. Advanced training and understanding of the tool was required for manual operations, which are not included in the attached SOP.

The Floyd sputter-down system contains a load-lock chamber with six platen shelves that are loaded individually into the process chamber for the deposition. Tantalum coated wafers are positioned on a circular platen 16.5 cm in diameter, shown in Figure 3.4. The aluminum deposition rate was between ~9 and 12 nm/min depending on the life of the target, temperature of the target, and the governing mode selected for deposition.

Figure 3.4. The six-platen shelf holder that is loaded into the Floyd load-lock with substrates prior to deposition. The image contains top (left) and side views (right).

Deposition thickness onto wafers in the Floyd system is independent of the position on the platen, as platens are rotated from the center point of the shelf during deposition. Controlled parameters were similar to those during tantalum sputtering. Samples were removed from the chamber and stored until further processing.

3.2.2 Northern Alberta Institute of Technology (NAIT) Fabrication Facility

3.2.2.1 Sputtering

Some tantalum coatings were sputtered on wafer substrates at NAIT using a Materials Research Corporation magnetron sputter system (see Figure 3.5). Silicon wafer substrates were purchased at nanoFAB and supplied to NAIT. Wafers did not undergo cleaning prior to deposition. A tantalum 20.32 cm (8") sputtering target of 99.95% purity (Kurt J. Lesker Company, Jefferson Hills, PA) was used.

Figure 3.5. NAIT magnetron sputter system used for the deposition of tantalum onto wafers.

For tantalum deposition at NAIT a DC planar magnetron sputtering system was used, but the following changes should be noted. This system requires manual operation. Samples were placed in the load-lock one at a time and transferred into the deposition chamber. The tantalum was sputtered onto a static substrate, held parallel to the target. A base pressure in the range of 10^{-6} Torr was achieved in the process chamber prior to sputtering. Argon gas of 99.9995% purity was pumped into the chamber to attain a gas pressure of 10 mTorr with a flow rate of 132 sccm. The power density was maintained at 1.54 W/cm^2 through constant power mode. A working distance of ~7 cm exists between the parallel target and substrates. In this sputter-down system, the samples are placed on a circular platen ~20 cm in diameter. Then the specimens were removed from the chamber and stored in containers until further processing.

3.2.3 Wafer Cleaving

Following deposition of aluminum and tantalum metallic films on wafer substrates, the wafers were cleaved into smaller sizes in Dr. Burrell's lab in the Research Transition Facility. To achieve consistent cleaving of the multilayer wafers a tool was designed using Solid Edge ST8 (©2015 Siemens Product Lifestyle Management Software, Munich, DE) and 3D printed at Cameron Library (Central Academic Building, University of Alberta). A draft of the cleaving tool is shown in Figure 3.6. A flat notch was used along the inner diameter of the tool to orient the wafer in the desired position for cleaving.

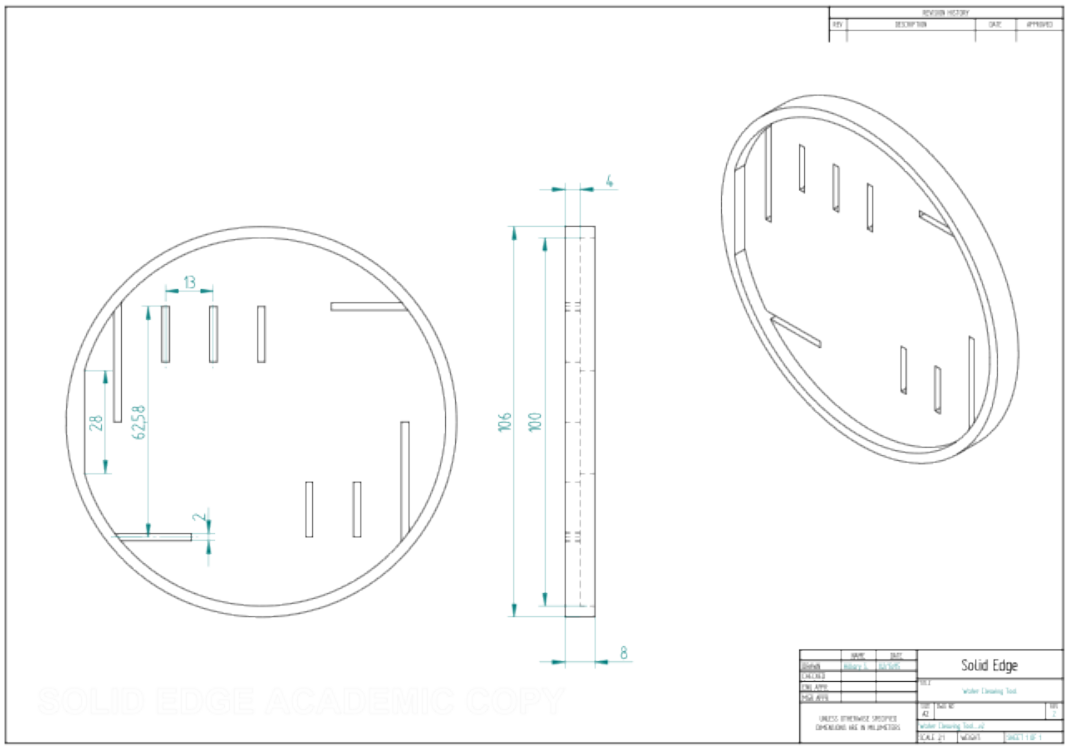

Figure 3.6. Draft of the cleaving tool designed for fracturing wafers along lines parallel and perpendicular to the flat notch along the inner diameter of the tool to create devices of a consistent size.

To cleave the wafer, the 3D printed stencil was placed over the wafer with the deposited layers adjacent to the stencil, and the notch was oriented in the correct location. The wafer and tool were positioned on a flat surface with the cleaving tool on top. A diamond scribe was run along the slots, contacting the deposited layers on the wafer surface with enough pressure to create lines in the surface layer. Next, the wafer was removed from the stencil tool, gripped on either side of the mark, and by applying a small amount of force was cleaved. Lines perpendicular to the notch should be cleaved first, followed by lines parallel to the notch along the edge of the remaining wafer. Rectangular pieces were ~1.3×6.3 cm, with an area of ~8.2 cm^2. Throughout this procedure gloves were worn to minimize surface contamination. The cleaving tool was typically used prior to or following anodizing. In cases when anodizing a full wafer was ideal, the cleaving tool was used subsequent to oxidation.

3.2.4 Electrochemical Oxidation

Electrochemical oxidation was conducted in Dr. Burrell's lab in the Research Transition Facility. One power supply was used throughout trials to control voltage parameters; a

Princeton Applied Research Model 273A Potentiostat/Galvanostat (Ametek® Scientific Instruments, Berwyn, Pennsylvania). The potentiostat monitored current and voltage while maintaining constant applied potential. The potentiostat was used for anodizing samples at ≤10 V. The system was controlled and analyzed using PowerSuite software (Ametek® Scientific Instruments, Berwyn, Pennsylvania) and an accumet™ saturated potassium chloride calomel reference electrode (Thermo Fisher, Waltham, MA) to ensure a consistent and accurate voltage.

Prior to anodization, the thin film sample was rinsed with deionized water. Multilayer thin film samples were dried and placed in the 3D printed holding apparatus and the anodizing cell, shown in Figure 3.7.

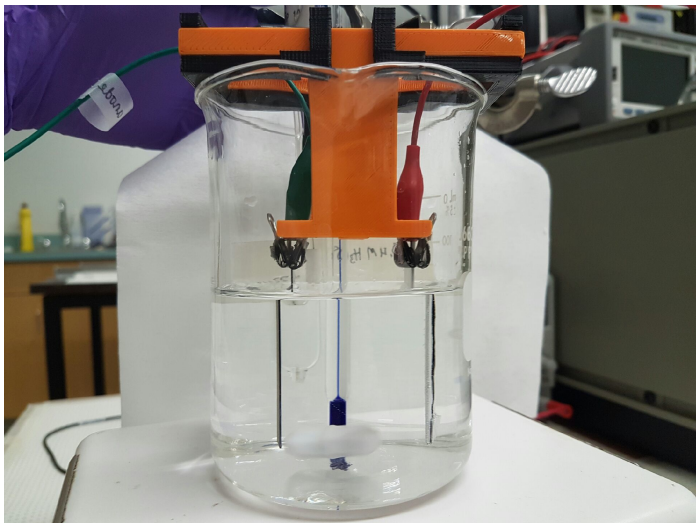

Figure 3.7. The electrochemical cell used for anodization of individual slides. The beaker contains electrolyte, a stir bar, a thermometer, a calomel reference electrode, and the anode and cathode held parallel and 4 cm apart by the 3D printed holder.

For anodization of an individual slide ~300 ml of electrolyte was used at room temperature (20±2°C) in a 500 ml beaker. The most common electrolyte used was 0.4 M phosphoric acid (H_3PO_4) however 0.4 M and 1.0 M concentrations of phosphoric, sulfuric (H_2SO_4), and oxalic acids ($C_2H_2O_4$) were employed for various experiments (o-phosphoric acid, sulfuric acid, and oxalic acid dihydrate: Thermo Fisher, Waltham, MA). Experiments were carried out with a magnetic stir bar set to 300 rpm. The anode, sputtered layers to be oxidized, and cathode, glass microscope slide covered with aluminum foil (Thermo Fisher, Waltham, MA), were held parallel to one another with 4 cm of separation unless otherwise

stated. Different voltages were employed during potentiostatic oxidation with 8 V being the most frequent. In some cases, full wafers were anodized in a 2500 ml beaker with ~1800 ml electrolyte under otherwise identical conditions.

Samples were anodized to one of three different stages of formation depending on the experiment, shown in Figure 3.8. Critical stages include the start of the first linear decline in current density following the equilibrium phase of porous aluminum oxide formation (a), when current density is approximately zero (b), and a constant period of 15 minutes (c).

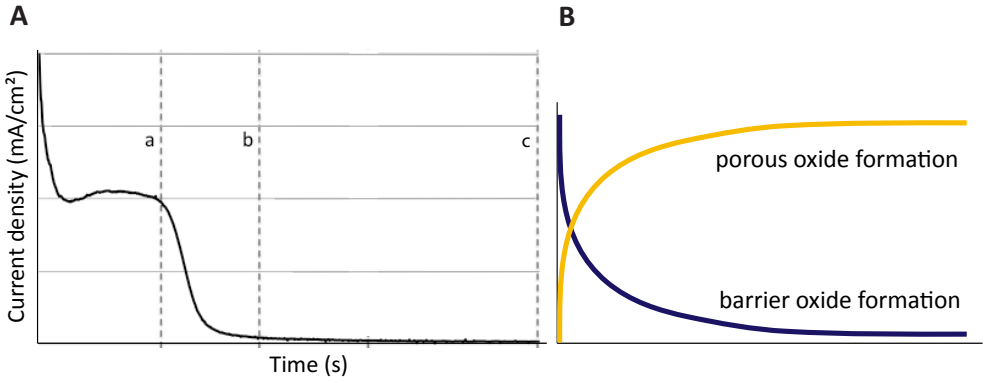

Figure 3.8. Current density as a function of time with (A) critical stages labelled as a, b, and c and (B) current density trends with oxidation generating a porous oxide film and a barrier oxide film.

With a known area and measured current values, current density was monitored and used to determine the stage of oxidation for sample selection. Critical stages selected were based on current density with the exception of stage c. Stage a was governed by initiation of the rapid decline in current density >0.1mA/cm^2 from the plateau where pore formation occurs. Stage b of formation was achieved after a linear decline in current density to <0.07 mA/cm^2 and lastly stage c was achieved after oxidation for a constant period of 15 minutes.

The desired anodization voltage and period of time, if relevant, were input into the PowerSuite software. For stage a and b where the length of time was variable, the process was halted manually when the desired current density was achieved. The anode and cathode were positioned in the holder with the corresponding electrodes attached to each. The reference electrode and stir bar (300 rpm) were positioned in the electrolyte beaker. The holder was lowered into the electrolyte and the anodization process immediately started. Upon completion, the applied potential was turned off and samples were quickly removed from the electrolyte, rinsed thoroughly with deionized water, and dried with oil free compressed air

(Staples®, Framingham, MA). Following chapters will provide specifics of the parameters applied during oxidation if different than those outlined above.

3.3 Protein Exposure and Adsorption

Various protein suppliers were used over the duration of this thesis. Lyophilized purified human prothrombin from citrated human plasma in 20 mM Tris-HCl, 0.1 M NaCl buffer at pH 7.4 and lyophilized affinity purified polyclonal immunoglobulin G (IgG) anti-human prothrombin (rabbit) with 4.5 mg sodium chloride (NaCl) in glycine buffer at pH 7.5 both from Hyphen (Aniara, West Chester, OH) were reconstituted with deionized water and used. These products were discontinued early on in this thesis, so the majority of work was completed with lyophilized human prothrombin in 50 mM Tris-HCl, 50 mM NaCl, 1 mM ethylenediaminetetraacetic acid (EDTA), and 2 mM benzamidine at pH 7.4 from ACOA (Aniara, West Chester, OH) and was reconstituted with deionized water. The replacement antibody was an affinity purified IgG anti-human prothrombin (sheep) in 10 mM 4-(2-hydroxyethyl)-1-piperazineethanesulfonic acid (HEPES), 150 mM NaCl, and 50% (v/v) glycerol at pH 7.4 also from ACOA (Aniara, West Chester, OH). This anti-prothrombin solution required dialysis to ensure minimal binding of anti-prothrombin or excipients to the bare surface. In cases where other proteins were used, details are given in the respective chapters.

To control the surface area exposed, 1 cm diameter hydrophobic circles were created with a Sharpie® marker, shown in Figure 3.9. A 20 µl drop of protein solution at the desired concentration was then pipetted onto the surface within the outlines circle and spread to the edges using the pipette tip. Solutions were left for the desired exposure time in a 100% relative humidity environment at room temperature. To create this environment samples were placed in a Petri dish on a wet cloth. The solution was then removed with a pipette, rinsed with deionized water, and dried with oil free compressed air.

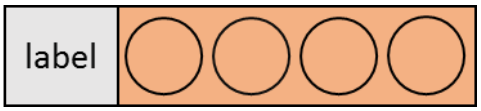

Figure 3.9. Schematic of the 1 cm diameter circles outlined on an anodized slide.

To form an antibody-antigen complex on the surface the same exposure process was complete with the desired concentration of anti-prothrombin on locations where the prothrombin was previously immobilized. Control spots of anti-prothrombin were placed on the bare surface, and in some instances non-specific antibodies were tested on spots with bound prothrombin and the bare surface also. Details on these protein solutions are provided in respective chapters.

In some cases, antibody delivered in solution as opposed to lyophilized, bound to the bare device surface and caused a visible colour shift. In these cases, dialysis into phosphate-buffered saline (PBS) at pH 7.4 eliminated non-specific binding. For dialysis Spectra/por 6 tubing with 10 kDa molecular weight cut-off and 12 mm flat-width (Rancho Dominguez, CA) was used. A known volume and concentration of protein solution was clamped into dialysis tubing and placed in ~300 ml of stirred buffer for 2 to 3 hours. The tubing was transferred into fresh buffer twice and left for 2 to 3 hours in each. The solution was then removed from the tubing and the concentration calculated. Protein solutions were stored at 4°C for use within the week, or aliquot and stored at -80°C for later use.

3.4 Custom Optics Viewing System

In the custom optics system controls were in place to ensure a constant viewing angle of 75° from the surface normal, in turn generating reproducible optical path differences, and illumination. Optical post holders, posts, rails, carriers and bar clamps were secured on a bench plate (all materials: Edmund Optics Inc., Barrington, NJ). The optical components were used to maintain the distance from the surface being analyzed to the light source and the detector.

A tunable white benchtop ScopeLED™ illuminator (Edmund Optics Inc., Barrington, NJ) was used to generate incident light on the slide surface, while tuning the CCT (2700 to 6500 K) and intensity (1 to 8). Parameters were set to a CCT of 5600 K and an intensity of 4 based on preliminary work. A randomized light guide (Dolan-Jenner, Setra Systems Inc.,

Boxborough, MA) with a 0.25" diameter fiber bundle, comprised of 0.55 numerical aperture glass fibers, was secured to the light source. The light guide eliminated the prism effect and mixed the red, green, and blue light. To help obtain saturated colour signals from the device surface a polarizing filter was placed between the slide and the detector, and a system cover was constructed out of white cardstock that acted as a diffuser. Under these conditions the custom viewing system, for capturing images of the slide surface, was highly reproducible.

Images were captured using a phone or digital camera. The detection source was kept consistent throughout each set of experiments. RGB colour coordinates were collected using ImageJ, or an online software, from each surface spot and converted to Yxy coordinates online (http://colormine.org/convert/rgb-to-yxy). The Yxy coordinate system was employed to compare colour shifts. The x and y chromaticity coordinates were plot on CIE diagrams for some experiments to allow for 2D plots of chromaticity coordinates and aid in colour shift interpretation. The colours listed for slides were typically determined using a CIE chart, similar to the one shown in Figure 2.14A, with labelled colour regions. Plotting the chromaticity coordinates from the images of the device surface, determined the region on the CIE chart and ultimately the colour. Statistical analysis was completed on the chromaticity coordinates.

Additionally, visible colour identification was used along with the custom viewing system for unaided colour comparisons. When viewing by eye, the device was positioned along the fold of white cardstock to achieve a white background and viewed at angles near 75° from the surface normal with a polarizing filter.

3.5 Calculating Sensitivities

To determine the limit of detection a statistical analysis between colour coordinates for the prothrombin control and the prothrombin followed by anti-prothrombin solutions of increasing concentrations were compared. The lowest anti-prothrombin concentration showing a statistical significance in the x and y coordinates from the prothrombin coordinates, was determined to be the limit of detection. For the analytical sensitivity the difference between spots with exposed prothrombin followed by anti-prothrombin solutions were compared. The smallest difference in anti-prothrombin concentration showing a statistical significance in both x and y coordinates was determined to be the analytical sensitivity.

3.6 Analytical Techniques

3.6.1 Profilometry

Tantalum and aluminum thicknesses were measured with an Alpha-Step IQ profilometer following the protocol provided in Appendix 2 – Alpha Step IQ Profilometer SOP. Even with frequent profilometer calibration this measurement technique proved to be difficult for achieving accurate and precise thickness measurements at the nanometer scale. For future work alternate techniques such as an optical profilometer and X-ray fluorescence spectroscopy (XRF) should be explored for quantifying thin film thicknesses. The optical profiler uses scanning white light interferometry that requires a scratch or step height in the film of interest, and XRF uses X-ray radiation for excitation and measures the fluorescence radiation for material analysis and thickness measurements. Both techniques are non-destructive and may provide a more accurate method of quantifying the metallic thin film thicknesses.

3.6.2 Scanning Electron Microscopy

Topographic and cross-sectional images were captured for examining surface morphology and layer thickness using a Sigma field emission scanning electron microscope (FESEM)(Carl Zeiss Canada Ltd., Toronto, ON). All SEM images were collected under ultra-high vacuum conditions $<1x10^{-8}$ Torr on prepared samples. For imaging device surfaces and cross-sections, a small portion of the thin film devices were cleaved with a diamond scribe, ~5 by 13 mm, and mounted onto 1 cm diameter aluminum stubs with PELCO Tabs™ (double sided carbon conductive tabs with a 9 mm outer diameter) or PELCO® conductive carbon glue (all materials: Ted Pella Inc., Redding, CA). To image cross-sections, the edge of interest was placed ~1 mm over the side of the stub for best results. Unanodized samples were viewed with an accelerating voltage of 4 keV, an aperture size of 20 μm, and a working distance of ~5 mm. Anodized samples were viewed with an accelerating voltage of 3 keV, an aperture size of 15 μm, and a working distance of ~5 mm. Prepared samples were placed in an airtight holding container and examined shortly after preparation in attempts to minimize sample oxidation and contamination.

Images were mainly captured with the through-the-lens secondary electron detector and analysed using ImageJ open source software (National Institutes of Health, Bethesda, MD,

https://imagej.nih.gov/ij/). Surface and cross-sectional images captured from samples were used for subsequent analysis. Surface pore features were measured along 3 vertical and 3 horizontal lines and thickness measurements were completed at 20 points in each image.

The SEM system integrates the AZtecSynergy system (Oxford Instruments, Abindon, Oxfordshire, UK) with electron backscattered detector (EBSD) and energy dispersive X-ray (EDX) data acquisition. The use of EBSD generates images based mainly on composition. Backscattering occurs when incident beam electrons interact with specimen atoms and are elastically scattered. Numerous deflections can eventually result in electrons exiting the specimen. The likelihood of elastic scattering increases with atomic number, as the nucleus of heavier atoms maintain a greater positive charge, and decreases with increasing electron energy, as the occurrence of a reaction is less likely. These detectors provide elemental mapping and phase identification of local regions of interest identified using the SEM. During analysis with the EBSD, using the NordlysNano detector (Oxford Instruments, Abington, Oxfordshire, UK), the SEM voltage was typically 5 or 10 keV, an aperture of 20 or 15 μm, and a working distance of ~8 mm, which was required for the detector. For EDX, the X-MaxN 150 mm^2 Silicon Drift Detector (Oxford Instruments, Abingdon, Oxfordshire, UK) was used. All EDX data was analyzed using AZtecEnergy EDS software (Oxford Instruments, Abingdon, Oxfordshire, UK)

3.6.3 Ellipsometry

Data collected with a variable angle spectroscopic M-2000V ellipsometer (J.A. Woollam Co., Lincoln, NE) was used to generate thickness, optical constant (refractive index and extinction coefficient), percent void, and standard error values for the final layers. Data was analysed using the CompleteEASE software (J.A. Woollam Co., Lincoln, NE). Psi (ψ) and delta (Δ) values were recorded over wavelengths of 370 to 700 nm at angles of 45, 55, 65, and 75° from the surface normal. The model was constructed layer-by-layer with a bottom-up approach. For each layer Ψ and Δ values were collected and fit to the thin film model with approximate values. When fitting data to the model, thickness and optical constants were varied to achieve the best fit. Optical constants were saved for tantalum and tantala layers and used in subsequent models, until the three layers of tantalum, tantalum oxide, and porous alumina were complete.

Modelling was carried out over the visible spectrum with B-spline, Cauchy, and effective medium approximation (EMA) fittings for the tantalum, tantalum oxide, and alumina layers respectively. For the EMA layer, with materials of alumina and void (i.e. air), an anisotropic Bruggeman EMA model was used. Depolarization constants for the EMA layer were set to x-y plane=0.5 and z plane=0 to correspond to the columnar alumina structure.

3.6.4 X-ray Diffraction

XRD was used to detect microstructural differences in the thin film samples. An Ultimate IV (Cu-source) diffraction system (Rigaku, Scottsdale, AZ) was used with the thin film stage. Data was collected between 10 and 80° 2θ at 5 °/min, using a DHL slit of 10 mm and glancing angle of ω=0.5° unless otherwise stated. JADE 9™ software (Materials Data Inc., Livermore, CA) was used along with International Center for Diffraction Data (Newtown Square, PA) to analyze the scans collected. Peaks in the database were used to match the resulting peaks. Note that no difference was observed with slower scan rates.

3.6.5 Spectrophotometer

The U-3900H Spectrophotometer (Hitachi, Chiyoda, Tokyo, JP) was used to collect reflectance measurements off varying thin film surfaces created with different preparation procedures. Reflectance sample mounts compatible with this system have incident angles of 5 and 45°. With an upgraded system larger angles of incidence that generate optimal interference colours on the device surface could be employed while obtaining spectrum data.

3.6.6 X-ray Photoelectron Spectroscopy

XPS, formerly known as electron spectroscopy for chemical analysis (ESCA), was performed at the University of Alberta nanoFAB by trained technicians. A spectrometer with monochromatized Al K_α ($h\upsilon$=1486.71 eV) (Kratos Analytical Ltd., Manchester, UK) was calibrated with the binding energy of Au $4f_{7/2}$ (84.0 eV) with reference to the Fermi level. During analysis the chamber pressure was $<5x10^{-10}$ Torr. A hemispherical electron-energy analyzer working at a pass energy of 20 eV was used to collect core-level spectra while a survey spectrum in the range of binding energies from 0 to 1100 eV was collected at an analyzer pass energy of 160 eV. After data collection Casa XPS software (© 2018 Casa Software Ltd., Cheshire, UK) was used to complete data processing and analysis.

3.6.7 Secondary Ion Mass Spectroscopy

The time-of-flight (ToF) SIMS IV instrument (IONTOF GmbH, Münster, DE) was used to characterize the thin film device before and after exposure to biologics in attempts to evaluate protein penetration into the pores. SIMS is an extremely sensitive surface analysis technique for ion detection, in parts-per-million for some elements, that provides elemental and molecular information about the multilayer device. Before the SIMS depth profiling experiments, the pressure of the analysis chamber was $<3.75 \times 10^{-9}$ Torr. During depth profiling, Bi^+ ions were operated at 25 keV and used as the analytical source. Cs^+ ions were operated at 500 eV and used as the sputtering source, with an ion current of ~10 nA. Depth profiles were generated by alternating these two ion beams on the samples. The craters sputtered were ~250x250 μm, while a 40x40 μm area in the center of the craters was used for data acquisition. After data collection SurfaceLab 6 software (IONTOF GmbH, Münster, DE) was used to complete data processing and analysis.

3.6.8 Statistics

Statistical analysis was used to compare findings and determine statistically significant differences using IBM SPSS Statistics, Version 24.0 (IBM Corp., Released 2017, Armonk, NY). A Levene's homogeneity of variances test was used to determine if variances were equal between groups. For comparing two independent groups and independent t-test was used. To compare groups ($n>2$) when variances were equal a one-way analysis of variance (ANOVA) test was used and a Tukey post hoc test whereas, when variances were unequal a Welch's t-test was used to compare groups and a Games-Howell post hoc test. A 5% level of significance was used for all tests and plot error bars show standard deviations (SD) unless otherwise stated.

Chapter 4 – The Effect of Anodization Parameters and Aluminum Deposition on the Device Structure and Operation

4.1 Introduction

Studies have demonstrated that anodizing aluminum can produce a wide range of anodic alumina properties and structures. [1] For instance changes in electrolyte pH vary the microstructure (i.e. nanotubes, nanowires), composition and voltage govern the feature dimensions (i.e. structure diameter and wall thickness), and temperature and applied field alter the rates of oxidation and dissolution. Additionally, oxidation time can impact the dissolution and final oxide thickness, and pre or post treatments (i.e. annealing, polishing, cleaning, and etching) can drastically alter the final material. These anodization conditions, among others, play a critical role in the resulting anodic films.

The number of times a sample is anodized influences the formation mechanism and the resulting structure. Electrochemical oxidation can be carried out with a one or two-step process both of which convert aluminum into a porous oxide. Typically, a two-step process is carried out to achieve highly uniform porous membranes, yet a one-step process can also be used to create a less ordered porous film. The first anodization step grows an oxide layer, which creates the resulting structure in a single step process. However, for a two-step process the surface is placed in an acid solution to etch the previously formed oxide and expose the metal layer. The structure of this base metal layer, due to the first anodization process, contains an ordered template to guide formation of the next porous layer. During the second anodization process a highly ordered and uniform porous structure forms. [2,3]

Furthermore, to achieve ordered porous films the applied voltage is dependent on the electrolyte composition. The self-ordering region for sulfuric acid electrolyte is between 19 and 25 V, oxalic acid is between 40 and 70 V, and phosphoric acid is between 160 and 195 V. [4] These voltage regions can change depending on the anodization set up and electrolyte concentrations, as shown for phosphoric acid formed at a voltage of 115 V. [5]

Anodization is governed by constant applied voltage in this work, as opposed to constant current. For pore formation it is useful to apply a constant voltage to achieve the desired pore diameter. [6] Constant current is commonly suggested to prevent a decrease in the applied voltage with oxide layer growth and depends on the concentration, temperature, and

material. However, in this application very thin, low resistance alumina does not stop the current or oxidation process. Furthermore, the underlying tantalum is converted to a tantala barrier layer and halts the process after a consistent thickness has formed.

A number of applications employ anodic alumina films created through a two-step anodization process to achieve highly ordered pores. [7-11] With that said, few studies compare porous alumina formed in one and two-step processes with identical apparatus and parameters. A study by Sulka et al. found that a single oxidation process with anodization in 3.8 M sulfuric acid at 1ºC between 15 and 25 V does not result in ordered porous films, while double and triple oxidation processes generate ordered pores. There was no etching prior to surface analysis, only to remove the oxide layer. [7] A recent comparison of one and two-step processes for anodic titanium oxide nanotubes showed that a two-step process leads to more order and uniformity. [12] However, most two-step methods employ surface pre-treatment, low electrolyte temperatures, and a lengthy initial anodization time[13,14] making it difficult to conclude which condition allows for improved pore order.

Two-step anodization processes with low applied voltages have resulted in uniform pore distribution. Work by León-Patiño et al. used 1.0 to 1.5 M sulfuric acid between 10 and 20 V for both oxidation processes. No pre-treatment was completed and the final anodization step of 24 hours created at 20 μm film. [15] A pore widening step was complete in 0.9 M phosphoric acid at 32ºC for 10 minutes. [16] Work by Bwana used 0.4 M sulfuric acid at 15ºC between 5 and 25 V. Sputtered 2 μm films were electropolished prior to oxidation and anodized for 30 minutes. [17] Additional works using two-step processes at self-ordering voltages were reported with oxidation in sulfuric, [18-22] oxalic, [10,11,13,14,23-26] and phosphoric acids. [6-9] Mixed electrolyte solutions have also been used.[27]

A study by Voon et al. demonstrates a one-step process for the synthesis of ordered porous alumina films to oxidize a polished aluminum film in 0.3 M oxalic acid at 15ºC at 50 V for 60 minutes. Post etching in a chromic and phosphoric acid mixture enhanced the uniformity by revealing the underlying metal surface. [28] Increasing the length of oxidation will eventually create a uniform pore distribution at an underlying layer by controlling the depth of feature growth into the oxide layer through a stress gradient. [23] Anodic films with irregular pore distribution contain higher compressive stress in high pore density areas and lower stress in areas where the pore density decreases Therefore, prolonged anodization or a post etching

treatment to remove the surface layer is likely to reveal a more uniform pore distribution. Chemical etching with a combination of 0.6 to 1.7 M phosphoric and 0.2 to 1.0 M chromic acids at a temperature of 55ºC was found to be optimal for etching. [47] However, other ratios and temperatures can be employed.[2]Work by Zhang et al. showed that even with subsequent pore widening, anodic alumina films from two-step processes were more uniform than those from one-step processes and continued to improve with longer first anodization times. [29]

Minimal work has been completed to date on single step anodization of aluminum in phosphoric, sulfuric, and oxalic acid electrolytes at low voltages, let alone on sputtered aluminum films in the nanometer thickness range. The following are one-step processes in relevant electrolytes that lead to acceptable pore order. Ono and Masuko conducted work on anodization in sulfuric, oxalic, phosphoric, and chromic electrolytes, at temperatures between 20 and 40°C, and applied voltages between 1 and 40 V. Aluminum sheets were utilized and no pre or post oxidation treatment was carried out. [30] In addition, Yim et al. oxidized evaporated aluminum films in 0.3 and 6 M sulfuric acid between 5 and 37°C with the voltage ranging from 10 to 60 V. Post treatment pore widening was completed. [31] Work by De Laet et al. in 0.4 M phosphoric acid at 35°C under constant current density, with a steady state voltage <25 V, and resulted in an ordered array with 50 nm pores. [32] Single oxidation processes in sulfuric, oxalic, and phosphoric acid electrolytes are commonly carried out at 30 V or higher. [32,33] Testing anodization parameters in the experimental apparatus, governed by a constant low voltage at room temperature, will provide insight on the resulting device structures and changes in the thin film interference that result.

The purpose of this study was to determine the effect of different anodization conditions on the device generated from a one-step process on sputtered aluminum-tantalum thin films with no pre or post anodization treatments. Electrolyte type and concentration, voltage, and initial aluminum deposition energy and time were varied, and parameters of the device layers were analyzed. It is important that 1) the alumina surface layer refractive indices are in the proper range and can be finely tuned to the refractive indices of the analyte to prevent scatter at this interface, 2) that the pore diameter is large enough to achieve the desired refractive index, yet small enough to prevent the analyte from diffusing deep into the porous alumina film, and 3) the tantala and tantalum interface creates minimal scatter at the interface and

leads to strong visible colour. By developing a better understanding of the key factors that impact this specific anodization process and the device characteristics, a higher degree of tunability can be achieved.

4.2 Materials and Methods

See Chapter 3 – General Methods and Materials for details on device preparation and analysis techniques. Unless otherwise stated anodization was carried out until the end of tantala formation (stage b).

4.2.1 Electrolyte Type and Concentration

The tantalum and aluminum layers were deposited at the nanoFAB. Tantalum deposition (~200 nm) was followed by an aluminum deposition for 770 seconds at ~10.8 nm/min, resulting in an initial aluminum thickness of ~138 nm. Multilayer films were anodized in 0.4 and 1.0 M phosphoric, sulfuric, and oxalic acid electrolytes at 8 V. Tantalum thin films were anodized without the surface aluminum layer to assess the resulting structure and colour formed with an applied potential of 8 V in each electrolyte. All slides created were imaged with *s* and *p*-polarization. Applied Potential

Sputtered tantalum and aluminum films were deposited in the nanoFAB systems. Tantalum deposition (~200 nm) was followed by an aluminum deposition for 560 seconds at ~10.8 nm/min, resulting in aluminum thicknesses of ~101 nm. Oxidation was conducted in 0.4 M phosphoric acid at 2, 5, 8, and 10 V. Plots were modelled with linear trendlines, or order 2 or 3 polynomial trendlines depending on the parameter.

4.2.2 Current Density

Sputtered tantalum films were deposited in the NAIT system and aluminum films in the nanoFAB system. Tantalum was ~200 nm and aluminum films were 109.2±4.7 nm, 115.0±4.6 nm, and 117.0±4.1 nm. Anodization was carried out in 0.4 M phosphoric acid under potentiostatic conditions at 8 V until stage b of formation.

4.2.3 Sputtered Aluminum Thickness

Tantalum films (~200 nm) were deposited in the NAIT system and aluminum films were deposited in the nanoFAB system for varying lengths of time between 580 and 750 seconds.

4.2.3.1 Part A – Aluminum Deposition in Constant Power Mode

Tantalum depositions took place and wafers were stored under atmospheric conditions for up to 5 months. Aluminum depositions took place at an argon pressure of 7 mTorr and a constant power of 300 W applied at a power density of 6.6 W/cm^2 (current=0.72 mA, voltage=420 V). Tantalum and aluminum layers were deposited at average rates of 66.2±0.91 nm/min and 10.7±0.31 nm/min, respectively. Aluminum slides were deposited for 580, 620, 660, 680, 700, and 720 seconds. Subsequent processes of anodization and ellipsometry were completed within a week and after seven months, respectively.

4.2.3.2 Part B – Aluminum Deposition in Constant Current Mode

Tantalum depositions took place and wafers were stored under atmospheric conditions for 13 months. Aluminum depositions took place at an argon pressure of 7 mTorr and constant current of 0.72 mA applied at a power density of 6.0 W/cm^2 (power=275 W, voltage=380 V). Tantalum and aluminum layers were deposited at average rates of 65.9±0.9 nm/min and 10.3±0.4 nm/min, respectively. Subsequent processes, anodization and ellipsometry, were carried out within 24 hours of the prior step.

4.2.4 Analysis

Profilometry measurements were used to determine the aluminum film thickness. SEM images were captured and analyzed to measure pore diameter, wall thickness, and interpore spacing of surface alumina films. Ellipsometry data was captured from devices composed of anodic alumina, anodic tantala, and tantalum. Modeling generated mean standard error (MSE), thickness, refractive index, and percent void of the device films.

The anodized slides were viewed at 75° from normal through a polarizing lens. Images were captured using a phone or digital camera. For images analyzed with colour coordinates, a

custom optics system with controlled lighting and angle was used for improved interference colour visibility and reproducibility.

A UV-VIS spectrophotometer was employed with a 45° sample mount to collect the reflectivity across the visible spectrum. To achieve the reflectivity of horizontally polarized (*s*-pol) and vertically polarized (*p*-pol) light a polarizer was positioned in the desired orientation before the detector.

Statistical analyses were completed with SPSS. A Levene's equality of variance test was complete for each data set.

4.3 Results

4.3.1 Electrolyte Type and Concentration

Current density as a function of time is shown in Figure 4.1 for anodization at 8 V in 0.4 M and 1.0 M solutions of (a) phosphoric, (b) sulfuric, and (c) oxalic electrolytes.

a)

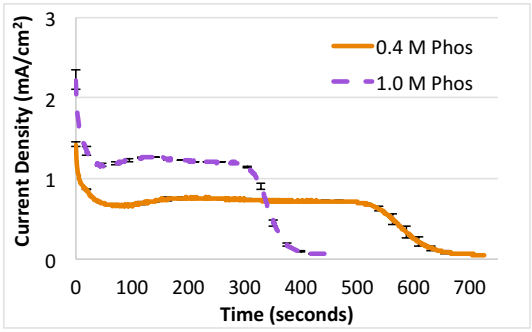

b)

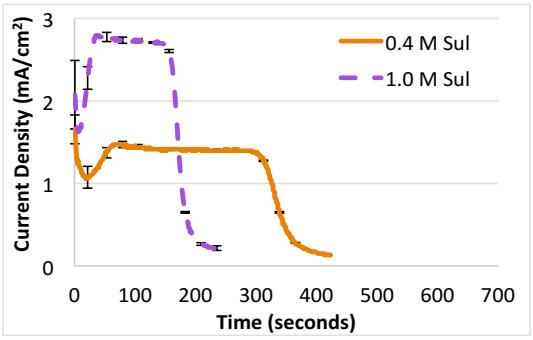

c)

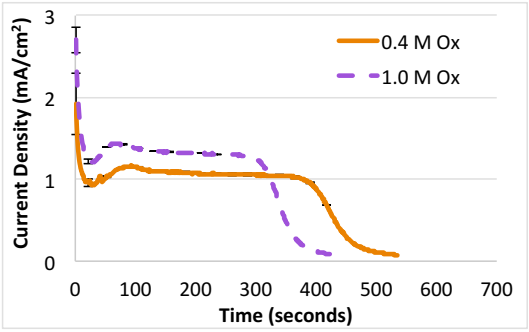

Figure 4.1. Current density as a function of time during anodization in 0.4 M and 1.0 M solutions of (a) phosphoric (Phos), (b) sulfuric (Sul), and (c) oxalic (Ox) acid electrolytes at 8 V.

Changes in the current density and length of anodization vary with electrolyte composition. All electrolytes showed an increase in the rate of oxidation with concentration. Table 4.1 shows current density and time values at critical stages of oxidation.

Table 4.1. Summary of average current density (J) and time values for critical oxidation points. Devices were formed in 0.4 M and 1.0 M solutions of phosphoric, sulfuric, and oxalic acid electrolytes at 8 V.

Electrolyte Type and Concentration		Minimum Before Plateau		Middle of Plateau		Final	
		J (mA/cm^2)	Time (s)	J (mA/cm^2)	Time (s)	J (mA/cm^2)	Time (s)
Phosphoric Acid	**0.4 M**	0.66	83	0.7	300	0.05	725
	1.0 M	1.16	51	1.2	201	0.06	446
Sulfuric Acid	**0.4 M**	1.06	16	1.4	176	0.13	381
	1.0 M	1.63	5	2.7	76	0.17	219
Oxalic Acid	**0.4 M**	0.92	25	1.1	225	0.07	481
	1.0 M	1.21	23	1.3	201	0.08	386

SEM images were captured of devices anodized in each electrolyte composition of interest. Topographic images are shown in Figure 4.2 and cross-sectional images 45° from normal are shown in Figure 4.3.

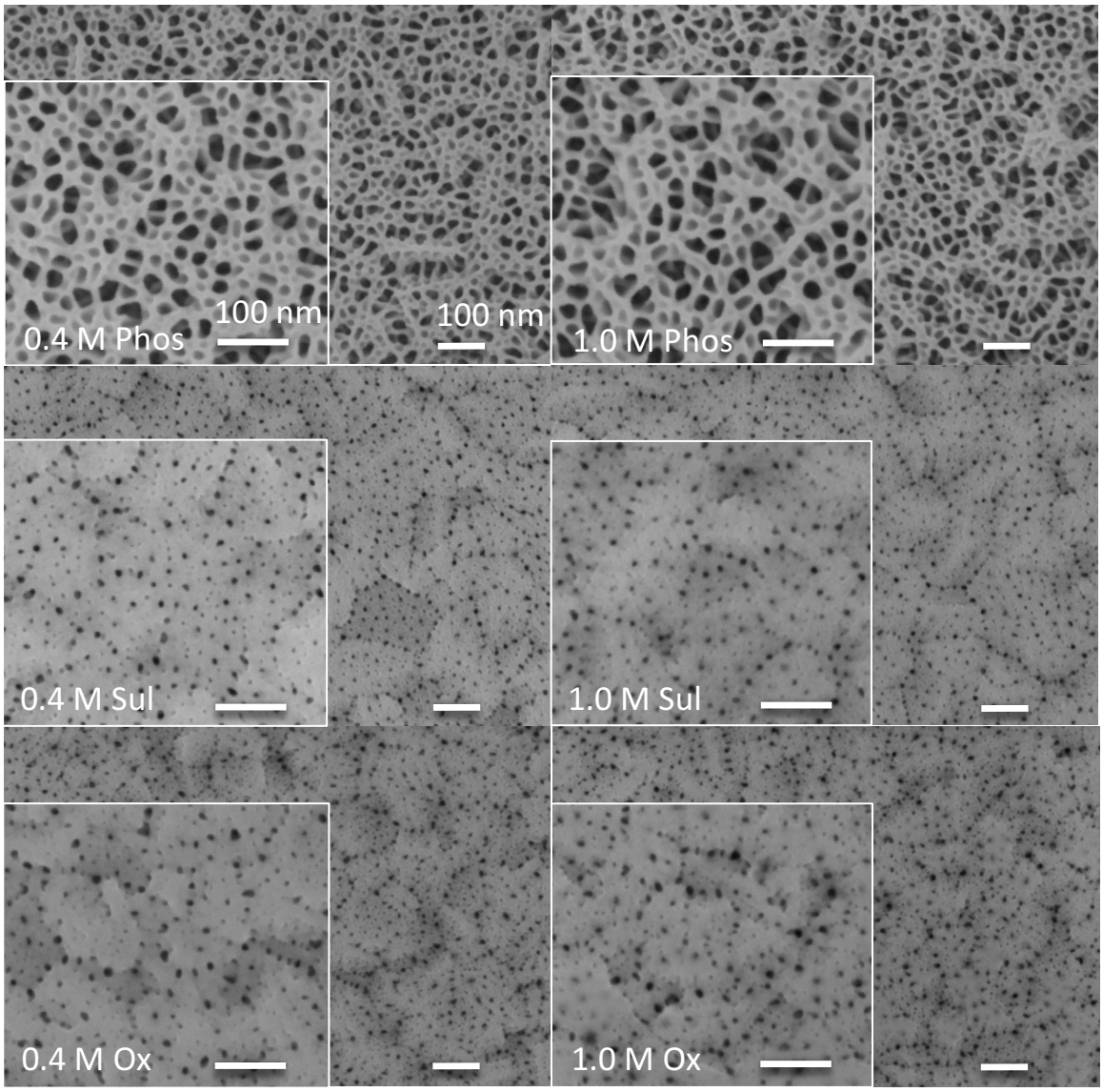

Figure 4.2. SEM images of alumina surfaces anodized in 0.4 M and 1.0 M solutions of phosphoric (Phos), sulfuric (Sul), and oxalic (Ox) acid electrolytes at 8 V. Scale bars show 100 nm at different magnifications.

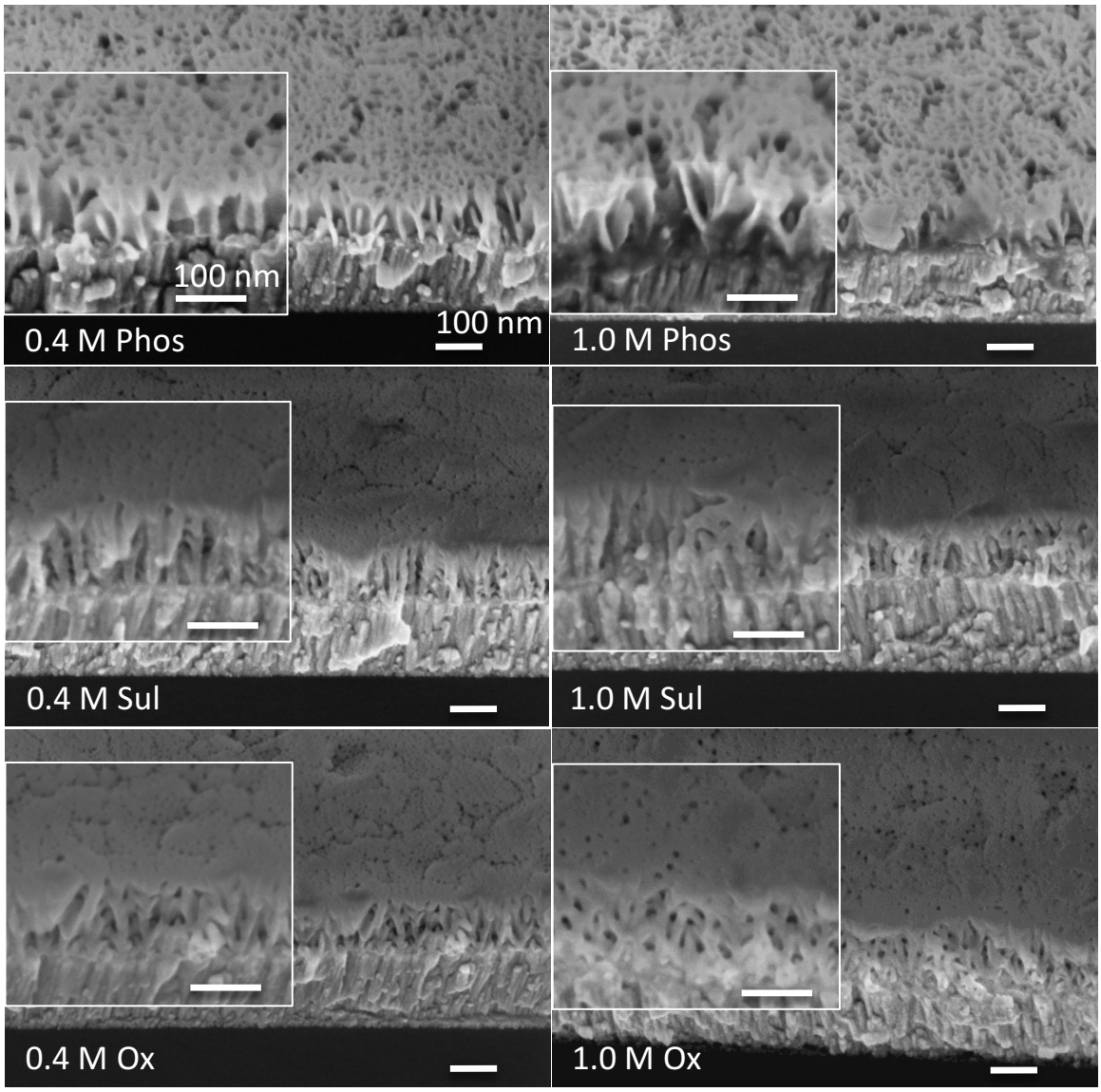

Figure 4.3. SEM images 45 °from the sample surfaces anodized in 0.4 M and 1.0 M solutions of phosphoric (Phos), sulfuric (Sul), and oxalic (Ox) acid electrolytes at 8 V. Scale bars show 100 nm at different magnifications.

The phosphoric acid electrolyte creates an alumina layer that is highly porous with noticeable surface etching. Samples anodized in sulfuric or oxalic acid electrolytes result in wavy, dense, columns and significantly lower alumina surface porosity with small pores that are predominant along grain boundaries. SEM images of alumina surfaces formed in different electrolytes were used to measure the average pore diameter, wall thickness, and interpore spacing, listed in Table 4.2.

Table 4.2. Parameters measured from SEM images for samples anodized in 0.4 M and 1.0 M of phosphoric, sulfuric, and oxalic acid electrolytes at 8 V.

Electrolyte Type and Concentration		Pore Diameter ± SD (nm)		Total Wall Thickness ± SD (nm)		Interpore Spacing ± SD (nm)	
Phos Acid	**0.4 M**	18.3	5.3	10.2	2.2	28.1	4.1
	1.0 M	19.1	5.9	9.3	1.9	29.4	4.2
Sul Acid	**0.4 M**	5.8	1.4	17.2	5.1	24.1	5.8
	1.0 M	6.4	1.5	14.3	3.7	23.1	4.6
Ox Acid	**0.4 M**	6.5	2.2	15.6	6.3	21.4	6.3
	1.0 M	6.5	1.9	14.8	5.8	21.9	5.4

Figure 4.4 shows trends in pore diameter, total wall thickness, and interpore spacing that result with oxidation in different electrolyte compositions.

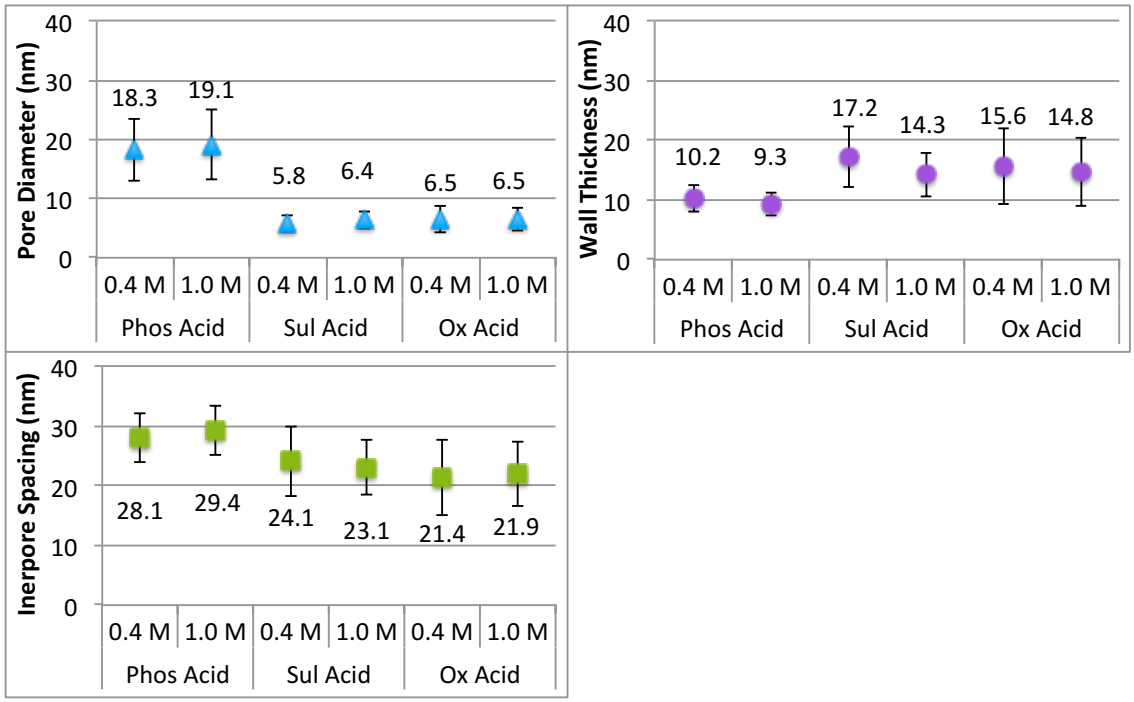

Figure 4.4. Changes in feature sizes with anodization in different electrolyte compositions.

Films formed in phosphoric acid show larger fluctuations in pore diameter and smaller fluctuations in wall thickness, whereas sulfuric and oxalic electrolytes demonstrate opposite trends. Anodizing using phosphoric acid created pore sizes twice as large as the sulfuric and oxalic electrolytes ($p<.001$). The samples created in sulfuric and oxalic acids had greater surface area with smaller pores and larger wall thicknesses ($p<.001$).

Ellipsometry results from samples anodized in different electrolyte compositions are shown in Table 4.3.

Table 4.3. Parameters measured from ellipsometry for samples anodized in 0.4 M and 1.0 M of phosphoric, sulfuric, and oxalic acid electrolytes at 8 V.

Electrolyte Type and Concentration		Tantala Thickness ± SD (nm)		Alumina Thickness ± SD (nm)		Percent Alumina ± SD (%)		Alumina Refractive Index (min & max)		MSE
Phosphoric Acid	**0.4 M**	15.1	0.8	122.8	0.4	46.8	1.5	1.35	1.39	13.4
	1.0 M	15.2	0.2	125.9	0.2	41.8	1.0	1.31	1.35	12.3
Sulfuric Acid	**0.4 M**	3.9	0.1	168.4	5.4	82.1	4.2	1.56	1.62	6.2
	1.0 M	6.3	0.2	177.3	3.5	80.1	3.1	1.55	1.61	13.5
Oxalic Acid	**0.4 M**	8.1	0.4	149.4	1.8	82.0	2.0	1.56	1.61	11.2
	1.0 M	6.9	0.3	160.2	2.7	79.3	2.7	1.55	1.60	10.9

Figure 4.5 depicts the trends for (a) tantala and alumina thicknesses, (b) percent alumina present at each surface, and (c) alumina layer refractive indices from data in Table 4.3.

a)

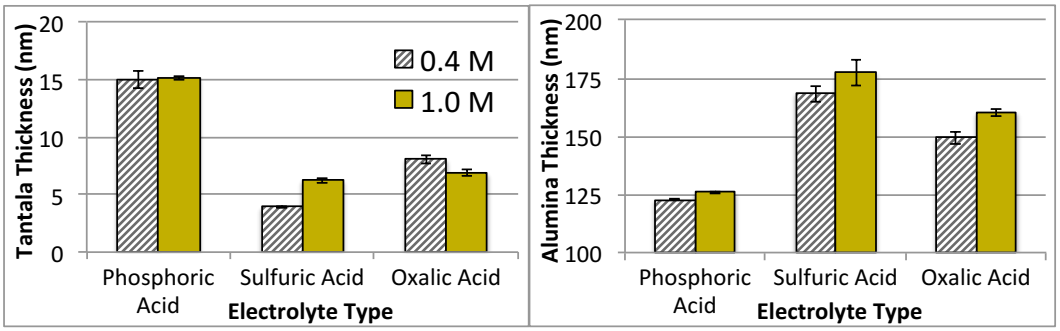

b)

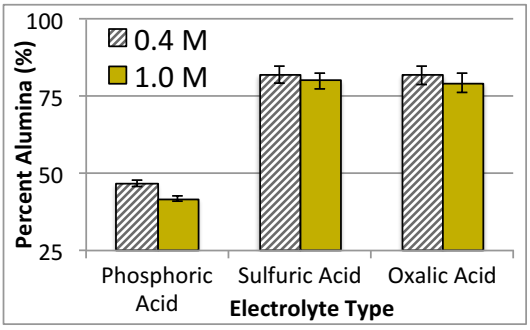

c)

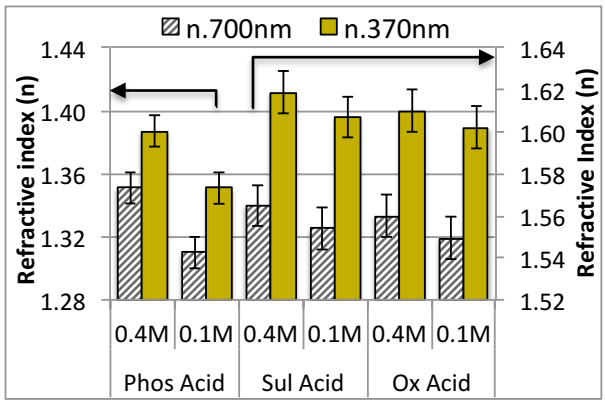

Figure 4.5. Variability in the (a) tantala and alumina thicknesses, (b) percent alumina at each surface, and (c) alumina layer refractive indices of samples anodized in 0.4 M and 1.0 M solutions of phosphoric (Phos), sulfuric (Sul), and oxalic (Ox) acid electrolytes at 8 V.

Notable differences were found between parameters of films created in phosphoric acid versus sulfuric and oxalic acids. Visible surface colours were assessed to better understand the device interference. Anodic tantala on tantalum and the alumina/tantala/tantalum structures were both analyzed. Figure 4.6 shows the anodic tantala formed in each electrolyte viewed with horizontal and vertical polarization at (a) ~75º and (b) ~5º from normal.

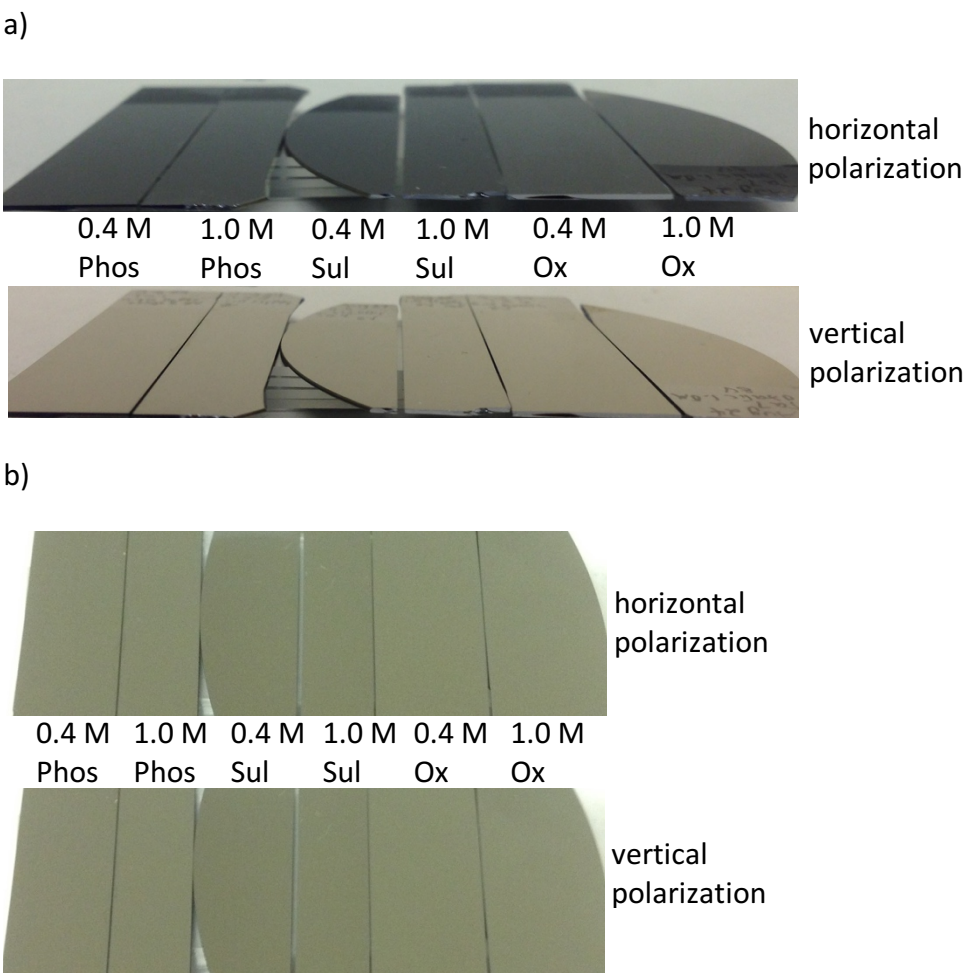

Figure 4.6. Anodic tantala on tantalum formed in each electrolyte composition at 8 V. Surfaces were viewed with horizontal and vertical polarization at (a) ~75° and (b) ~5° from normal.

Additionally, Fresnel equations were used to produce theoretical reflectivity values at 5°, 45°, and 75° for both polarization states and are listed in Table 4.4. A tantala refractive index of 2.5 was applied for calculations and tantalum theoretical R_s and R_p values at each angle were used.

Table 4.4. Fresnel equations were used to calculate the reflectivity of horizontally and vertically polarized light off the anodic tantala and tantalum surface and varying angles of incidence.

Surface	Angle of Incidence	Total R_s at Surfaces	Total R_p at Surfaces
Tantala	5°	17	17
Tantalum		13	9
Tantala	45°	28	8
Tantalum		10	12
Tantala	75°	62	4
Tantalum		2	9

Ellipsometry data for anodic tantala films formed at 8 V films is shown in Table 4.5 along with spectrophotometry data in Figure 4.7 for films formed in each electrolyte.

Table 4.5. Ellipsometry measured values of anodic tantala layers formed in electrolytes at 8 V.

Electrolyte Type and Concentration	Tantala Thickness ± SD (nm)		Tantala Refractive Index (min and max)		MSE ± SD	
Phosphoric Acid	12.0	0.4	2.03	2.58	3.58	0.23
Sulfuric Acid	10.3	0.3	2.57	3.02	5.51	0.37
Oxalic Acid	12.1	0.6	2.12	2.63	4.05	0.15

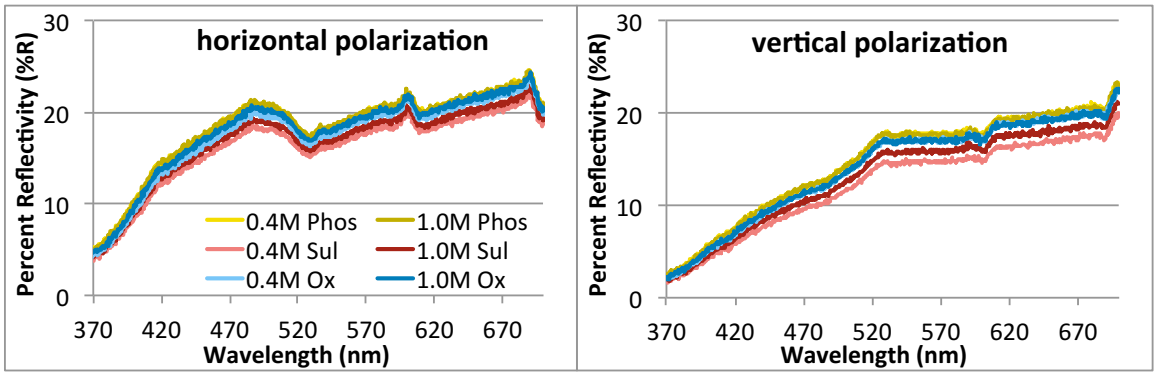

Figure 4.7. Spectrophotometric data from the surface of tantalum oxide films formed at 8 V in 0.4 and 1.0 M phosphoric (Phos), sulfuric (Sul), and oxalic (Ox) acid electrolytes. Reflections were captured at 45° from normal to the surface. (n=2)

Visible surface interference colours for the multilayer device were captured for samples anodized in each acid with horizontal and vertical polarization, shown in Figure 4.8.

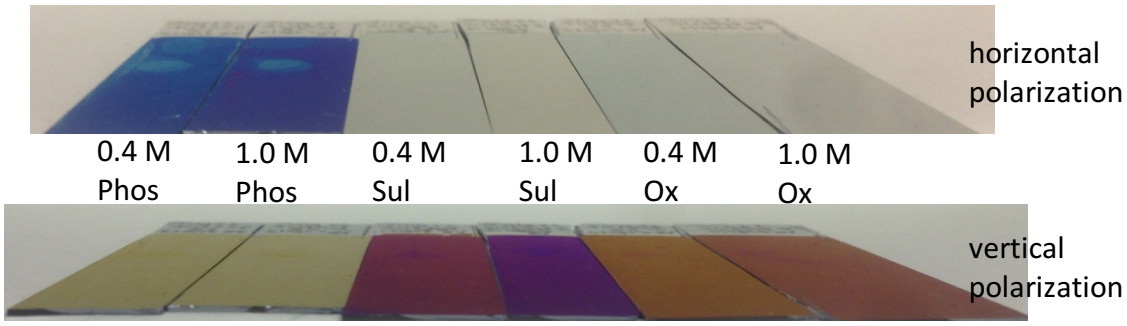

Figure 4.8. Samples anodized in different electrolyte solutions at 8 V viewed through a polarizing filter for horizontal and vertical polarization at ~75 ° from normal.

Slides anodized in phosphoric acid when horizontally polarized produce a blue surface colour, whereas the vertically polarized interference produces a yellowish-gold surface colour. Devices created in sulfuric and oxalic acids with horizontal polarization generate a mirror like, colourless, surface and with vertical polarization produces a red/purple and tan/orange, respectively. The change in concentration altered the alumina thickness more than the refractive index, changing the OPL and shifting the colour. The devices generated visible colour contrast that was optimal in one polarization, regardless of the concentration.

Colour shifts in Figure 4.8 are confirmed with spectrophotometric reflectivity data in Figure 4.9. Data was collected at 45° from the surface.

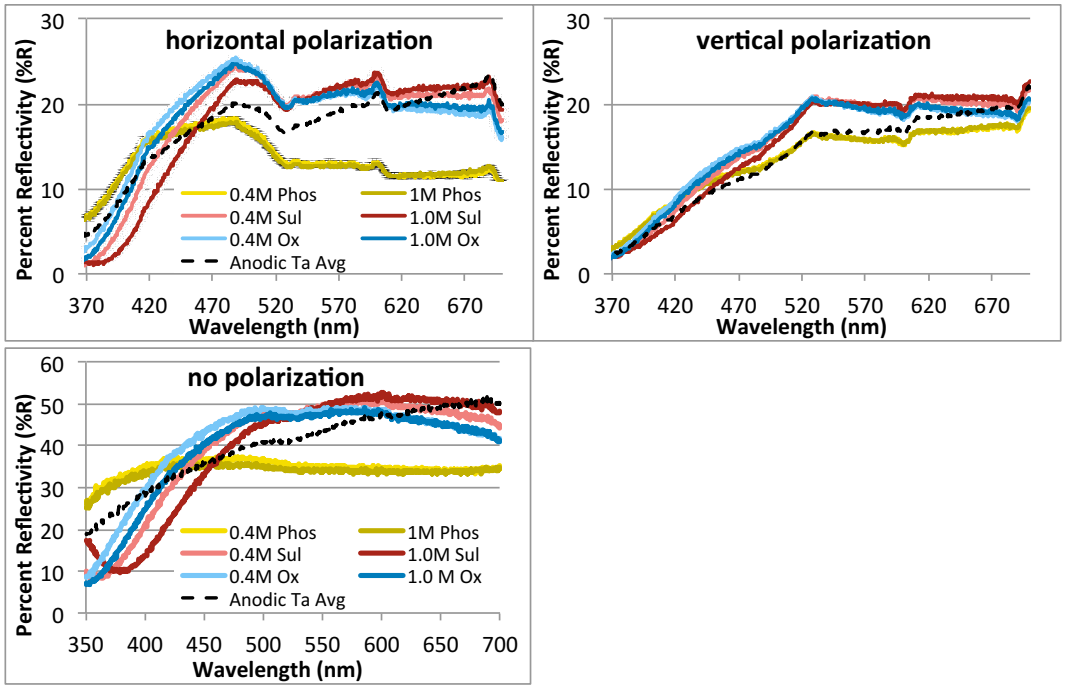

Figure 4.9. Reflectivity data with horizontal, vertical, and no polarization for device surfaces prepared with anodization at 8 V in 0.4 and 1.0 M solutions of phosphoric (Phos), sulfuric (Sul), and oxalic (Ox) electrolytes. Reflections were captured at 45° from normal to the surface.

Fresnel calculations were used to show R_s, R_p, and R in the multilayer system and an anodized tantalum model. A tantalum refractive index of 2.5 was used along with measured reflectivity values in difference polarization states and angles of incidence. An alumina refractive index of 1.35 was used for films created in phosphoric (Phos) acid and 1.58 for films created in sulfuric (Sul) and oxalic (Ox) acid.

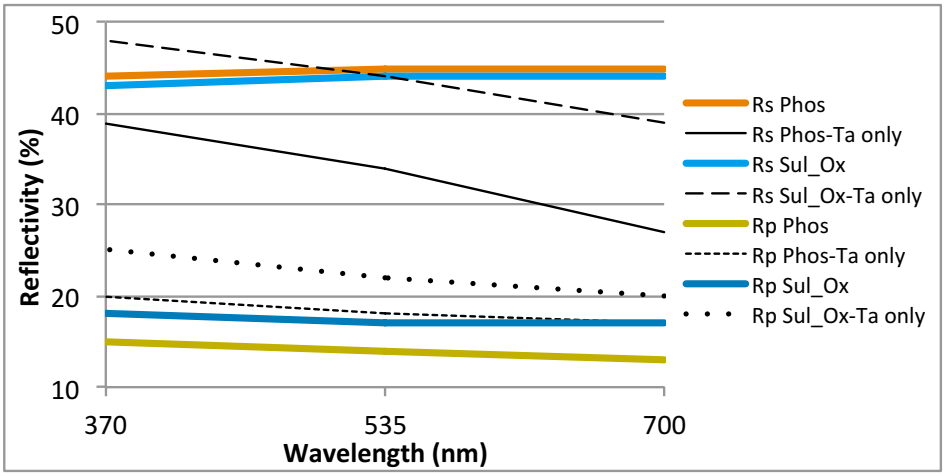

Figure 4.10. Theoretical R_s and R_p values are shown for alumina/tantala/tantalum and tantala/tantalum (labelled Ta only) devices. The refractive indices of the alumina and tantala films created in phosphoric, sulfuric, and oxalic electrolytes were used in the equations. Fresnel equations were used and a viewing angle of 45°.

Table 4.6. A comparison of the reflectivity values obtained with experimental (spectrophotometer) and theoretical (Fresnel equation) techniques.

Electrolyte	Measurement	Rs (%)	Rp (%)	R (%)	Ratio of Spec. R to Fresnel R (%)		
Phos	Spectrophotometer	12	17	35	27%	121%	59%
	Fresnel Equations	45	14	59			
Sul & Ox	Spectrophotometer	23	21	48	52%	124%	79%
	Fresnel Equations	44	17	61			

Based on the spectrophotometer data at a wavelength of ~520 nm the reflectivity for surfaces prepared in sulfuric and oxalic acids reaches a maximum of 48%, whereas surfaces prepared in phosphoric acid reach a maximum of 35%. These values are lower than the theoretical reflectivity values calculated using Fresnel equations.

4.3.2 Applied Potential

Specific attention was given to anodization in phosphoric acid electrolyte at voltages known to result in nanometer scale surface pores. Figure 4.11 shows representative the current density plots for constant aluminum and tantalum thickness devices anodized at 2, 5, 8, and 10 V.

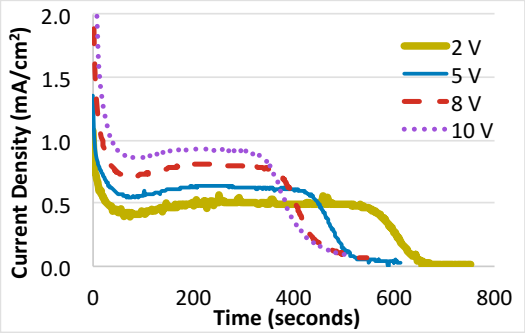

Figure 4.11. Current density as a function of time for samples anodized at 2, 5, 8, and 10 V.

Samples anodized at higher voltages achieve a higher current density during pore formation, reaching stage b faster than samples anodized at lower voltages. Topographic SEM images are shown in Figure 4.12 and cross-sectional images 45° from normal are shown in Figure 4.13 for devices anodized at applied potentials of 2, 5, 8, and 10 V.

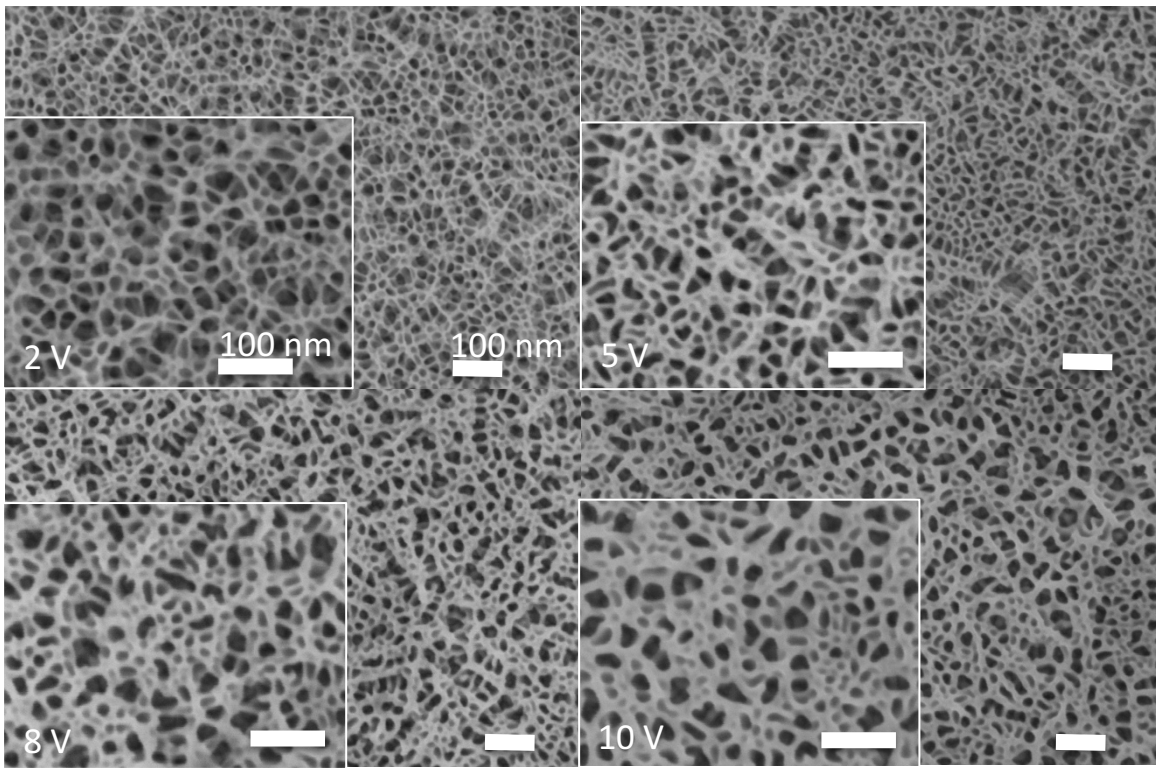

Figure 4.12. SEM images of alumina surfaces anodized in 0.4 M phosphoric acid at 2, 5, 8, and 10 V. Scale bars show 100 nm at different magnifications.

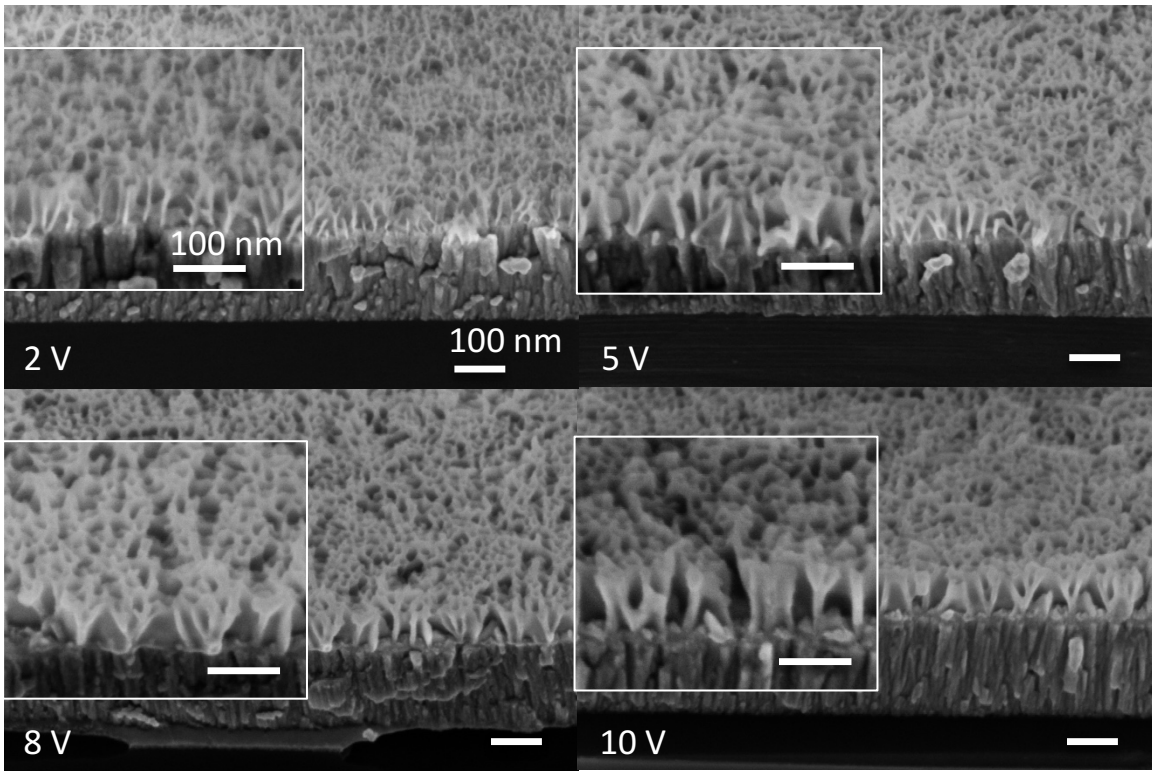

Figure 4.13. SEM images 45° from the sample surfaces anodized in 0.4 M phosphoric acid at 2, 5, 8, and 10 V. Scale bars show 100 nm at different magnifications.

SEM topographic images of alumina were used to measure the average pore diameter, total wall thickness, and interpore spacing, listed in Table 4.7 and depicted in Figure 4.14.

Table 4.7. Parameters measured from SEM topographic images for samples anodized in 0.4 M phosphoric acid electrolyte at applied potentials of 2, 5, 8, and 10 V.

Applied Potential During Anodization	Pore Diameter ± SD (nm)		Total Wall Thickness ± SD (nm)		Interpore Spacing ± SD (nm)	
2 V	15.5	4.8	7.3	1.7	22.8	5.1
5 V	14.4	4.3	8.2	1.6	22.6	4.6
8 V	20.8	6.6	9.2	1.8	30.0	6.8
10 V	21.9	6.9	9.6	2.1	31.5	7.2

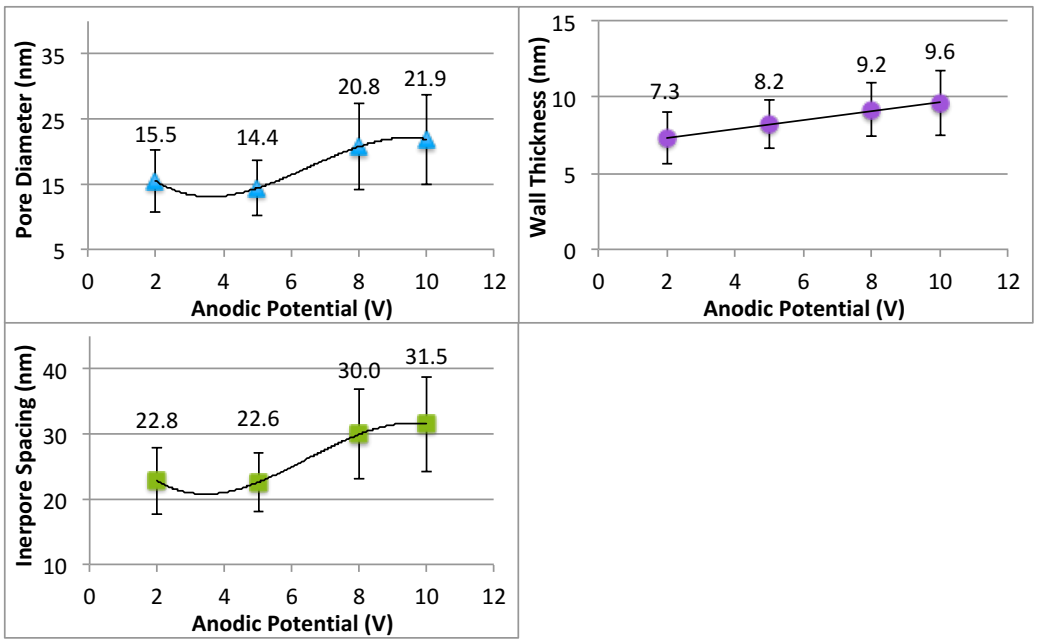

Figure 4.14. Variability in feature sizes with different applied potentials during anodization in 0.4 M phosphoric acid. (n=2)

Pore size and interpore distance follow the same trend with a local minimum at ~4 V, whereas the wall thickness linearly increases with voltage. Ellipsometry results of samples anodized at various applied potentials are shown in Table 4.8 and depicted in Figure 4.15.

Table 4.8. Summary of ellipsometry analysis for multilayer devices created with anodization in 0.4 M phosphoric acid electrolyte at 2, 5, 8, and 10 V.

Applied Potential During Anodization	Tantala Thickness ± SD (nm)		Alumina Thickness ± SD (nm)		Percent Alumina ± SD (%)		Alumina Refractive Index at 500nm ± SD (η)		MSE
2 V	4.0	0.6	76.0	0.4	35.5	0.9	1.28	0.01	4.3
5 V	7.6	0.5	85.5	0.2	45.3	0.4	1.35	0.01	5.4
8 V	10.9	0.5	84.7	0.4	49.8	0.8	1.38	0.01	8.1
10 V	14.6	0.3	83.6	0.2	53.5	0.5	1.40	0.01	6.5

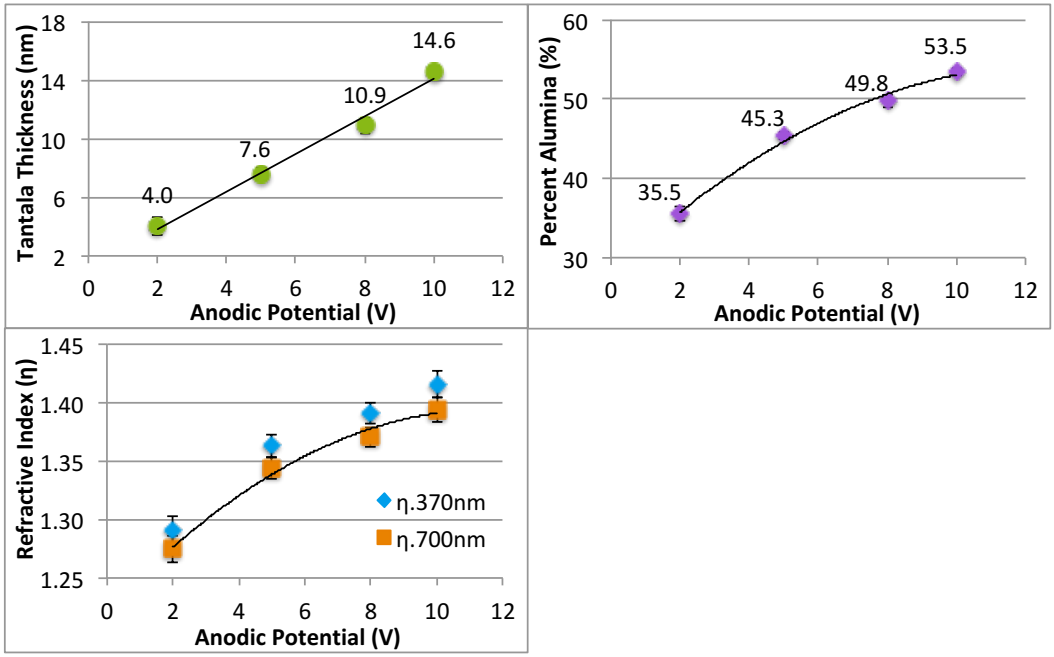

Figure 4.15. The tantala thickness, percent alumina and refractive indices over the visible spectrum resulting from samples anodized in 0.4 M phosphoric at applied potentials of 2, 5, 8, and 10 V.

Adjusting the voltage leads to significant changes to device thin film parameters. Figure 4.16 shows the visible surface colours apparent on slides prepared with different voltages.

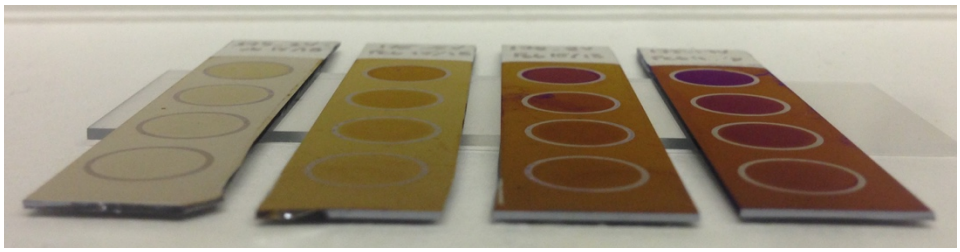

Figure 4.16. Device surfaces after anodization in 0.4 M phosphoric acid electrolyte at 2, 5, 8, and 10 V.

4.3.3 Current Density

The average current density as a function of time is depicted in Figure 4.17 for aluminum thicknesses of 109.2, 114.0, and 117.5 nm. Average current density curves were taken across three intra wafer slides for three inter wafer sets for each aluminum thickness. (n=9)

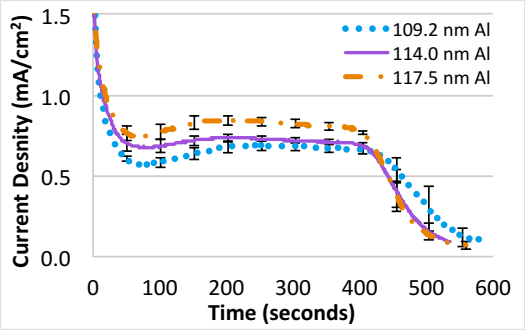

Figure 4.17. Average current density plots for aluminum thicknesses of 109.2, 114.0, and 117.5 nm collected from the anodization of intra (n=3) and inter (n=3) wafer sets. (n=9)

Average electrolyte temperatures and anodization times are provided in Table 4.9.

Table 4.9. Average temperature and anodization length across intra and inter wafer sets.

Initial Aluminum	Electrolyte Temperature ± SD (°C)		Anodization Time ± SD (sec)	
109.2 nm	19.8	0.6	591	34
114.0 nm	20.6	0.6	551	26
117.5 nm	21.4	0.3	556	9

Averages of multiple current density curves shows inaccurate current density trends and slopes from individual curves. Figure 4.18 shows the average current density curves for intra and inter wafer sets. The average electrolyte temperatures and anodization times are provided in Table 4.10.

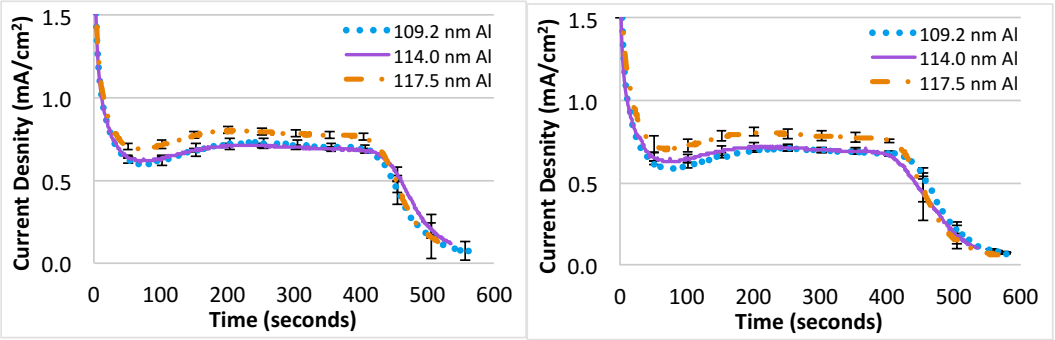

Figure 4.18. Individual current density plots for aluminum thicknesses of 109.2, 114.0, and 117.5 nm collected from the anodization of inter (left) and intra (right) wafer slides. (n=3)

Table 4.10. Average temperature and anodization length in intra and inter wafer sets.

Intra wafer set				
Initial Aluminum	Electrolyte Temperature ± SD (°C)		Anodization Time ± SD (sec)	
109.2 nm	20.5	0.2	558	9
114.0 nm	20.4	0.2	587	10
117.5 nm	21.0	0.1	566	9
Inter wafer set				
Initial Aluminum	Electrolyte Temperature ± SD (°C)		Anodization Time ± SD (sec)	
109.2 nm	20.1	0.2	572	10
114.0 nm	20.8	0.8	561	37
117.5 nm	20.9	0.0	565	7

4.3.4 Sputtered Aluminum

4.3.4.1 Part A – Aluminum Deposition in Constant Power Mode

Table 4.11 shows the slide and alumina thickness with resulting anodization parameters.

Table 4.11. Anodization parameters of slides with aluminum sputtered in constant power mode.

Slide	Alumina Thickness (nm)	SD	Anodization Time (min)	SD	Final Current Density (mA/cm^2)	SD	Plateau Current Density (mA/cm^2)	SD
1_a	102.1	1.6	7.8	0.1	0.07	0.01	0.87	0.00
2_a	107.9	0.6	8.3	0.1	0.07	0.01	0.88	0.01
3_a	114.2	0.5	9.4	0.2	0.06	0.01	0.72	0.03
4_a	123.7	1.7	8.9	0.1	0.07	0.00	0.90	0.06
5_a	128.1	2.8	9.1	0.5	0.07	0.01	0.88	0.10
6_a	133.0	1.5	9.1	0.5	0.07	0.01	0.88	0.04

Ellipsometry parameters of the alumina layer have been recorded in Table 4.12.

Table 4.12. Multilayer devices created with different aluminum thicknesses, under constant power, lead to changes in the resulting alumina film parameters following anodization.

Slides	Aluminum Thickness (nm)	SD	Alumina Thickness (nm)	SD	n.370nm	SD	n.700nm	SD	MSE	SD	Percent Void (%)	SD
1_a	106	3	102	0	1.359	0.008	1.349	0.008	10.8	1.0	47.4	0.1
2_a	114	3	108	0	1.366	0.005	1.355	0.005	9.8	0.5	46.7	0.1
3_a	121	3	114	0	1.356	0.004	1.345	0.004	9.5	0.7	47.4	0.4
4_a	125	3	124	1	1.344	0.006	1.333	0.006	11.2	4.7	49.3	0.1
5_a	128	4	128	0	1.338	0.011	1.329	0.012	12.9	6.2	50.0	0.1
6_a	132	4	133	0	1.331	0.004	1.320	0.004	14.8	3.8	50.9	0.1

The changes in refractive index with alumina thickness have been recorded in Figure. At a wavelength of 370 nm, there was a decrease in refractive index with increased alumina thickness from 1.359±0.008 at 102 nm to 1.331±0.004 at 133 nm. The linear equation and coefficient of determination in the plot are for the refractive index at 370 nm, as well as the statistical analysis shown in Table 4.13.

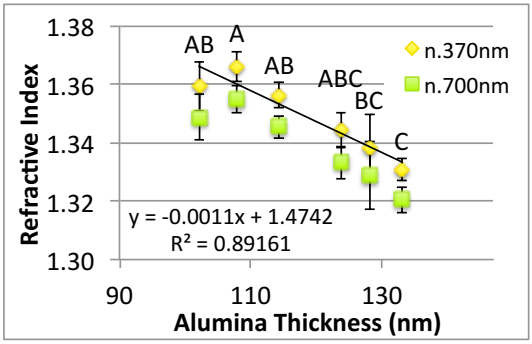

Figure 4.19. Refractive indices resulting with different alumina thicknesses. The mean category letter above points indicates significant differences and correlates with Table 4.13. (n=3)

Table 4.13. Statistical analysis showed the effect of alumina thickness on refractive index of the alumina layer sputtered in constant power mode. (Tukey's HSD test, F(5,12)=7.413, p=.002.

Slide	Alumina Thickness, Mean Refractive Index, and Mean Category	P values (Tukey's HSD test, p<.005)
1_a	102 nm 1.3593 AB	2_a to 5_a >.091 8_a =.016
2_a	108 nm 1.3660 A	3_a and 4_a >.078 7_a =.018 6_a =.003
3_a	114 nm 1.3563 AB	4_a and 5_a >.178 6_a =.032
4_a	124 nm 1.3443 ABC	5_a and 6_a >.444
5_a	128 nm 1.3383 BC	6_a =.893
6_a	133 nm 1.3310 C	

Figure 4.20 shows slides 1_a to 6_a with alumina thickness increasing. Spots show areas exposed to protein solutions.

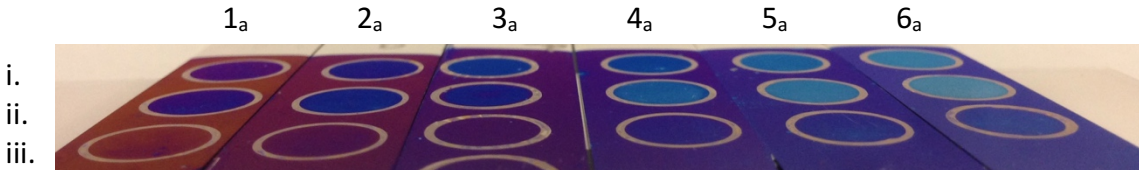

Figure 4.20. Colour shifts of slides with increasing alumina thicknesses from left to right. Spot rows from top to bottom show (i) prothrombin (II), (ii) II and anti-II, and (iii) anti-II. Slide labels 1_a to 6_a correspond with table information.

4.3.4.2 Part B – Aluminum Deposition in Constant Current Mode

Table 4.14 shows the slide, alumina thickness with resulting anodization parameters.

Table 4.14. Anodization parameters of slides with aluminum sputtered in constant current mode.

Slide	Alumina Thickness (nm)	SD	Anodization Time (min)	SD	Final Current Density (mA/cm^2)	SD	Plateau Current Density (mA/cm^2)	SD
1_b	76.0	0.1	7.1	0.2	0.07	0.01	0.65	0.02
2_b	83.9	0.4	7.5	0.2	0.06	0.00	0.68	0.02
3_b	92.7	0.3	8.4	0.1	0.06	0.00	0.62	0.01
4_b	100.4	0.8	9.2	0.1	0.06	0.00	0.64	0.03
5_b	108.8	0.5	9.7	0.5	0.06	0.00	0.65	0.04
6_b	117.2	1.0	10.1	0.5	0.07	0.00	0.61	0.05

Ellipsometry parameters of the alumina layer have been recorded in Table 4.15.

Table 4.15. Multilayer devices created with different aluminum thicknesses, under constant current, lead to changes in the resulting alumina film parameters following anodization.

Slides	Aluminum Thickness (nm)	SD	Alumina Thickness (nm)	SD	n.370nm	SD	n.700nm	SD	MSE	SD	Percent Void (%)	SD
1_b	86	3	76	0	1.362	0.002	1.351	0.002	15.0	2.8	47.1	0.3
2_b	94	4	84	0	1.350	0.003	1.339	0.003	15.6	2.1	48.5	0.6
3_b	103	4	93	0	1.342	0.003	1.332	0.002	14.6	1.5	49.5	0.4
4_b	112	4	100	0	1.338	0.002	1.328	0.003	13.5	0.9	50.0	0.4
5_b	120	5	109	0	1.330	0.000	1.320	0.000	12.1	0.4	51.3	0.2
6_b	129	5	117	0	1.325	0.004	1.315	0.004	10.8	0.8	51.8	0.4

The changes in refractive index with alumina thickness have been recorded in Figure 4.21. At a wavelength of 370 nm the refractive index decreased from 1.362±0.002 at 76 nm alumina to 1.325±0.004 at 117 nm. The linear equation and coefficient of determination in the plot are for refractive index at 370 nm. Data points with a different letter are significantly different, for the data series at 370 nm. The results of the statistical analysis for the 370 nm data series are shown in Table 4.16.

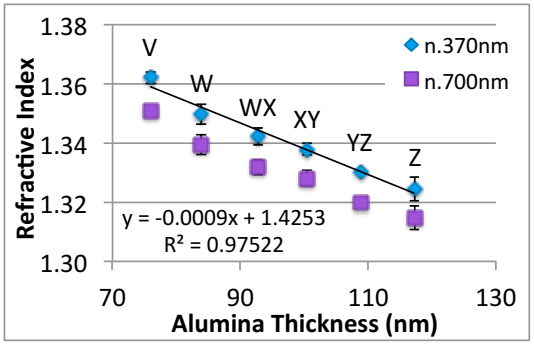

Figure 4.21. Refractive indices resulting at different alumina thicknesses. Means with a different letter above points indicate a significant difference. The mean category letter indicates significant differences and correlates with Table 4.16. (n=3)

Table 4.16. Statistical analysis comparing the effect of alumina thickness on refractive index of the alumina layer sputtered in constant current mode. (Tukey's HSD test, F(5,12)=52.797, p=.000)

Slide	Alumina Thickness, Mean Refractive Index, and Mean Category	P values (Tukey's HSD test, p<.001)
1_b	76 nm 1.362 V	2_b =.006 3_b to 6_b =.000
2_b	84 nm 1.350 W	3_b =.089 4_b =.007 5_b and 6_b =.000
3_b	93 nm 1.342 WX	4_b =.669 5_b =.007 6_b =.000
4_b	100 nm 1.338 XY	5_b =.089 6_b =.003
5_b	109 nm 1.330 YZ	6_b =.393
6_b	117 nm 1.325 Z	

Figure 4.22 shows the device surfaces with alumina thickness increasing from left to right.

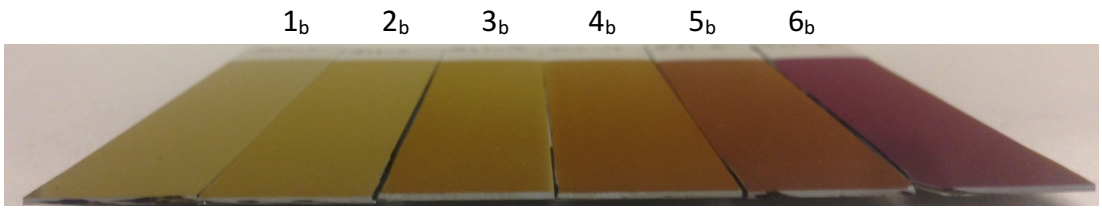

Figure 4.22. Anodized slides comprised of different alumina thicknesses overlying the tantalum oxide and tantalum layers. Alumina increases from left to right: 76, 84, 93, 100, 109, and 117 nm. Slide labels 1_b to 6_b correspond with table information.

4.3.4.3 Comparison of Aluminum Deposition Modes

Table 4.17 shows results of independent t-tests comparing the effect of the aluminum deposition mode on the alumina film refractive index in the device. Slides with similar final alumina thicknesses were selected for comparison.

Table 4.17. Statistical analysis comparing the effect of the aluminum sputtering mode on refractive index of the alumina layer. Selected slides were close in alumina thicknesses.

Slide	Alumina Thickness, and Mean Refractive Index	P values (Independent t-test)
1_a	102 nm 1.359	t(4)=-3.456, p=.026
4_b	100 nm 1.338	
2_a	108 nm 1.366	t(2)=-10.251, p=.009
5_b	109 nm 1.330	
3_a	114 nm 1.3563	t(4)=-7.236, p=.002
6_b	117 nm 1.325	

Aluminum films of the same thickness generated refractive indices that were statistically significant under constant power and current sputter modes.

4.4 Discussion

Devices should be tailored to tune the resulting surface interference colours, based on the findings in this work. Firstly, when the tantala layer was formed in different electrolytes it altered the final thickness, colour generation, and surface reflectivity. The porous structure is highly tunable as well. Alumina formed in phosphoric acid was highly porous (45% alumina at the surface) whereas, structures formed in sulfuric and oxalic are significantly less porous

(80% alumina at the surface). Changes in the alumina porosity of devices prepared in sulfuric and oxalic acids showed ~50% higher reflectivity than surfaces prepared in phosphoric acid, and strong interference colours with *p*-polarization as opposed to *s*-polarization. In addition to electrolyte type, voltage had a large influence on the resulting pore size and interpore spacing of the alumina film. The minimum pore size in phosphoric acid was generated at ~4 V and the interpore spacing increased linearly with voltage. Increasing the voltage from 2 to 10 V, the percent of surface alumina increased from 34 to 54% and the alumina refractive indices ranged from 1.28 to 1.40. Furthermore, the voltage controlled the thickness of the barrier tantala layer which contributes to the surface colour, providing an alternate method to tailor the device. Current density curves, used to govern device oxidation, showed variation with slight changes (~4°C) in the electrolyte bath temperature. For increased temperature regulation, a temperature bath could be used. Lastly, anodization of sputtered aluminum films to create the porous alumina layer, showed a greater decrease in thickness on slides with lower energy depositions. These slides likely contained more defects and voids in the microstructure. A statistical difference in the alumina refractive index resulted with changes in the energy during aluminum deposition although it was not determined if interference colours were influenced.

4.4.1 Temperature

The temperature of the bath during oxidation was controlled at room temperature (20±2°C). Pore size and interpore spacing of alumina surfaces showed no significant difference at constant anodization voltage and concentration, with changes in temperature between 5 and 37°C with anodization in 0.3 to 6.0 M sulfuric acid in the range of 10 to 60 V. [31] Some films created in oxalic acid show constant pore size and interpore spacing at constant voltage and concentration, and changes in temperature, [34] while others show an increase with increasing the electrolyte temperatures. [6,35] Work by Ba and Li found electrolyte temperature to have a lower impact on the resulting ordered pore size than electrolyte concentration. However, lower temperatures during oxidation showed higher pore symmetry. [23] In addition, low temperature electrolyte for the anodization of aluminum leads to a more resistant oxide, whereas higher temperature causes thinner and less durable oxides in comparison to films grown at room temperature. [36] Barrier layer thickness, linked to wall thickness, is affected by

temperature and has shown changes with adjusting the temperature from 16 to 40°C. [37] For the purpose of this work it is important to keep the temperature constant during anodization to ensure reproducibility.

4.4.2 Electrolyte Type and Concentration

4.4.2.1 Tantalum Films

For knowledge on interference colours and device operations, an anodic tantala barrier layer was formed and analyzed in the absence of the alumina layer. The tantala layer, similar to the tantalum metal, gradually increased in percent reflectivity with wavelength, ranging between 20%R at 350 nm to 50%R at 700 nm. Horizontal and vertical polarization images of the anodic tantala surfaces viewed at ~75º, showed greater differences in visible colour than at a lower angle (see Figure 4.6). Horizontal polarization at ~75º created a greyish tantalum surface, meaning equal contributions of blue, green, and red peaks leading to a relatively flat reflectivity line across the visible spectrum (see Chapter 2 for details on colour) and vertical polarization created a slight tan surface colour. Spectrophotometer data at 45º showed that R_s was higher than R_p in blue and green wavelength regions (see Figure 4.7). Optimal surface colour is perceived when the reflected light intensity off the tantala and tantalum layers is balanced. For the anodic tantala on tantalum system, optimal viewing angles are between 5 and 45º, where a light tan colour is perceived.

The resulting tantala thickness regardless of electrolyte type was ~12 nm when formed without the overlying alumina layer. With the porous alumina layer, no reduction in tantala thickness was observed in phosphoric acid; however, a 56% and 35% reduction was observed with formation in sulfuric and oxalic electrolytes. The smaller pore diameters in alumina formed in sulfuric and oxalic electrolytes likely restricted the formation of a complete tantalum oxide layer. Sulfuric oxides were halted before the 0.7 mA/cm^2 current density, which may have contributed to the slightly thinner layer; however, this does not account for 10 nm of thickness loss. Electrolyte concentration showed no significant change in tantala thicknesses when the overlying alumina layer was present.

Work by Mozalev et al. showed the mechanism of growth for tantalum hillocks formed under a porous alumina layer and proved the hillock density corresponds with that of the

overlying pores. [5,38] Anodization in 1.0 M oxalic acid at 35°C and a constant voltage of 21.5 V, created an approximate tantalum width between the oxide hillocks of <10 nm. [38] With a lower voltage, the alumina pore size and interpore spacing at the tantalum interface will decrease. The tantala thickness will decrease as well, resulting in less pronounced hillock formation. The decrease in tantala thickness alters the colour generation from the tantala layer, shown by prior work. It is important to consider this when attempting to produce highly saturated colours and when comparing the anodic tantala reflectivity to the device reflectivity in Figure 4.9.

The tantala layer could be formed in different electrolytes from the alumina layer to alter the formation rate and final thickness, colour generation, and surface reflectivity, in order to tune the interference generated. Table 4.5 shows the differences in tantala thickness and refractive indices with electrolyte type and Figure 4.7 shows the reflectivity. A slight increase in reflectivity is apparent for films anodized in phosphoric and oxalic acid over sulfuric acid, with an increased tantala thicknesses and equal or lower refractive indices. Fresnel calculations carried out based on the applied conditions, showed that an increase in the tantala refractive index is expected to cause a minor increase in the total reflectivity. However, this was not the case for device created in sulfuric acid. The experimental decrease of ~5% reflectivity can be explained by the change in tantala thickness and electrolyte type. Anion integration into the outer tantala barrier layer demonstrated in past works, [39-41] may affect the change in thickness and reflectivity observed. A gradient in refractive index due to anion incorporation can increase the vertical distance that the change in refractive index occurs over. A gradient in the film is accompanied by more adsorption, known as the adiabatic effect[42] and would explain why tantala films formed in sulfuric acid adsorb more light and reflect less light.

4.4.2.2 Aluminum/Tantalum Films

Sulfuric anodization occurred at the highest field (current density) and rate of formation for both concentrations, and thus had the shortest oxidation periods. For all three electrolytes the 1.0 M concentrations, with a lower pH, resulted in a faster oxidation. Current density curves showed that by increasing the concentration from 0.4 to 1.0 M, anodization in phosphoric, sulfuric, and oxalic acids of equal aluminum thickness occurred in 62, 57, and

80% of the time respectively. Although variance is minor, the greatest deviation in average current density plots was observed prior to and following the pore formation plateau, as any shifts in time are more influential in these regions.

The change in applied field during alumina formation relates to the anions integrated from the electrolyte into the exterior alumina layer, and the actual field strength at the pure alumina. The highest field is found in films oxidized in the order of: sulfuric>oxalic>phosphoric>chromic electrolytes.[43] A portion of the migrating Al^{3+} ions are ejected into solution and do not contribute to the formation of the solid oxide film. [36,44] However, the interaction of these ejected ions with anions from the electrolyte could contribute to changes in the alumina thicknesses that result in different electrolyte compositions. Changes to the aluminum barrier layer thickness were found in 4% phosphoric acid, 15% sulfuric acid, and 2% oxalic acid to be: 1.0, 1.2, and 1.2 nm/V respectively. [45-47] The aluminum barrier layers formed in phosphoric acid were shown to decrease with increasing concentration and could influence the resulting structure of the device in varying phosphoric acid concentrations.[48]

Changes in alumina structure (e.g. pore diameter or alumina thickness) with electrolyte composition can be linked to altering the threshold for field-assisted dissolution at the oxide and electrolyte interface. This explains why parameters resulting in a higher applied field (i.e. electrolyte, or greater concentrations) formed alumina layers in a shorter period of time, (see Figure 4.1) as the alumina growth rate is increased with more anions present and the resulting alumina layers were thicker. Furthermore, the anodization process occurring in sulfuric acid at 8 V is closest to the identified self-ordering region and therefore the reaction was carried out at a greater efficiency. For sulfuric acid the self-ordering region is between 19 and 25 V, whereas phosphoric and oxalic acids are in the range of 160 to 195 V and 40 to 70 V, respectively. [4]

SEM images provide information on the resulting film structure. Phosphoric acid leads to a highly porous film (45% alumina) with thin columnar structures that are vertically oriented. The surface structures formed in sulfuric acid and oxalic are significantly less porous (80% alumina), with smaller pore sizes and greater wall thicknesses. The grain structure is still visible following oxidation in sulfuric and oxalic electrolytes with lower surface etching and significantly more volume expansion. Average ratios of alumina to aluminum thickness

for phosphoric, sulfuric, and oxalic electrolytes from this work were 0.9, 1.25, and 1.12 respectively. Volume expansion is strongly dependent on the electrolyte type and demonstrates variability between 1.32 and 2.08 in the self-ordered regime. [49,50] This supports that processes carried out at low efficiencies result in less alumina growth.

Cross-sections reveal that the sulfuric electrolyte creates a columnar structure with variable width along the height of each column while alumina formed in oxalic acid has a branching structure with more uniform column widths. The phosphoric acid creates a uniform column with a significantly smaller wall thickness throughout the entire alumina layer, demonstrated at the surface by the higher percent void. SEM topographic images of samples formed in 0.1 M sulfuric acid were difficult to resolve at high magnification (see Figure 4.2), which may result from greater surface charging due to the amount of sulfate anions integrated into the surface layer. This was also found in work conducted by Thompson and Wood.[43]

Work by Yim et al. showed that a large increase in electrolyte concentration led to only slightly larger and denser alumina pores. [31] In other work the concentration has demonstrated a slight influence on the pore diameter. [44] Work by Sullivan and Wood found that in increasing concentration from 0.4 to 2.25 M of phosphoric acid showed little variation in pore diameter when measured on film sections, whereas surface etching resulted. [48] Out of the concentrations tested, alumina films formed in 0.4 and 1.0 M phosphoric acid showed no statistical difference in the average pore diameters (18.3±5.3 and 19.1±5.9 nm) ($p=.776$) or refractive indices ($p=.217$), yet there was a statistical difference in the total wall thicknesses ($p<.001$). The discrepancy in significant differences with correlated parameters is likely due to the size of variance. With larger variance in pore diameter and refractive indices no significant difference results. Work in chapter 6 shows that refractive index is typically a better indicator of differences in the alumina porosity, with higher accuracy than SEM measurements. Therefore, it is likely that higher sample numbers or greater changes in concentration are needed to produce significant differences in the refractive index and pore size. [44]

Porous anodic alumina films formed in phosphoric, sulfuric, and oxalic acids typically show greater pore size, wall thickness, and interpore spacing than in these findings due to higher voltages typically employed. A comparison of wall thickness from this work and Keller et al. [47] are shown in Table 4.18.

Electrolyte	Concentration (M)	Temperature (°C)	Voltage (V)	Wall thickness formation (nm/V)	References
Phosphoric	0.4	24	20-60	1.00	Keller et al.
	0.4	20±2	8	0.65	-
	1.0	20±2	8	0.60	-
Sulfuric	0.4	20±2	8	1.08	-
	1.0	20±2	8	0.89	-
	1.7	24	15-30	0.80	Keller et al.
Oxalic	0.2	24	20-60	1.09	Keller et al.
	0.4	20±2	8	0.98	-
	1.0	20±2	8	0.93	-

Table 4.18. A comparison of wall thickness values obtained in low voltage work in different electrolyte conditions.

For sulfuric, oxalic, and phosphoric electrolytes formed in self-ordered regions, interpore distances of 50 to 60 nm, 90 to 140 nm, and 405 to 500 nm result. [4] With anodization for 15 minutes in 0.3 M sulfuric acid under constant voltage of 10 V at 22°C, with post anodization physical and chemical etching the interpore distance was found to be 30±4.5 nm. With increasing the voltage between 10 and 40 V the interpore distance increased up to 72 nm, as well as the pore shape uniformity.[31]Again these values are significantly higher than interpore distances found at lower voltages, due to lower efficiencies of formation and the introduction of a one step process.

Multilayer device surfaces prepared in sulfuric and oxalic acids showed ~50% more reflectivity than surfaces prepared in phosphoric acid (see Figure 4.9). This is a result of changes in surface area and effective refractive indices of alumina films. Surfaces generated in sulfuric and oxalic acids have ~80% surface alumina as opposed to those generated in phosphoric acid which have 45% surface alumina (see Table 4.3). The increased alumina surface area for sulfuric and oxalic over phosphoric acid, results in an increased reflectivity at the air and oxide interface. A portion of light contacting the solid alumina is converted to horizontally polarized light (i.e. glare), proportional to the surface area leaving a lower intensity reflected in the vertical polarization (see Chapter 2 section on polarization). This change in microstructure and interface reflections alters the optimal polarization state for viewing thickness changes, such as prothrombin detection, on the alumina layer.

When a change in polarization states leads to an intensity shift it is due to a change in percent reflection, whereas a colour shift means a change in OPL (i.e. refractive index or thickness) has occurred. In this work the colour shifts that are apparent with different

polarization are caused by a change in the refractive index and thickness of alumina. Horizontal and vertical polarized light interact differently within the alumina layer. The s-polarized light sees the material with one refractive index in the x-y plane (parallel to the alumina surface), whereas the p-polarized light sees the alumina as an anisotropic film with the x-y plane and z plane (perpendicular to the alumina surface) creating two different refractive indices due to the columnar nature of the pores. Therefore, there is increased scattering of *p*-polarized light travelling in a direction that is impacted by the split x-y plane refractive index as well as the z plane refractive index. Other factors may influence the reflectance and interference within the multilayer device that was not accounted for such as scattering due to surface roughness. [51]

Furthermore, different viewing conditions are required to balance the reflectance off tantalum and alumina interfaces. Fresnel equations for the anodized multilayer structure provide an estimate of the reflectivity of each polarized state, shown in Table 4.19. Films formed in sulfuric and oxalic electrolyte showed less sensitive protein detection, as the difference in refractive index between the protein layer and alumina is likely greater.

Table 4.19. Calculations using Fresnel equations to determine the R_s and R_p to balance the intensity off the alumina and tantalum layers. Highlighted boxes show conditions for optimal colour generation.

		Alumina η=1.35		Alumina η=1.58	
Surface	**Angle of Incidence**	**Total R_s at Surfaces**	**Total R_p at Surfaces**	**Total R_s at Surfaces**	**Total R_p at Surfaces**
Alumina	5°	2	2	5	5
Tantalum		36	6	34	10
Alumina	45°	6	0	11	1
Tantalum		31	10	28	14
Alumina	75°	32	11	43	10
Tantalum		6	8	4	8

Although the calculated reflectance off the alumina and tantalum layers is not balanced at the experimentally determined optimal viewing angle of ~75° (highlighted boxes), we have yet to compensate for the porosity. Films formed in phosphate have a refractive index of approximately 1.4 and a porosity of 55%. This likely decreases the actual alumina reflectance by 55% changing R_s from 32 to 15 and increases the tantalum reflectance to 9. Demonstrating an optimal viewing angle for balanced R_s interference, between 71 and 73°. For alumina films at higher refractive indices of 1.6 formed in sulfuric and oxalic electrolytes, the porosity was ~20%. Therefore, decreasing the alumina reflectance (R_p) from 10 to 5 and increasing the

tantalum reflectance to 13. Balanced R_p interference is ~77°. Table 4.20 shows the total reflectivity off alumina and tantalum interfaces at near optimal angles after accounting for porosity.

Table 4.20. Fresnel reflectivity values corrected to account for alumina surface porosities of ~55 and 20% for η=1.35 and η=1.58 respectively. Nearly balanced reflectance off the alumina and tantala layers are highlighted for R_s and R_p.

		Alumina η=1.35		Alumina η=1.58	
Surface	**Angle of Incidence**	**Total R_s at Surfaces**	**Total R_p at Surfaces**	**Total R_s at Surfaces**	**Total R_p at Surfaces**
Alumina	71°	11	3	16	2
Tantalum		13	13	11	16
Alumina	73°	13	4	17	3
Tantalum		11	12	9	14
Alumina	75°	15	5	19	5
Tantalum		9	11	7	13
Alumina	77°	17	7	22	6
Tantalum		6	10	4	10

Discrepancies between Fresnel values and measured theoretical and experimental values further support that the theoretical calculations assuming a uniform alumina layer do not account for some critical property of this device. Polarized reflectance at 45° was compared from spectrophotometry measurements and Fresnel calculations. The experimental spectrophotometry reflectance for films generated in phosphoric acid was 59% of the theoretical reflectance (with 44% surface alumina), and sulfuric and oxalic generated films showed 79% of the theoretical reflectance (with 81% surface alumina) (see Table 4.6). These calculations were done without accounting for the surface porosity.

Work by Aschalew et al. [52] showed that nanometer scale pores and porosity, both influence the way visible light interacts with the surface. Commercial nanoporous anodic alumina membranes, that are 100 μm thick and contains pore sizes between 18 and 150 nm with various pore densities were tested. As pore size increases the transmittance and reflectance decreases and absorbance increases. [52] Reflectance appears to be influenced by porosity, in addition to pore size. Increasing porosity was calculated for films with pore sizes of 35, 80, 55, 18, 100, and 150 nm and showed decreasing reflectance in this order, with the exception of the 80 nm sample. It is possible that the pore density value was inaccurately measured for the 80 nm sample.

Another possible explanation for the contradictory theoretical and experimental reflectivity could be a result of the tantalum metal and tantala hillock interface. Hillocks form under the alumina pores and changes in the alumina structures will influence their shape and potentially the reflected light. In sulfuric and oxalic films smaller tantala widths and more tantalum metal is expected to be contacting the alumina oxide layer and wall thicknesses are smaller. Whereas, in phosphoric films the alumina pores are larger and thus the oxide hillocks that result will be wider and less tantalum metal will exist at the alumina interface. The tantala layer does not significantly alter the reflectance; however, the tantalum amount and shape contacting the alumina may impact the interference.

The reflectance of horizontal and vertical polarized light off the alumina and tantalum layers is nearly balanced at 75° while having an OPL large enough to generate interference in the visible range. Porous alumina reflectivity is decreased from solid alumina depending on the pore size or void fraction, taken into account by Fresnel equations with a decrease in the refractive indices. Previous work on nanoporous anodic alumina films 1580 nm thick (formed in 0.3 M oxalic acid at 40 V and 5°C for 20 hours) showed the reflectivity to be ~90%R at 400 nm and ~80%R at 700 nm. A slight increase in the average reflectivity resulted with an increase in pore size, from 39 to 90 nm, and porosity from 14 to 71%.[53] The increased reflectance with a higher pore size and porosity presented in this work goes against the prior literature. However, with an aluminum substrate, higher scatter results with lower porosity and greater surface roughness and higher reflectance occurs with greater porosity. Hence, explaining why the reflectivity is 45 to 55% higher than off the devices in this work consisting of porous alumina surfaces on a tantalum substrate that absorbs approximately 45% of the incoming visible light.

With pore sizes ≥400 nm the specular reflectance begins to decrease and diffuse reflectance (i.e. scatter) increases. In a highly uniform film, specular reflected light results when the wavelength is greater than pore diameter multiplied by $\sqrt{3}/2$ (a factor of 1.225). [42] For nanometer pores the conclusion can be made that the majority of light is specularly reflected light and little scatter results. Diffuse light would be a result of the surface roughness and non-uniformity that becomes more apparent in films generated in phosphoric acid and

may contribute to the decrease in total reflectance. On a flat alumina film 5 to 7% of incident light is scattered.[42]

Figure 4.9 shows destructive and constructive wavelengths in the first order of interference through changes in reflectivity. These maximum and minimum values shift towards higher wavelengths with alumina thickness, ultimately causing a change in the surface colour. Prikulis et al. [54] demonstrated dominant peaks that shift to higher wavelengths for alumina thicknesses increasing from 75 to 280 nm with pore sizes in the range of 18 to 25 nm, amplified with 10 to 20 nm gold coatings on the surface. Reflectance peaks in the near-IR range, 600 and 1000 nm, showed more distinguishable spectral shifts with alumina thickness than the UV-VIS range of 350 to 600 nm, and could lead to increased detection sensitivity.[54]Visible surface colour shifts are similar to those found with alumina thicknesses in our work; however, the surface reflectance is amplified with a highly reflective coating, to balance the reflectance off the aluminum substrate reflectance.

4.4.2.3 Birefringence

Anisotropic materials demonstrate interactions with light that are related to the orientation, as distinct axes exist in the material. [55] Various studies on porous alumina films with a columnar structure have shown and evaluated anisotropy. [56,57] A study by Luitch et al. measured the changes in birefringence of alumina thin films with changes in the porosity. [58] Birefringence, or double refraction, occurs when light of mixed polarization contacts the film at oblique angles of incidence. Different polarizations are influenced by different refractive indices, resulting in two rays propagating through the material with different velocities and angles of refraction. Subsequent to passing through the birefringent layer, the *s* and *p*-polarized light interfere and can lead to birefringence. [58]

The possibility of birefringence was considered early on in the optics design process. To confirm that structural birefringence was not contributing to additional colour variation, the visible interference colour shifts were observed with polarization of the input and output beams. No difference resulted in the visible colour observed, and therefore birefringence was deemed irrelevant when using a polarizing filter to view interference colours on the device surface.

4.4.2.4 Hydration

During oxidation in sulfuric acid, significantly more hydrogen evolution occurred. This was not quantified but based solely on the visible observation of gas bubbles generated at the cathode surface, relative to the amount generated from oxidation in phosphoric and oxalic electrolytes. In addition, slides anodized in sulfuric acid were noticeably more hydrophilic than other slides, as residual rinse water was difficult to remove. Porous films created in sulfuric and oxalic acids can contain up to 15% w/w water[59,60]in the form of hydroxide and/or hydrated oxide.[61,62]Films created in phosphoric acid showed ~5% water. [63] It is generally accepted that the amount of water in a porous alumina layer depends on the anodization conditions, sample handling, and measuring technique used.[61]Anions incorporated into the outer alumina layer may affect the hydrogen bonding properties of the layer and composition, with sulfuric acid having the largest anion integration followed by oxalic, and phosphoric acids.[43]Work by Alvey in 1974 confirmed the integration of 11.1% sulfate, 7.6% phosphate, 2.4% oxalate, and 0.1% chromate with various detection techniques. [64] Anion integration was found to decrease with temperature for oxalate[59] and increase with current density for sulfates and phosphates. [65]

Work by Ye et al. showed that wider and deeper pores as well as the length of anodization were the main factors governing the hydrophilic property of anodic alumina films formed in 0.3 M phosphoric acid at 25°C using a single oxidation process. [66] However, when comparing alumina created in different electrolytes these factors were disproven. Films formed in sulfuric acid had smaller pore diameters and a smoother surface than samples formed in phosphoric acid. Furthermore, these samples were anodized in the shortest time period. It is possible that the pore wall roughness, resulting in oxides formed in sulfuric acid, may be influential to the higher wettability due to capillary effects outlined in other works. [67] If sulfuric electrolyte is used in future device preparation; additional work should be completed to ensure the hydrophilic alumina does not negatively affect the protein-surface interactions and impact protein immobilization.

The non-uniform nanoscale pores and surface properties may also influence the hydrophilic nature of these anodic films. Leese et al. demonstrated that smaller pores formed in sulfuric acid followed by oxalic acid, lead to a lower contact angle with a decrease from 20

to 10 nm pore size causing a decrease in contact angle of ~20°.[68] However, this would not explain the difference between sulfuric and oxalic hydration experiences in this work, as alumina pore sizes are similar in both electrolytes.

4.4.3 Applied Potential

Anodization voltage, electrolyte type and concentration, and temperature have demonstrated effects on the resulting anodic alumina structure.[69,70] Of these parameters voltage has been recognized as the greatest contributing factor to the pore size and interpore spacing followed by concentration.[31] Prior electrolyte tests proved phosphoric acid to be optimal with simpler horizontal polarized colour generation and increased uniformity of the tantala layer.

In phosphoric acid the conversion of aluminum to porous alumina was faster with increasing applied potentials, leading to a greater applied field and plateau current density, demonstrated in Figure 4.11. For low voltages between 2 and 10 V the plateau regions were flat, indicating uniform pore formation.[33] Reports on anodization in acid electrolytes with <20 V on thin sputtered films <200 nm are limited in the literature.[17,22,24,30,31,33] However, in phosphoric acid the process is significantly less common due to the self-ordered pore formation occurring at significantly higher voltages. Work by Ono and Masuko showed a minimum pore size of ~21 nm at 5 V in phosphoric, sulfuric, oxalic, and chromic acid.[30,71] This trend was dominant with oxidation in phosphoric acid with the larger pore size and porosity that resulted. Our findings agree with the non-linear increase in pore size with low voltages. A linear increase in pore size was noted in films formed at 5 to 10 V; however, the 2 V films were found to contain a larger pore diameter than the 5 V samples ($p=.037$). Mean pore sizes were significantly different at all voltages, except 8 and 10 V ($p=.320$). Based on the polynomial trendline the minimum pore size exists at ~4 V. Pore diameters resulting after anodization in phosphoric acid at low voltages do not follow the majority of relationships outlined in literature. A previously reported equation for pore diameter (nm) was 1.29 nm/anodizing voltage (V) was disproven for all voltages tested.[44] For the 2 V samples it is possible that chemical dissolution widens the pores at the oxide and electrolyte interface leading to pore diameters that are larger at the surface,[44]as etching in phosphoric acid for pore widening is a common procedure.[50] However, the cross-sectional alumina layer formed at 2 V

in this work appeared to have consistent pore sizes and the smallest wall thickness, meaning any etching was uniform. The pore diameter in a 2 V sample was larger than the 5 V sample and therefore, the increased pore size due to the low field has a greater effect than the low voltage governing a smaller pore size.

Work by Zhang et al. showed a linear relationship between interpore spacing and voltage[72] and Yim et al. showed that interpore distance is reduced at lower voltages.[31] Our work showed a non-linear increase in interpore spacing with oxidation in phosphoric acid at low voltages between 2 and 10 V. However, the non-linear pore diameters translate to the interpore spacing.

The percent alumina increased from 34 to 54% and the alumina refractive indices from 1.28 to 1.40 with increasing the applied potential from 2 to 10 V. The refractive indices at 370 nm are significantly different. ($p=.014$) In addition, alumina films formed at 2 V are 76 nm thick, whereas the 5 to 10 V films are ~84 nm. Lower efficiency film formation occurred at 2 V with the lowest current density of <0.75 mA/cm^2 during pore formation, resulting in a greater loss of aluminum ions.[73,74] The longer pore formation periods at low field strength allows for greater etching. The alumina thickness change demonstrates significantly greater etching as the initial aluminum was the same thickness for all slides. Changes in the alumina optical path length (i.e. refractive index and thickness) lead to various colours from light tan to dark orange and the application of protein spots showed further colour shifts with increased thicknesses.

MSE values of samples formed at 8 and 10 V indicated greater standard errors in the generated values for this sample. Other work showed tantalum oxide thickness had the greatest influence by a larger MSE, however the alumina thickness or refractive index could be slightly affected also (see next section 4.4.4).

Films formed at this voltage allow for close matching of adsorbed protein layers on the surface. A trade off exists between the refractive indices and pore size. Ideally smaller pores will prevent protein diffusion into the pores, however the refractive index must match the refractive indices of protein layers and lead to colour generation. With a protein refractive index of ~1.5 if we assume a minimum 80% of the protein layer contains protein and the remainder is void, the refractive index of the protein layer is 1.4. Therefore, a slightly larger or smaller refractive index may be necessary to match the alumina to proteins for optimal

detection. Alumina films formed at 8 V generate η=1.38 and at 5 V have η=1.35 measured a 500 nm. Depending on the refractive index of the protein of interest the voltage is yet another parameter that could be adjusted to tune the alumina layer. The tantala barrier layer thickness can also be linearly controlled with voltage as it formed at: tantala thickness (nm)=1.28 (nm/V) × voltage (V) + 1.27 (nm). Increasing the voltage after formation is complete to increase the tantala thickness may provide a means to improve the base device colour contrast.

Future work was carried out in 0.4 M phosphoric electrolyte at 8 V. However, the anodization process allows for numerous methods to tailor the device that are now better understood. Other areas of exploration that were not completed include: temperature, electrolyte mixes, voltage or oxidation steps, and pre and post anodization processes.

4.4.4 Current Density

While anodizing sputtered films, current density was used to regulate the device based on the growth of an electrically resistant tantala barrier layer. This study was carried out to determine the variability of the sputtered device films and anodization. The average current density curves for initial aluminum thicknesses of 109, 114, and 118 nm of intra and inter wafer sets were averaged for each thickness (shown in Figure 4.17). An increase in electrolyte temperature can increase the current density plateau and decrease the length of anodization, or vice versa, shifting the oxidation time. When plots are averaged the shift in time alters the original trends and the final slope. Electrolyte temperature fluctuations alter the field and anodization length of time (see Table 4.9). The data for the 109 nm film contained the greatest temperature and time deviations, explaining the skewed current density curve that resulted. Figure 4.18 provides an accurate representation of the current density curves with averaged intra and inter wafer slides for each thickness at similar electrolyte temperatures. (n=3)

The shape of the graph showed the formation of the porous alumina layer followed by the oxidation of tantalum for each thickness. Thicker aluminum films can result in a longer period of pore formation and total anodization time; however, the sputtered aluminum thicknesses tested are not significantly different and therefore, it was expected that the length of pore formation would be comparable between sets. The maximum difference in current density occurred between periods of 80 and 180 seconds, when the alumina barrier layer exists and begins to form micro cracks prior to pore formation, and between periods of 450 and 510

seconds, when the tantala layer was forming. In the first region the absolute difference was <0.15 mA/cm^2, a maximum of 21% deviation from the average current density. Whereas in the second region the deviation was between 0.15 and 0.20 mA/cm^2, which appears larger due to shifts in the anodization time and the current density approaching zero.

Large changes in current density could influence the rate and the length of aluminum conversion to alumina. In this case the variation is due to changes in the electrolyte temperature. It is possible that anodization parameters other than temperature contribute to the variability. Overall, the use of current density was effectively utilized to monitor the porous alumina formation and govern the tantala barrier layer thickness that resulted. For better reproducibility a temperature bath should be utilized.[35,75]

4.4.5 Sputtered Aluminum Thickness

The decrease in alumina refractive index that occurred with increased aluminum deposition, regardless of the governing mode, was due to a change in the final alumina structure. Sputtered aluminum was converted to a porous anodic alumina by anodization, and the thicker the aluminum layer the greater the time required for conversion. The slide was submersed in phosphoric acid electrolyte for the entirety of anodization and resulted in increased etching with time. The amorphous alumina is an amphoteric oxide with the following etching reactions of $2OH^- + Al_2O_3 \rightarrow 2AlO^{2-} + H_2O$ and $6H^+ + Al_2O_3 \rightarrow 2Al^{3+} + 3H_2O$. [76] Studies on porous anodic alumina use low concentration solutions of phosphoric acid as a chemical etch following anodization to increase the pore sizes. [77-79] Gâlca et al. found that phosphoric acid achieved chemical etching at rates of 0.3 and 0.9 nm/min with 0.35 to 0.84 M phosphoric acid at room temperature respectively. [77] Work by Bellemare et al. found an etch rate of 4.1 nm/min in 0.8 M phosphoric acid at 50°C. [80] The difference between these results and past studies is that these anodization processes were completed in phosphoric acid and etching is expected to occur simultaneously with oxidation as opposed to a post anodization pore widening treatment. The refractive index of a solid alumina layer has a refractive index between 1.53 and 1.70 in the visible spectrum[81-83]and an increase in aluminum dissolution during formation generates a porous alumina layer with higher void fraction, accompanied by a decrease in the refractive index, or effective refractive index. The equation below provides a simplified relation of the refractive index and porosity. [84,85] Ellipsometry modelling applies a

complex version called anisotropic Bruggeman EMA equation, which can be found in the literature.[86]

$$\eta_{\text{porous alumina}} = \eta_{\text{effective}} = \eta_{\text{air}}(\text{porosity}) + \eta_{\text{alumina}}(1 - \text{porosity}) \qquad \text{Equation 4-1}$$

Another decrease in alumina refractive index occurs with changes in the aluminum microstructure sputtered. Aluminum sputtering conditions, in this case governing modes of constant current and power, influence the flux and energy of incoming atoms. Slides with aluminum sputtered in constant power versus constant current mode had higher power and voltage by 25 W and 40 V respectively, and equal currents of 0.72 mA. In sputtering the current corresponds with the number of ions that contact the target and voltage corresponds with the energy of ions. Therefore, in higher energy aluminum depositions, in this case constant power mode, ad atom diffusion occurs more easily, reducing defects and grain boundaries. Defects are areas of high energy where dissolution occurs more rapidly; hence changing the amount affects the dissolution of aluminum during anodization. The thickness change between initial aluminum and alumina was greater for slides with lower energy depositions, predicted to contain increased defects. Average aluminum thickness decreases 1±3.4 nm and 11±0.6 nm for the high energy (i.e. constant power) and low energy slides (i.e. constant current) respectively. Measuring the aluminum grain size would further support microstructural changes due to sputtering.

Anodization was carried out at a constant voltage and slides sputtered at a lower energy, that contain increased defects, resulted in a decreased current density during the pore formation region. At a constant voltage (V), a decrease in current (I) stems from an increase in resistance (R) as shown in Ohm's law below.[87]

$$V=IR \qquad \text{Equation 4-2}$$

Therefore, changes in the sputtered film resistances, influence the oxidation process. The lower the plateau current, the slower the anodization process, further increasing conversion time and the amount of aluminum dissolution. Data is shown for constant power and current slides in Table 4.11 and Table 4.13 respectively.

The alumina layer refractive index of slides with sputtered aluminum under higher energy deposition showed greater variability than those under constant current mode, and in some cases high associated MSE values. Higher variability is thought to have resulted from

tantalum deposition in the NAIT system, which was found to have intermittent leaks in the chamber. Average tantalum and tantalum oxide parameters were applied to ellipsometry models of resulting devices. However, when the corresponding wafer tantalum and tantalum oxide parameters were substituted into the device model, a reduction in the MSE between 3 and 18% was found. The alumina thickness, tantala thickness, percent void, and refractive index values showed fluctuation less than 0.70, 32.50, 2.10 and 0.65%. The main change was in tantalum oxide thickness with minimal effects on alumina parameters. This analysis was completed on slides with aluminum sputtered under constant current.

Alumina refractive index as a function of thickness shows a linear trend line for constant power and current modes (see Figure 4.19 and Figure 4.21). With the generated equations predictions can be made for the refractive indices at various alumina thicknesses, within the tested range. In this work the change in refractive index due to the sputtering energy during aluminum deposition was significant. A significant difference was found between these groups ($p \leq 0.026$) (see Table 4.17). It is clear that sputtering conditions play a large role in the resulting device structure and should be meticulously calibrated and controlled for each sputtering system and material for optimal reproducibility. Less etching would be desirable to reduce and eliminate differences in the final alumina refractive indices or thicknesses.

4.5 Future Work

It is important to notice that with non-uniform porous alumina surfaces, SEM and ellipsometry measurements may lead to inaccurate conclusions depending on the size of the variances. Future work may involve the use of Brunauer-Emmett-Teller (BET) for porosity and surface area information of the porous layer. In addition, further studies on the tantala layer uniformity could lead to tailored scatter at the metal and oxide interface. This may include exposing the oxidized films to a higher voltage to grow the tantala layer thickness in attempts to generate a more uniform layer or anodizing in multiple acids.

4.6 Conclusions

It is apparent that by determining the results of anodization under various conditions the thickness and optical constants of the alumina and tantala layers that form can be tailored. The following conclusions were reached:

4.6.1 Electrolyte Type and Concentrations

1. Electrolyte composition changes the wettability of thin anodic films formed at low voltages.
2. Device formation in sulfuric and oxalic acids creates a thinner tantala layer under the alumina layer than in phosphoric acid. The thinner tantala layer decreases the contribution to colour generation.
3. Fresnel equations can be used along with the alumina layer refractive index and the incident angle to calculate the reflectance off alumina and tantalum surfaces with horizontal and vertical polarization. Accounting for porosity was crucial to explain conditions with balanced reflectivity.
4. Optimal surface colours for films formed in phosphoric acid occur with horizontal polarization (*s*-pol), whereas for films formed in sulfuric and oxalic acids viewing was optimal with vertical polarization (*p*-pol). Alumina anisotropy makes *p*-polarized light more complex than *s*-polarized light.

4.6.2 Applied Potential

5. Stronger colour generation resulted when tantala thickness increased from 5 to 10 V samples.
6. Alumina refractive indices between 1.28 and 1.40 can be obtained with low voltages in the range of 2 to 10 V.
7. The minimum pore size occurred at ~4 V, however at less than 8 V the average pore size of 21 nm was thought to prevent protein penetration deep into pores while allowing a greater surface alumina for binding.

4.6.3 Current Density

8. Monitoring current density provides an effective method to govern the alumina pore formation and the tantala barrier layer creation.
9. Temperature changes between 18 and 22°C can lead to absolute differences in current density before and after the pore formation region of up to <0.2 mA/cm^2. A temperature bath should be used to mitigate temperature fluctuation.

4.6.4 Sputtered Aluminum Thickness

10. The sputtered aluminum microstructure influences the aluminum dissolution during anodization, and ultimately the final alumina layer parameters (i.e. thickness, porosity, and refractive index). A greater decrease in thickness was observed for slides with lower energy aluminum depositions. The average aluminum thickness decreased 1±3.4 nm and 11±0.6 nm for high energy (i.e. constant power in this work) and low energy slides (i.e. constant current in this work) respectively.
11. Increasing the initial aluminum thickness caused a decrease in the alumina layer refractive indices of the slides.
    a. Aluminum depositions in constant power mode (in this case high energy) generated an alumina layer with η=1.359±0.008 and t=102 nm and decreased to η=1.331±0.004 when t=133 nm.
    b. Aluminum depositions in constant current mode (in this case low energy) generated an alumina layer with η=1.362±0.002 and with alumina t=76 nm and decreased to η=1.325±0.004 when t=117 nm.
12. When the corresponding wafer tantalum and tantalum oxide parameters are used instead of average values the MSE was reduced between 3 and 18%. The alumina thickness, tantala thickness, percent void, and refractive index values showed fluctuation less than 0.70, 32.50, 2.10 and 0.65%.

Chapter 5 – Adsorption of Prothrombin and Anti-prothrombin Layers onto Porous Anodic Alumina: an XPS and SIMS Investigation

5.1 Introduction

The adsorption of biologics onto surfaces is a phenomenon well studied on bulk materials through numerous techniques. [1-11] The majority of intended applications consist of biomedical devices such as: instruments, implants, monitoring cells, and functionality *in situ*. Investigating protein adsorption onto porous structures becomes arduous and as a result is less common. Analyses for porous membranes are conducted for tissue or bone integration on implant surfaces, separation or adsorption onto filters, and changes with alternate treatment processes on a porous material.[12-17]

This study aims to characterize a thin film device using XPS and SIMS prior to and following exposure to biologics in order to investigate protein adsorption and penetration into the porous alumina surface. The multilayer device consists of alumina, tantala, and tantalum thin films on a silicon wafer. An antigen-antibody prototype of prothrombin and anti-prothrombin were immobilized on the porous alumina layer, increasing the physical path length and altering the optical constants of the alumina if any penetration occurs. Ideally no protein penetration occurs, meaning the change in OPL results from a thickness increase. Regardless of the reason for the change in OPL, areas with adsorbed proteins create a difference from the device surface, observed by the generation of interference at wavelengths in the visible spectrum. Prothrombin and anti-prothrombin are the two protein layers used for adsorption during this study. A complex was formed on the surface by exposing anti-prothrombin to the prothrombin-coated surface.

Prothrombin solution is placed on the surface and is immobilized as a result of alumina's high affinity to vitamin K dependent proteins. [18,19] Carboxyglutamic acid residues, which are present in proteins of this type, have been shown to bind securely to alumina, possibly through an esterification type reaction. [20-23] Fragment 1 of prothrombin contains 55% of the glutamic acid residues of the entire protein, and 100% of the carboxyglutamic acid residues. [24,25] It is expected then that prothrombin binds to the alumina in a consistent orientation, normal to the alumina surface with fragment 1 closest to the alumina. Prior use of

alumina as a separation filter demonstrates this capability further.[26] See Chapter 2 for more details.

In this work, we report the relationship between protein immobilization on and within different device surface structures. Multilayered devices oxidized at 8 V generate an increased pore size and decreased porosity of the alumina films compared to films oxidized at 5 V, showing a 5% increase in surface alumina (supported by work in Chapter 4). The change in effective surface area of alumina in the anodized structure[27] ultimately changes the protein interaction. Characteristics of the porous alumina surfaces are examined using ellipsometry, FESEM, XPS, and SIMS. Furthermore, the adsorption and penetration of a single prothrombin layer will be compared against a prothrombin/anti-prothrombin complex to investigate protein binding sites as well as binding efficiency. Results of this study will further the understanding of prothrombin interactions with a porous anodic alumina film along with optimization of process conditions, and ultimately the efficiency and stability of the thin film device.

5.2 Materials and Methods

5.2.1 Device Preparation

Prior to sputtering the wafers were cleaned using a piranha solution and dried using nitrogen gas in a spin rinse dryer. Coatings were deposited using two planar magnetron sputtering systems. First (~200nm) 202±27.2 nm of tantalum was deposited in the nanoFAB (Bob) system followed by 95±2.6 nm of aluminum in the second nanoFAB (Floyd) system sputter. Systems operated under constant power at a power density of ~6.58W/cm^2.

The wafers were cleaved into slides ~2 cm by ~6 cm. Unanodized controls were used from each wafer. Samples to be oxidized were rinsed with deionized water and samples were anodized at either 5 V or 8 V in an aqueous solution of 0.4 M phosphoric acid. The process was halted after the tantala barrier layer formed and the current density declined to <0.07 mA/cm^2 (stage b). This anodization stage was chosen as an end point to ensure the complete transformation of the aluminum into porous alumina with minimal etching. See Chapter 3 for more details on device preparation.

5.2.2 Adsorption of Biologics

Human prothrombin and anti-prothrombin (Hyphen, Aniara, West Chester, OH) were received in a lyophilized state. To create a prothrombin layer, a 20 µl drop of prothrombin at 1 mg/ml was pipetted onto the surface and left for 15 minutes in a relative humidity environment of 100%. The majority of solution was pipetted off the surface and the slide rinsed with deionized water. After every rinse the slides were dried in air. For the slides with a double protein layer, a 20 µl drop of anti-prothrombin solution at 0.2 mg/ml was pipetted onto the prothrombin-coated surface and left for 15 minutes in a relative humidity environment of 100%. The excess protein was then removed with a pipette, and the slide was rinsed with deionized water and air dried.

5.2.3 Analysis

5.2.3.1 SEM

Topographic images were taken before the introduction of protein complexes. ImageJ software (NIH open source software) was used to conduct average pore diameter measurements. Pores were measured along three horizontal and three vertical lines to obtain mean and standard deviation values. See Chapter 3 for more details.

5.2.3.2 Ellipsometry

Following preparation of the thin film samples, ellipsometry was used to collect data and generate models of the multilayer structure. From models the thicknesses of alumina and tantala layers, and optical constants of alumina layers were estimated. Values for the alumina layer surface porosity were also generated as a result. See Chapter 3 for more details.

5.2.3.3 XPS

Room-temperature XPS experiments were performed at the University of Alberta nanoFAB using a Kratos spectrometer. No electron flood gun was used and therefore the C 1s peak was calibrated to 285.0 eV for every sample. Casa XPS software was used for data processing and analysis. A Shirley background was applied to subtract the inelastic background of core-level peaks. A non-linear optimization, the Marquardt Algorithm, was used to determine the peak model parameters such as peak positions, widths, and peak

intensities. The model peak to describe XPS core-level lines for curve fitting was a product of Gaussian and Lorentzian functions. Survey scans were taken in triplicate for every sample.

Surface behaviour diagrams were employed to plot XPS measured elemental compositions following equations in work by Davis et al. [28] Determining the compositions can be completed using the following equations.

$$x = K(C_{Al} - C_P) \quad \text{Equation 5-1}$$

$$y = 2KC_P \quad \text{Equation 5-2}$$

$$z = K(2C_O - 3C_{Al} - 5C_P) = 1 - x - y \quad \text{Equation 5-3}$$

Relative compositions of aluminum (Al), phophorous (P), and oxygen (O) are shown by C with the corresponding elemental subscript, and K is the normalization factor. Compositions were then plot on surface behaviour diagrams as points (x, y, z).

5.2.3.4 SIMS

Depth profiles were obtained using a time of flight (ToF) SIMS IV instrument (ION-TOF GmbH). Analysis was carried out using ToF-SIMS software where negative secondary ion mass spectra were obtained. H^-, C^-, and Al^- ion peaks were used to calibrate the mass scale. CN^-, AlO^-, and TaO_2^- ion spectra will be the primary focus of this study as these ions were found to be the best representation of their respective regimes. Negative ion spectra was collected for the detection of electronegative elements that contain a stable negative species, and the type of protein did not need to be distinguished which can be done more easily with positive spectra. [29,30] The CN^- ion (m/z 26) spectrum was chosen to represent organic species as it demonstrated the strongest signal of any ion originating from organics. Negative ions CN^- and CNO^- are linked to the poly(amide) protein backbone. [30] AlO^- ions (m/z 43) demonstrated the strongest signal of the aluminum oxides and were chosen to represent the porous alumina region. In the unanodized control samples, the Al_2^- ion (m/z 54) was used to represent the bulk aluminum. TaO_2^- ions (m/z 213) demonstrated the strongest signal of the tantalum oxides and were chosen to represent the tantala barrier layer region. Any large momentary spikes in the depth profile data during testing are due to beam current instabilities and were disregarded during analysis.

To compare depth profiles, ratios of signal intensity were taken as a form of normalization. Each ion intensity was normalized to their respective scan's AlO^- ion average intensity to account for differences in each scan. Scan time is related to depth of the sample by sputtering rate of the species but, as sputtering rate is not consistent across all species the different regimes cannot be directly compared. The time scale for each spectrum was normalized in a similar fashion to the intensities of each spectrum. The method used to quantify the elastic regime of metals in stress-strain curves was adapted for this purpose. [31] Each region was truncated in a systematic way using the linear portions of the ion spectra. A line was drawn covering the linear portion of the data at either end of each regime. The midpoint of these linear regions was then taken as the start or end point of their respective regime. Each of these truncated regions were then expressed as a percentage of their scan's respective AlO^- region. This method sought to account for interface regions and best represent the bulk of that region for further quantification.

5.2.3.5 Statistical Analysis

Independent two sample unpaired t-tests, one-way ANOVA, and Welch's t-tests were performed on values obtained from SIMS and XPS scans performed in triplicate to determine statistical significance of the difference between the means of the different sets. A significance level of 5% was used to determine statistical significance.

5.3 Results

Ellipsometry and SEM results in Table 5.1 highlight differences in the multilayer films generated at 5 and 8 V.

Table 5.1. Ellipsometry and SEM data on the device structures formed with anodization at 5 and 8 V in 0.4 M phosphoric acid.

Parameter	Anodization Potential Employed			
	5 V		8V	
MSE ± SD	1.3	0.2	2.8	1.2
Alumina Thickness ± SD (nm)	79.8	3.5	78.6	3.9
Tantala Thickness ± SD (nm)	6.1	0.7	10.7	0.9

The percent alumina at the surface, indicated that there was 1.1 times the amount of surface alumina in the 8 V samples compared to the 5 V samples. Pore size of the 5 V and 8 V

anodized samples indicated a 34% increase in the 8 V samples. Pore diameter distributions are shown in Figure 5.1 for thin films anodized at 5 V and 8 V respectively.

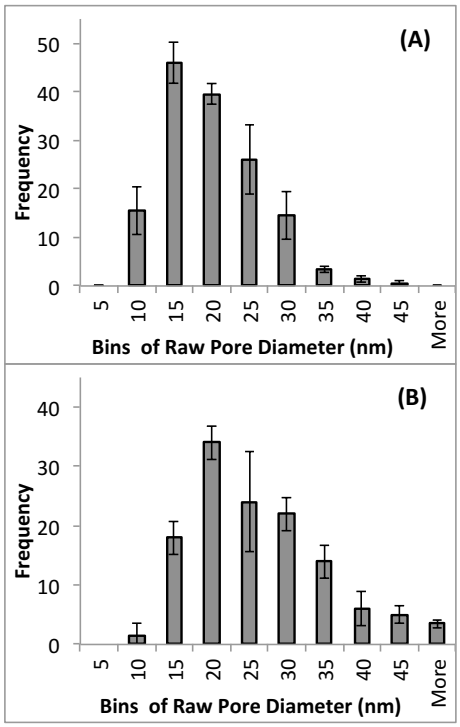

Figure 5.1. Pore diameter distributions following oxidation at (A) 5 V and (B) 8 V respectively. Anodization procedures both were carried out in 0.4 M phosphoric acid.

5.3.1 XPS

5.3.1.1 Phosphorous Content

Table 5.2 compares the phosphorous content of the samples in the form of P (2s)/Al (2p) ratios. The P 2s peak was chosen as opposed to the P 2p peak, because the P 2p was displayed in unanodized samples that had never been exposed to any form of phosphate or phosphorous. In those sample spectrums the P 2s peak was not displayed and it was determined that an aluminum plasmon loss peak was being expressed at the same binding energy of the P 2p peak.

Table 5.2. Summary of average P (2s)/Al (2p) ratios for unanodized, 5 V, and 8 V samples with exposure to no protein, prothrombin for 15 minutes, and prothrombin followed by anti-prothrombin for 15 minutes each. (n=3)

Protein Layers	P (2s)/Al (2p)		
	Unanodized	5 V	8 V
None	0.00±0.00	0.08±0.01	0.08±0.00
Prothrombin	0.00±0.00	0.07±0.00	0.09±0.03
Prothrombin & Anti-prothrombin	0.00±0.00	0.07±0.00	0.07±0.00

The low resolution XPS spectra are shown in Appendix 3. Anodized slides showed no statistical difference between ratios of P/Al regardless of the device formation applied voltage or the protein solutions exposed with a Welch's test [F(5,4.727)=1.192, p=.431].

5.3.1.2 Surface Behavior Diagrams

Davis et al. showed that the application of surface behavior diagrams could help study the hydration of aluminum anodized in phosphoric acid, among other surface structures. [28,32,33] Using these equations and the atomic composition data recorded from XPS analysis was plotted on the proposed diagrams. Three data points from 5 V and 8 V samples are shown on each of the tertiary diagrams in Figure 5.2. The 8 V data points showed higher consistency, and overlap is apparent. The marks in Figure 2 (A) were triplicate samples from one wafer and in Figure 2 (B) were triplicate samples from another wafer.

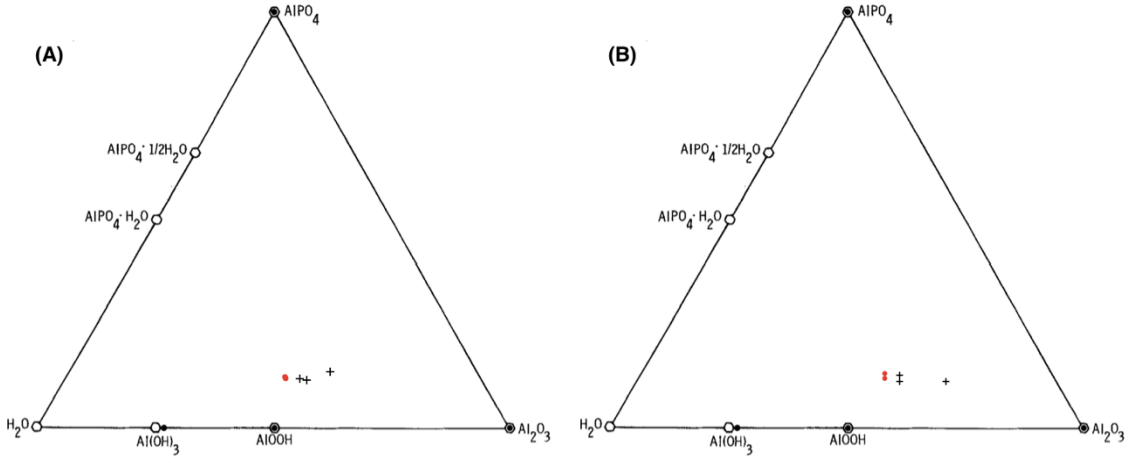

Figure 5.2. The 5 V (black +) and 8 V (red circle) anodized sample data plotted on tertiary surface chemistry diagrams from (A) wafer 1 and (B) wafer 2. (n=3 for each diagram)

Equivalent amounts of $AlPO_4$ were found in all films [t(10)=0.261, p=.800]. In both wafers 8 V samples showed greater H_2O [t(10)=2.430, p=.035] and lower Al_2O_3 [t(10)=2.539,

p=.029] in comparison to 5 V samples. However, difference wafers showed shifts on the diagram.

5.3.1.3 Nitrogen Content

To qualitatively evaluate binding of adsorbed proteins to the alumina, the N (1s)/Al (2p) intensity ratio was used. This ratio was chosen as the nitrogen signal originates exclusively from the protein layer and the aluminum signal was exclusively from the underlying alumina layer. Table 5.3 shows ratios of N/Al for various samples.

Table 5.3. Summary of average N (1s)/Al (2p) ratios for unanodized, 5 V, and 8 V samples with exposure to no protein, prothrombin for 15 minutes, and prothrombin followed by anti-prothrombin for 15 minutes each. (n=3)

Protein Layers	N (1s)/Al (2p)		
	Unanodized	5 V	8 V
None	0.00±0.00	0.00±0.00	0.10±0.07
Prothrombin	0.50±0.01	0.23±0.01	0.28±0.04
Prothrombin & Anti-prothrombin	1.06±0.37	0.63±0.00	0.56±0.03

Ratios of N/Al for each sample were found to increase across all samples as the number of protein layers increased. No significant difference resulted in the N/Al ratio between 5 and 8 V surfaces exposed to prothrombin [t(2.187)=1.710, p=.219] and prothrombin and anti-prothrombin [t(2.001)=3.378, p=.078]. the unanodized samples showed greater ratios regardless of the number of protein layers.

5.3.2 SIMS

SIMS allows for the investigation of the device structure and chemistry through the depth of the sample. Figure 5.3 shows a typical SIMS scan of an unanodized control sample. The large bulk aluminum region represented by the Al_2^- ion is clearly visible with the protein signal at the very beginning of the scan represented by CN^- ions. A second alumina region (AlO^- ion) at the tantalum interface was present due to aluminum reducing the native tantala (TaO_2^- ion) that forms when transferring the sample between sputtering machines. [34-36] The tantala (TaO_2^- ion) from exposure to atmosphere between depositions is minimal as a result of largely being reduced.

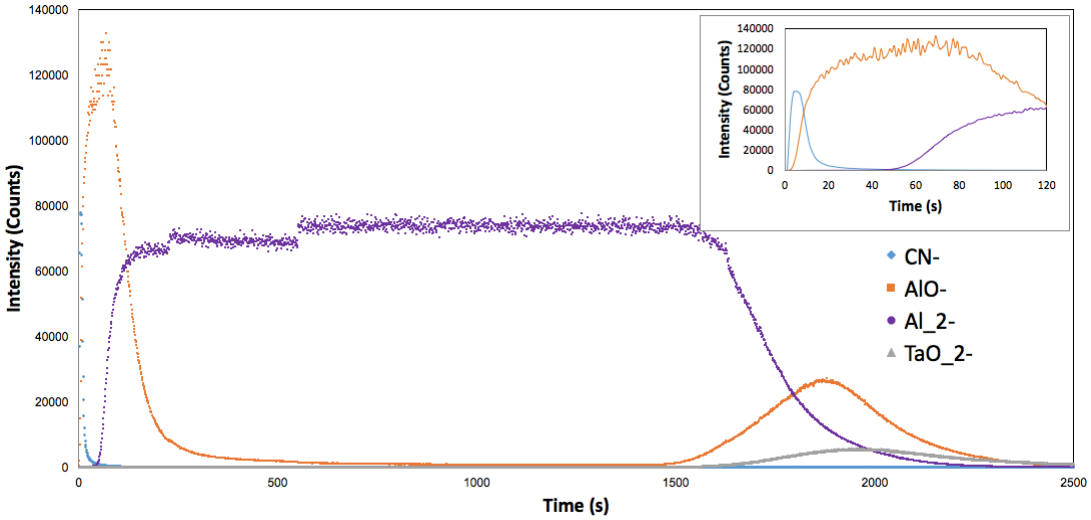

Figure 5.3. Typical ToF-SIMS depth profile of a typical unanodized control sample exposed to prothrombin for 15 minutes. Insert shows the first 120 seconds of the same scan magnified.

Figure 5.4 shows a typical scan of an anodized sample that was not exposed to protein, the insert showing the isolated CN^- ion curve.

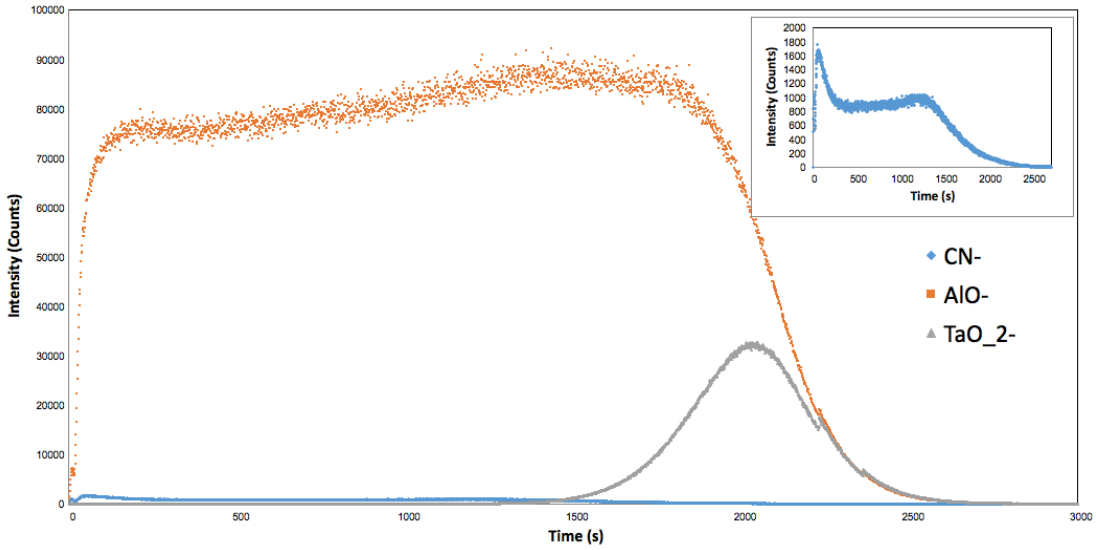

Figure 5.4. ToF-SIMS depth profile of a sample anodized at 5 V with no subsequent protein exposure. Insert shows the isolated and magnified CN^- ion curve.

In samples that were not exposed to protein solution a CN^- ion signal was detected, demonstrating a similar shape to the CN^- ion spectrum of samples that were exposed to protein solutions, although at significantly lower counts (<8.4%).

Figure 5.5 shows a typical SIMS scan of an anodized sample with relevant regions and designations of other important points on the CN^- curve (P1, P2, and P3) that will be referenced.

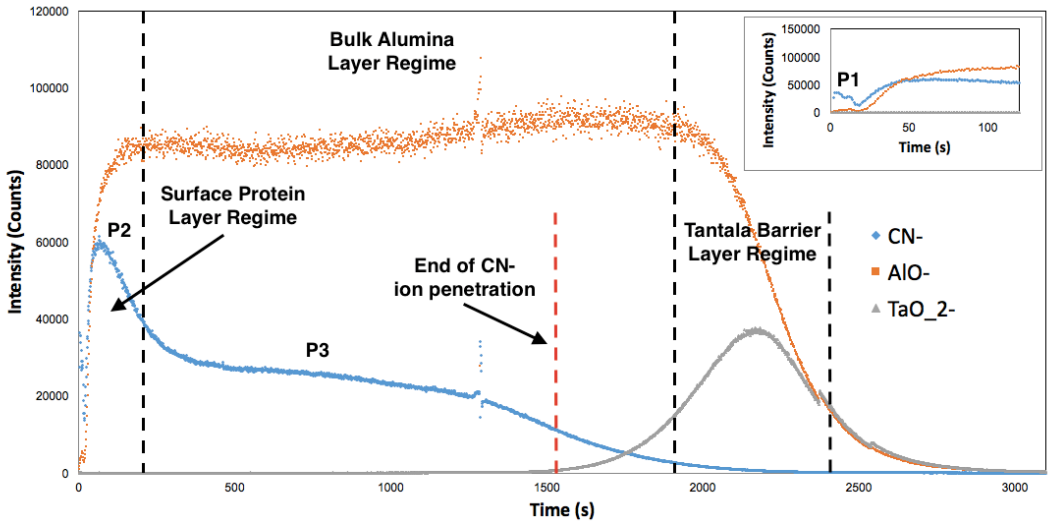

Figure 5.5. ToF-SIMS depth profile with regimes and important points labelled. Insert shows the first 120 seconds of the same scan magnified. The sample was anodized at 5 V and exposed to prothrombin for 15 minutes.

There was a peak in all signals after the first 15 to 20 seconds in anodized samples, denoted as P1 in Figure 5.5. The next peak of the CN^- ion in the first 300 seconds of the scan, denoted by P2 in Figure 5.5, represents the surface layer of protein. P3 in Figure 5.5 shows the protein species within the pores. The large plateau of the AlO^- ion represents the alumina bulk and the peak of the TaO_2^- ion represents the tantalum oxide barrier film.

5.3.2.1 Surface Ions

Other ions that showed the same general shape of spectra as the CN^- ion spectra were the H^- (m/z 1), OH^- (m/z 17), and CNO^- (m/z 42) curves. A typical depth profile with these four spectrums isolated is shown in Figure 5.6. The CNO^- ion likely represents the same type of materials that are detected by the CN^- ion, with a lower sputtering probability than the CN^- ion. The CNO^- ion was detected in similar proportions to the CN^- ion both in samples that were exposed to the protein solution as well as in samples that were not exposed to the protein. The H^- and OH^- ions were demonstrated in similar proportions regardless of if proteins were present or not.

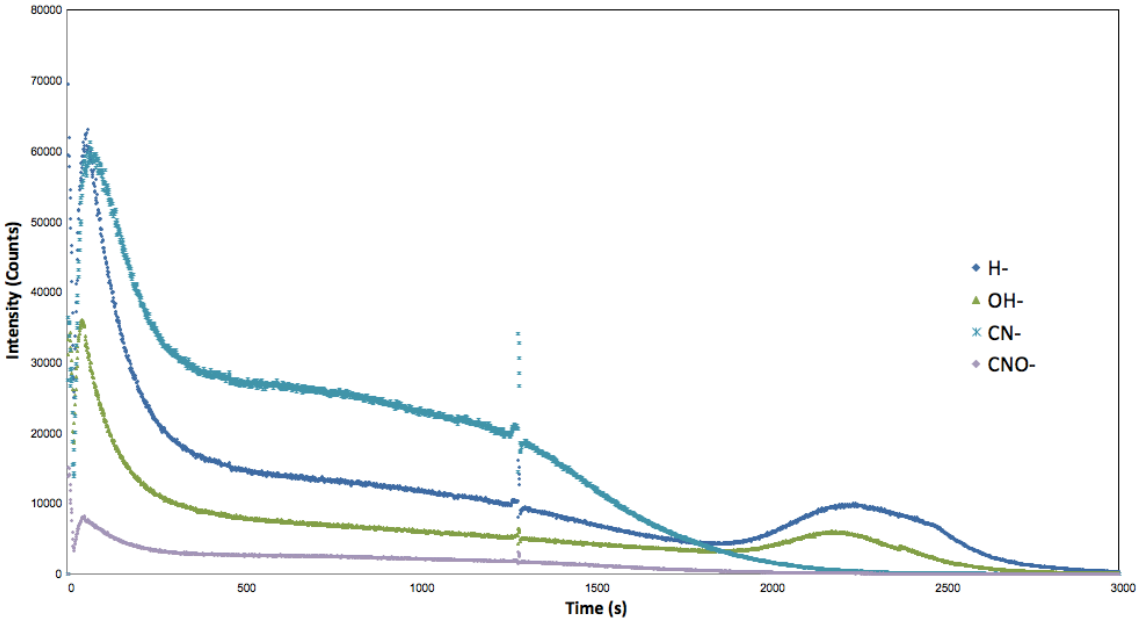

Figure 5.6. ToF-SIMS depth profile of a sample anodized at 5 V and exposed to prothrombin for 15 minutes. The CN, H, OH, and CNO curves have been isolated to demonstrate their comparable trend.

5.3.2.2 Protein Depth

SIMS depth profiles of 5 V and 8 V samples that were exposed to prothrombin for 15 minutes are shown in Figure 5.7.

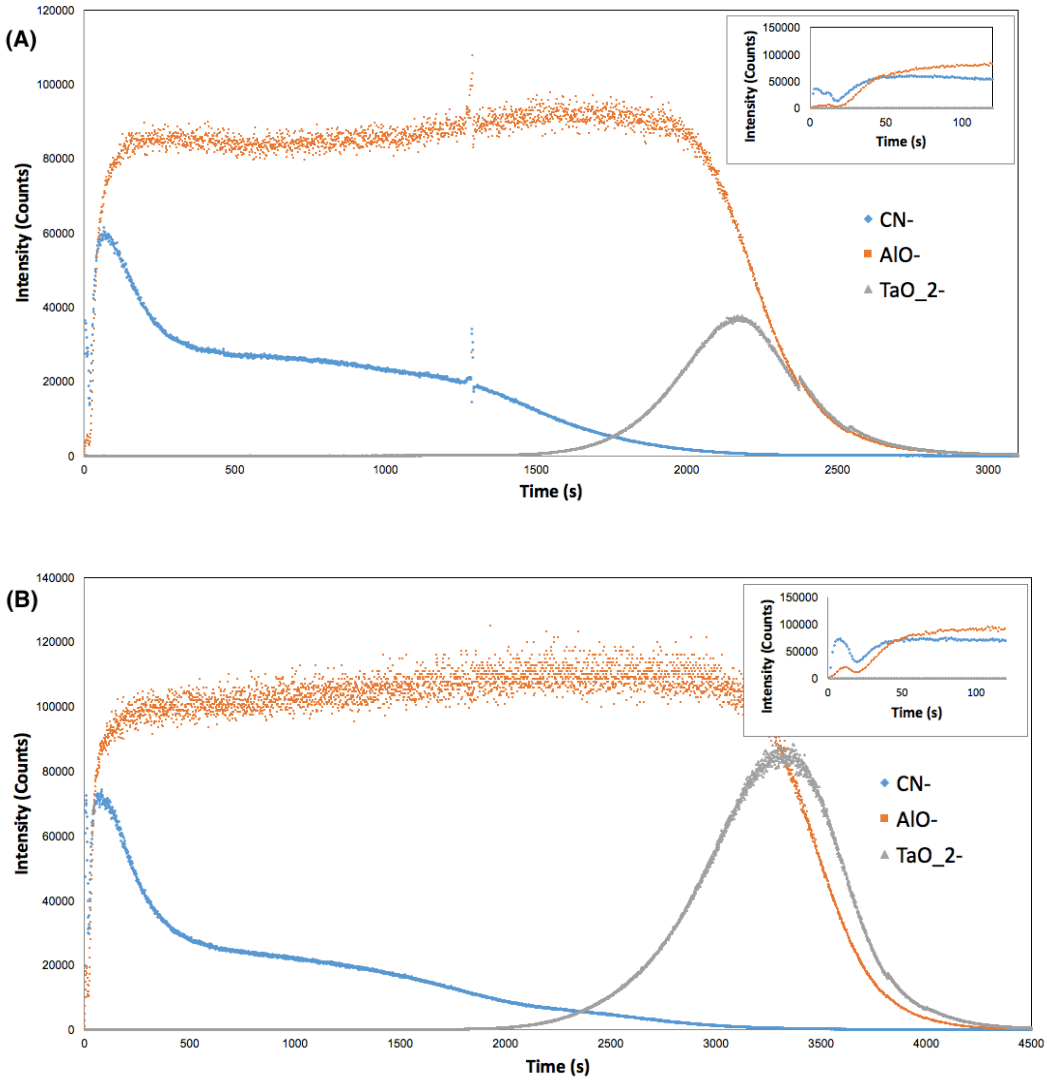

Figure 5.7. ToF-SIMS depth profiles of a typical sample anodized at (A) 5 V with exposure to prothrombin for 15 minutes and a typical sample anodized at (B) 8 V and exposed to prothrombin for 15 minutes. Inserts show the first 120 seconds of their respective scans magnified.

On 5 and 8 V samples exposed to prothrombin, the strength of P2 showed no statistical difference between the 5 V and 8 V samples, determined by an independent t-test [t(4)=0.239, (p=.822)]. However, there was a statistical difference between the strength [t(4)=5.329, (p=.006)] and depth of protein penetration [t(4)=3.349, (p=.029)] in the 5 V samples and 8 V samples based on the P3 region of the CN^- signal.

5.4 Discussion

5.4.1 XPS

5.4.1.1 Phosphorous Content

The phosphorous composition in the surface alumina film was investigated, as anodization in phosphoric acid allows for integration of phosphate anions into the porous anodic alumina. The phosphate incorporation from electrolyte creates a film that is resistant to hydration and relatively inert in aqueous environments.[37,38] Changes in the stability of these films, whether anodized at 5 V and 8 V, could influence the protein adsorption that results. Typically, porous films grown in phosphoric acid have been reported to contain 6-8 wt.% phosphate,[27,39,40] yet further increasing the phosphate content in the alumina may increase film stability. There was no statistical difference between the P/Al ratios for films oxidized at 5 or 8 V regardless of the number of protein layers exposed to the surface (p=.431). This data was a good indication that the oxidation procedure carried out in phosphoric acid electrolyte had a consistent effect on the phosphorous content of the top ~10 nm of the anodized slides. Techniques that are capable of analyzing deeper into the alumina films may reveal differences.

5.4.1.2 Surface Behavior Diagrams

Changes in composition of the 5 and 8 V slides, as well as between different wafers, were determined from surface behaviour diagrams. The 5 V samples showed no significant difference across the two sets of wafers, whereas the 8 V samples showed a significant difference. The difference illustrates the importance of the storage and handling procedures. The only difference between each wafer was when they were prepared, and the time between when they were prepared and tested. Tertiary diagrams in Figure 5.2 showed no statistical difference in the percentage of $AlPO_4$, with values were between 7.5 and 11% across all samples (p=.800). Studies by Davis et al., showed $AlPO_4$ compositions with anodization in 10 wt.% phosphoric acid at 10 V generated films with ~20% $AlPO_4$ and rinsing post-anodization samples with acetone instead of water showed ~53%.[28] It is expected that an increase in the presence of $AlPO_4$ on or within Al_2O_3 will help stabilize the surface, as the $AlPO_4$ phase prevents a change in microstructure due to surface hydration.[28,37,38,41,42] Increased surface

stability will likely allow for the product to have a longer shelf life and may influence protein adsorption.

The 5 V and the 8 V samples showed averages of 34.0% and 40.7% H_2O respectively (p=.035). It is important to understand that the H_2O content depicted in the surface behavior diagrams is not present exclusively as H_2O but reflects the overall hydration of the surface. This hydration can be present as H_2O or as an aluminum hydroxide (i.e. bayerite ($Al(OH)_3$) or boehmite (AlOOH)). The composition of H_2O increases at the expense of the measured composition of Al_2O_3. A difference was also measured in Al_2O_3 between the 5 V and 8 V samples (p=.029). Composition changes in the probed surface area could be due to the increased presence of oxygen resulting from the increase in surface alumina in the 8 V sample or some effects introduced by the change in microstructure. With low levels of phosphate, the alumina is exposed and becomes hydrated, and thus less underlying alumina is detected with XPS. Another reason supporting why increasing the phosphate content would result in greater surface reproducibility and stability.

5.4.1.3 Nitrogen Content

Ratios of N/Al for each sample increased as the number of protein layers increase, and values were higher on the unanodized surface. The majority of the nitrogen content was expected to be from the protein species. The N/Al noted when comparing unanodized to anodized samples showed a decrease. The anodized surfaces appear to impede the ideal, organized binding that occurred on the planar unanodized surfaces. However, it is difficult to compare these structures based on XPS data, as the aluminum changes structure and density and the probing distance is likely altered as a result.

There was no statistical difference between the N/Al ratios for the 8 V sample with prothrombin compared to the 5 V sample with prothrombin (p=.219) or prothrombin and anti-prothrombin layers (p=.078). An increase in the absolute N/Al ratio with complex formation is favorable for the device, as an increase in available antigen on the surface would allow for an increase in the anti-prothrombin binding and the limit of detection. This variation in comparative N/Al ratios indicates that no difference exists between 5 V and 8 V samples with a prothrombin or prothrombin and anti-prothrombin layers on the device surface. This supports that no difference in prothrombin binding orientation or efficiency exists between the

5 and 8 V samples, however with a greater change in the surface area, steric hindrance could limit the complex formation when exposed.

The unanodized sample with a protein complex, prothrombin and anti-prothrombin, as well as the 8 V sample with no protein layers showed a greater relative variance than other samples, likely due to surface contamination. XPS is a highly sensitive technique so any form of contamination will be magnified compared to other analytical techniques.

5.4.2 SIMS

5.4.2.1 Surface Ions and Surface Hydration

It stands to reason that the shape of H^-, OH^-, CN^-, and CNO^- ions maybe indicative of the microstructure in some way. A combination of the proposed protein penetration effects as well as species implantation during sputtering is a possible explanation. Species implantation during the sputtering process of a porous film is known to occur and would cause the continual decline observed throughout the P3 region, adding further explanation to this spectra shape.

H^- and OH^- ions demonstrate a peak at the tantalum interface, another region which was likely hydrated during exposure to atmosphere before the aluminum layer was sputtered. The H^- fragment is easily created during SIMS, as the protein contains hydrogen as well as the surface alumina that is hydrated prior to exposure to the ultra-high vacuum system for analysis. Only the physisorbed hydrogen would be removed from the surface by the vacuum, while any chemisorbed hydrogen would require stronger forces to fragmentize. Similarly, the hydroxides are integrated into the portion of the alumina that forms close to the electrolyte.

It is assumed that all of these ions are located mainly at the exposed alumina interfaces through hydration or electrolyte integration of these species, and that the spectra curve shape was indicative of a material that lines the pore walls. This would provide further explanation of the CN^- and CNO^- curve shapes. A more precise measure of aluminum hydration would be the $AlOH^-$ ion but unfortunately the m/z ratio of $AlOH^-$ is 43.99 is essentially identical to the m/z ratio of COO^-, which is 44.01. There showed significant broadening of the signal at this mass ratio and so it was deemed an unviable method to quantify hydration.

5.4.2.2 Protein Depth Penetration

SIMS data demonstrates where proteins sit in regard to the aluminum or alumina layer. Taking the CN^- ion as the indicator of protein showed that on unanodized control samples, with a non-porous native alumina, the protein species does not penetrate into the surface film. On alumina layers (see Figure 5.5) the first peak, denoted P1, can be explained by the fact that there is a significant structure change from a semi-dense monolayer of protein on the alumina surface to a highly porous structure at the time of P1. Furthermore, the early stages of a SIMS profile often exhibit such matrix effects as it is considered a pre-equilibrium period. [43] Whereas, the main surface peak (P2) in the CN^- ion shows a large quantity of prothrombin was built up at the surface and the P3 region showed penetration into the porous alumina structure occurred. Depth of the protein within the anodic alumina layer changed depending on the applied potential.

The intensity of the CN^- signal decreases by 50 to 65% across all samples when comparing P2 to P3. The CN^- ion signal at P3 penetrated the porous alumina 21.7% more and P3 was 19.7% stronger in the 5 V samples compared to the 8 V samples. The increased amount of protein within the pores of the 5 V samples demonstrates alterations between the 5 V and 8 V devices, and interactions with the exposed protein solutions. Consistency and minimization of protein penetration are essential to maintain sensitivity of the device. Prothrombin in the pores may provide inconsistent binding sites for the analyte as well as increase the effective refractive index of the alumina layer contributing to scatter in the system.

The CN^- ion spectrum was representative of a non-specific organic species and therefore it cannot be determined whether intact prothrombin detected at the surface differs in structure from proteins detected within the bulk. Alumina has demonstrated catalytic properties towards adsorbed proteins (see Chapter 9 Introduction). Should prothrombin contact the alumina surface in a way that prevents the glutamic acid residues from securely binding and protecting the protein from degradation, other regions of the protein may be degraded. Fragments of denatured protein may fall into the pores by diffusion and generate the CN^- ion signal in the bulk of the sample. It is possible that with smaller pores in the surface formed at 5 V, fragment 1 of prothrombin binds to the alumina and positions the molecule perpendicular to

the pore wall, allowing the molecule to reach the other side of the pore and be degraded (see Figure 5.1). The increased occurrence of proteins spanning the pore could translate to more organic-based fragments being created and therefore an increase in the CN^- ion signal penetrating the bulk of the alumina.

The size of the protein molecules further supports this idea. A prothrombin molecule is 11 nm long and 4.5 nm wide at its widest point. [24] If there were whole prothrombin molecules located within the pores, one would expect a reduction in pore size to reduce the penetration of the CN^- ion signal. With an average pore diameter of 23.9±9.3 nm in the 8 V samples a single prothrombin molecule cannot block the entire pore and prevent other molecules from entering. With an average pore diameter of 17.9±6.7 nm in the 5 V samples, should a single prothrombin molecule bind normal to the wall of the pore, other prothrombin molecules would have great difficulty in being able to enter. This fact would reduce the probability that protein could enter the pores and result in a decline of the CN^- ion counts near the alumina surface however, this was not the case. Furthermore, it is possible that the higher porosity of surface alumina in the 5 V samples allowed for the SIMS sputter process to push protein molecules or fragments into the pores more easily.

Additional observations are apparent in the SIMS scans regarding the differences in tantalum structures of the 5 and 8 V samples. The TaO_2^- ion peak was more prominent in the 8 V samples compared to the 5 V samples which was consistent with the tantalum oxide barrier layer growing at a rate between 1.6 to 1.8 nm/V, [44-47] and larger diameter pores in the 8 V samples will allow for more exposed tantalum hillocks to grow into the bottom of the alumina structure.

5.5 Future Work

Repeating XPS and SIMS work with lower prothrombin concentrations may generate less protein penetration into the alumina film. Base on the radiolabelled work conducted in Chapter 9 it was determine that a monolayer of prothrombin forms on the surface with exposing a solution of ~0.2 mg/ml for 15 minutes.

Furthermore, different SIMS scan parameters could be used in attempts to confirm protein location with greater accuracy. Numerous studies used positive spectra detection as well as different sputtering and probing molecules for analysing protein-surface interactions.

[29,30,48,49] Different charge neutralization during the measurement process can be used with insulating substrates, [30] and the use of Bi_3^+ primary ions for analysis of complex surfaces has shown improvement over Ga^+ and Cs^+ primary ion sources.[49]

5.6 Conclusions

Subsequent to device fabrication, biologics were exposed to the porous anodic alumina surfaces leading to adsorption and penetration into the pores of the thin film. Anodization at potentiostatic voltages of 5 V and 8 V led to changes in the average pore diameter and the porosity. Exposing protein layers for 15 minutes, first prothrombin and in some cases a second layer of anti-prothrombin, created notable differences in the XPS and SIMS data, investigating both surface adsorption and penetration. The following conclusions were made.

1. Surface behavior diagrams and XPS data determined that the storage and handling of samples have a noticeable impact on their surface chemistry.
2. N/Al ratios showed with no difference with prothrombin incubation on 5 and 8 V films. The same result was found for anti-prothrombin incubation.
3. The surface protein in the alumina layer, measured by the P2 peak, showed no difference in strength between the 5 and 8 V samples.
4. $AlPO_4$ content was constant in all samples with between 7.5 and 11%. Samples oxidized at 8 V showed greater H_2O content and lower Al_2O_3 compared to the 5 V sample.
5. The phosphoric acid electrolyte had a consistent effect on the phosphorous content of the slide surface probed with XPS between films created at 5 and 8 V.
6. Investigation of SIMS data for H^-, OH^-, CN^-, and CNO^- ion signals support that the shape of the depth profile curves may be indicative of the porous nature of the samples.
7. Devices created at 5 V showed greater protein penetration within the alumina layer. SIMS systematic quantification methods showed an increase in the protein signal by 21.7% in depth penetration and 19.7% in intensity in the 5 V samples over the 8 V samples.

The investigation of protein interaction on porous alumina structures anodized at 5 V and 8 V will contribute to future analysis and understanding. The 8 V samples showed less protein diffusion into the pores and will be used for future tests. This technique used to measure protein depth in porous films may be useful in other adsorption-based studies.

Chapter 6 – Point-of-Care Detection Platform Using Tunable Anodic Alumina Surfaces[1]

6.1 Introduction

The current clinical laboratory testing paradigm is based primarily on ELISA testing protocols with biomarker assessments in heart disease, [1,2] cancer, [3,4] and infectious disease[5-8] forming the bulk of testing. Thus, biomarker testing typically involves hospital laboratory facilities. Rapid or "STAT" testing typically requires extensive resources invested into specialized device readers or to transport specimens for centralized processing. Thus cost, time, and complexity remain substantial barriers to testing protocols for front-line physicians or emergency personnel. Home tests for diabetes or coagulation disorders have similar barriers and as a consequence, systematic reviews and evidence-based assessments reveal that the impact of these testing protocols on clinical decision-making is limited. [9-12] The need for point-of-care testing continues to grow. For example, the prevalence of anticoagulation in general population has increased dramatically over the past decade. [12] Rapid home testing would be a significant advance in the treatment of these patients that need to make routine trips to and from specialist clinics or laboratory facilities to follow their coagulation status.[13]

Langmuir and Schaefer[14] first reported the adsorption of proteins from a solution through the production of light interference. The device consisted of a reflective substrate, and a single film of barium stearate along with an antibody layer that created light interference. Succeeding this, Rothen and Landsteiner[15] developed a device using a similar technique comprised of different materials. However, both experienced limitations with regards to colour contrast and glancing angles. The roadblock of glancing angle was overcome in the 1970's through patents published by Giaever (1974, 1975, and 1976) that reduced the

[1]A version of this chapter has been submitted to the Journal of Thin Solid Films. Sweet, HM, Burrell RE, Moxham K, Nickel M, McMullen T. Characterization of Thin Anodic Tantala-Alumina Films for a Protein Detection Platform.

substrate reflection. His first patent used a method to produce voids in a thin film where adsorption of large biological particles to the antibody-coated substrate had occurred. Subsequent variations utilized different surfaces, but the synthesis of these devices was complex, and difficult to reproduce. The problem of glancing angle was overcome but the contrast of the interference remained weak.

The patent by Burrell et al. [16] helped solve the sensitivity problem with earlier thin film diagnostic platforms by using a porous anodic alumina layer on tantalum. The aluminum oxide layer minimized light scattering and differences in the refractive index between the aluminum oxide and adsorbed protein layer to produce highly sensitive thin films. These thin film devices have detected protein in the nanomolar range in as little as 5 min. [17] With improved knowledge in the field of anodization, also known as oxidation, the resulting porous alumina layer is tunable. The main governing factors, specific to thin alumina films, include the electrolyte type, [18-21] strength (i.e., concentration or pH), [22-24] temperature, [21,24,25] and applied voltage. [18,20-22,24,26,27] See Chapter 4 for details. These parameters control the porosity through pore diameter and pore wall thickness, [28] and ultimately the refractive indices. Further tuning of the porous alumina can be achieved based on the applied anodization cycle conditions, [29] pre-treatment, [26,29] and post-treatment, [29-31] but was not examined during this work as it was not necessary for device detection. Future work may investigate these processes.

We propose and derive a tunable thin film platform suitable as a point-of-care diagnostic for detecting protein-protein, and peptide-protein complexes. The technology allows for visible interference colour shifts through changes in the OPL of light, a product of the refractive index and physical path length. We examine how the initial aluminum thickness and oxidation process generate different alumina nanostructures. The process variables affect end components of thickness, porosity, and refractive index. Understanding these changes in the structural components allow the surface to be tuned for visible analysis of various proteins, while ensuring that the resulting color shifts are in regions of first and second order interference for high sensitivity.

To create a thin film diagnostic capable of use with many different proteins and under varying conditions, we also documented a novel protein immobilization methodology suited to the highly reactive environment of aluminum oxide surfaces. [32] In the list of anions that

react with alumina in water, formate is observed to have a high affinity towards alumina, which is analogous to carboxyl groups under a pH which deprotonates the aspartic acid and glutamic acid groups. [33,34] We characterize this system by examining the hydrated surface alumina that securely binds vitamin K dependent proteins, such as prothrombin, likely through an esterification reaction. Prothrombin, a three-domain protein of 72 kDa contains Fragment 1, Fragment 2, and thrombin. Fragment 1 contains 10 gamma-carboxyglutamic acid residues in the first 33 amino acids[35] These 20 carboxyl groups have a high binding affinity for alumina[36-38] and govern the orientation of binding on the surface.

Since sensitivity and specificity can be optimized for individual proteins and test purposes, we demonstrate that the device is tunable using the example of a coagulation protein, prothrombin, using an antigen-antibody complex on our hydrated alumina surface. We demonstrate that aluminum deposition and the oxidation process influence the initial device surface and the colour changes with immobilizing prothrombin and anti-prothrombin on the surface. These experiments demonstrate the utility of a tunable thin film device to perform point-of-care testing for antigen-antibody complexes.

6.2 Materials and Methods

6.2.1 Thin Film Deposition

Unprocessed silicon wafer substrates 100 mm in diameter (University Wafer, South Boston, MA) were cleaned in a piranha solution (J.T. Baker, Center Valley, PA). Wafers were dried using nitrogen gas in a spin rinse dryer and coated using planar magnetron sputtering systems. A tantalum target of 99.95% purity and aluminum target of 99.9995% purity were used (Kurt J. Lesker Company, Jefferson Hills, PA). Tantalum deposition was at constant power with a power density of 1.54 W/cm^2 or 6.6 W/cm^2 with an argon pressure between 7 and 10 mTorr. Aluminum deposition was at constant power with a power density of 6.6 W/cm^2 and an argon pressure of 7 mTorr. A tantalum layer of ~200 nm was sputtered and above subsequent aluminum layers between 20 and 150 nm on different substrates. Tantalum and aluminum film uniformities were 13 and 2.4% respectively. Tantalum was sputtered, and the substrates were switched to a different sputter system, exposing them to atmosphere, prior to aluminum deposition.

6.2.2 Thin Film Oxidation

Wafers were cleaved into pieces ~6.3x1.3 cm and one-step anodization was carried out at 8 V under potentiostatic conditions. The anode, sputtered layers to be oxidized, and cathode, aluminum foil, were kept parallel to one another with 4 cm of separation. The electrolyte consisted of 0.4 M phosphoric acid, at room temperature (21±2°C). See Chapter 3 for additional details.

Devices at three critical stages were constructed, depicted in Figure 6.1. Stage a, was carried out until the aluminum was fully converted to a porous alumina layer and the current density plateau, that results with pore formation, undergoes a rapid decline to >0.1 mA/cm^2. Following pore formation, the tantalum oxide barrier layer forms causing a decline in current density. Anodization for stage b was halted when ~87% of the tantala thickness (compared to the thickness at stage c) had formed and a current density of <0.07 mA/cm^2 was reached. Lastly, stage c, was anodized for a constant period of 15 minutes.

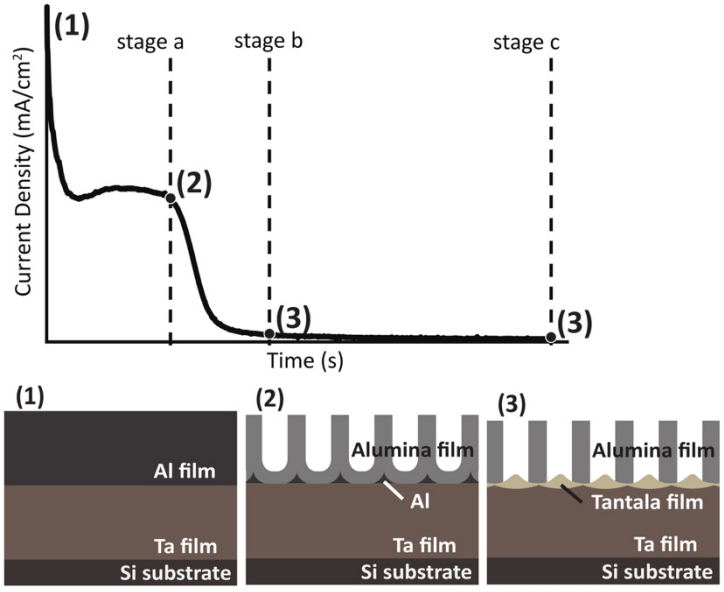

Figure 6.1. Shows a typical anodization current density versus time plot with critical stages labelled (top) along with cross-sections of the devices at these stages (bottom). Formation consists of (1) as sputtered, (2) after anodization at 8 V in 0.4 M phosphoric acid until the end of pore formation - stage a, and (3) oxidation until the majority of tantala formed or a period of 900 seconds - stage b/stage c.

6.2.3 SEM

FE SEM images were taken using a through-the-lens detector. An accelerating voltage of 3 or 4 keV was used with apertures of 15 or 20 μm for alumina and aluminum, respectively. All SEM images were collected under vacuum conditions on prepared samples with a pixel dwell time of 64 μs, and a probe current of 35 pA. Images were captured of the surface and average pore diameters and cross-sectional thicknesses measured. ImageJ (National Institutes of Health, Bethesda, MD, https://imagej.nih.gov/ij/) was used for collecting measurements. Average pore diameters were extracted from pores measurements along three horizontal and three vertical lines (n=3).

6.2.4 Ellipsometry

Variable angle spectroscopic ellipsometer (M-2000V) was used to analyze the optical constants, porosity, and thicknesses of the thin film layers. Models were built using a bottom up approach on the CompleteEASE® software (J. A. Woollam Co., Inc, Lincoln, NE). The base layer in the model is an optically thick 200 nm tantalum layer with an overlying barrier tantalum pentoxide (Ta_2O_5) and porous alumina (Al_2O_3) layer formed during the anodization process.

Scans were conducted with incident light from 370 to 700 nm between 45 and 75° at 10° intervals. Standard data was fit to a model comprised of a B-spline layer for the tantalum metal, a Cauchy layer for the tantala, and an anisotropic Bruggeman EMA layer for the porous alumina. The EMA layer was fit with depolarization factors of 0 for the z axis and 0.5 for the x-y split axis, which correlate with a porous columnar structure. The refractive index values were recorded in the x-y plane. Alumina and tantala thickness values were fit along with the percent void in the EMA to generate optical constants of each layer. No improvements in MSE occurred while using an EMA layer to model the surface roughness, and scans to confirm that depolarization during examination of the porous alumina layer were negligible.

6.2.5 Adsorption of Biologics

A hydrophobic outline of 1 cm diameter circles were created for each test using a Sharpie® marker. Purified human prothrombin in 20 mM Tris-HCl, 0.1 M NaCl buffer at pH 7.4, (ACOA, Aniara, West Chester, OH) was pipetted onto the surface within the constant

area. Volumes consisted of 20 µl at 1 mg/ml and were left for 15 minutes at room temperature in a 100% relative humidity environment, to minimize evaporation. The solution was then removed with a pipette, and the slide was rinsed thoroughly with deionized water. The affinity purified anti-human prothrombin (sheep) in 10 mM HEPES, 150 mM NaCl, and 50% (v/v) glycerol (ACOA, Aniara, West Chester, OH) was dialyzed in phosphate buffered saline at pH 7.4. Anti-prothrombin was pipetted onto areas with prothrombin and directly onto the surface as a control. Solutions consisted of 20 µl at 100 µg/ml and were exposed for 15 minutes. Excess protein was removed with a pipette and the surface rinsed with deionized water and dried.

As controls for non-specific binding, 3 IgG antibodies were exposed to the device surface, previously coated in prothrombin. Anti-PDGFR-α (C-20) affinity purified rabbit polyclonal antibody (Santa Cruz Biotechnology, Santa Cruz, CA), anti-thyroid transcription factor (TTF)-1 (8G7G3/1) mouse monoclonal antibody (Santa Cruz Biotechnology, Santa Cruz, CA), and anti-rubella mouse monoclonal antibody (specific for E1) (Millipore Corporation, Temecula, CA) were exposed to the device surface for 15 minutes using the same procedure as described above. All solutions were at 200 µg/ml in PBS.

6.2.6 Visible Interference Colour Detection

Colour shifts were observable by eye with a polarizing film to eliminate p-polarized light off the device surface and viewed at an incidence angle of 75° to generate the strongest colour contrast. Raw images were captured to obtain colour coordinates. To obtain luminance-chrominance Yxy coordinates for quantification of the surface colours, the same conditions were used as viewing by eye and images were captured using a camera. Images were uploaded to a colour coordinate generating software (http://www.ginifab.com/feeds/pms/pms_color_in_image.php & http://colormine.org/convert/rgb-to-yxy) and coordinates were averaged over five consistent positions for each protein spot (n=3). The bare surface was averaged over four values around the exterior of each protein spot (n=9).

6.2.7 Statistical Analysis

When conditions of random sample representation of the population, homogeneity of variance, and nearly normal distributions were met, a one-way ANOVA test was run. In cases where variances were not equal a Welch's t-test test was run. The respective post hoc tests were completed to determine which groups were different. A 5% level of significance was used for all tests.

6.3 Results

6.3.1 Aluminum Thin Film Deposition and Oxidation

We created thin film templates with aluminum and tantalum sputtered on a substrate that were then subjected to anodization analyzed at three stages as shown in Figure 6.1. The anodization process was started from four different initial aluminum thicknesses; 78±2.2, 95±1.9, 115±2.8, and 149±3.1 nm. For each starting thickness, the pore size during anodization was followed with representative SEM images outlined in Figure 6.2 for the three stages of anodization. The mean pore size for each stage of formation (a, b, and c) was quantified in Figure 6.3. In all cases, the pore diameter increases with anodization length of time.

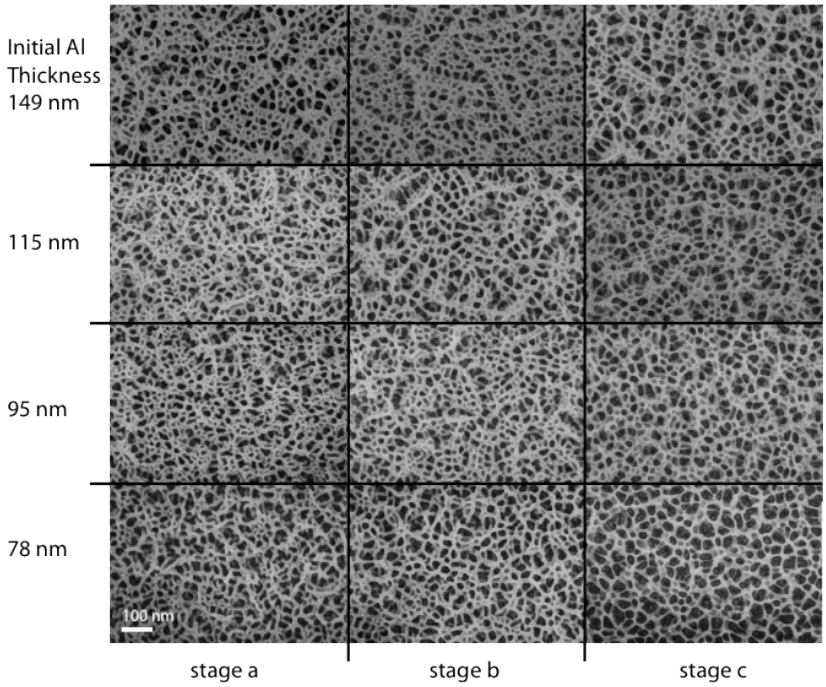

Figure 6.2. SEM images of porous alumina surfaces from four initial aluminum thicknesses. Anodization was conducted at 8 V in 0.4 M phosphoric acid until stage a, b, and c.

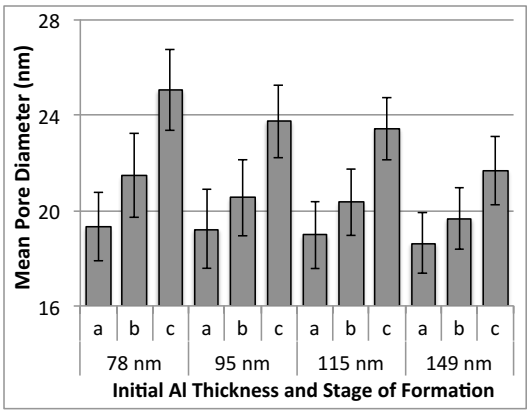

Figure 6.3. Mean pore diameters at the alumina surface from four sputtered aluminum thicknesses.

The mean pore diameters at each anodization stage for one aluminum thickness were found to be significantly different regardless of the thickness (p=.000). When comparing the pore diameters of all four aluminum thicknesses anodized to stage a (p=.129) or b (p=.471), no significant differences were documented. When anodized to stage c there was a significant difference between the pore size of all devices (p≤.017) except between those with aluminum layers of 78 and 95 (p=.149) as well as 95 and 115 nm (p=.859). While the overall mean pore

size increased with anodization time, the overall distribution about the mean was similar for each of the four starting films as shown in Figure 6.4.

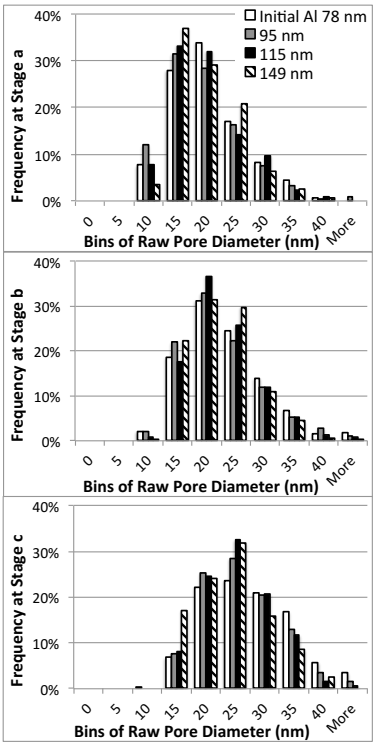

Figure 6.4. Frequency of pore diameter resulting from devices with four initial aluminum thicknesses following anodization at 8 V in 0.4 M phosphoric acid. Plots are shown from top to bottom for anodization to stage a, b, and c respectively.

6.3.2 Variable Angle Spectroscopic Ellipsometry

Ellipsometry from wavelengths 370 to 700 nm provided refractive indices for thin film devices when anodized to stages b and c, shown in Figure 6.5.

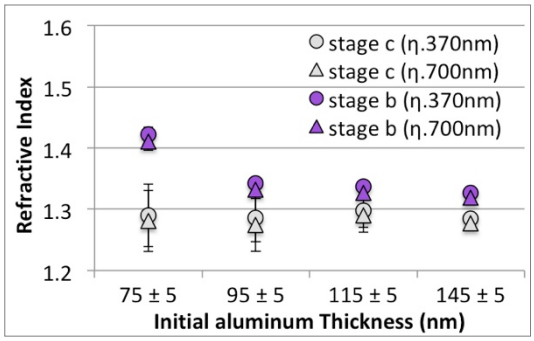

Figure 6.5. Optical constants in the xy plane for devices with different initial aluminum thicknesses anodized until stage b or c are shown at wavelengths of 370 and 700 nm. Extinction coefficients were zero.

A decrease in the refractive index was observed for anodization to stage b with increasing aluminum thickness. Aluminum depositions of ~75 and ~145 nm showed significant differences in the resulting refractive index values between anodization to stage b and stage c ($p<.05$ and $p<.001$, respectively). See Table 6.1 for details. Aluminum of ~95 and ~115 nm anodized to stage b resulted in refractive indices that showed no statistical significance, ($p=.537$) whereas all other combinations of thicknesses anodized to stage b showed refractive indices that were statistically significant ($p<.05$). At stage c for all thicknesses no significant differences were found between the refractive indices ($p=.959$). Table 6.1 shows the statistical analysis results of the effect on alumina refractive indices with anodization to stage b and c with the same initial sputtered aluminum.

Table 6.1. Statistical analysis comparing the effect of anodization stage on the alumina layer refractive index. (n=3)

Anodization Stage	Aluminum Thickness, and Mean Refractive Index	p Values (Independent t-test)
stage b stage c	70 nm, 1.423±0.012 78 nm, 1.290±0.050	t(4)=4.47, *p<.05*
stage b stage c	95 nm, 1.342±0.004 95 nm, 1.287±0.040	t(2.04)=2.37, p>.1
stage b stage c	120 nm, 1.337±0.002 115 nm, 1.300±0.026	t(2.03)=2.44, p>.1
stage b stage c	145 nm, 1.327±0.003 149 nm, 1.287±0.006	t(4)=11.18, *p<.001*

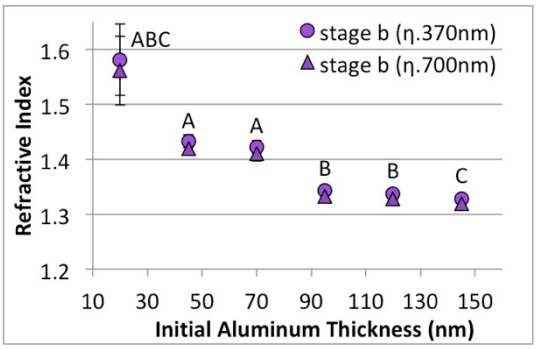

Figure 6.6. Optical constants in the xy plane for devices with initial aluminum thicknesses from ~20 to 150 nm, anodized until stage b are shown at wavelengths of 370 and 700 nm. Letters shown above markers categorizes statistically significant mean values. Extinction coefficients were zero.

Letters above markers in Figure 6.6 show significant differences between the mean refractive index values of alumina films. Slides with 36 and 60 nm, 86 and 111 nm, and 135 nm alumina generate layers with the same refractive index values. The refractive index of slides with 14 nm alumina films were included in the mean of all groups, likely due to the large variability shown at low aluminum thicknesses. The statistical analysis for the effect of alumina thickness on the resulting alumina refractive index with anodization to stage b is shown in Table 6.2.

Table 6.2. Statistical analysis comparing the effect of alumina thickness on the alumina layer refractive index at 370 nm anodized to stage b. (Welch's t-test, F(5,5.35)=57.65, p=.000) (n=3)

Slide	Alumina Thickness, Mean Refractive Index, and Mean Category	Vs. Slide	p Values (Welch's t-test, p<.001)
1	14 nm 1.581±0.065 ABC	2 to 6	p>.05
2	36 nm 1.433±0.012 A	3 4 to 6	p>.5 *p<.015*
3	60 nm 1.423±0.012 A	4 to 6	*p<.015*
4	86 nm 1.342±0.004 B	5 6	p>.5 *p<.05*
5	111 nm 1.337±0.002 B	6	*p<.05*
6	135 nm 1.327±0.003 C		

Ellipsometry was used to assess how the alumina thickness changes with anodization as well as quantify the formation of the tantala layer (see Figure 6.7). It was observed that the alumina film thickness decreases the most with the 78 nm aluminum film, with progressively smaller changes as the starting thickness increases. The tantala layer formation is generally uniform (around 12 nm) for all starting conditions and was primarily completed by anodization to stage b (see Figure 6.7).

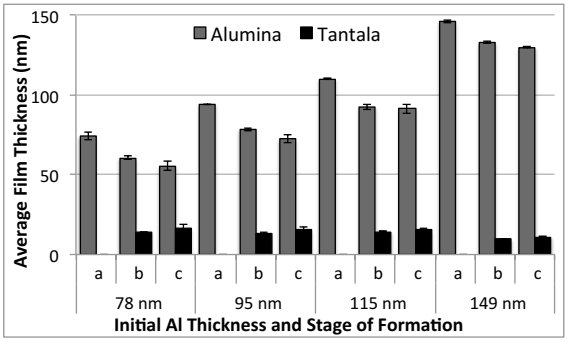

Figure 6.7. Alumina and tantala thicknesses following anodization at 8 V in 0.4 M stirred phosphoric acid until stage a, b, and c. Sputtered aluminum thicknesses were 78, 95, 115, and 149 nm.

Figure 6.8 compares differences in alumina thicknesses measured with ellipsometry and SEM techniques after anodization to stages a and b.

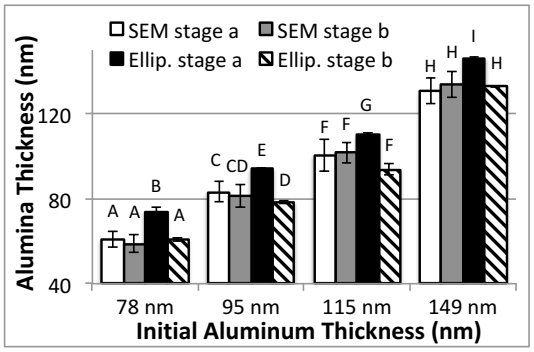

Figure 6.8. A comparison of alumina thicknesses with oxidation to stage a and b of formation, measured with ellipsometry and SEM techniques. Separate tests were carried out for each of the four initial aluminum thicknesses. Letters shown above bars categorizes statistically significant means.

Variations in the sputtered aluminum thickness and anodization time altered the resulting alumina film thickness. Statistically significant means are shown with different letters above bars in Figure 6.8. One-way ANOVA or Welch's t-tests were complete on the alumina thicknesses measured from the four aluminum thicknesses depending on results of the Levene's tests (78 nm Al one-way ANOVA results [$F(3,22)=11.967$, $p=.000$]; 95 nm Al Welch's t-test results [$F(3, 8.541)=350.625$, $p=.000$]; 115 nm Al Welch's t-test results [$F(3, 7.606)=34.168$, $p=.000$]; 149 nm Al Welch's t-test results [$F(3, 9.609)=158.707$, $p=.000$)]. Statistical analysis results are shown in Table 6.3.

Table 6.3. Statistical analysis comparing the effect of the measurement technique (SEM or variable angle spectroscopic ellipsometry (VASE)) used to obtain the alumina thicknesses with anodization to stage a and b. Separate tests were carried out for each of the four different initial aluminum films. (n=3)

Aluminum Thickness and Measurement Tool	Anodization Stage and Alumina Thickness ± SD (nm)	Vs. Test	p Values (Welch's t-test or ANOVA*)
78 nm, SEM*	Stage a, 61.08 ± 3.82	SEM, stage b	p>.5
		VASE, stage a	*p<.001*
		VASE, stage b	p>.9
	Stage b, 58.86 ± 4.09	VASE, stage a	*p<.001*
		VASE, stage b	p>.9
78 nm, VASE*	Stage a, 74.14 ± 1.79	VASE, stage b	*p<.01*
	Stage b, 60.67 ± 0.64		
95 nm, SEM	Stage a, 83.24 ±4.63	SEM, stage b	p>.7
		VASE, stage a	*p=.000*
		VASE, stage b	*p<.05*
	Stage b, 81.22 ±5.18	VASE, stage a	*p<.001*
		VASE, stage b	p>.4
95 nm, VASE	Stage a, 94.16 ± 0.23	VASE, stage b	*p<.005*
	Stage b, 78.40 ± 0.62		
115 nm, SEM	Stage a, 100.48 ± 7.5	SEM, stage b	p>.9
		VASE, stage a	*p<.01*
		VASE, stage b	p>.1
	Stage b, 101.8 ± 4.91	VASE, stage a	*p<.005*
		VASE, stage b	p>.05
115 nm, VASE	Stage a, 110.22 ± 0.50	VASE, stage b	*p<.05*
	Stage b, 93.74 ± 2.51		
149 nm, SEM	Stage a, 130.88 ± 6.04	SEM, stage b	p>.6
		VASE, stage a	*p<.001*
		VASE, stage b	p>.6
	Stage b, 133.73 ± 5.93	VASE, stage a	*p<.001*
		VASE, stage b	p>.9
149nm, VASE	Stage a, 146.29 ± 0.71	VASE, stage b	*p<.001*
	Stage b, 133.01 ± 0.39		

6.3.3 Alumina Etch Rates and Tantala Growth Rates

The alumina etch rates and tantala growth rates at each stage of anodization were calculated using SEM profiles and ellipsometry scans.

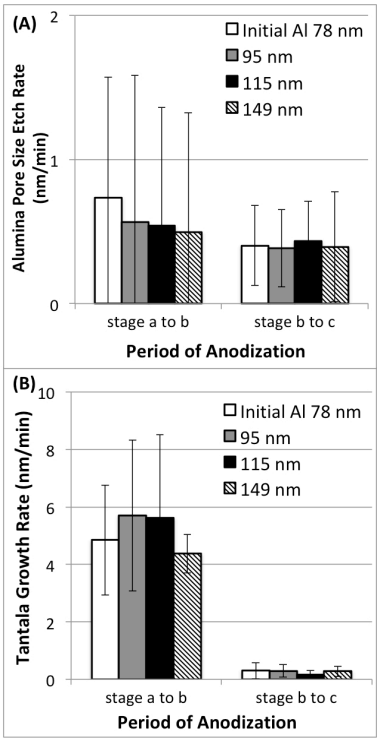

Figure 6.9. Alumina surface pore diameter etch rates (A) and tantala growth rates (B) at each stage of anodization. Rates are shown for all initial aluminum thicknesses and anodized at 8 V in 0.4 M phosphoric acid until stage a, b, and c. Rates were shown from the start of oxidation to stage a, from stage a to stage b, and from stage b to stage c.

A reduction in the alumina thickness occurs at an average rate of 3.83±0.4 nm/min from the start of anodization to stage a, from stage a to b the alumina thickness shows no significant difference, ($p \geq .574$) and from stage b to c the etching occurs at an average rate of 0.5±0.2 nm/min. The alumina pores (see Figure 6.9A) from stage a to b were etched at 0.6±0.41 nm/min, which decreases slightly after stage b etching at an average rate of 0.4±0.15 nm/min from stage b to c. The tantala film growth rate was altered based on the current density applied, or the stage of anodization shown in Figure 6.9B. Oxidation to stages b and c creates tantala film thicknesses of 12.8±2.1nm and 14.8±2.5 nm, hence anodization to stage b results in ~87% of the total tantala thickness achieved in stage c. The average growth rate of tantala decreased from 5.1±1.1 nm/min to 0.3±0.1 nm/min after stage b with a drop in current density to <7.4% of the plateau value during pore formation.

6.3.4 Visible Interference Colour Detection

Visible colours were used to determine when tuning of the alumina layer was optimal. Thin films showed colour contrast after exposing prothrombin and anti-prothrombin solutions to the device surfaces. The antibody was placed on the device surfaces as a negative control; these spots were not visible. Devices with protein exposed to the surface are shown in Figure 6.10 with colour coordinates listed in Table 6.4. Images were captured through a polarizing film to optimize interference. Control non-specific antibodies showed no visual colour change after being exposed to the prothrombin coated surface for 15 minutes.

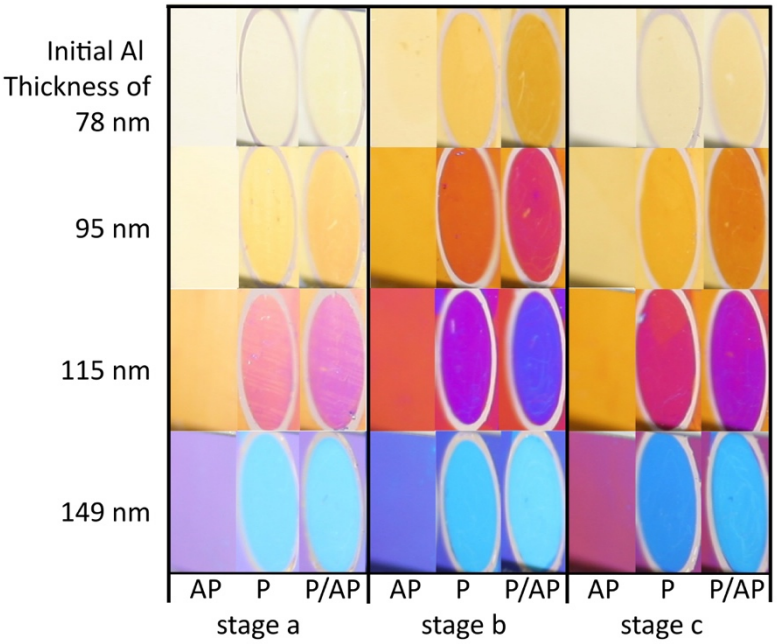

Figure 6.10. Interference colours of films after protein exposure. Initial aluminum thicknesses are shown to the left of images and stages of oxidation as well as the protein solution exposed are shown at the bottom of the image. Solutions consist of prothrombin (P) and anti-prothrombin (AP). The images were taken at 75 degrees from normal.

Table 6.4. Visible colours and Yxy coordinates from the surface of anodized slides prior to and following protein immobilization. Three different initial aluminum thicknesses were deposited and anodized at 8 V in 0.4 M phosphoric acid until stage a, b, and c.

Stage of Formation	Alumina Surface Composition	Initial Al of 78 nm		Initial Al of 95 nm		Initial Al of 115 nm		Initial Al of 149 nm	
		Colour	Coordinates (Yxy)	Colour	Coordinates (Yxy)	Colour	Coordinates (Yxy)	Colour	Coordinates (Yxy)
a	Anodized Alumina Surface	light tan	91.99, 0.32, 0.34	light yellow-tan	87.81, 0.35, 0.37	strong tan	79.97, 0.36, 0.38	light purple	53.12, 0.26, 0.26
b		yellow-tan	76.38, 0.37, 0.39	gold	49.61,0.47, 0.45	orange	36.14, 0.45, 0.37	royal blue	33.88, 0.21, 0.21
c		tan	83.66, 0.34, 0.36	yellow	72.52, 0.38, 0.40	gold-yellow	50.29, 0.42, 0.43	red-purple	20.55, 0.29, 0.20
a	Prothrombin	light tan	90.03, 0.33, 0.35	light yellow	82.34, 0.37, 0.40	light red	71.49, 0.34, 0.37	cyan	71.12, 0.25, 0.30
b		yellow-tan	68.77, 0.41, 0.42	orange-brown	30.26, 0.52, 0.39	purple	22.39, 0.28, 0.26	cyan	59.96, 0.23, 0.28
c		tan	77.48, 0.36, 0.38	yellow-brown	58.40, 0.45, 0.45	magenta	19.48, 0.38, 0.23	royal blue	39.34, 0.21, 0.23
a	Prothrombin & Antiprothrombin	light tan	90.22, 0.33, 0.36	light-tan	77.42, 0.38, 0.40	light purple	66.06, 0.34, 0.35	cyan	73.39, 0.25, 0.31
b		brown-tan	58.92, 0.43, 0.44	magenta	25.48, 0.49, 0.33	violet-blue	25.70, 0.25, 0.20	light cyan	66.72, 0.24, 0.30
c		stronger tan	75.90, 0.37, 0.39	light orange	48.48, 0.47, 0.44	purple	26.13, 0.39, 0.23	light blue	46.90, 0.21, 0.25
a	Antiprothrombin	light tan	92.69, 0.32, 0.34	light yellow-tan	88.87, 0.34, 0.37	strong tan	86.70, 0.35, 0.37	light purple	52.92, 0.26, 0.25
b		yellow-tan	76.57, 0.37, 0.39	gold	51.80, 0.47, 0.45	orange	42.97, 0.44, 0.42	royal blue	37.89, 0.20, 0.22
c		tan	84.44, 0.35, 0.37	yellow	70.95, 0.38, 0.40	gold-yellow	73.69, 0.39, 0.42	red-purple	20.63, 0.28, 0.18

6.4 Discussion

We address the challenges of low visible colour contrast and sensitivity in thin film diagnostics by tuning the platform, resulting in a hand held thin film prototype that detects biological substrates and generates colour changes within minutes. Devices generate visible colour shifts as the alumina thickness and refractive indices vary. The tunable device allows for the surface and protein refractive indices to be matched. The colour shift with protein binding is a result of the OPL change and leads to the detection of specific monolayers of biological molecules. A constant potential of 8 V was chosen to closely match the optical constants. Preliminary work and studies at low applied potentials, where the range of 1 to 40 V was experimentally tested in various electrolytes, provided insight for this work. [18,39] We found that the initial aluminum deposition and the anodization time also influence the OPL. As the OPL difference increases, the resulting interference moves from first order to higher order colours where colour shifts become less distinguishable. For this test first-order colours are generated on devices with aluminum layers between 95 and 115 nm, oxidized to stage b or c (OPLs between 127 and 184 nm).

When comparing the aluminum thicknesses, differences were expected with anodization to various stages because the conversion to porous alumina takes varying lengths of time depending on the initial thickness. Moreover, the surface pore size exhibits significant differences at stage c of formation when the aluminum thicknesses change by ≥34nm. Therefore, when tuning devices to generate first order colour shifts for future applications, it

must be considered that the change in aluminum thicknesses should be <34 nm to eliminate changes in surface etching and pore size. Ellipsometry showed that the refractive index values of the porous alumina changes during anodization. Values appear relatively constant within each stage. Devices at stage a possess the highest refractive index with minimal time for etching, however at stage a MSE values were 4 times that of stage b and c indicating greater error in the generated thicknesses and refractive indices and was excluded from Figure 6.5 for this reason. In addition, at stage a, no anodic tantala has formed which is known to contribute to the colour generation. The device at stage a would be hard to tune with the large error and weak colour shifts. Prior work demonstrates that the thickness of anodic tantala barrier layers control the surface colour as a result of the interference between the interfaces of air-oxide and oxide-metal. [40,41] Oxidation to stage b and c allows for the collection of accurate refractive index values and the generation of better colour contrast with protein binding, as >80% of tantala is present. A tantala film >10 nm is the minimum thickness necessary for reproducible formation and colour generation under the anodizing parameters tested. However, a comparison of the significantly different surface pore diameters and refractive indices showed no correlation. From this we can conclude that pore sizes at the alumina surfaces are not representative of changes in the refractive index of the alumina layer and differ from the bulk pore size. Alumina thickness offers a higher degree of device tunability over the alumina refractive index. Furthermore, the acceptable threshold for the alumina refractive indices is narrow to ensure the protein layer is closely matched.

The refractive index values of stage b films showed lower standard deviations than those anodized to stage c. With a constant anodization time for stage c, the length of time for pore formation is dependent on the aluminum thickness and oxidation parameters. More on the impact of changing current density on the length of oxidation and plateau current density can be found in Chapter 4. Films anodized to stage c with thicker sputtered aluminum, showed a decrease in variability because the oxidation period after the pores form was reduced. Furthermore, with thicker films the anodization time to reach stage b and stage c converges and brings the alumina refractive indices closer. However, changes in the variance of alumina refractive index impact which values are determined to be statistically significant. Even though the thickest alumina films oxidized to stage b and c show converging refractive

indices, the difference between the two was significant. Increasing the number of samples would provide a better representation of the population variance. A trade off exists in alumina refractive indices at stages b and c, between obtaining lower variability and consistent values over changing sputtered aluminum thicknesses.

Measured alumina thicknesses of stage a and b films generated with the same initial aluminum thickness, showed a significant difference ($p \leq .024$) with ellipsometry, however using SEM cross-sections showed no difference ($p \geq .574$). A greater error resulted in ellipsometry models at stage a, in part to no tantalum oxide, and therefore, the precision of the mean is farther from the actual mean. As a result, the alumina thicknesses after oxidation to stage b, measured with ellipsometry, were applied to stage a thickness values, for the respective sputtered aluminum devices. These thicknesses more accurately depict the alumina thickness at the end of pore formation and were used to determine alumina thickness etch rates.

After pore formation, devices show a decrease from the initial aluminum layer thickness going against the notion that aluminum grows in thickness when converted to alumina. [42] However, volumetric growth depends on the electrolyte type, concentration, and anodizing voltage. [43] Typically, anodization in phosphoric acid to achieve self-ordered pore membranes is carried out at higher voltages. [42,44] With a voltage decrease the efficiency of the process is altered, accounting for the decrease in thickness observed. [43] Halting anodization at three sequential periods led to the determination of etching and growth rates and improved the ability to tailor the device. The alumina etch rate was maximal during pore formation, up to stage a. The alumina etch rate, from commencing anodization to stage a, varied between initial aluminum thicknesses of 78 and 149 nm ($p=.000$). The change in etch rate may stem from the large difference in thickness or changes in the power density during the tantalum deposition. Changes in the tantalum microstructure may influence the aluminum anodization by altering the current flow. Unlike the alumina, the majority of tantala growth occurs between stage a and b at a rate of 5.14 ± 1.5 nm/min, after which growth was minimal. There was no difference in the tantala growth rate with initial aluminum thickness ($p=.551$). Tantalum is insoluble in phosphoric acid and any hillock formation that resulted was not influenced by the change in alumina film thicknesses. Growth rates from this work with anodization to stage b ($J \cong$

0.07mA/cm^2) and c (J≅0.02mA/cm^2) were 1.60 nm/V and 1.87 nm/V, respectively. These values fall within the range of literature findings, showing tantala barrier growth rates in phosphoric acid range from 1.67 to 2.21 nm/V. [45-49] The variance is likely a result of the parameters of anodization used and the final current density achieved. Over the anodization period, with a constant applied potential, the barrier layer continues to slowly grow as the current density decreases until the maximum thickness is achieved. Thus, barrier formation rates are highly dependent on the final current density and should be reported.

Optimal conditions for matching the refractive index of analyte to the effective refractive index of alumina were achieved with anodization to stage b and c. Adsorbed prothrombin layers have a refractive index value between 1.36+i0 and 1.55+i0. [50-53] The refractive indices of protein are dependent on the structure and the hydration of the protein following adsorption. Taking into account that the porous alumina layer is ~40% air this may lead to a discontinuous protein layer with a refractive index slightly lower than predicted values above, assuming the protein layer contains the same void fraction as the alumina. Considering the protein layer may range from discontinuous to solid, the alumina properties are near the predicted optimum that strives to match protein and alumina effective refractive index values and minimize scatter. When tuning the alumina surface to match the refractive indices of different protein layers, the length of anodization between stage b and c will allow for fine adjustments. We used our model system of prothrombin and anti-prothrombin to demonstrate a tunable diagnostic device utilizing thin anodic alumina films. Little to no colour shift occurred after exposing the antibody solution to the surface, as antibodies have demonstrated relatively low affinity for porous alumina with weak interactions at pH 7.4. [54] We also found that OPL's between ≥127 and <230 nm generate an optimal device for prothrombin and prothrombin-antibody detection when calculated and viewed at 75° from normal. This work demonstrates that alumina thickness is more influential than the refractive index in terms of generating strong colour shifts, as alumina layers in devices oxidized to stage b and c shown no significant difference in their refractive indices. Initial aluminum thickness and stages of formation that were not ideal for this prototype but provided insight to tailor the device for the detection of other proteins. Controlling the refractive index and thickness of the porous alumina specific to each compound can create strong visible colour

contrast with adsorption. Additional work on changing acid type, concentration, and applied potential may further enhance tunability and the resulting interference colours.

Other immobilization techniques for attaching biological molecules to alumina could benefit from this work including organophosphates[55,56] and aminosilanes.[57,58] Improvement in detection of biological markers using tunable alumina device surfaces will dramatically improve point-of-care diagnosis and medical treatment. Device tunability allows for optimization based on structure; antigen-antibody, avidin-biotin, and aptamers could also be detected with this device.

6.5 Conclusions

This work provided insight on the alumina-tantala thin film device structure, and device colour contrast, as a function of oxidation and aluminum deposition time. The optimal structure for strong colour contrast with the prothrombin and prothrombin-antibody complex consists of an initial aluminum thickness between 95 and 115 nm anodized to stage b or c (OPL's between ≥127 and <230 nm). The final alumina thicknesses are between 72.8±1.9 nm and 92.7±1.7 nm with a tantala thickness between 13.3±0.8 and 16.5±0.9 nm. The porous alumina layer effective refractive index values for these devices range from 1.27±0.04 to 1.39±0.02 over the visible spectrum. Device tunability allows for optimization based on structure; antigen-antibody, avidin-biotin, and aptamers could also be detected with this device.

Further conclusions from this work include:

1. Refractive index values provide a better indication of differences between devices over pore diameter values.
2. Oxidation to the end of pore formation (stage a) generates a large standard error in ellipsometry models and result in low colour contrast.
3. Alumina thickness is more influential than the refractive index in terms of generating strong colour shifts.
4. Tantalum thickness should be >10 nm to generate strong colour shifts with protein binding.
5. Out of the three stages of formation evaluated, stage b creates devices with the lowest standard deviation in terms of refractive index and alumina thicknesses.

We have outlined a process for creating a point-of-care device that can be used by frontline medical professions in either general family practice settings or in remote settings. The colour change generated through our approach of tuning a thin film system allows for a rapid assessment of analytes with potential applications in diagnosing and managing health problems where target molecules are produced.

Chapter 7 – The Impact of Layers at the Tantalum and Aluminum Interface

7.1 Introduction

Although the porous alumina, barrier tantala, and tantalum thin film device generates visible interference colours, the contribution of layers at the tantalum and aluminum interface are unknown. The influence of the tantalum properties and the presence of a native or anodic tantalum oxide layer before aluminum deposition are specific areas of interest. To produce a device with high sensitivity and create products containing tantalum and aluminum interfaces with optimal function, further knowledge surrounding the interface is critical. Chapter 7 compares two tantalum films sputtered in different magnetron sputter systems with native and anodic tantala barrier layers generated. Subsequently, aluminum films were sputtered on these tantalum slides with native or anodic tantalum oxide layers and the standard anodization process was completed.

7.1.1 Interstitial native and anodic oxide layers

Exposing a sputtered valve metal such as tantalum to the atmosphere leads to a native oxide film that is ~2.1 nm thick, [1] while anodization leads to a thicker barrier anodic oxide film on the metallic surface with a thickness that correlates to the applied voltage (~1.7 nm/V) (see the discussion section in Chapter 6). The resulting surfaces are uniform amorphous layers and for valve metals this process leads to uniform interference colours. [2,3]

When valve metals are anodized with an overlying porous layer, hillocks form. The porous alumina overlay largely influence the geometry of the underlying metal oxide that forms, as the hillocks extend into the pores. With the drop in current density the oxide nucleation begins and eventually leads to the expansion of the hillock, in vertical and horizontal directions, into the base of the pore. The shape, geometry, population density, chemical composition, the nature of the underlying metal, electrolyte solution, and anodizing conditions all govern the structure and characteristics of the resulting anodic oxide layer. [4] Furthermore, hillocks only form when an oxide layer of higher resistivity (i.e. resistivity of Al_2O_3 > resistivity of Ta_2O_5) is superimposed on a layer with a lower resistivity. It is likely that the system becomes electrically unbalanced during anodizing, which is relieved within the system by the lower resistivity oxide protruding through the porous oxide layer with a higher

resistivity. These finger-like protrusions at the interface of the two oxide films, attempts to short-circuit the porous oxide to allow the current to flow through the protruding layer. [5]

7.1.2 Tantalum Oxide Reduction with Adjacent Aluminum Deposition

The first film of the multilayer device is tantalum with either a native or anodic oxide on the surface. When the second aluminum layer is sputtered the reaction at the interface can be foreseen with an Ellingham diagram. Ellingham diagrams show the relative affinity of various metals for oxygen as a function of temperature by the position of the reaction line. Unstable oxides have reaction lines closer to the top of the diagram and are easily reduced. Towards the bottom of the diagram metals have lower formation energies and become progressively more reactive, their oxides are harder to reduce, and they have the capability to reduce oxide layers of all metals with reaction lines above theirs on the diagram. [6] Figure 7.1 shows an Ellingham diagram with aluminum and tantalum reactions highlighted.

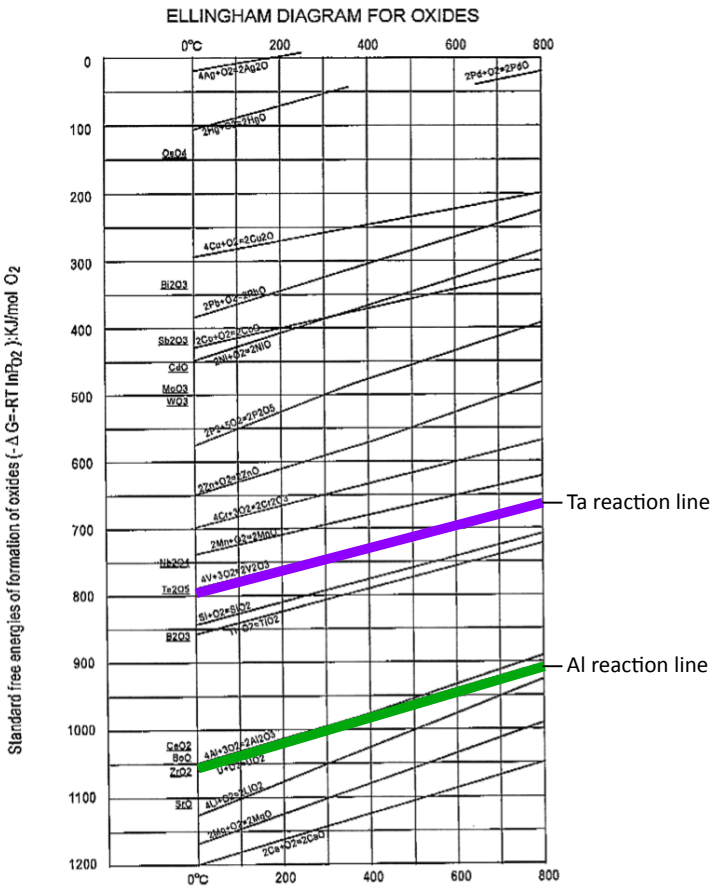

Figure 7.1. The Ellingham diagram outlines the stability of various metal oxides with respect to temperature. Image from Sato et al.[7] *with modifications to highlight the tantalum (purple) and aluminum (green) reaction lines.*

Theoretically, aluminum deposition over the native or anodic tantalum oxide layer converts the adjacent aluminum to an aluminum oxide layer and metallic tantalum remains, as the $\frac{4}{3}Al + O_2 = \frac{2}{3}Al_2O_3$ reaction line is below the $\frac{4}{5}Ta + O_2 = \frac{2}{5}Ta_2O_5$ reaction line. [8]

It is concluded that the aluminum reduces some or all of the tantalum pentoxide, which makes up 85% of native tantalum oxide. Therefore, the reduction of tantalum oxide by the adjacent aluminum coating occurs spontaneously. The equation below shows the reduction reaction.

$$10\ Al + 3Ta_2O_5 \rightarrow 5Al_2O_3 + 6Ta \qquad \text{Equation 7-1}$$

When tantalum coatings are exposed to air a native oxide forms (~2.1 nm), [1] the subsequent deposition of aluminum creates a 3 to 5 nm amorphous alumina layer by reducing the native tantalum oxide. [8] With an anodic oxide layer (~13 nm) on the tantalum coating, it is

likely that the deposition of aluminum reduced some, if not all, of the tantalum pentoxide, leading to an increase in volume and resistivity. The standard anodization process likely regenerates the tantalum oxide that was reduced and leads to a device structure shown in Figure 7.2.

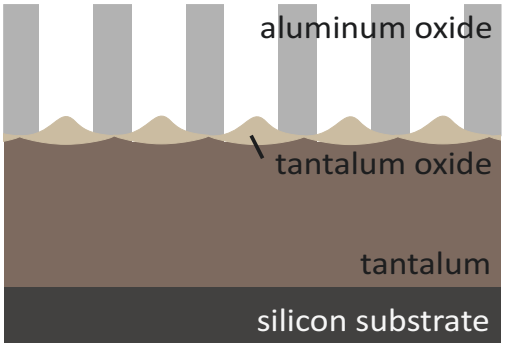

Figure 7.2. The device structure following the standard anodization in 0.4 M phosphoric acid at 8 V, regardless of whether a native tantalum oxide layer was present at the interface of the tantalum and aluminum layers prior to anodization.

7.1.3 Characteristic Properties of Sputtered Thin Films

The majority of sputtered films are under stress, with total stress being comprised of thermal stress and intrinsic stress. [9] Thermal stress results when sputtered films are placed at a temperature that differs from the deposition temperature. Thermal expansion coefficients of the coating and substrate materials can be used to assess the resulting forces. A comparison of thermal expansion forces to the yield strength of the coating can provide insight on the likelihood of failure when film stresses are over the tolerable limit. Intrinsic stress is a result of flaws in the crystal structure that can occur during the sputtering process and depend on the deposition parameters. [9]

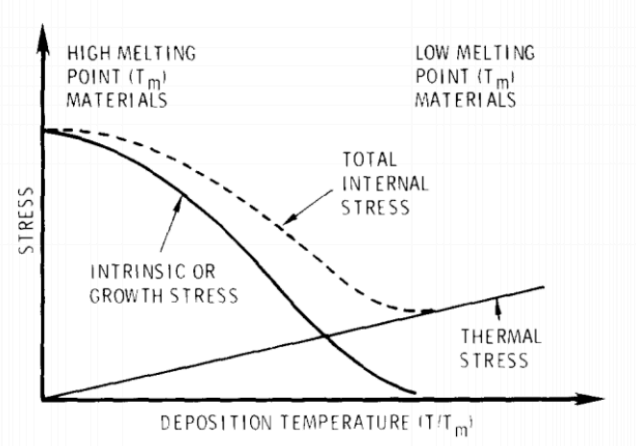

Figure 7.3. Depicts the thermal and intrinsic stresses contributing to the total stress in a sputtered coating. Image from Thornton and Hoffman. [9]

The parameter substrate temperature, T (K), divided by the melting temperature of the thin film material, Tm (K), aids in understanding microstructure and stress induced behaviours of vacuum-deposited thin films. Materials with high melting temperatures and a relatively low T/Tm ratio (i.e. tantalum) tend to contain higher levels of intrinsic stress over thermal stress. On the contrary, materials with low melting points and a relatively high T/Tm (i.e. aluminum) when sputtered at low temperatures lead to films where thermal stress dominates over intrinsic stress. Bulk diffusion prevents the accumulation of internal stresses. The relationship between thermal and intrinsic stress in a sputtered film is visually explained in Figure 7.3.

It is apparent from Figure 7.3 above that at low T/Tm the intrinsic stress is dominant and at higher T/Tm, typically greater than 0.25 to 0.3, the thermal stress becomes dominant. Recovery and recrystallization at T/Tm higher than 0.2 can relax intrinsic stresses and reduce their build up in a growing film. [9] Furthermore, the intrinsic stress builds in the coating during deposition whereas thermal stress forms subsequent to deposition when the substrate has reached room temperature.[9]

Further classification of microstructures is attainable by comparing the visual appearance and parameters that correspond to different zones in the structure zone diagram. These diagrams focus on a select few deposition parameters and illustrate the microstructural trends on the coating structure. However, these models are basic and provide a depiction of structural changes that require clarification for specific applications. Thornton's structure zone

diagram for plasma vapour deposition relates the final deposition structures that occur with changing T/Tm and argon sputter pressure, is shown in Figure 7.4.

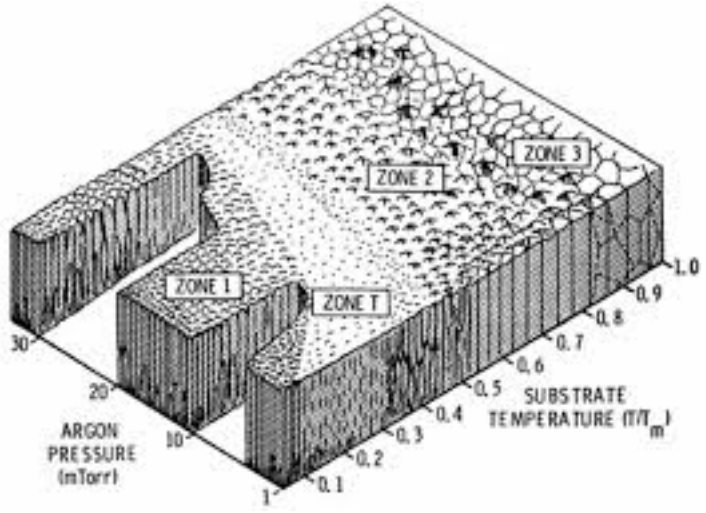

Figure 7.4. Thornton's structure zone diagram[10] outlines the influence of substrate temperature and argon pressure on the structure of sputtered coatings deposited in a cylindrical magnetron system. With the substrate temperature, T (K), and the melting point of the deposited material, Tm (K).

Films in zone 1 consist of highly columnar structures, separated by voided boundaries. Shadowing effects amplify peaks and valleys in this region, either from initial substrate roughness or when the coating flux is at a large angle to the substrate. Extreme zone 1 films are unable to withstand stresses and have poor reflectivity. Zone T (transition) regions have dense fibrous structures with smooth surfaces and a high reflectivity. These structures are commonly formed on smooth substrates when the coating flux arrives from normal to the surface and shadowing effects are negligible. Significant intrinsic stress can result in a zone T structure. Zone 2 structures are columnar with distinct separation between grains. Recovery occurs in zone 2 structures and limits the intrinsic stress that remains in sputtered films. Coatings with zone 3 structures encompass a range of sputter conditions that are governed by bulk diffusion. Recovery and recrystallization occurs in zone 3 structures and limit the intrinsic stresses that result. Thornton's diagram provides a reference of the location and typical structures one can expect with changing thermal and kinetic deposition parameters; yet, alternate models exist. Extensions of prior structure zone diagram concepts can be found in other works. [11]

For strong adhesion in a multilayer device, depositions must result in a bond between the coating and substrate that can resist the forces produced within the films. Otherwise failure

will result as cracking, buckling, or poor adhesion. Strong adhesion is critical and in situations where failure occurs, investigation into the deposition parameters and the substrate surface to ensure it is free of oils and contaminates will be beneficial. The oxidation processes on sputtered films will change material properties and can alter stresses within the multilayer device.

The purpose of work completed in this chapter was to compare how changes at the porous alumina and tantalum interface effect the device in terms of structure, to determine the optimal manufacturing procedure. Firstly, this work compares the tantalum coatings deposited in nanoFAB and NAIT sputtering systems in terms of structure, composition, crystalline phase, and the surface colours that result with the formation of an anodic tantala layer on tantalum films. Subsequently, the structure and colours that result after sputtering identical aluminum coatings on the two tantalum films and anodizing will be analyzed. Lastly, experiments comparing the resulting device structures and colours were complete for devices with native or anodic tantalum oxide layers created on tantalum layers before aluminum deposition and anodization processes, at varying voltages. Work in these areas has led to new insight on the device layers and interfaces, including film microstructures and optical path lengths, adhesion, and surface colour shifts.

7.2 Materials and Methods

7.2.1 Device Preparation

Tantalum layers were deposited using the nanoFAB and NAIT sputter systems, and aluminum depositions were carried out in the nanoFAB system. For test samples two anodization processes were completed, both in stirred 0.4 M phosphoric acid. The tantalum-coated wafer was cleaved into 6 slides using the cleaving tool. Half of the tantalum slides were exposed to a primary anodization process at 6 V, creating a tantalum oxide barrier layer prior to the aluminum deposition. Subsequently, aluminum layers of 99.0±11.2 nm and 103.8±9.2 nm (~10.9 nm/min 540 and 575 seconds) were deposited onto anodized and unanodized tantalum coatings from the same wafer simultaneously, ensuring constant aluminum thickness. Aluminum depositions were carried out in constant power mode with a set point of 300 W (see Chapter 3 for details). The standard anodization process was then carried out at applied potentials of 4, 6, and 8 V. Control samples containing identical

tantalum and aluminum thicknesses were anodized at equivalent voltages (4, 6, and 8 V) following the standard anodization process. Following tantalum deposition two methods created tantala films on the surface. Firstly, when the wafer was exposed to the atmosphere and a native tantalum oxide grown, and alternatively when the primary anodization process was used to create an anodic tantalum oxide. The multilayer thin film device with tantalum oxide between the aluminum and tantalum layers is illustrated in Figure 7.5.

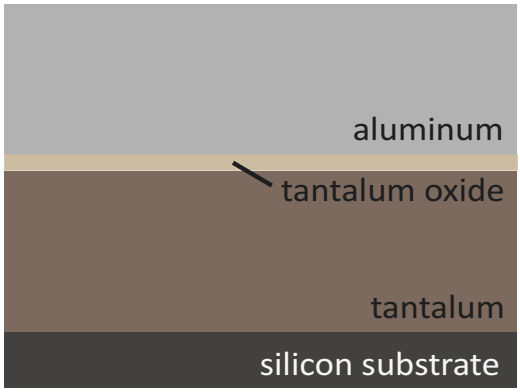

Figure 7.5. Device structure after sputtering tantalum and aluminum thin films on a silicon wafer in two separate sputter systems with exposure to atmosphere between or primary anodization of the tantalum before aluminum deposition.

All anodization steps were carried out in 0.4 M stirred phosphoric acid electrolyte to stage b (current density ≤0.7 mA/cm^2). See Chapter 3 for more details on the preparation process (i.e. cleaving wafers and the standard anodization process).

7.2.2 Analysis

7.2.2.1 SEM

Identical aluminum thicknesses were sputtered on the contrasting tantalum surfaces and thicknesses were confirmed using SEM images captured at 90°. Surface porosity values were determined based on SEM topographic images.

7.2.2.2 Time Calculation of Barrier Oxide Formation

The length of time for tantala barrier layer formation was calculated from the current density plots. A relatively horizontal line along the pore formation plateau and a second line along the negative slope that occurs after pore formation during the barrier oxide formation.

The intersection point of these two lines was used as the initial time of barrier formation and the final time was the last current density point collected. The absolute difference between these two values was calculated and provided the time required for tantala formation.

7.2.2.3 Ellipsometry

Standard fitting procedures were used to generate an ellipsometry model for multilayer devices using a bottom up approach.

7.2.2.4 EDS

SEM-EDS Analysis was conducted at 5 and 10 V, for generation of data shown in Table 7.1 and Table 7.14 respectively. See Chapter 3 for more details.

7.2.2.5 Sensitivity Analysis with Protein Adsorption

Protein exposure in this work used 20 μl of prothrombin (0.1 mg/ml) and anti-prothrombin solutions (range of 0.015 to 0.05 mg/ml) from ACOA, incubated on the surface for 15 minutes. TBS solution was exposed to the surface prior to protein work for 15 minutes to equilibrate the slides. Solutions were exposed to the surface following protein adsorption procedures outlined in Chapter 3.

The surface colours after protein exposure were compared across different device structures (n=1). ImageJ was used to collect the average RGB coordinates from the spots and an open source ColorMine library was used to perform calculations on these coordinates. Firstly, a site (http://colormine.org/delta-e-calculator) was used to determine the ΔE* between resulting RGB coordinates between prothrombin-coated surfaces and the subsequent anti-prothrombin exposure at various concentrations. This site uses a calculation method that ensures the difference is in regard to how the human eye perceives colours. Another site was used to convert RGB coordinates to Yxy coordinates (http://colormine.org/convert/rgb-to-yxy) to allow colours to be plot on a CIE chromaticity diagram for a 2D representation and visual comparison. A just noticeable difference of ~2.3 ΔE*, means the colours are perceived to be equivalent when the differences are less than this value.[12]

7.3 Results

7.3.1 As Sputtered Tantalum and Anodic Tantala Films

Metallic tantalum films deposited in nanoFAB and NAIT sputter systems demonstrate different microstructures. Figure 7.6 shows topographic and cross-sectional SEM images of the two tantalum films as sputtered and anodized.

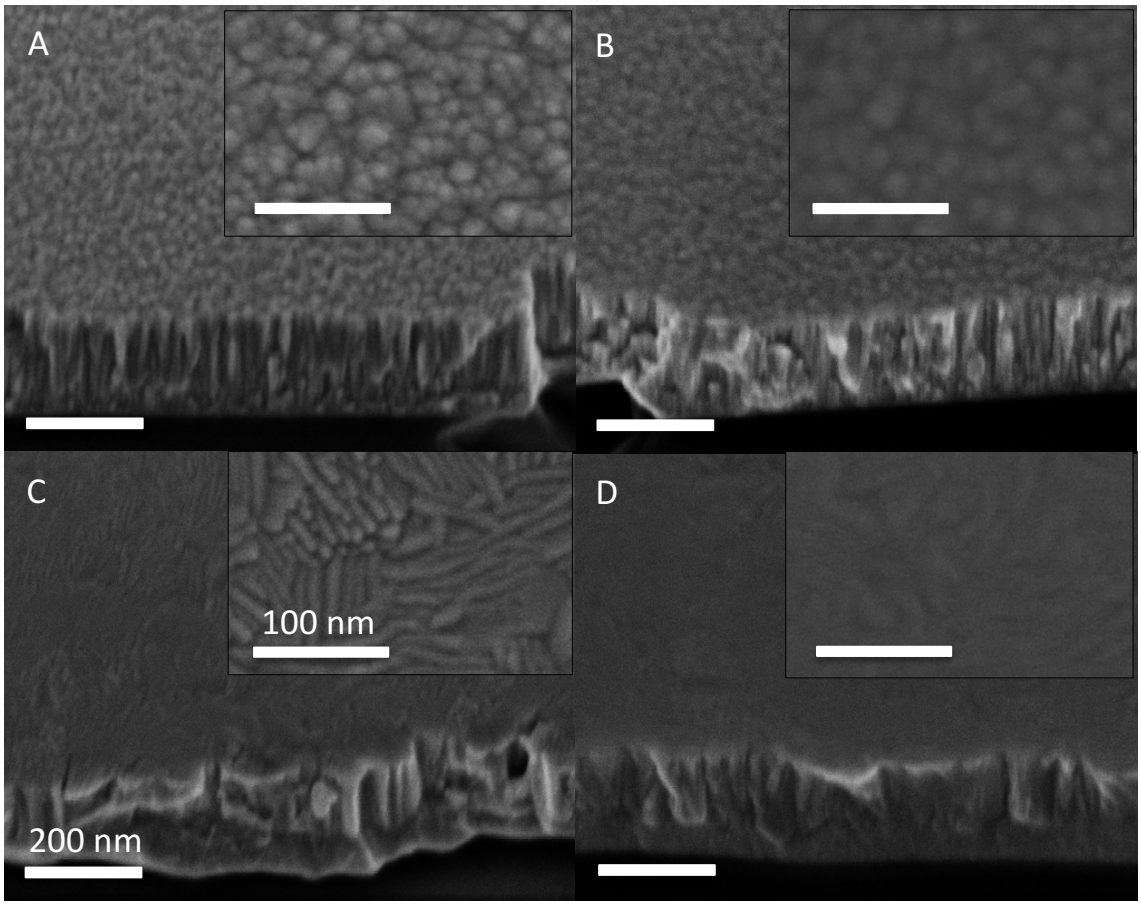

Figure 7.6. SEM images at 0° (upper right) and 45° from the tantalum surfaces were captured of films deposited in the nanoFAB system (A) as sputtered and (B) anodized films, and tantalum surfaces deposited in the NAIT system (C) as sputtered and (D) anodized films. Anodized films were obtained by oxidation in 0.4 M phosphoric acid at 6 V under potentiostatic conditions. All topographic and cross-sectional images have the same scales as those shown on (C) lower left images.

The tantalum coating deposited in the nanoFAB system generated a columnar structure with a range of circular surface grains from 10 to 30 nm. The coating deposited in the NAIT system generated a transition structure with a fibrous surface showing elongated grains with a constant width of ~12 nm and lengths of ≤80 nm. Figure 7.7 provides a representation of the surface roughness in cross-sectional images of tantalum from both systems.

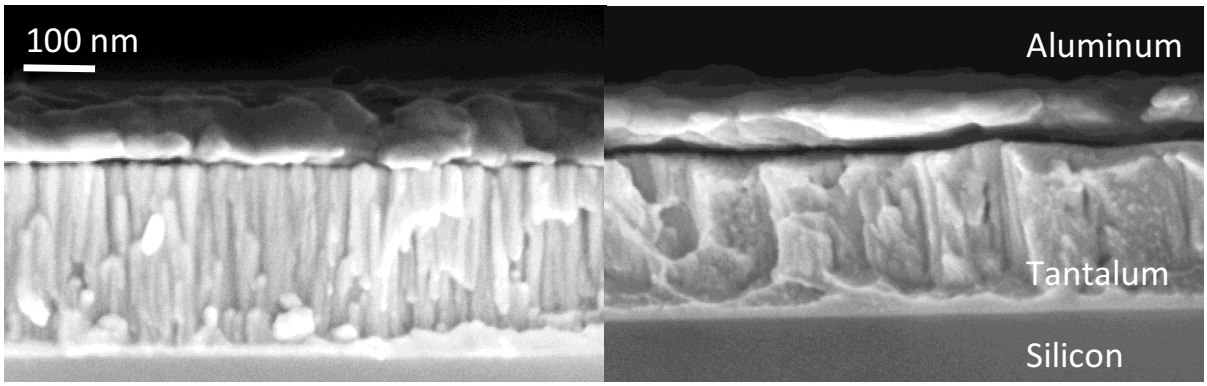

Figure 7.7. Roughness of the sputtered tantalum layers in as sputtered multilayer devices containing tantalum from nanoFAB (left) and NAIT (right) sputter systems with subsequent aluminum films deposited in the nanoFAB system. The scale bar is pertinent to both images.

Apparent changes in structure are notable between the two sputter systems. The interface between tantalum and aluminum in devices with nanoFAB tantalum appear to have increased roughness, whereas NAIT tantalum appears much smoother.

7.3.1.1 SEM with EBSD

SEM-EBSD was used to gather elemental data from tantalum surfaces from both sputter systems, as sputtered and anodized.

Table 7.1. Elemental data and standard deviations (SD) from as sputtered and anodized tantalum layers. Elements found were carbon (C), tantalum (Ta), oxygen (O), and nitrogen (N). (n=3, except nanoFAB as sputtered n=2)

Tantalum Film	C (at%)	SD	Ta (at%)	SD	O (at%)	SD	N (at%)	SD	O/Ta Ratio	SD
nanoFAB as sputtered	63.2	1.0	29.7	2.7	7.1	1.7	0.0	0.0	0.2	0.2
nanoFAB anodized (6V)	59.3	1.0	26.2	0.7	14.5	0.5	0.0	0.0	0.6	0.1
NAIT as sputtered	52.1	2.7	41.9	2.3	4.8	0.5	1.3	0.2	0.1	0.0
NAIT anodized (6V)	54.8	1.1	30.1	0.7	14.0	0.4	1.1	0.8	0.5	0.6

7.3.1.2 XRD

The tantalum crystallinity from as sputtered films deposited in the two systems were assessed with XRD. Tantalum films and tantalum with an anodic oxide layer showed identical peaks, as the tantalum oxide is 85% amorphous, which does not develop the long-range crystalline structure necessary for peaks. However, in all tantalum coatings prepared in the nanoFAB system, anodization decreased the intensity of the dominant beta tantalum crystalline peak (002). XRD scans of tantalum sputtered in the nanoFAB and NAIT systems are shown in Figure 7.8.

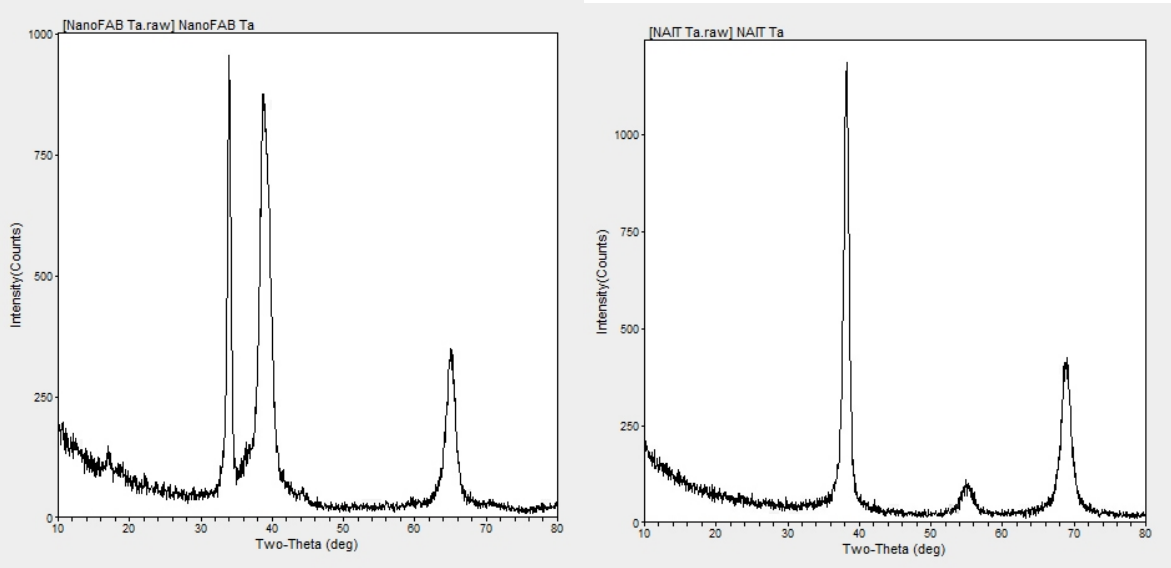

Figure 7.8. Tantalum peaks present in the XRD scans of films sputtered in the nanoFAB (left) and NAIT (right) deposition systems. Crystallite orientations in nanoFAB and NAIT as sputtered films correspond with mixed alpha-beta (α-β) tantalum and α-Ta, respectively.

Information on peaks is provided in Table 7.2. The nanoFAB tantalum coating showed dominant peaks for alpha and beta tantalum, whereas NAIT tantalum showed dominant peaks for only alpha tantalum.

Table 7.2. XRD peaks identified in tantalum slides deposited in nanoFAB and NAIT magnetron sputter systems, and corresponding peak information.

Crystal Peaks 2θ (°)	Depostion System	d-spacing (Å)	Tantalum Phase and Plane (hkℓ)
34	nanoFAB	2.63	β (002)
38.6		2.33	α (110) and/or β (202)
39.4		2.28	β (211) - overlay with 38.6° peak
65		1.43	β (304)
38.5	NAIT	2.35	α (110)
55		1.67	α (200)
68.9		1.36	α (211)

A low intensity β-Ta (410) peak may also exist at 2θ of 36° in the nanoFAB scan. Films with the anodic oxide layer showed the same peaks, some of which were broader, and the 55° peak was not identified by the software, but still exists.

7.3.1.3 Surface Colour

The tantalum surfaces showed visible colour differences between coatings sputtered in the two systems. At high angles of incidence, ~75° from normal to the surface, differences

were hard to distinguish, but viewing the surface at close to normal (0°) amplified the colour shifts along with higher anodization voltages, shown in Figure 7.9.

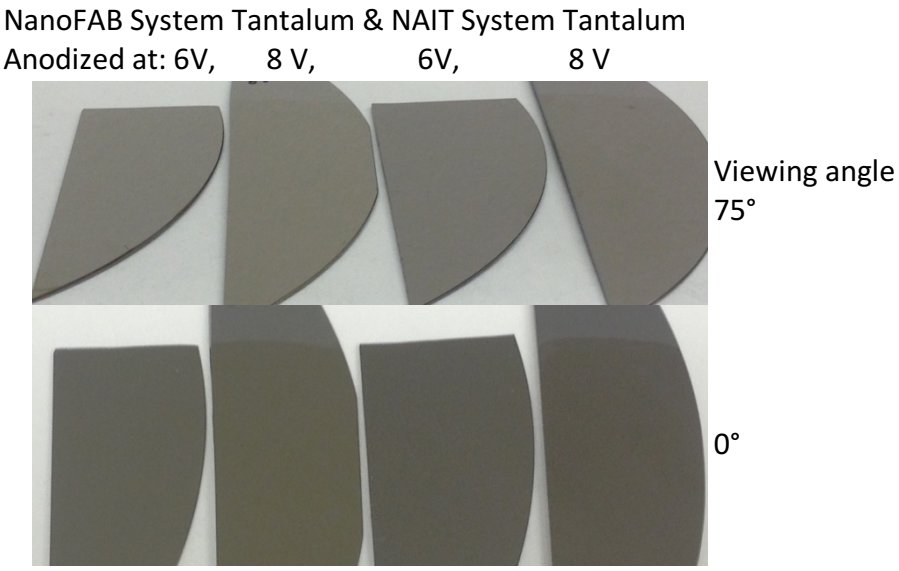

Figure 7.9. Tantalum thin films on silicon wafers sputtered in nanoFAB and NAIT sputter systems viewed at a high angle of incidence (top) and perpendicular to the surface (bottom). Slides from left to right contain: tantalum deposited in the nanoFAB system anodized at 6 V and 8 V, and tantalum deposited in the NAIT system anodized at 6 V and 8 V. Anodization was carried out in 0.4 M phosphoric acid.

A spectrophotometer collected reflectance values of tantalum and tantalum oxide films over the visible spectrum, as shown in Table 7.15. The data was collected at 5° from normal and allowed for a quantitative analysis of the reflectivity.

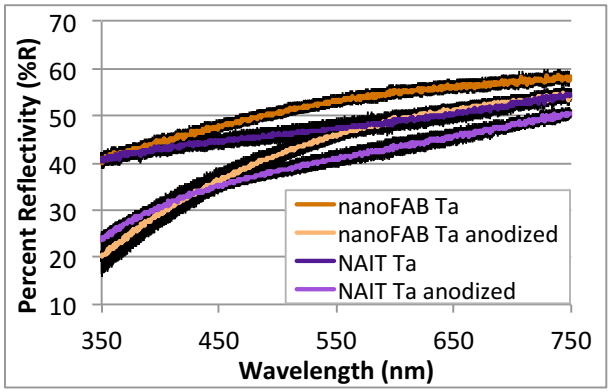

Figure 7.10. Reflectivity off tantalum surfaces over the visible spectrum at 5° from the surface normal. Samples were tantalum as sputtered from nanoFAB and NAIT systems and anodized tantalum samples at 6 V under potentiostatic condition in 0.4 M phosphoric acid. The error is shown in black for each sample. (n=2)

The tantalum deposition parameters influenced the reflectivity of the device and ultimately the final colours observed. Table 7.3 summarizes the reflectivity findings at a wavelength of 550 nm in the two deposition systems.

Table 7.3. Reflectivity values at 550 nm are shown for tantalum films deposited in the nanoFAB or NAIT systems. Tantalum films were analyzed in as sputtered and anodized states. Anodization was carried out at 6 V in 0.4 M phosphoric acid.

Tantalum Film	nanoFAB Reflectivity (%R)	NAIT Reflectivity (%R)	p Value
as sputtered	53.1±0.4	47.3±2.1	0.008
anodized (6V)	46.0±1.7	41.0±1.7	0.022

The average percent reflectivity values were statistically different between nanoFAB and NAIT tantalum (p=.008) and anodic tantalum oxide (p=.022) at a wavelength of 550 nm (p=0.008). At lower wavelengths the difference in reflectivity increased and vice versa. Ellipsometry measured values of tantalum films as sputtered and anodized are shown in Table 7.4. Differences in optical constants were apparent in films deposited in the different sputter systems.

Table 7.4. Ellipsometry generated thicknesses and optical constants for tantalum coatings deposited in nanoFAB and NAIT systems and anodized in 0.4 M phosphoric acid at 8 V. As sputtered and anodized tantalum films were analyzed to generate tantalum and tantalum oxide layer data.

Parameter Measured	Tantalum		Tantalum Oxide	
	nanoFAB	NAIT	nanoFAB	NAIT
Mean Std. Error (MSE)	5.45	1.88	1.92	3.11
Thickness (nm)	-	-	13.97	12.40
n_370	1.84	2.22	2.09	2.29
n_700	2.84	2.41	1.73	1.96
k_370	2.23	2.34	-	-
k_700	3.49	3.40	-	-

7.3.2 Standard Anodization of Aluminum on α and Mixed α-β Tantalum Structures

The control slides, created with a single standard anodization process, were analyzed on tantalum from the nanoFAB and NAIT systems. Devices with identical aluminum thicknesses on nanoFAB and NAIT tantalum layers were anodized under identical parameters. Ellipsometry was used to model the multilayer systems and investigate differences between devices at each step of formation. Table 7.5 shows results of anodized aluminum and tantalum devices. The optical constants of the tantalum thin films were used as a base layer in the

model created for the anodized tantalum and subsequently the anodized aluminum and tantalum devices.

Table 7.5. Ellipsometry generated thickness and optical constant values obtained from devices containing aluminum and tantalum coatings, deposited in nanoFAB and NAIT systems, anodized following the standard process at 8 V.

Parameter Measured	Alumina formed on (Initial Al=99 nm)				Alumina formed on (Initial Al=104 nm)			
	nanoFAB Ta	SD	NAIT Ta	SD	nanoFAB Ta	SD	NAIT Ta	SD
Mean Std. Error (MSE)	20.58	0.02	10.75	0.17	14.48	0.16	11.07	0.32
Alumina Thickness (nm)	84.37	0.27	95.08	0.20	94.95	0.24	101.80	0.75
Tantala Thickness (nm)	13.97	0.00	8.26	0.64	11.02	0.47	7.76	0.83
Percent Void (%)	48.20	0.60	49.00	0.70	49.40	0.64	49.00	1.05
n_370_xy	1.35	0.00	1.35	0.01	1.34	0.01	1.34	0.01
n_700_xy	1.34	0.00	1.34	0.01	1.33	0.01	1.33	0.01
n_370_z	1.46	0.00	1.46	0.01	1.46	0.01	1.45	0.01
n_700_z	1.45	0.00	1.44	0.00	1.44	0.01	1.44	0.01

Measurements of SEM images provide an alternate method for collecting alumina thicknesses and surface porosity values. Topographic and cross-sectional SEM images were measured using ImageJ software, and the results are shown in Table 7.6.

Table 7.6. Measurements of alumina thicknesses and surface porosity values from SEM images of aluminum and tantalum coatings, deposited in nanoFAB and NAIT systems, anodized following the standard process at 8 V.

Parameter Measured	Alumina formed on (Initial Al=99 nm)				Alumina formed on (Initial Al=104 nm)			
	nanoFAB Ta	SD	NAIT Ta	SD	nanoFAB Ta	SD	NAIT Ta	SD
Alumina Thickness (nm)	84.9	8.0	92.7	7.1	89.9	7.7	97.6	6.8
Surface Porosity (%)	42.6	3.5	42.2	1.5	40.0	0.1	40.6	0.4

The difference between the initial aluminum thicknesses was 5 nm, which remained after anodization. The difference between the resulting alumina thicknesses of devices with nanoFAB tantalum was 5.1±11.1 nm and with NAIT tantalum was 4.9±9.8 nm. SEM measurements showed no differences between the alumina thicknesses from ellipsometry for nanoFAB ($p=.953$) and NAIT ($p=.760$) tantalum devices. Furthermore, the surface porosity values showed no differences from ellipsometry percent void for nanoFAB ($p=.448$) and NAIT ($p=.100$) tantalum devices.

The resulting interference colours on the two device surfaces, when viewed at low angles, differed depending on the underlying tantalum structure. Interestingly, ellipsometry and SEM measurements showed that the final alumina thickness differs depending on the underlying tantalum layers present in the device. The changes in alumina thicknesses were

thought to be the predominant cause of the colour shifts, in addition to the differences in anodic tantalum surface colours with primary anodization. Two aluminum thicknesses of ~99 and ~104 nm were used to assess the resulting colour shifts after the standard anodization process, as shown in Figure 7.11.

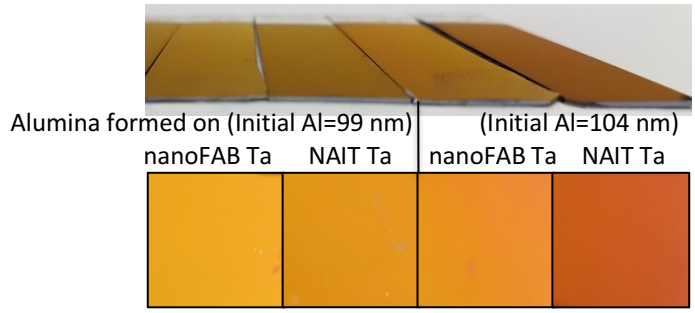

Figure 7.11. Slides consisting of identical aluminum thicknesses on tantalum layers from nanoFAB and NAIT systems, anodized to stage b in 0.4 M phosphoric acid at 8 V. Images show the surfaces captured at 75° from normal. From left to right: nanoFAB and NAIT tantalum with 99 nm aluminum followed by nanoFAB and NAIT tantalum with 104 nm of aluminum.

A comparison of the detection limits was carried out on devices with nanoFAB and NAIT tantalum for both aluminum thicknesses. Figure 7.12 shows images of control device surfaces with exposing 28 picomoles of prothrombin (20 µl at 0.1 mg/ml) and subsequently 2, 3.3 and 6.7 picomoles of anti-prothrombin (20 µl at 0.015, 0.025, and 0.050 mg/ml) to the surfaces.

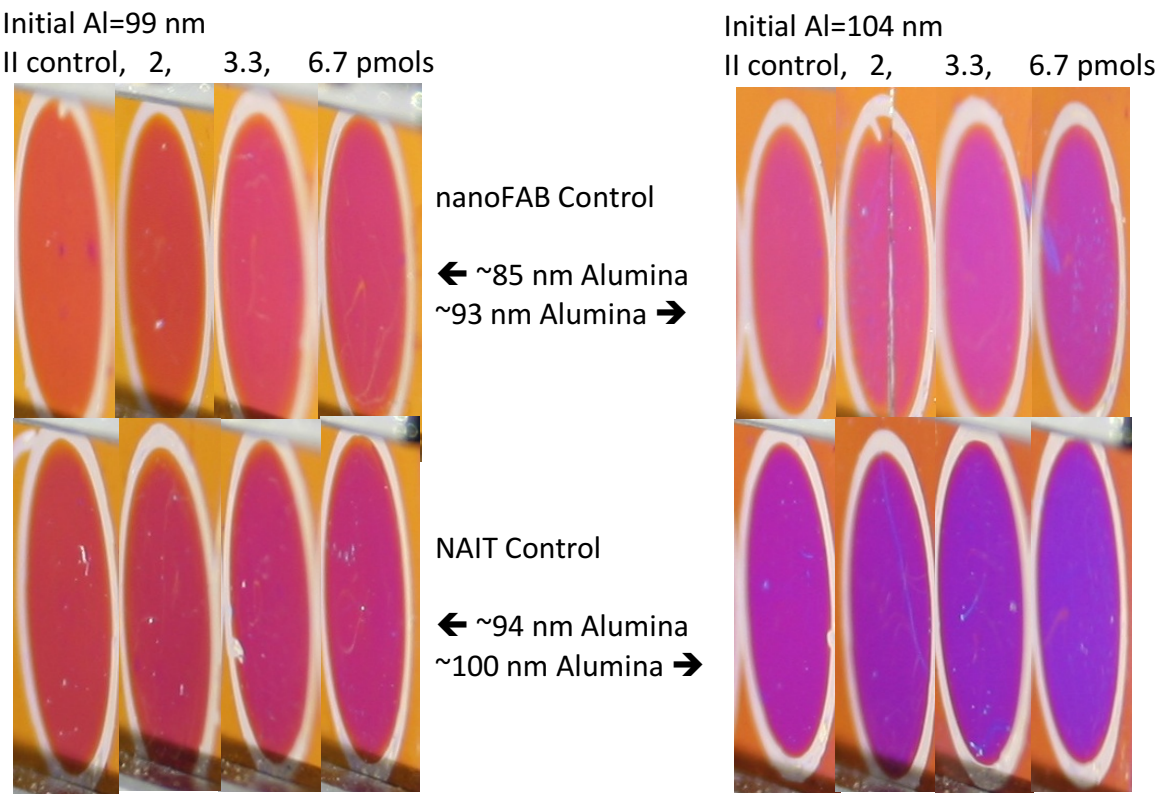

Figure 7.12. Shows the visible surface colours resulting with exposing 28 picomoles of prothrombin (20 µl at 0.1 mg/ml) and subsequently 2, 3.3 and 6.7 picomoles of anti-prothrombin (20 µl at 0.015, 0.025, and 0.050 mg/ml) to the control slide surfaces formed on nanoFAB and NAIT tantalum. Images were taken using the custom optics system. (n=1)

The prothrombin control spots for the thinner aluminum films created on nanoFAB and NAIT tantalum layers were orange pink and pinkish red respectively. Subsequent shifts with anti-prothrombin appear to be equivalent sensitivities. With highest anti-prothrombin solutions on slides with nanoFAB tantalum shifting to red purple and NAIT tantalum shifting to pink. Films created with a thicker initial aluminum layer showed prothrombin control spots for slides with nanoFAB tantalum and NAIT tantalum of pink and reddish purple and move towards reddish purple and purple with anti-prothrombin bound, respectively.

Table 7.7 shows RGB coordinates and differences between colours perceived by the human eye (ΔE*). These values allow for a comparison of which colour shifts are more sensitive with anti-prothrombin exposed to a prothrombin-coated surface.

Table 7.7. RGB coordinates and differences in colour between prothrombin-coated surfaced exposed to anti-prothrombin solutions (ΔE) at varying concentrations.*

Protein Concentrations Exposed to Surface and Colour Coordinates		Initial Aluminum of 99 nm						Initial Aluminum of 104 nm					
		nanoFAB Control			NAIT Control			nanoFAB Control			NAIT Control		
		Average	SD	**ΔE* (vs II)**	Average	SD	**ΔE* (vs II)**	Average	SD	**ΔE* (vs II)**	Average	SD	**ΔE* (vs II)**
II (0.1 mg/ml)	R	217.14	2.77		189.19	6.16		216.28	1.899		176.37	3.31	
	G	87.24	3.34		61.65	9.65		82.42	2.981		40.45	4.57	
	B	60.03	8.55		73.85	9.42		132.77	8.969		174.53	5.69	
II & AP (0.015 mg/ml)	R	202.87	3.22	7.61± 4.90	182.91	5.52	9.27± 3.07	216.78	4.526	6.95± 8.05	155.55	5.20	8.58± 1.12
	G	72.91	6.89		54.10	8.05		86.97	6.525		39.11	5.35	
	B	59.47	10.08		83.57	7.02		147.53	11.958		176.93	6.90	
II & AP (0.025 mg/ml)	R	216.51	2.80	27.14± 6.71	187.09	5.27	23.22± 2.91	211.77	2.237	25.52± 6.67	149.89	4.87	15.05± 1.67
	G	74.85	4.09		50.52	6.55		77.18	3.069		42.14	6.53	
	B	101.96	9.62		107.46	6.53		174.65	7.892		190.26	7.02	
II & AP (0.05 mg/ml)	R	208.88	2.86	31.99± 6.13	190.10	5.13	27.17± 4.02	192.99	4.677	30.77± 5.87	148.39	4.68	20.38± 1.24
	G	70.60	5.05		51.54	8.21		70.42	5.288		51.63	4.82	
	B	105.66	9.22		115.86	9.07		173.11	9.176		205.60	4.65	

Table 7.8 shows Yxy coordinates transformed from RGB values, to plot on the chromaticity chart in Figure 7.13 below.

Table 7.8. Yxy chromaticity coordinates were transformed from RGB colour coordinates to plot coordinates on the CIE chart.

Protein Concentrations Exposed to Surface and Colour Coordinates		Initial Aluminum of 99 nm		Initial Aluminum of 104 nm	
		nanoFAB Control	NAIT Control	nanoFAB Control	NAIT Control
II (0.1 mg/ml)	Y	21.96	14.74	22.43	13.90
	x	0.53	0.51	0.43	0.32
	y	0.36	0.32	0.27	0.17
II & AP (0.015 mg/ml)	Y	17.75	13.34	23.65	11.65
	x	0.54	0.49	0.41	0.29
	y	0.34	0.29	0.26	0.15
II & AP (0.025 mg/ml)	Y	20.61	13.97	22.38	11.87
	x	0.48	0.45	0.37	0.27
	y	0.30	0.26	0.22	0.14
II & AP (0.05 mg/ml)	Y	19.03	14.63	18.79	13.19
	x	0.47	0.44	0.34	0.25
	y	0.29	0.25	0.20	0.14

Chromaticity colour coordinates from images of the prothrombin exposure and the shifts with subsequent anti-prothrombin exposure on each of the four tantalum slides were mapped on CIE charts in Figure 7.13.

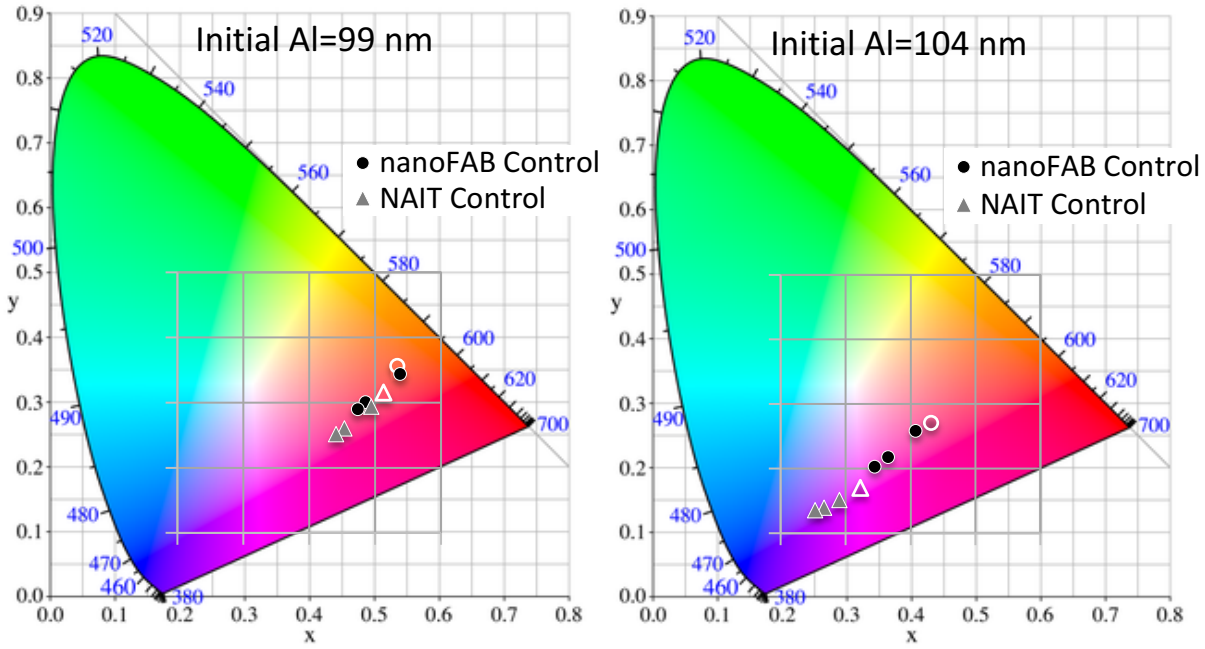

Figure 7.13. Colour plots showing the colours resulting with 0.1 mg/ml prothrombin (outlined shape) and subsequently 0.015, 0.025, and 0.050 mg/ml anti-prothrombin (from top right to bottom left). Plots compare colours on control slides with NAIT tantalum and nanoFAB tantalum layers.

7.3.3 Primary and Standard Anodization on Mixed α-β Tantalum Films

Current density plots for anodization of the two aluminum thicknesses, produced during the standard anodization for test and control samples are shown in Figure 7.14. Test samples underwent a primary tantalum anodization prior to aluminum deposition and following, the standard anodization process, whereas control samples were created using the standard anodization process. The impact of the initial tantala barrier layer, or the alumina barrier layer formed by the reduction of the anodic tantala layer, results in changes to the current density curves of test and control samples. The effect was more significant when the standard potential was higher than that applied during the primary anodization process. However,

differences are still noticeable with standard anodization potentials of 4 and 6 V.

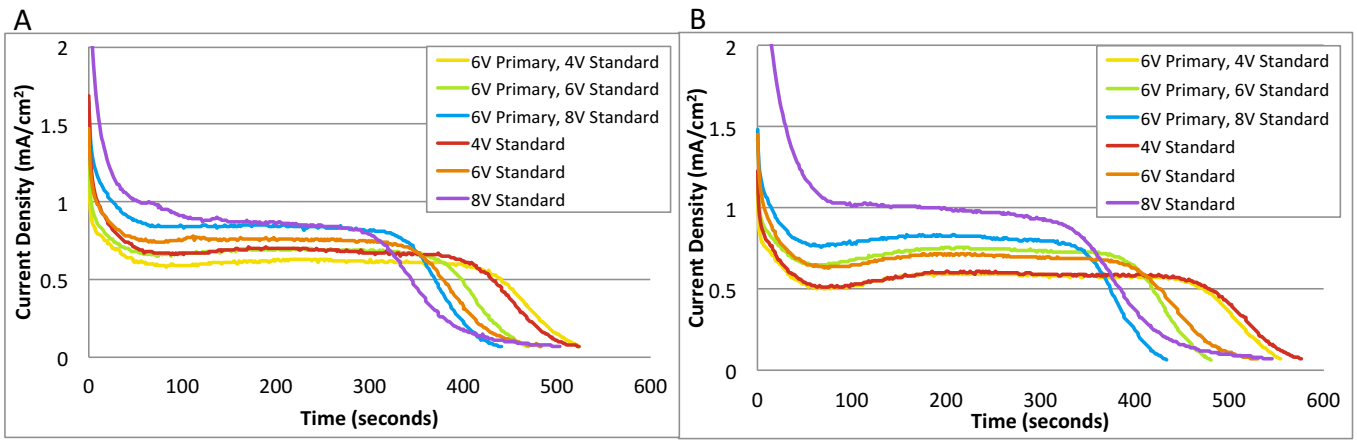

Figure 7.14. Current density plots show anodization curves from initial aluminum thicknesses of 99±11.2 nm (A) and 104±9.2 nm (B) that represent the trends shown in each set of triplicates. Curves were generated for the standard anodization process. Test samples had the primary anodization of tantalum at 6 V prior to aluminum deposition, followed by the standard anodization process. Control samples had one standard anodization process. Current density curves for test (primary and standard anodization) and control (standard anodization) samples were generated from oxidation of devices with identical aluminum thicknesses at voltages of 4, 6, and 8 V in 0.4 M phosphoric acid electrolyte.

Table 7.9 shows the average anodization time for the barrier oxide layer to form during the standard anodization process for test and control slides.

Table 7.9. Average time required to form the barrier oxide layer during the standard oxidation process in 0.4 M phosphoric acid electrolyte. The difference between oxide formation time for slides with only the standard anodization versus slides with primary and standard anodization were compared at the respective voltages used for the standard anodization process (4, 6, or 8 V).

Time for Tantala Barrier Layer Formation (seconds)			
Samples		Average	SD
Control	4V Standard	113	4
	6V Standard	133	5
	8V Standard	189	20
Test	6V Primary, 4V Standard	90	3
	6V Primary, 6V Standard	92	4
	6V Primary, 8V Standard	100	10
Delta (Control-Test)	Δ4V Standard	23	5
	Δ6V Standard	42	6
	Δ8V Standard	88	22

Slides with primary anodization of the tantalum layer at 6 V resulted in a shorter barrier oxide formation period during the standard anodization process, regardless of the applied voltage. Ellipsometry was conducted on all films with an initial aluminum thickness of 99 nm.

Table 7.10. Ellipsometry data for slides formed with the standard anodization process or primary and standard anodization processes. The standard anodization was carried out at 4, 6, and 8 V on devices with an initial aluminum thickness of 99 nm.

Parameters Measured	Alumina formed on nanoFAB Ta films with the following anodization processes (Initial Al=99 nm)											
	4V standard	SD	6V primary, 4V standard	SD	6V standard	SD	6V primary, 6V standard	SD	8V standard	SD	6V primary, 8V standard	SD
Mean Std. Error (MSE)	20.26	0.74	27.95	5.24	20.48	0.53	33.62	0.38	20.40	0.14	31.69	1.52
Alumina Thickness (nm)	88.93	1.26	71.10	7.81	86.94	0.19	80.25	0.70	84.57	0.13	81.78	0.69
Tantala Thickness (nm)	5.33	0.45	15.94	0.19	9.69	0.23	18.07	0.58	13.20	0.49	19.03	0.16
Percent Void (%)	52.05	0.45	49.00	0.30	48.70	0.60	44.65	0.35	47.60	0.90	41.40	1.00
n_370_xy	1.32	0.01	1.35	0.00	1.35	0.00	1.38	0.00	1.36	0.01	1.41	0.01
n_700_xy	1.31	0.00	1.34	0.00	1.34	0.00	1.37	0.00	1.34	0.00	1.40	0.01
n_370_z	1.43	0.00	1.46	0.00	1.46	0.00	1.49	0.00	1.46	0.00	1.52	0.01
n_700_z	1.42	0.00	1.44	0.00	1.44	0.00	1.47	0.00	1.45	0.01	1.50	0.01

SEM topographic and cross-sectional images were captured of test and control slides. Topographic and cross-sectional images were measured to generate aluminum surface porosity and thickness values using an alternate method to ellipsometry.

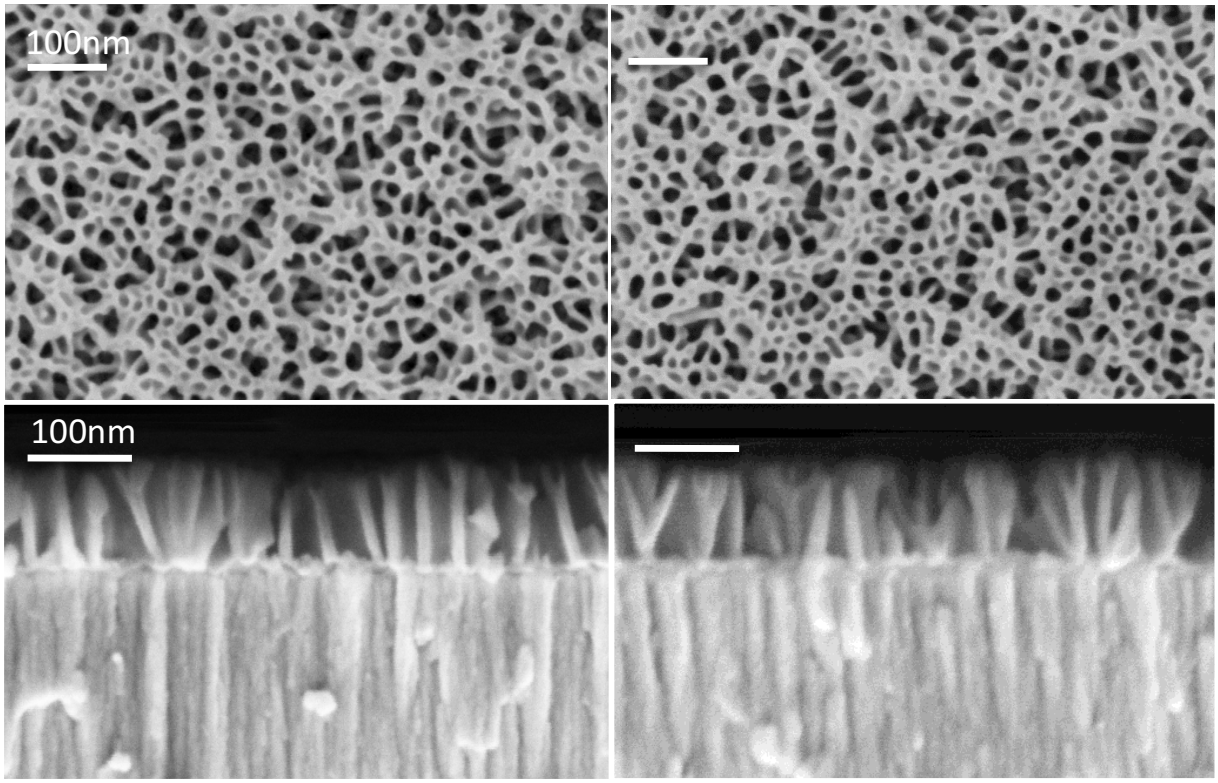

Figure 7.15. Topographic and cross-sectional images of a slide formed with the standard anodization process (left) and a slide formed with primary and standard anodization processes (right). The standard anodization was carried out at 8 V and the initial aluminum thicknesses for both slides were 99 nm. All scale bars show 100 nm.

One set of SEM images was shown, as all alumina films were visibly indifferent. Measurements of alumina thickness and porosity are shown in Table 7.11.

Table 7.11. Measurements of alumina thicknesses and surface porosity values from SEM images of aluminum and tantalum coatings, deposited in the nanoFAB system, anodized following the primary and 8 V standard processes for test samples or with the standard process at 8 V for control samples.

Parameter Measured	Alumina formed on (Initial Al=99 nm)				Alumina formed on (Initial Al=104 nm)			
	nFAB control	SD	nFAB test	SD	nFAB control	SD	nFAB test	SD
Alumina Thickness (nm)	84.9	8.0	88.5	6.5	89.9	7.7	96.3	6.2
Surface Porosity (%)	42.60	3.50	41.60	0.90	40.00	0.10	39.10	1.30

Comparing the alumina thicknesses of devices formed on nanoFAB tantalum for control and test slides, showed no significant difference regardless of the initial aluminum layers ($p=.428$). Furthermore, surface porosity between control and test slides showed no statistical difference either ($p>.754$). The final method used to evaluate the interface and confirm the oxide layer thicknesses was SIMS. Figure 7.16 shows the result of SIMS scans of control and test samples formed with 99 nm of aluminum on nanoFAB tantalum.

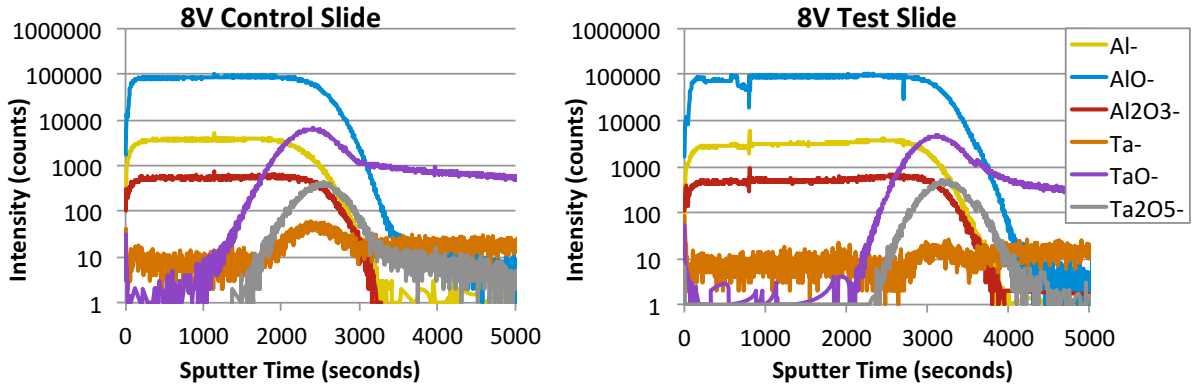

Figure 7.16. SIMS scans of control (left) and test (right) samples formed with the standard anodization processes completed at 8 V.

All aluminum and aluminum oxide species confirmed that the alumina layer was thicker in the test sample versus the control sample. The tantalum oxide species (TaO- and Ta2O5-) showed a greater FWHM in the control sample and showed a lower slope for tantala species, increasing at an earlier sputter time than in the test sample scan. For TaO- the signal began increasing at 27% of the way through the AlO- signal in the control slide versus an onset at 61% of the way through the AlO- in the test slide. The TaO- signal showed a gradual increase and decrease in the tantala signals on the control slide in comparison to the test slide making the FWHM harder to measure. Correlating TaO-/AlO- to the known alumina thickness

measured from SEM images showed a tantala thickness of ~29 nm for both control and test slides respectively.

Visible surface colour shifts shown in Figure 7.17, further indicated changes between the test and control devices. An increase in the optical path length caused the visible colour to shift further into the first order region and towards second order colours. The only parameters that lead to an increase in the optical path length are increasing the distance travelled through the film or the refractive index of the layers.

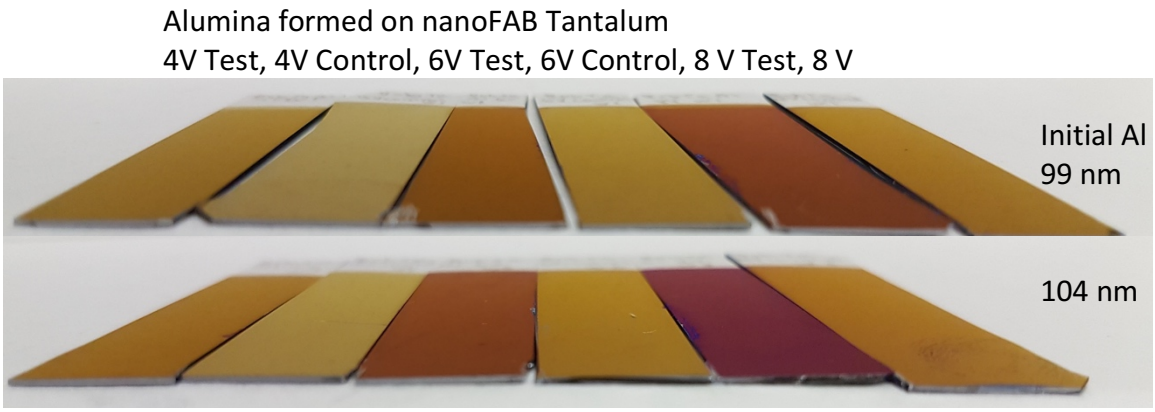

Figure 7.17. Images show slides in order of (left to right): 4 V test, 4 V control, 6 V test, 6 V control, 8 V test, and 8 V control. The test samples were prepared by primary anodization of the tantalum layer at 6 V and subsequently, aluminum deposition and the standard anodization process at 4, 6, or 8 V. The anodization of control samples, containing aluminum and tantalum, were carried out at 4, 6, or 8 V.

Differences were apparent between control and test surfaces formed at the same standard anodization process applied voltage. A comparison of the detection limits was carried out on devices with nanoFAB tantalum for control and test slides. Figure 7.18 shows images of control and test surfaces formed with a standard anodization process at 8 V. Surfaces were exposed to 28 picomoles of prothrombin (20 µl at 0.1 mg/ml) and subsequently 2, 3.3 and 6.7 picomoles of anti-prothrombin (20 µl at 0.015, 0.025, and 0.050 mg/ml).

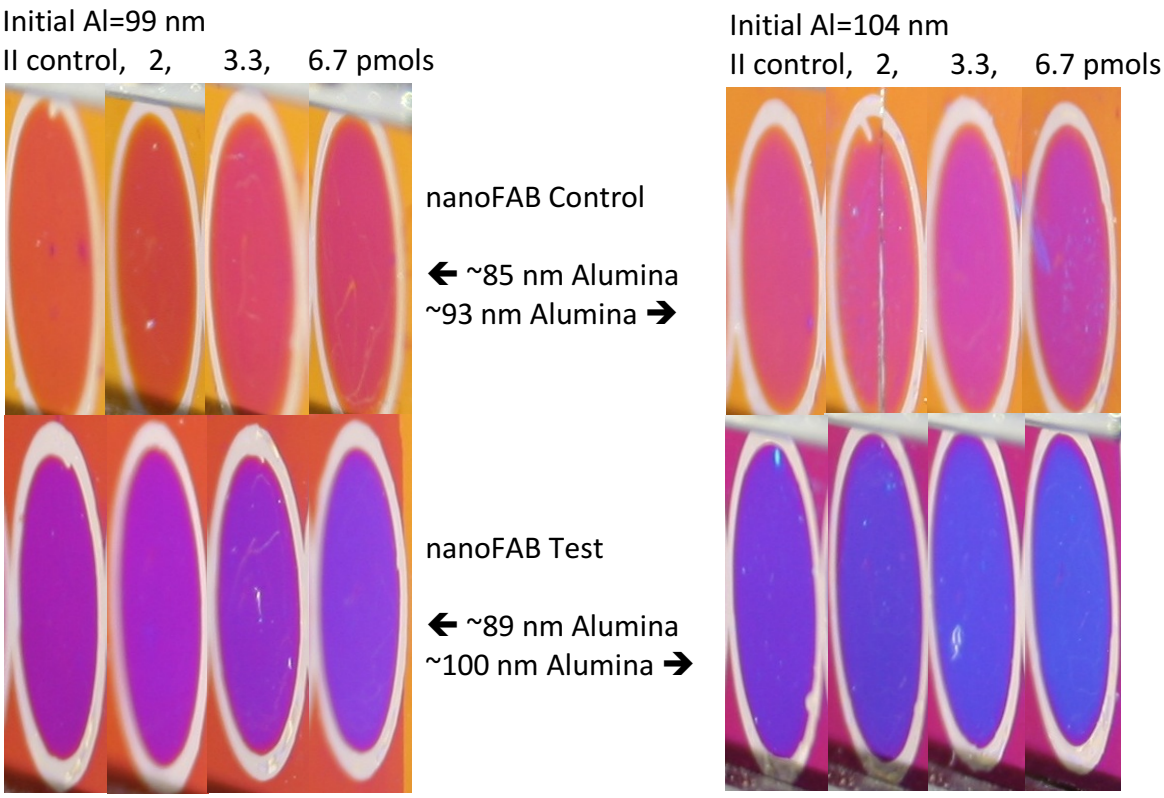

Figure 7.18. Shows the visible surface colours resulting with exposing 28 picomoles of prothrombin (20 µl at 0.1 mg/ml) and subsequently 2, 3.3 and 6.7 picomoles of anti-prothrombin (20 µl at 0.015, 0.025, and 0.050 mg/ml) to the control and test slide surfaces formed on nanoFAB tantalum. Images were taken using the custom optics system. (n=1)

The prothrombin control spots for the thinner aluminum films created on control and test slides were orange pink and purple respectively. Subsequent shifts with anti-prothrombin appear to be equivalent sensitivities. With highest anti-prothrombin solutions on control slides shifting to pink and test slides shifting to bluish purple. Films created with a thicker initial aluminum layer showed prothrombin control spots for control and test slides of pink and bluish purple, and move towards reddish purple and purplish blue, respectively.

Table 7.12 shows RGB coordinates and differences between colours perceived by the human eye (ΔE*). These values allow for a comparison of which colour shifts are more sensitive with anti-prothrombin exposed to a prothrombin-coated surface.

Table 7.12. RGB coordinates and differences in colour between prothrombin-coated surfaced exposed to anti-prothrombin solutions (ΔE) at varying concentrations.*

Protein Concentrations Exposed to Surface and Colour Coordinates		Initial Aluminum of 99 nm						Initial Aluminum of 104 nm					
		nanoFAB Test			nanoFAB Control			nanoFAB Test			nanoFAB Control		
		Average	SD	**ΔE* (vs II)**	Average	SD	**ΔE* (vs II)**	Average	SD	**ΔE* (vs II)**	Average	SD	**ΔE* (vs II)**
II (0.1 mg/ml)	R	163.52	3.77		217.14	2.77		119.12	3.85		216.28	1.90	
	G	33.82	2.13		87.24	3.34		58.97	3.41		82.42	2.98	
	B	175.76	4.81		60.03	8.55		216.93	4.05		132.77	8.97	
II & AP (0.015 mg/ml)	R	168.23	4.40	9.80± 3.31	202.87	3.22	7.61± 4.90	100.06	5.53	8.27± 0.62	216.78	4.53	6.95± 8.05
	G	39.09	1.87		72.91	6.89		67.00	5.13		86.97	6.53	
	B	198.21	4.78		59.47	10.08		212.88	5.00		147.53	11.96	
II & AP (0.025 mg/ml)	R	149.36	6.79	12.84± 0.95	216.51	2.80	27.14± 6.71	98.06	7.88	11.08± 2.75	211.77	2.24	25.52± 6.67
	G	50.06	8.71		74.85	4.09		79.82	7.53		77.18	3.07	
	B	199.93	5.36		101.96	9.62		231.05	3.85		174.65	7.89	
II & AP (0.05 mg/ml)	R	142.00	3.54	21.41± 0.81	208.88	2.86	31.99± 6.13	87.44	4.86	17.21± 1.63	192.99	4.68	30.77± 5.87
	G	66.23	3.22		70.60	5.05		88.46	4.52		70.42	5.29	
	B	221.31	2.04		105.66	9.22		231.70	3.79		173.11	9.18	

Table 7.13 shows Yxy coordinates transformed from RGB values, to plot on the CIE charts in Figure 7.19.

Table 7.13. Yxy chromaticity coordinates were transformed from RGB colour coordinates in order to plot coordinates on the CIE chart.

Protein Concentrations Exposed to Surface and Colour Coordinates		Initial Aluminum of 99 nm		Initial Aluminum of 104 nm	
		nanoFAB Test	nanoFAB Control	nanoFAB Test	nanoFAB Control
II (0.1 mg/ml)	Y	12.10	21.96	12.06	22.43
	x	0.30	0.53	0.22	0.43
	y	0.16	0.36	0.12	0.27
II & AP (0.015 mg/ml)	Y	13.89	17.75	11.52	23.65
	x	0.28	0.54	0.20	0.41
	y	0.14	0.34	0.12	0.26
II & AP (0.025 mg/ml)	Y	12.88	20.61	14.08	22.38
	x	0.26	0.48	0.20	0.37
	y	0.14	0.30	0.12	0.22
II & AP (0.05 mg/ml)	Y	14.91	19.03	14.91	18.79
	x	0.24	0.47	0.19	0.34
	y	0.13	0.29	0.13	0.20

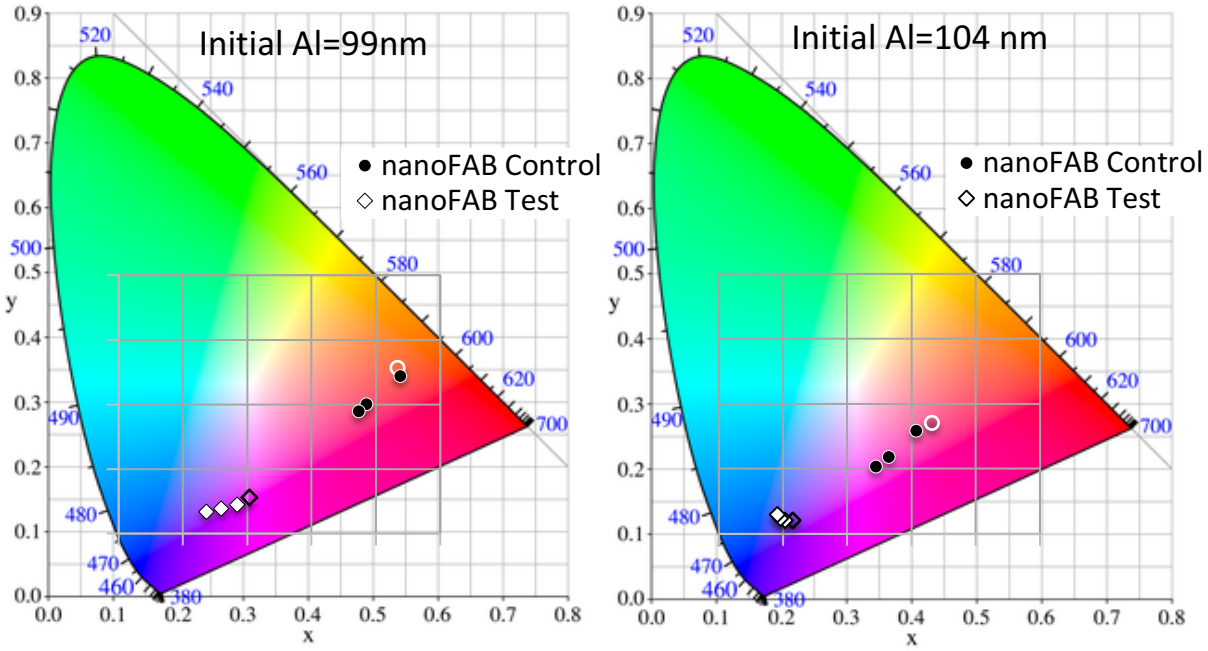

Figure 7.19. Colour plots showing the colours resulting with 0.1 mg/ml prothrombin (outlined shape) and subsequently 0.015, 0.025, and 0.050 mg/ml anti-prothrombin (from right to left). Plots compare colours on control and test slides with nanoFAB tantalum layers.

7.3.4 Primary and Standard Anodization on α Tantalum Film

When completing the standard anodization on tantalum films formed in the NAIT system failure of the thin film occurred. Initially delamination of slide surfaces became visible during the standard oxidation process of test samples, but subsequently showed occasional delamination on control samples also. Midway through the pore formation region, the current density plot showed a peak at the same time as visible spots appeared on the anode surface in the electrolyte bath. Figure 7.20 shows the current density plots of 5 devices with apparent delamination during anodization.

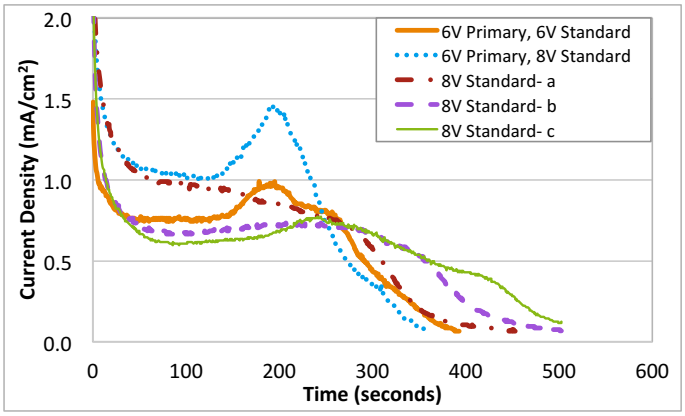

Figure 7.20. Current density curves for samples that lead to areas of delamination following the standard anodization process. The legend provides sample information on which anodization processes were carried out with the applied voltages.

When viewed perpendicular to the surface, effected regions appeared lighter in colour than the fully anodized alumina and tantala, but when viewed at a high angle (~75°) they were colourless and appeared to be similar in colour to a metallic film.

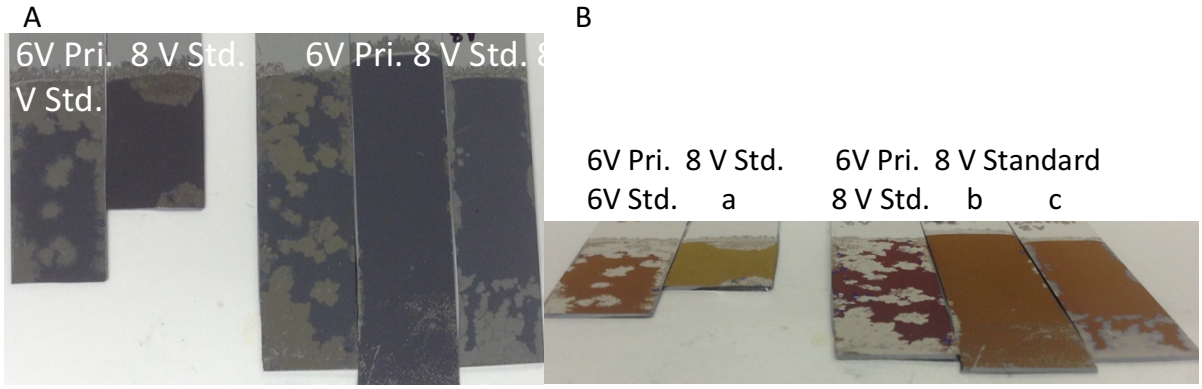

Figure 7.21. Images of slides showing delamination captured at incident angles of (A) 0° and (B) 75°. Samples were prepared with primary (Pri.) anodization at 6V followed by standard (Std.) anodization at 6 or 8 V, or standard (Std.) anodization at 8 V. Anodization processes used are labelled above the corresponding slides. These films correspond with current density plots shown in the figure above.

Test slides with primary and standard anodization processes showed significantly more delamination.

7.3.4.1 NAIT Tantalum Surfaces

Prior to aluminum deposition, wafers with tantalum films sputtered in the NAIT system were viewed in a bright light box to check for fine particulate or contamination on the surface

that may affect the aluminum adhesion. Figure 7.22 shows 4 tantalum wafers sputtered in the NAIT system.

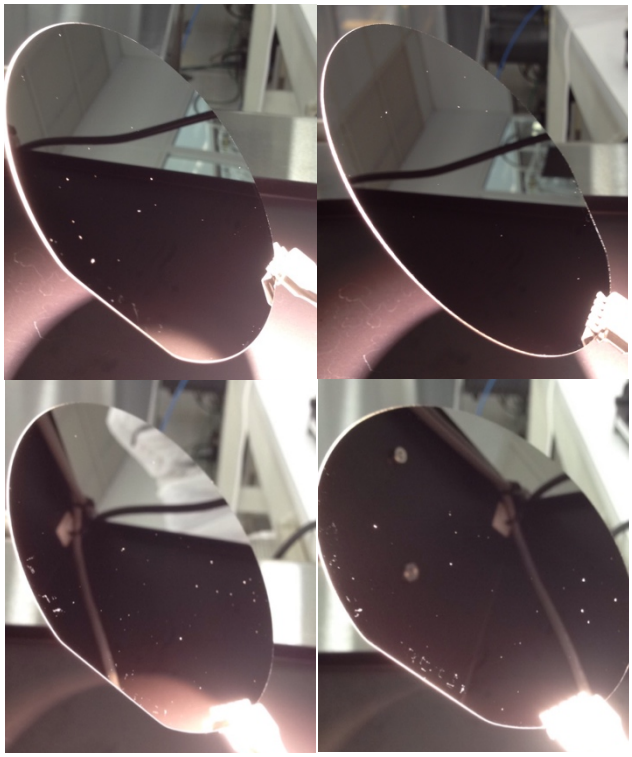

Figure 7.22. Wafers viewed in a bright box to examine tantalum coatings deposited in the NAIT sputter system.

Particulate was found on the surface of all wafers. Wafer tweezer marks were noticeable, close to notches, on 3 out of the 4 tantalum wafers viewed.

7.3.4.2 Analysis of Film Failure

SEM images of slides showing delamination were used to interpret the surface interface when adhesion issues presented.

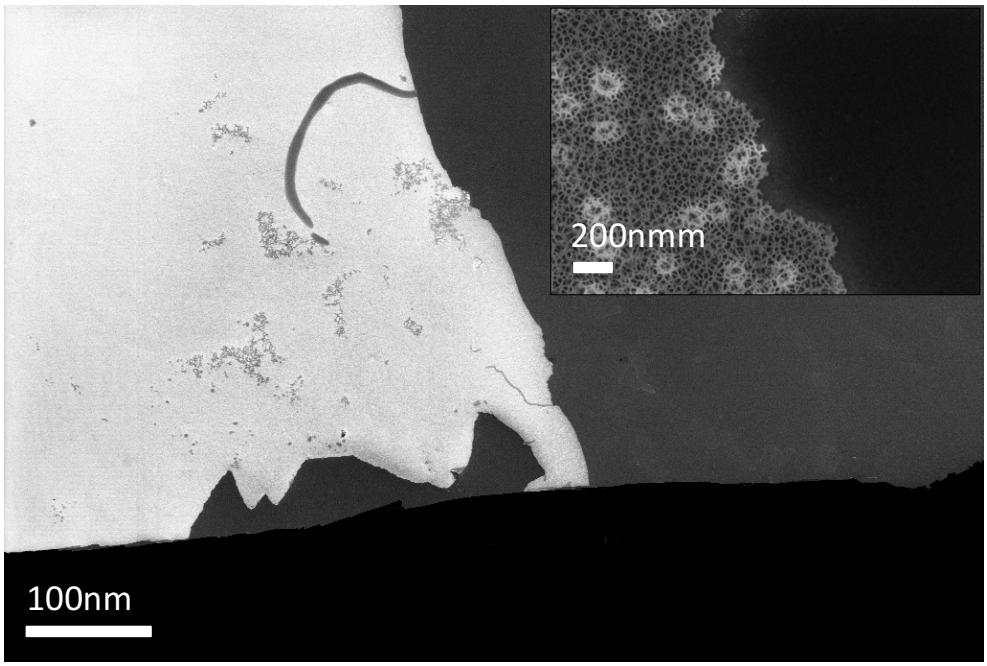

Figure 7.23. A sample with delamination after primary anodization at 6 V, aluminum deposition, and standard anodization at 6 V. The image shows porous alumina on the left of both images and removal of this layer on the right.

EDS confirmed the composition of films remaining on delaminated sections of the slide, with a shiny metallic colour after anodization, as opposed to typical surface colour. Results of the map scan are shown in Figure 7.24 and location sites for the point analysis. Results of the point analysis are shown in Table 7.14.

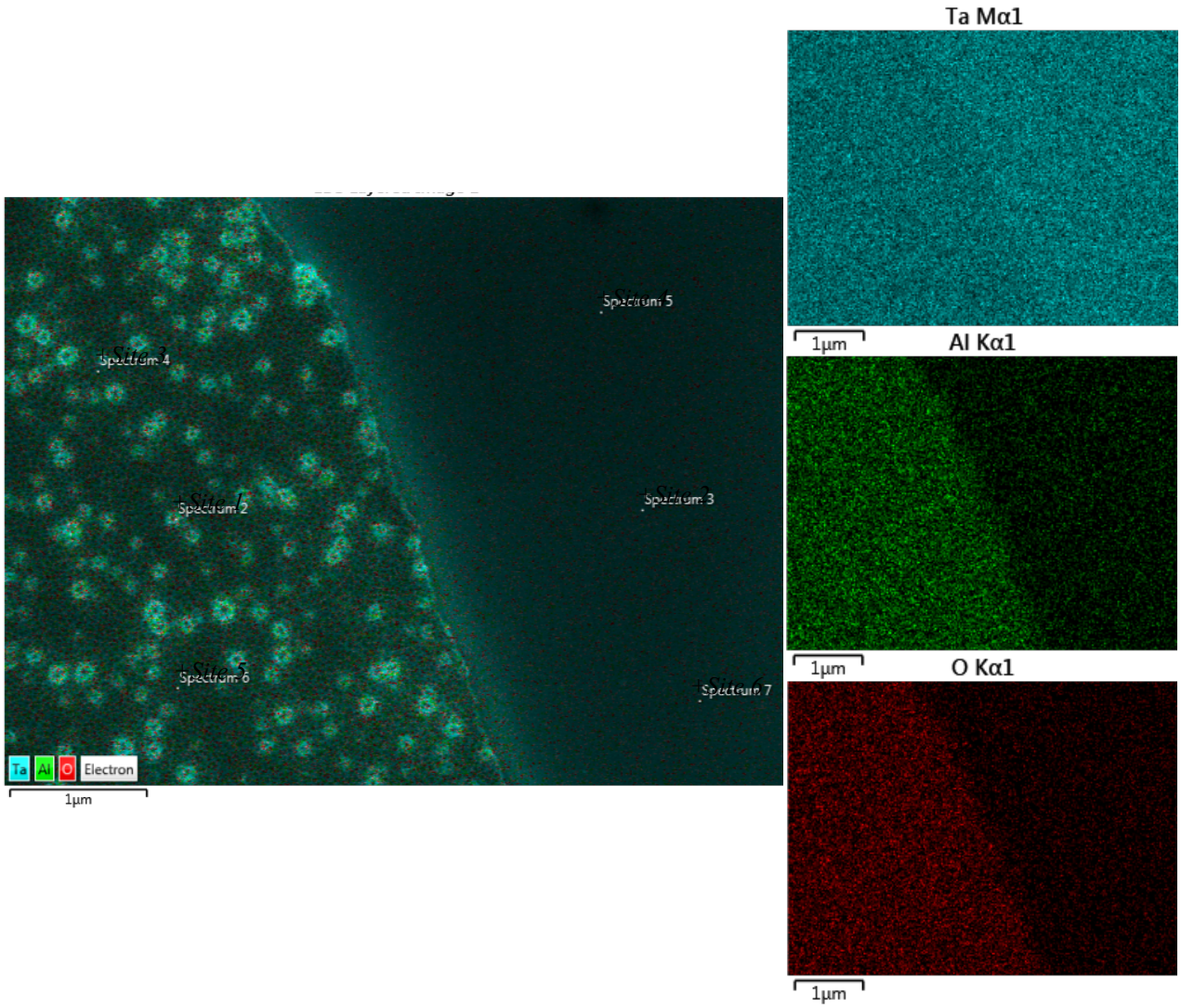

Figure 7.24. EDS map scan and sites used for point analysis on the alumina (left side) and a region where delamination occurred (left side). Individual elements were mapped for tantalum (Ta), aluminum (Al), and oxygen (O), which are shown alongside the SEM map scan.

Table 7.14. Elemental point analysis data collected from the locations depicted in Figure 7.24. Elemental compositions of the porous alumina and the to-be-determined (TBD) locations are shown with standard deviations.

Material	Sites	C (at%)	SD	N (at%)	SD	O (at%)	SD	Al (at%)	SD	Si (at%)	SD	Ta (at%)	SD	O/Al Ratio	SD
Alumina	1,3,5	1.1	0.1	0.7	0.6	8.8	0.3	2.7	0.1	0.7	0.0	86.0	0.3	3.2	0.1
TBD	2,4,6	0.0	0.0	0.0	0.0	2.4	0.1	0.0	0.0	0.8	0.1	96.6	0.3	undefined	

Based on the elements detected, the main composition of the TBD material was tantalum with a small amount of oxygen, either native or anodic tantala. The TBD region contained no aluminum, and thus the porous anodic alumina was fully removed in the

electrolyte solution during anodization. Minor amounts of silicon were found on the surface of both regions. Note that elemental values in the table above cannot be compared to EDS data in Table 7.1 because the probing voltage was changed from 5 kV to 10 kV.

Additional SEM images of surfaces provided insight on the failure mechanism leading to delamination. Figure 7.25 shows SEM images of a sample (8 V Standard-b in Figure 7.20) containing aluminum on NAIT tantalum coatings that was anodized following the standard process at 8 V. The bright areas in the images show porous alumina where numerous electrons contact the surface and return to the detector. Darker regions show tantalum, a conducting layer, from which lower levels of electrons are reflected back to the detector.

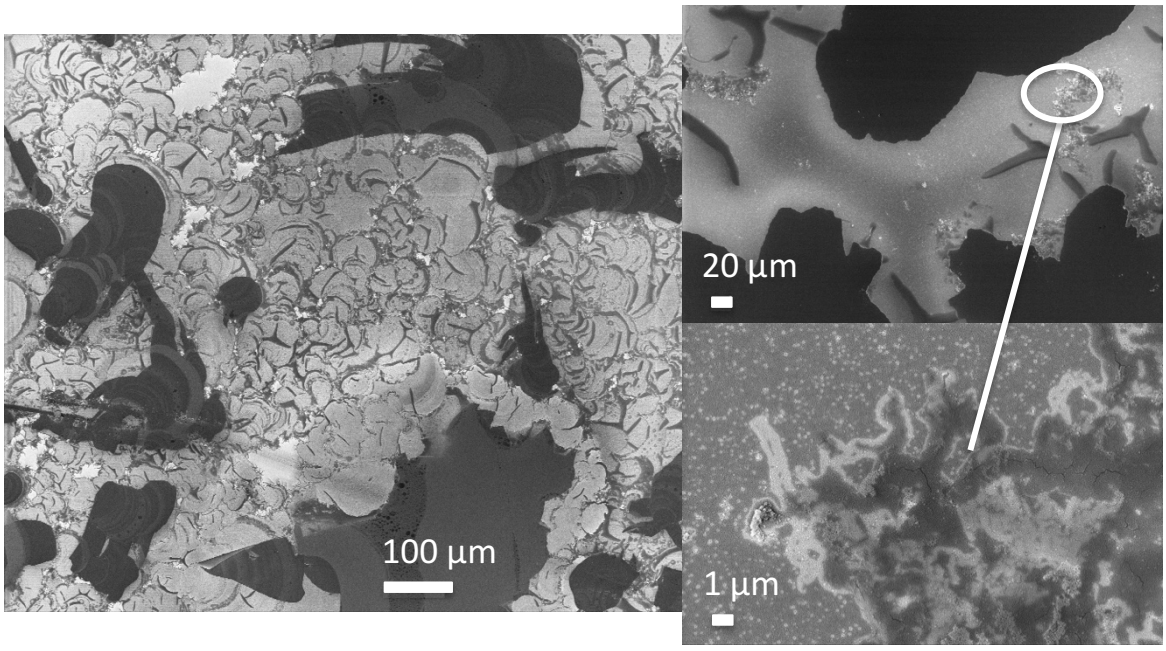

Figure 7.25. A sample with delamination shows a larger field of view and allows for the observation of failure lines. The device had tantalum and aluminum thin films with exposure to atmosphere between sputtering and the standard oxidation process was complete at 8 V in 0.4 M phosphoric acid electrolyte. Bright regions are alumina and darker regions are tantalum.

Failure lines and regions of delamination are visible in these images. Figure 7.26 showed the visible "worm-tracks" in the SEM images from the same sample shown in Figure 7.25.

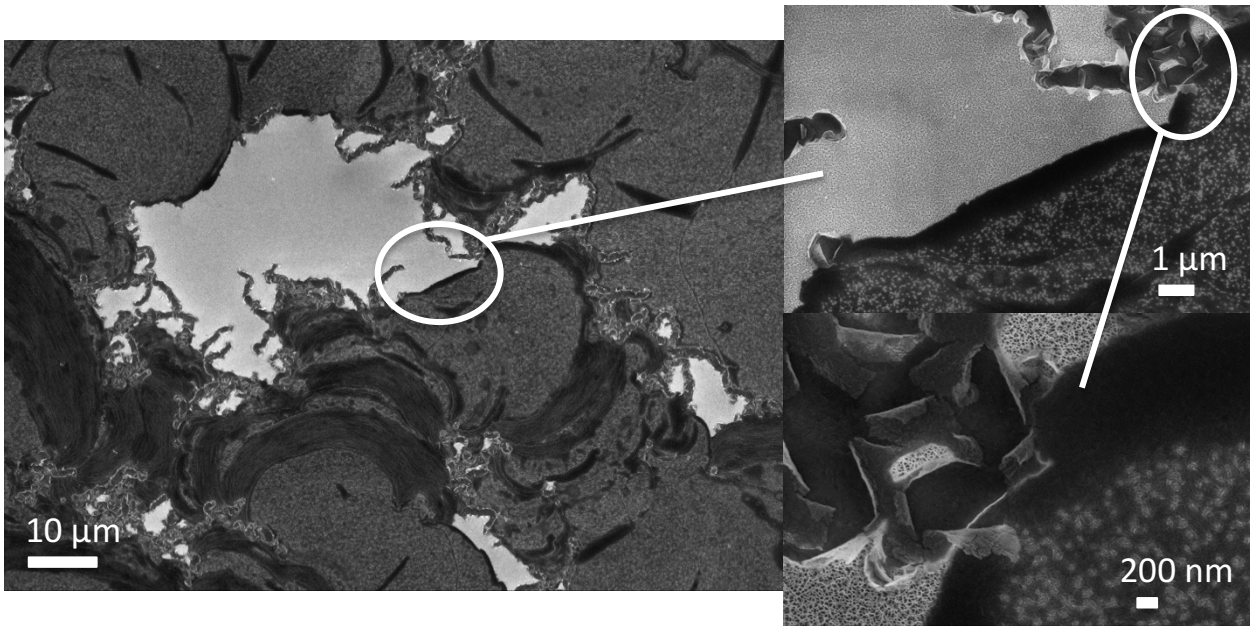

Figure 7.26. Delamination that resulted during the standard oxidation process, completed at 8 V in 0.4 M phosphoric acid electrolyte. "Worm-tracks" are visible where delamination and rolling of the porous alumina layer results. Bright regions are alumina and darker regions are tantalum.

Cross-sectional images of a sample at 45° from the surface, showed the transition from porous alumina to where film delamination occurred. On the right side of the image porous alumina was present and on the left side none remains.

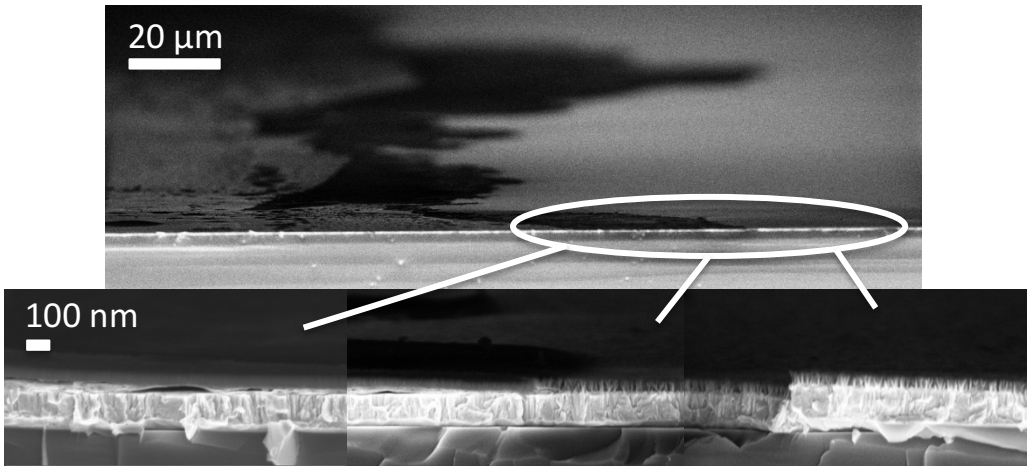

Figure 7.27. Delamination of the alumina layer shown at 45° from normal to the surface. The sample contains tantalum and aluminum thin films, exposed to atmosphere between film depositions, and the standard oxidation process was complete at 8 V in 0.4 M phosphoric acid electrolyte. Bottom images at a higher field of view show from left to right: complete alumina delamination, the transition point where there is both no alumina and alumina, and the alumina layer.

In Figure 7.28, images on the left were captured moving from the top of the film towards the remaining alumina layer. Images on the right show a higher field-of-view of select locations.

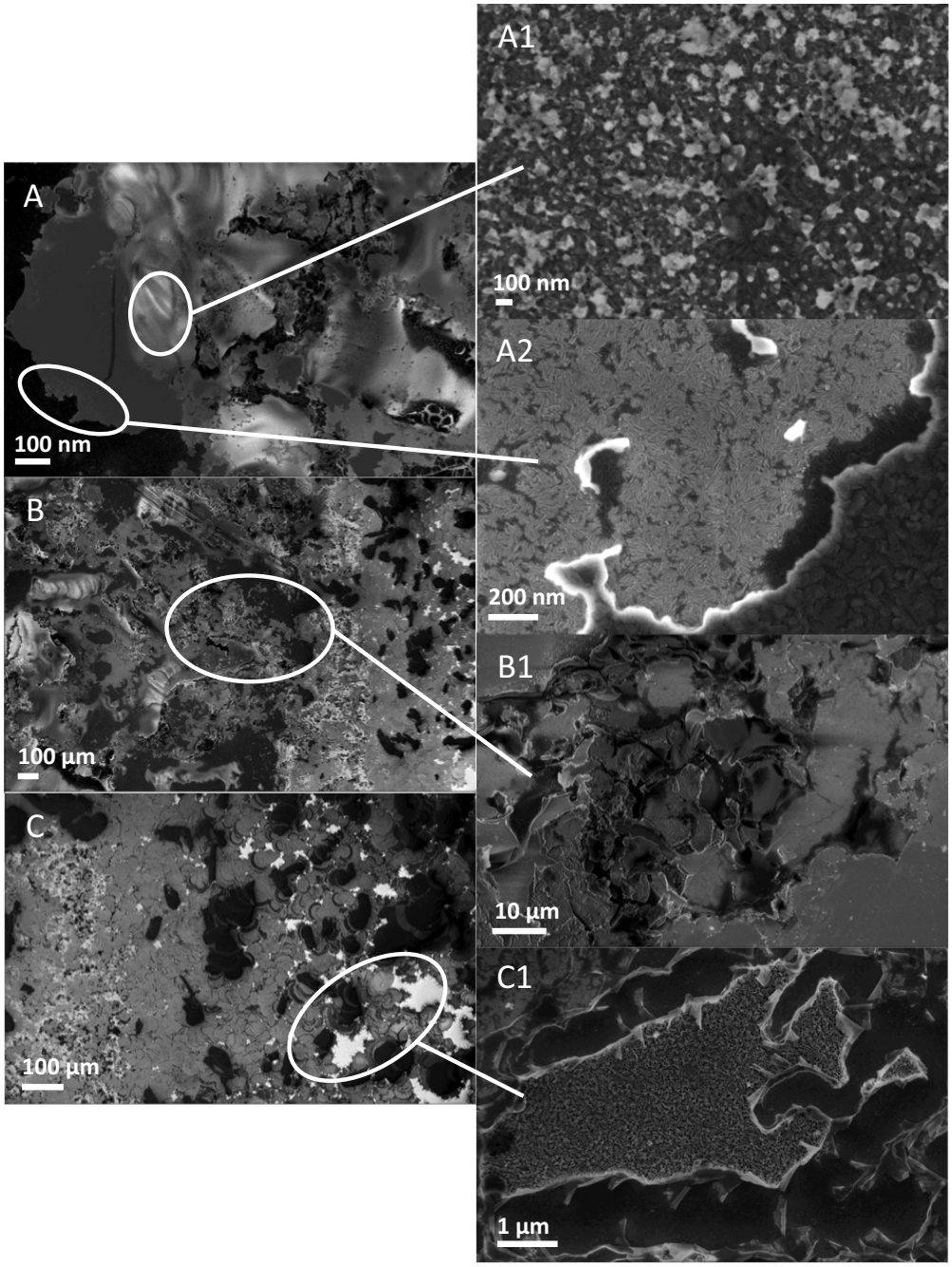

Figure 7.28. SEM images of the top area of an anodized sample showing delamination. Images in the left column start at (A) the electrolyte line and (B and C) move down towards an area with less delamination. The right column shows select areas at an increased field-of-view.

Various structures are visible in these SEM images, none of which look like the typical porous alumina surface, except a central region of the bottom right image (C1). Similar to Figure 7.28 (A, B, and C) above, Figure 7.29 (A, B, and C) shows SEM images with EDS mapping. Tantalum, aluminum, and oxygen were the three highest elements present, and in some cases phosphorous. A breakdown of the composition was shown for Figure 7.29 (A).

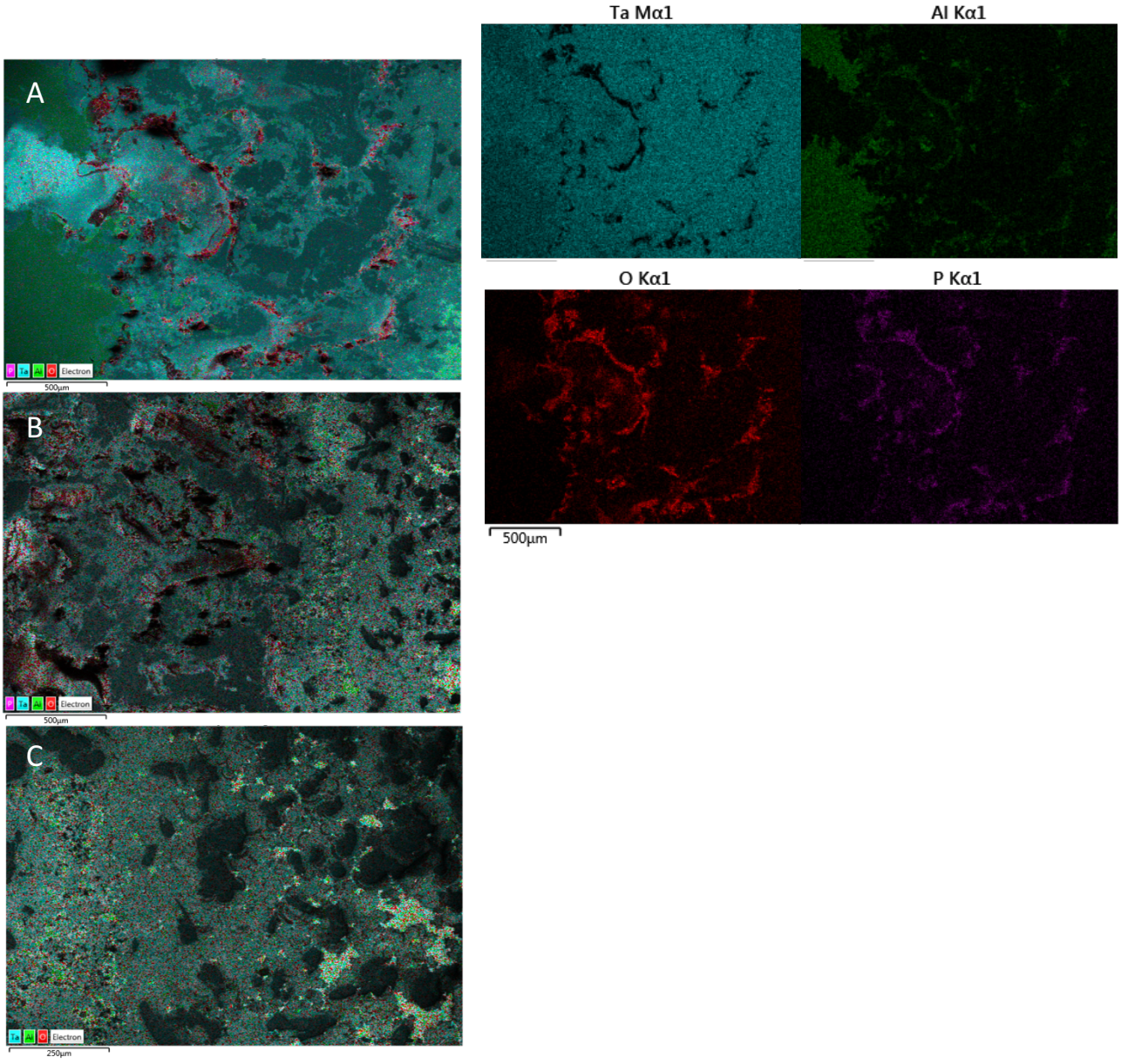

Figure 7.29. SEM with EDS map scans of the top portion of an anodized sample showing delamination. Images from top to bottom show the non-uniform region at the electrolyte line and move towards the area where porous alumina remains.

Comparing the SEM and SEM-EDS images shown in Figure 7.28 and Figure 7.29 allowed for a better understanding of the surface structures. From the individual element maps, it is apparent where porous alumina exists from the element distribution of aluminum, oxygen, and phosphorous. Furthermore, in Figure 7.28 (A2) the aluminum and tantalum grains were visible. Some of the non-uniform portion near the electrolyte line was tantalum with little oxide present. Porous alumina sections were visible in Figure 7.28 (C and C1) and Figure 7.29 (A and C). As you continue to move further down the slide these fragments become larger and eventually connect in areas where failure did not result. Structures in many areas along the top of the slide were unrecognizable and likely result due to delamination.

7.4 Discussion

7.4.1 As Sputtered Tantalum and Anodic Tantala Films

From visual observation, tantalum films formed in the nanoFAB system created a zone 1 structure and films formed at NAIT created a Zone T structure. The nanoFAB tantalum films were highly columnar with circular grains and occasional voids. NAIT tantalum films showed a dense structure with a smooth fibrous surface. The difference in power densities, and in turn deposition rates, likely resulted in the alternate tantalum microstructures. The higher power density in the NAIT system leads to a deposition rate more than 6 times that of films sputtered in the nanoFAB system. With increased deposition rates, higher energy and temperatures can be expected. Ad atom diffusion is a function of energy and thus occurs more readily in the NAIT tantalum thin films. Furthermore, a large sputter target was used perpendicular to the substrate in the NAIT system and thus no shadowing results and the sputtered coatings are smoother than those formed in the nanoFAB system which uses a target smaller than the substrate at a slight angle to the substrate. Deposition parameters in the two sputter systems differ, as shown in Table 7.15.

Table 7.15. Deposition parameters used for tantalum deposition in the nanoFAB and NAIT sputter systems.

Sputter System	Base Pressure (Torr)	Power Density (W/cm^2)	Current (A)	Voltage (V)	Ar Pressure (mTorr)	Flow Rate (sccm)	Working Distance (cm)	Deposition Rate (nm/min)
nanoFAB	10^{-6} to 10^{-7}	6.6	0.6 to 0.8	375 to 440	7	10	12	9
NAIT	10^{-5} to 10^{-6}	1.54	1.7	200 to 300	10	135	7	60

Using the structure zone diagram as a model, tantalum deposition at 40°C have a T/Tm ratio of 0.1 and are a zone 1 structure. The microstructure of tantalum coatings deposited at temperatures between 56 and 715°C (329 K and 988 K) theoretically shifts from a zone 1 to zone T. However, the two tantalum films created in this work should not be compared as if they are on the same structure zone diagram, as the zone trends of each deposition system are unknown. Figure 7.4 provides an outline of the microstructures expected for a sputtered coating deposited using a cylindrical magnetron sputter system. Variance in the deposited coatings will result with different types of sputter systems and from one system to the next.

7.4.1.1 SEM with EBSD

Elemental data from as sputtered and anodized tantalum films provide another method for film analysis. Oxygen values in as sputtered tantalum films produced in the nanoFAB and NAIT systems were statistically different (p=.066), however, after anodization no significant difference in the oxygen content remained (p=.238). As shown in Table 7.15, the argon flow rate in the nanoFAB system was low compared to the NAIT system and may have contributed to larger amounts of oxygen throughout the tantalum layer. The increased oxygen and carbon content in the nanoFAB films can be explained by the longer shelf time prior to analysis. With longer periods of exposure to atmosphere after sputtering the native oxide continues to thicken. Nitrogen was present in NAIT tantalum as sputtered and anodized films, which has been linked to an intermittent leak in the process chamber. Additionally, the base pressure in the NAIT system was slightly higher than that achieved in the nanoFAB system, meaning the chamber may contain more residual gasses during the deposition system. Contamination of residual gas in the process chamber during sputtering may further alter the colour of the deposited film due to the integration of contaminants into the structure.

A study with reactive sputtering showed that changes in the nitrogen concentration present during sputtering demonstrate phase changes that were dependent on the sputtering voltage. Small amounts of nitrogen, 2-3 at%, were found to alter the phase and lead to

reflectance changes in the sputtered films. [13] It is possible that alternate sputter conditions such as temperature also influence the solubility limit of nitrogen in the coating and the tantalum phase that results.

7.4.1.2 XRD

Following XRD it was determined that not only are the zone structures different, but the crystal peaks differ as well. Deposition in the nanoFAB system created a mixture of alpha and beta tantalum. Deposition in the NAIT system generated an α-Ta structure. The beta structure is a tetragonal or hexagonal subcell and the alpha structure is body-centered-cubic (bcc).

The nanoFAB tantalum film showed 4 β-Ta peaks and 1 α-Ta peak. The first peak was beta (002), reported in the majority of studies with β-Ta sputtered films as the preferential orientation with a distance between crystal planes (d-spacing) of 2.627 Å. [14] The second peak (not visible) was beta (410), located between the beta (002) and α-Ta (110) peaks. Additionally, the α-Ta (110) main peak overlaps with another β-Ta peak oriented in the (202) plane. Hence why the peak at ~39° appears wide and has a jagged top. With oxidation the peak becomes wider and the combination of beta and alpha phases becomes more apparent and was distinguishable with the analysis software. The NAIT tantalum film showed 3 α-Ta peaks with crystal orientations of (110), (200), and (211). In the mixed phase, the ratios of alpha to beta tantalum cannot be determined because overlapping peaks prevent identification of peaks in the 2θ region of 38 to 40° with certainty (see Table 7.2). A technique to accurately confirm these peaks can be found in the literature. [15,16]

In sputtered tantalum thin films two phases exist, a stable alpha (bcc) phase with needle shaped grains and a metastable beta (tetragonal) phase with circular grains. The deposition energy has shown to be highly influential to the phase and structure that results, with higher energy leading to the growth of α-Ta.[17,18]With typical deposition in magnetron sputter systems a β-Ta crystal structure results. The α-Ta phase can be achieved by transforming β-Ta to α-Ta with heating above 750 °C[19]or heating during deposition.[20]

Surface morphology of β-Ta has been shown to change with sputter parameters such as pressure. The topographic structures and XRD peaks in samples sputtered at 5 mTorr in work by Navid and Hodge, validated that the phase formed in the NAIT sputter system was α-Ta.

[21]The NAIT system employed a deposition rate 10 times greater than Navid and Hodge's work, hence why the beta structure had enough energy to form at a slightly higher pressure (10 mTorr).

Changes in the crystal structure have proven to generate differences in the resulting film residual stress. [19,21] Clevenger et al. showed heating a film during deposition demonstrated an increase in tensile stress. [19] Furthermore, his work showed that elastic and plastic deformations are methods of stress relief that occur at low and medium temperature ranges, and beta to alpha transformation at high temperatures. Lower intrinsic stress resulted in films deposited with lower rates of ion bombardment, due to the open microstructure. Lower stresses within sputtered films allow larger elastic deformation before the yield stress is reached and plastic deformation begins. [19] Navid and Hodge showed residual stresses that were tensile for β-Ta (202) and (002) and high compressive stresses for α-Ta (211) and (110). [21] Lower stresses are shown to result in β-Ta structures, which allows for a reduced chance of failure and ultimately better film adhesion with sputtering and oxidizing. In addition, tantalum films containing both alpha and beta phases may have increased adhesion due to the complex dislocation structure of the mixed phases.[22]

The nucleation of α and β-Ta phases has shown to be decisive in the resulting structure. [23] Increasing substrate temperature increases the alpha phase formation. Temperatures between (177 to 327 °C) 450 and 600 K showed nucleation of both tantalum phases, and (>327 °C) >600 K showed only α-Ta. [23]

7.4.1.3 Surface Colour

The surface reflectivity off tantalum films created in the nanoFAB and NAIT systems was statistically different for both as sputtered and anodized tantalum. The anodization process was required to alter the metallic surface and generate surface colours, and in doing so the reflectance off the surface decreased. The higher the anodic tantala thickness the greater the visible difference between tantalum and anodic tantalum surfaces. Tantalum surface colours were more dominant when viewed at 0°. The change in optical constants between nanoFAB and NAIT provides additional confirmation that the surface colours and intensities between films formed in the two sputter systems vary.

Work by Thornton et al. looked at reflectivity of tantalum thin films with various microstructures by altering the deposition pressure. [9] A cylindrical magnetron sputtering system was used which are different from the planar magnetron sputter systems under consideration. In Thornton's work the deposition rate was between 45 to 60 nm/min, which is comparable to that of films generated in the NAIT system. Reflectance was measured at a wavelength of 550 nm as ~52 %R, for a film deposited at working pressure of 10 mTorr in the cylindrical sputter system. The reflectivity of the tantalum deposited in the NAIT system at 10 mTorr was measured at a wavelength of 550 nm as 47.3±2.1 %R. A cylindrical sputter system has an increased angular flux of incoming atoms, increasing the roughness and decreasing the surface reflectivity from films produced in a magnetron sputter system at the same pressures. Therefore, the comparison to Thornton's work shows comparable values, yet considering only the change from cylindrical to planar magnetron sputtering one would predict higher reflectance values at identical pressures to those used by Thornton. It is likely that other changes between deposition systems exist that account for the lower reflectivity.

Thornton's work also stated that a Zone 1 structure would have a decreased reflectivity with a greater number of voids present in the film leading to scattering whereas, zone T structures contain dense fibrous films, with increased reflectivity. With the nanoFAB mixed alpha and beta tantalum a zone 1 microstructure and NAIT alpha tantalum coating resulting in a zone T structure, one would expect that the zone T structure to generate a higher reflectance. However, with tantalum formed in different sputter systems the percent reflectance values cannot be compared as if structures exist on the same diagram. Furthermore, other sputtering parameters such as power density, deposition rate, and film thickness among others, can influence a films reflectivity. In order to compare the reflectivity of a zone T and zone 1 structure, the use of one sputter system to produce coatings in both structural regimes must be carried out.

The optical constants of the tantalum films were measured and showed a significant difference. Alpha tantalum films showed higher refractive index and extinction coefficients in this work. Work by Muth, supported that differences in optical constants exist between the two tantalum phases, however, he demonstrated that beta tantalum values were higher than alpha (β -Ta: η=3.43-3.66*i*, α-Ta: η=2.90-2.41*i* collected at λ=546 nm). [24] The anodic tantala

layer showed (η=2.22) by Muth is similar to the values obtained on both tantalum layers in this work. It is possible that changes in the sputtering conditions between these two experiments have allowed for the alpha optical constants to become larger than beta.

7.4.2 Standard Anodization of Aluminum on α and Mixed α-β Tantalum Structures

Multilayer structures of aluminum and tantalum from the different sputter systems resulted in different and visible surface colours. Structures formed on the nanoFAB tantalum resulted in thinner final alumina layers and thicker tantala layers following oxidation than films generated on the NAIT tantalum. The slides with thicker alumina on NAIT tantalum shifted towards higher colour orders. It is possible that the changes in tantalum structures and properties effect the conversion of aluminum to alumina and hence the resulting layer thickness. The α-Ta layers are 13 to 50 μΩcm and β-Ta layers are 170 to 220 μΩcm. [14,23] Different resistances *in situ* and various barrier thicknesses or complex oxide layers could all effect the device formation and surface colour. The tantalum layer surface roughness may further influence hillock integration into the overlying pores during formation, making it difficult for the ellipsometry model to decipher between alumina and tantala. The MSE values are higher for slides with nanoFAB tantalum, further supporting this theory. Current density plots showed no significant changes between oxidation of slides containing different tantalum.

Changes to the alumina thicknesses for constant aluminum thickness deposited on nanoFAB and NAIT tantalum layers, were confirmed with ellipsometry and SEM measurements of cross-sectional images. Therefore, changes in the surface colours likely result from a change in optical path length of the tantala or composite tantala and alumina oxide (i.e. thickness or refractive index) and/or the variance in the porous alumina film thicknesses. The sensitivity of prothrombin-coated surfaces exposed to anti-prothrombin solutions was compared using ΔE* values. Antibodies generally showed larger visible colour shifts on nanoFAB tantalum devices, however a greater deviation was found on these devices in comparison to devices with NAIT tantalum layers. Work demonstrates that there are differences in the apparent change in anti-prothrombin sensitivity on beta and alpha tantalum coatings, although increasing the number of samples would allow for a statistical analysis to be complete on the coordinates. Therefore, changing the tantalum base layer influenced the resulting device structures (i.e. tantala and alumina properties or the oxide composition at the

interface) and the protein detection limit. All colours generated with protein incubation and adsorption, were within the first and second order regions of high sensitivity, however tests should be redone with prothrombin control spots on each device of the same colour.

Although the α-Ta layer with a bcc crystal structure and a deposition rate 6 times greater than the deposition rate required to obtain the mixed α-β-Ta layer, devices with the mixed α-β-Ta layer appear to have a greater colour shift when anti-prothrombin solutions are exposed to the prothrombin-coated surface.

7.4.3 Primary and Standard Anodization Processes on Mixed α-β Tantalum Films

A primary anodization of the tantalum layer to generate an anodic tantalum oxide barrier film on the surface prior to aluminum deposition produces an oxide more than 4 times thicker than that of the native oxide at the interface. The creation of an oxide layer without an overlying porous alumina layer eliminates the hillock structure that results when the anodic tantala was formed under the porous alumina. However, sputtering the aluminum layer on the tantala surface results in some unknown amount of tantalum oxide reduction by the adjacent aluminum, before the second standard anodization process is completed. The aluminum has a higher affinity for the oxide layer, as demonstrated in the Ellingham diagram (see Figure 7.1). With the oxide layer formed at 6 V having a thickness of ~10 nm it was not resolved in SEM images and was measured using ellipsometry and SIMS techniques. Visible surface colours for test samples anodized twice showed higher colour orders than control samples, regardless of the standard applied potential or the initial aluminum thickness. Therefore, an increase in the optical path length, meaning either the thickness or refractive index, occurred. Only tantalum deposited at the nanoFAB was examined in this set of experiments. When the process was carried out on tantalum deposited in the NAIT system, adhesion issues became apparent during the anodization process, see the following section.

Deposition of aluminum on a 3 to 5 nm tantalum native oxide layer fully reduced the tantala layer.[8] Reduction of the tantala layer creates oxygen vacancies and a disordered tantalum surface under tension.[25] Whereas, the alumina layer that forms under the deposited aluminum would be in compression with a larger alumina lattice than aluminum.

When samples undergo a second anodization process, a steeper negative slope occurs during the formation of the barrier oxide layer due to the current pushing through a dielectric

layer, with a higher resistance, that already exists. Regardless of the complex oxide structure, the presence of these dielectric layers will reduce the amount of tantala oxide that forms during the standard oxidation process to reach the final current density. The primary anodization process creates a dielectric layer that acts as a barrier for the current and oxygen species, making it harder to move into the multilayer device. The time of barrier layer formation was used as a measure and was always larger for control standard anodization than for tests slides at the same applied potential. The difference in time of formation increased with increasing standard anodization applied potential.

Ellipsometry values from slides showed that the oxidation process efficiency and volume expansion increase at lower voltages for the standard anodization process, with the thickest alumina film resulting at 4 V (see Chapter 4). The ellipsometry method showed that test slides had thinner alumina layers than control slides; the opposite trends were showed using SEM, SIMS, and visual surface colour analysis techniques. The test samples showed MSE values 1.5 times higher than the control samples, regardless of the standard oxidation applied voltage. It is known that a rough interface exists between the tantalum and aluminum layers initially and with test samples having two anodization processes it is possible that the complex oxide layers that result at the interface, lead to an increase in error for ellipsometry values.

Various equations and layer parameters were applied to the ellipsometry model in attempts to best fit the experimental data, and generate a low MSE value, without creating a model with highly correlated parameters. Applying an EMA layer at the interface with alumina and tantala, led to a 100% tantala layer and grading the porous alumina EMA layer, to determine if the refractive index had a gradient, resulted in only one slice. Only one change from the standard fitting procedure for test slides on nanoFAB tantalum showed lower MSE values and decreased correlation in the fit parameters. The method consisted of using a tantala layer with material properties in the software, instead of the previously fit tantala optical constants. When using this method on test slides the alumina thickness increases up to 5 nm and the tantala thickness decreases up to 5 nm. When applied to control slides the MSE showed no major improvement and the layer thicknesses fluctuated by <2 nm for alumina and tantala.

The change in tantalum oxide (increase) and alumina (decrease) thicknesses measured with ellipsometry from the actual thicknesses in the test slides are likely a misinterpretation of a composite layer containing tantala and alumina with either a solid or porous structure and thus may have a different refractive index combining both the porous alumina and barrier tantala layers. A study by Muth, showed the formation of an alumina and tantala layer with a refractive index of 2.12 and a different dielectric constant than tantala only. [24] SIMS work showed ~29 nm for both control and test samples tantala thicknesses. Taking into account that the material was likely detected through the pores prior to sputtering the entire alumina layer, the tantala layer was likely similar in thickness in each device structure (<29 nm). Matching the control and test tantala thickness and adding the difference to the alumina thicknesses from the ellipsometry model creates alumina thicknesses that are similar to the SEM alumina thickness measurements. Furthermore, based on the observed colour the test slides have a significant increase in OPL over the control slides.

The presence of tantala hillocks may introduce an issue for device sensitivity, as increased light scatter will occur at a rough tantala-alumina interface. Use of the primary anodization process on the tantalum layers was thought to be a method to prevent the formation of hillocks and create a uniform anodic tantala layer prior to aluminum deposition. However, it was determined that this makes it difficult to measure device parameters and tune the layers. More work is needed in this area to determine if tantala was more uniform than in control slides. Current tests revealed that antibodies showed similar visible colour shifts on control and test slides with nanoFAB tantalum, however a greater deviation was found on control slides regardless of the alumina thickness of the device. The change in structure brought on with completing primary and standard anodization processes alters the structure and reflectivity, making detection of colour shifts after exposing anti-prothrombin solutions less dominant.

7.4.4 Primary and Standard Anodization Processes on α Tantalum Films

SEM images, EDS compositional data, and visible interference showed that delamination of films during the standard anodization on NAIT tantalum, leads to removal of the porous alumina film. Problems with film adhesion became apparent when spot formations became visible on the device surfaces during the standard anodization step. Films that failed

were on α-Ta coatings deposited in the NAIT system with the majority containing a tantala barrier layer prior to the aluminum deposition and standard anodization process. Partial delamination of the aluminum layer occurred during the anodization process, due to poor adhesion that results from contamination or changes in the thin film structures.

Adhesion problems generally appeared on device surfaces between the middle and end of alumina pore formation (see Figure 7.20). Typically, an increase in current density resulted at the oxidation time when affected areas became visible. The spike in current density likely resulted when oxidation reached the interface between the aluminum and tantalum coatings where an oxide layer existed. Micro-cracks in the alumina barrier layer result in increased surface area and decreased resistance, ultimately causing the current to increase. In slides where a primary oxidation process was carried out, the oxide layer at the interface was thicker than a native oxide layer and showed an increase in current density. Most devices that underwent only the standard anodization process did not result in delamination; however, abnormal curves and delamination occurred on a few slides and conditions could not be replicated.

It is likely that the introduction of the anodic tantalum layer induced failure by lowering the manageable stress threshold of the tantala and tantalum films. The few slides showing delamination with only the standard anodization process may have grown a thicker native oxide film on the tantalum surface, prior to aluminum deposition and oxidation, than other slides. The NAIT tantalum layer was unable to contain the stresses that resulted in the porous alumina layer, whereas nanoFAB tantalum showed no delamination issues. Prior evaluation of the two tantalum films in section 7.4.1 showed differences in the composition, grain shape, zone structure, and crystalline phase. With anodic tantala layers on the NAIT tantalum films, it was found that aluminum deposition onto the dense, zone T structures, commonly resulted in failure during subsequent oxidation. The zone T structure can form with a large amount of intrinsic stress. It is likely that zone 1 microstructures with voids and a rough surface from the nanoFAB system, have increased adhesion. More finger-like protrusions may exist at the Ta/Al interface over those that form at the smooth and dense NAIT tantalum surfaces. The increased roughness and surface area at the tantalum surface may improve stress relief that can occur and prevent delamination.

Other work carried out under galvanostatic (constant current) oxidation in phosphoric acid, found anodization generates stress in the oxide and at the metal-oxide interface. [26] Stress was linked to changes in the interfacial volume (due to reactions and transport processes). In this work the alumina, which was generated from reducing the tantalum oxide formed in the primary anodization is likely under compressive stress and the tantalum layer would be under tensile stress. Anodization of aluminum in phosphoric acid showed that porous oxide formation at current densities of <3 mA/cm^2 generate a tensile force in the oxide and at higher current densities a compressive force. [26] Compressive stress build-up in the oxide has been used to explain the formation of self-ordering pores by flow-assisted mechanisms. [26-29] Therefore, stress alone does not explain failure, as it is common occurrence during pore formation.

An alternate source of stress in thin films occurs with oxidation, as the resulting oxide has a larger volume than the original metal and increases lattice distortion and compression of the film. Pure aluminum coatings typically contain low stresses under the sputter conditions used in this work, [30] which explains why failure was not visible until anodization of the aluminum layer and conversion to alumina. In the oxidized, porous thin film, further contamination by impurities including water vapour, hydrogen, and oxygen can occur. [31] Intrinsic stresses increase with coating thickness. Therefore, a maximum coating thickness exits that can be tolerated by the coating-substrate bond before adhesion fails.

It is common that interface shear stress concentrates at the film edges, [9] explaining why some slides in Figure 7.21 showed spots along the edges. If the coated film experiences poor adhesion at some surface point, then redistribution is necessary for substrate and coating strains to rematch. If redistribution of stress does not occur, it often leads to failure of the coating adhesion. In all slides, areas of delamination showed no interference colours at low viewing angles but had a shiny metallic surface at high viewing angles, as shown in Figure 7.21.

The oxygen to aluminum ratio for the porous alumina region was ~3 times greater than 1.5 for Al_2O_3 (see Table 7.14). This high ratio of oxygen to aluminum was due to the tantalum oxide signal contributing to the total oxygen detected. Assuming a ratio of 1.5 for the alumina layer, the remaining 4.7 at% of oxygen signal would be from the underlying tantala film. The unknown region where failure occurred was determined to be mainly tantalum, containing

approximately half of the oxygen present in the tantalum oxide coating under the porous alumina. From this it can be said that only a portion of native or anodic tantala remains on the substrate.

It is important that the silicon wafer substrate is clean, as well as the tantalum surface, to achieve strong adhesion between device layers. It is possible that delamination occurs where some contaminant was on the tantalum surface prior to the aluminum depositions. However, no trends were observed on slides from the same wafers or in the area of delamination. Furthermore, wafer surfaces with tantalum coatings showed minimal particulate (see Figure 7.22). Additional work is required to determine if the silicon wafer was contaminated. Alternate suppliers could be used to obtain silicon wafers of higher consistency and cleanliness, or an initial wafer cleaning process used. Depositions of the tantalum and aluminum coatings without an intervening air-exposure or using a tantalum nitride layer would ensure that no oxide layer exists between the aluminum and tantalum interface prior to anodization.

SEM images of surfaces showed a variety of structures after failure. Combinations of straight and circular failure lines were visible in Figure 7.25. “Worm-tracks” were a common observation surrounding areas of porous alumina that remained on the device surface (see Figure 7.26). The cross-sectional images of an area where delamination begins, further confirmed alumina films were released from the underlying tantalum layer with a thickness decrease visible (see Figure 7.27). All slides with delamination during anodization showed a build-up of material along the electrolyte line of the slide. SEM-EDS analysis on this region starting at the electrolyte surface where the non-uniformity begins and moving down the slide toward the homogeneous oxide film with normal interference showed a wide variety of structures and compositions (see Figure 7.28).

The build-up at the top of the device showed unique structures and little porous alumina. In the EDS maps high levels of oxygen, phosphorous, and aluminum were visible as a result of aluminum oxidation in the phosphoric acid electrolyte. Areas with only high aluminum signal and no oxygen or phosphorous show unanodized aluminum. These compositional images were helpful in identifying the alumina in areas where structures were abnormal. As small areas of anodic alumina become more apparent in areas of delamination, “worm-tracks” were commonly visible around these sections. Compressive stress in sputtered films often

leads to relief by buckling and, with isotropic stress, the generation of "worm-tracks".[32] The creation of "worm-tracks" relieved stress from within the thin film device and resulted in delamination and ultimately areas of non-uniform interference colours.

7.5 Future Work

Future work may delve into alternate colour generating films that allow for a smooth interface in attempts to minimize light scattering. The alumina and tantala interface plays a critical role on the interference colours that result.

Tantalum deposition with various parameters would create a zone structure diagram in one sputter system and aid in the understanding of alpha and beta tantalum structures (i.e. the optical constants and reflectivity) and how to prevent failure. To determine the exact transition temperature for these tantalum coatings, sputtering over a range of argon pressures and deposition temperatures (T/Tm), in each sputter system, would be required. It is possible that changing the tantalum structure to a zone 2 or 3 could reduce the stress in tantalum coatings prior to or following the aluminum deposition. The know-how of creating a zone 2 or 3 structure should be revealed from the structure zone diagram or may require heating during deposition or a post-annealing step.

The tantalum microstructure and tantalum oxide layer require further investigation to select the optimal structure and phase of tantalum for future work. An irreversible transformation of tantalum to a stable bcc structure with heating in vac to ~725 °C may be beneficial in the future to ensure consistent device parameters and colour shifts.[13] In addition, the tantalum surface oxide, native or anodic, could be removed with RF sputtering prior to aluminum deposition, or the two metals may be sputtered in the same system eliminating exposure to atmosphere in between depositions. The use of RF etch back prior to aluminum deposition may eliminate film delamination by improving the adhesion to the surfaces. Furthermore, the use of a valve metal lower than aluminum on the reaction line of an Ellingham diagram should maintain a flat barrier oxide structure with primary oxidation followed by aluminum deposition and oxidation. A uniform oxide at the interface may increase sensitivity by eliminated scatter off the hillocks.

Measuring the stress in each layer of the multilayer device during formation would provide further confirmation into the reason for failure. Lastly, TEM scans has the ability to

show the composition changes between the aluminum and tantalum layers and contribute to the composition and structure at the interface in various samples.

7.6 Conclusions

The preparation of different tantalum structures prior to aluminum deposition revealed new information about the multilayer device. Although additional work is necessary, the findings are critical for manufacturing a thin film device with strong adhesion between layers. The following conclusions were made for work completed in this chapter.

1. Changes in the deposition energy generate different crystalline tantalum structures. In the nanoFAB sputter system a low deposition energy formed a mixed α-β-Ta and in the NAIT system a high deposition energy formed α-Ta structures.
2. Differences in reflectivity and optical constants were apparent on these mixed α-β-Ta and α-Ta films. As a result, slight changes can be expected in the surface interference colours that are generated on these different tantalum films.
3. Aluminum and tantalum prepared devices showed differences in the resulting visible surface colour. Alumina was thinner on devices with mixed α-β-Ta than on devices with α-Ta. The colour shifts with anti-prothrombin on prothrombin-coated surfaces were larger on nanoFAB tantalum (mixed α-β-Ta) however, values overlapped with NAIT tantalum (α-Ta).
4. Whether an anodic tantala layer was formed prior to or after the aluminum deposition, changed the surface colour generated. The creation of an anodic tantalum layer on mixed α-β-Ta, followed by aluminum deposition and anodization, resulted in a greater OPL (i.e. visible surface colour) than when no anodic tantalum layer was created prior to aluminum deposition. The resulting test devices had thicker alumina than control devices.
5. The tantala oxide detection in SIMS commenced closer to the alumina surface in control samples, formed with only the standard anodization, than in test samples, formed with two anodization processes, which may indicate test samples showed less dominate hillock structures in the interfacial oxide film.

6. The colour shifts with anti-prothrombin on prothrombin-coated surfaces were larger on nanoFAB tantalum (mixed α-β-Ta) control slides than test slides. Values overlapped between the two types of samples, however the number of samples should be increased, as the standard deviation on the control slides were large.
7. The creation of an anodic tantalum layer on α-Ta resulted in delamination. In a few instances, even control slides on NAIT tantalum showed failure. Hence, the α- Ta structure is likely under a higher stress or unable to relieve the multilayer stresses during the standard oxidation process.

Chapter 8 – Detection of Vitamin K-dependent Proteins

8.1 Introduction

The vitamin K-dependent protein, prothrombin, has been used extensively in the development of this thin film technology. It has been found that vitamin K-dependent proteins have an unusually high affinity for the aluminum oxide surface. [1] Vitamin K-dependent proteins are unique in that they contain a γ-carboxyglutamic acid (Gla) domain, where post-translational modification converts glutamic acid residues to Gla residues by the process of carboxylation. [2] These Gla domains require vitamin K for the synthesis and are dependent on divalent metal ions to achieve membrane binding. [2] There are several vitamin K-dependent proteins including: clotting factors involved in the coagulation cascade (Factor II or prothrombin, VII, IX, X), anticoagulants (protein C, S, and Z), matrix Gla protein (MGP) and some proteins for hard and soft tissue mineralization (osteocalcin or bone Gla protein (BGP)). [3] Figure 8.1 shows a schematic of the structure of some vitamin K-dependent proteins.

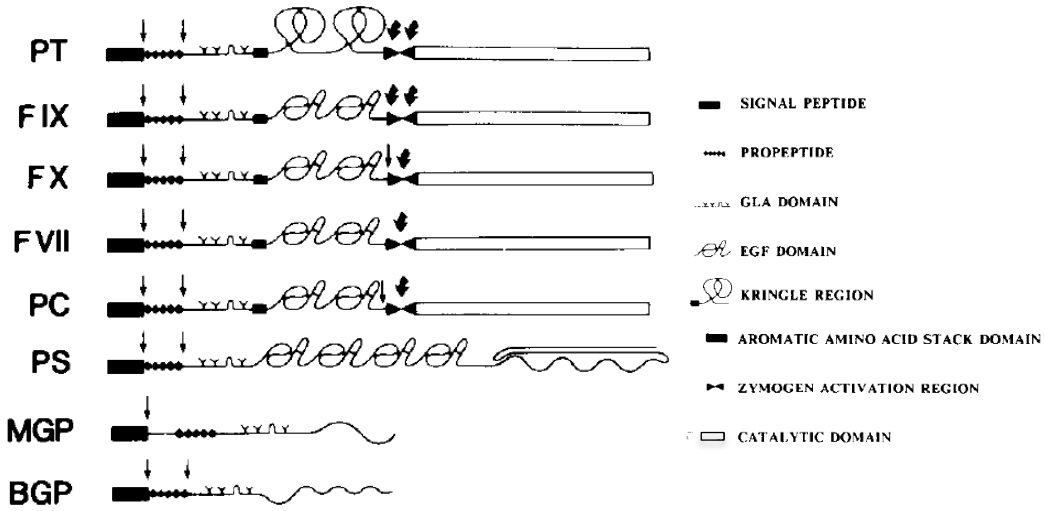

Figure 8.1. Depicts the structural domains of vitamin K-dependent proteins prothrombin (PT), factor IX (FIX), factor X (FX), factor VII (FVII), protein C (PC), protein S (PS), matrix Gla protein (MGP), and bone Gla protein (BGP). The legend identifies protein components. Proteolytic cleavage sites are shown with thin arrows when cleaving occurs to create the mature protein structure, and cleavage sites are indicated by thick arrows when linked to enzymatic activation. Images from Furie and Furie (1988).[2]

The structure of vitamin K-dependent proteins contains a Gla domain, at least two epidermal growth factor (EGF) domains – except prothrombin which has two kringle domains instead of EGF domains[2]–, and a catalytic or serine protease domain – except for protein S

which has a unique carboxy-terminal structure.[4] A greater understanding of these domains comes from analyzing regions individually and in combination. For instance, in the clotting process prothrombin is cleaved into various fragments and thrombin components (see Figure 8.2), making it an ideal protein to demonstrate domain binding and functional differences.

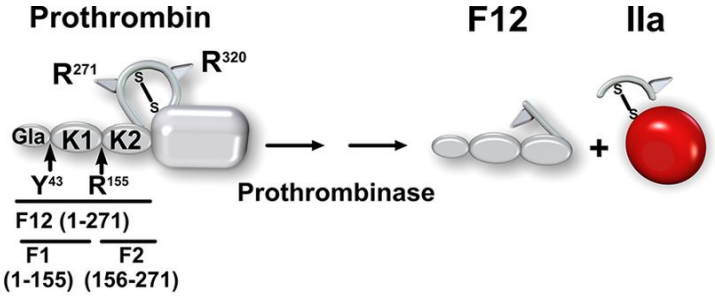

Figure 8.2. An image from the literature[5] depicts prothrombin activation with cleavage at Arg320 (R320 in FASTA sequence) and Arg271 (R271) which leads to fragment 12 (F12) and thrombin (IIa). F12 contains the Gla and both kringle domains (Gla-K1-K2). Further cleavage at Arg155 (R155) separates F12 into fragment 1 (F1) and fragment 2 (F2). It is possible to remove the Gla domain with cleaving at Tyr43 (Y43). Other components of prothrombin can be found in the literature.[6,7]

To predict protein binding on the porous alumina surface, the Gla domain position and protein structure are likely the leading indicators. Prothrombin, factor IX, and protein S were compared due to differences in protein composition, dissociation constants, isoelectric points, and the number of Gla residues.

8.1.1 Vitamin K-dependent Proteins

Investigation of molecular size, dissociation constants, isoelectric points, and mass-to-charge ratios was conducted to select different proteins to determine if immobilization and sensitivity on the alumina surface changes. Table 8.1 shows tabulated parameters; however, other dissociation constants of vitamin K proteins for phospholipid layers were found in the literature.[8]A broad base support was deemed ideal for stable adsorption of protein to the surface and to ensure the protein regions without exposed carboxyl groups do not contact the surface and bind or degrade. These factors are important to achieve consistent optical path length changes and the resulting visible colour shift on the device surface.

*Table 8.1. A comparison of vitamin K-dependent proteins involved in the coagulation cascade. Blank spaces indicate parameters that are not present in some proteins and * represents a value that was not present in the literature.*

Protein	Molecular weight (kDa)	Plasma concentration (μmol/L)	Dissociation constant, k_d (μmol/L)	Isoelectric point, pI	Carboxy-glutamic acid residues	Other metal ion binding sites	Refs.
II	70 to 72	1.4	1.04	4.7 to 4.9	10		9-15
FIX	52 to 55	0.09	<1.0	4.0 to 4.5	12	12	8,15-18
FX	59	0.17	0.19	4.9 to 5.2	11		15,19-21
FVII	50	0.01	15	4.8 to 5.1	10		8,15,22-25
PC	62	0.08	0.23	4.4 to 4.8	9		15,26-29
PS	~75	0.14	0.005	5.0 to 5.5	11		
PZ	62	0.05	0.32	*	13		15,27,30-36

The large Gla domains in vitamin K-dependent proteins will enable them to bind to the device surface at a relatively constant orientation and generate a consistent optical path length and visible colour shift. Prothrombin, factor IX, and protein S were chosen for these experiments. These proteins range in sizes from 52 to 75 kDa, and the number of γ-carboxyglutamic acid residues varies, with prothrombin containing the lowest carboxyl-to-mass ratio and factor IX containing the largest. The dissociation constants range from 5 nM to 1 μM, [2] with protein S showing a significantly lower dissociation constant than prothrombin, which may influence the binding at lower concentrations, assuming that binding to the phospholipid membrane is similar to the alumina surface. The reported binding affinity of each protein was in association with phosphatidyl-serine-phosphatidylcholine membranes, and the lower the dissociation constant the higher the affinity. Protein S shows a significantly (five-fold) higher affinity than other coagulation proteins. Protein C and factor X also show very high affinities for the protein-membrane interactions. Typically, a lower dissociation constant suggests that a molecule will have a higher affinity to a metal substrate. [37]

Consideration was also given to the isoelectric point of proteins, which influence the net charge. The amphoteric nature of protein allows a positive, negative, or neutral net charge based on the pH of the surrounding environment. The pH where net zero charge result is known as the isoelectric point (pI). When pH>pI the protein exhibits a net negative charge and when pH<pI a net positive charge. Together the solution pH and pI influence the mobility of proteins, regarding magnitude and direction of migration. Proteins with a range of pI values were selected to test the influence of this parameter at a pH of 7.4.

8.1.2 Gla Domain Metal Ion Binding Sites

Each vitamin K-dependent protein contains a Gla domain at the amine terminus, containing 9 to 12 Gla residues.[37] These regions of proteins are membrane anchoring domains with an affinity for metal ions.[38] Two classes of metal binding sites have been identified in the Gla domain with different affinities and specificities for metal ions, as well as varying effects on the protein tertiary structure and functional roles.[39-43] Mg^{2+} and Ca^{2+} interact with vitamin-K dependent proteins in physiological solutions, depending on the type and concentration of each ion in the solution.[44] These metal binding sites are commonly classified as high and low affinity sites. A high affinity site requires an intact disulphide bond that stabilizes the protein and results in multiple Gla residues in close proximity. These sites bind to metal ions reversibly and create an intramolecular bridge; however, if unoccupied, the high affinity Gla residues repel one another, and significantly change the tertiary structure.[39] Low affinity sites result when one or two Gla residues bind a metal ion. Studies show that these metal binding sites may bridge proteins to other proteins or membrane surfaces.

Exterior sites on the protein structure are likely to be the direct contributor to the phosphatidylserine binding,[45,46] with two or more of the three external divalent metal binding sites containing Mg^{2+} when Ca^{2+} and Mg^{2+} are present.[19-24] The number of sites containing Mg ions is dependent on the ion concentrations and the vitamin K-dependent protein.[47-52] Models suggest that Ca ions have two distinct roles based on location. The four central ions are highly influential in achieving the proper conformation of the protein for binding, and the outer ions help directly fasten the protein to the lipid membrane.[46] Although the influence of metal ions on the Gla domain has been studied with respect to phospholipid membrane binding, the mechanism of binding remains unclear. Figure 8.3 depicts metal ions binding to the Gla domain of factor VIIa. Metal ion binding to all Gla domains in vitamin K-dependent proteins is thought to be similar, as the position and number of γ-carboxyglutamic acid groups are nearly identical.

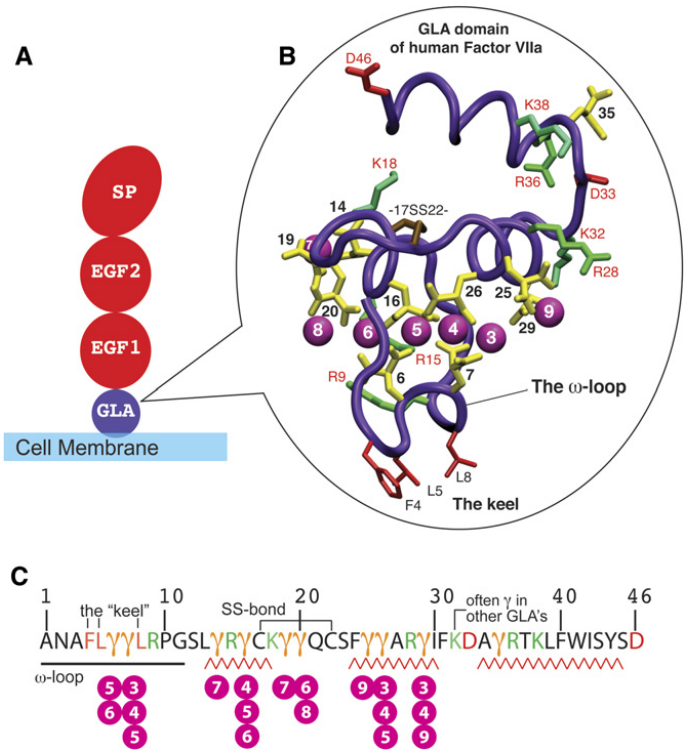

Figure 8.3. Images from Ohkubo and Tajkhorshid (2008) provide a detailed outline of the Gla domain of vitamin K-dependent proteins. [46] *(A) Shows the typical structure of vitamin K-dependent proteins. (B) The Gla domain structure of FVIIa with the backbone of the structure shown as tubing and the Ca^{2+} ions as numbered spheres. (C) The first 46 amino groups of the Gla domain sequence have γ-carboxyglutamic acid groups depicted as gamma (γ) and the bound Ca^{2+} are positioned under the residue(s) that bind them to the Gla domain.*

Modelling the Gla domain interaction with a phospholipid membrane shows that Ca ions bound to the protein to interact with the negative lipid membrane. Work by Kromis[53]supported a 'Ca^{2+} bridging' mechanism to aid in understanding the binding of prothrombin fragment 1 to lipid membranes with Ca ions present. Throughout the simulation ionic bonds were retained between the Ca ions and phosphatidylserine molecules with up to 8 Ca ions. [53] Rodríguez et al. determined two binding sites connecting prothrombin to the phosphatidylserine membrane secure the protein by electrostatic interactions. The first binding site includes Ca1, Gla30, and Lys11 and the second Ca5, Ca6, Ca7, Lys3, and Arg10. In this model the Gla loop was ~0.7 nm inside the membrane (see ω-loop label in Figure 8.3).[54]

The roles of each Gla residue with metal ion binding were determined by substituting one glutamic acid residue at a time from the prothrombin molecule. Little impact on the prothrombin function was noticed with removing the carboxyl group at residue 6, as it binds two Ca ions but has no importance to the structure or function of the Gla domain. Functionality and phospholipid

binding were attributed to Ca interactions with prothrombin residues 7, 14, 19, 20, 25, and 32. Stabilization of the Gla domain was linked to Ca interactions with residues 16, 26, and 29 and was crucial for protein function. [55] For a visual depiction refer to Figure 8.3 of Factor VIIa Gla domain. The main difference between Factor VIIa and prothrombin is that the carboxyl group in residue 35 of prothrombin is removed and a carboxyl group at residue 32 of prothrombin is added. Tai et al. [44] indicated that structural changes brought on by metal binding were localized to the Gla domain (1-42 residues). However, Armstrong et al. showed the opposite, indicating that structural changes with the presence of metal ions extend beyond fragment 1 to thrombin.[56]

Although work has examined the binding of vitamin K-dependent proteins to phospholipid membranes, the adsorption of these proteins to alumina surfaces, with the presence of low metal ions in solution, is novel.

The purpose of this study was to assess the influence of binding different vitamin K-dependent proteins and the exposure of prothrombin solutions containing metal ions. Visible interference colours on the device surface were analyzed to measure the relative sensitivity and changes in the optical path lengths of different protein solutions. In future operation, the immobilized protein layer may act as a cross-linking agent for other antigens or antibodies, to achieve specific protein detection. Hence the immobilized layer is crucial for the successful operation of this point-of-care test. Improving the protein adhesion or the efficiency of binding and activity has the potential to increase the limit of detection. Furthermore, improved understanding allows for tailoring the visible colour shifts to achieve optimal sensitivity. It was predicted that the negative charged Gla region and the protein conformation were the main factors governing protein immobilization.

8.2 Materials and Method

8.2.1 Device Preparation

Multilayer devices were prepared with tantalum deposition in the NAIT sputter system and subsequent aluminum deposition in the University of Alberta NanoFAB, Floyd magnetron sputtering system (see Chapter 3 – General Materials and Methods). Sputtered tantalum films were 225 nm and aluminum films ranged from 100 to 120 nm. SEM cross-sectional images, profilometry, or sputter rates were utilized to determine thicknesses of the resulting aluminum layers for each test. Individual slides or full wafers were anodized at 8 V under potentiostatic

conditions in 0.4 M phosphoric acid. Anodization was carried out at 20°C±2°C until the end of alumina pore formation and tantala barrier layer growth, also known as stage b. Stage b was reached when current density was <0.07 mA/cm^2. Typical procedures were followed for cleaving and anodizing unless otherwise stated. See Chapter 3 – General Materials and Methods for additional details.

8.2.2 Protein Modelling

I-TASSER (Iterative Threading Assembly Refinement) was used to model and predict various 3D protein structures and biological functions from amino acid sequences. [57-59] Federal Acquisition Streaming Act (FASTA) format of amino acid sequences were input into the online server (http://zhanglab.ccmb.med.umich.edu/I-TASSER/). Additional templates without alignment were input with Protein Data Bank identification (PDB ID) and the chain identification (Chain ID) to guide modelling. For prothrombin, factor IX, and protein S the PDB IDs and chain IDs of P00734[10] and 5EDM: A, [60] P00740[16] and 1NL0: G, [61] and P07225[30] and 1NL0: G were used. I-TASSER collects the PDB structure and generates the target-template alignment with an in-house alignment tool called Multi-Sources ThreadER (MUSTER). For more information on this threading algorithm see work by Wu and Zhang 2008. [62]

Running I-TASSER led to an output of the top five models. The predicted models were analysed based on their C-score, a quantitative measurement of confidence, and the local structure error profile that shows the estimated accuracy in the distance deviation between residue positions in the model and the native structure. Typically, the first model is the highest quality with the greatest C-score; however, in rare cases lower ranked models have highest C-scores, and the local structure error profile needs to be analyzed to select the optimal model. The model with the best fit and typically the highest C-score (a confidence score used to estimate the accuracy of the predicted models) was selected. A typical C-score value is in the range of -5 to 2 with a higher value indicating a model with greater confidence. All models had scores within this range.

The model with the best fit was visualized using the Molsoft ICM-Browser (http://www.molsoft.com/icm_browser.html). Results provided annotated 3D images depicting a potential position of the Gla domain within each vitamin-k dependent protein selected. The longest plausible dimensions of the models were obtained by choosing two atoms, one from the

Gla domain to the farthest atom. Dimensions of protein widths were measured at the widest point of the molecule. For the three proteins chosen the broadest part was at the opposite end of the protein from the Gla domain.

To calculate the volume of the highly charged Gla domain, this region was selected, and others hidden. Under the display settings, the option to measure the distance between two atoms was selected. Two points were then chosen to generate length, width, and height dimensions for the area of interest. The product of these dimensions equals the volume of the Gla domain or charged region depending on the molecule.

8.2.3 Protein Adsorption

Protein adsorption was completed following the procedure outlined in the General Methods section. All experiments below followed the same processes for exposing proteins or wash solutions to the device surface, however the solutions and in some cases time of exposure were varied. Sharpie markers were used to describe hydrophobic 1 cm diameter circles. The alumina area inside these regions was re-equilibrated by exposing a 20 µl spot of TBS at pH 7.4 for 15 minutes. TBS solution was removed with a pipette and slides were rinsed and dried. Immediately following vitamin K-dependent protein solutions of 20 µl were exposed for 15 minutes (see specific tests below for details). After this period the liquid was removed with a pipette from the surface, rinsed with deionized water, and subsequently dried with oil free compressed air. All protein tests solutions were mixed and diluted in Eppendorf® LoBind micro-centrifuge tubes (Sigma-Aldrich, St. Louis, MO) unless otherwise stated.

Part A – Detection of Vitamin K-dependent Proteins

8.2.3.1 Prothrombin Loss in Ordinary Micro-centrifuge Tubes

Initial prothrombin adsorption was tested with concentrations of 0.001, 0.01, 0.03, 0.06, 0.08, 0.1, and 1 mg/ml. Solutions were prepared in ordinary 1.5 ml micro-centrifuge tubes and mixed thoroughly after dilutions to ensure uniform distribution of the protein in the TBS. Solutions were exposed to the alumina surface following steps outlined in section 8.2.3 Protein Adsorption.

8.2.3.2 Sensitivity of Vitamin K-dependent Proteins

Tests looking at prothrombin, factor IX, and protein S on the surface, employed initial prothrombin concentrations that were converted into molar concentrations to expose the same number of moles to the surface for each protein solution. Prothrombin concentrations of 0.007, 0.015, 0.025, 0.035, 0.05, 0.08, and 0.1 mg/ml were exposed to the surface. The equivalent molar concentrations were determined to ensure the same molar concentration was exposed to the surface for each of the three vitamin K-dependent proteins, with different molar masses (n=3). The varying concentrations and picomoles exposed to the surface for prothrombin solutions are shown in Table 8.2.

Table 8.2. Outlines the prothrombin concentrations, moles present in 20µl spots, and the number of times this quantity can cover the nominal surface area within a 1 cm diameter spot with short and long side molecule binding. The effective alumina surface area has a porosity of ~50% of the nominal are, not taking into account surface roughness.

Prothrombin Concentration (mg/ml)	Prothrombin in 20 µl (picomoles)	Times the Nominal Surface Area Covered with		Times the Effective Surface Area Covered with	
		short side	long side	short side	long side
1	286.00	35.10	96.60	70.10	193.80
0.1	28.60	3.50	9.60	7.00	19.30
0.08	22.30	2.73	7.52	5.47	15.04
0.06	15.70	1.93	5.30	3.86	10.60
0.03	9.43	1.16	3.18	2.31	6.36
0.01	2.86	0.40	1.00	0.70	1.90
0.001	0.29	0.04	0.10	0.07	0.19

Anti-prothrombin polyclonal and anti-influenza B virus nucleoprotein monoclonal (MyBioSource, San Diego, CA) antibodies were each exposed to spots where 28 picomoles of prothrombin, factor IX, and protein S had been exposed to the device surface (0.1 mg/ml of prothrombin). Antibody solutions of 0.1 mg/ml were utilized and 20 µl were exposed to each spot for 15 minutes. Further details on the procedure for exposing protein solution to the surface are outlined in section 8.2.3 Protein Adsorption.

Initial prothrombin control solutions and prothrombin solutions exposed to the alumina surface 0.035, 0.05, and 0.1 mg/ml for 15 minutes, were collected for liquid chromatography mass spectrometry (LCMS) by the Department of Chemistry (Lab EB-38, University of Alberta, AB). Samples were stored in low-bind tubes at 4°C until analyzed.

8.2.3.3 Time Dependence of Vitamin K-dependent Proteins

Constant molar concentrations of each vitamin K-dependent protein were exposed to an alumina surface of one thickness for 45, 50, and 55 minute periods (n=3). Solutions contained 3 picomoles, equivalent to a prothrombin concentration of 0.01 mg/ml. Calculations of total protein charges were completed online at ProteinCalculator v3.4 (http://protcalc.sourceforge.net/) to aid in analysis and solutions were exposed to the alumina surface following steps outlined in section 8.2.3 Protein Adsorption.

Part B – Detection of Prothrombin with Metal Ions in Solution

8.2.3.4 Binding of Prothrombin from Solutions Containing Metal Ions

Reagents used included calcium chloride dihydrate, and magnesium chloride hexahydrate (Sigma-Aldrich, Oakville, ON). Solutions of Ca^{2+} (1 mM to 10 mM), Mg^{2+} (1 mM to 5 mM), and Ca^{2+}/Mg^{2+} mixes were made with the respective reagents listed above in 1X TBS (see Table 8.3). The TBS buffer solution contains 50 mM Tris-Cl and 150 mM NaCl with a pH of 7.4 at room temperature.

Table 8.3. Concentrations of various metal ion solutions applied to the alumina surface with other constituents, typically prothrombin.

Metal ions in solution	Ca^{2+}	Mg^{2+}	Ca^{2+}/ Mg^{2+}	
Concentrations (mM)	1		1/ 1	
	2.5	1	2.5/1	2.5/5
	10	5	10/1	10/5

The solution pH levels were measured and adjusted to 7.4 using small volumes of HCl or NaOH. A final concentration of 0.1 mg/ml prothrombin was achieved by adding 0.01 ml of 1 mg/ml prothrombin solution to 0.09 ml of the metal ion solutions. Solutions were incubated at room temperature with periodic mixing for 30 minutes before surface exposure. Solutions were exposed to the alumina surface following steps outlined in section 8.2.3 Protein Adsorption.

Anti-prothrombin volumes of 20 µl at increasing cumulative concentrations of 0.015, 0.025, 0.05, and 0.1 mg/ml were exposed to select prothrombin-coated spots for 15 minutes to test for active binding sites and changes in the detection limit. Spots coated with prothrombin

and prothrombin mixtures containing 5 mM Mg, 1 mM Ca, and 1 mM Mg/Ca ion solutions were exposed to anti-prothrombin.

8.2.3.5 The Effect of Metal Ions and Chelators in Solution

A metal ion solution of 1 mM Mg ions and 2.5 mM Ca ions was created in TBS. The device surface was coated with a prothrombin solution of 0.1 mg/ml and subsequently exposed to the mixed Mg and Ca metal ion solution. Control solutions exposed to the slide for visual comparison included; the metal ion mixture, prothrombin control, and prothrombin with metal ions. All metal ion solutions and prothrombin dilutions were complete in 1X TBS at pH 7.4.

Prothrombin and metal ion solution mixes were created using the same procedure previously outlined, with the additional step of adding 1 mM EDTA to the solution prior to the incubation period. Control solutions exposed to each surface included prothrombin control and Ca ions and EDTA for visual comparison. The final concentration of these constituents in all solutions was 0.1 mg/ml of prothrombin, 1 mM Ca ions, and 1 mM EDTA. See section 8.2.3 for more information on exposing the protein solution to the device surface and preparing metal ion solutions.

8.2.4 Characterization

8.2.5 Liquid Chromatography Mass Spectrometry

For protein molecular weight determination reverse phase high-performance liquid chromatography followed by detection using ultraviolet absorption and mass spectrometry (RP-HPLC-UV-MS) was performed. An Agilent 1200 SL HPLC System was used with an Aeris™ WIDEPORE XB-C8, 3.6 μm particle size, 200 Å pore size, 50x2.1 mm column (Phenomenex®, Torrance, CA), with a guard trap cartridge, and thermostatic at 40°C. A buffer gradient system composed 0.1% formic acid in water as the mobile phase A and 0.1% formic acid in acetonitrile as the mobile phase B was used. A sample volume between 15 and 20 μl was chosen and kept constant for prothrombin unexposed and exposed solutions at each initial concentration to allow for a comparison of intensity in data. The sample was loaded into the column at a flow rate of 0.50 ml/min and an initial buffer composition of 90% mobile phase A and 10% mobile phase B. After injection, the column was washed using the initial loading conditions for 2 minutes to remove salts. Elution of the proteins was completed using a linear gradient from 10% to 30%

mobile phase B over a period of 3 minutes, 30% to 38% mobile phase B over a period of 10 minutes, 38% to 98% mobile phase B over a period of 1 minute, held at 98% mobile phase B for 3 minutes and back to 10% over 1 minute. UV absorbance was monitored at 210, 214, 254, and 280 nm. Mass spectra were acquired in the positive mode of ionization using an Agilent 6220 Accurate-Mass time-of-flight HR-LC/MS system (Santa Clara, CA) equipped with a dual sprayer electrospray ionization source with the second sprayer providing a reference mass solution. A mass correction was performed for each spectrum using peaks at mass-to-charge ratios (m/z) of 121.0509 and 922.0098 from the reference solution. Mass spectrometric conditions consisted of; drying gas 10 L/min at 325°C, nebulizer 20 psi, acquisition rate of ~1.03 spectra/sec, fragmentor 275 V, skimmer 65 V, capillary 4000 V, and instrument state 4 GHz high resolution. Data analysis was performed using the Agilent MassHunter Qualitative Analysis software package version B.03.01 SP3 (Agilent, Santa Clara, CA).

8.3 Results

8.3.1 Protein Modelling

A 3D structure of prothrombin in Figure 8.4 and Figure 8.5 illustrate the localization of the Gla domain. The FASTA sequence for prothrombin contains 622 amino acid residues. The signal peptide and propeptide (groups 1 to 43) were ignored. [10]

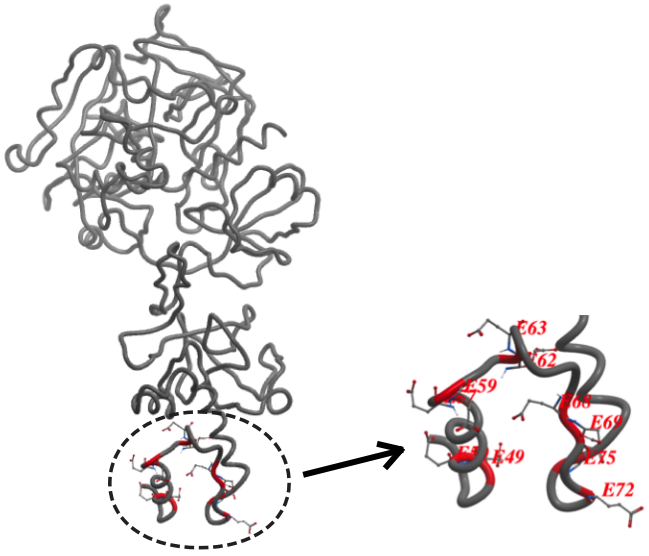

Figure 8.4. The 3D structure of prothrombin generated using I-TASSER. The 10 Gla residues (red) are located at sites 49, 50, 57, 59, 62, 63, 68, 69, 72, 75 on the protein (excluding signal peptide and propeptide sites: 6, 7, 14, 16, 19, 20, 25, 26, 29, and 32).

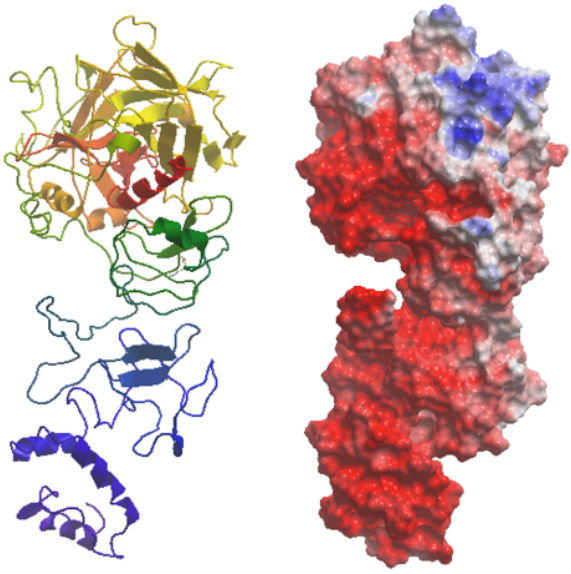

Figure 8.5. A 3D structure of prothrombin (left) and surface charge map (right) in same orientation. The 10 Gla residues form an 8.3 nm^3 carboxyglutamic domain at the base of the structure where binding to the alumina

Figure 8.6 and Figure 8.7 show the 3D structure generated for factor IX and the Gla domain containing 12 γ-carboxyglutamic acid residues and 12 other metal binding sites on

varying amino acids. The protein sequence consists of 461 amino acids. The prepeptide and propeptide (groups 1 to 46) were ignored. [61,63,64]

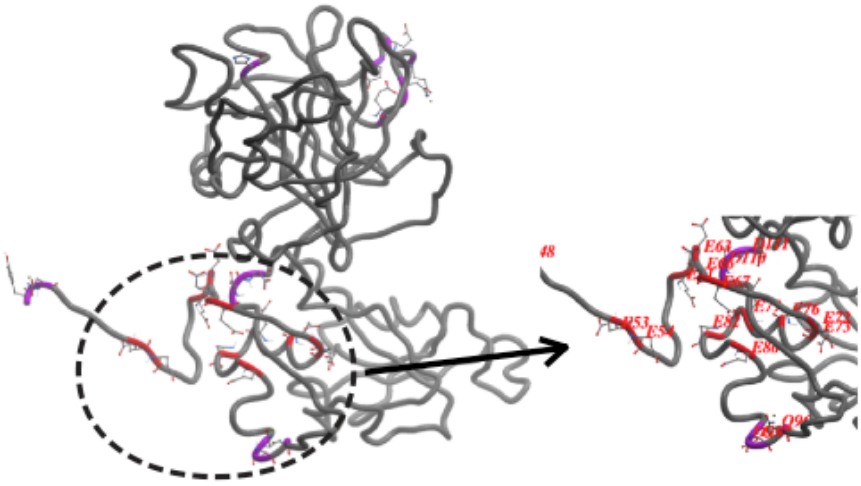

Figure 8.6. The 3D structure of human coagulation factor IX generated using I-TASSER. The 12 Gla residues (red) are located at sites 53, 54, 61, 63, 66, 67, 72, 73, 76, 79, 82, and 86 on the protein (excluding signal peptide and propeptide sites: 7, 8, 15, 17, 20, 21, 26, 27, 30, 33, 36, and 40). Additional metal binding sites (purple) are 47, 48, 93, 94, 96, 110, 111, 281, 283, 286, 288, and 291 (excluding signal peptide and propeptide sites: 1, 2, 47, 48, 50, 64, 65, 235, 237, 240, 242, and 245).

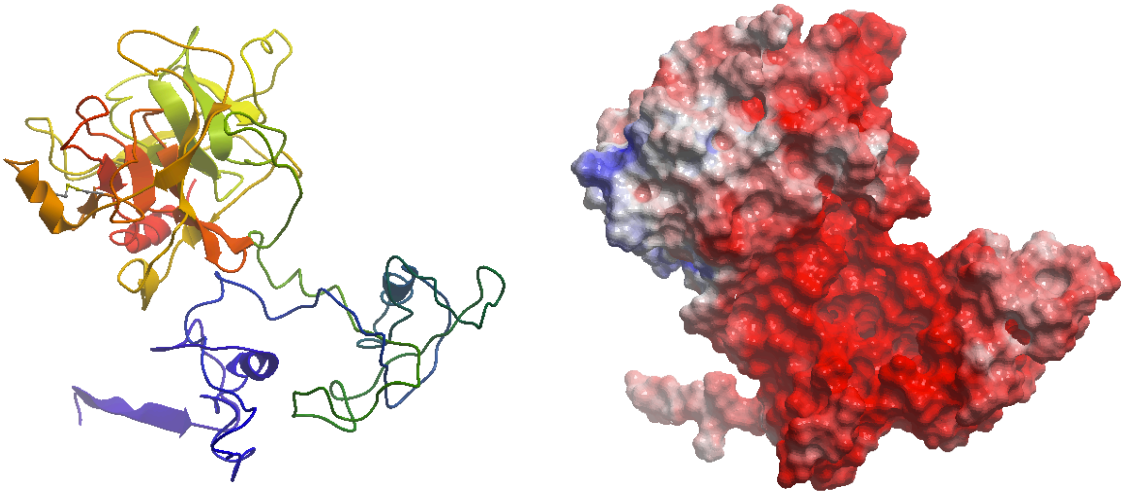

Figure 8.7. The 3D structure of human coagulation factor IX (left) and surface charge map (right) in same orientation. The 12 Gla residues form an 17 nm^3 carboxyglutamic domain at the base of the structure where binding to the alumina substrate occurs.

Figure 8.8 and Figure 8.9 show the modelled 3D structure of protein S with the charged residues. The structure was built from 676 amino acid residues and the signal peptide and propeptide (groups 1 to 41) were ignored. [30]

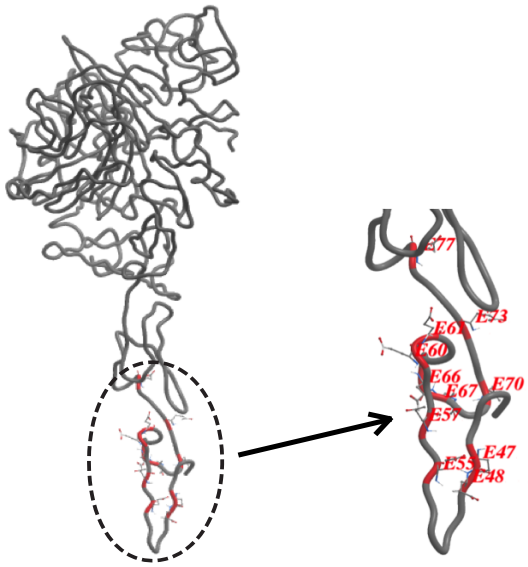

Figure 8.8. The 3D structure of protein S generated using I-TASSER. The 11 Gla residues are located at sites 47, 48, 55, 57, 60, 61, 66, 67, 70, 73, and 77 (excluding signal peptide and propeptide sites: 6, 7, 14, 16, 19, 20, 25, 26, 29, 32, and 36). [30]

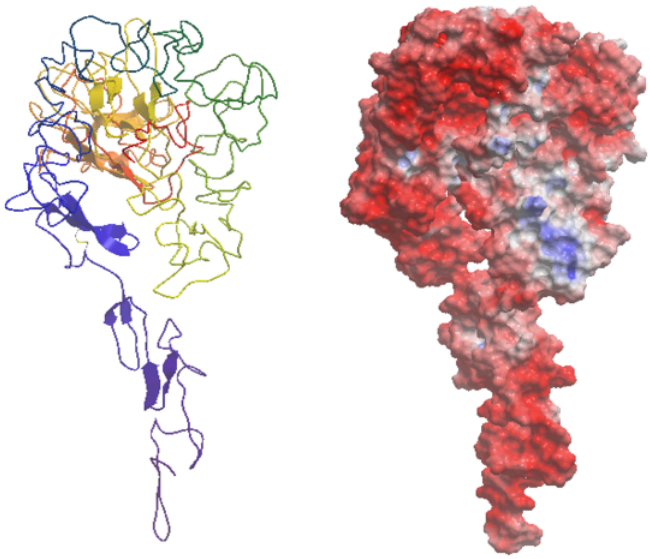

Figure 8.9. A 3D structure of protein S (left) and surface charge map (right) in the same orientation. The 11 Gla residues form a 12.3 nm^3 carboxyglutamic domain at the base of the structure where binding to the alumina substrate occurs.

8.3.2 Protein Adsorption to Alumina

Part A – Detection of Vitamin K-dependent Proteins

8.3.2.1 Prothrombin Loss in Ordinary Tubes

Figure 8.10 shows the alumina surface after prothrombin solutions between 0.001 and 1 mg/ml were exposed.

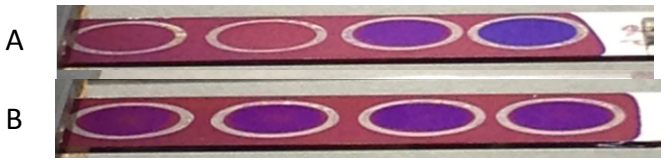

Figure 8.10. The alumina surface after prothrombin exposure. Spots on (A) show concentrations from left to right of 0.001, 0.01, 0.1, and 1 mg/ml and (B) shows concentrations from left to right of 0.03, 0.06, 0.08, and 0.1 mg/ml.

Figure 8.11 outlines the dimensions of micro-centrifuge tubes used to dilute and store proteins prior to exposure to the alumina surface.

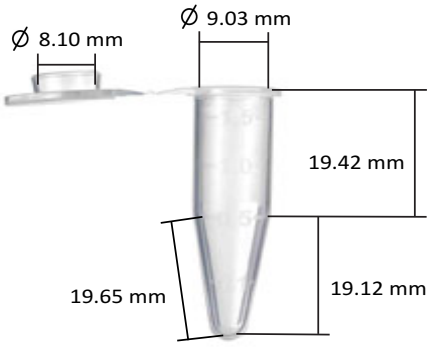

Figure 8.11. The dimensions of polypropylene micro-centrifuge tubes used for mixing and storing proteins.

The inner surface area was calculated to be 8.8 cm^2. Based on the available surface for protein loss, as well as the maximum adsorption of prothrombin based on the size, the final concentration of the exposed solution was determined and is shown in Table 8.4.

Table 8.4. The initial concentration and molarity of prothrombin in solution were used along with a maximum adsorption value of 570 ng/cm^2 and the centrifuge tube internal surface area of 8.8 cm^2 to determine the moles adsorbed and the final concentration exposed.

Initial Concentration (mg/ml)	Molarity (moles/l)	Moles in 200 µl (picomoles)	Moles of Protein Adsorbed to Tube (picomoles)	Final Concentration (mg/ml)
1.00	1.4E-05	2857	72	0.975
0.10	1.4E-06	286	72	0.075
0.08	1.1E-06	223	72	0.053
0.06	7.9E-07	157	72	0.030
0.03	4.7E-07	94	72	0.008
0.01	1.4E-07	29	29	0.000
0.001	1.4E-08	3	3	0.000

In tubes with initial concentrations of 0.010 and 0.001 mg/ml, no protein remains. Therefore, not enough protein remained in solution to create a monolayer on the thin film surface. Under the same conditions for prothrombin solution at 0.033 mg/ml, the concentration of the solution pipetted onto the surface contained enough protein to form a monolayer on the centrifuge tube surface while reducing the prothrombin solution to ~8 µg/ml.

8.3.2.2 Sensitivity of Vitamin K-dependent Proteins

Figure 8.12 depicts the visible colour changes that resulted from exposing protein solutions of II, FIX, and PS containing 0.1, 0.2, 0.3, 0.5, 0.7, 1.1, and 1.4 µM to the surface of the thin film. This is equivalent to 1, 4, 6, 9, 13, 22, and 27 picomoles of prothrombin.

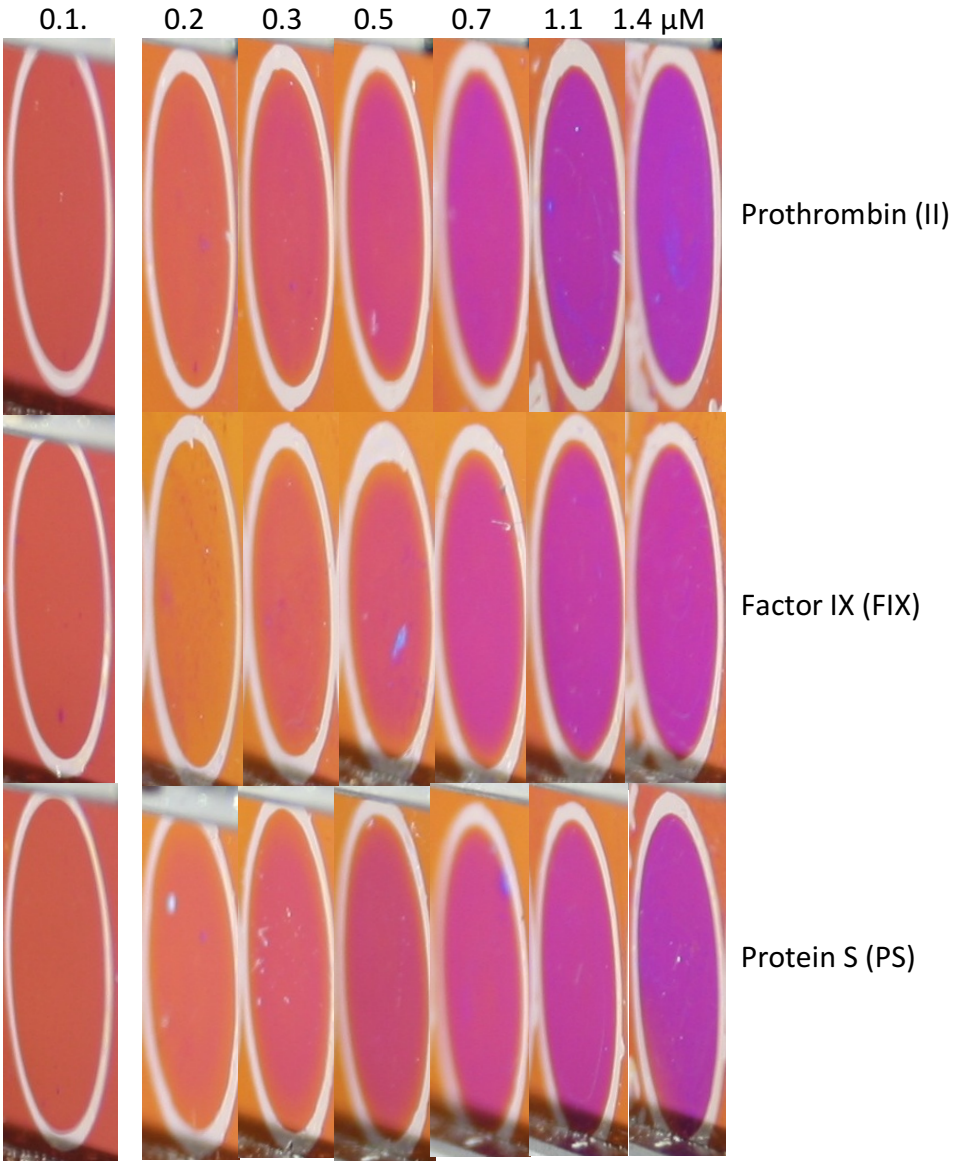

Figure 8.12. Prothrombin, factor IX, and protein S solutions exposed and adsorbed to the device surface are shown from top to bottom. Spots on each slide show molar concentrations from left to right of 0.1, 0.2, 0.3, 0.5, 0.7, 1.1, and 1.4 µM.

Spots with 0.1 µM exposed show the colours resulting after exposing protein solutions of the lowest molar concentration to a device with a different alumina thickness and base surface colour than the devices used for all other concentrations. Therefore, a comparison of the three spots with 0.1 µM can only be carried out between the three proteins. Colour shifts varied slightly after exposing larger concentrations of the three vitamin K-dependent proteins at constant molar concentrations.

8.3.2.3 Time Dependence of Vitamin K-dependent Proteins

Protein migration is a function of the molecular weight, shape, and overall net charge. Correlations were helpful to predict the diffusion coefficients of proteins ranging in size and shape, along with the radius of gyration and molecular weight. The radius of prothrombin, factor IX, and protein S were found in the literature and used to calculate if any significant change in diffusion time from the outermost region of the drop to the alumina surface was expected. Protein diffusion coefficients were calculated with the following equation.

$$D = \frac{6.85 \times 10^{-8}\, T}{v \cdot \sqrt{M^{1/3} \cdot R_G}} \qquad \text{Equation 8-1}$$

In the above equation, the constant of 6.85 x 10^{-8} is from fitting past literature, T is the temperature in K, $v$is the solvent viscosity in cP, M is molecular weight in g/mol, R_G is the radius of gyration in Å, and D is the diffusion coefficient in cm^2/s. [65] For all calculations, a temperature value of 21°C was utilized and a water solvent with a viscosity of 0.98 cP. [66] With the solvent containing buffer constituents an increased viscosity would result and extend the diffusion time slightly. For PBS at 19°C the viscosity equals 1.05 cP but drops to 0.70 cP at 37°C. [67] TBS is assumed to be very close to both water and PBS solvent viscosities. In TBS at 21°C, the prothrombin radius of gyration is 35.5 Å without metal ions in solution and 39.5 Å when Ca ions are in solution. [68] The radius of gyration for factor IX without metal ions present is 34.5 Å while with metal ions in solution and bound to the protein the value is 32.8 Å. [69] Literature for protein S was incomplete and hence proven trends between the molecular weight and radius of gyration of globular proteins were used to estimate an approximate radius of gyration. [70] Except for prothrombin, all vitamin-K dependent proteins are globular proteins. [71] Therefore, taking into consideration that the globular structure results in a slightly larger radius of gyration at the same molecular weight, a radius of gyration value of 40.0 Å was approximated.

The maximum diffusion distance from the air-surface interface of the spot to the alumina surface was measured to be ~0.8 mm. Using the obtained values and assuming the underlying mechanism was momentum transfer, generates time for the maximum net displacement (i.e. protein to move from the outermost surface of the droplet to the alumina surface)

$$t = \frac{a^2}{n2D} \qquad \text{Equation 8-2}$$

Where d is the net distance of diffusion in time t with units of cm (the maximum distance), D is the diffusion coefficient in cm^2/s, n is the dimension of diffusion (associated with 1D diffusion), and t is the elapsed time in seconds. [72] Table 8.5 shows input and output values from the two equations above.

Table 8.5. Protein molecular weight and radius of gyration values were used to calculate diffusion coefficients in water at 21°C and the length of time for diffusion from the surface of a 20 µl spot to the alumina surface.

proteins	molecular weight (g/mol)	Rg with metal ions	Rg without metal ions	average Rg (Å)	diffusion coefficient (cm^2/s)	time (min)
Prothrombin	71,000	39.5	35.5	37.5	5.22E-07	51
Factor IX	53,000	32.8	34.5	33.6	5.79E-07	46
Protein S	75,000			40.0	5.01E-07	53
					Average	50
					SD	3 min 41 sec

Little change in the calculated diffusion time resulted between the three proteins. The diffusion coefficient and diffusion time calculation do not take the protein and alumina charges into consideration. Table 8.6 shows the net negative charges and mass-to-charge ratios for prothrombin, factor IX, and protein S. With a low m/z ratio, proteins are expected to reach the alumina surface and bind more quickly.

Table 8.6. Shows the calculated net charges and mass-to-charge ratios for the vitamin k-dependent proteins of interest.

Molecule	Net Charge	Mass-to-Charge Ratio (m/z)
Prothrombin	-13.7	5182
Factor IX	-14.9	3557
Protein S	-15.7	4777

Figure 8.13 shows the device surface after exposing a prothrombin solution containing 0.007 mg/ml and with equivalent moles of factor IX and protein S to the surface for longer than 15 minutes. Figure 8.13 shows the colour shifts present after solutions of prothrombin, factor IX, and protein S containing 0.1 µM of protein were placed on the alumina surface for 45, 50, and 55 minutes. The purpose was to observe the influence of protein diffusion with different mass-to-charge ratios.

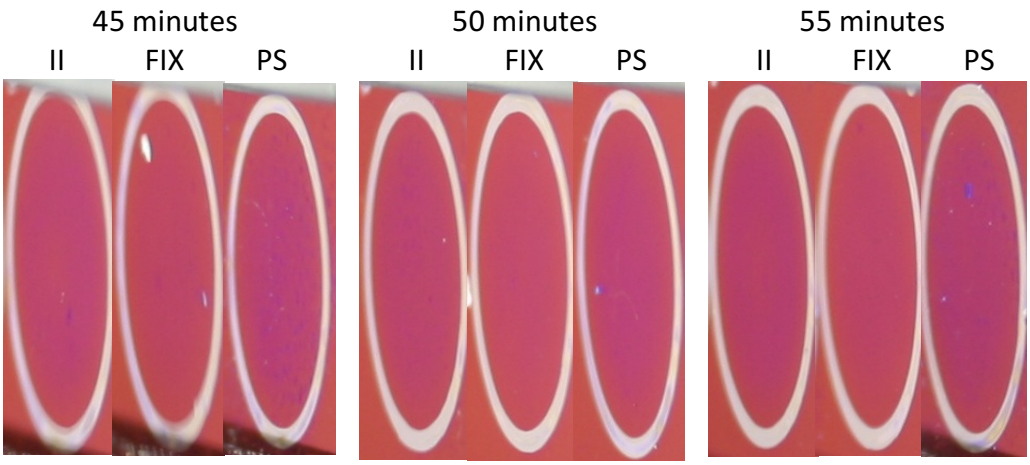

Figure 8.13. Colour shifts resulting when 2 picomoles of prothrombin, factor IX, and protein S solutions are in contact with the surface for periods of 45, 50, and 55 minutes.

Part B – Detection of Prothrombin with Metal Ions in Solution

8.3.2.4 Binding of Prothrombin from Solutions Containing Metal Ions

To test the effect of EDTA on protein binding to the alumina, prothrombin, from solutions with various concentrations of metal ions and EDTA, was immobilized and the resulting visible colour shifts were observed to assess differences.

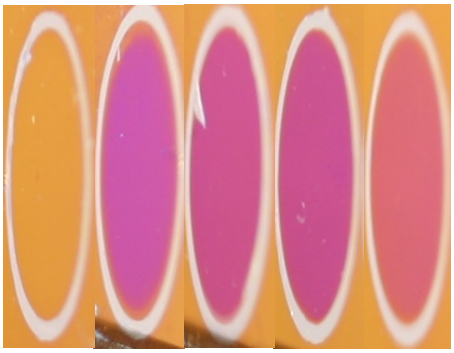

Figure 8.14. Alumina surface with exposure to (left to right) Ca and EDTA, prothrombin with Ca, prothrombin with Ca and EDTA, prothrombin control, and prothrombin with EDTA. All solutions of prothrombin were at concentrations of 0.1 mg/ml with constituents of 1 mM Ca and 1 mM EDTA.

The buffer solution consisting of Ca ions and EDTA had no influence on the bare device surface colour. A buffer solution with Ca ions and EDTA showed no colour shift. Figure 8.15 and Figure 8.16 show two slides containing six spots each with varying metal ion and prothrombin solutions. Each slide surface contains a prothrombin control spot for the comparison of resulting colour shifts.

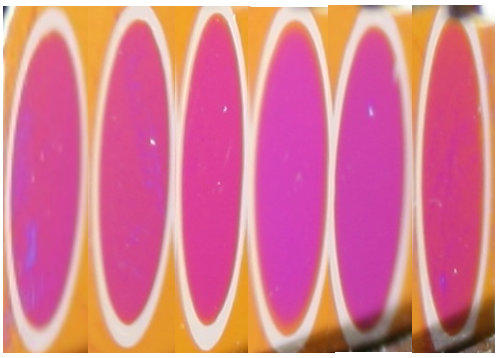

Figure 8.15. Colour shifts (left to right) from solutions of: prothrombin and 1 mM Mg, prothrombin and 5 mM Mg, prothrombin control, prothrombin and 1 mM Ca, prothrombin and 2.5 mM Ca, prothrombin and 10 mM Ca. All solutions contain a final prothrombin concentration of 0.1 mg/ml.

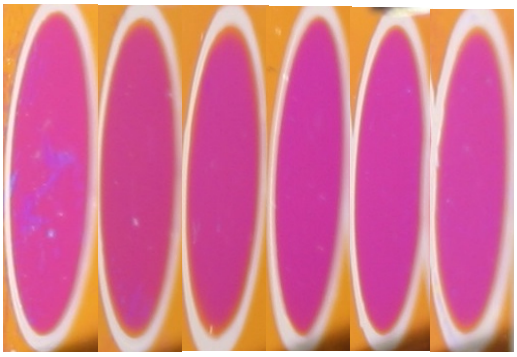

Figure 8.16. Colour shifts (left to right) from solutions of: prothrombin and 5/2.5 mM Mg/Ca, prothrombin and 5/10 mM Mg/Ca, prothrombin control, prothrombin and 1/1 mM Mg/Ca, prothrombin and 1/2.5 mM Mg/Ca, prothrombin and 1/10 mM Mg/Ca. All solutions contain a final prothrombin concentration of 0.1 mg/ml.

Measuring the Yxy coordinates from the protein spots and the bare surfaces images and plotting on a CIE chart makes colour shifts more apparent. Figure 8.17 shows three colour plots that outline shifts when Ca ions, Mg ions, and combinations of the two ions are mixed with prothrombin prior to surface exposure. Coordinates of the bare surface and prothrombin control solution are shown on each plot.

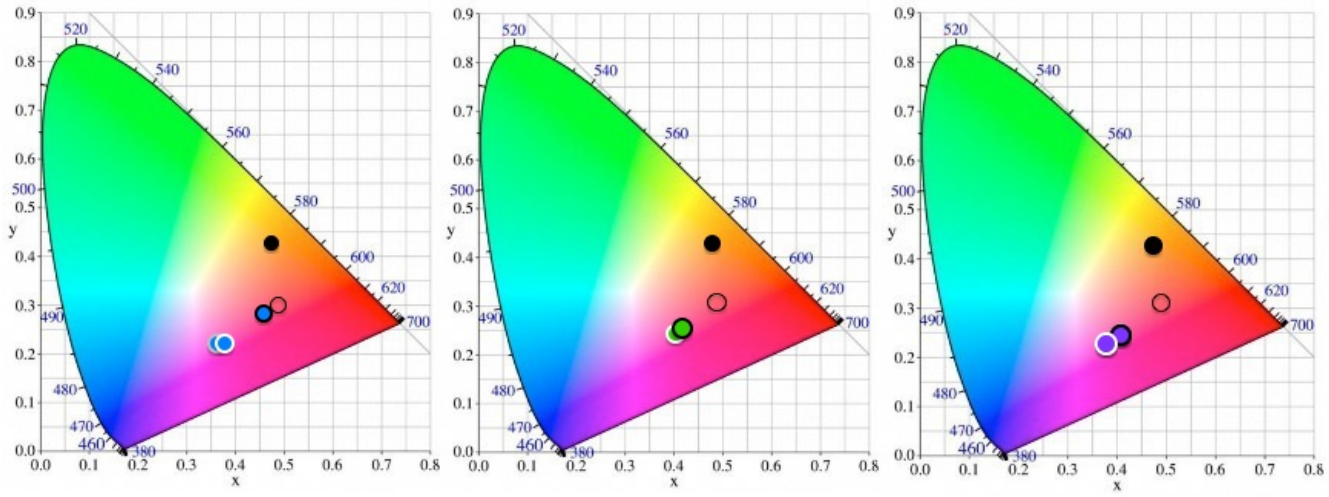

Figure 8.17. Colour coordinates shown on each plot show the average surface coordinates (solid black) and the prothrombin control solution (black outline). Plots from left to right show prothrombin with Ca ions (blue), prothrombin with Mg ions (green), and Ca/Mg ions (purple). The marker outlines provide information on the ion concentration in the protein solutions with white indicating the lowest, grey the middle value (if one exists), and black the largest. Solutions containing both Ca and Mg ions show coordinate averages of the lowest and highest Mg ions with all Ca concentrations.

Work on prothrombin has shown that binding 2 or 3 metal ions were necessary for prothrombin membrane binding. [41,73] When 2 to 3 multivalent metal ions were bound a higher stability protein with a different conformational state results. [11,74,75] Occupancy of 4 or 5 metal ion binding sites allows prothrombin to bind securely to phospholipid membranes that have a net negative charge. The metal ion binding sites are specific for calcium ions, however other alkaline earth and lanthanide metal ions can substitute with lower efficiency.[76,77]

Images captured of cumulative antibody solutions on prothrombin with different metal ions are shown in Figure 8.18 and Figure 8.19. Similar to images showing prothrombin solution subsequently exposed to the metal ion solution, images with multiple antibody solutions appear to have less homogeneous surface colours.

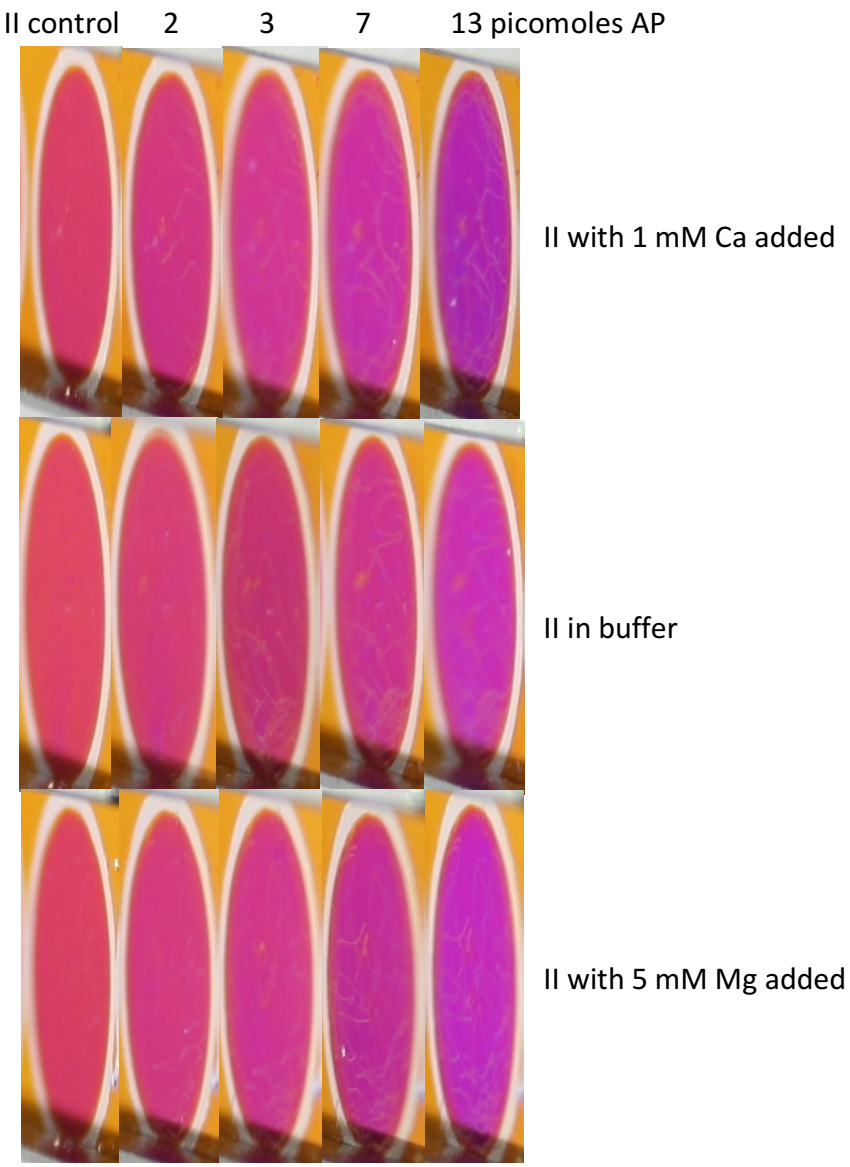

Figure 8.18. Anti-prothrombin visual detection sensitivity with exposed cumulative concentrations from left to right of no anti-prothrombin solution, 2, 3, 7, and 13 picomoles (20 μl of 0.015, 0.025, 0.05, and 0.1 mg/ml). Solutions were exposed to surfaces initially coated with 28 picomoles prothrombin solutions containing various amounts of Ca or Mg ions for 30 minutes.

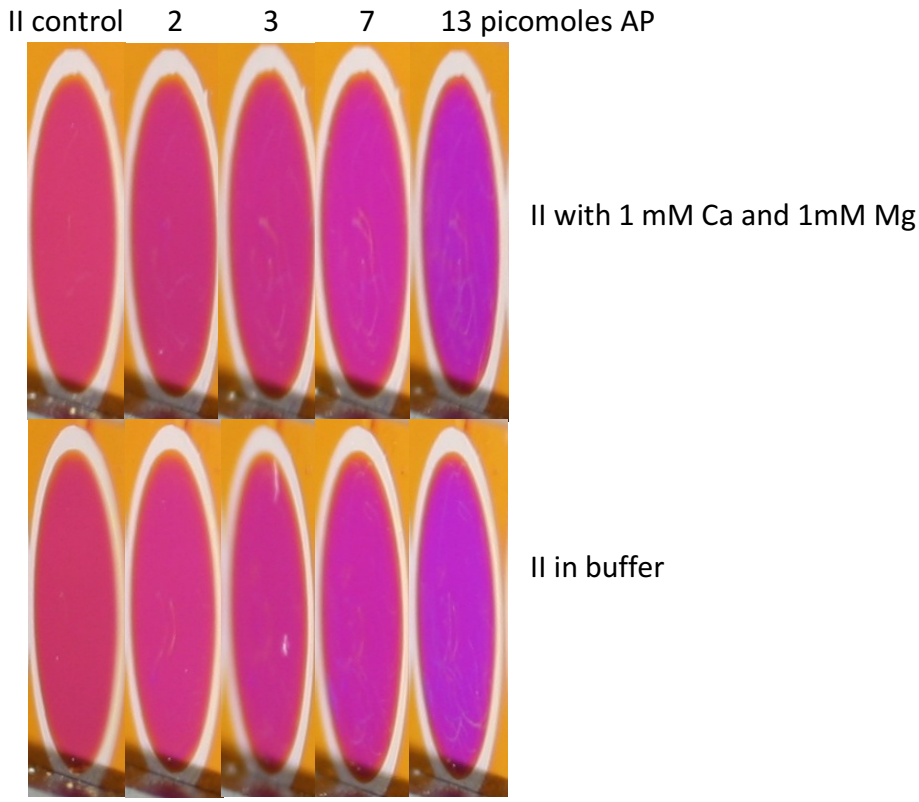

Figure 8.19. Anti-prothrombin visual detection sensitivity with exposed cumulative concentrations from left to right of no anti-prothrombin solution, 2, 3, 7, and 13 picomoles (20 μl of 0.015, 0.025, 0.05, and 0.1 mg/ml). Solutions were exposed to device surfaces coated with 28 picomoles of prothrombin solutions with 1 mM Ca and 1mM Mg ions for 30 minutes.

Regardless of the protein and metal ion mixture on the surface, the anti-prothrombin led to an increase in the colour shift with larger concentrations. Anti-prothrombin sensitivity on each surface appears to be the same.

8.3.2.5 The Effect of Metal Ions and Chelators in Solution

Figure 8.20 shows an anodized slide with spots exposed to (left to right) the metal ion buffer solution, prothrombin control, prothrombin bound with subsequent exposure to a metal ion buffer solution, and prothrombin with metal ions in solution.

Figure 8.20. The alumina surface exposed to (left to right) Mg/Ca ions in solution, prothrombin with Mg/Ca ions, prothrombin control, and prothrombin followed by Mg/Ca ion solution. All prothrombin solutions were at 0.1 mg/ml, Mg ion solutions were at 1 mM, and Ca ion solutions were at 2.5 mM.

Exposing the metal ion solution to the slide surface for 15 minutes results in no colour shift. Furthermore, no colour shift was apparent between the prothrombin control and the spot of immobilized prothrombin with subsequent exposure to the metal ion solution, although the surface colour appears less homogenous after removal of the second solution.

8.3.3 Liquid Chromatography Mass Spectrometry

Figure 8.21 shows an overlay of low mass areas of the 0.1 mg/ml prothrombin control solution (red) and the solution after exposure to the alumina surface (black).

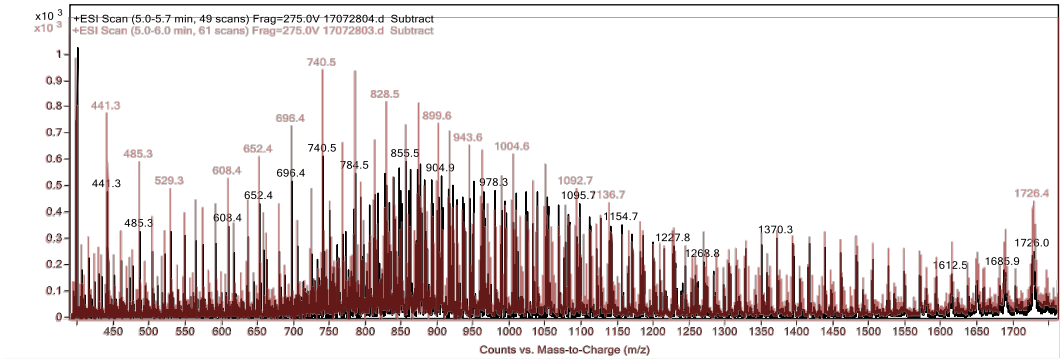

Figure 8.21. An overlay of the low mass regions (counts vs mass-to-charge) obtained from LCMS where the polymer is detectable. The prothrombin initial solution (orange) and the solution after exposure to the alumina surface for 15 minutes before examination (black) are shown to outline differences between the two.

Deconvoluted plots of the control and exposed prothrombin solutions with an initial concentration of 0.1 mg/ml are shown in Figure 8.22.

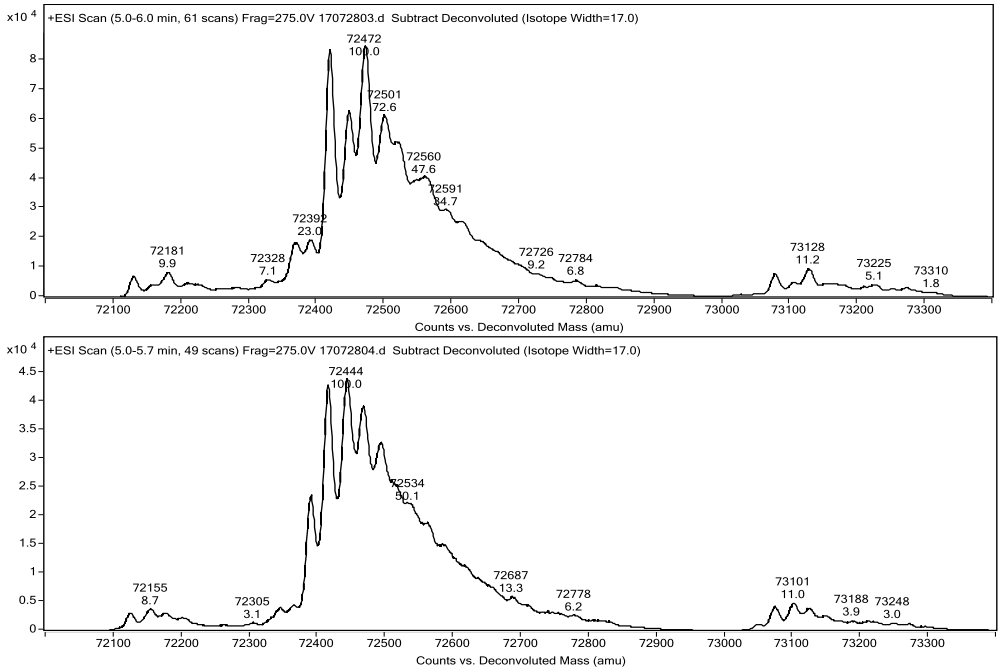

Figure 8.22. Deconvoluted plots show the 3 sets of peaks in a prothrombin control solution (top) and the solution after exposure to the alumina surface (bottom) with an initial concentration of 0.1 mg/ml. Set 1 was in the 72100 amu range, set 2 was in the 72400 amu range, and set 3 was in the 73100 amu range.

All prothrombin solutions produce curves with three sets of peaks regardless of the concentration under evaluation. The average shift between peak sets 1 and 2 was calculated to be 291±2 amu and between set 2 and 3 was 657±1 amu. These shift values were present in all prothrombin solutions regardless of exposure to the alumina surface or initial concentration. The maximum peaks in set 1, 2, and 3 were consistently 72181±1, 72472±1, and 73128±1 amu for the control solution and 72153±2, 72444±1, and 73101±1 amu for the alumina exposed prothrombin solution, respectively. Between the control and alumina exposed prothrombin solutions the peak positions shifted ~28 amu.

Figure 8.23 shows set 2 for prothrombin solutions before and after exposure to the device surface for initial prothrombin concentrations of 0.035, 0.05, and 0.1mg/ml.

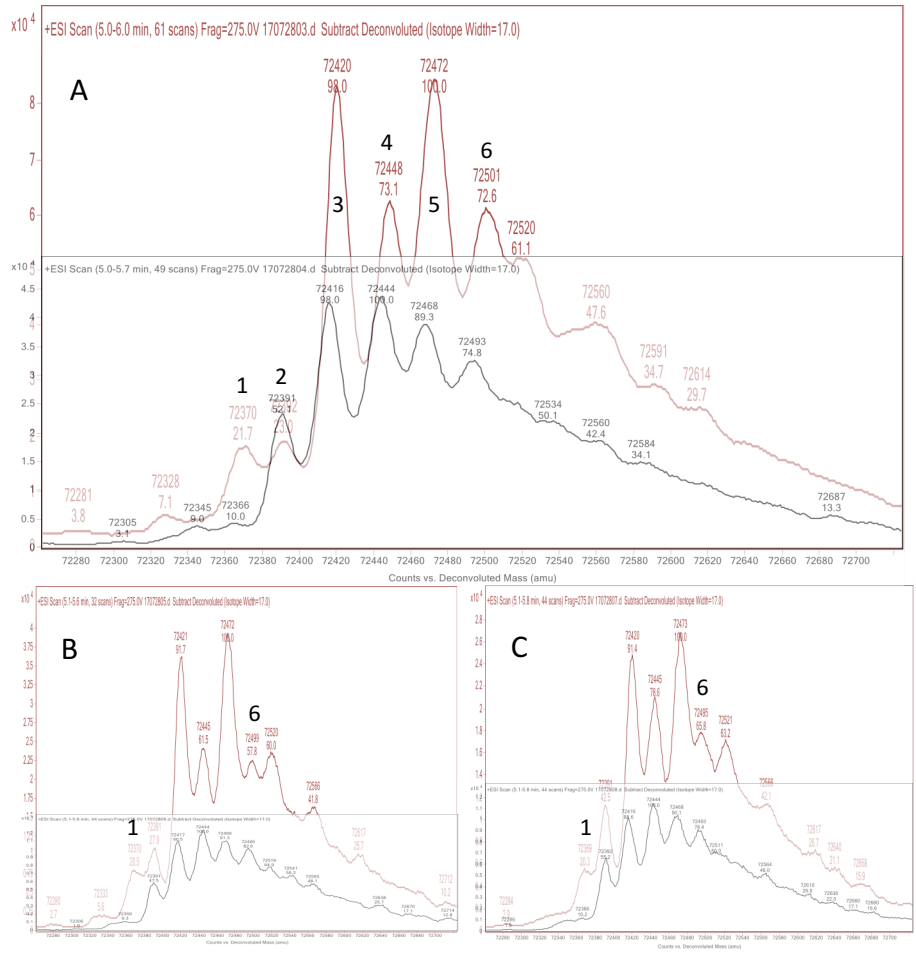

Figure 8.23. Deconvoluted plots show peaks from set 2 for the initial prothrombin solution (red) and the prothrombin solution exposed to the porous alumina surface for 15 minutes (black). The initial prothrombin concentrations were (A) 0.1, (B) 0.05, and (C) 0.035 mg/ml for plots shown. The main peaks are labelled 1 to 6.

An average shift of 26±2 amu was calculated between peaks in set 2 of all prothrombin solutions run. Table 8.7 shows a comparison of peak intensities resulting from the control solution and the alumina exposed prothrombin solution was completed for concentrations of 0.035, 0.05, and 0.1 mg/ml. The average intensity of each sub-peak in set 2 was determined relative to the maximum peak intensity of the control prothrombin solution.

Table 8.7. Average peak intensity of prothrombin control solutions and prothrombin solutions exposed to the alumina surface as a percentage of the maximum control peak intensity (bold). Average percentages and standard deviations

were achieved from solutions of 0.035, 0.05, and 0.1 mg/ml. Standard deviations (SD) and coefficient of variations (CV) were shown for peak percentage values of control and exposed solutions.

Peak Label	Peak Regions (amu)	Peak Intensity in Prothrombin Control Solution (% of Max Peak)			Peak Intensity in Prothrombin Solution Exposed to Alumina (% of Max Control Peak)			Decrease in Peak Intensity (%)	
		Average	SD	CV	Average	SD	CV	Average	SD
1	72359 to 72370	21	1	0.04	4	1	0.05	17	1
2	72391 to 72392	31	10	0.33	22	6	0.08	9	12
3	72416 to 72421	94	4	0.04	39	11	0.05	55	8
4	72444 to 72448	71	9	0.12	42	10	0.00	29	7
5	72468 to 72473	**100**	**0**	0.00	38	9	0.01	62	9
6	72493 to 72501	65	7	0.11	33	6	0.05	33	1

The largest peak intensity decreases were found to be 62 and 55% with exposure to the alumina surface for peak regions of ~72416 and ~72468 amu respectively (peaks 3 and 5).

8.4 Discussion

8.4.1 Protein Modelling

Although the membrane anchoring domain of all vitamin K-dependent proteins are similar, generating models for the three proteins selected allowed for a visual depiction of how the structure could influence binding to the alumina. Prothrombin binds to the alumina surface at the Gla domain because the numerous carboxyglutamic residues have a high affinity for metal oxides such as alumina.[9] With the high concentration of Gla residues at the base of the molecule, it is likely that vitamin K-dependent proteins will bind to the surface through the Gla domain, at a particular orientation.[19] Reliable binding is crucial for the device operation as it results in consistent optical path length and visible colour shifts on the surface. The prothrombin I-TASSER generated models are shown between Figure 8.4 and Figure 8.9.

Prothrombin is a unique vitamin K-dependent protein as it contains two 'kringle' domains.[50] These domains exist in other proteins in the blood coagulation process but not in other vitamin K-dependent proteins. It has been proven that the kringle domains contain no sites participating in the protein and membrane binding.[14] The predicted binding orientation of factor IX to the alumina substrate is similar to prothrombin through the Gla domain. In the I-TASSER models, the protein appears to have a broad base and was expected to generate a thinner monolayer than prothrombin based on the lower molar mass. A reproducible orientation was expected; however, the width and curvature of the protein may allow portions of the structure to fold and contact the alumina surface and cause protein denaturing or instability. Seven of the additional metal ion

binding sites exist within the Gla domain which may or may not benefit binding to the alumina surface, and the remaining 5 are at the opposite end and may hinder binding to the surface.

No documents unveil the detailed structure of protein S. However, I-TASSER was employed to use the amino acid sequence and the same chain alignment as for factor IX to generate a structure based off the folding of similar protein sequences (see Figure 8.8 and Figure 8.9). The stability of a narrow base is undetermined and may allow flexibility in the upper portion of the protein, exposing it to the surface and potentially denaturing or becoming unstable.

Prothrombin, factor IX, and protein S models had C-scores of -1.05, -1.67, and -2.74, with the range of C-score values for low to high quality being -5 to 2. The 3D models provided visualization for assessing protein-surface interactions such as interpreting the colour generation and stability of the Gla domain on the alumina surface. Optimal molecules for linking additional proteins, and building the detection platform, should contain a high charge density region to orient molecules and ensure stable positioning on the surface and reproducibility.

Table 8.8. Gla residue density of vitamin K-dependent linker molecule.

Molecule	Number of Gla residues	Gla Domain Volume (nm^3)	Gla Residue Density (Gla Residues/nm^3)
Prothrombin	10	8.3	1.20
Factor IX	12	17.0	0.71
Protein S	11	12.3	0.89

A consistent binding orientation of the initial protein monolayer is necessary for reproducible colour shifts on the surface of the slide and subsequent cross-linking to create a detection platform for different analytes. Further experimental testing is required to confirm the exact protein structure including the location and orientation of the Gla domain (see more on orientation in Chapter 9).

8.4.2 Protein Adsorption to Alumina

Part A – Detection of Vitamin K-dependent Proteins

8.4.2.1 Prothrombin Loss in Ordinary Tubes

Initial work carried out to determine the approximate sensitivity of the device, exposed Prothrombin solutions between 0.001 and 1 mg/ml (0.3 to 285.7 picomoles). The resulting visible colours observed showed different hues of purple with protein solutions of 1 and 0.1

mg/ml exposed and no visible colour change with ≤0.01 mg/ml. Exposing higher concentration solutions resulted in a colour shift towards the blue region, demonstrating an increase in the optical path length with more protein binding to the surface. Additional concentrations between 0.1 and 0.01 mg/ml showed visible colour changes until solutions <0.3 mg/ml. The drop-off in protein adsorption may be due to the proteins in solution adsorbing to the centrifuge tube that protein dilutions are carried out in or the pipet tip. A decrease in the concentration changes the diffusion coefficient and absorption coefficient of proteins within the droplet toward the surface. It is also possible that when the concentration becomes too low, diffusion towards the surface is the rate-limiting factor and prevents significant adsorption in the allotted period. If this is the case, increased time should result in increased binding and sensitivity.

From the literature, the amount of protein that adsorbs to a hydrophobic surface is in the range of 100 to 1000 ng/cm^2 depending on the binding orientation and dimension of the protein. [78,79] A geometrical maximum of prothrombin binding to the surface in one layer with short and long sides of the protein was determined. Prothrombin was modelled as an ellipsoid based on its globular structure with dimensions of 4.5×5×11 nm. [80] The densest packing of these molecules in long side and short side binding positions led to the determination that the maximum amounts of prothrombin that can bind to the surface are 207 and 570 ng/cm^2 respectively. Work completed by Esser provides a demonstration of these calculations. [81] The centrifuge tube (see Figure 8.11) was divided into three components and the inner surface area available to bind protein was determined to be 8.8 cm^2. The maximum amount of protein that could adsorb to the surface of the centrifuge tube allowed for adjustments of the protein concentration accordingly and showed the importance of using low-bind tubes. A maximum geometrical adsorption value of 570 ng/cm^2 for a monolayer of prothrombin was employed for calculations, leading to a maximum adsorption of 5 μg (72 picomoles). Table 8.4 outlines the initial concentration and molarity of prothrombin, the moles in a dilution volume of 200 μl within the centrifuge tube, the moles adsorbed to the tube surface, and the final concentration of the solution exposed to the surface.

The pipet tip inner surface area contacted by 20 μl of solution, was 1.03 cm^2. With close packed order of prothrombin this can result in an additional 0.59 μg of protein adsorption. Decreasing the 20 μl solution by 29 μg/ml if the tip was filled once and potentially decreasing the 0.2 ml solution in the centrifuge tube by 2.9 μg/ml if the tip was filled and released multiple

times. The theoretical mass adsorbed by a pipet tip is an order of magnitude less than a centrifuge tube. Furthermore, filling and releasing of protein solution from the pipette tip multiple times before pipetting, ensures saturation of the tip and reduces the impact on concentration. Adsorption to the pipet tips was assumed to be zero for these calculations.

These results confirm that the lack of a visible colour below 0.03 mg/ml was due to protein being removed from solution during the dilution process. Solutions containing <5 μg (72 picomoles) loose the majority of protein in solution during the formation of a monolayer on the tube surface leaving no protein in solution. The actual sensitivity was closer to ~15 μg/ml, which aligns with the sensitivity of prothrombin determined with low bind tubes (see section 8.4.2.2) To increase the precision of the protein concentration in solution, it is essential to mitigate protein adsorption to the micro-centrifuge tube surface. Options include using an alternate protein solution (e.g., BSA) to coat the tube surface before diluting the protein solutions or using a pre-coated or special tube to minimize protein adsorption to the surface. Alternatively, the dilution could be carried out on the alumina surface by pipetting the necessary volume of TBS and subsequently the small volume of protein at a higher concentration than desired to achieve the final concentration with a greater accuracy. For remaining tests low binding micro-centrifuge tubes will be used to mitigate adsorption during mixing and diluting. In cases when ordinary micro-centrifuge tubes are used for prothrombin solutions, or protein of a similar mass, a protein loss of ~5 μg should be accounted for. Accurate concentrations are crucial when examining colour shifts on device surfaces, at low concentrations, shown in chapter 9 and 10.

8.4.2.2 Sensitivity of Vitamin K-dependent Proteins

Applying the same number of moles for prothrombin, factor IX, and protein S allowed proteins with different molar masses, charges, and structure to be compared base on the resulting colours generated and sensitivity. The dimensions measured from these I-TASSER models of prothrombin, factor IX and protein S were 10 by 4.4 nm, 6.2 by 4 nm, and 11.8 by 5 nm, respectively. Protein thicknesses showed a stronger indication of colour shift than charge density explaining why factor IX generated a less distinguishable colour than prothrombin and protein S and was ultimately less sensitive for detection by eye. The Gla domain binds to the membrane surface on the short side of the molecules and thus with protein binding the colour shift and thickness of protein monolayers would be expected to increase in the order of factor

IX<prothrombin<protein S. It was expected that protein S would be ~2 nm thicker than prothrombin and shift slightly further into higher colour orders, however, they appeared similar. It is plausible that the structure of protein S was less stable, and binding created a layer that was thinner than that generated by prothrombin binding. Consistent colour shifts were observed and led to the conclusion that binding of proteins to the surface is reproducible. With molar solutions of each protein showing different colour shifts with immobilization, it is difficult to determine if diffusion and binding occur at the same rate. The sensitivity, or visual detection limit, for molar concentrations of prothrombin, factor IX, and protein S equate to 0.2, 0.3, and 0.2 μM respectively.

Anti-prothrombin and influenza B antibodies were exposed to each protein spots to confirm device specificity. Anti-prothrombin generated a colour shift when exposed to immobilized prothrombin spots, but no colour change when exposed to factor IX or protein S spots. The influenza B antibody showed no colour shift on any of the three immobilized vitamin K-dependent protein spots, interpreted by eye.

8.4.2.3 Time Dependence of Vitamin K-dependent Proteins

Prothrombin solutions at a concentration of 1 mg/ml contain over 35 times the amount of protein required to saturate the nominal alumina surface of a 1 cm diameter spot with a monolayer of protein, regardless of the binding orientation. With similar dimensions for factor IX and protein S, concentrations of ~1 mg/ml solutions likely contain significantly more protein than that required for a monolayer as well. Table 8.2 shows the amount of prothrombin present in solutions at different concentrations to cover the surface. For prothrombin solutions, the number of molecules present in a 20 μl spot of 0.007 mg/ml (1 picomole) covers the nominal surface between 0.2 and 1.3 times. The nominal surface area differs from the actual porous alumina layer due to porosity and roughness, however, this provides a rough indication of short and long side binding to the alumina. Calculations were completed using dimensions from Lim et al. [23]

At lower concentrations it was thought that the orientation of binding and diffusion to the surface may be more influential to the resulting colour shift. Lower concentrations and increased exposure time of the protein solution, was carried out to determine if differences in diffusion or mass-to-charge ratios change the sensitivity of the protein solutions. An average diffusion time for the vitamin K-dependent proteins of 50 minutes±3 minutes and 41 seconds was calculated.

With similar diffusion times it was expected that stronger colour shifts would result from the exposure of protein solutions containing a lower mass-to-charge ratio (m/z). Mass-to-charge ratios are in order of prothrombin>protein S>factor IX and were expected to better represent the impact of the charged Gla region on the molecule. However, the net negative charges are in order of protein S>factor IX>prothrombin. Theoretical calculations showed that prothrombin solutions between 0.2 and 0.5 μM (see Table 8.2) must be exposed to the surface for 15 minutes to create a colour shift. Loss in the low bind tubes showed that the actual exposed protein was ~ 0.1 M (see Table 8.4).

The surface colour change increased with longer exposure periods for all protein solution. However, in the protein m/z ratios did not appear to impact binding differently with increased exposure time, as factor IX with the lowest mass-to-charge ratio had the weakest colour shift. These results further demonstrate the importance of thickness change and protein conformation for colour shifts and indicate that the density of Gla residues in each molecule between the vitamin K-dependent protein testes was not influential to the protein binding.

When selecting a base protein layer to build an antigen-antibody detection test low concentration of the linking protein are not likely to be used. The exposure of high concentration solutions would saturate the surface and minimize the necessary exposure time period. However, the greater the affinity of the protein for the alumina surface, the better to achieve high device stability.

Part B – Detection of Prothrombin with Metal Ions in Solution

8.4.2.4 Binding Effects of Prothrombin Solutions Containing Metal Ions

This work tested various concentrations of Ca and Mg ions individually and in combinations to determine how the addition of metal ions to prothrombin solutions influenced the binding, and ultimately the colour shifts on the surface. Metal ion solutions shown in Table 8.3 create mixtures of prothrombin solutions with a final concentration of 0.1 mg/ml. Images of spots are shown in Figure 8.16 and Figure 8.17 and visual differences were observable by eye. However, CIE chromaticity diagrams were useful for assessing the colour shifts in these images, which were otherwise difficult to interpret by eye. Colour interpretation by eye leads to a perceived reduction in the protein layer thickness with the 10 mM Ca ion protein solution.

However, mapping the coordinates showed that a shift towards a higher optical path length did occur; it was just not an easy change for our eyes to detect.

Protein solutions with added Ca and Mg ions resulted in greater colour shifts than the prothrombin control by increasing in optical path length. The most significant colour shifts were observed after protein solutions with 2.5 and 1 mM Ca ions were exposed to the surface. A close second were solutions with mixtures of Mg at 1 mM and any of the Ca concentrations tested (1, 2.5, and 10 mM) followed by Mg at 5 mM and Ca concentrations of 2.5 and 10 mM with smaller colour shifts from the prothrombin control. The protein solution with 10 mM Ca ions resulted in a colour very close to the prothrombin control.

Altering concentrations of calcium and magnesium ions has demonstrated changes in prothrombin binding to the alumina surface and was thought to be caused by the number of ions bound to sites in the Gla domain. [82] Assuming that the Gla domain of all vitamin K-dependent proteins interact similarly with metal ions and binding to a membrane or alumina surface, the well-researched proteins can be used to interpret the effect on prothrombin and other proteins with less available background. Solutions employed for this work were close to what exists in normal human plasma. The prothrombin concentration was 0.1 mg/ml and the midpoint of Ca and Mg ions used were 2.5 and 1 mM, respectively. Whereas the native concentration of prothrombin ranges from 0.05 to 0.15 mg/ml[83] and contains ~1.25 mM free Ca^{2+} and ~0.5 mM Mg^{2+}.[84]

Prothrombin has high and low affinity metal binding sites that bind a single metal ion with a single or multiple Gla residues. [39] A study on factor X, identified classes of metal binding sites in the Gla domain unique to Ca ions. With Gd(III), one high affinity metal binding site was found (K_d=0.55 μM) and between four and six low binding sites (K_d=4 to 8 μM). [39,77] The affinity of each binding site in the prothrombin molecule is unknown, yet the intermolecular bridge that results from two high affinity sites is known to stabilize the tertiary structure of prothrombin. [9,60]

Studies showed that vitamin K-dependent proteins require calcium ions to configure in a way that allows them to bind to membranes. At supraphysiologic concentrations of Ca^{2+}, Gla domains in factors VII, IX, and X are known to bind 7 to 9 Ca^{2+} when no other metal ions are present. [2,22,85,86] Supraphysiologic Ca^{2+} concentrations of 2.5 to 5mM Ca^{2+} were employed in clotting studies to ensure saturation of the Gla domains for maximal enzymatic activity and

membrane binding. [87] However, based on the visible colour shifts this work showed binding of prothrombin with 2.5 mM and 1 mM Ca ions were nearly identical, whereas at 10 mM Ca ions showed, almost no change from the prothrombin control solution colour shift. If a greater number of sites contain Ca ions the structure differs and binds less preferentially to the alumina surface.

At plasma ion levels, between 2 and 4 of the metal binding sites in Gla domains of factor VII (inactivated or VIIa) and X are filled by Mg^{2+}.[48,87] The addition of Mg ions to protein solutions with Ca ions at physiological levels was found to enhance membrane binding to FVIIa and activated protein C. [39] Solutions with 1 mM Mg ion concentrations were found to show slightly greater colour shifts than solutions with 5 mM Mg ion concentrations, regardless of the Ca ion concentrations. Even solutions with Mg and 10 mM Ca ions result in a greater optical path difference than solutions containing only 10 mM of Ca ions. This change demonstrates an improvement in protein stability and/or conformation. In previous work the occupancy of Mg^{2+} improved the stability of binding sites in the Gla domain compared to when only Ca^{2+} is present.[88]

Exposing anti-prothrombin to spots where prothrombin was bound demonstrates immobilization and that metal ion solutions did not denature binding sites. Colour shifts were notable on all spots, and therefore the assumption can be made that prothrombin receptor sites remain intact. The sensitivity of anti-prothrombin detection was tested on each of the spots by exposing initially low concentrations of antibody to the surfaces. The increase in cumulative concentrations (0.015, 0.025, 0.05, and 0.1 mg/ml) ensured visible detection (see Figure 8.19). Preliminary work compared the colour shifts of anti-prothrombin on prothrombin with the exposure of cumulative antibody solutions versus a single solution and found no visible differences.

With noticeable differences in the prothrombin colour shifts, it is likely that ion mixtures altered the conformation or binding efficiency of the molecules resulting in a thicker or denser protein layer and increasing the colour change. However, with antibodies showing equivalent colour shifts, the assumption was made that the prothrombin layer density remains constant and that colour differences result from a change in the protein layer thickness. The sensitivity of anti-prothrombin appeared to be equal on surfaces with all prothrombin solutions regardless of the metal ions combined in solution.

Exposing multiple antibody solutions and in some cases prothrombin and metal ion solution leads to less homogenous colour shifts or lines within the exposed area. It is possible that these visible inhomogeneities are a result of contaminants or multiple protein layers.

8.4.2.5 The Effect of Metal Ions and Chelators in Solution

Additional tests were run to determine if bound prothrombin molecules are influenced by the exposure of metal ions in a buffer solution and how the addition of metal ions and a chelator impact the visible colour changes on the device surface. A buffer solution containing metal ions, near physiological levels, was placed on the surface with immobilized prothrombin to determine the influence on the colour shift. Furthermore, the influence of metal ion solutions on the alumina surface tests whether ions interact with the surface and lead to colour shifts. A study by Natishan and O'Grady showed that chloride ions interact with aluminum hydroxide and can lead to corrosion. [89] If any oxidation of the alumina occurs from Ca and Mg ions reducing the alumina, it is extremely minimal and caused no noticeable colour shift. After prothrombin has bound to the surface, the metal ion solution had no visible influence on the protein. The mixture of prothrombin with metal ions demonstrates the resulting colour shift on the same slide, which was slightly different from the original prothrombin solution as expected.

Introducing a chelator, EDTA, to protein solutions and exposing these solutions to the alumina surface, reduced the visible colour shifts that result. It was expected that EDTA would bind to metal ions in solution or, in solutions with low free ions, from ions initially bound to the protein molecules changing the conformation of the protein and potentially influencing binding. It is known that the Gla domain becomes unstable with the addition of EDTA because the Ca^{2+} dependent folding is disrupted, [5] hence supporting that resulting colour changes were not from metal ions interacting with the alumina surface.

A comparison of the surface colours showed that protein solutions with equal ratios of Ca ions and EDTA generated the same visible colour shift as the prothrombin control solution whereas, prothrombin solutions with Ca ions resulted in an increased OPL and stronger colour shift than the protein control solution. Prothrombin solutions with EDTA led to a decrease in OPL and a less significant colour change than the prothrombin control solution. Solutions with balanced EDTA and Ca ions resulted in no visual difference from the prothrombin control surface. Equal ratios likely completely mitigate any impact of the Ca ions, as EDTA is a

chelating agent with a high affinity for metal ions. The use of EDTA reduces the prothrombin binding when no additional or free metal ions exist in solution, likely removing metal ions from the Gla domain. The change in structure creates a layer with a reduced OPL, decreasing either the refractive index or thickness.

Based on the literature two possibilities exist for *in situ* binding of prothrombin. Firstly, the Gla residue maybe the binding mechanism or secondly, the metal ions positioned in the Gla domain expose some other binding site on the prothrombin molecule that is otherwise not exposed. [44] A combination of these two mechanisms is also possible. Work by Mann et al. [90] supports that the γ-carboxyglutamic acids bind to the membrane surfaces through the bridges containing calcium whereas Borowski et al. [91] demonstrated that the protein structure was altered adjacent to the Gla domain, exposing a site that binds directly to the membrane.

In addition to the carboxyl groups binding with hydroxides at the alumina surface, it is possible that higher valence Al ions at the device surface may displace Ca and Mg ions from the Gla domain or bind to available sites due to a higher charge and binding affinity. However, it was demonstrated that removing the Ca and Mg ions with EDTA was detrimental to the prothrombin structure and reduced the OPL from that of the prothrombin control solution. If immobilization occurred through only carboxyl groups, then less ions bound to the Gla domain would leave more sites for membrane binding with the addition of EDTA, hence a structural change in the protein molecule that prevents efficient binding seems more likely.

8.4.3 Liquid Chromatography Mass Spectrometry

HR-LC/MS provided mass data in the range of 100 to 100,000 amu. Polymer contamination was observed in the low mass region of prothrombin samples shown in Figure 8.21. Polyethylene glycol (PEG) and other ethoxylated polymers – detergent residues and surfactants – demonstrate a 44 amu ion mass series with some number (n) of repeat units $(OCH_2CH_2)n$. The polymer was likely some non-ionic surfactant such as tween, triton, polyethylene glycol or some ethylene oxide with a repeating group. The deconvolution of this region was unattainable, and therefore exact polymer masses are unknown. The most probable cause is that the polymer was an additive to the protein solution for a stabilizing agent. However, the polymer may be from plastic ware/silicon coatings, organic solvents, calibration solution, sample detergents, glassware or cleaning solutions used during manufacturing. [92] Analysis of the

low mass region between prothrombin control solutions and those exposed to the alumina surface, showed lower intensity signals from protein solutions after exposure to the alumina surface (see Figure 8.21). It is likely that some polymer remains immobilized on, or trapped in, the porous alumina film. The polymer may remain on the alumina film or may rinse off following the removal of the protein solution. When testing immobilization of different protein solutions in future work, LCMS may be a useful tool to confirm the approximate amount of low mass fragments that are present and binding to the surface to ensure the amount is minimal and has no contribution to the thickness increase and colour shift. Future tests could expose the device surface to an intentionally high amount of polymer contamination to see if any colour shift results.

In the higher mass region near prothrombin (~72000 amu) deconvoluted plots show three distinct peak sets in all prothrombin solutions tested. Each set of peaks is labelled as 1 to 3 from lowest to highest mass for this work with set 2 consistently displaying a significantly higher intensity than other sets (see Figure 8.22). The max peak shifting between control and exposed solutions is thought to be from preferential adsorption. Analysis of monosaccharide residue masses provides a viable explanation for the fragments of prothrombin leading to three sets of peaks. As previously mentioned from set 1 to set 2 peaks a consistent increase 291±2 amu was measured and between set 2 and 3 peaks an increase of 657±1 amu. The ~291 amu difference was likely from the addition or subtraction of one SA, N-acetylneuraminic acid (NeuAc), bound at a glycan region. The ~657 amu shift is likely a result of HexNAc – specifically N-acetylglucosamine – with a mass of 203 amu, NeuAc with a mass of 291 amu, and Hex – either fructose, galactose, glucose, or mannose – with a mass of 162 amu added at glycan regions. Therefore, accounting for a total mass increase of 656 amu. [93] Calculations employed underivatized monoisotopic monosaccharide residue masses. Prothrombin is a glycoprotein with three N-linked glycans at amino groups of asparagine 121, 143, and 416. [16,94,95] Theses N-linked glycans are complex (UnitProt Consortium 2017). This purified protein contains by weight ~90% amino acid residues with the remaining ~10% consisting of carbohydrates present include 2.8 to 4.1% Hexose (Hex), 2.3 to 3.4% sialic acid (SA), and 2.4 to 3.1% N-acetyl hexosamine (HexNAc). [83,96,97] Optimization of the LCMS parameters may reduce fragmentation of glycan groups off prothrombin molecules if these losses occur prior to or during analysis. It is also

possible that the prothrombin solution was non-homogeneous, contributing to the three sets of peaks.

Within the three peak sets, sub-peaks were observed. Set 2 was selected for sub-peak analysis as it contains the majority of protein and provides the most distinguishable shifts, shown in Figure 8.23. The mass spectrometry tool used to collect data assigns masses with an accuracy of 0.001 amu[98] and therefore, this shift between sub-peaks was deemed significant. The available databases provided no insight on the spacing within sets. In all protein solutions between 7 and 9 sub-peaks were visible within peak sets. Sub-peaks showed an average shift of 26±2 amu for all prothrombin concentrations run. The number of sub-peaks correlates with the number of metal ion binding sites that exist in the Gla domain. The explanation is that ions or molecules (i.e., Ca and Mg ions) are bound to areas of localized charge in the Gla domain during the isolation process. Changes in the type and number of ions bound to the Gla domain of a vitamin K-dependent protein are known to alter the conformational structure. When comparing peaks from the mass spectrometry data of all prothrombin solutions, preferential binding of prothrombin to the alumina surface took place at peaks in the range of 72416 to 72421 and 72468 to 72473 amu (see Table 8.7). It is likely that the Gla domains of these molecules contained optimal combinations of metal ions for binding to the alumina surface to occur. The coefficient of variation values for the normalized intensities of initial solutions and wash solutions were ≤ 0.33, demonstrating low variance. For improved accuracy, the area under each curve should be compared to account for the total intensity, however using the normalized intensity data provided a method to highlight the observed trend. An important concept that remains unknown is whether the optimal presence of metal ions bound to prothrombin allows these ions to be replaced more easily by aluminum ions at the surface, or if changes in the protein conformation with ion binding unmask membrane binding sites.

8.5 Future Work

Work conducted in this chapter looks at the adsorption of three vitamin K-dependent proteins; prothrombin, factor IX, and protein S. Numerous other vitamin K-dependent proteins exist and may reveal a device with greater sensitivity due to different protein-surface interactions and binding. Furthermore, exposing the corresponding antibody solution after the immobilized vitamin K-dependent protein may show differences in the limits of detection. Testing subsequent

wash solutions on surfaces coated with protein maybe indicative of changes in protein charge and stability based on protein removal, but this was outside the scope of this work.

With various metal ions in solution any changes to the pH of the solution may provide valuable insight on the protein-surface interaction. Both parameters would allow for conformational change of the protein including the sites exposed and net charge. However, it was excluded from this work because biologics on the device surface will be at a pH of ~7.4 and proteins are stable at this value. The use of radiolabelling with prothrombin solution containing metal ions would confirm if the change in OPL resulted from a change in the protein layer density or thickness. The first would show an increased radioactivity whereas the second would show no change in radioactivity.

A continuation of the protein modelling work has the potential to show protein interactions with the porous alumina layer. However, the theoretical models may not accurately depict the protein structure; let alone how it interacts with the surface.

Inductively coupled plasma mass spectrometry (ICPMS) may confirm that the mass spectrometry sub-peaks occurring at 26 amu increments result from metal ions and the type (e.g. Ca, Mg, Na, or Al), if amounts were above the detection limit. Solution preparation would be necessary to ensure a high purity solution initially and following steps to separate the protein from any attached ions.

Future work could apply Triton X-100, a non-ionic detergent that shows minor disruption of protein-protein interactions, to the affected areas in attempts to remove protein-proteins interactions. The binding of antigen and antibodies are typically unaffected. [99] If unsuccessful in achieving surface homogeneity stronger detergents of sodium deoxycholate and sodium dodecyl sulphate (SDS) could be used. These solutions have a greater ability to disrupt protein-protein interactions and may denature proteins. Antigen and antibody interactions are typically preserved but work by Herrmann et al. showed this is not always the case, as deoxycholate was found to reversibly change the antigen structure and did not bind to the corresponding antibody. [100] Protocol details for exposing these detergents can be found in the literature.[99]

8.6 Conclusions

1. This work compared the binding properties and sensitivities of three vitamin K-dependent proteins to the alumina surface. It was apparent by visible detection that

larger proteins of prothrombin and protein S had sensitivities of 0.2 μM, whereas factor IX had a sensitivity of 0.3 μM.

2. Tests exposing prothrombin solutions to the surface after mixing and diluting concentrations in ordinary micro-centrifuge tubes, showed a detection limit between 10 and 30 μg/ml (0.1 to 0.4 μM). However, a loss of 5 μg to the tube surface must be accounted for when ordinary tubes are used. Low bind tubes should be used for all sensitivity work.
3. When metal ions were introduced to prothrombin solutions prior to exposing to the alumina surface, larger colour shifts resulted from conformational changes. The strongest colour shifts were present with prothrombin solutions containing 2.5 and 1 mM Ca ions, closely followed by the 1mM Mg and 2.5 mM Ca mixed ion solution. The binding efficiency may have been impacted as well but further work is needed to confirm this.
4. The addition of near physiological Mg ion concentrations to a protein solution with 10 mM Ca stabilized prothrombin and generated a greater OPL and higher order colour than compared to protein solutions with only 10 mM Ca.
5. Prothrombin solutions showed one main set of peaks with 7 to 9 distinguishable sub-peaks separated by ~26 amu. The mass shift was likely from metal ions bound in the Gla domain, as the number of peaks correlates with the number of metal ion binding sites. Preferential adsorption of prothrombin to the alumina surface was noticeable in molecules containing 3 or more ions, where conformation was optimal.

Overall, this work demonstrates that the protein structure and thickness change were the most influential factors of the sensitivity and colour generation. The molecule size is self-determining however; the type and number of metal ions bound could be adjusted to produce larger shifts in the OPL, and ultimately the colour.

Chapter 9 – Prothrombin Surface Density and the Effect of Wash Solutions on the Alumina/Tantala Device

9.1 Introduction

Porous alumina membranes have been used in numerous biological applications[1] such as sensors,[2,3] protein separation,[4,5] and drug delivery.[6] The biocompatibility of alumina varies in the literature;[7,8] however aluminum and aluminum oxide biomaterials typically undergo surface modifications to increase biocompatibility and chemical stability,[9] or alter the structure.[4,5] The surface area of the alumina controls the amount of protein binding to the device, and pore size determines the ability of protein to bind within the porous film.[10] The alumina pore shape, dimension, and distribution can also influence how biologics interact with the surface.[11-13]

Methods to immobilize specific proteins to aluminum and aluminum oxide include exposing anions that have a high affinity and react with alumina (i.e. sulphates and phosphates).[14-17] Phosphates bind to reactive alumina sites[18-21] and reduce future reactions, increasing the film stability. Furthermore, studies using silanization and physical adsorption polyethyleneimine immobilization chemistries where polyethylene glycol (PEG) coatings were bound to the alumina surface showed significant improvements in anti-biofouling properties of the membrane.[22,23] For this device it is important to keep protein off the surface as alumina is catalytic and has demonstrated proteolytic degradation[24-26] resulting in the loss of biological activity.[27,28] Biomaterial implantation, or exposure to blood, is known to coat a surface with proteins almost immediately.[29-32] Therefore, bridging molecules will not only coat the surface but also act as a spacer between target proteins and the potentially catalytic surface.[33] Vitamin K-dependent proteins will be used as the bridging molecule to create stable binding and a consistent change in path length. Prothrombin, once immobilized on alumina, is stable due to the polyanionic nature of the Gla domain with a relatively high charge density that allows for binding at the N-terminus end while positioning the rest of the protein off the alumina surface (see Chapter 2 and Chapter 8 for more on the Gla domain and alumina binding mechanisms). The charged region of prothrombin binds to alumina through exposed surface hydroxyl groups or unorganized aluminum atoms exposing high-energy edge or defect sites.[34,35] Exposing a prothrombin solution, that creates a monolayer on the surface, is

expected to minimize protein degradation and non-specific binding to the alumina. Future work will require crosslinking to immobilize receptor proteins to the bridging molecules, and subsequent detection of the target protein by exposing the prepared surface to the biological sample of interest.

The purpose of this work was to better understand how prothrombin functions as a bridging molecule on the alumina surface. Radiolabelled prothrombin studies measured the surface density after slides were exposed to prothrombin solutions at various concentrations and times. The prothrombin concentration in solution that is required to form a monolayer on the surface was determined from adsorption isotherms along with the surface density. The experimental monolayer surface density was compared with the theoretical surface density values for short side and long side binding, to determine the binding orientation. Additionally, biological wash solutions were exposed to prothrombin-coated slides to determine the radioactivity that remains and gain insight into how biological solutions may impact the resulting device. Lastly, the colour shifts resulting after the exposure of different prothrombin concentrations to the alumina surface for 15 minutes were analysed. Colour coordinates were used to quantify the colours and a statistical analysis was carried out to determine if significant differences between the coordinates exists.

Understanding protein-surface interactions are critical to ensure non-specific proteins in the detection sample do not adhere to or remove the initial protein layer and result in a false positive or false negative, respectively.

9.2 Materials and Method

9.2.1 Device Preparation

9.2.1.1 Gold Conjugated Anti-prothrombin

The standard procedures for thin film device preparation were employed with anodization to stage b (see Chapter 3 – General Materials and Methods). Aluminum deposition was completed in the nanoFAB system for 610 seconds leading to a thickness of ~120 nm.

9.2.1.2 Radiolabelled Prothrombin

Tantalum thin films of 225 nm and aluminum films between 90 and 110 nm were sputtered onto silicon wafers. Anodization of the multilayer device was completed in 0.4 M phosphoric acid at a constant potential of 8 V until the aluminum layer was converted into porous alumina and the majority of tantala had formed. Growth of the tantala barrier layer results in a decline in current density to ≤0.7 mA/cm^2, where the anodization was stopped.

Hydrophobic 1 cm diameter outlines were created. Surfaces were equilibrated prior to conducting the test to ensure relatively consistent hydration. A 20 µl volume of TBS solution was pipetted within each 1 cm diameter circle and spread to the edge using the pipette tip. After 15 minutes the spots were removed with a pipette tip, rinsed with deionized water, and dried with oil free compressed air. Individual spots were placed in wells of BioLite 6 well plates (Fisher scientific company, Ottawa, ON) with TechniCloth® (Texwipe, Kernersville, NC) covering the bottom of each well. The cloth was then saturated with water (~0.5 ml).

9.2.2 Anti-prothrombin Gold Conjugation

The anti-prothrombin polyclonal antibody solution (ACOA, Aniara, West Chester, OH) was dialyzed to remove glycine from the solution and ensure the gold particles bind to proteins and not non-protein amino groups. Spectra/Por 6 Dialysis Membrane (Spectrum Labs, Rancho Dominguez, CA) with a molecular weight cut off of 10 kDa was used along with fresh dialysate solution of 0.1 M sodium phosphate at pH 7.4. A sodium phosphate solution was used for conjugation to ensure the solution was free of amino acids, protein additives (i.e. bovine serum albumin (BSA)), EDTA, primary amine containing buffers or components, (i.e. Tris) and strong buffers that might change the pH.

The gold nanoparticle kit contained: 10 nm NHS-activated gold particles, quenching solution, reaction buffer, and protein resuspension buffer. A storage buffer was made of 20 mM Tris at pH 8.0, 150 mM NaCl, 1% (w/v) BSA, and 0.025% (v/v) Tween20. Reagents were equilibrated to room temperature. The supplied protein resuspension buffer was used to dilute protein to a final concentration of ~1 mg/ml. The protein solution, 48 µl, was combined with 60 µl of reaction buffer. A portion of the protein mix from the previous step, 90 µl, was transferred to one of the vials containing gold nanoparticles and immediately mixed well by

pipetting up and down. The vial was incubated at room temperature for 2 hours. For some tests an incubation time between 4 and 6 hours was used for increased conjugation efficiency. Next, 10 µl of the quenching solution was added to the vial to stop the reaction and the vial was placed in a microcentrifuge for 1 hour using 17000g. The transparent supernatant was removed, typically 70-80 µl, and 100 µl of gold conjugate storage buffer was added to the vial. UV-VIS spectrums of the anti-prothrombin solution prior to and following conjugation were measured using a spectrophotometer. The control and conjugated anti-prothrombin spectrums were compared to ensure a ~3 nm shift occurred with the gold conjugation. The protein conjugate solution was stored at 4°C until use.

To confirm gold conjugation to antibodies the following procedure adapted from Moeremans et al. was completed. [36] Spots of 1 µl prothrombin dilutions, between 100 µg/µl and 10 ng/µl in PBS with 0.05 µg/µl of BSA, were placed on the nitrocellulose membrane (Bio-Rad Laboratories Inc., Hercules, CA) and was left to dry. The membrane was blocked for 30 minutes using 1% (w/v) dry milk (Smuckers Foods of Canada Corp., Markham, ON) in 1X PBS at room temperature and then incubated for at least 2 hours at room temperature with gold conjugate antibody diluted 1:10 with 0.2% dry milk in PBS. Blocking solution was used to wash 3 times for 5 minutes. The membrane was dried and observed.

9.2.3 Prothrombin Radiolabelling Materials

The chelator 2-*S*-(4-isothiocyanatobenzyl)-1,4,7-triazacyclononane-1,4,7-triacetic acid (*p*-SCN-Bn-NOTA) (Macrocyclics Inc., Plano, TX) was purified on RP-HPLC (H_2O, 0.2% trifluoroacetic acid (TFA)/acetonitrile (CH_3CN)) yielding *p*-SCN-Bn-NOTA·3TFA. The protein concentration was determined by using a Beckman Coulter DU 730 (Beckman Coutler, Brea, CA) to obtain A_{280} measurements with a percent solution extinction coefficient of $\varepsilon^{1\%}$=13.8 $(g/100ml)^{-1}cm^{-1}$ for prothrombin. [37] Amicon Ultra 0.5 ml 50k spin filters (Millipore Ltd., Etobicoke, ON) were used. The sodium bicarbonate ($NaHCO_3$), TBS, and sodium acetate (NaOAc) buffers were pre-treated with Chelex 100 resin and prepared freshly using trace metal grade salts. Econo-Pac 10DG (PD10) desalting columns (Bio-Rad Laboratories Inc., Hercules, CA) and thin layer chromatography (TLC) silica gel 60 F_{254} plates (Merck KGaA, Darmstadt, DE) were used. Radio-TLC plates were analyzed using a Bioscan AR-2000 TLC scanner. Miniprotean TGX precast 12% polyacrylamide gels with 50

µl wells (Bio-Rad Laboratories Inc., Hercules, CA) were used for sodium dodecyl sulphate-polyacrylamide gel electrophoresis (SDS-PAGE) analysis. Gels were evaluated on a BAS-IP MS 2025 phosphor imager plate (Fuji), which was read on a molecular dynamics Typhoon 9400. Radioactivity was measured on a Biodex Atomlab 400 dose calibrator. The gamma counter used for measuring radioactivity of the plates and the washings is a PerkinElmer Wizard² 2480 Automatic Gamma Counter (PerkinElmer, Woodbridge, ON). A $^{64}CuCl_2$ molecule in 0.1 N HCl (Mallinckrodt Institute of Radiology, St. Louis, MO) was used to label the prothrombin. The labelled protein solutions for the adsorption experiments were handled in Eppendorf® LoBind microcentrifuge tubes.

9.2.3.1 NOTA Conjugation

Prothrombin was conjugated to the macrocyclic chelator NOTA via isothiocyanate bioconjugation reaction with lysine residues of the protein. The prothrombin solution (TBS, 100 µl, 10 mg/ml) (ACOA, Aniara, West Chester, OH) was subjected to spin filtration to achieve buffer exchange into $NaHCO_3$ (0.15 M, pH 8.8). The resulting solution (500 µl, 852 µg, 1.7 mg/ml) was reacted overnight with *p*-SCN-Bn-NOTA·3TFA (0.112 mg, 141 nmol, 12 eq.) as a $NaHCO_3$ buffer solution at 37°C and 300 rpm. The solution was purified using a size exclusion column while achieving buffer exchange into TBS (pH 7.4). The solution containing the conjugate was split. A portion was aliquoted and used *1)* for LCMS analysis to establish the number of bound chelators and *2)* for assessing the device colour change of the modified protein.

The remainder was subjected to spin filtration into NaOAc (0.25 M, pH 5.5) suitable for ^{64}Cu labeling. The solution was aliquoted (100 µg in 61.4 µl buffer) and stored at −78°C.

9.2.3.2 ^{64}Cu Labeling

The prothrombin labelling was complete with Cu-64 (Mallinckrodt Institute of Radiology, St. Louis, MO). 126-163.8 MBq $[^{64}Cu]CuCl_2$ in 20 µl NaOAc buffer was added to the NOTA-prothrombin solution (100 µg, in 61.4 µl NaOAc). The reaction mixture was shaken for 1 hour at 30°C at 550 rpm. Next, 10 µl of an EDTA solution (50 mM) was added. After 10 minutes, the incorporation was determined using TLC (SiO_2, 50 mM EDTA, R_f(Protein)=0, R_f(^{64}Cu-EDTA)=1). The solution was purified using size exclusion

chromatography while achieving buffer exchange into TBS pH 7.4. The fraction containing the highest amount of radioactivity was used for the following experiments. The purity was determined using TLC and SDS-PAGE.

9.2.4 Protein Adsorption

9.2.4.1 Gold Conjugated Anti-prothrombin

Pipette 20 µl prothrombin solution (ACOA, Aniara, West Chester, OH) at 1 mg/ml onto the alumina surfaces for 30 minutes, remove excess, and rinse. Next pipette 20 µl gold conjugate anti-prothrombin on the same locations for 1.5 hours, remove excess, and rinse. For control, pipette 20 µl gold conjugated anti-prothrombin onto the surface for 1.5 hours, remove excess, and rinse. Examine surface using SEM to locate the conjugated nanoparticles on the device surface.

9.2.4.2 Radiolabelled Prothrombin

Prothrombin solutions were created in TBS at pH 7.4 with the desired final concentrations and ~100-1000 kBq of ^{64}Cu-NOTA-prothrombin. The final concentration of protein was adjusted using the specific activity. Pipette 20 µl of the protein solution onto the surface within the 1 cm diameter hydrophobic outline and incubate at room temperature (20±2°C) in a 100% relative humidity environment for the indicated time. After the indicated times the solution was removed by pipette and plates were washed three times with TBS buffer. The liquid and the alumina surfaces were transferred into separate scintillation vials and the associated radioactivities were measured. The formula below was employed to calculate the adsorbed protein surface density based on the radioactivity measured. The radioactivity of the combined wash solutions and the plates were counted separately.

$$A = \frac{\frac{(a_b)\,[Bq]}{a_b + a_w\,[Bq]} \times 100 \times m\,[\mu g]}{s\,[cm^2]} \qquad \text{Equation 9-1}$$

Where A is the resulting adsorbate surface density, a_b is the radioactivity bound, a_w is the radioactivity in the washed solution, m is the mass of protein in solution, and s is the surface area over which protein was exposed. All studies were done in triplicate.

9.2.4.3 Radioactivity Variation

The amount of radiolabelled prothrombin was varied in a starting 0.1 mg/ml prothrombin concentration and exposed to the device surface for 15 minutes. Solutions contained 2.3, 4.6, 9.2, 12.2, and 13.4 μg/ml of radiolabelled prothrombin, equivalent to 2, 4, 8, 11, and 12% modified prothrombin in solutions, respectively. The following adsorption isotherm was used to compensate for the slight increase in surface density with increasing concentration.

9.2.4.4 Adsorption Isotherm

The total prothrombin concentration in solution was varied from ~0.009 to 1 mg/ml. Incubation time on the device surface was fixed to 15 minutes. Curve fitting and graphics were done using Origin 2016.

9.2.4.5 Time Variation

The effect of changing the protein exposure time was determined for prothrombin concentrations of 0.105 and 1 mg/ml. The two prothrombin solutions were exposed to the device surface at separate locations, for incubation periods ranging from 5 minutes to 2 hours. After removal the radioactivities were measured and compared.

9.2.4.6 Protein Competition

A binary protein solution of 0.017 mg/ml labelled prothrombin and an increasing concentration from 0 to 1 mg/ml of human serum albumin (HSA) was exposed to the device surface. The incubation time was fixed to 15 minutes and the human serum albumin was not labelled. Salt-free lyophilized human serum albumin (Millipore Ltd., Etobicoke, ON) with a PI of 4.7 was used.

9.2.4.7 Wash-out of Radioactivity

Different wash solutions and incubation times were selected to expose the prothrombin-coated device to different protein solutions.

Human serum albumin and fetal bovine serum (FBS) – 1 hour

The prepared alumina surfaces were exposed to a total prothrombin concentration of ~0.02 or ~0.1 mg/ml for 30 minutes. The surfaces were then incubated with human serum albumin (5 mg/ml) or FBS for 1 hour. The same human serum albumin source for the protein competition test was used and FBS (Life Technologies, Grand Island, NY) was used at physiological concentrations with a pH of 7.2.

Human serum (HS) and Prothrombin – 1 and 12 hours

Alumina surfaces were exposed to a total protein concentration of ~0.1 and ~1.0 mg/ml incubated on the surface for 30 minutes were subsequently incubated with solutions of prothrombin (5 mg/ml) or human AB serum (Corning™, Manassas, VA) for 1 hour. Next, ~0.1 mg/ml prothrombin was exposed for 30 minutes, followed by wash solutions of prothrombin (5 mg/ml) or human AB serum for 1 and 12 hours.

9.2.5 Protein Analysis

UV-VIS spectrophotometer and bicinchonic acid protein assay (BCA) were used to determine the total concentration of protein in the solution following the purification step. A SDS-PAGE to check that one dominant band remained following modification as well as after the HS wash removed prothrombin.

9.2.6 Surface Analysis

FESEM in-lens detector and the EBSD were used to gather information on samples exposed to the conjugated anti-prothrombin. Variable angle ellipsometry (J.A. Woollam Co., Inc., Lincoln, NE) provided information on the alumina layer and the prothrombin binding. See Chapter 3 General Materials and Methods for details on SEM and ellipsometry techniques and parameters applied.

Images of visible surface colours were taken at 15° from the surface with an s-polarizing filter under controlled lighting parameters. Measuring colour coordinates from the surface images allowed for placement of colours on a CIE plot and a quantitative evaluation of the resulting colour shifts with varying concentrations. Using ImageJ software to analyze the colour coordinates over the full protein spot versus analyzing the colour at five locations provided coordinates with no significant difference ($p>0.4$). The method for analyzing

coordinates measured and compared the coordinates over five locations. Statistical analysis was complete on the chromaticity coordinates of x and y individually.

9.3 Results

9.3.1 Gold Conjugated Anti-prothrombin

The standard immunogold blotting protocol on a nitrocellulose membrane showed visible colours from strong pink to slight pink with pipetting and drying 1 µl drops of prothrombin solution between 100 µg/µl and 10 ng/µl. Furthermore, spectrophotometer results showed a peak shift after conjugation. Proving the conjugation was successful. Figure 9.1 to Figure 9.4 show SEM images of the porous alumina surfaces with and without a series of protein layers. Images were captured using the SEM with the in-lens detector and the EBSD.

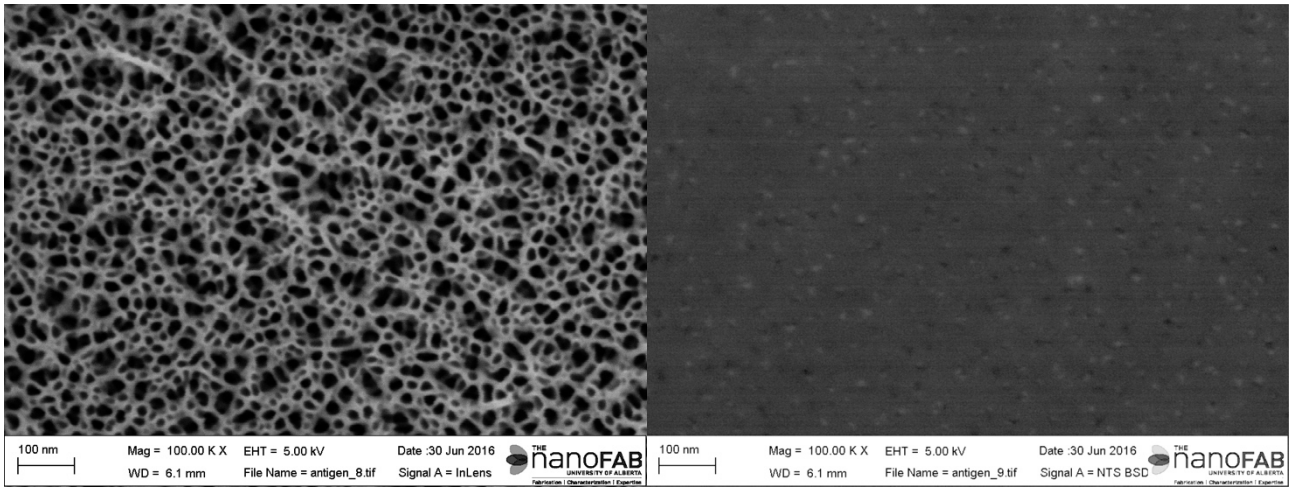

Figure 9.1. SEM in-lens image (left) and EBSD image (right) of the bare anodic alumina surface.

Bright and dark specks are visible in the backscattered detector images of the bare anodic alumina surface.

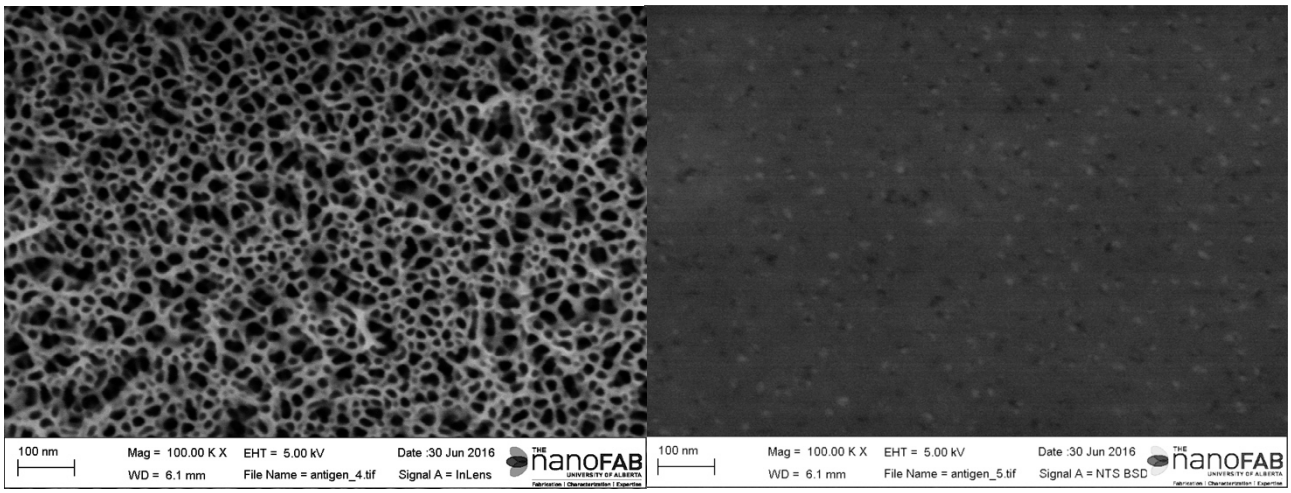

Figure 9.2. SEM in-lens image (left) and EBSD image (right) of the anodic alumina surface exposed to a prothrombin solution at 1 mg/ml for 15 minutes.

No differences in the surface images are present after prothrombin solution was immobilized. A complex was created with prothrombin immobilization and subsequently exposing gold conjugated anti-prothrombin, shown in 9.3.

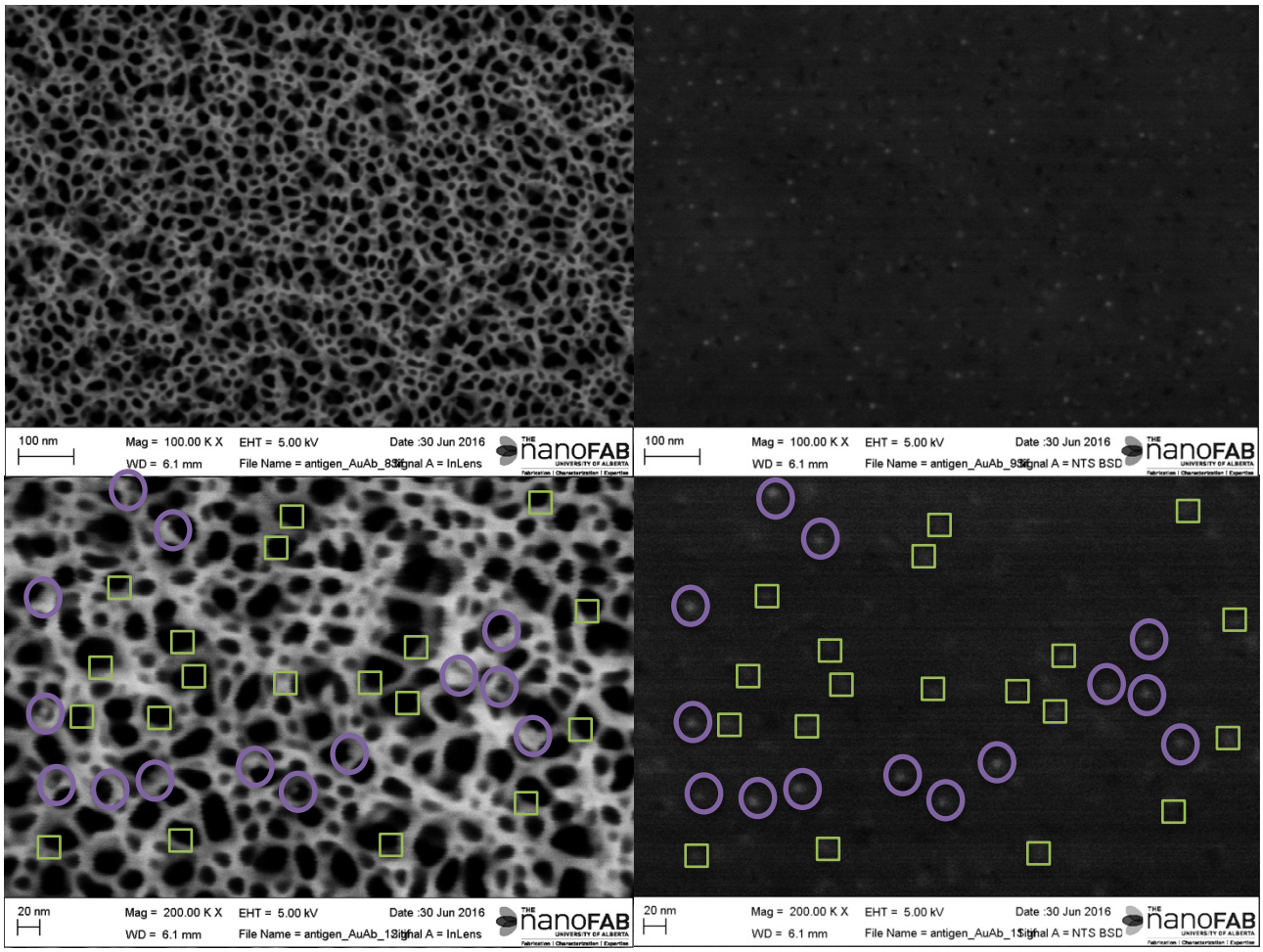

Figure 9.3. SEM in-lens image (left) and EBSD image (right) of the anodic alumina exposed to a prothrombin solution at 1 mg/ml for 15 minutes and following an anti-prothrombin solution with gold conjugated antibodies at ~0.6 mg/ml for 1.5 hours. A greater magnification was used for images shown in the bottom row to locate the gold nanoparticles. Gold nanoparticles are outlined with circles and bright specks are outlined with squares.

The negative control consisted of exposing only the gold conjugated anti-prothrombin to the alumina surface, shown in Figure 9.4.

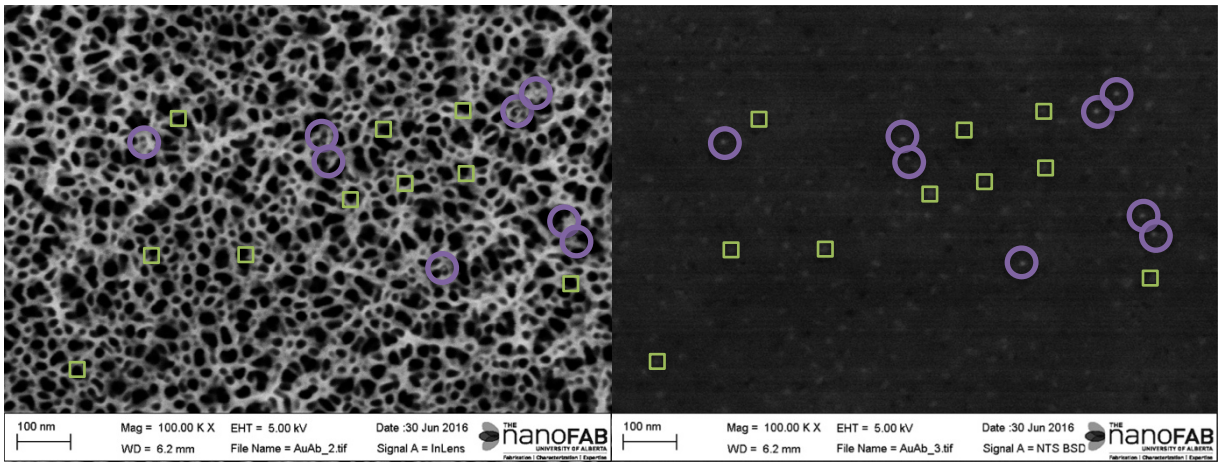

Figure 9.4. SEM in-lens image (left) and EBSD image (right) of the anodic alumina exposed to a gold conjugated anti-prothrombin solution at ~0.6 mg/ml for 1.5 hours. Gold nanoparticles are outlined with circles and bright specs are outlined with squares.

Immobilization of the conjugates anti-prothrombin to the bare alumina surface was apparent.

9.3.2 Characterization of Prepared Devices

Figure 9.5 shows the bare anodic surfaces of prepared slides used in radioactivity variation, adsorption isotherm, and time variation tests. Having a similar bare surface colour was important for quantifying colour shifts after protein exposure.

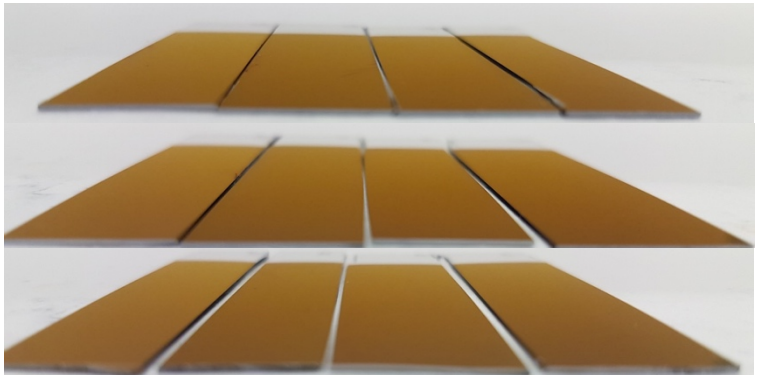

Figure 9.5. Prepared bare anodic slides used for radiolabel tests.

Ellipsometry results in Table 9.1 shows details of the bare surfaces that were exposed to radiolabelled prothrombin or the repeat tests with the original, unmodified, prothrombin solutions.

Table 9.1. Parameters of the bare anodic multilayer slides that were exposed to radiolabelled or original prothrombin solutions.

	Radiolabelled Prothrombin		Original Prothrombin	
Measured Parameter	Bare Slides ± SD		Bare Slides ± SD	
MSE	14	2	23	5
Alumina Thickness (nm)	94.8	0.1	94.0	0.3
Tantala Thickness (nm)	9.9	0.6	9.4	0.7
Percent Void (%)	45.9	1.1	47.6	0.4
η.370 nm	1.37	0.01	1.36	0.01
η.700 nm	1.36	0.01	1.35	0.01

A change in the mean standard error values was noted along with slight changes in the porous alumina percent void and refractive indices.

9.3.3 Prothrombin Radiolabelling

Mass spectrometry results of the modified prothrombin with *p*-SCN-Bn-NOTA chelator groups attached were confirmed by peak shifts corresponding to the chelator molecular weight (~450 Da), shown in Figure 9.6. The original prothrombin solution contains one main peak at ~72397 Da (see Chapter 8 for LCMS scans of control prothrombin solutions).

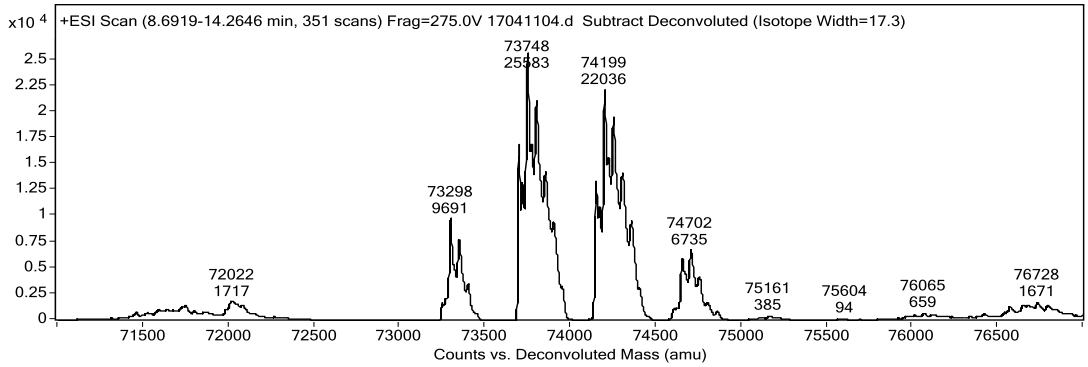

Figure 9.6. LCMS scan of prothrombin modified with a chelator, NOTA, bound to the protein for radiolabelling.

Prothrombin exposed to chelator groups show that the original prothrombin mass increases by a factor of ~450 Da with each group that binds. Four sets of distinguishable prothrombin masses were visible at 73298, 73748, 74199, and 74702 Da indicating successful modification. The last peak was measured from a different sub-peak than others, making it appears to shift >450 kDa in Figure 9.6. Prothrombin was bound to chelator groups, which then captured the ^{64}Cu radioactive label. Figure 9.7 shows the gel run to assess the purity and

mass of the modified prothrombin solution after binding the active label and completing the purification step.

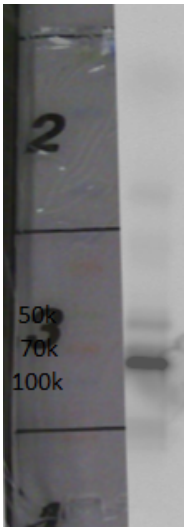

Figure 9.7. The resulting bands from an SDS-PAGE of the labelled prothrombin solution.

One predominant band from the labelled prothrombin solution exists between 75 and 85 kDa and implies little or no impact on size resulted with labelling.

9.3.4 Adsorption of Radiolabelled Prothrombin

9.3.4.1 Radioactivity Variation

Figure 9.8 compares the affinity of radiolabelled prothrombin and original prothrombin for the surface. All solutions had a total protein concentration of ~0.1 mg/ml, however the percent of ^{64}Cu labelled prothrombin differed in each.

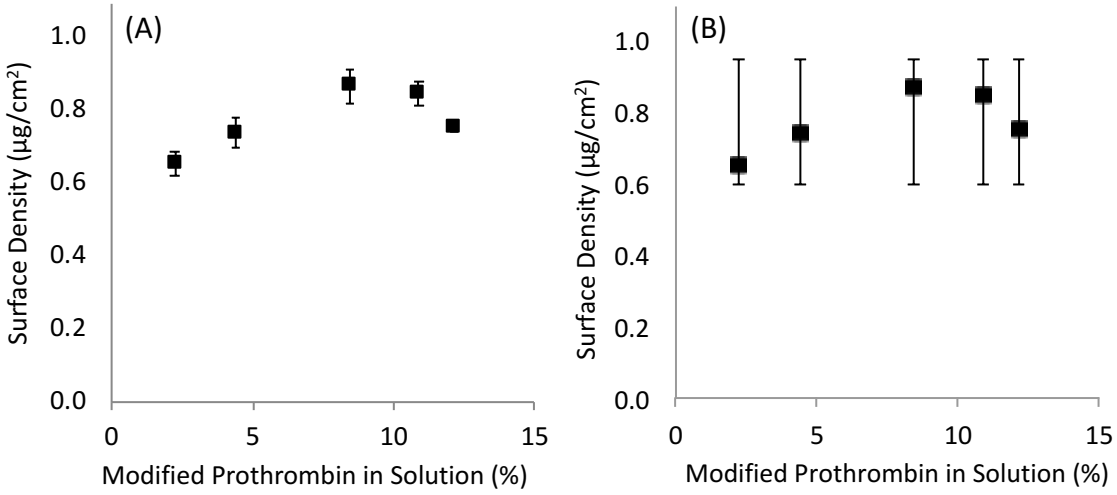

Figure 9.8. Prothrombin surface density with exposed solutions of 2, 4, 9, 11, and 12% modified prothrombin in a ~0.1 mg/ml prothrombin solution. Plot (A) shows the slope and intercept with standard deviations and plot (B) shows 2σ standard error lines from the mean.

Solutions in the range of 2 to 12% modified prothrombin in solution showed no significant difference in the resulting surface density. The slope and intercept standard deviations are inclusive of all data points and lie within 2σ from the mean. These results are indicative of the experimental error that can be expected from this procedure.

9.3.4.2 Adsorption Isotherm

The prothrombin surface density resulting from concentrations of 0.009, 0.014, 0.019, 0.024, 0.034, 0.045, 0.06, 0.1, 0.5, and 1 mg/ml exposed to the surface for 15 minutes is shown in Figure 9.9.

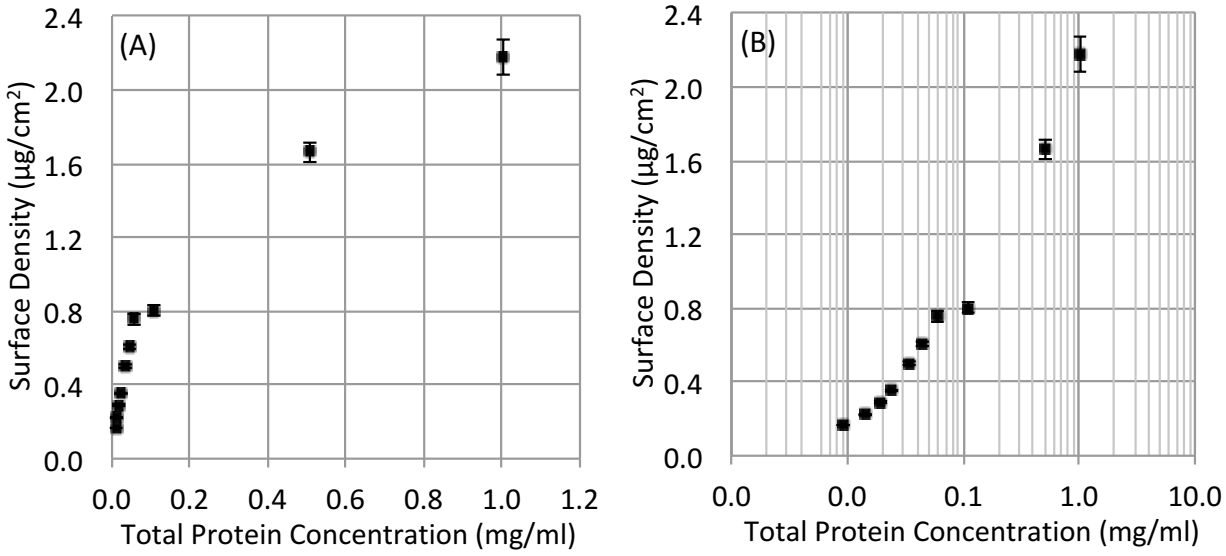

Figure 9.9. The adsorption isotherm for modified prothrombin on the alumina surface for 15 minutes shown as a standard (A) and log (B) plot.

Langmuir-Freundlich (LF) and Guggenheim-Anderson-de Boer (GAB) equations were used to model the adsorption data shown in Table 9.2. These equations led to determining when a monolayer of prothrombin forms on the surface, among other parameters.

Table 9.2. Parameters determined with fitting LF and GAB equations to the adsorption isotherm data. Adsorption data was collected using varying prothrombin concentrations exposed to the surface for 15 minutes

Measured Parameter	Langmuir-Freundlich (LF)	Guggenheim-Anderson-de Boer (GAB)
R^2	0.959	0.980
Monolayer Surface Density and Exposed Concentration	1.32±0.17 μg/cm^2, 0.2 mg/ml	1.49±0.35 μg/cm^2, 0.25 mg/ml
K (L/g)	17.3±4.3	12.76 weak K=0.38
Parameters in Equation	2	3

Ellipsometry data was used to model the multilayer slides and changes with protein immobilization on the surface. Radiolabelled prothrombin slides were evaluated as well as replicated slides using the original, unmodified, prothrombin solutions. The mean standard error and combined alumina and prothrombin thickness of devices with radiolabelled and original prothrombin solutions exposed are shown in Table 9.3. The assumption that alumina and prothrombin have the same refractive indices was made.

Table 9.3. Ellipsometry values with radiolabelled and original prothrombin solutions exposed to slide surfaces. It was assumed that alumina and prothrombin have the same refractive index for data generation.

Radiolabelled Prothrombin Slides					Original Prothrombin Slides				
Exposed II Concentration (mg/ml)	MSE ± SD		Alumina & II Thickness (nm) ± SD		Exposed II Concentration (mg/ml)	MSE ± SD		Alumina & II Thickness (nm) ± SD	
0.000	14	2	94.8	0.1	0.000	23	5	94.0	0.3
					0.003	19	5	97.0	1.0
					0.005	13	1	96.5	0.4
0.009	21	3	97.6	0.8	0.010	15	2	97.6	0.6
0.014	21	6	97.7	0.8	0.015	17	3	98.6	1.0
0.019	24	3	98.8	1.2					
0.024	24	5	99.9	0.7	0.025	22	5	100.0	1.2
0.034	40	6	102.9	0.9	0.035	25	6	100.0	1.2
0.040	47	0	104.1	0.3					
0.060	43	12	104.8	0.5	0.050	34	3	102.5	1.1
0.100	59	10	106.7	0.6	0.100	55	4	106.2	0.7
0.500	84	13	109.9	2.3	0.500	73	2	109.7	0.5
1.000	84	11	112.2	0.9	1.000	81	11	111.2	1.7

Greater MSE values were found when modelling the slides used for the original prothrombin solution compared to the slides used to collect radiolabelled data. However, after protein solutions were exposed, the radiolabelled prothrombin solution consistently led to slide models with greater error. Due to lower MSE values on slides exposed to the original prothrombin solution, the colour analysis was completed on these slides and correlated with the surface density measured on the radiolabelled prothrombin slides. Table 9.4 shows the

thickness increase from the bare device alumina with radiolabelled prothrombin and original prothrombin solutions exposed.

Table 9.4. The thickness increase and change in mean standard error (MSE) from the base device with various radiolabelled prothrombin and original prothrombin solutions exposed.

Radiolabelled Prothrombin Slides					Original Prothrombin Slides				
Exposed II Concentration (mg/ml)	Thickness Increase (nm) ± SD		ΔMSE ± SD		Exposed II Concentration (mg/ml)	Thickness Increase (nm) ± SD		ΔMSE ± SD	
					0.003	3.0	1.1	4.2	7.6
					0.005	2.5	0.5	9.3	5.5
0.009	2.9	0.8	7.8	3.5	0.010	3.5	0.6	7.4	5.6
0.014	2.9	0.9	7.0	6.2	0.015	4.5	1.0	6.0	6.3
0.019	4.0	1.2	10.8	3.5					
0.024	5.1	0.7	10.0	5.8	0.025	6.0	1.2	0.8	7.7
0.034	8.1	1.0	26.5	6.0	0.035	6.0	1.3	2.3	8.2
0.040	9.3	0.3	32.9	1.8					
0.060	10.0	0.5	29.8	12.1	0.050	8.5	1.1	11.7	6.4
0.100	11.9	0.6	45.5	10.2	0.100	12.2	0.7	32.6	6.6
0.500	15.1	2.3	70.0	13.0	0.500	15.6	0.6	50.1	5.9
1.000	17.4	0.9	70.3	11.1	1.000	17.1	1.7	58.5	12.6

The measured thickness increase of the surface layer provides an indication of how the protein layer changes. Note slight difference in the exposed prothrombin concentrations in Table 9.3 and Table 9.4.

Changes in the total alumina and protein thickness measured with ellipsometry were compared after exposing radiolabelled prothrombin and original prothrombin solutions at varying concentrations.

Table 9.5. Results of statistical analyzes on the effect of radiolabelled vs the original prothrombin solution exposed to slides on the change in thickness measured. Statistically significant results are in italics.

Exposed II Concentration (mg/ml)	Test	Alumina and Protein Thickness (nm) ± SD	vs. Test	p Value	ΔMSE ± SD
0.000	Radiolabelled II Original II	94.8 ± 0.1 94.0 ± 0.3	Original II	t(4)=3.801, *p=.019*	9 ± 6
0.009/0.010	Radiolabelled II Original II	97.6 ± 0.8 97.6 ± 0.6	Original II	t(4)=0.126, p=.905	6 ± 3
0.014/0.015	Radiolabelled II Original II	97.7 ± 0.8 98.6 ± 1.0	Original II	t(4)=-1.201, p=.296	4 ± 6
0.024/0.025	Radiolabelled II Original II	99.9 ± 0.7 100.0 ± 1.2	Original II	t(4)=-0.124, p=.907	2 ± 6
0.034/0.035	Radiolabelled II Original II	102.9 ± 0.9 100.0 ± 1.2	Original II	t(4)=3.203, *p=.033*	15 ± 7
0.044/0.050	Radiolabelled II Original II	104.1 ± 0.3 102.5 ± 1.1	Original II	t(4)=1.950, p=.146	12 ± 3
0.060/0.050	Radiolabelled II Original II	104.8 ± 0.5 102.5 ± 1.1	Original II	t(4)=2.722, p=.072	9 ± 9
0.100	Radiolabelled II Original II	106.7 ± 0.6 106.2 ± 0.7	Original II	t(4)=0.819, p=.459	4 ± 9
0.500	Radiolabelled II Original II	109.9 ± 2.3 109.6 ± 0.5	Original II	t(4)=0.168, p=.875	11 ± 11
1.000	Radiolabelled II Original II	112.2 ± 0.9 111.2 ± 1.7	Original II	t(4)=0.906, p=.461	3 ± 13

A significant difference was found between the initial alumina thicknesses of 94.8 and 94.0 nm (p=.019) with low variance in these samples and in the slides with exposed protein at 0.035 mg/ml (p=.033) with the greatest difference in mean standard error between slides compared. The other eight prothrombin concentrations exposed to slides showed no significant differences between the final thicknesses resulting from exposing radiolabelled and original prothrombin solutions.

9.3.4.3 Time Variation

Figure 9.10 shows the surface density changes with prothrombin incubation on the surface for 5, 15, 30 minutes, 1, and 2 hours. Total prothrombin concentrations of 0.1 and 1 mg/ml were utilized.

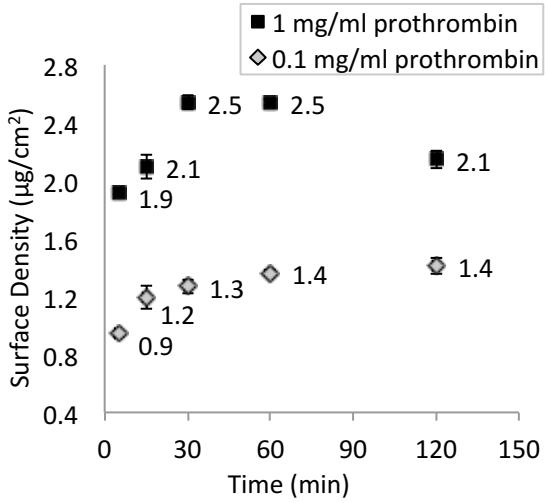

Figure 9.10. The effect of varying prothrombin incubation time on the resulting surface density. Total prothrombin concentrations of 0.1 and 1 mg/ml were used.

A comparison of the resulting surface density with exposing 0.1 and 1 mg/ml prothrombin solutions to the surface for 15 minutes in the adsorption isotherm (section 9.3.4.2) and time tests was completed using independent t-tests, shown in Table 9.6.

Table 9.6. Results of statistical analyzes on the effect of varying the test on the surface density with 0.1 and 1 mg/ml prothrombin solutions exposed to the surface for 15 minutes. Statistically significant results are in italics.

Exposed II Concentration (mg/ml)	Test	Surface Density (µg/cm²) ± SD	vs. Test	Independent t-test p Value
0.1	Time Adsorption	1.193 ± 0.113 0.903 ± 0.015	0.1 Adsorption	t(4)=4.381, *p=.012*
1	Time Adsorption	2.077 ± 0.783 2.259 ± 0.238	1 Adsorption	t(4)=-.383, p=.712

The 0.1 mg/ml prothrombin solution on the surface for 15 minutes leads to a surface density that is higher than in the adsorption isotherm experiment (p=.012) and the 1 mg/ml concentration shows no change in surface density (p=.712).

9.3.4.4 Protein Competition

A binary solution of human serum albumin and prothrombin was exposed to the surface to determine if prothrombin had a greater affinity for the surface. The competition curve is shown as "HSA Added" where human serum albumin was added to a low concentration of labelled prothrombin solution shown in Figure 9.11. The prothrombin adsorption isotherm from Figure 9.9 is shown on the plot as "Prothrombin Added" where prothrombin was added

to a low concentration of labelled prothrombin solution to reach the total protein in solution. Labelled prothrombin concentrations of 0.017 and 0.009 mg/ml were assumed identical for experiments with "HSA Added" and "Prothrombin Added", respectively.

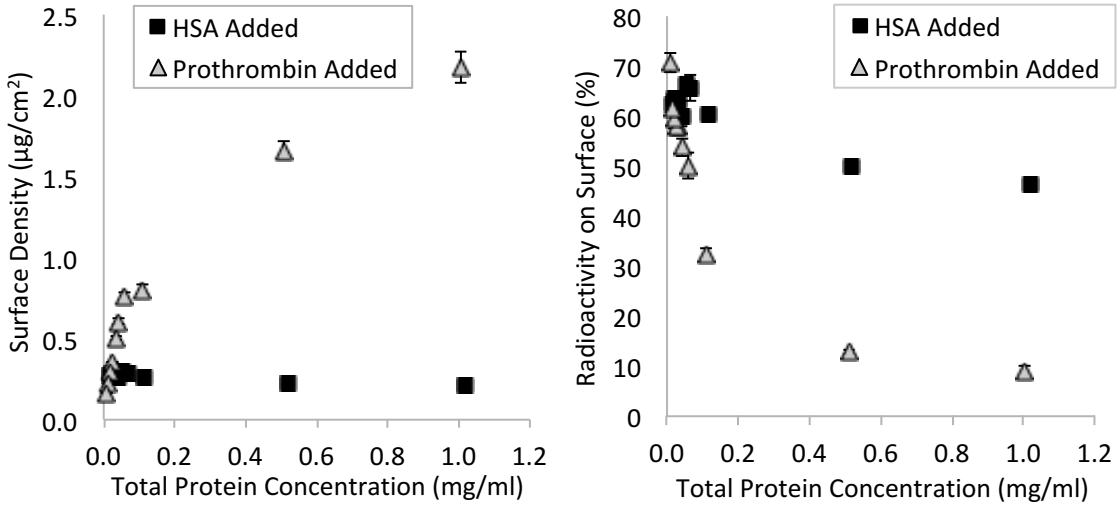

Figure 9.11. Prothrombin surface density that results with ~0.01 mg/ml labelled prothrombin in solution with human serum albumin (HSA) or prothrombin added to achieve the total protein concentration.

The addition of human serum albumin to the labelled prothrombin shows a comparison of prothrombin binding at low and high total protein concentrations with ratios of human serum albumin to prothrombin between 0 and 58. The percent of radioactive prothrombin on the surface from solutions with added prothrombin was lower than with human serum albumin added. Therefore, prothrombin competitively displaced the labelled prothrombin as expected if the process relies on negatively charged residues at the alumina interface.

Table 9.7 shows results of the statistical analysis on the effect of human serum albumin to prothrombin ratios in solutions exposed to the surface on the amount of radioactivity that binds. A one-way ANOVA test was used [$F(9,20)=18.556$, $p=.000$] and a subsequent Tukey post hoc test.

Table 9.7. Post hoc test results on the effect of human serum albumin to prothrombin ratios in solutions exposed to the surface on the amount of radioactive prothrombin that binds. (n=3)

Post Hoc Test Results			
Ratio HSA to II (mg/ml)	Amount of II Bound (%) ± SD	vs. Ratio	p Value
58	46.37 ± 0.25	29	p>.7
		5.8	*p<.001*
		2.9	*p<.001*
		2.0	*p<.001*
		1.3	*p<.001*
		0.9	*p<.001*
		0.6	*p<.001*
		0.3	*p<.001*
		0	*p<.001*
29	50.09 ± 0.95	5.8	*p<.005*
		2.9	*p<.001*
		2.0	*p<.001*
		1.3	*p<.01*
		0.9	*p<.001*
		0.6	*p<.005*
		0.3	*p<.001*
		0	*p<.001*
5.8	60.17 ± 2.64	2.9	p>.2
		2.0	p>.2
		1.3	p=1
		0.9	p>.9
		0.6	p>.9
		0.3	p>.8
		0	p>.9
2.9	65.7 ± 3.49	2.0	p=1
		1.3	p>.2
		0.9	p>.9
		0.6	p>.8
		0.3	p>.8
		0	p>.8
2.0	66.18 ± 2.21	1.3	p>.1
		0.9	p>.8
		0.6	p>.7
		0.3	p>.8
		0	p>.7
1.3	59.66 ± 4.41	0.9	p>.8
		0.6	p>.9
		0.3	p>.7
		0	p>.9
0.9	62.88 ± 2.67	0.6	p=1
		0.3	p=1
		0	p=1
0.6	62.22 ± 2.53	0.3	p=1
		0	p=1
0.3	63.5 ± 1.42	0	p=1
0	62.4 ± 3.04		

9.3.4.5 Wash-out of Radioactivity

Human serum albumin and FBS – 1 hour

Figure 9.12 shows the effect of human serum albumin (5 mg/ml) and FBS solutions after 1 hour of incubation on alumina surfaces previously exposed to prothrombin solutions of 0.02 and 0.1 mg/ml for 30 minutes.

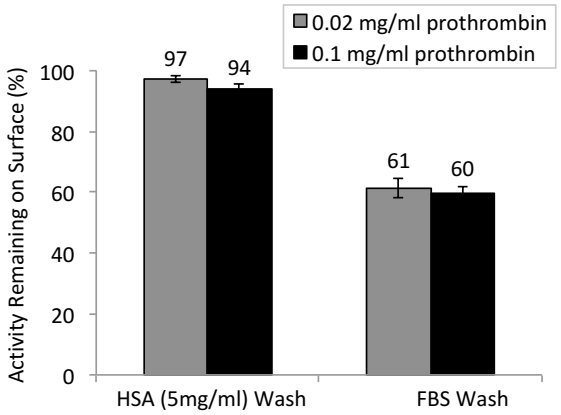

Figure 9.12. The effect of human serum albumin and FBS wash solutions for 1 hours on prothrombin activity. Prothrombin was immobilized from 0.02 and 0.1 mg/ml solutions for 30 minutes.

Washing with human serum albumin removed less prothrombin radioactivity and then FBS with immobilized prothrombin solutions of 0.02 and 0.1 mg/ml. A statistical analysis of the conditions tested in Figure 9.12 is shown in Table 9.8.

Table 9.8. Results of statistical analyzes on the effect of varying the exposed prothrombin solution on the radioactivity that remains bound after exposing wash solutions of human serum albumin and FBS. Statistically significant results are in italics.

Exposed II Concentration (mg/ml)	Test	Amount of II Bound (%) ± SD	vs.	Independent t-test p Value
0.02 0.1	HSA	97.08 ± 1.01 93.96 ± 1.39	0.02 vs 0.1 HSA	t(4)=3.142, *p=.035*
0.02 0.1	FBS	61.46 ± 4.05 59.64 ± 2.69	0.02 vs. 0.1 FBS	t(4)=0.650, p=.551

No significant decrease in the radiolabelled activity on the alumina surface was noticed between prothrombin concentrations of 0.02 and 0.1 mg/ml when exposed to FBS (p=.551) whereas exposure to human serum albumin showed a significant difference (p=.035).

HS and II – 1 and 12 hours

Figure 9.13 shows changes in bound prothrombin radioactivity when a subsequent wash with prothrombin solution (5 mg/ml) with 1 hour of incubation time. The initial prothrombin layer was bound to the surface from prothrombin solutions of 0.1 and 1 mg/ml for 30 minutes.

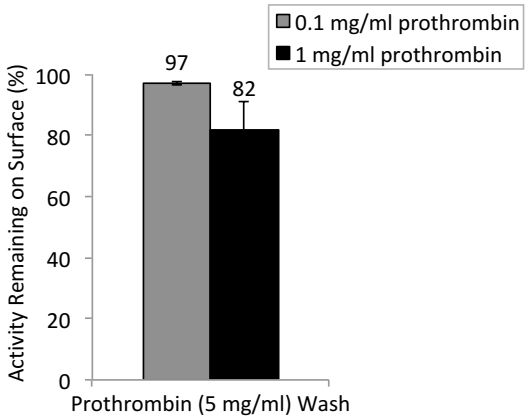

Figure 9.13. The effect of prothrombin wash solution at 5 mg/ml for 1 hour on prothrombin activity. Prothrombin was immobilized from 0.1 and 1 mg/ml solutions for 30 minutes.

A greater decrease and variance in radioactivity resulted after washing surfaces with 1 mg/ml prothrombin solutions used for immobilization. Prothrombin (5 mg/ml) and HS wash solutions were exposed to prothrombin-coated alumina (0.1 mg/ml for 30 minutes) for 1 hour and 12 hours, as shown in Figure 9.14.

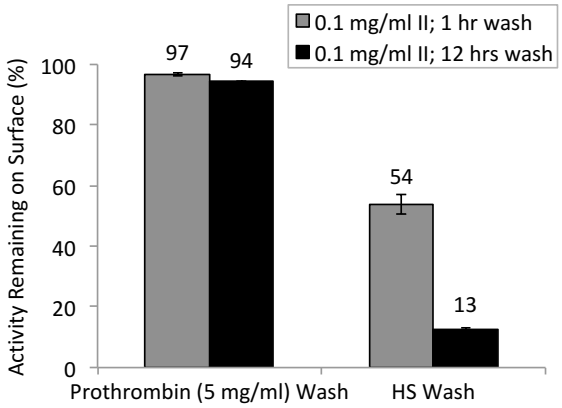

Figure 9.14. The effect of prothrombin wash solution at 5 mg/ml and HS wash solution at physiological concentrations for 1 hour and 12 hours on prothrombin activity. Prothrombin was immobilized from a 0.1 mg/ml solution for 30 minutes.

Wash solutions of prothrombin and HS with incubation for 1 and 12 hours showed decreases in radioactivity. For the prothrombin wash solution, the decrease after 12 hours was minor, whereas the HS wash solution showed a drastic decrease in activity after 1 hour and

even more after 12 hours. A gel was run of the removed HS wash solution in attempts to determine the size of active prothrombin removed from the surface. The resulting SDS-PAGE is shown in Figure 9.15.

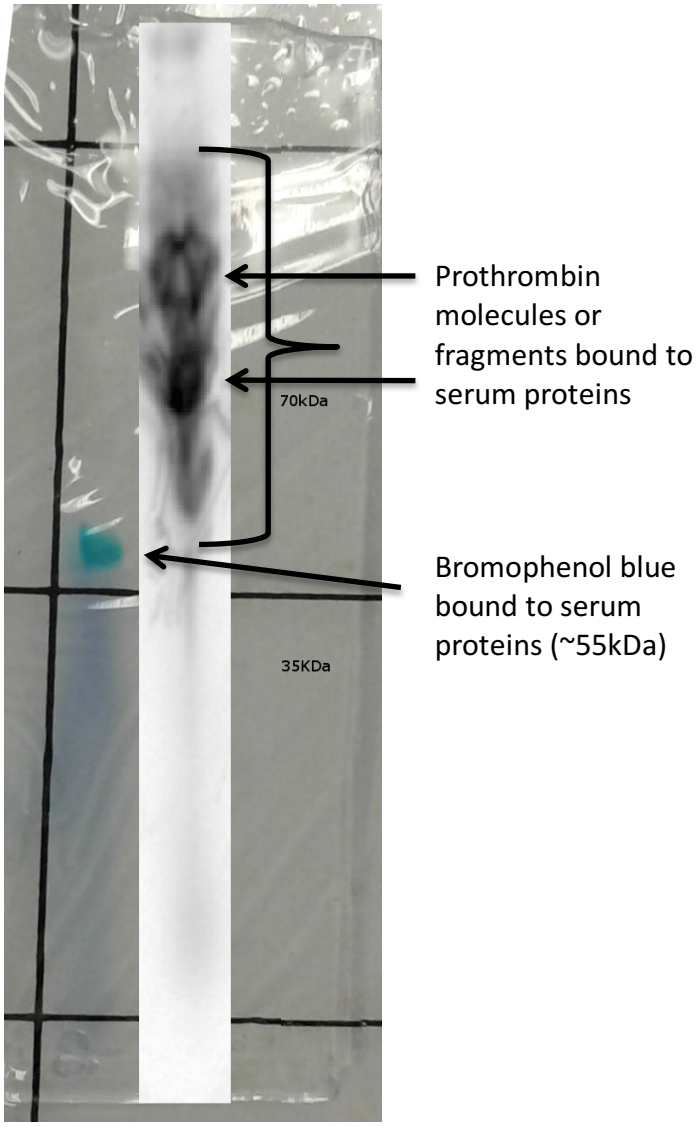

Figure 9.15. The resulting band from an SDS-PAGE of the HS wash solution after exposure to the prothrombin-coated surface shows a complex mixture of protein and fragments.

Bromophenol blue showed strong adsorption at ~55 kDa to serum proteins in solution. It is likely that these proteins also bind to the radiolabelled fragments released from the surface. The smear reached as low as 45 and as high as 95 kDa (see Figure 9.15) Regions with dominant bands include 65-75 kDa and 85-95 kDa. Each copper label was 63.5 Da and no free copper was found, as the SDS buffer showed no radioactivity after completing the gel.

Figure 9.16 compares the percent radioactivity remaining after various wash solutions on an immobilized prothrombin monolayer. Wash solutions were exposed for 1 hour and include human serum albumin and FBS from Figure 9.12, and prothrombin and HS from Figure 9.14.

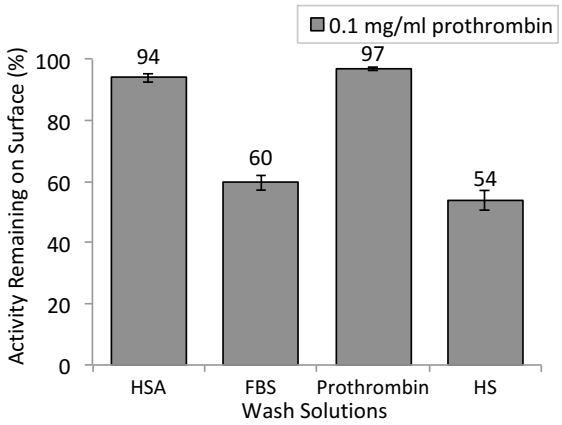

Figure 9.16. Prothrombin radioactivity change with different wash solutions after forming a monolayer of prothrombin on the surface. Wash solutions were human serum albumin at 5 mg/ml, prothrombin at 5 mg/ml, FBS, and HS for 1 hour.

A summary of the radioactivity remaining after various wash solutions are summarized in Table 9.9.

Table 9.9. The radioactivity remaining on surfaces coated with 0.1 mg/ml prothrombin solutions and subsequently exposed to varying wash solutions for 1 and 12 hours.

Wash Solution	Activity Remaining with 1 Hour Wash ± SD (%)	Activity Remaining with 12 Hours Wash ± SD (%)
human serum albumin	94±1.4	-
FBS	60±2.3	-
Prothrombin	97±0.6	94±0.5
HS	54±3.3	13±0.8

A minor reduction in prothrombin radioactivity on the device surface results with prothrombin and human serum albumin washes, and more significant reductions with FBS and HS washes.

9.3.5 Quantification of Immobilized Prothrombin with Colour Coordinates

9.3.5.1 Alumina Thickness of ~95 nm

Surface colours generated on the slides exposed to radiolabelled prothrombin while determining the protein surface density were compared to the slides created with exposing the

original prothrombin solution. Images shown in Figure 9.17 were captured using the custom optics system.

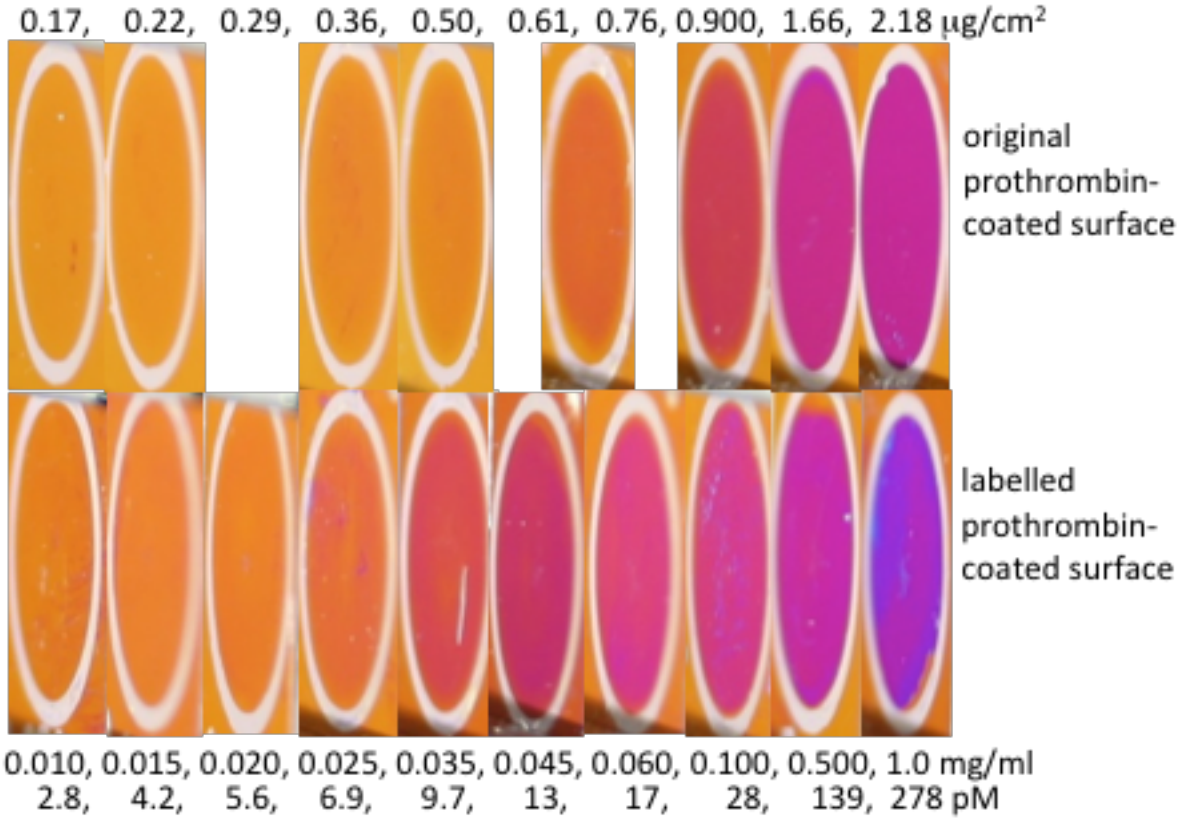

Figure 9.17. Images of surfaces exposed to labelled (bottom) and original prothrombin solutions (top). The exposed prothrombin concentrations are shown under the corresponding images and the resulting surface densities above.

Figure 9.18 shows the surface colours generated with exposing original prothrombin solutions, with no modification or label, at all concentrations tested including those used for the comparison in Figure 9.17. Concentrations of prothrombin were between 0.003 and 1 mg/ml.

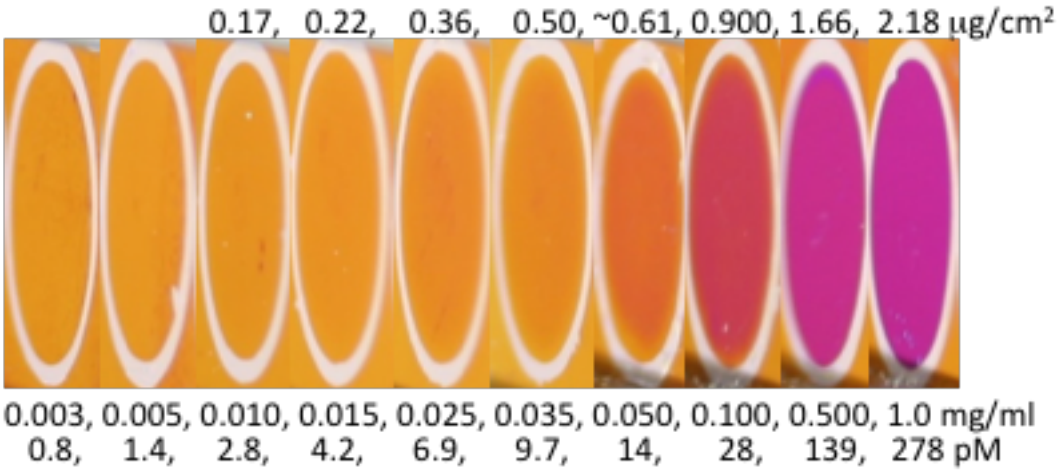

Figure 9.18. Images captured of the slide surfaces after original prothrombin solutions were exposed to the surface. The exposed prothrombin concentrations are shown under the corresponding image and the resulting surface densities above.

RGB colour coordinates were collected and converted into Yxy coordinates to analyze the base slide as well as the colour shift following exposure and adsorption of each concentration. The base colour coordinates for triplicate slides are provided in Table 9.10.

Table 9.10. Yxy colour coordinates of the bare surfaces for slides with a 95 nm alumina layer. Coordinates were collected from four points around the exterior of each protein spot. (n=3 for average of set, 10 spots per set)

Bare Surface	Colour Coordinates					
	Y ± SD		x ± SD		y ± SD	
Set 1	39.003	4.379	0.491	0.012	0.432	0.009
Set 2	37.024	2.496	0.494	0.008	0.430	0.005
Set 3	34.917	2.242	0.499	0.008	0.427	0.006
Average of Sets	36.981	3.596	0.494	0.010	0.430	0.007

Additional colour coordinates for surfaces following exposed protein concentrations are provided in Table 9.11

Table 9.11. Yxy colour coordinates for slides with 95 nm alumina layers with immobilized protein layers created by placing ten prothrombin concentrations on the surface for 15 minutes. Coordinates were collected from five points within each protein spot for each set. (n=3 for average of sets)

Exposed Concentration (mg/ml) and Coordinate ±SD		Colour Coordinates							
		Set 1		Set 2		Set 3		Average of Sets	
0.003	x ± SD	0.493	0.001	0.498	0.004	0.510	0.000	0.500	0.007
0.005		0.494	0.002	0.500	0.000	0.498	0.004	0.497	0.002
0.010		0.494	0.002	0.498	0.004	0.502	0.004	0.498	0.003
0.015		0.497	0.003	0.502	0.004	0.512	0.004	0.504	0.006
0.025		0.503	0.003	0.510	0.000	0.520	0.006	0.511	0.007
0.035		0.506	0.002	0.510	0.000	0.520	0.000	0.512	0.006
0.050		0.530	0.001	0.530	0.000	0.530	0.000	0.530	0.000
0.100		0.485	0.010	0.500	0.000	0.490	0.006	0.492	0.006
0.500		0.415	0.003	0.410	0.000	0.404	0.005	0.410	0.004
1.000		0.390	0.002	0.354	0.005	0.390	0.006	0.378	0.017
0.003	y ± SD	0.433	0.001	0.424	0.005	0.420	0.000	0.426	0.005
0.005		0.433	0.001	0.430	0.000	0.430	0.000	0.431	0.001
0.010		0.432	0.002	0.430	0.000	0.424	0.005	0.429	0.003
0.015		0.428	0.003	0.420	0.000	0.410	0.000	0.419	0.007
0.025		0.418	0.006	0.408	0.004	0.386	0.005	0.404	0.013
0.035		0.419	0.003	0.406	0.005	0.386	0.005	0.404	0.014
0.050		0.359	0.006	0.380	0.000	0.358	0.004	0.366	0.010
0.100		0.284	0.008	0.308	0.004	0.290	0.006	0.294	0.010
0.500		0.228	0.002	0.220	0.000	0.220	0.000	0.223	0.004
1.000		0.210	0.001	0.188	0.004	0.210	0.006	0.203	0.010

Table 9.12 shows results of the statistical analysis on the effect of exposed prothrombin concentration on the average surface colour. The surface colour was quantified with chromaticity coordinates (x and y) and compared to difference in the measured surface density. The coordinates were analyzed based on the Levene's test results, the x coordinates using an independent t-test [$t(7.470)=11.939$, $p=.000$] and the y coordinates using a one-way ANOVA test [$F(9,20)=195.586$, $p=.000$].

Table 9.12. Results of the statistical analysis of the effect of exposed prothrombin concentration on the average chromaticity coordinates collected from surface images. The base alumina layer was 95 nm. Statistically significant results are in italics. (n=3 spots, 5 locations within each spot)

Post Hoc Test Results			
Exposed Prothrombin Concentration and Surface Density	vs. Concentration (mg/ml)	x Coord. p Values	y Coord. p Values
0.003 mg/ml	0.005	p>.9	p=1
	0.010	p=1	p=1
	0.015	p=1	p>.9
	0.025	p>.8	p>.3
	0.035	p>.7	p>.3
	0.050	p>.1	*p<.001*
	0.100	p>.9	*p<.001*
	0.500	*p<.005*	*p<.001*
	1.000	*p<.05*	*p<.001*
0.005 mg/ml	0.010	p=1	p=1
	0.015	p>.8	p>.9
	0.025	p>.4	p>.1
	0.035	p>.3	p>.1
	0.050	*p<.05*	*p<.001*
	0.100	p>.9	*p<.001*
	0.500	*p<.005*	*p<.001*
	1.000	*p<.05*	*p<.001*
0.010 mg/ml 0.017 ± 0.00 μg/cm^2	0.015	p>.9	p>.9
	0.025	p>.5	p>.2
	0.035	p>.3	p>.1
	0.050	*p<.05*	*p<.001*
	0.100	p>.9	*p<.001*
	0.500	*p<.001*	*p<.001*
	1.000	*p<.05*	*p<.001*
0.015 mg/ml 0.022 ± 0.01 μg/cm^2	0.025	p>.9	p>.7
	0.035	p>.8	p>.7
	0.050	p>.1	*p<.001*
	0.100	p>.6	*p<.001*
	0.500	*p<.005*	*p<.001*
	1.000	*p<.05*	*p<.001*
0.025 mg/ml 0.036 ± 0.01 μg/cm^2	0.035	p=1	p=1
	0.050	p>.2	*p<.05*
	0.100	p>.3	*p<.001*
	0.500	*p<.005*	*p<.001*
	1.000	*p<.05*	*p<.001*
0.035 mg/ml 0.050 ± 0.01 μg/cm^2	0.050	p>.2	*p<.05*
	0.100	p>.2	*p<.001*
	0.500	*p<.005*	*p<.001*
	1.000	*p<.05*	*p<.001*
0.05 mg/ml between 0.061 ± 0.02 and 0.076 ± 0.03 μg/cm^2	0.100	p>.05	*p<.001*
	0.500	*p<.005*	*p<.001*
	1.000	*p<.05*	*p<.001*
0.1 mg/ml 0.90 ± 0.03 μg/cm^2	0.500	*p<.005*	*p<.001*
	1.000	*p<.05*	*p<.001*
0.5 mg/ml 1.66 ± 0.050 μg/cm^2	1.000	p>.4	p>.4
1 mg/ml 2.18 ± 0.22 μg/cm^2			

The average chromaticity coordinates for concentrations were plot on a CIE diagram shown in Figure 9.19.

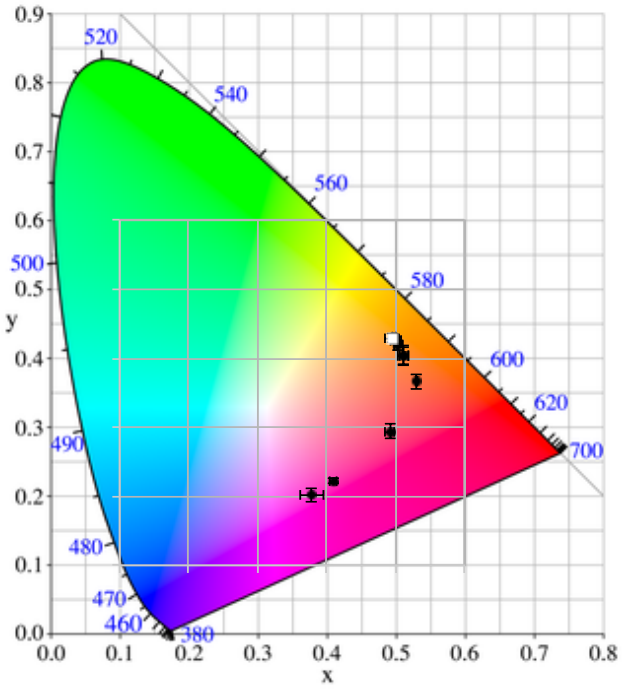

Figure 9.19. Average chromaticity coordinates and standard deviations are shown on the CIE chart for 95 nm alumina layers exposed to various prothrombin concentrations. With increasing exposed concentration and colour order the trajectory moves from the tan/orange region toward the purple region. Increasing concentrations of 0.003, 0.005, 0.01, 0.015, 0.025, 0.035, 0.05, 0.1, 0.5, and 1.0 mg/ml are mapped however the lowest six concentrations are difficult to separate on the plot (upper right markers). The white marker shows the average bare surface coordinates.

Markers show the Yxy coordinates from the base surface colour (white) and the colour shifts from protein binding to the surface (black) with error bars showing standard deviation. Coordinates for concentrations of 0.003, 0.005, 0.01, 0.015, 0.025, and 0.035 mg/ml were hard to distinguish on the CIE plot. The coordinates for the remaining concentrations of 0.05, 0.1, 0.5, and 1 mg/ml were visibly different on the CIE plot, and moving towards the lower left blue region.

Table 9.13 shows results of the statistical analysis on the effect of exposed prothrombin concentration on the set 1 surface colour coordinates. The x and y coordinates were analyzed using independent t-test's and showed [t(15.981)=36.839, p=.000] and [t(15.750)=126.796, p=.000] respectively.

Table 9.13. Results of the statistical analysis on the effect of exposed prothrombin concentration on set 1 chromaticity coordinates collected from the surface images. The base alumina layer was 95 nm. Statistically significant results are in italics and differences that became significant when analyzing the set 1 coordinates are in bold. (n=5 locations within one spot)

Post Hoc Test Results			
Exposed Prothrombin Concentration (mg/ml)	vs. Concentration (mg/ml)	x Coord. p Values	y Coord. p Values
0.003	0.005	p>.9	p=1
	0.010	p=1	p=1
	0.015	p>.7	p=1
	0.025	***p=.05***	p>.5
	0.035	***p<.005***	p>.5
	0.050	***p<.001***	*p<.001*
	0.100	p>.7	*p<.001*
	0.500	*p<.001*	*p<.001*
	1.000	*p<.001*	*p<.001*
0.005	0.010	p=1	p>.9
	0.015	p>.9	p>.2
	0.025	***p>.05***	p>.05
	0.035	***p<.005***	***p<.005***
	0.050	*p<.001*	*p<.001*
	0.100	p>.6	*p<.001*
	0.500	*p<.001*	*p<.001*
	1.000	*p<.001*	*p<.001*
0.010	0.015	p>.9	p>.9
	0.025	***p<.05***	p>.3
	0.035	***p<.005***	p>.2
	0.050	*p<.001*	*p<.001*
	0.100	p>.7	*p<.001*
	0.500	*p<.001*	*p<.001*
	1.000	*p<.001*	*p<.001*
0.015	0.025	p>.3	p>.8
	0.035	***p<.05***	p>.7
	0.050	***p<0.001***	*p<.005*
	0.100	p>0.5	*p<.001*
	0.500	*p<.001*	*p<.001*
	1.000	*p<.001*	*p<.001*
0.025	0.035	p>.8	p=1
	0.050	***p<.001***	*p<.05*
	0.100	p>.1	*p<.001*
	0.500	*p<.001*	*p<.001*
	1.000	*p<.001*	*p<.001*
0.035	0.050	***p<.001***	*p<.05*
	0.100	p>.1	*p<.001*
	0.500	*p<.001*	*p<.001*
	1.000	*p<.001*	*p<.001*
0.050	0.100	p<.01	*p<.001*
	0.500	*p<.001*	*p<.001*
	1.000	*p<.001*	*p<.001*
0.100	0.500	*p<.01*	*p<.001*
	1.000	*p<.001*	*p<.001*
0.500	1.000	*p<0.001*	p>.4
1.000			

Testing colour coordinates from one set of slides, measured from within one protein spot for each exposed concentration, showed an increase in the number of statistically significant results between concentrations for x and y coordinates.

9.3.5.2 Alumina Thickness of ~100 nm

The colours resulting from prothrombin tests in Chapter 8 were compared as they showed a lower limit of detection. It was assumed that a slight increase in alumina thickness had no effect on protein adsorption and binding, as the surface density calculated on ~95 nm alumina films was also applied to ~100 nm alumina films. Figure 9.20 shows surface colours after exposing prothrombin solutions between concentrations of 0.015 to 0.100 mg/ml for 15 minutes.

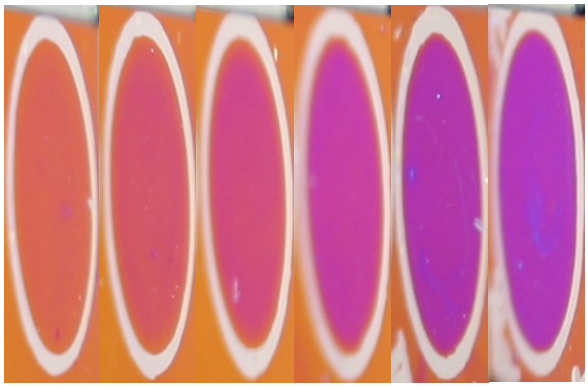

Figure 9.20. Images of the surfaces after prothrombin solutions were exposed to the surface. Exposed prothrombin concentrations are shown under the corresponding images.

The base colour coordinates for triplicate sets used in the slides with ~100 nm of alumina is provided in Table 9.14.

Table 9.14. Yxy colour coordinates of the bare surfaces for sides with ~100 nm alumina layers. Coordinates were collected from four points around the exterior of each protein spot. (n=3 for average of set, 6 spots per set)

Bare Surface	Colour Coordinates		
	Y ± SD	x ± SD	y ± SD
Set 1 Slides	31.498 3.421	0.466 0.007	0.383 0.024
Set 2 Slides	36.114 3.066	0.455 0.019	0.393 0.008
Set 3 Slides	35.374 3.245	0.463 0.007	0.402 0.008
Average of Sets	34.329 3.827	0.462 0.013	0.393 0.017

Additional colour coordinates for surfaces following exposed protein concentrations are provided in Table 9.15.

Table 9.15. Yxy colour coordinates for slides with 100 nm alumina layers with immobilized protein layers created by placing six prothrombin concentrations on the surface for 15 minutes. Coordinates were collected from five points within each protein spot for each set. (n=3 for average of sets)

Exposed Concentration (mg/ml) and Colour Coordinates ± SD		Colour Coordinates							
		Set 1		Set 2		Set 3		Average of Sets	
0.015	x ± SD	0.453	0.005	0.453	0.007	0.470	0.005	0.459	0.008
0.025		0.439	0.004	0.437	0.004	0.452	0.005	0.443	0.007
0.035		0.413	0.007	0.385	0.006	0.419	0.009	0.406	0.015
0.050		0.354	0.004	0.385	0.006	0.385	0.006	0.375	0.015
0.080		0.328	0.009	0.363	0.003	0.370	0.005	0.353	0.018
0.100		0.326	0.010	0.358	0.007	0.384	0.006	0.356	0.023
0.015	y ± SD	0.354	0.007	0.348	0.007	0.384	0.008	0.362	0.016
0.025		0.321	0.007	0.327	0.003	0.337	0.012	0.328	0.006
0.035		0.281	0.009	0.265	0.006	0.295	0.006	0.280	0.012
0.050		0.231	0.005	0.266	0.006	0.262	0.005	0.253	0.016
0.080		0.205	0.008	0.239	0.003	0.245	0.004	0.230	0.018
0.100		0.206	0.011	0.231	0.009	0.256	0.009	0.231	0.020

Results of a statistical analysis on the effect of exposed prothrombin concentration on the average surface colour quantified using coordinates, are shown in Table 9.16. One-way ANOVA tests for x and y coordinates showed [$F(5,12)=16.657$, $p=.000$] and [$F(5,12)=24.997$, $p=.000$] respectively.

Table 9.16. Results of the statistical analysis of the effect of exposed prothrombin concentration on the average chromaticity coordinates collected from images of the device surface. The base alumina layer was 100 nm. Statistically significant results are in italics. (n=3 spots, 5 locations within each spot)

Post Hoc Test Results			
Exposed Prothrombin Concentration (mg/ml)	vs. Concentration (mg/ml)	x Coord. p values	y Coord. p Values
0.015	0.025	p>.8	p>.3
	0.035	*p<.05*	*p<.005*
	0.050	*p<.005*	*p<.001*
	0.080	*p<.001*	*p<.001*
	0.100	*p<.001*	*p<.001*
0.025	0.035	p>.2	p>.05
	0.050	*p<.01*	*p<.005*
	0.080	*p<.005*	*p<.001*
	0.100	*p<.005*	*p<.001*
0.035	0.050	p>.3	p>.5
	0.080	*p=.05*	p>.05
	0.100	p>.05	p>.05
0.050	0.080	p>.7	p>.6
	0.100	p>.8	p>.7
0.080	0.100	p=1	p=1
0.100			

The average chromaticity coordinates for concentrations were plot on a CIE diagram shown in Figure 9.21.

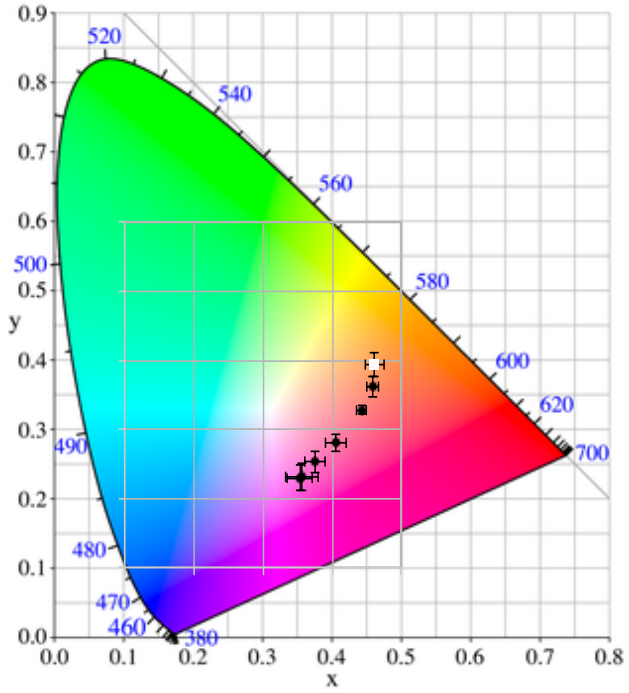

Figure 9.21. Average chromaticity coordinates and standard deviations are shown on the CIE chart for 100 nm alumina layers exposed to various prothrombin concentrations. With increasing exposed concentration and colour

order the trajectory moves from the tan/orange region toward the purple region. Increasing concentrations of 0.015, 0.025, 0.035, 0.050, 0.08, and 0.1 mg/ml are mapped however the two highest concentration markers are difficult to separate on the plot. The white marker shows the average bare surface coordinates.

Markers show the Yxy coordinates from the base surface colour (white) and the colour shifts from protein binding to the surface (black) with error bars showing standard deviation. Coordinates for concentrations were distinguishable with the exception of exposed concentrations of 0.08 and 0.1 mg/ml. The thicker alumina layer pushed the coordinates further along the trajectory with an increased OPL.

Table 9.17 shows results of the statistical analysis on the effect of exposed prothrombin concentration on the set 1 surface colour coordinates. The x and y coordinates were analyzed using ANOVA and Tukey post hoc tests that showed [F(5,24)=268.861, p=.000] and [F(5,24)=251.200, p=.000] respectively.

Table 9.17. Results of the statistical analysis on the effect of exposed prothrombin concentration on set 1 chromaticity coordinates collected from surface images. The base alumina layer was 100 nm. Statistically significant results are in italics and differences that became significant when analyzing set 1 coordinates are in bold. (n=5 locations within one spot)

Post Hoc Test Results			
Exposed Prothrombin Concentration (mg/ml)	vs. Concentration (mg/ml)	x Coord. p Values	y Coord. p Values
0.015	0.025	p>.07	***p<.001***
	0.035	*p<.001*	*p<.001*
	0.050	*p<.001*	*p<.001*
	0.080	*p<.001*	*p<.001*
	0.100	*p<.001*	*p<.001*
0.025	0.035	***p<.001***	***p<.001***
	0.050	*p<.001*	*p<.001*
	0.080	*p<.001*	*p<.001*
	0.100	*p<.001*	*p<.001*
0.035	0.050	***p<.001***	***p<.001***
	0.080	*p<.001*	***p<.001***
	0.100	***p<.001***	***p<.001***
0.050	0.080	***p<.001***	***p<.005***
	0.100	***p<.001***	***p<.005***
0.080	0.100	p=1	p>.9
0.100			

An evaluation of the average chromaticity coordinates shows statistically significantly results between all but one of the prothrombin concentrations tested.

9.4 Discussion

9.4.1 Gold Nanoparticle Conjugation

In attempts to discover the surface density and distribution of prothrombin bound to the alumina surface, 10 nm gold nanoparticles were covalently conjugated to anti-prothrombin and exposed to the prothrombin-coated surfaces. Conjugation was confirmed with an immunogold blotting procedure and a 3 nm shift in the UV-VIS spectrum. Particles were hard to locate in images captured with the in-lens detector; however, the EBSD provided images with compositional contrast to confirm gold particle locations. In these images, light and dark specks were visible in all samples, including the bare surface (Figure 9.1) and prothrombin-coated surfaces (Figure 9.2). The elemental composition of specks could not be determined using EDX, and likely result from the porous surface layer.

The electron penetration distance into the multilayered sample was approximated using expressions specific to aluminum in the low voltage region for (5 keV down to 100 eV) shown in Figure 9.22.[38]

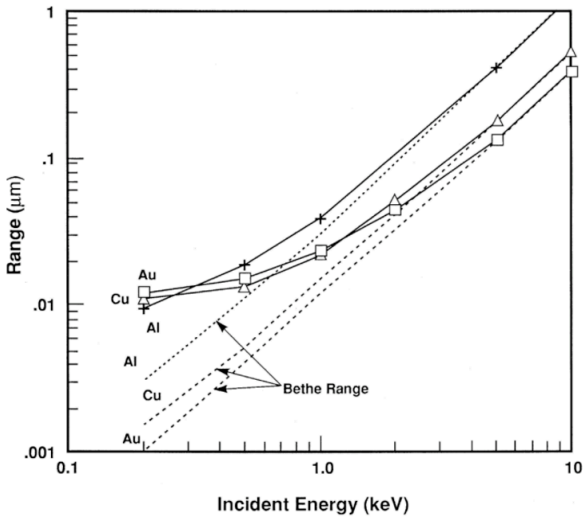

Figure 9.22. Electron penetration distance into Al, Cu, and Au samples calculated using the Bethe expression computed by Rao-Sahib and Wittry (1972) and modified expressions extended by Joy and Luo (1989). [38]

It was predicted that an aluminum sample bombarded with 5 keV penetrates to a depth of roughly 400 nm. With the porous anodic alumina layer, the distance electrons travelled would increase in void (i.e. air) regions and decrease in the dielectric alumina regions. Atoms with high atomic numbers (i.e. Ta and Au) increase the elastic scattering, reflecting larger

amounts of backscattered electrons, and appear brighter. In the thin film device, brighter areas occur where voids allow electrons to contact the tantalum layer and reflect back to the detector as well as where gold nanoparticles are bound on the surface. Atoms with lower atomic numbers (i.e. Al and O) reflect fewer electrons and appear darker, especially in areas with dense corners of intersecting pore walls and barrier layers. The porous structure creates bright and dark regions that are not clearly distinguishable and appear as specks with blurred outlines. Specks were distinguishable from gold nanoparticles because they generated stronger contrast (brighter) and were circular with well-defined edges in comparison to the specks. Outlining the gold particles and bright specs in Figure 9.3 and Figure 9.4 make gold particles in the SEM in-lens images easier to locate and shows that bright specks occur over voids, supporting that the signal was from backscattering off the underlying tantalum.

Gold particles were found on prothrombin-coated surfaces exposed to conjugated anti-prothrombin (see Figure 9.3) and surface exposed to the conjugated anti-prothrombin solution (see Figure 9.4). In comparison to the number of gold nanoparticles that bound to a set surface area on the prothrombin coated slides, just over half the number of gold nanoparticles were visible on the bare surface within the same surface area. With non-specific binding to the bare device surface, the location and density of immobilized gold nanoparticles were not evaluated on the prothrombin-coated surfaces. It is possible that small amounts of anti-prothrombin typically bind the surface in an orientation that does not cause a significant increase in the path length. However, binding could also be a result of the gold particle interfering with anti-prothrombin and surface interactions. The drastic size increase of ~6110 kDa with conjugation or the gold coating may result in non-specific binding to the surface.

In attempts to improve gold conjugation, smaller particles were considered to minimize the impact on protein binding; however, 10 nm particles were needed to separate the conjugated and unconjugated antibodies. Further work is necessary to optimize this procedure to generate meaningful data in regard to the prothrombin binding. Alternate anti-prothrombin solutions could be tested for conjugation including MES, MOPS, and HEPES. However, due to interactions between the conjugated nanoparticles and the alumina surface of interest, an alternate method was used to determine the prothrombin surface density.

9.4.2 Radiolabelled Prothrombin

9.4.2.1 Protein Labelling

The NOTA chelator was used as the gold standard for ^{64}Cu introduction, [39] which gave very good incorporation yields (84-97%) and stability. LCMS of the protein conjugate showed the successful introduction of 2-5 chelators on the protein. The majority of proteins had 3 and 4 chelator groups bound and a small amount had 2 and 5 groups bound (see Figure 9.6). The protein conjugate showed comparable colour shifts in relation to the unmodified prothrombin. The radiochemical purity of the isolated ^{64}Cu-NOTA-prothrombin was greater than >95% as determined by SDS-PAGE and TLC. The SDS-PAGE of labelled prothrombin solution confirmed that one dominant band exists at slightly greater than 70 kDa (see Figure 9.7) supporting that the prothrombin was unaffected by the modification process. The specific radioactivity after purification was between 0.94 and 1.51 GBq/mg.

9.4.2.2 Radioactivity Variation

No significant difference was found when a prothrombin solution with 2-12% modified prothrombin was exposed to the surface. The trendline and standard deviations, along with 2σ standard error encompass all data points (see Figure 9.8). Thus, the binding affinity of the radiolabelled and original prothrombin for the alumina surface can be treated as equal when the labelled prothrombin is between 2 and 12% of the total prothrombin in solution. The test conducted provides an indication of variability expected with these trials. Experimental variability may result from solution exposure to the hydrophobic outer surface area, adsorption to Eppendorf tubes or pipette tips, and variability in the alumina surface.

9.4.2.3 Adsorption Isotherm

The adsorption isotherm data allowed for the calculation of prothrombin surface density values (see Figure 9.9). Langmuir-Freundlich (LF) (strong and cooperativity) and Guggenheim-Anderson-de Boer (GAB) (strong and unselective) equations fit to the curve gave monolayer densities of 1.32 μg/cm^2 (18.3 pmol/cm^2) and 1.49 μg/cm^2 (20.7 pmol/cm^2) after exposing ~0.2 and 0.25 mg/ml for 15 minutes, respectively. LF is used for energetically heterogeneous surfaces and does not assume uniformity, [40] whereas GAB is used for

multilayer adsorption modelling.[41] More information on LF and GAB equations can be found in the literature.[42]

The adsorption showed a Langmuir-like shape with additional protein binding for higher concentrations. The adsorption and desorption equilibrium constant (K) of prothrombin for the alumina surface was determined to be 17.3±4.3 L/g from which $\Delta G°$ was estimated[43] to be −35 kJ/mol. The reaction is governed by numerous parameters including: surface (i.e. area, structure, chemistry), pore size and distribution, wettability, pH, point of zero charge, and temperature.[24,44,45] Demonstrating the importance of exposing TBS to the surface to equilibrate the alumina surface prior to conducting radiolabelled experiments in attempts to achieve constant alumina chemistry and wettability.

Theoretical calculations for binding prothrombin using the footprint of 11×5×4 nm shows that a closely packed monolayer on the nominal surface area requires 0.7 μg/cm^2 (9.7 pmol/cm^2) and 0.3 μg/cm^2 (4.2 pmol/cm^2) for short and long side binding, respectively. The experimentally determined surface density was approximately twice the theoretical value obtained for the short prothrombin side binding. The short ends of prothrombin with the Gla domain and multiple γ-carboxyglutamic acid residues,[40] are attracted to the alumina surface or the upper regions of internal pore walls (see Chapter 2 and Chapter 6) while forming a denser than anticipated monolayer. Two molecules bound to the upper region of the alumina layer likely decrease the effective pore diameter and block the pore, preventing additional diffusion. The porous structure results in a greater surface area than the nominal value used, and potentially some diffusion into the surface region of the alumina film. The adsorption curve supports the hypothesis that the short end of prothrombin binds to the alumina surface.

Protein adsorption to nanoporous alumina has found pore size to influence the degree of biologics that bind. Surface pores of 200 nm resulted in greater protein adsorption than 20 nm pores, regardless of the protein solution exposed.[10] A study with 200 nm pores in a silicon substrate were filled with BSA in 3 minutes.[46] human serum albumin was able to diffuse into porous silicon matrices with a mean pore diameter >11 nm up to thicknesses of 1 μm.[47] It was difficult to compare these slides to this work as the protein solution has an affinity to the surface. Moreover, the parameters differ, the pores have a mean diameter of ~20 nm and the incubation time was 15 minutes.

Gispert et. al showed adsorption of BSA onto alumina reached saturation at 0.11 μg/cm^2 with exposing ~0.5 to 1 mg/ml solutions and continues to increase to 0.15 μg/cm^2 with exposing a 4 mg/ml solution and 0.2 μg/cm^2 with exposing 9 mg/ml.[48] BSA binding to alumina resulted in higher surface densities,[48,49] however plots were the same shape. Likely indicating the same adsorption mechanism.[42] Protein-protein interactions, after monolayer formation, may continue to increase surface density. The initial adsorption corresponds to immobilization onto the positively charged alumina surface. After the first layer was adsorbed the surface charge of the alumina becomes masked and during the second adsorption stage the arriving proteins interact with the immobilized molecules to form dimers. Further supporting that the adsorption process leads to a saturation value close to that of one end-on monolayer, yet after this point adsorption continues.[48]

Prior works on porous substrates have shown continuously increasing surface density values due to protein penetration into the pores.[47,50] The log plot (see Figure 9.9 B) shows a plateau with exposing a concentration of ~0.1 mg/ml; however, at greater concentrations the surface density appears to increase linearly. These findings lead to conclusions that increasing the exposed protein concentration leads to an increase in the protein loading within the porous alumina film.

Ellipsometry shows an increase in thickness that correlates with prothrombin concentrations exposed and the increasing surface density. Exposing a 0.1 mg/ml prothrombin solution leads to a thickness change equivalent to the prothrombin thickness assuming short side binding. At greater concentrations the measured surface density and thickness continued to increase. However, during ellipsometry modelling correlations exist between the refractive index and thickness of a layer. The ellipsometry model applied the alumina refractive index for the protein layer, as the refractive index of prothrombin is inconclusive and voids in the protein layer would result in additional changes to the effective refractive index. There are two possible explanations for a 17 nm increase in the surface film after a 1 mg/ml prothrombin solution was exposed to the alumina device. Either the protein layer refractive index was higher than the value used in the model leading to a thickness greater than the actual protein layer or a bilayer of prothrombin formed. The increase in optical thickness measured using ellipsometry corresponds with the radiolabelled increase in surface density.

The alumina thickness between radiolabelled and original prothrombin slides differed by 0.8 nm but the mean standard error values were 14 and 23 respectively. However, after proteins were exposed the labelled slides showed a greater mean standard error, likely because the copper label on a percent of bound prothrombin and the surface was not dried completely before storage. The changes introduce more error into the model. However, even with differences in the mean standard error values the thicknesses measured in Table 9.3 showed significant differences between radiolabelled and original prothrombin exposed to the slide surface for only two out of the ten exposed prothrombin concentrations (see Table 9.5). Likely due to the variances being very low in one case and a large difference in mean standard error in the other case.

9.4.2.4 Time Variation

Varying time experiments support that either protein-protein interactions lead to a bilayer or saturation was incomplete and a monolayer continues to form. In both cases diffusion through solution causes subsequent protein interactions to result. The higher concentration of 1 mg/ml showed a greater fluctuation with exposure time and the surface density after 15 minutes of exposure was 1.7 times larger than the 0.1 mg/ml solution. Exposing prothrombin solutions of 0.1 mg/ml, leads to saturation after 15 minutes, and shows minimal increase in surface density with longer incubation times. With the incubation time increasing to 30 minutes, 1 hour, and 2 hours the surface density increased by 6, 12, and 15%.

A significant difference resulted between the adsorbed protein from 0.1 mg/ml solutions in time and adsorption isotherm experiments. This change could result from higher variability between tests until monolayer formation is complete. The surface density values in the initial variability test showed a maximum difference of 0.25 $\mu g/cm^2$, which accounts for the difference found between these tests. With increasing the number of samples, it is expected that no significant difference would result.

It is possible that with greater concentrations or exposure times, deeper diffusion into the pores may occur. For both concentrations tested, a plateau in surface density was observed by 30 minutes. Rezwan et al. supported the concept that higher concentrations lead to greater pore diffusion into porous silicon. [49] Prothrombin solutions that indicate a monolayer on the

surface will be exposed for 15 to 30 minutes in future tests to balance test efficiency and monolayer formation.

9.4.2.5 Protein Competition

An evaluation of prothrombin adsorption to the alumina surface in competition with human serum albumin showed the affinity of prothrombin for the alumina was greater than human serum albumin. human serum albumin was selected because it makes up a large component of the human blood plasma. [51] Furthermore, human serum albumin and prothrombin are similar sizes, 69 kDa[52] and 72 kDa, [53] and dimensions, 9×5.5×5.5 nm[49,54] and 11×5×4 nm, [33] respectively. Therefore, in competition studies the size and diffusion can be deemed extraneous. Lastly, an albumin-coated surface is less susceptible to platelet adhesion, [55] so there may be some benefit in exposing albumin to block the surface if whole blood samples are used.

Total protein concentrations ranging from 0.017 to 1 mg/ml were employed. It was concluded that prothrombin selectively binds to the alumina due to a higher affinity to the surface over human serum albumin. Exposing solutions with ratios of human serum albumin to prothrombin of 0 to 5.8 led to surface densities in the range of 0.26±0.01 to 0.29±0.01 μg/cm^2, and a ratio of 58 led to 0.21±0.01 μg/cm^2. A 12% decrease in surface density resulted when testing labelled prothrombin solutions with the highest amounts of human serum albumin, showing a significant difference in the resulting labelled prothrombin bound when the ratio was ≥29 (p=.000) (see post hoc results in Table 9.7).

As previously mentioned, the Gibbs energy for prothrombin on alumina was -35 kJ/mol and work by Gispert et al. shows the BSA adsorption onto alumina powder to be -38.5 kJ/mol or -46 kJ/mol depending on the concentration range. [48] The surface area or structure of the alumina powder used by Gispert et al. likely effects the binding and shows an increase in the Gibbs energy for BSA from what would result with exposure to the porous alumina surface used in this work. Results showed prothrombin adsorption to alumina to have a higher driving force than BSA (see Figure 9.11), however, this was not represented by Gibbs energy values. Karlsson et al. (2006) found that nanoporous alumina binds albumin better than fibrinogen and IgG, [56] and therefore, we expect fibrinogen and IgG will have less impact on prothrombin binding than human serum albumin.

It is undetermined whether biologics adsorb better to hydrophobic or hydrophilic alumina surfaces and is likely surface and protein dependent. Some reports show increased protein adsorption on hydrophilic substrates, [57] whereas the majority show that proteins adsorb more extensively onto hydrophobic surfaces, such as starch-based biomaterials. [58,59] Proteins with low conformational stability (i.e. BSA) [58,60] adsorb to hydrophilic or hydrophobic surfaces. [48] With anodic alumina being hydrophilic after anodization and becoming hydrophobic with time, the surface was equilibrated and rehydrated with TBS prior to tests to ensure hydration consistency. Exposing prothrombin to a hydrated surface presents an environment similar to *in vivo* situations and may diminish the likelihood of proteins changing conformation from hydrophobic interactions during adhesion.[56,61]

9.4.2.6 Wash-out of Radioactivity

The device operation requires that a stable protein monolayer be immobilized on the surface to create a detection platform for a specific antigen or antibody. Subsequent binding of receptor proteins and detection will require exposing the device surface to patient samples (i.e. serum, blood, or urine). To model the impact of these solutions on the prothrombin-coated surface, prothrombin was immobilized to the alumina surface and subsequent wash solutions exposed. It was found that with increased II concentration a greater loss in radioactivity with the wash solution was noted. This may be a result of more protein bound and weaker protein-protein interactions. Likely influenced by the lower variances resulting with human serum albumin wash solution.

The prothrombin wash on the 1 mg/ml prothrombin-coated surfaces showed a higher level of wash-out than when the 0.1 mg/ml prothrombin-coated surfaces were exposed. This could be due to weak protein-protein interactions on the surface. Additionally, proteins with an equal or higher affinity for the surface (i.e. vitamin K-dependent proteins or fragments) may displace the labelled prothrombin.

Human serum albumin wash solutions exposed for 1 hour removed 4.5±1.8% radioactivity whereas FBS removed 40.5±4% radioactivity of the previously exposed 0.02 and 0.1 mg/ml prothrombin solutions. Serum contains 6 to 8% of blood proteins with the majority being albumin and the remainder globulin. With the human serum albumin wash showing a minor reduction in prothrombin radioactivity (Figure 9.12) and a lower affinity for the surface

than prothrombin, it is unlikely that the serum albumin displaces the labelled prothrombin. The size of BSA is 66.4 kDa and contains 76% of the same sequence as human serum albumin. [62] It is possible that serum (i.e. FBS and HS) contains prothrombin and other proteolytic enzymes that cleave prothrombin into thrombin or smaller fragments. Thrombin remaining in the serum, or created by proteolytic cleavage of bound prothrombin, acts as a catalyst for prothrombin cleaving. The radiolabel was coupled to prothrombin with NOTA chelator groups that bind to the protein through an amide linkage. [63] Within prothrombin, amino acids with amine side groups (i.e. arginine, lysine, asparagine, and glutamine) are distributed 54% in thrombin and 46% in fragment 1 and 2. Therefore, if the radiolabel is uniformly distributed among potential binding sites and thrombin was removed, a ~54% decrease in radioactivity would result.

Blood coagulation produces a clot and serum upon separation. Fibrinogen and most proteins involved in the coagulation cascade are consumed during clot formation; however, remnants include some clotting factors, proteins not involved in the clotting process, electrolyte, antibodies, antigens, hormones, and exogenous substances. During induced coagulation that cut fibrinogen and platelet levels in half, a 10% decrease in the available prothrombin and a 15 to 30% decrease in FVII, FIX, and FX occurred. [64] Past work demonstrates that prothrombin conversion in blood to produce serum typically results in the production of thrombin and fragment 1·2 peptides, with the presence of FX.[65-67]Aronson et al. showed fragment 1·2 was the main prothrombin fragment that remained in serum, accounting for more than 90% of the prothrombin originally in the sample. The serum contained fragment 1, however less than 10% of the original prothrombin was present as this amine terminal end. [68] The cleavage of fragment 1 from prothrombin or fragment 1·2 is predominantly due to thrombin. [65,69-72] However this process is slow compared to cleaving fragment 1·2 from prothrombin, and only results when thrombin remains active. [65,70,72] Ware and Seegers showed that the concentration of thrombin in solution impacts the prothrombin stability. With low concentrations destroying prothrombin, medium concentrations temporarily preventing the conversion of prothrombin to thrombin, and high concentrations showing no influence on prothrombin. [73]

After 1 hour of FBS and HS exposure a 40 and 45% decrease in radioactivity resulted respectively. With 12 hours HS exposure 13% radioactivity remained with a longer cleaving time and potentially more thrombin in solution acting as a catalyst for prothrombin cleaving, so smaller fragments remain bound. Figure 9.16 presents data that is beneficial for device design and function. The 12 hours of incubation demonstrates a maximum exposure time, as detection is expected to require <1 hour. However, it is important to understand and prevent removal of the immobilized protein layers for detection.

Running an SDS-PAGE of the HS wash removed from the prothrombin-coated surface was completed (see Figure 9.15) to determine the prothrombin fragments present. Regions with dominant bands include 65-75 kDa and 85-95 kDa. Therefore, the first is likely fragment 2 (12.8 kDa) bound to serum proteins shown to exist mainly at 55kDa and the second is likely thrombin (36.7 kDa) bound to serum proteins. Molecular weights smaller than prothrombin are fragments of prothrombin that were cleaved and may or may not be bound to serum proteins. Serum proteins caused greater mass differentiation and prevented distinct bands from forming. If the entire prothrombin molecule were chipped from the surface it is unlikely that a smear, especially over such a wide range, would result.

9.4.3 Quantification of Immobilized Prothrombin with Colour Coordinates

This work evaluates the limit of detection and whether quantification of protein on the surface is possible using the initial prothrombin layer. A custom optics system captured images of the surface while maintaining constant viewing parameters. The images were then used to obtain colour coordinates for the bare slide and slides exposed to protein solutions (see Table 9.10 and Table 9.14). Slides used for radiolabelled work, resulted in larger colour shifts than the original, unmodified, prothrombin solution, shown in Figure 9.17. In both cases the prothrombin solutions were exposed to slides with a ~95 nm alumina layer. From this it can be interpreted that the modification process increased the labelled prothrombin size and the protein layer OPL. Therefore, the radiolabelled data was used to generate the surface density and slides exposed to original prothrombin solutions with the same alumina thickness were used to analyze the resulting colour shifts. Ellipsometry and visible analysis were completed on slides exposed to labelled and original prothrombin solutions. The addition colour change resulting on slides exposed to radiolabelled prothrombin helps explain the higher mean

standard error values associated with models of surfaces exposed to labelled prothrombin (see section 9.3.4.2) because the copper label would not be accounted for in the model of the system.

Slides used for tests in Chapter 8 showed a lower limit of detection and will be analysed for the purpose of quantification in this chapter (see Figure 9.20). Ellipsometry confirmed the alumina thickness of these slides was 100 nm. Assuming protein immobilization was the same for thicker alumina layers the colour shifts can also be related to the surface densities measured on the 95 nm alumina slides.

Colour coordinates of the bare device and with protein immobilization are shown in Table 9.10 and Table 9.11 for slides with 95 nm of alumina and Table 9.14 and Table 9.15 for thicker slides with 100 nm of alumina. Individual protein sets showed the lowest variance, measuring locations within 1 spot (each protein-coated spot covers an area of ~0.8 cm^2). The second lowest variance was noticed in the individual bare surface sets that used coordinates from locations external to a minimum of 6 protein spots. Lastly, the averages showed increases in the standard deviations when comparing coordinates from locations across all three sets (coordinates from a minimum of 18 spots). In each case the number and separation of locations where coordinates were collected increases. Comparing coordinates collected for the 95 nm and 100 nm alumina slides a difference in variance was observed. This shows the importance of keeping the imaging device consistent; however, the image collector is also likely to introduce variability depending on the level of caution exercised by the image collector.

Chromaticity coordinates were plotted on CIE charts for both alumina thicknesses of 95 and 100 nm (see Figure 9.19 and Figure 9.21). Colour shifts occur in an elliptical pattern with increasing OPL and colour order. Work by Sandström et al. showed changes in chromaticity coordinates for interference colours generated on a multilayer device comprised of a silica film, (η=1.5) between 0 to 600 nm, and a silicon substrate (η=2.25), shown in Figure 2.13. [74]

In the first order colour region where sensitivity is highest, the detection limit was found to be 0.7 nm or 0.1 $\mu g/cm^2$ by Sandstrom et al. [74] Chromaticity coordinates on CIE plots from this work, showed similar trends to those demonstrated in prior work. Taking into account the decrease in the refractive index of alumina and the colour generation from the underlying

tantalum oxide layer, the film thicknesses required to transition from red to purplish blue were increased slightly. The 95 nm alumina films showed an initial colour slightly prior to the highest saturation yellow (closest to the outer edge) was achieved and a visible detection limit of 50 mg/ml. The 100 nm alumina films were closer to the optimal sensitivity region, which explains the lower detection limit on these slides after exposing 15 mg/ml.

A statistical analysis for x and y coordinates with different exposed concentrations were carried out for slides with each alumina thickness. The thicker 100 nm alumina slides showed an increase in the number of statistically significant x coordinates. The increase in sensitivity was due to the change in surface colour coordinates which resulted in x coordinates decreasing with increasing OPL. Whereas, the 95 nm alumina slides were less sensitive with surface coordinates that resulted in the x coordinates to first increase and then decrease with an increasing OPL. Exposing prothrombin solutions from 0.003 to 0.035 mg/ml showed increases in the x coordinates, after which they decreased with exposed solutions from 0.05 to 1 mg/ml. For both alumina thickness the y coordinates showed a similar number of significant differences in coordinates. Therefore, depending on the base device colour, the chromaticity coordinate that provides a better indication of significant difference will change. With that said, it was proven beneficial for quantification purposes to have coordinates moving in one direction with an increasing OPL. The first order colour region generated optimal sensitivity and shifts the interference colours from tan to purple. The number of statistically significant results between the same exposed protein concentrations and resulting colour coordinates on the two alumina thicknesses, further supports this importance.

When comparing the surface coordinates generated after exposing 0.015 to 0.1 mg/ml solutions on ~95 and 100 nm alumina layers, the thicker film shows a greater significance at low concentrations. For the thicker 100 nm alumina slides exposed solutions of 0.015 and 0.035 mg/ml show that colour coordinates are statistically significant for both the x and y coordinates, whereas the 95 nm alumina film was not statistically significant for the y coordinate until comparing 0.015 and 0.05 mg/ml and 0.015 and 0.5 mg/ml for x and y coordinates. The 95 nm alumina films showed increased significance between the coordinates with exposed solutions of 0.05 and 0.1 mg/ml that were statistically significant for y coordinates, whereas neither coordinate differed for the thicker alumina film. Lastly, it is important to note the effect of multi-directional shifting in coordinates with increasing OPL.

The 95 nm alumina slides demonstrate multi-directional shifting; placing the x coordinates of surfaces exposed to the 0.1 mg/ml solutions very close to x coordinates of low concentrations. Ultimately, results in the x coordinates between 0.1 mg/ml and from 0.003 to 0.025 mg/ml surfaces showing higher p values than expected.

Analyzing the 95 nm alumina average of sets showed statistically significant results for chromaticity coordinates between groups of 0.003-0.035, 0.05, 0.1, 0.5, and 1 mg/ml (≤0.50, ~0.68, 0.90, 1.66 and 2.18 μg/cm^2). The limit of detection using coordinates showed solutions of 0.003-0.035 and 0.050 mg/ml generated significant differences for the y coordinate. Analyzing the 100 nm alumina average of sets showed statistically significant results for chromaticity coordinates between groups of 0.015-0.025, 0.025-0.035, 0.05-0.1 mg/ml (0. 22-0.36, 0.36-0.50, ~0.68-0.90, 1.66, and 2.18 μg/cm^2)[2]. The limit of detection using coordinates showed solutions of 0.015 and 0.035 mg/ml generated significant differences for x and y coordinates. The coordinate and visible limits of detection were both improved on the 100 nm alumina slide with greater sensitivity.

On these slides the statistical differences in colour coordinates were found after exposure of a prothrombin solution at 0.035 mg/ml (9.7 pM). Taking the surface densities that result with a statistical difference in the colour coordinates (0.50 μg/cm^2) and after the formation of a protein monolayer (1.32 and 1.49 μg/cm^2) it was determined that colour shifts are detected when 34 to 38% of the monolayer has formed. This can be extrapolated to estimate the adsorbed amounts of various proteins that will be required to achieve a shift in the colour coordinates. With the assumption that one anti-prothrombin molecule is immobilized for every prothrombin molecule required to achieve between 34 and 38% surface coverage, a colour shift can be expected with ~2.7 pM (1.0 μg/cm^2) immobilized on the surface (see Chapter 10 for experimentally determined anti-prothrombin limit of detection).

---

[2]Assumes that the resulting prothrombin surface density on slides with 95 nm of alumina is the same as slides with 100 nm of alumina for the respective concentration exposed

Furthermore, comparing the average of one individual set versus three sets leads to an increase in the number of statistically significant coordinates. Testing colour coordinates from one set of slides generates intra spot variance, while testing the average produces inter spot variance. These tests along with the increase in standard deviation with coordinates collected from a greater number of locations shows that the manufacturing process itself creates variance in colour coordinates between trials. The alumina thickness, among other parameters, must be precisely controlled to achieve reproducible quantification of protein solutions.

Results show that prothrombin binding to the device surface can be quantified using visible interference colour shifts when viewed with a polarizing film at 75° from normal to the surface. Areas of weakness such as the variance in the base device surface colour and the removal of bound prothrombin with subsequent exposure to human and bovine serum should be investigated in future work to further improve the quantification and device stability.

9.5 Future Work

Future work should examine the influence of pore size and hydration of the alumina surface layer on prothrombin adsorption. Radiolabelled work on an anodic barrier layer and films created at different voltages could provide a better indication of the amount of protein binding within the pores by comparing the surface densities that result. Looking at adsorption of different proteins is important, as unprocessed biological solutions will contain a large number of various sized molecules. The device structure must be adapted to control whether proteins diffuse and bind to the internal surface of pores or if binding occurs mainly at the macroscopic surface.

The combination of radiolabelling and ellipsometry supports the conclusion that prothrombin is strongly bound to the alumina; however, more work is necessary to provide detail on the protein distribution within the porous alumina. (see SIMS work in Chapter 5)

Anti-coagulated whole blood and plasma, urine, sputum, exudate, and environmental samples exposed to the device surface would provide insight into which fluids can be used for protein detection. Whole blood and plasma solutions differ from serum samples because no coagulation is required and hence little to no thrombin will be present in solution. Furthermore, the plasma and whole blood contain fibrinogen and the whole blood also contains cells (i.e., white and red blood cells, and platelets). Prior work found anodic tantalum

and silicon samples to preferentially adsorb fibrinogen out of plasma. [75] It would be beneficial to determine components that preferentially adsorb to the device surface.

9.6 Conclusions

This chapter analyzed the adsorption of prothrombin onto a porous anodic alumina surface and provided valuable information on the surface density, monolayer formation, and protein orientation. Findings from this work include:

1. A monolayer of prothrombin containing between 18 and 21 pmol/cm^2 (1.32 and 1.49 μg/cm^2) was formed by exposing 20 μl of ~0.2 mg/ml prothrombin solution (60 pM) on the surface after 15 minutes. Exposing higher protein concentrations caused the surface density to continue increasing; however, after 15 minutes little increase in surface density was noticed with longer incubation periods up to 2 hours. It is possible that a bilayer of prothrombin formed or that protein loading in the porous alumina structure increases with concentration.
2. The theoretical surface density for short and long side prothrombin binding were 0.7 μg/cm^2 (9.7 pmol/cm^2) and 0.3 μg/cm^2 (4.2 pmol/cm^2) using the nominal surface area. The experimentally determined surface density with a monolayer of protein was ~2 times the theoretical value calculated using short side binding; however, calculations did not account for the increase in surface area on the porous structure from the plane alumina. The increase in experimental surface density supports that the molecule is binding at the short side and that the surface density doubles due to the porous nature of the film.
3. Prothrombin in a binary solution with human serum albumin was not influenced during adsorption to the alumina surface until very large ratios of human serum albumin to prothrombin were used. A significant difference in the resulting prothrombin bound was observed when the ratio was ≥29 ($p=.000$). The surface density decreased by 20% and 26% when exposed solutions contained ratios of human serum albumin to prothrombin of 29 and 58, respectively.
4. Wash solutions of prothrombin and albumin at 5 mg/ml concentrations showed little wash-out of radioactivity on the prothrombin-coated surface. However, serum (i.e. HS and FBS) which consists largely of albumin proteins, showed

significant removal of radioactivity after 1 and 12 hours on the coated surface. This can be explained by the presence of enzymes and other proteolytic factors, such as thrombin, which cleave the bound prothrombin when exposed for long periods of time.

5. The colour shifts that result with protein binding can be quantified using colour coordinates. Averaged coordinates on the 95 nm alumina slides generated significant differences between exposed solutions of 0.003-0.035, 0.05, 0.1, 0.5, and 1 mg/ml. Average coordinates on the 100 nm alumina slide generated significant difference between exposed solutions of 0.015-0.025, 0.025-0.035, 0.05-0.1 mg/ml. The limits of detection using coordinate and visible identification for the 95 nm alumina slides was 0.050 mg/ml (14 pmol) and for the 100 nm alumina slides was 0.035 mg/ml (9.7 pmol) respectively. When comparing individual sets as opposed to the averaged coordinates, the number of statistically significant results increased dramatically. This was caused by the decrease in variance observed with a lower separation between the locations that coordinates were collected over
6. Using the prothrombin limit of detection and surface densities measured with radiolabelling, on the most sensitive slides, it was found that 34 to 38% prothrombin surface coverage was required to generate a detectable difference in the colour coordinates. Extrapolating this information for subsequent protein layers can provide estimates on the limit of detection based on the specific molecule. For anti-prothrombin one can expect a statistical difference in the colour coordinates with 1 $\mu g/cm^2$ (5.5 pM) immobilized on the surface.
7. Lastly, the base slide colour is critical for generating statistically significant coordinates with low protein concentrations. The aluminum sputtered thickness and anodization require a high degree of consistency to achieve alumina thicknesses with accuracy to ±2 nm. The starting colour position on the CIE chart was optimal when x and y coordinates moved in only one direction.

‡Chapter 10 – Anti-Prothrombin Sensitivity on a Prothrombin-Coated Multilayer Device

10.1 Introduction

Arguably the most important immune system response, for removing foreign organism from within the body, results from antibody-antigen interactions. With an increase in time from exposure, the affinity of generated antibodies towards the antigen increases. This is known as affinity maturation. [1] The antigenic determinant, or epitope binds to the antibody at the paratope. [2] The strength of the bond between an antigen and antibody depends on the available area for contact and the ability of molecules to move within nanometers of one another. [2] Antibodies generated from an immune response in the human body are generally in concentrations ranging from 1 to 10 mg/ml in serum. [3,4]

ELISA is the gold standard for detection of antigen-antibody pairs and operates by forming complexes with an immobilized molecule, and subsequently amplifying the signal. Sensitivity of ELISAs can be as low as 1 pg/ml while using solution volumes between 10 and 100 µl, incubated on the plate surface for 2-4.5 hours. [5] Hence the amount of protein required for detection is typically between 0.1 to 100 fmols, but can be less with certain amplification techniques. [5,6] See Chapter 2 for more on the operation of ELISAs. In the case of ELISA, as well as the multilayered device of interest, the protein complex forms on a surface as opposed to in solution. Affinities of antigen-antibody interactions are generally highest when proteins are in their native environment and binding in solution. Antigen-antibody complexes formed in serums and PBS showed differences in size and affinity. [7] Work by Oda et al. showed the inability of some immobilized antibody's to form complexes with the corresponding antigens in the same stoichiometry that occurred in solution. [8] Another study showed that antigens

‡ A version of this chapter has been submitted to Nanomedicine: Nanotechnology, Biology and Medicine. Sweet HM, McMullen T, and Burrell RE. A visual immunoassay for the rapid validation of antibody specificity prior to experimentation.

bound to a surface were able to form complexes when exposed to free antibodies, similarly to in solution.[9] The immobilized protein orientation likely influences the ability of complex formation. The surface charge of the material used for antibody immobilization can affect subsequent antigen binding also.[10] Additional factors that affect the strength of the reaction are: temperature, pH, ionic strength, concentration and size of proteins, and the duration of incubation.[2,8,11] Enhancing antigen-antibody binding was demonstrated in some tests with the presence of albumin to address issues of non-specific binding and protein stability.[12-15] A comparison of streptavidin and anti-streptavidin IgG2 binding affinities in buffer and serum showed no difference, yet binding was ~3-fold tighter in serum.[16] Molecule crowding in the solution was proven to partially account for the tighter binding in serum.

To create a platform test, the ability to immobilize a receptor protein to the surface is required. Procedures for binding proteins to anodic alumina surfaces have been demonstrated,[17] but will not be explored in this work (see Chapter 9 Introduction for more details). To evaluate the complex formation on the device surface, the prototype of prothrombin and anti-prothrombin was used. With prothrombin being a native human protein, the anti-prothrombin molecules are typically raised in other mammals (i.e. rabbit, sheep, goat, etc.).

The purpose of this work was to determine the limit of detection for an IgG in solution with the antigen immobilized on the device surface. Furthermore, this work builds on radiolabelled data that showed a statistical difference in chromaticity coordinates with 34-38% of a prothrombin monolayer formed (see Chapter 9). Based on results for the initial protein layer, the anti-prothrombin limit of detection was theoretically calculated, and in this chapter was experimentally determined and compared to the theoretical limit. The IgG limit of detection on the antigen-coated device is critical to ensure that detection is possible for antigens and antibodies, with small volumes. The current sensitivity of the device will help select target markets of benefit that are in the necessary protein range for detection with the current device. The prototype test avoids the need for a bridging molecule and linker, and hence the complex efficiency should be maximized.

10.2 Methods

10.2.1 Theoretical Calculations for Anti-Prothrombin Limit of Detection

The prothrombin limit of detection and the radiolabelled data (see Chapter 9) was used to determine the number of moles on the surface when a visible shift in colour was achieved. For prothrombin the limit of detection occurred with 5.5 pmols bound to the surface, achieving 34-38% surface coverage. The prothrombin dimensions are 11×4×5 nm[18] and the anti-prothrombin IgG dimensions are ~14.5×8.5×4 nm. [19,20] Based on these dimensions, it can be assumed that the anti-prothrombin limit of detection will result when one anti-prothrombin molecule has bound for every two prothrombin molecules needed to achieve 34-38% surface coverage. Therefore, the theoretical limit of detection for anti-prothrombin was calculated to be 2.7 pmols. With antibody detection it is predicted that the Fab regions bind in an orientation that prevents at least one adjacent prothrombin molecule from binding to another antibody, however to achieve 34-38% surface coverage steric hindrance will not be an issue. Based on this, 20 µl of anti-prothrombin solution at 0.045 mg/ml (6 pmols) exposed to the surface for 15 minutes, with ~45% of protein in solution binding to the antigen-coated surface, would be required to bind 2.7 pmols and generate a colour shift. The percent binding from solution was approximated based on the radiolabelled prothrombin data.

10.2.2 Device Preparation

Tantalum thin films of 225 nm and subsequent aluminum films between 100 and 140 nm were sputtered onto silicon wafers. Deposition equipment at NAIT was used to create the tantalum films and at the University of Alberta's nanoFAB to create the aluminum thin film. The slides with 97 nm of alumina, used to evaluate shifts with increasing anti-prothrombin concentration, had aluminum films sputtered at a constant current of 0.72 mA with a resulting power of 279 W and voltage of 385 V. Depositions were carried out for 610 seconds and created aluminum films of ~105 nm. Other sets of slides with alumina thicknesses of 102, 108, and 124 nm were created and characterized as in Chapter 4 (Section 4.2.4. Part A). Tantalum films were deposited following the same process outlined above and aluminum films were deposited for lengths of time of 580, 620, and 680 seconds. Deposition parameters were the same as above with current of 0.72 mA leading to a power of 300 W and

voltage of 420 V). Tantalum and aluminum layers were deposited at average rates of 66.2±0.91 nm/min and 10.7±0.31 nm/min, respectively.

For all slides a standard anodization process was carried out until the end of pore formation (stage b), with the exception of the full wafer being anodized at one time instead of individual slides. See Chapter 3 for details on the standard device preparation procedures.

10.2.3 Prothrombin Immobilization and Complex Formation

Twenty microliter volumes of prothrombin solutions (ACOA, Aniara, West Chester, OH) containing 1.4 μM (28 picomoles) were exposed within all hydrophobic circles on the device surface and spread to the edges using the pipette tip. Solutions were left for 15 minutes in a high humidity environment at room temperature. The solution was removed with a pipette, rinsed with deionized water, and dried with oil free compressed air. Volumes (20 μl) of polyclonal anti-prothrombin solution (ACOA, Aniara, West Chester, OH) were pipetted within outlined circles previously coated with prothrombin, following the same process outlined for the prothrombin solution above. Anti-prothrombin polyclonal IgG antibody solutions, ranging from 20 nM to 1.3 μM, were placed on the alumina surface with a pipette and removed after 15 minutes. Subsequently, the surface was rinsed with deionized water and dried with compressed air. In addition, anti-prothrombin solution was exposed to the device surface and an influenza B antibody solution was exposed to the prothrombin-coated surface. No colour shifts resulted, interpreting the surface by eye. These solutions tested for non-specific binding.

10.2.4 Analysis

Images of visible surface colours were taken at an incidence angle of 75° with an *s*-polarizing filter and controlled lighting parameters. See Chapter 3 for more details.

10.3 Results

Parameters of the resulting slides following anodization are shown in Table 10.1.

Table 10.1. Parameters of various slides observed and measured with ellipsometry after device preparation.

Visible Device Colors with Different Alumina Thicknesses and Protein Exposure			
Alumina Thickness (nm)	**Surface Color**	**Prothrombin Color**	**Anti-prothrombin Color (0.67 µM)**
97±0.8	Orange	Pink	Purple
102±1.6	Orangish-pink	Purple	Bluish-purple
108±0.6	Reddish-purple	Purplish-blue	Blue
124±1.7	Bluish-purple	Light blue	Cyan

Figure 10.1 shows slides with an alumina layer of 97 nm exposed to varying concentrations of anti-prothrombin solutions on prothrombin-coated device surfaces. A prothrombin control was shown on each slide to confirm similar colour generation with the initial protein layer.

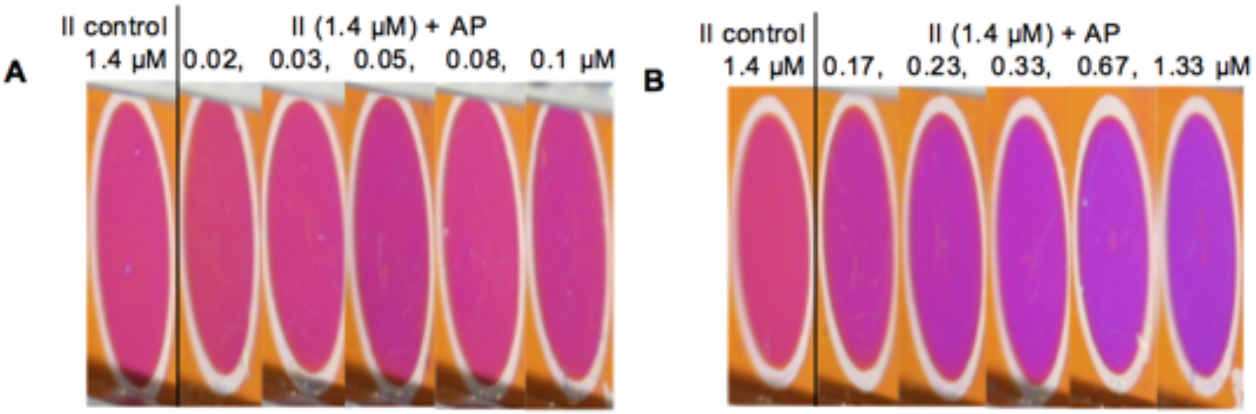

Figure 10.1. Anti-prothrombin solutions of different molar concentrations were exposed to spots previously coated with prothrombin (II) solutions (20 µl at 1.4 µM). Solutions were exposed to the surface for 15 minutes. Slides (A) and (B) are from the same wafer and prothrombin control spots are shown on each.

The initial device surface colour was an orange or orangish-pink. After a monolayer of prothrombin formed, the colour shifted to pink, and continued moving toward the purple region of the second colour order with anti-prothrombin solution exposure and complex formation on the device surface. The amount of anti-prothrombin incubated on the antigen-coated alumina surface varied from 20 µl volumes containing 0.02 µM to 1.33 µM.

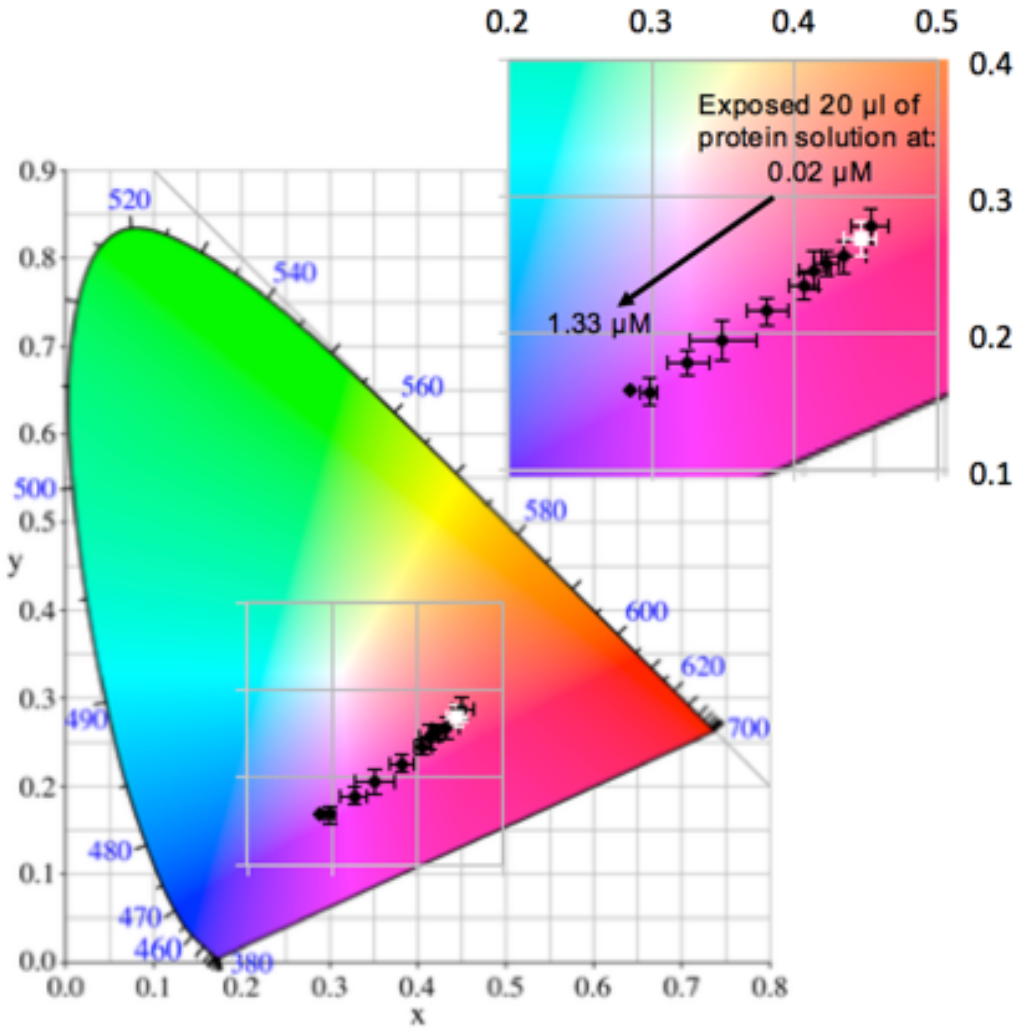

Figure 10.2. Average chromaticity coordinates and standard deviations are shown on the CIE chart for 97 nm alumina layers coated with a monolayer of prothrombin and subsequently exposed to various anti-prothrombin solutions. Increasing molar concentrations between 0.02 and 1.33 µM are mapped from right to left on the plot (black markers). The white marker shows the average prothrombin-coated surface coordinates from all slides.

Mapping the colour coordinates of the device, prothrombin monolayer and after incubating various amounts of anti-prothrombin on the prothrombin-coated surface, helped interpret the chromaticity differences. Markers show the Yxy coordinates from the prothrombin-coated surface (white), and the colour shifts from anti-prothrombin binding to the surface (black). Statistically significant results were found between chromaticity coordinates of surfaces exposed to only prothrombin solution versus prothrombin followed by anti-prothrombin solutions when the 20 µl volume exposed was ≥0.17 µM. Exposing anti-

prothrombin solutions containing 0.23, 0.33, 0.67, and 1.33 μM to the prothrombin-coated surface, leads to three and two different means for x and y coordinates, respectively.

Table 10.2 shows results of the statistical analysis on the effects of various anti-prothrombin concentrations incubated on the prothrombin-coated surface on the chromaticity coordinates. The x and y coordinates were analyzed using one-way ANOVA tests that showed [F(10, 22)=57.393, p=.000] and [F(10, 22)=40.033, p=.000], respectively.

Table 10.2. Results of the statistical analysis on the effect of exposed anti-prothrombin molar concentrations on chromaticity coordinates collected from the surface images. The base alumina layer was 97 nm and was coated with a monolayer of prothrombin. Statistically significant results are in italics. (n=3) (A) Shows the limit of detection by eye and using colour coordinates and (B) shows the analytical sensitivity determined from analyzing the colour coordinates.

A

Visual and Coordinate Analysis for AP Limit of Detection on the II-Coated Surface

Exposed Protein, Concentration, Color, and Coordinates	Vs. II + AP Test (μM)	Difference Detectable by Eye from II Control (yes/no)	x Coord. + p Values	y Coord. + p Values
II control 1.4 μM pink x=0.45±0.02 y=0.27±0.02	0.02	no	x=0.45±0.02; p=1	y=0.28±0.01; p>.9
	0.03	no	x=0.43±0.02; p>.9	y=0.26±0.01; p>.9
	0.05	no	x= 0.41±0.01; p>.05	y=0.23±0.01; *p<.05*
	0.08	no	x=0.42±0.01; p>.6	y=0.25±0.01; p>.7
	0.10	no	x= 0.41±0.01; p>.1	y=0.25±0.01; p>.4
	0.17	yes	x=0.38±0.01; *p<.001*	y=0.22±0.01; *p<.005*
	0.23	yes	x=0.35±0.02; *p<.001*	y=0.19±0.01; *p<.001*
	0.33	yes	x=0.33±0.02; *p<.001*	y=0.18±0.01; *p<.001*
	0.67	yes	x=0.30±0.01; *p<.001*	y=0.16±0.01; *p<.001*
	1.33	yes	x=0.29±0.00; *p<.001*	y=0.16±0.00; *p<.001*

B

Color Coordinate Analysis for AP Analytical Sensitivity on the II-Coated Surface

Exposed Protein, Concentration, and Color	Vs. II + AP Test (μM)	x Coord. p Values	y Coord. p Values
II (1.4 μM) + AP (0.02 μM) pink	0.03	p>.8	p=.5
	0.05	p>.05	*p<.01*
	0.08	p>.2	p>.2
	0.10	p>.05	p=.1
	0.17	*p<.001*	*p<.001*
	0.23	*p<.001*	*p<.001*
	0.33	*p<.001*	*p<.001*
	0.67	*p<.001*	*p<.001*
	1.33	*p<.001*	*p<.001*
II (1.4 μM) + AP (0.03 μM) pink	0.05	p>.3	p>.5
	0.08	p>.9	p=1
	0.10	p>.7	p>.9
	0.17	*p<.005*	*p<.05*
	0.23	*p<.001*	*p<.001*
	0.33	*p<.001*	*p<.001*
	0.67	*p<.001*	*p<.001*
	1.33	*p<.001*	*p<.001*
II (1.4 μM) + AP (0.05 μM) purplish pink	0.08	p>.8	p>.8
	0.10	p=1	p>.9
	0.17	p>.4	p>.7
	0.23	*p<.005*	*p<.05*
	0.33	*p<.001*	*p<.001*
	0.67	*p<.001*	*p<.001*
	1.33	*p<.001*	*p<.001*
II (1.4 μM) + AP (0.08 μM) purplish pink	0.10	p>.9	p=1
	0.17	*p<.05*	*p=.05*
	0.23	*p<.001*	*p<.001*
	0.33	*p<.001*	*p<.001*
	0.67	*p<.001*	*p<.001*
	1.33	*p<.001*	*p<.001*
II (1.4 μM) + AP (0.10 μM) purplish pink	0.17	p>.1	p>.1
	0.23	*p<.001*	*p<.001*
	0.33	*p<.001*	*p<.001*
	0.67	*p<.001*	*p<.001*
	1.33	*p<.001*	*p<.001*

Slides with different alumina thicknesses and the same alumina refractive indices (p>.078) (ranging from η=1.345 to 1.366, see Chapter 4) were visually evaluated by eye to compare the anti-prothrombin limit of detection with different alumina thicknesses. Figure 10.3 shows slides exposed to prothrombin and anti-prothrombin solutions near the detection limit. Figure 9.4 shows the same slides as in Figure 10.3, but individual protein spots were imaged using the custom optics system for improved surface colour analysis.

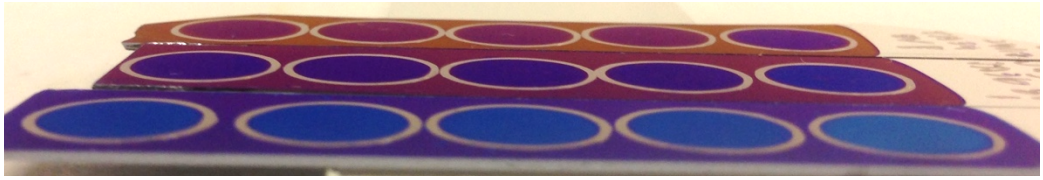

Figure 10.3. Visible interference colours resulting on prothrombin-coated slides 20 µl at 1.4 µM with alumina thicknesses from top to bottom of 102, 108, and 124 nm with subsequent anti-prothrombin solution incubation on the surface at concentrations (from left to right) of II control only, 0.03, 0.05, 0.08, and 0.067 µM.

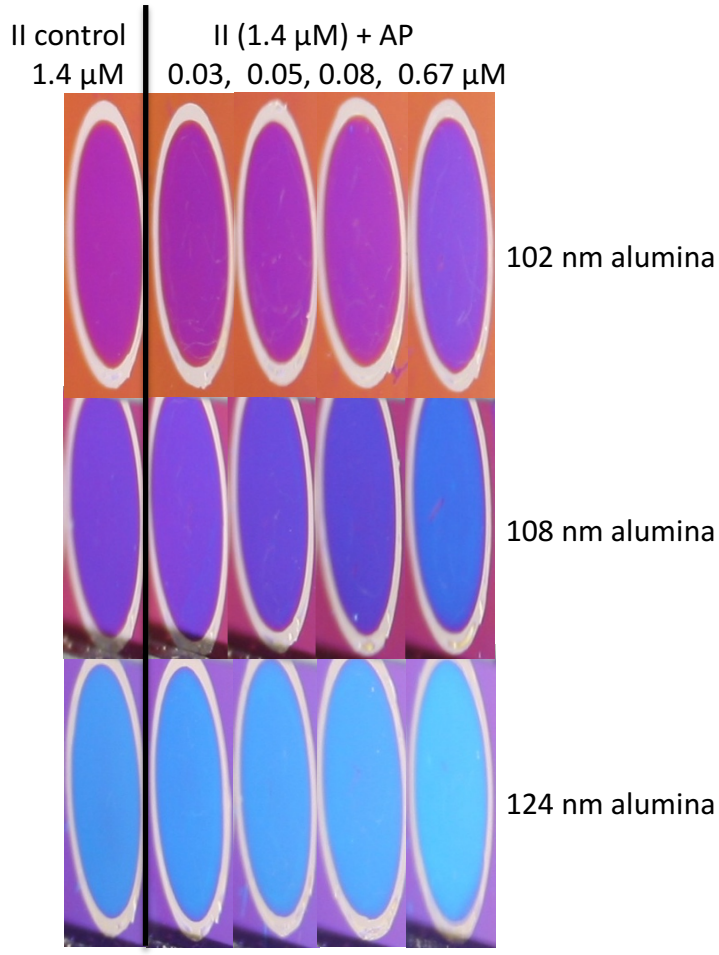

Figure 10.4. Visible surface colours on slides with 102, 108, and 124 nm alumina film thicknesses exposed to prothrombin (II) solutions (20 µl at 1.4 µM) and varying anti-prothrombin molar concentrations (20 µl volumes for µM solutions labelled above). Protein solutions were exposed for 15 minutes in all cases.

The base colours differ with alumina thicknesses and influence the visible detection by the unaided eye. With additional protein layers immobilized on each slide the interference colours shift towards higher colour orders. A difference in the limit of detection was apparent

for different alumina thicknesses. Base colours and prothrombin-coated surface colours with and without exposure to antibodies are given in Table 10.1.

10.4 Discussion

The experimental limit of detection for anti-prothrombin on the antigen-coated surface occurred when 20 µl protein solutions of 0.17 µM (3.3 pmols) were exposed to the device surface. The analytical sensitivity was 0.09 µM (1.7 pmols) comparing spots exposed to 20 µl solutions of 0.08 and 0.17 µM. Prior radiolabeling work evaluating (Chapter 9) the adsorption of prothrombin solutions incubated on the surface for 15 minutes showed between 37 and 42% of the protein in solution binds for concentrations exposed above. Between 22 and 71% of the protein in solutions binds to the surface from concentrations of 0.200 to 0.009 mg/ml, respectively. This was supported by work surrounding adsorption kinetics showed that with 15 minutes of incubation with a protein solution on a surface ~40% of the protein in a solution binds to a surface, and in 1 hour uptake increases to 87% of protein in solution. [21] The amount of protein in each anti-prothrombin solution was known, but radiolabelled tests were not completed and therefore, assumptions were made about the amount of anti-prothrombin that binds to the surface from solutions. Therefore, assuming ~40% of the protein in solution binds to the surface, the limit of detection and analytical sensitivity was achieved when ~1.3 pmols and ~0.7 pmols of anti-prothrombin bound to the antigen-coated surface.

A comparison of experimental and theoretical calculations, assuming one anti-prothrombin binds for every two prothrombin molecules for theoretical calculations, showed the experimentally determined limit of detection was lower than the theoretical limit by 1.4 pmols. A number of assumptions were made that could account for this discrepancy. Assumptions include the ratio of prothrombin to anti-prothrombin binding and the percentage of antibody that binds to the surface from solution at a specific concentration. In addition, the anti-prothrombin likely creates a thicker layer on the surface than prothrombin and could lead to a lower limit of detection as a result similar to findings with the vitamin K-dependent proteins size influencing sensitivity (see chapter 8 for details). An increase in the refractive index of the protein, or the layer density, may cause an additional increase in the OPL and colour shift. Lastly, a portion of the prothrombin surface coverage during radiolabelled work in chapter 9, may bind within the surface pores in an orientation that prevents antibody

binding. Therefore, the required surface coverage to generate a visible colour shift would appear higher than necessary for detection.

Based on the results obtained with the current methods, detecting an antibody from solution with an immobilized antigen on the device surface showed a lower sensitivity than ELISAs. However, the use of an amplification process, as in other immunoassays, would improve the sensitivity as well as changes in the exposure procedure such as increasing the length of time or volume. The limit of detection for ELISAs is in the femtomole range when comparing the amount of protein. However, to achieve these levels of sensitivity an amplification step is required and incubation times between 2 and 4 hours[5] at an increased temperature. [2] With longer incubation times and higher exposure volumes, the detection limit of the current device would decrease, improving the device sensitivity. On the current device with the exposure parameters employed, quantitative protein detection can be achieved. Antibodies generated in response to an immunogen are in the mg/ml range in serum, [3,4] along with virulence factors, from sputum or other sources, which are present in the μg/ml range. [22] Higher sensitivities are necessary for detecting biomarkers and signal proteins and would require modifications to the device or exposure procedure in order to amplify the signal.

The statistical analysis results showed no difference in the x and y coordinates between exposing 0.67 and 1.33 μM of anti-prothrombin solution to the antigen-coated device. The second protein layer is likely reaching saturation with higher concentrations. Additional chromaticity coordinates for higher anti-prothrombin concentrations would be needed to confirm this.

Lastly, observations by eye of device surfaces containing three different alumina thicknesses showed that a lower limit of detection was achievable in certain regions of the second colour order. Slides with different alumina thicknesses and the same alumina refractive indices ($p>.078$) (ranging from $\eta=1.345$ to 1.366 at $\lambda=370$ nm) were visually evaluated by eye to compare the anti-prothrombin limit of detection with different alumina thicknesses. With the anti-prothrombin solutions of 0.08 μM exposed to the antigen-coated surface a stronger colour shift was apparent on the 108 nm alumina device.

10.5 Future Work

To complete sensitivity and specificity work that provide more information, additional tests should be completed. Anti-prothrombin should be diluted in biological samples (i.e. serum, anti-coagulated plasma, anti-coagulated whole blood, sputum etc.) to determine the influence on the sensitivity. This will evaluate the antigen-antibody binding in a complex solution with non-specific proteins. Alternate antigen-antibody pairs should be tested, using a bridging molecule and linking method to immobilized other antigens as receptors. Lastly, devices with a variety of alumina thicknesses and refractive indices should be tested for anti-prothrombin detection to ensure maximum sensitivity.

10.6 Conclusions

The exposure of various amounts of anti-prothrombin to the prothrombin-coated alumina surface, and analysis of the chromaticity coordinates allowed for interpretation of the data. Findings from the work are important for understanding the limit of detection and potential detection applications, as well as areas that can improve the limit of detection. The following conclusions were made.

1. The antibody sensitivity was assessed, finding the limit of detection on the prepared surface was ~1.3 pmols (20 µl at 0.17 µM) and the analytical sensitivity was ~0.7 pmols with a difference of 0.09 µM (between 20 µl at 0.08 and 0.17 µM), assuming 40% of the protein in solution binds to the surface in the incubation period. A difference in the x and/or y coordinates were observed to quantify differences in chromaticity coordinates.
2. The theoretical detection limit showed that 2.7 pmols of anti-prothrombin are required to bind to the antigen-coated surface to generate a colour shift (over 2 times the experimental limit of detection). The theoretical limit was equivalent to exposing 20 µl of anti-prothrombin solution at 0.3 µM (6 pmols).
3. Protein solutions used in future tests should be quantified. This work demonstrates that a change in the IgG solution concentrations of 0.09 µM, with 15 minutes of incubation on the surface, can result in a statistical difference in

chromaticity coordinates. Techniques for quantification could include Western Blot or UV-VIS spectrophotometry.

Bibliography

Chapter 1

1. McMullen T, Lai R, inventors. The Governors Of The University Of Alberta, assignee. Use of PDGFR-alpha as diagnostic marker for papillary thyroid cancer. US patent 20150010582A1. 2015 Jan. 08.

2. Zhang J, Wang P, Dykstra M, Gelebart P, Williams D, Ingham R, et al. Platelet-derived growth factor receptor-alpha promotes lymphatic metastases in papillary thyroid cancer. The Journal of Pathology 2012;228(2):241-250.

3. Ito Y, Miyauchi A. Lateral lymph node dissection guided by preoperative and intraoperative findings in differentiated thyroid carcinoma. World Journal of Surgery 2008;32(5):729-739.

4. Lorne R. The role of lymphadenectomy in the management of papillary carcinoma of the thyroid. Journal of Surgical Oncology 2009;99(4):186-188.

5. Machens A, Hinze R, Thomusch O, Dralle H. Pattern of nodal metastasis for primary and reoperative thyroid cancer. World Journal of Surgery 2002;26(1):22-28.

6. Lopez-Campistrous A, Adewuyi EE, Benesch MGK, Ko YM, Lai R, Thiesen A, et al. PDGFRα regulates follicular cell differentiation driving treatment resistance and disease recurrence in papillary thyroid cancer. EBioMedicine 2016;12:86-97.

7. Campbell S, Landry ML. Rapid antigen tests. In: Yi-Wei T, Stratton CW, editors. Advanced Techniques in Diagnostic Microbiology New York, NY: Springer; 2006. p. 23-41.

8. Nazarpour S. Thin films and coatings in biology. Dordrecht: Springer; 2013.

9. Burrell RE, Naylor AG, Rosenfeld AM, inventors. Alcan International Ltd, assignee. Thin film diagnostic device. US patent 5,124,172. 1992 Jun. 23.

Chapter 2

1. Loonen AJM, Schuurman R, van den Brule, Adriaan J. C. Highlights from the 7th European meeting on molecular diagnostics. Expert Review of Molecular Diagnostics 2012;12(1):17-19.

2. Engvall E, Perlmann P. Enzyme-linked immunosorbent assay (ELISA) quantitative assay of immunoglobulin G. Immunochemistry 1971;8(9):871-874.

3. Kellogg MD. Measurement of biological materials.In: Robertson D, Williams GH, editors. Clinical and Translational Science. 2nd ed. London, UK: Academic Press; 2017. p. 137-155.

4. Hnasko R. ELISA: Methods and protocols. New York: Humana Press; 2015.

5. Crowther JR. The ELISA guidebook. 2nd ed. New York: Humana Press; 2009.

6. Thermo Fisher Scientific Inc. ELISA technical guide and protocols. 2010;2018(01/03).

7. AppliCations. Improving quality and stability of ELISA. 2010; Available from: https://www.applichem.com/fileadmin/Application_Notes/AppliCations_No4_AppliCoat_CrossDown_en.pdf. [cited 11/06/2014].

8. Byrne B, Stack E, Gilmartin N, Richard O'Kennedy. Antibody-based sensors: principles, problems and potential for detection of pathogens and associated toxins. Sensors 2009;9(6):4407-4445.

9. Gubala V, Harris LF, Ricco AJ, Tan MX, Williams DE. Point of care diagnostics: status and future. Analytical Chemistry 2012;84(2):487-515.

10. Yager P, Domingo GJ, Gerdes J. Point-of-care diagnostics for global health. Annual Review of Biomedical Engineering 2008;10(1):107-144.

11. Holland CA, Kiechle FL. Point-of-care molecular diagnostic systems — past, present and future. Current Opinion in Microbiology 2005;8(5):504-509.

12. Cepheid. Cepheid Solutions. 2018; Available from: http://www.cepheid.com/us/. [cited 05/07/2018].

13. F. Hoffman La Roche Ltd. Roche aquires IQ^{uum} to strengthen offerings in moelcular diagnostics. 2018; Available from: https://www.roche.com/media/store/releases/med-cor-2014-04-07.htm. [cited 05/07/2018].

14. Valle C. The year ahead: What to expect in 2017. 2017; Available from: https://www.luminexcorp.com/blog/the-year-ahead-what-to-expect-in-2017/. [cited 05/07/2018].

15. ERBA MDX. ERBA diagnostics Mannheim aquires Lumora. 2015; Available from: http://www.erbamdx.co.uk/news/175-erba-diagnostics-mannheim-acquires-lumora.html. [cited 07/05/2018].

16. Dunbar SA. Applications of Luminex® xMAP™ technology for rapid, high-throughput multiplexed nucleic acid detection. Clinica Chimica Acta 2006;363(1):71-82.

17. Luminex Coorporation. xMAP® Technology. 2018; Available from: https://www.luminexcorp.com/research/our-technology/xmap-technology/. [cited 05/10/2018].

18. Chin CD, Linder V, Sia SK. Commercialization of microfluidic point-of-care diagnostic devices. Lab On A Chip 2012;12(12):2118-2134.

19. Warsinke A. Point-of-care testing of proteins. Analytical and Bioanalytical Chemistry 2009;393(5):1393-1405.

20. Song Y, Huang Y, Liu X, Zhang X, Ferrari M, Qin L. Point-of-care technologies for molecular diagnostics using a drop of blood. Trends in Biotechnology 2014;32:132-139.

21. Myers FB, Lee LP. Innovations in optical microfluidic technologies for point-of-care diagnostics. Lab on a Chip 2008;8(12):2015-2031.

22. Koczula K, Gallotta A. Lateral flow assays. Essays in Biochemistry 2016;60(1):111-120.

23. Tetracore Inc. BioThreat Alert®. n/a; Available from: http://www.tetracore.com/bio-warfare/index.html. [cited 05/08/2018].

24. Townsend MB, MacNeil A, Reynolds MG, Hughes CM, Olson VA, Damon IK, et al. Evaluation of the Tetracore Orthopox BioThreat® antigen detection assay using laboratory grown orthopoxviruses and rash illness clinical specimens. Journal of Virological Methods 2013;187(1):37-42.

25. Cliawaived Inc. Rapid test for elevated TSH. 2015; Available from: http://thyrochek.com/. [cited 05/08/2018].

26. You DJ, Park TS, Yoon J. Cell-phone-based measurement of TSH using Mie scatter optimized lateral flow assays. Biosensors and Bioelectronics 2013;40:180-185.

27. Sajid M, Kawde A, Daud M. Designs, formats and applications of lateral flow assay: A literature review. Journal of Saudi Chemical Society 2015;19(6):689-705.

28. Chui BW, Kenny TW, Mamin HJ, Terris BD, Rugar D. Independent detection of vertical and lateral forces with a sidewall-implanted dual-axis piezoresistive cantilever. Applied Physics Letters 1998;72(11):1388-1390.

29. Harley JA, Kenny TW. 1/F noise considerations for the design and process optimization of piezoresistive cantilevers. Journal of Microelectromechanical Systems 2000;9(2):226-235.

30. Wu J, Gu M. Microfluidic sensing: State of the art fabrication and detection techniques. Journal of Biomedical Optics 2011;16(8):1-12.

31. Dianax. Products. 2018; Available from: https://dianax.eu/. [cited 05/07/2018].

32. Gervais L, de Rooij N, Delamarche E. Microfluidic chips for point-of-care immunodiagnostics. Advanced Materials 2011;23(24):H151-H176.

33. Dincer C, Bruch R, Kling A, Dittrich PS, Urban GA. Multiplexed point-of-care testing – xPOCT. Trends in Biotechnology 2017;35(8):728-742.

34. Abbott. i-Stat handheld. 2017; Available from: https://www.pointofcare.abbott/int/en/offerings/istat/istat-handheld. [cited 05/07/2018].

35. Ismail F, Mackay WG, Kerry A, Staines H, Rooney KD. The accuracy and timeliness of a point of care lactate measurement in patients with sepsis. Scandinavian Journal of Trauma, Resuscitation and Emergency Medicine 2015;23(1):68-74.

36. Bogue R. MEMS sensors: Past, present and future. Sensor Review 2007;27(1):7-13.

37. Kim SH, Asay DB, Dugger MT. Nanotribology and MEMS. Nano Today 2007;2(5):22-29.

38. Ravishankar D. Analysis of the global in vitro diagnostics market: Slowing US and European markets demand alignment with global market needs. PR Newswire (USA) 2014 10/01.

39. Frost & Sullivan. Research and markets: US companion diagnostics market trends and insights 2014. Business Wire 2014.

40. Ritchie RH, Arakawa ET, Cowan JJ, Hamm RN. Surface-plasmon resonance effect in grating diffraction. Physical Review Letters 1968;21(22):1530-1533.

41. Otto A. Excitation of surface plasma waves in silver by the method of frustrated total reflection . Zeitschrift Für Physik a Hadrons and Nuclei 1968;216(4):398-410.

42. Kretschmann E., Raether H. Radiative decay of non radiative surface plasmons excited by light. Zeitschrift für Naturforschung A 1968;23(12):2135.

43. Liedberg B, Nylander C, Lunström I. Surface plasmon resonance for gas detection and biosensing. Sensors and Actuators 1983;4:299-304.

44. Singh P. SPR biosensors: Historical perspectives and current challenges. Sensors and Actuators B: Chemical 2016;229:110-130.

45. Wijaya E, Lenaerts C, Maricot S, Hastanin J, Habraken S, Vilcot J, et al. Surface plasmon resonance-based biosensors: From the development of different SPR structures to novel surface functionalization strategies. Current Opinion in Solid State and Materials Science 2011;15(5):208-224.

46. Liu Y, Liu Q, Chen S, Cheng F, Wang H, Peng W. Surface plasmon resonance biosensor based on smart phone platforms. Scientific Reports 2015;5(12864):1-9.

47. Van Dorpe P, Ryken J, Li J, Steylaerts T, Vos R, Loo J, et al. Biosensing with SiO2-covered SPR substrates in a commercial SPR-tool. Sensors and Actuators B-Chemical 2014;200:167-172.

48. Guner H, Ozgur E, Kokturk G, Celik M, Esen E, Topal AE, et al. A smartphone based surface plasmon resonance imaging (SPRi) platform for on-site biodetection. Sensors and Actuators B: Chemical 2017;239:571-577.

49. Preechaburana P, Gonzalez MC, Suska A, Filippini D. Surface plasmon resonance chemical sensing on cell phones. Angew Chem Int Ed 2012;51(46):11585-11588.

50. Bremer K, Roth B. Fibre optic surface plasmon resonance sensor system designed for smartphones. Opt Express 2015;23(13):17179-17184.

51. Roche PJR, Filion-Côté S, Cheung MC-, Chodavarapu VP, Kirk AG. A camera phone localised surface plasmon biosensing platform towards low-cost label-free diagnostic testing. Journal of Sensors 2011;2011(406425):1-7.

52. Dutta S, Saikia K, Nath P. Smartphone based LSPR sensing platform for bio-conjugation detection and quantification. RSC Adv 2016;6(26):21871-21880.

53. Langmuir I, Schaefer VJ. Monolayers and multilayers of chlorophyll. J Am Chem Soc 1937;59(10):2075-2076.

54. Rothen A, Landsteiner K. Serological reactions of protein films and denatured proteins. J Exp Med 1942;76(5):437-450.

55. Giaever I, inventor. General Electric Company, assignee. Method and apparatus for immunological detection of biological particles. US patent 3,853,467. 1974 Dec. 10.

56. Giaever I, inventor. General Electric Company, assignee. Substrate for immunological tests and method of fabrication thereof. US patent 3,926,564. 1975 Dec. 16.

57. Giaever I, inventor. General Electric Company, assignee. Diagnostic device for visually detecting presence of biological particles. US patent 3,979,184. 1976 Sept. 7.

58. Nygren BH, Sandstrom ET, Stenberg JE, Stiblert LB, inventors. Sagax Instrument AB, assignee. Method and member for detecting and/or measuring the concentration of a chemical substance. US patent 4,558,012. 1985 Dec. 10.

59. Adams AL, Klings M, Fischer GC, Vroman L. Three simple ways to detect antibody-antigen complex on flat surfaces. J Immunol Methods 1973;3(3):227-232.

60. Burrell RE, Naylor AG, Rosenfeld AM, inventors. Alcan International Ltd, assignee. Thin film diagnostic device. US patent 5,124,172. 1992 Jun. 23.

61. Djokić SS, Burrell RE. Visual detection of protein adsorption onto electrochemically oxidized aluminum surfaces. Biosens Bioelectron 1998;13(3–4):271-278.

62. Ettinger A, Ostroff R, Brien J, Polisky B. In-process monitoring of protein purification with thin film silicon sensor technology. BioTechniques 2002;32(4):934-938.

63. Harbeck RJ, Teague J, Crossen GR, Maul DM, Childers PL. Novel, rapid optical immunoassay technique for detection of group A streptococci from pharyngeal specimens: Comparison with standard culture methods. Journal of Clinical Microbiology 1993;31(4):839-844.

64. Van Dong L, Khoo HE, Quyen LK, Gopalakrishnakone P. Optical immunoassay for snake venom detection. Biosensors and Bioelectronics 2004;19(10):1285-1294.

65. Maul DM, Crider DG, Bilodeau RJ, Bogart GR, inventors. Biostar I, assignee. Highly sensitive optical immunoassay using enzyme-labeled reagents. EP patent 0 546 222 B1. 1997 09/10.

66. Datta P. Immunoassay design and mechanisms of interferences.In: Dasgupta A, Sepulveda JL, editors. Accurate Results in the Clinical Laboratory San Diego: Elsevier; 2013. p. 63-73.

67. Stevenson RL. Review of HPLC 2014: Advances in HPLC and so much more. American Laboratory 2014;46(7):4-9.

68. Larson JR, Tingstad JE, Swadesh JK. Introduction.In: Swadesh JK, editor. HPLC: Practical and industrial applications. 2nd ed. Boca Raton, FL: CRC Press; 2001. p. 1-70.

69. Brunstein J. PCR: The basics of the polymerase chain reaction. Medical Laboratory Observer 2013;45(4):32-35.

70. Lyshevski SE. Nano- and micro-electromechanical systems: Fundamentals of nano- and microengineering. 2nd ed. Boca Raton, FL: CRC Press; 2005.

71. Bogue R. Recent developments in MEMS sensors: A review of applications, markets and technologies. Sensor Review 2013;33(4):300-304.

72. Pilarski LM, Mehta MD, Caulfield T, Kaler KVIS, Backhouse CJ. Microsystems and nanoscience for biomedical applications: A view to the future. Bulletin of Science, Technology and Society 2004;24(1):40-45.

73. Backhouse CJ, inventor. Micralyne Incorporated, assignee. Fluidic devices. US patent 6,318,970. 2001 Nov. 20.

74. Peeling RW, Holmes KK, Mabey D, Ronald A. Rapid tests for sexually transmitted infections (STIs): the way forward. Sexually Transmitted Infections 2006;82(Suppl V):v1-v6.

75. Macleod HA. Thin-film optical filters. 4th ed. Boca Raton: Taylor & Francis; 2010.

76. Nave R. Oil film interference. 2000; Available from: http://hyperphysics.phy-astr.gsu.edu/hbase/phyopt/oilfilm.html. [cited 10/24/2015].

77. J. A. Woollam Company. Guide to using WVASE 32®. 2008.

78. Hecht E. Optics. 4th ed. San Francisco; Toronto: Addison-Wesley; 2002.

79. Bunk T, Eisenkraft A, Kirkpatrick LD. Color creation. Quantoons: Metaphysical Illustrations by Tomas Bunk, physical explanations by Arthur Eisenkraft and Larry D. Kirkpatrick. 2006:140.

80. Malacara D. Color vision and colorimetry: Theory and applications. 2nd ed. Bellingham, WA: SPIE; 2011.

81. Lugolole R, Sam KO. The effect of thickness of aluminium films on optical reflectance. Journal of Ceramics 2015;2015:1-6.

82. Sandström T, Stenberg M, Nygren H. Visual detection of organic monomolecular films by interference colors. Applied Optics 1985;24(4):472-479.

83. Kinoshita S. Structural colors in the realm of nature. Singapore: World Scientific Publishing Co. Pte. Ltd.; 2008.

84. Kern W, Schuegraf KK. Deposition technolgoies and applications: introduction and overview.In: Seshan K, editor. Handbook of Thin Film Deposition: Processes and Technologues. 2nd ed. Norwich, NY: Noyes Publications; 2002. p. 11-43.

85. Greene JE. Review Article: Tracing the recorded history of thin-film sputter deposition: From the 1800s to 2017. Journal of Vacuum Science & Technology A 2017;35(5):1-60.

86. Swann S. Magnetron sputtering. Physics in Technology 1988;19(2):67-75.

87. Jenison RD, Bucala R, Maul D, Ward DC. Thin-film technology for direct visual detection of nucleic acid sequences: Applications in clinical research. Expert Review of Molecular Diagnostics 2006;6(1):89-99.

88. Frey H. Cathode sputtering.In: Frey H, Khan HR, editors. Handbook of Thin Film Technology Berlin: Springer; 2015. p. 133-165.

89. Depla D, Mahieu S, Greene JE. Sputter deposition processes.In: Martin PM, editor. Handbook of Deposition Technologies for Films and Coatings : Science, Applications and Technology. 3rd ed. Amsterdam: William Andrew; 2010. p. 253-294.

90. Eichner HW, Schowalter WE. 1950;1813.

91. Kabayashi GS, Donnelly DJ. 1974;DG-41517.

92. Rogers NL, inventor. Bell Aerospace Corporation, assignee. Bondable coating on aluminum and method of applying it. US patent 3,414,489. 1966 .

93. Venables JD, McNamara DK, Chen JM, Sun TS, Hopping RL. Oxide morphologies on aluminum prepared for adhesive bonding. Applications of Surface Science 1979;3(1):88-98.

94. Masuda H, Fukuda K. Ordered metal nanohole arrays made by a two-step replication of honeycomb structures of anodic alumina. Science 1995;268(5216):1466-1468.

95. Piao Y, Kim H. Fabrication of nanostructured materials using porous alumina template and their applications for sensing and electrocatalysis. Journal of Nanoscience and Nanotechnology 2009;9(4):2215-2233.

96. Chen B, Xu Q, Zhao X, Zhu X, Kong M, Meng G. Branched silicon nanotubes and metal nanowires via AAO-template-assistant approach. Advanced functional materials 2010;20(21):3791-3796.

97. Yanagishita T, Nishio K, Masuda H. Fabrication of metal nanohole arrays with high aspect ratios using two-step replication of anodic porous alumina. Advanced Materials 2005;17(18):2241-2243.

98. Drury A, Chaure S, Kröll M, Nicolosi V, Chaure N, Blau WJ. Fabrication and characterization of silver/polyaniline composite nanowires in porous anodic alumina. Chemistry of Materials 2007;19(17):4252-4258.

99. Zhu Z, Garcia-Gancedo L, Qiang L, Flewitt A, Milne WI, Moussy F. Size-tunable porous anodic alumina nano-structure for biosensing. Soft Nanoscience Letters 2011;1(3):55-60.

100. Shi H, Yeh JI. Part I: Recent developments in nanoelectrodes for biological measurements. Nanomedicine 2007;2(5):587-598.

101. Young DJ. High temperature oxidation and corrosion of metals. 1st ed. Amsterdam; Boston; London: Elsevier; 2008.

102. Mozalev A, Sakairi M, Saeki I, Takahashi H. Nucleation and growth of the nanostructured anodic oxides on tantalum and niobium under the porous alumina film. Electrochimica Acta 2003;48(20):3155-3170.

103. Macagno V, Schultze J. The growth and properties of thin oxide layers on tantalum electrodes. J Electroanal Chem Interfacial Electrochem 1984;180(1-2):157-170.

104. Charlesby A, Polling JJ. The optical properties of thin oxide films on tantalum. Proc R Soc Lond A Math Phys Sci 1955;227(1171):434-447.

105. Cui-Cui S, Yun-Yu C, En-Mei D, Chang-Hao L. Tunable structural color of anodic tantalum oxide films. Chin Phys B 2012;21(8):1-5.

106. Lee W, Park S. Porous anodic aluminum oxide: Anodization and templated synthesis of functional nanostructures. Chem Rev 2014;114(15):7487-7556.

107. Sulka GD. Highly ordered anodic porous alumina formation by self-organized anodizing.In: Eftekhari A, editor. Nanostructured Materials in Electrochemistry Weinheim: Wiley-VCH: John Wiley & Sons; 2008. p. 1-97.

108. Ono S, Masuko N. Evaluation of pore diameter of anodic porous films formed on aluminum. Surface and Coatings Technology 2003;169-170:139-142.

109. Zhou F. Growth mechanism of porous anodic films on aluminum. Unpublished, The University of Manchester, 2011.

110. Hunter MS, Fowle P. Natural and thermally formed oxide films on aluminum. Journal of the Electrochemical Society 1956;103(9):482-485.

111. Bocchetta P, Sunseri C, Masi R, Piazza S, Di Quarto F. Influence of initial treatments of aluminium on the morphological features of electrochemically formed alumina membranes. Materials Science and Engineering: C 2003;23(6):1021-1026.

112. Kasprzyk-Hordern B. Chemistry of alumina, reactions in aqueous solution and its application in water treatment. Adv Colloid Interface Sci 2004;110(1):19-48.

113. Aramesh M, Cervenka J. Surface modification of porous anodic alumina for medical and biological applications.In: Seifalian A, de Mel A, Kalaskar DM, editors. Nanomedicine. 1st ed. VIC, AU: One Central Press; 2014. p. 439-467.

114. Hu G, Zhang H, Di W, Zhao T. Study on wet etching of AAO template. Applied Physics Research 2009;1(2):78-83.

115. Morterra C, Magnacca G. A case study: surface chemistry and surface structure of catalytic aluminas, as studied by vibrational spectroscopy of adsorbed species. Catalysis Today 1996;27(3):497-532.

116. Wefers K, Misra C. Oxides and hydroxides of aluminum. Pennsilvania, USA: Alcoa Research Laboratories; 1987.

117. Cornelius EB, Milliken TH, Mills GA, Oblad AG. Surface Strain in Oxide Catalysts-Alumina. The Journal of Physical Chemistry 1955;59(9):809-813.

118. Flockhart BD, Leith IR, Pink RC. Electron-transfer at alumina surfaces. Part 2. - Electron-donor properties of aluminas. Transactions of the Faraday Society 1969;65:542-551.

119. Mardilovich PP, Paterson R, Govyadinov AN, Mukhurov NI, Rzhevskii AM. New and modified anodic alumina membranes Part I. Thermotreatment of anodic alumina membranes. Journal of Membrane Science 1995;98(1-2):131-142.

120. Yopps JA, Fuerstenau DW. The zero point of charge of alpha-alumina. Journal of Colloid Science 1964;19(1):61-71.

121. Bowen WR, Hughes DT. Properties of microfiltration membranes: The surface electrochemistry of anodic film membranes. Journal of Colloid and Interface Science 1991;143(1):252-265.

122. Gervais F. Aluminum Oxide (Al_2O_3).In: Palik ED, editor. Handbook of Optical Constants of Solids. 2nd ed. San Diego, CA: Academic Press; 1998. p. 761-775.

123. Suárez-García A, Gonzalo J, Afonso CN. Low-loss Al_2O_3 waveguides produced by pulsed laser deposition at room temperature. Applied Physics A 2003;77(6):779-783.

124. Aslan MM, Webster NA, Byard CL, Pereira MB, Hayes CM, Wiederkehr RS, et al. Low-loss optical waveguides for the near ultra-violet and visible spectral regions with Al_2O_3 thin films from atomic layer deposition. Thin Solid Films 2010;518(17):4935-4940.

125. Smit MK, Acket GA, van der Laan CJ. Al_2O_3 films for integrated optics. Thin Solid Films 1986;138(2):171-181.

126. Kawaguchi T, Shiro T, Iwata K. Device for visual detection of antigens and antibodies by means of light interference. Thin Solid Films 1990;191(2):369-381.

127. Stroeve P, Ileri N. Biotechnical and other applications of nanoporous membranes. Trends in Biotechnology 2011;29(6):259-266.

128. Platschek B, Keilbach A, Bein T. Mesoporous structures confined in anodic alumina membranes. Advanced Materials 2011;23(21):2395-2412.

129. Kumeria T, Kurkuri MD, Diener KR, Parkinson L, Losic D. Label-free reflectometric interference microchip biosensor based on nanoporous alumina for detection of circulating tumour cells. Biosensors and Bioelectronics 2012;35(1):167-173.

130. Shi W, Shen Y, Ge D, Xue M, Cao H, Huang S, et al. Functionalized anodic aluminum oxide (AAO) membranes for affinity protein separation. Journal of Membrane Science 2008;325(2):801-808.

131. Fu J, Mao P, Han J. Artificial molecular sieves and filters: A new paradigm for biomolecule separation. Trends in Biotechnology 2008;26(6):311-320.

132. Manzano M, Vallet-Regi M. New developments in ordered mesoporous materials for drug delivery. Journal of Materials Chemistry 2010;20(27):5593-5604.

133. de la Escosura-Muñiz A, Espinoza-Castañeda M, Chamorro-García A, Rodríguez-Hernández CJ, de Torres C, Merkoçi A. In situ monitoring of PTHLH secretion in

neuroblastoma cells cultured onto nanoporous membranes. Biosens Bioelectron 2018;107:62-68.

134. Tian F, Lyu J, Shi J, Tan F, Yang M. A polymeric microfluidic device integrated with nanoporous alumina membranes for simultaneous detection of multiple foodborne pathogens. Sens Actuators B Chem 2016;225:312-318.

135. Peh AEK, Li SFY. Dengue virus detection using impedance measured across nanoporous alumina membrane. Biosens Bioelectron 2013;42:391-396.

136. Nguyen BTT, Peh AEK, Chee CYL, Fink K, Chow VTK, Ng MML, et al. Electrochemical impedance spectroscopy characterization of nanoporous alumina dengue virus biosensor. Bioelectrochemistry 2012;88:15-21.

137. Cheng MS, Ho JS, Tan CH, Wong JPS, Ng LC, Toh C. Development of an electrochemical membrane-based nanobiosensor for ultrasensitive detection of Dengue virus. Anal Chim Acta 2012;725:74-80.

138. Jin Z, Meng F, Liu J, Li M, Kong L, Liu J. A novel porous anodic alumina based capacitive sensor towards trace detection of PCBs. Sens Actuators B Chem 2011;157(2):641-646.

139. Chen Z, Shen G, Li Y, Zhang P, Ji H, Liu S, et al. A novel biomimetic logic gate for sensitive and selective detection of Pb(II) base on porous alumina nanochannels. Electrochem Commun 2015;60:83-87.

140. Wu S, Ye W, Yang M, Taghipoor M, Meissner R, Brugger J, et al. Impedance sensing of DNA immobilization and hybridization by microfabricated alumina nanopore membranes. Sens Actuators B Chem 2015;216:105-112.

141. Rai V, Hapuarachchi HC, Lee CN, Siew HS, Yee SL, Chee- ST, et al. Ultrasensitive cDNA detection of Dengue virus RNA using electrochemical nanoporous membrane-based biosensor. PLoS ONE 2012;7(8):1-7.

142. Deng J, Chee-Seng Toh. Impedimetric DNA biosensor based on a nanoporous alumina membrane for the detection of the specific oligonucleotide sequence of Dengue virus. Sensors 2013;13(6):7774-7785.

143. Rai V, Deng J, Toh C. Electrochemical nanoporous alumina membrane-based label-free DNA biosensor for the detection of Legionella sp. Talanta 2012;98:112-117.

144. Ye W, Xu Y, Zheng L, Zhang Y, Yang M, Sun P. A nanoporous alumina membrane based electrochemical biosensor for histamine determination with biofunctionalized magnetic nanoparticles concentration and signal amplification. Sensors 2016;16(10):1-12.

145. Li S, Xia N, Yuan B, Du W, Sun Z, Zhou B. A novel DNA sensor using a sandwich format by electrochemical measurement of marker ion fluxes across nanoporous alumina membrane. Electrochim Acta 2015;159:234-241.

146. Largueze J, Kirat KE, Morandat S. Preparation of an electrochemical biosensor based on lipid membranes in nanoporous alumina. Colloids Surf B Biointerfaces 2010;79(1):33-40.

147. Tanvir S, Pantigny J, Boulnois P, Pulvin S. Covalent immobilization of recombinant human cytochrome CYP2E1 and glucose-6-phosphate dehydrogenase in alumina membrane for drug screening applications. J Membr Sci Technol 2009;329(1):85-90.

148. Yang Z, Zhang C. Single-enzyme nanoparticles based urea biosensor. Sens Actuators B Chem 2013;188:313-317.

149. Kim J, Mauk M, Chen D, Qiu X, Kim J, Gale B, et al. A PCR reactor with an integrated alumina membrane for nucleic acid isolation. Analyst 2010;135(9):2408-2414.

150. Vasiliev AA, Pavelko RG, Gogish-Klushin S, Kharitonov DY, Gogish-Klushina O, Sokolov AV, et al. Alumina MEMS platform for impulse semiconductor and IR optic gas sensors. Sens Actuators B Chem 2008;132(1):216-223.

151. Tsou P, Sreenivasappa H, Hong S, Yasuike M, Miyamoto H, Nakano K, et al. Rapid antibiotic efficacy screening with aluminum oxide nanoporous membrane filter-chip and optical detection system. Biosens Bioelectron 2010;26(1):289-294.

152. Liu Z, Zhang Y, Yu J, Mak AF, Li Y, Yang M. A microfluidic chip with poly(ethylene glycol) hydrogel microarray on nanoporous alumina membrane for cell patterning and drug testing. Sens Actuators B Chem 2010;143(2):776-783.

153. Álvarez J, Sola L, Cretich M, Swann MJ, Gylfason KB, Volden T, et al. Real time optical immunosensing with flow-through porous alumina membranes. Sens Actuators B Chem 2014;202:834-839.

154. Liu Y, Wang HH, Indacochea JE, Wang ML. A colorimetric sensor based on anodized aluminum oxide (AAO) substrate for the detection of nitroaromatics. Sens Actuators B Chem 2011;160(1):1149-1158.

155. Ayas S, Bakan G, Ozgur E, Celebi K, Torunoglu G, Dana A. Colorimetric detection of ultrathin dielectrics on strong interference coatings. Opt Lett 2018;43(6):1379-1382.

156. Wang J, Zhang Y, Feng C, Li J, Li G. Adsorption capacity for phosphorus comparison among activated alumina, silica sand and anthracite coal. Journal of Water Resource and Protection 2009;1(4):260-264.

157. Schmitt GL, Pietrzyk DJ. Liquid chromatographic separation of inorganic anions on an alumina column. Analytical Chemistry 1985;52(12):2247-2253.

158. Hyndman D, Burrell R, Lever G, Flynn TG. Protein immobilization to alumina supports: I. Characterization of alumina-organophosphate ligand interactions and use in the attachment of papain. Biotechnology and Bioengineering 1992;40(11):1319-1327.

159. Hyndman D, Burrell R, Lever G, and Flynn G. Protein immobilization to alumina supports: II. Papain immobilization to alumina via organophosphate linkers. Biotechnology and Bioengineering 1992;40(11):1328-1336.

160. Vasudevan PT, Thakur DS. Soluble and immobilized catalase. Applied Biochemistry and Biotechnology 1994;49(3):173-189.

161. Leary Swan EE, Popat KC, Desai TA. Peptide-immobilized nanoporous alumina membranes for enhanced osteoblast adhesion. Biomaterials 2005;26(14):1969-1976.

162. Kummert R, Stumm W. The surface complexation of organic acids on hydrous γ-Al2O3. Journal of Colloid and Interface Science 1980;75(2):373-385.

163. Somasundaran P, Krishnakumar S. Adsorption of surfactants and polymers at the solid-liquid interface. Colloids and Surfaces A: Physicochemical and Engineering Aspects 1997;123-124:491-513.

164. Evans H, Weinberg W. A comparison of the vibrational structures of ethanol, acetic acid, and acetaldehyde adsorbed on alumina. The Journal of Chemical Physics 1979;71(12):4789-4798.

165. Anderson JA, Rochester CH. Infrared study of the adsorption of acetone, acrolein, ethanoic acid and propene-NO mixtures on Rh/Al2O3 catalysts. Journal of the Chemical

Society, Faraday Transactions 1: Physical Chemistry in Condensed Phases 1989;85(5):1117-1128.

166. Wijnja H, Schulthess CP. ATR–FTIR and DRIFT spectroscopy of carbonate species at the aged γ-Al2O3/water interface. Spectrochimica Acta Part A: Molecular and Biomolecular Spectroscopy 1999;55(4):861-872.

167. van den Brand J, Blajiev O, Beentjes PCJ, Terryn H, de Wit, J. H. W. Interaction of anhydride and carboxylic acid compounds with aluminum oxide surfaces studied using infrared reflection absorption spectroscopy. Langmuir 2004;20(15):6308-6317.

168. Hall JT, Hansma PK. Chemisorption of monocarboxylic acids on alumina: A tunneling spectroscopy study. Surface Science 1978;77(1):61-76.

169. Nara M, Torii H, Tasumi M. Correlation between the vibrational frequencies of the carboxylate group and the types of its coordination to a metal Ion: An *ab initio* molecular orbital study. The Journal of physical chemistry 1996;100(51):19812-19817.

170. Ohe C, Ando H, Sato N, Urai Y, Yamamoto M, Itoh K. Carboxylate-counterion interactions and changes in these interactions during photopolymerization of a long-chain diacetylene monocarboxylic acid at air-water Interfaces: External infrared reflection absorption spectroscopic study. The Journal of Physical Chemistry B 1999;103(3):435-444.

171. Deacon GB, Phillips RJ. Relationships between the carbon-oxygen stretching frequencies of carboxylato complexes and the type of carboxylate coordination. Coordination Chemistry Reviews 1980;33(3):227-250.

172. Ulrich HJ, Stumm W, Cosovlc B. Adsorption of aliphatic fatty acids on aquatic interfaces. Comparison between two model surfaces: the mercury electrode and d-Al2O3 colloids. Environmental Science and Technology 1988;22(1):37-41.

173. Karaman ME, Antelmi DA, Pashley RM. The production of stable hydrophobic surfaces by the adsorption of hydrocarbon and fluorocarbon carboxylic acids onto alumina substrates. Colloids and Surfaces A: Physicochemical and Engineering Aspects 2001;182(1):285-298.

174. Ramsier RD, Henriksen PN, Gent AN. Adsorption of phosphorus acids on alumina. Surface Science 1988;203(1-2):72-88.

175. Crowell JE, Chen JG, Yates JT. A vibrational study of the adsorption and decomposition of formic acid and surface formate on Al(111). The Journal of Chemical Physics 1986;85(5):3111-3122.

176. Koide Y, Barron AR. $Al_5(^tBu)_5(\mu_3\text{-}O)_2(\mu_3\text{-}OH)_2(\mu\text{-}OH)_2(\mu\text{-}O_2CPh)_2]$: A model for the interaction of carboxylic acids with boehmite. Organometallics 1995;14(8):4026-4029.

177. Bethley CE, Aitken CL, Harlan CJ, Koide Y, Bott SG, Barron AR. Structural characterization of dialkylaluminum carboxylates: Models for carboxylate alumoxanes. Organometallics 1997;16(3):329-341.

178. Walz DA, Hewett-Emmett D, Seegers WH. Amino acid sequence of human prothrombin fragments 1 and 2. Proceedings of the National Academy of Sciences of the United States of America 1977;74(5):1969.

179. Gitzen WH. Alumina as a ceramic material. Columbus, Ohio: American Ceramic Society; 1970.

180. do Carmo DR, Filho NLD. Adsorption at silica, alumina, and related surfaces.In: Somasundaran P, editor. Encylopedia of Surface and Colloid Science. 3rd ed.: Taylor & Francis; 2015. p. 122-140.

181. Pozzi N, Chen Z, Di Cera E. (PDB ID: 5EDM) How the linker connecting the two kringles influences activation and conformational plasticity of prothrombin. The Journal of Biological Chemistry 2016;291(19):6071-6082.

182. Lim TK, Bloomfield VA, Nelsestuen GL. Structure of the prothrombin-and blood clotting factor X-membrane complexes. Biochemistry 1977;16(19):4177-4181.

183. Thurman RB, Gerba CP. Characterization of the effect of aluminum metal on poliovirus. Journal of Industrial Microbiology 1988;3(1):33-38.

184. Murray JP, Laband SJ. Degradation of poliovirus by adsorption on inorganic surfaces. Applied and Environmental Microbiology 1979;37(3):480-486.

185. Wittayanukulluk A, Jiang D, Regnier FE, Hem SL. Effect of microenvironment pH of aluminum hydroxide adjuvant on the chemical stability of adsorbed antigen. Vaccine 2004;22(9):1172-1176.

186. Clapp T, Siebert P, Chen D, Jones Braun L. Vaccines with aluminum-containing adjuvants: Optimizing vaccine efficacy and thermal stability. Journal of Pharmaceutical Sciences 2011;100(2):388-401.

187. Chu BY, Chui HC, Hsu CR, Chung CK. Characteristic resonance reflection spectra of nanoporous alumina films and its application to precise thickness measurement. ECS Journal of Solid State Science and Technology 2017;6(7):N92-N96.

188. Sorensen BE. A revised Michel-Levy interference colour chart based on first-principles calculations. European Journal of Mineralogy 2013;25(1):5-10.

189. Fernandez-Maloigne C. Advanced color image processing and analysis. New York: Springer; 2013.

190. Schubert EF. Colorimetry.Light-Emitting Diodes. 2nd ed. Cambridge: Cambridge University Press; 2006. p. 292-305.

191. Smith WJ. Optics Overview.Modern optical engineering: The design of optical systems. 4th ed. New York: McGraw-Hill; 2008. p. 1-20.

192. Fortner B, Meyer TE. Defining colours - the CIE color diagram.Number by colors: a guide to using color to understand technical data. 2nd ed. New York: Springer; 1997. p. 87-117.

193. Cronin TW, Johnsen S, Marshall NJ, Warrant EJ. Visual ecology. 1st ed. Princeton, New Jersey ;Oxfordshire, England: Princeton University Press; 2014.

194. Matsumoto F, Nishio K, Masuda H. Flow-through-type DNA array based on ideally ordered anodic porous alumina substrate. Advanced Materials 2004;16(23-24):2105-2108.

195. Wang M, Meng G, Li M, Li Z, Tang C, Huang Q. Fluorescence detection of trace PCB101 based on PITC immobilized on porous AAO membrane. Analyst 2011;136(2):278-281.

196. Macias G, Hernández-Eguía LP, Ferré-Borrull J, Pallares J, Marsal LF. Gold-coated ordered nanoporous anodic alumina bilayers for future label-free interferometric biosensors. ACS Applied Materials and Interfaces 2013;5(16):8093-8098.

197. Pan S, Rothberg LJ. Interferometric sensing of biomolecular binding using nanoporous aluminum oxide templates. Nano Letters 2003;3(6):811-814.

198. Wang X, Smirnov S. Label-free DNA sensor based on surface charge modulated ionic conductance. ACS Nano 2009;3(4):1004-1010.

199. Muchhala N, Johnsen S, Smith SD. Competition for hummingbird pollination shapes flower color variation in Andean solanaceae. International Journal of Organic Evolution 2014;68(8):2275-2286.

200. Endler JA, Mielke Jr. PW. Comparing entire colour patterns as birds see them. Biological Journal of the Linnean Society 2005;86(4):405-431.

201. Troscianko J, Stevens M. Image calibration and analysis toolbox – a free software suite for objectively measuring reflectance, colour and pattern. Methods in Ecology and Evolution 2015;6(11):1320-1331.

202. Kendal D, Hauser CE, Garrard GE, Jellinek S, Giljohann KM, Moore JL. Quantifying plant colour and colour difference as perceived by humans using digital images. PLOS ONE 2013;8(8):1-11.

203. Taylor CH, Gilbert F, Reader T. Distance transform: A tool for the study of animal colour patterns. Methods in Ecology and Evolution 2013;4(8):771-781.

204. Garcia JE, Girard MB, Kasumovic M, Petersen P, Wilksch PA, Dyer AG. Differentiating biological colours with few and many sensors: Spectral reconstruction with RGB and hyperspectral cameras. PLOS ONE 2015;10(5):1-31.

205. Garcia JE, Greentree AD, Shrestha M, Dorin A, Dyer AG. Flower colours through the lens: Quantitative measurement with visible and ultraviolet digital photography. PLOS ONE 2014;9(5):1-10.

206. Stevens M, Párraga CA, Cuthill IC, Partridge JC, Troscianko TS. Using digital photography to study animal coloration. Biological Journal of the Linnean Society 2007;90(2):211-237.

207. Tapia-McClung H, Ajuria Ibarra H, Rao D. Quantifying human visible color variation from high definition digital images of orb web spiders. PLOS ONE 2016;11(11):1-15.

208. Martin CH, Sönke Johnsen. A field test of the Hamilton–Zuk hypothesis in the Trinidadian guppy (Poecilia reticulata). Behavioral Ecology and Sociobiology 2007;61(12):1897-1909.

209. Cramer JD, Gaetano T, Gray JP, Grobler P, Lorenz JG, Freimer NB, et al. Variation in scrotal color among widely distributed vervet monkey populations (Chlorocebus

aethiops pygerythrus and Chlorocebus aethiops sabaeus). American Journal of Primatology 2013;75(7):752-762.

210. Johnsen S. How to measure color using spectrometers and calibrated photographs. Journal of Experimental Biology 2016;219(6):772-778.

211. Tedore C, Johnsen S. Weaponry, color, and contest success in the jumping spider Lyssomanes viridis. Behavioural Processes 2012;89(3):203-211.

212. Gage S. Optoelectronics/fiber-optics applications manual. 2nd ed. New York: McGraw-Hill; 1981.

213. Ito H, Ogawa M, Sunaga S. Evaluation of an organic light-emitting diode display for precise visual stimulation. Journal of Vision 2013;13(7):6-6.

214. Bachalla N. Identification of synthetic food colors adulteration by paper chromatography and spectrophotometric methods. International Archives of Integrated Medicine 2016;3(6):182-191.

215. Kasperová¡ J, Nagy J, Popelka P, Dičáková Z, Nagyová A, Mal'a P. Physico-chemical indicators and identification of selected Slovak honeys based on colour measurement. Acta Veterinaria Brno 2012;81(1):57-61.

216. Biancalana RC, Freitas Vincenti SA, Alves dS, Carvalho PP. Color stability of dental restorative materials submitted to cold temperatures for forensic purposes. Journal of Forensic and Legal Medicine 2017;51:63-68.

217. Araújo M, Martínez J, Ordóñez C, Vilán JA. Identification of granite varieties from colour spectrum data. Sensors 2010;10(9):8572-8584.

218. Wang Q, Xie J, Li X, Ding L, Liang J, Luo P, et al. Development of a nano-SiO_2 based enzyme-linked ligand binding assay for the determination of ibuprofen in human urine. Talanta 2017;167:617-622.

219. Shinde S, Dae-Young Kim, Saratale RG, Syed A, Ameen F, Ghodake G. A spectral probe for detection of aluminum (III) ions using surface functionalized gold nanoparticles. Nanomaterials 2017;7(10):1-16.

220. Capitán-Vallvey LF, Asensio LJ, López-González J, Fernández-Ramos MD, Palma AJ. Oxygen-sensing film coated photodetectors for portable instrumentation. Analytica Chimica Acta 2007;583:166-173.

221. Claycomb RW, Delwiche MJ. Biosensor for on-line measurement of bovine progesterone during milking. Biosensors and Bioelectronics 1998;13(11):1173-1180.

222. Moehrs S, Del Guerra A, Herbert DJ, Mandelkern MA. A detector head design for small-animal PET with silicon photomultipliers (SiPM). Physics in Medicine and Biology 2006;51(5):1113-1127.

223. Tibbe AB, de Grooth BG, Greve J, Liberti PA, Dolan GJ, Terstappen LW. Cell analysis system based on immunomagnetic cell selection and alignment followed by immunofluorescent analysis using compact disk technologies. Cytometry 2001;43(1):31-37.

224. Tsukagoshi K, Jinno N, Nakajima R. Development of a micro total analysis system incorporating chemiluminescence detection and application to detection of cancer markers. Analytical Chemistry 2005;77(6):1684-1688.

225. Collett E. Field guide to polarization. Bellingham, WA: SPIE; 2005.

Chapter 4

1. Belwalkar A, Grasing E, Van Geertruyden W, Huang Z, Misiolek WZ. Effect of processing parameters on pore structure and thickness of anodic aluminum oxide (AAO) tubular membranes. Journal of Membrane Science 2008;319(1-2):192-198.

2. Erdogan P, Yuksel B, Birol Y. Effect of chemical etching on the morphology of anodic aluminum oxides in the two-step anodization process. Applied Surface Science 2012;258(10):4544-4550.

3. Zhou J, He J, Zhao G, Zhang C, Zhao J, Hu H. Alumina nanostructures prepared by two-step anodization process. Transactions of Nonferrous Metals Society of China 2007;17(1):82-86.

4. Jani AMM, Losic D, Voelcker NH. Nanoporous anodic aluminium oxide: Advances in surface engineering and emerging applications. Progress in Materials Science 2013;58(5):636-704.

5. Mozalev A, Sakairi M, Saeki I, Takahashi H. Nucleation and growth of the nanostructured anodic oxides on tantalum and niobium under the porous alumina film. Electrochimica Acta 2003;48(20):3155-3170.

6. Li F, Zhang L, Metzger RM. On the growth of highly ordered pores in anodized aluminum oxide. Chemistry of Materials 1998;10(9):2470-2480.

7. Sulka GD, Stroobants S, Moshchalkov V, Borghs G, Celis J-. Synthesis of well-ordered nanopores by anodizing aluminum foils in sulfuric acid. J Electrochem Soc 2002;149(7):D97-D103.

8. Li A, Muller F, Birner A, Nielsch K, Gosele U. Fabrication and microstructuring of hexagonally ordered two-dimensional nanopore arrays in anodic alumina. Advanced Materials 1999;11(6):483-487.

9. Li AP, Muller F, Gosele U. Polycrystalline and monocrystalline pore arrays with large interpore distance in anodic alumina. Electrochemical and Solid-State Letters 2000;3(3):131-134.

10. Masuda H, Satoh M. Fabrication of gold nanodot array using anodic porous alumina as an evaporation mask. Japanese Journal of Applied Physics 1996;35(1):L126-L129.

11. Shingubara S, Okino O, Sayama Y, Sakaue H, Takahagi T. Ordered two-dimensional nanowire array formation using self-organized nanoholes of anodically oxidized aluminum. Japanese Journal of Applied Physics 1997;36(12):7791-7795.

12. Yan S, Chen Y, Wang Z, Han A, Shan Z, Yang X, et al. Essential distinction between one-step anodization and two-step anodization of Ti. Materials Research Bulletin 2017;95:444-450.

13. Masuda H, Fukuda K. Ordered metal nanohole arrays made by a two-step replication of honeycomb structures of anodic alumina. Science 1995;268(5216):1466-1468.

14. Asoh H, Nishio K, Nakao M, Tamamura T, Masuda H. Conditions for fabrication of ideally ordered anodic porous alumina using pretextured Al. Journal of the Electrochemical Society 2001;148(4):B152-B156.

15. León-Patiño CA, Aguilar-Reyes E, Ruiz-Aguilar C. Fabrication and characterization of highly ordered porous alumina templates by a two-step anodization process. Materials Science Forum 2013;755:75-81.

16. Pérez Bueno JJ, Rodríguez ME, Zelaya-Angel O, Baquero R, Gonzalez-Hernández J, Baños L, et al. Growth and characterization of $Cd_{1-x}Zn_xTe$ crystals with high Zn concentrations. Journal of Crystal Growth 2000;209(4):701-708.

17. Bwana NN. Synthesis of highly ordered nanopores on alumina by two-step anodization process. Journal of Nanoparticle Research 2008;10(2):313-319.

18. Masuda H, Hasegwa F, Ono S. Self-ordering of cell arrangement of anodic porous alumina formed in sulfuric acid solution. Journal of The Electrochemical Society 1997;144(5):L127-L130.

19. Li AP, Müller F, Birner A, Nielsch K, Gösele U. Polycrystalline nanopore arrays with hexagonal ordering on aluminum. Journal of Vacuum Science & Technology A 1999;17(4):1428-1431.

20. Zhou W, Li Y, Liu Z, Tang D, Zou X, Wang G. Self-organized formation of hexagonal nanopore arrays in anodic alumina. Chinese Physics 2001;10(3):218-222.

21. Wood GC, O'Sullivan JP. The anodizing of aluminium in sulphate solutions. Electrochimica Acta 1970;15(12):1865-1876.

22. Sulka GD, Parkoła KG. Anodising potential influence on well-ordered nanostructures formed by anodisation of aluminium in sulphuric acid. Thin Solid Films 2006;515(1):338-345.

23. Ba L, Li WS. Influence of anodizing conditions on the ordered pore formation in anodic alumina. Journal of Physics D: Applied Physics 2000;33(20):2527-2531.

24. Stępniowski WJ, Norek M, Michalska-Domańska M, Bojar Z. Ultra-small nanopores obtained by self-organized anodization of aluminum in oxalic acid at low voltages. Materials Letters 2013;111:20-3.

25. Sulka GD, Stępniowski WJ. Structural features of self-organized nanopore arrays formed by anodization of aluminum in oxalic acid at relatively high temperatures. Electrochimica Acta 2009;54(14):3683-3691.

26. Montero-Moreno J, Sarret M, MÃ¼ller C. Self-ordered porous alumina by two-step anodizing at constant current: Behaviour and evolution of the structure. Microporous and Mesoporous Materials 2010;136(1):68-74.

27. Xu Y, Liu H, Li X, Kang W, Cheng B, Li X. A novel method for fabricating self-ordered porous anodic alumina with wide interpore distance using phosphoric/oxalic acid mixed electrolyte. Materials Letters 2015;151:79-81.

28. Voon CH, Derman MN, Hashim U, Ahmad KR, Ho LN. A simple one-step anodising method for the synthesis of ordered porous anodic alumina. Journal of Experimental Nanoscience 2014;9(2):106-112.

29. Zhang J, Kielbasa JE, Carroll DL. Controllable fabrication of porous alumina templates for nanostructures synthesis. Materials Chemistry and Physics 2010;122(1):295-300.

30. Ono S, Masuko N. Evaluation of pore diameter of anodic porous films formed on aluminum. Surface and Coatings Technology 2003;169-170:139-142.

31. Yim S, Bonhôte C, Lille J, Wu T. Parameter effects for the growth of thin porous anodic aluminum oxides. ECS Transactions 2007;6(8):267-274.

32. De Laet J, Terryn H, Vereecken J. Development of an optical model for steady state porous anodic films on aluminium formed in phosphoric acid. Thin Solid Films 1998;320(2):241-252.

33. Choi YC, Hyeon JY, Bu S, Bae TS. Effects of anodizing voltages and corresponding current densities on self-ordering process of nanopores in porous anodic aluminas anodized in oxalic and sulfuric acids. Journal of the Korean Physical Society 2009;55(2):835-840.

34. Kashi MA, Ramazani A. The effect of temperature and concentration on the self-organized pore formation in anodic alumina. Journal of Physics D: Applied Physics 2005;38(14):2396-2399.

35. Zhang YN, Chen M, Liu ZL, Zhao YC. A novel approach to large-scale formation of through-hole porous anodic aluminum template. Chinese Chemical Letters 2008;19(11):1371-1374.

36. Thompson GE. Porous anodic alumina: Fabrication, characterization and applications. Thin Solid Films 1997;297(1):192-201.

37. Song Y, Jiang L, Qi W, Lu C, Zhu X, Jia H. High-field anodization of aluminum in concentrated acid solutions and at higher temperatures. Journal of Electroanalytical Chemistry 2012;673:24-31.

38. Mozalev A, Gorokh G, Sakairi M, Takahashi H. The growth and electrical transport properties of self-organized metal/oxide nanostructures formed by anodizing Ta-Al thin-film bilayers. Journal of Materials Science 2005;40(24):6399-6407.

39. Lu Q, Mato S, Skeldon P, Thompson GE, Masheder D, Habazaki H, et al. Anodic film growth on tantalum in dilute phosphoric acid solution at 20 and 85 °C. Electrochim Acta 2002;47(17):2761-2767.

40. Sloppy JD, Macdonald DD, Dickey EC. Growth laws of bilayer anodized tantalum oxide films formed in phosphoric acid. Journal of the Electrochemical Society 2010;157(5):157-165.

41. Lu Q, Mato S, Skeldon P, Thompson GE, Masheder D. Dielectric properties of anodic films formed on sputtering-deposited tantalum in phosphoric acid solution. Thin Solid Films 2003;429(1):238-242.

42. Tsao Y, Sondergaard T, Skovsen E, Gurevich L, Pedersen K, Pedersen TG. Pore size dependence of diffuse light scattering from anodized aluminum solar cell backside reflectors. Optics Express 2013;21(1):A84-A95.

43. Thompson GE, Wood GC. Porous anodic film formation on aluminium. Nature 1981;290:230-232.

44. Eftekhari A. Nanostructured materials in electrochemistry. Chichester: Weinheim: Wiley-VCH; 2008.

45. Hunter MS, Fowle P. Determination of barrier layer thickness of anodic oxide coatings. Journal of the Electrochemical Society 1954;101(9):481-485.

46. Hunter MS, Fowle P. Factors affecting the formation of anodic oxide coatings. Journal of the Electrochemical Society 1954;101(10):514-519.

47. Keller F, Hunter MS, Robinson DL. Structural features of oxide coatings on aluminum. Journal of the Electrochemical Society 1953;100(9):411-419.

48. O'Sullivan JP, Wood GC. The morphology and mechanism of formation of porous anodic films on aluminium. Proceeding of the Royal Society A 1970;317(1531):511-543.

49. Abd-Elnaiem A, Mebed AM, Gaber A, Abdel-Rahim M. Effect of the anodization parameters on the volume expansion of anodized aluminum films. Int J of Electrochem Sci 2013;8(8):10515-10525.

50. Zhu Z, Garcia-Gancedo L, Qiang L, Flewitt A, Milne WI, Moussy F. Size-tunable porous anodic alumina nano-structure for biosensing. Soft Nanoscience Letters 2011;1(3):55-60.

51. Ibn-Elhaj M, Schadt M. Optical polymer thin films with isotropic and anisotropic nano-corrugated surface topologies. Nature 2001;410(6830):796-799.

52. Optical characterization of nanoporous AAO sensor substrate. ; 2014.

53. Hernández-Eguía L,P., Ferré-Borrull J, Macias G, Pallarès J, Marsal LF. Engineering optical properties of gold-coated nanoporous anodic alumina for biosensing. Nanoscale Research Letters 2014;9(1):414-414.

54. Prikulis J, Tamulevicius T, Poplausks R, Bergs G, Apsite I, Malinovskis U, et al. Optical properties of thin metal films with nanohole arrays on porous alumina-aluminum structures. RSC Advances 2015;5(83):68143-68150.

55. Landau LD, Lifshitz EM. Chapter XI - Electromagnetic waves in anisotropic media.In: Lifshitz EM, Pitaevkii LP, editors. Electrodynamics of Continuous Media. 2nd ed. Amsterdam: Pergamon; 1984. p. 331-357.

56. Lutich AA, Gaponenko SV, Gaponenko NV, Molchan IS, Sokol VA, Parkhutik V. Anisotropic light scattering in nanoporous materials: A photon density of states effect. Nano Letters 2004;4(9):1755-1758.

57. Thompson DW, Snyder PG, Castro L, Yan L, Kaipa P, Woollam JA. Optical characterization of porous alumina from vacuum ultraviolet to midinfrared. Journal of Applied Physics 2005;97(11):1-9.

58. Lutich AA, Danailov MB, Volchek S, Yakovtseva VA, Sokol VA, Gaponenko SV. Birefringence of nanoporous alumina: Dependence on structure parameters. Applied Physics B: Lasers & Optics 2006;84(1):327-331.

59. Thompson GE, Wood GC. Anodic films on aluminium. Treatise on Materials Science and Technology 1983;23:205-329.

60. Pullen ND. Some physical characteristics of oxide films on aluminium. Transactions of the IMF 1939;15(1):69-78.

61. Diggle JW, Downie TC, Goulding CW. Anodic oxide films on aluminum. Chemical Reviews 2009;69(3):365-405.

62. Despic A, Parkhutik VP. Electrochemistry of aluminum in aqueous solutions and physics of its anodic oxide.In: Bockris JO, White RE, Conway BE, editors. Modern Aspects of Electrochemistry. 20th ed. Boston, MA: Springer US; 1989. p. 401-503.

63. Kasprzyk-Hordern B. Chemistry of alumina, reactions in aqueous solution and its application in water treatment. Adv Colloid Interface Sci 2004;110(1):19-48.

64. Alvey CE. The mechanical properties of porous anodic oxide films on aluminium. The University of Manchester; 1974.

65. Tajima S, Baba N, Shimura FM. Einfluss von anionen und Inhibitoren auf die primären wachstumsvorgänge der anodischen oxidschichten auf aluminium. Electrochimica Acta 1967;12(8):955-966.

66. Ye J, Yin Q, Zhou Y. Superhydrophilicity of anodic aluminum oxide films: From “honeycomb” to “bird's nest”. Thin Solid Films 2009;517(21):6012-6015.

67. Bico J, Tordeux C, Quéré D. Rough wetting. Europhsics Letters 2001;55(2):214-221.

68. Leese H, Bhurtun V, Lee KP, Mattia D. Wetting behaviour of hydrophilic and hydrophobic nanostructured porous anodic alumina. Colloids and Surfaces A: Physicochemical and Engineering Aspects 2013;420:53-58.

69. Sander MS, Prieto AL, Gronsky R, Sands T, Stacy AM. Fabrication of high-density, high aspect ratio, large-area bismuth telluride nanowire arrays by electrodeposition into porous anodic alumina templates. Advanced Materials 2002;14(9):665-667.

70. Lee KH, Wong CC. Decoupling two-step anodization in anodic aluminum oxide. Journal of Applied Physics 2009;106(10).

71. Ono S, Baba N, Masuko N. Cell and pore diameters of anodic oxide films on aluminum. Journal of the Surface Finishing Society of Japan 1991;42(1):133.

72. Zhang F, Liu X, Pan C, Zhu J. Nano-porous anodic aluminium oxide membranes with 6-19 nm pore diameters formed by a low-potential anodizing process. Nanotechnology 2007;18(34):345302.

73. Thompson GE, Furneaux RC, Wood GC, Richardson JA, Goode JS. Nucleation and growth of porous anodic films on aluminium. Nature 1978;272(5652):433-435.

74. Dell'Oca CJ, Fleming PJ. Initial stages of oxide growth and pore initiation in the porous anodization of aluminum. Journal of the Electrochemical Society 1976;123(10):1487-1493.

75. Zhao Y, Chen M, Zhang Y, Xu T, Liu W. A facile approach to formation of through-hole porous anodic aluminum oxide film. Materials Letters 2005;59(1):40-43.

76. Hu G, Zhang H, Di W, Zhao T. Study on wet etching of AAO template. Applied Physics Research 2009;1(2):78-83.

77. Gâlca AC, Kooij ES, Wormeester H, Salm C, Leca V, Rector JH, et al. Structural and optical characterization of porous anodic aluminum oxide. Journal of Applied Physics 2003;94(7):4296-4305.

78. Stefan Kooij E, Wormeester H, Gâlcă AC, Poelsema B. Optical anisotropy and porosity of anodic aluminum oxide characterized by spectroscopic ellipsometry. Electrochemical and Solid-State Letters 2003;6(11):B52-B54.

79. Jung YW, Byun JS, Woo DH, Kim YD. Ellipsometric analysis of porous anodized aluminum oxide films. Thin Solid Films 2009;517(13):3726-3730.

80. Bellemare J, Carignan L, Sirois F, Ménard D. Etching the oxide barrier of micrometer-scale self-organized porous anodic alumina membranes. Journal of the Electrochemical Society 2015;162(4):E47-E50.

81. Aslan MM, Webster NA, Byard CL, Pereira MB, Hayes CM, Wiederkehr RS, et al. Low-loss optical waveguides for the near ultra-violet and visible spectral regions with Al_2O_3 thin films from atomic layer deposition. Thin Solid Films 2010;518(17):4935-4940.

82. Smit MK, Acket GA, van der Laan CJ. Al_2O_3 films for integrated optics. Thin Solid Films 1986;138(2):171-181.

83. Zeković LD, Urošević VV, Jovanić BR. Determination of the refractive index of porous anodic oxide films on aluminium by a photoluminescence method. Thin Solid Films 1986;139:109-113.

84. Taylor DJ, Fleig PF, Hietala SL. Technique for characterization of thin film porosity. Thin Solid Films 1998;332(1):257-261.

85. Braun M,M., Pilon L. Effective optical properties of non-absorbing nanoporous thin films. Thin Solid Films 2006;496(2):505-514.

86. Rodenhausen KB, Schmidt D, Rice C, Hofmann T, Schubert E, Schubert M. Detection of organic attachment onto highly ordered three-dimensional nanostructure thin films by generalized ellipsometry and quartz crystal microbalance with dissipation techniques.In: Hinrichs K, Eichhorn K, editors. Ellipsometry of Functional Organic Surfaces and Films Berlin, Heidelberg: Springer Berlin Heidelberg; 2014. p. 135-154.

87. Makarov S,N., Ludwig R, Bitar SJ. Major circuit elements.In: N. Makarov S, Ludwig R, Bitar SJ, editors. Practical Electrical Engineering Cham: Springer International Publishing; 2016. p. 29-87.

88. Rahman MM, Garcia-Caurel E, Santos A, Marsal LF, Pallarès J, Ferré-Borrull J. Effect of the anodization voltage on the pore-widening rate of nanoporous anodic alumina. Nanoscale Research Letters 2012;7(1):474-474.

89. Wu Z, Richter C, Menon L. A study of anodization process during pore formation in nanoporous alumina templates. Journal of the Electrochemical Society 2007;154(1):E8-E12.

90. Hale GM, Querry MR. Optical constants of water in the 200-nm to 200-um wavelength region. Applied Optics 1973;12(3):555-563.

91. Ciddor PE. Refractive index of air: New equations for the visible and near infrared. Applied Optics 1996;35(9):1566-1573.

Chapter 5

1. Aoyagi S. TOF-SIMS applications to bioimaging and biomolecule evaluation methods.In: Lee MS, editor. Mass Spectrometry Handbook. 1st ed. Hoboken, NJ: John Wiley & Sons; 2012. p. 243-258.

2. Boxer SG, Kraft ML, Weber PK. Advances in imaging secondary ion mass spectrometry for biological samples. Annual Review of Biophysics 2009;38:53-74.

3. Cai K, Bossert J, Jandt K. Does the nanometre scale topography of titanium influence protein adsorption and cell proliferation? Colloids and Surfaces B-Biointerfaces 2006;49(2):136-144.

4. Feng B, Weng J, Yang B, Chen J, Zhao J, He L, et al. Surface characterization of titanium and adsorption of bovine serum albumin. Materials Characterization 2002;49(2):129-137.

5. Han C, Johansson CB, Wennerberg A, Albrektsson T. Quantitative and qualitative investigations of surface enlarged titanium and titanium alloy implants. Clinical Oral Implants Research 1998;9(1):1-10.

6. Kempson IM, Martin AL, Denman JA, French PW, Prestidge CA, Barnes TJ. Detecting the presence of denatured human serum albumin in an adsorbed protein monolayer using TOF-SIMS. Langmuir 2010;26(14):12075-12080.

7. Lausmaa J, Linder L. Surface spectroscopic characterization of titanium implants after separation from plastic-embedded tissue. Biomaterials 1988;9(3):277-280.

8. Malmberg P, Nygren H. Methods for the analysis of the composition of bone tissue, with a focus on imaging mass spectrometry (TOF-SIMS). Proteomics 2008;8(18):3755-3762.

9. Nakanishi K, Sakiyama T, Imamura K. On the adsorption of proteins on solid surfaces, a common but very complicated phenomenon. Journal of Bioscience and Bioengineering 2001;91(3):233-244.

10. Palmquist A, Snis A, Emanuelsson L, Browne M, Thomsen P. Long-term biocompatibility and osseointegration of electron beam melted, free-form-fabricated solid and porous titanium alloy: experimental studies in sheep. Journal of Biomaterials Applications 2013;27(8):1003-1016.

11. Schmidt DR, Waldeck H, Kao WJ. Protein adsorption to biomaterials.In: Puleo DA, Bizios R, editors. Biological Interactions on Materials Surfaces: Understanding and Controlling Protein, Cell, and Tissue Responses New York: Springer; 2009. p. 1-18.

12. Aoyagi S, Hayama M, Hasegawa U, Sakai K, Tozu M, Hoshi T, et al. Estimation of protein adsorption on dialysis membrane by means of TOF-SIMS imaging. Journal of Membrane Science 2004;236(1):91-99.

13. Kempson IM, Barnes TJ, Prestidge CA. Use of TOF-SIMS to study adsorption and loading behavior of methylene blue and papain in a nano-porous silicon layer. Journal of the American Society for Mass Spectrometry 2010;21(2):254-260.

14. Lazzara TD, Mey I, Steinem C, Janshoff A. Benefits and limitations of porous substrates as biosensors for protein adsorption. Analytical Chemistry 2011;83(14):5624-5630.

15. Suh C, Kim M, Choo J, Kim J, Kim H, Lee E. Analysis of protein adsorption characteristics to nano-pore silica particles by using confocal laser scanning microscopy. Journal of Biotechnology 2004;112(3):267-277.

16. Velleman L, Triani G, Evans PJ, Shapter JG, Losic D. Structural and chemical modification of porous alumina membranes. Microporous and Mesoporous Materials 2009;126(1-2):87-94.

17. Wei J, Helm GS, Corner-Walker N, Hou X. Characterization of a non-fouling ultrafiltration membrane. Desalination 2006;192(1-3):252-261.

18. Filho NLD, Do Carmo DR. Adsorption at silica, alumina, and related surfaces.In: Somasundaran P, editor. Encyclopedia of Surface and Colloid Science. 2nd ed. New York: USA: Taylor & Francis; 2006. p. 209-228.

19. Gitzen WH. Alumina as a ceramic material. Columbus, Ohio: American Ceramic Society; 1970.

20. Templeton MK, Weinberg WH. Adsorption and decomposition of dimethyl methylphosphonate on an aluminum oxide surface. Journal of the American Chemical Society 1985;107(1):97-108.

21. Evans H, Weinberg W. A comparison of the vibrational structures of ethanol, acetic acid, and acetaldehyde adsorbed on alumina. The Journal of Chemical Physics 1979;71(12):4789-4798.

22. Hall JT, Hansma PK. Chemisorption of monocarboxylic acids on alumina: A tunneling spectroscopy study. Surface Science 1978;77(1):61-76.

23. Hirota K, Fueki K, Shindo K, Nakai Y. Studies on the state of formic acid adsorbed on silica and alumina by a combined method of nuclear magnetic resonance and infrared absorption. Bulletin of the Chemical Society of Japan 1959;32(11):1261-1263.

24. Lim TK, Bloomfield VA, Nelsestuen GL. Structure of the prothrombin-and blood clotting factor X-membrane complexes. Biochemistry 1977;16(19):4177-4181.

25. Walz DA, Hewett-Emmett D, Seegers WH. Amino acid sequence of human prothrombin fragments 1 and 2. Proceedings of the National Academy of Sciences of the United States of America 1977;74(5):1969.

26. Kasprzyk-Hordern B. Chemistry of alumina, reactions in aqueous solution and its application in water treatment. Advances in Colloid and Interface Science 2004;110(1-2):19-48.

27. Furneaux R, Rigby W, Davidson A. The formation of controlled-porosity membranes from anodically oxidized aluminium. Nature 1989;337(6203):147-149.

28. Davis G, Sun T, Ahearn J, Venables J. Application of surface behaviour diagrams to the study of hydration of phosphoric acid-anodized aluminium. Journal of Materials Science 1982;17(6):1807-1818.

29. Brown A, Vickerman JC. A comparison of positive and negative ion static SIMS spectra of polymer surfaces. Surface and Interface Analysis 1986;8(2):75-81.

30. Wagner MS, Castner DG. Characterization of adsorbed protein films by time-of-flight secondary ion mass spectrometry with principal component analysis. Langmuir 2001;17(15):4649-4660.

31. ASTM International. Standard test methods for tension testing of metallic materials. 2016 27 Oct 2016;E8/E8M-16a.

32. Davis G, Buchner S, Beck W, Byer N. Use of surface behavior diagrams to compare anodic and photochemical oxides of Hg 0.8 Cd 0.2 Te. Applications of Surface Science 1983;15(1):238-246.

33. Venables J. Adhesion and durability of metal-polymer bonds. Journal of Materials Science 1984;19(8):2431-2453.

34. Lee H. Chemical thermodynamics for metals and materials. 1st ed. London: Imperial College Press; 1999.

35. Transactions and Communications. Journal of the Society of Chemical Industry 1944;63(5):125-160.

36. Qin W, Volinsky AA, Werho D, Theodore ND, Kottke M, Ramiah C. Spontaneous oxide reduction in metal stacks. Thin Solid Films 2005;473(2):236-240.

37. Venables JD, Tadros ME, Ditchek BM, inventors. Lockheed Martin Corp, assignee. Durability of adhesively bonded aluminum structures and method for inhibiting the conversion of aluminum oxides to aluminum hydroxide. US patent 4308079. 1981 Dec. 29.

38. Marceau JA, Firminhac RH, Moji Y, inventors. The Boeing Company, assignee. Method for providing environmentally stable aluminum surfaces for adhesive bonding and product produced. US patent 4,085,012. 1978 Apr. 18.

39. Dorsey GAJ. The characterization of anodic aluminas I. Composition of films from acidic anodizing electrolytes. Journal of Electrochemical Society 1966;113(2):169-172.

40. Plumb RC. Studies of the anodic behavior of aluminum II. Coulometry of barrier layer production. Journal of Electrochemical Society 1958;105(9):498-502.

41. Critchlow G, Brewis D. Review of surface pretreatments for aluminium alloys. International Journal of Adhesion and Adhesives 1996;16(4):255-275.

42. Ondrus D, Boerio F. Effect of substrates on the structure of polymer interphases: I. Oxidation of aminosilane primers. Journal of Colloid and Interface Science 1988;124(1):349-357.

43. Vickerman JC, Brown A, Reed NM. Secondary ion mass spectrometry: principles and applications. Oxford: Clarendon Press; 1989.

44. Lu Q, Mato S, Skeldon P, Thompson G, Masheder D, Habazaki H, et al. Anodic film growth on tantalum in dilute phosphoric acid solution at 20 and 85 C. Electrochimica Acta 2002;47(17):2761-2767.

45. Lu Q, Mato S, Skeldon P, Thompson G, Masheder D. Dielectric properties of anodic films formed on sputtering-deposited tantalum in phosphoric acid solution. Thin Solid Films 2003;429(1):238-242.

46. Macagno V, Schultze J. The growth and properties of thin oxide layers on tantalum electrodes. J Electroanal Chem Interfacial Electrochem 1984;180(1-2):157-170.

47. Sloppy J, Macdonald D, Dickey E. Growth laws of bilayer anodized tantalum oxide films formed in phosphoric acid. J Electrochem Soc 2010;157(5):C157-C165.

48. Wagner M, Horbett T, Castner D. Characterization of the structure of binary and ternary adsorbed protein films using electron spectroscopy for chemical analysis, time-of-flight secondary ion mass spectrometry, and radiolabeling. Langmuir 2003;19(5):1708-1715.

49. Tyler BJ, Bruening C, Rangaranjan S, Arlinghaus HF. TOF-SIMS imaging of adsorbed proteins on topographically complex surfaces with Bi_3^+ primary ions. Biointerphases 2011;6(3):135-141.

50. Vickerman JC, Gilmore I. Surface analysis: The principal techniques. 2nd ed. Chichester, UK: Wiley; 2009.

Chapter 6

1. Qureshi A, Gurbuz Y, Niazi JH. Biosensors for cardiac biomarkers detection: A review. Sens Actuators B Chem 2012;171-172:62-76.

2. Addona TA, Shi X, Keshishian H, Mani DR, Burgess M, Gillette MA, et al. A pipeline that integrates the discovery and verification of plasma protein biomarkers reveals candidate markers for cardiovascular disease. Nature Biotechnology 2011;29(7):635-643.

3. Ambrosi A, Airò F, Merkoçi A. Enhanced gold nanoparticle based ELISA for a breast cancer biomarker. Analytical Chemistry 2010;82(3):1151-1156.

4. Zangar RC, Daly DS, White AM. ELISA microarray technology as a high-throughput system for cancer biomarker validation. Expert Review of Proteomics 2006;3(1):37-44.

5. Ruhwald M, Bjerregaard-Andersen M, Rabna P, Eugen-Olsen J, Ravn P. IP-10, MCP-1, MCP-2, MCP-3, and IL-1 RA hold promise as biomarkers for infection with M. tuberculosis in a whole blood based T-cell assay. BMC Research Notes 2009;2:1-6.

6. Katsuragi K, Noda A, Tachikawa T, Azuma A, Mukai F, Murakami K, et al. Highly sensitive urine-based enzyme-linked immunosorbent assay for detection of antibody to Helicobacter pylori. Helicobacter 1998;3(4):289-295.

7. Jalalypour F, Farajnia S, Mohammad HS, Hojabri Z, Yousefzadeh R, Saeedi N. Comparative evaluation of RUT, PCR and ELISA tests for detection of infection with cytotoxigenic H. pylori. Advanced Pharmaceutical Bulletin 2016;6(2):261-266.

8. Steinhagen K, Probst C, Radzimski C, Schmidt-Chanasit J, Emmerich P, van Esbroeck M, et al. Serodiagnosis of Zika virus (ZIKV) infections by a novel NS1-based ELISA devoid of cross-reactivity with dengue virus antibodies: a multicohort study of assay performance, 2015 to 2016. Eurosurveillance 2016;21(50):1-16.

9. St John A, Price C, P. Existing and emerging technologies for point-of-care testing. Clinical Biochemist Reviews 2014;35(3):155-167.

10. Pecoraro V, Banfi G, Germagnoli L, Trenti T. A systematic evaluation of immunoassay point-of care-testing to define impact on patients outcomes. Annals of Clinical Biochemistry Journal 2017;54(4):420-431.

11. Gialamas A, St John A, Laurence CO, Bubner TK. Point-of-care testing for patients with diabetes, hyperlipidaemia or coagulation disorders in the general practice setting: a systematic review. Family Practice 2010;27(1):17-24.

12. Gialamas A, Yelland LN, Ryan P, Willson K, Laurence CO, Bubner TK, et al. Does point-of-care testing lead to the same or better adherence to medication? A randomised controlled trial: the PoCT in general practice trial. The Medical Journal of Australia 2009;191(9):487-491.

13. Conway SE, Hwang AY, Ponte CD, Gums JG. Laboratory and clinical monitoring of direct acting oral anticoagulants: What clinicians need to know. Pharmacotherapy 2017;37(2):236-248.

14. Langmuir I, Schaefer VJ. Monolayers and multilayers of chlorophyll. J Am Chem Soc 1937;59(10):2075-2076.

15. Rothen A, Landsteiner K. Serological reactions of protein films and denatured proteins. J Exp Med 1942;76(5):437-450.

16. Burrell RE, Naylor AG, Rosenfeld AM, inventors. Alcan International Ltd, assignee. Thin film diagnostic device. US patent 5,124,172. 1992 Jun. 23.

17. Djokić SS, Burrell RE. Visual detection of protein adsorption onto electrochemically oxidized aluminum surfaces. Biosens Bioelectron 1998;13(3–4):271-278.

18. Ono S, Masuko N. Evaluation of pore diameter of anodic porous films formed on aluminum. Surface and Coatings Technology 2003;169-170:139-142.

19. Chu SZ, Wada K, Inoue S, Isogai M, Katsuta Y, Yasumori A. Large-scale fabrication of ordered nanoporous alumina films with arbitrary pore intervals by critical-potential anodization. Journal of the Electrochemical Society 2006;153(9):B384-B391.

20. Choi YC, Hyeon JY, Bu S, Bae TS. Effects of anodizing voltages and corresponding current densities on self-ordering process of nanopores in porous anodic aluminas anodized in oxalic and sulfuric acids. Journal of the Korean Physical Society 2009;55(2):835-840.

21. Abd-Elnaiem A, Gaber A. Parametric study on the anodization of pure aluminum thin film used in fabricating nano-pores template. International Journal of Electrochemical Science 2013;8(7):9741-9751.

22. Belwalkar A, Grasing E, Van Geertruyden W, Huang Z, Misiolek WZ. Effect of processing parameters on pore structure and thickness of anodic aluminum oxide (AAO) tubular membranes. Journal of Membrane Science 2008;319(1-2):192-198.

23. Araoyinbo AO, Ahmad Fauzi MN, Sreekantan S, Aziz A. A novel process to produce nanoporous aluminum oxide using titration technique to prepare the neutral electrolyte. Journal of Non-Crystalline Solids 2010;356(20-22):1057-1060.

24. Yim S, Bonhôte C, Lille J, Wu T. Parameter effects for the growth of thin porous anodic aluminum oxides. ECS Transactions 2007;6(8):267-274.

25. Li F, Zhang L, Metzger RM. On the growth of highly ordered pores in anodized aluminum oxide. Chemistry of Materials 1998;10(9):2470-2480.

26. Zhu Z, Garcia-Gancedo L, Qiang L, Flewitt A, Milne WI, Moussy F. Size-tunable porous anodic alumina nano-structure for biosensing. Soft Nanoscience Letters 2011;1(3):55-60.

27. Rahman MM, Garcia-Caurel E, Santos A, Marsal LF, Pallarès J, Ferré-Borrull J. Effect of the anodization voltage on the pore-widening rate of nanoporous anodic alumina. Nanoscale Research Letters 2012;7(1):474-474.

28. Van Overmeere Q, Blaffart F, Proost J. What controls the pore spacing in porous anodic oxides? Electrchem Commun 2010;12(9):1174-1176.

29. Sulka GD. Highly ordered anodic porous alumina formation by self-organized anodizing.In: Eftekhari A, editor. Nanostructured Materials in Electrochemistry Weinheim: Wiley-VCH: John Wiley & Sons; 2008. p. 1-97.

30. Zaraska L, Sulka GD, JaskuAa M. Anodic alumina membranes with defined pore diameters and thicknesses obtained by adjusting the anodizing duration and pore opening/widening time. Journal of Solid State Electrochemistry 2011(11-12):2427.

31. Masuda H, Yotsuya M, Asano M, Nishio K, Nakao M, Yokoo A, et al. Self-repair of ordered pattern of nanometer dimensions based on self-compensation properties of anodic porous alumina. Applied Physics Letters 2001;78(6):826-828.

32. Burrell RE, inventor. Prominent Medical Inc., assignee. Aluminum oxide surfaces and interface molecules. US Provisional Patent patent - Provisional. 2018 Filed Feb. 20.

33. Schmitt GL, Pietrzyk DJ. Liquid chromatographic separation of inorganic anions on an alumina column. Analytical Chemistry 1985;52(12):2247-2253.

34. Wang J, Zhang Y, Feng C, Li J, Li G. Adsorption capacity for phosphorus comparison among activated alumina, silica sand and anthracite coal. Journal of Water Resource and Protection 2009;1(4):260-264.

35. Walz DA, Hewett-Emmett D, Seegers WH. Amino acid sequence of human prothrombin fragments 1 and 2. Proceedings of the National Academy of Sciences of the United States of America 1977;74(5):1969-1972.

36. Kasprzyk-Hordern B. Chemistry of alumina, reactions in aqueous solution and its application in water treatment. Adv Colloid Interface Sci 2004;110(1):19-48.

37. Filho NLD, Do Carmo DR. Adsorption at silica, alumina, and related surfaces.In: Marcel Dekker Inc, editor. Encyclopedia of Surface and Colloid Science. 1st ed. Ilha Solteira, Brazil: Marcel Dekker Inc; 2004. p. 1-20.

38. Gitzen WH. Alumina as a ceramic material. Columbus, Ohio: American Ceramic Society; 1970.

39. Lee W, Park S. Porous anodic aluminum oxide: Anodization and templated synthesis of functional nanostructures. Chem Rev 2014;114(15):7487-7556.

40. Charlesby A, Polling JJ. The optical properties of thin oxide films on tantalum. Proc R Soc Lond A Math Phys Sci 1955;227(1171):434-447.

41. Cui-Cui S, Yun-Yu C, En-Mei D, Chang-Hao L. Tunable structural color of anodic tantalum oxide films. Chin Phys B 2012;21(8):1-5.

42. Abd-Elnaiem A, Mebed AM, Gaber A, Abdel-Rahim M. Effect of the anodization parameters on the volume expansion of anodized aluminum films. Int J of Electrochem Sci 2013;8(8):10515-10525.

43. Poinern GEJ, Ali N, Fawcett D. Progress in nano-engineered anodic aluminum oxide membrane development. Materials 2011;4(3):487-523.

44. Masuda H, Yada K, Osaka A. Self-ordering of cell configuration of anodic porous alumina with large-size pores in phosphoric acid solution. Jpn J Appl Phys 1998;37(11):1340-1342.

45. Macagno V, Schultze JW. The growth and properties of thin oxide layers on tantalum electrodes. J Electroanal Chem Interfacial Electrochem 1984;180(1):157-170.

46. Stella K, Franzka S, Burstel D, Diesing D, Mayer D, and Roddatis V. Electrochemical oxidation as vertical structuring tool for ultrathin (d < 10nm) valve metal film. ECS J Solid State Sci 2014;3(5):143-148.

47. Sloppy J, Macdonald D, Dickey E. Growth laws of bilayer anodized tantalum oxide films formed in phosphoric acid. J Electrochem Soc 2010;157(5):C157-C165.

48. Lu Q, Mato S, Skeldon P, Thompson GE, Masheder D, Habazaki H, et al. Anodic film growth on tantalum in dilute phosphoric acid solution at 20 and 85 °C. Electrochim Acta 2002;47(17):2761-2767.

49. Lu Q, Mato S, Skeldon P, Thompson GE, Masheder D. Dielectric properties of anodic films formed on sputtering-deposited tantalum in phosphoric acid solution. Thin Solid Films 2003;429(1):238-242.

50. Voros J. The density and refractive index of adsorbing protein layers. Biophys J 2004;87(1):553-561.

51. Jung LS, Campbell CT, Chinowsky TM, Mar MN, Yee SS. Quantitative interpretation of the response of surface plasmon resonance sensors to adsorbed films. Langmuir 1998;14(19):5636-5648.

52. Benesch J, Askendal A, Tengvall P. The determination of thickness and surface mass density of mesothick immunoprecipitate layers by null ellipsometry and protein (125)iodine labeling. J Colloid Interface Sci 2002;249(1):84-90.

53. Cuypers PA, Corsel JW, Janssen MP, Kop JM, Hermens WT, Hemker HC. The adsorption of prothrombin to phosphatidylserine multilayers quantitated by ellipsometry. J Biol Chem 1983;258(4):2426-2431.

54. Alvarez SD, Li C, Chiang CE, Schuller IK, Sailor MJ. A label-free porous alumina interferometric immunosensor. ACS Nano 2009;3(10):3301-3307.

55. Hyndman D, Burrell R, Lever G, Flynn TG. Protein immobilization to alumina supports: I. Characterization of alumina-organophosphate ligand interactions and use in the attachment of papain. Biotechnology and Bioengineering 1992;40(11):1319-1327.

56. Hyndman D, Burrell R, Lever G, and Flynn G. Protein immobilization to alumina supports: II. Papain immobilization to alumina via organophosphate linkers. Biotechnology and Bioengineering 1992;40(11):1328-1336.

57. Vasudevan PT, Thakur DS. Soluble and immobilized catalase. Applied Biochemistry and Biotechnology 1994;49(3):173-189.

58. Leary Swan EE, Popat KC, Desai TA. Peptide-immobilized nanoporous alumina membranes for enhanced osteoblast adhesion. Biomaterials 2005;26(14):1969-1976.

Chapter 7

1. Sloppy JD, Podraza NJ, Dickey EC, Macdonald DD. Complex dielectric functions of anodic bi-layer tantalum oxide. Electrochimica Acta 2010;55(28):8751-8757.

2. Charlesby A, Polling JJ. The optical properties of thin oxide films on tantalum. Proc R Soc Lond A Math Phys Sci 1955;227(1171):434-447.

3. Cui-Cui S, Yun-Yu C, En-Mei D, Chang-Hao L. Tunable structural color of anodic tantalum oxide films. Chin Phys B 2012;21(8):1-5.

4. Mozalev A, Sakairi M, Saeki I, Takahashi H. Nucleation and growth of the nanostructured anodic oxides on tantalum and niobium under the porous alumina film. Electrochimica Acta 2003;48(20):3155-3170.

5. Skeldon P, Shimizu K, Thompson G, Wood G. Direct observation of anodic film growth on superimposed aluminium and tantalum metallic layers. Philosophical Magazine B 1990;61(5):927-938.

6. Ragone DV. Thermodynamics of materials. New York: Wiley; 1995.

7. Sato T, Onoue T, Kajiwara T, inventors. WD Media Pte. Ltd., assignee. Perpendicular magnetic recording medium and method of manufacturing the same. US patent. 2013 Mar. 26.

8. Qin W, Volinsky AA, Werho D, Theodore ND, Kottke M, Ramiah C. Spontaneous oxide reduction in metal stacks. Thin Solid Films 2005;473(2):236-240.

9. Thornton JA, Hoffman DW. Stress-related effects in thin films. Thin Solid Films 1989;171(1):5-31.

10. Thornton JA. High rate thick film growth. Annual Review of Materials Science 1977;7(1):239-260.

11. Anders A. A structure zone diagram including plasma-based deposition and ion etching. Thin Solid Films 2010;518(15):4087-4090.

12. Mahy M, Van Eycken L, Oosterlinck A. Evaluation of uniform color spaces developed after the adoption of CIELAB and CIELUV. Color Research & Application 1994;19(2):105-121.

13. Huttemann R, Morabito J, Steidel C, Gerstenberg D. The effect of the light elements nitrogen, carbon and oxygen on the physical properties of sputtered tantalum films. Japanese Journal of Applied Physics 1974;13(S1):513.

14. Yohannan A. Characterization of alpha and beta phases of tantalum coatings. Unpublished, New Jersey Institute of Technology, 2001.

15. Read MH, Hensler DH. X-ray analysis of sputtered films of beta-tantalum and body-centered cubic tantalum. Thin Solid Films 1972;10(1):123-135.

16. Lee SL, Doxbeck M, Mueller J, Cipollo M, Cote P. Texture, structure and phase transformation in sputter beta tantalum coating. Surface and Coatings Technology 2004;177-178:44-51.

17. Ino K, Shinohara T, Ushiki T, Ohmi T. Ion energy, ion flux, and ion species effects on crystallographic and electrical properties of sputter-deposited Ta thin films. Journal of Vacuum Science and Technology A: Vacuum, Surfaces and Films 1997;15(5):2627-2635.

18. Catania P, Roy RA, Cuomo JJ. Phase formation and microstructure changes in tantalum thin films induced by bias sputtering. Journal of Applied Physics 1993;74(2):1008-1014.

19. Clevenger LA, Mutscheller A, Harper JME, Cabral C, Barmak K. The relationship between deposition conditions, the beta to alpha phase transformation, and stress relaxation in tantalum thin films. Journal of Applied Physics 1992;72(10):4918-24.

20. Shiojiri M, Shinkai S, Sasaki K, Yanagisawa H, Abe Y. Preparation of low-resistivity a-Ta thin films on (001) Si by conventional DC magnetron sputtering. Japanese Journal of Applied Physics, Part 1: Regular Papers and Short Notes and Review Papers 2003;42(7 A):4499-4500.

21. Navid AA, Hodge AM. Nanostructured alpha and beta tantalum formation—Relationship between plasma parameters and microstructure. Materials Science and Engineering: A 2012;536:49-56.

22. Seeger A. Progress and problems in the understanding of the dislocation relaxation processes in metals. Materials Science & Engineering A 2004;370(13):50-66.

23. Colin JJ, Abadias G, Michel A, Jaouen C. On the origin of the metastable β-Ta phase stabilization in tantalum sputtered thin films. Acta Materialia 2017;126:481-493.

24. Muth DG. Ellipsometer study of anodic oxides formed on sputtered tantalum and tantalum-aluminum alloy films. Journal of Vacuum Science and Technology 1969;6(4):749-752.

25. Zhu G, Lin T, Cui H, Zhao W, Zhang H, Huang F. Gray Ta2O5 nanowires with greatly enhanced photocatalytic performance. ACS Applied Materials and Interfaces 2016;8(1):122-127.

26. Çapraz ÖÖ, Shrotriya P, Skeldon P, Thompson GE, Hebert KR. Factors controlling stress generation during the initial growth of porous anodic aluminum oxide. Electrochimica Acta 2015 20 March 2015;159:16-22.

27. Skeldon P, Thompson GE, Garcia-Vergara SJ, Iglesias-Rubianes L, Blanco-Pinzon CE. A tracer study of porous anodic alumina. Electrochemical and Solid-State Letters 2006;9(11):B47-B51.

28. Houser JE, Hebert KR. The role of viscous flow of oxide in the growth of self-ordered porous anodic alumina films. Nature Materials 2009;8(5):415-420.

29. Oh J, Thompson CV. The role of electric field in pore formation during aluminum anodization. Electrochimica Acta 2011;56:4044-4051.

30. Hoffman DW, Thornton JA. The compressive stress transition in Al, V, Zr, Nb and W metal films sputtered at low working pressures. Thin Solid Films 1977;45(2):387-396.

31. Gioia G, Ortiz M. Delamination of compressed thin films. Advances in Applied Mechanics 1997;33(08):119-192.

32. Mattox DM. Atomistic film growth and resulting film properties: Residual film stress. Vacuum Technology & Coating 2001;November:22-23.

33. Fang W, Lo C. On the thermal expansion coefficients of thin films. Sensors and Actuators A: Physical 2000;84(3):310-314.

34. Richard Zhang X, Fisher T,S., Raman A, Sands T. Linear coefficient of thermal expansion of porous anodic alumina thin films from atomic force microscopy. Nanoscale and Microscale Thermophysical Engineering 2009;13(4):243-252.

35. Michaelis A. Valve metal systems.In: Alkire RC, Kolb DM, Lipkowski J, Ross PN, editors. Electrochemical surface modification: Thin films, functionalization and characterization Weinheim: WILEY-VCH; 2008. p. 15-73.

36. Braginsky VB, Samoilenko AA. Measurements of the optical mirror coating properties. Physics Letters A 2003;315(3):175-177.

Chapter 8

1. Burrell RE, Naylor AG, Rosenfeld AM, inventors. Alcan International Limited, assignee. Thin film diagnostic device. EP patent. 1992 .

2. Furie B, Furie BC. The molecular basis of blood coagulation. Cell 1988;53(4):505-518.

3. El Asmar MS, Naoum JJ, Arbid EJ. Vitamin K dependent proteins and the role of vitamin K2 in the modulation of vascular calcification: A review. Oman Medical Journal 2014;29(3):172-177.

4. Dahlbäck B, Lundwall A, Stenflo J. Primary structure of bovine vitamin K-dependent protein S. Proceedings of the National Academy of Sciences of the United States of America 1986;83(12):4199-4203.

5. Bradford HN, Krishnaswamy S. The fragment 1 region of prothrombin facilitates the favored binding of fragment 12 to zymogen and enforces zymogen-like character in the proteinase. The Journal of Biological Chemistry 2016;291(21):11114-11123.

6. Krishnaswamy S. The transition of prothrombin to thrombin. Journal of Thrombosis and Haemostasis 2013;11(Suppl. 1):265-276.

7. Haynes LM, Bouchard BA, Tracy PB, Mann KG. Prothrombin activation by platelet-associated prothrombinase proceeds through the prethrombin-2 pathway via a concerted mechanism. Journal of Biological Chemistry 2012;287(46):38647-38655.

8. Nelsestuen GL, Kisiel W, Di Scipio RG. Interaction of vitamin K dependent proteins with membranes. Biochemistry 1978;17(11):2134-2138.

9. Walz DA, Hewett-Emmett D, Seegers WH. Amino acid sequence of human prothrombin fragments 1 and 2. Proceedings of the National Academy of Sciences of the United States of America 1977;74(5):1969.

10. UnitProt Consortium. UniProtKB - P00734 (thrb_human). 2017; Available from: http://www.uniprot.org/uniprot/P00734. [cited 02/04/2017].

11. Bajaj SP, Butkowski RJ, Mann KG. Prothrombin fragments. Ca^{2+} binding and activation kinetics. The Journal of Biological Chemistry 1975;250(6):2150-2156.

12. Mann KG. Prothrombin. Methods Enzymol 1976;45(pt. B):123-156.

13. Nesheim ME, Abbott T, Jenny R, Mann KG. Evidence that the thrombin-catalyzed feedback cleavage of fragment 1.2 at Arg154-Ser155 promotes the release of thrombin from the catalytic surface during the activation of bovine prothrombin. The Journal of Biological Chemistry 1988;263(2):1037-1044.

14. Kotkow KJ, Furie B, Furie BC. The interaction of prothrombin with phospholipid membranes is independent of either kringle domain. The Journal of Biological Chemistry 1993;268(21):15633-15639.

15. DiScipio RG, Davie EW. Characterization of protein S, a gamma-carboxyglutamic acid containing protein from bovine and human plasma. Biochemistry 1979;18(5):899-904.

16. UnitProt Consortium. UniProtKB - P02768 (albu_human). 2018; Available from: http://www.uniprot.org/uniprot/P02768. [cited 03/05/2018].

17. Thompson AR. Structure, function, and molecular defects of factor IX. Blood 1986;67(3):565-572.

18. Amphlett GW, Byrne R, Castellino FJ. The binding of metal ions to bovine factor IX. The Journal of Biological Chemistry 1978;253(19):6774-6779.

19. Waart Pvd, Bruls H, Hemker HC, Lindhout T. Interaction of bovine blood clotting factor Va and its subunits with phospholipid vesicles. Biochemistry 1983;22(10):2427-2432.

20. Henriksen RA, Jackson CM. Cooperative calcium binding by the phospholipid binding region of bovine prothrombin: a requirement for intact disulfide bridges. Archives of Biochemistry and Biophysics 1975;170(1):149-159.

21. UnitProt Consortium. UniProtKB - P00742 (fa10_human). 2017; Available from: http://www.uniprot.org/uniprot/P00742. [cited 04/04/2017].

22. Banner DW, D'Arcy A, Chène C, Einkler FK, Guha A, Konigsberg WH, et al. The crystal structure of the complex of blood coagulation factor VIIa with soluble tissue factor. Nature 1996;380(6569):41-46.

23. Bajaj SP, Rapaport SI, Brown SF. Isolation and characterization of human factor VII. Activation of factor VII by factor Xa. The Journal of Biological Chemistry 1981;256(1):253-259.

24. Strickland DK, Castellino FJ. The binding of calcium to bovine factor VII. Archives of Biochemistry and Biophysics 1980;199(1):61-66.

25. UnitProt Consortium. UniProtKB - P08709 (fa7_human). 2017; Available from: http://www.uniprot.org/uniprot/P08709. [cited 04/04/2017].

26. Griffin JH. Clinical studies of protein C. Seminars in Thrombosis and Hemostasis 1984;10(2):162-166.

27. Walker FJ. Regulation of activated protein C by protein S. The role of phospholipid in factor Va inactivation. The Journal of Biological Chemistry 1981;256(21):11128-11131.

28. Amphlett GW, Kisiel W, Castellino FJ. Interaction of calcium with bovine plasma protein C. Biochemistry 1981;20(8):2156-2161.

29. UnitProt Consortium. UniProtKB - P04070 (proc_human). 2017; Available from: http://www.uniprot.org/uniprot/P04070. [cited 04/04/2017].

30. UnitProt Consortium. UniProtKB - P07225 (pros_human). 2017; Available from: http://www.uniprot.org/uniprot/P07225. [cited 03/18/2017].

31. Shikamoto Y, Morita T, Fujimoto Z, Mizuno H. (PDB ID: 1Z6C) Solution structure of the Ca(2+)-binding EGF3-4 pair from vitamin k-dependent protein S: Identification of an unusual fold in EGF3. The Journal of Biological Chemistry 2005;44(24):8782-8789.

32. Lundwall Å, Dackowski W, Cohen E, Shaffer M, Mahr A, Dahlbäck B, et al. Isolation and sequence of the cDNA for human protein S, a regulator of blood coagulation. Proceedings of the National Academy of Sciences of the United States of America 1986;83(18):6716-6720.

33. Sugo T, Dahlbäck B, Holmgren A, Stenflo J. Calcium binding of bovine protein S. Effect of thrombin cleavage and removal of the gamma-carboxyglutamic acid-containing region. The Journal of Biological Chemistry 1986;261(11):5116-5120.

34. Miletich JP, Broze GJ, J. Human plasma protein Z antigen: range in normal subjects and effect of warfarin therapy. Blood 1987;69(6):1580-1586.

35. Broze GJ, J., Miletich JP. Human Protein Z. The Journal of Clinical Investigation 1984;73(4):933-938.

36. UnitProt Consortium. UniProtKB - P22891 (proz_human). 2017; Available from: http://www.uniprot.org/uniprot/P22891. [cited 04/04/2017].

37. Mann KG, Nesheim ME, Church WR, Haley P, Krishnaswamy S. Surface-dependent reactions of the vitamin K-dependent enzyme complexes. Blood 1990;76(1):1-16.

38. Soriano-Garcia M, Padmanabhan K, De vos AM, Tulinsky A. The calcium ion and membrane binding structure of the Gla domain of calcium-prothrombin fragment 1. Biochemistry 1992;31(9):2554-2566.

39. Furie BC, Blumenstein M, Furie B. Metal binding sites of a gamma-carboxyglutamic acid-rich fragment of bovine prothrombin. The Journal of Biological Chemistry 1979;254(24):12521-12530.

40. Nelsestuen GL. Role of gamma-carboxyglutamic acid. An unusual protein transition required for the calcium-dependent binding of prothrombin to phospholipid. The Journal of Biological Chemistry 1976;251(18):5648-5656.

41. Prendergast FG, Mann KG. Differentiation of metal ion-induced transitions of prothrombin fragment 1. The Journal of Biological Chemistry 1977;252(3):840-850.

42. Nelsestuen GL, Broderius M, Martin G. Role of gamma-carboxyglutamic acid. Cation specificity of prothrombin and factor X-phospholipid binding. The Journal of Biological Chemistry 1976;251(22):6886-6893.

43. Nelsestuen GL, Broderius M. Interaction of prothrombin and blood clotting factor X with membranes of varying composition. Biochemistry Easton 1977;16(19):4172-4177.

44. Tai MM, Furie BC, Furie B. Localization of the metal-induced conformational transition of bovine prothrombin. The Journal of Biological Chemistry 1984;259(7):4162-4168.

45. Tavoosi N, Davis-Harrison R, Pogorelov TV, Ohkubo YZ, Arcario MJ, Clay MC, et al. Molecular determinants of phospholipid synergy in blood clotting. The Journal of Biological Chemistry 2011;286(26):23247-23253.

46. Ohkubo YZ, Tajkhorshid E. Distinct structural and adhesive roles of Ca^{2+} in membrane binding of blood coagulation factors. Structure 2008;16(1):72-81.

47. Bajaj SP, Schmidt AE, Agah S, Bajaj MS, Padmanabhan K. High resolution structures of p-aminobenzamidine- and benzamidine-VIIa/soluble tissue factor: Unpredicted conformation of the 192-193 peptide bond and mapping of Ca^{2+}, Mg^{2+}, Na^{+}, and Zn^{2+} sites in factor VIIa. Journal of Biological Chemistry 2006;281(34):24873-24888.

48. Vadivel K, Bajaj SP. Structural biology of factor VIIa/tissue factor initiated coagulation. Frontiers In Bioscience (Landmark Edition) 2012;17:2476-2494.

49. Shikamoto Y, Morita T, Fujimoto Z, Mizuno H. (PDB ID: IJ34) Crystal structure of Mg^{2+}- and Ca^{2+}-bound Gla domain of factor IX complexed with binding protein. The Journal of Biological Chemistry 2003;278(26):24090-24094.

50. Agah S, B, S. P. Role of magnesium in factor XIa catalyzed activation of factor IX: calcium binding to factor IX under physiologic magnesium. Journal of Thrombosis and Haemostasis 2009;7(8):1426-1428.

51. Sekiya F, Yamashita T, Atoda H, Komiyama Y, Morita T. Regulation of the tertiary structure and function of coagulation factor IX by magnesium (II) ions. The Journal of Biological Chemistry 1995;270(24):14325-14331.

52. Persson E, Østergaard A. Mg^{2+} binding to the Gla domain of factor X influences the interaction with tissue factor. Journal of Thrombosis and Haemostasis 2007;5(9):1977-1978.

53. Kromis TL. Molecular dynamic simulations provide insight into the interaction between bovine prothrombin fragment one and the lipid phosphatidylserine. Unpublished, The University of North Carolina at Chapel Hill, 1997.

54. Rodríguez Y, Mezei M, Osman R. The PT1-Ca^{2+} Gla domain binds to a membrane through two dipalmitoylphosphatidylserines. A computational study. Biochemistry 2008;47(50):13267-13278.

55. Ratcliffe JV, Furie B, Furie BC. The importance of specific gamma-carboxyglutamic acid residues in prothrombin. Evaluation by site-specific mutagenesis. Journal of Biological Chemistry 1993;268(32):24339-24345.

56. Armstrong SA, Husten EJ, Esmon CT, Johnson AE. The active site of membrane-bound meizothrombin. A fluorescence determination of its distance from the phospholipid surface and its conformational sensitivity to calcium and factor Va. Journal of Biological Chemistry 1990;265(11):6210-6218.

57. Zhang Y. I-TASSER server for protein 3D structure prediction. BioMed Central Bioinformatics 2008;9(40):1-8.

58. Roy A, Kucukural A, Zhang Y. I-TASSER: a unified platform for automated protein sturcture and function prediction. Nature Protocols 2010;5(4):725-738.

59. Yang J, Yan R, Xu D, Poisson J, Zhang Y. The I-TASSER suite: protein structure and function prediction. Nature Methods 2015;12(1):7-8.

60. Pozzi N, Chen Z, Di Cera E. (PDB ID: 5EDM) How the linker connecting the two kringles influences activation and conformational plasticity of prothrombin. The Journal of Biological Chemistry 2016;291(19):6071-6082.

61. Huang M, Furie BC, Furie B. (PDB ID: 1NL0) Crystal structure of the calcium-stabilized human factor IX Gla domain bound to a conformation-specific anti-factor IX antibody. The Journal of Biological Chemistry 2004;279(14):14338-14346.

62. Wu S, Zhang Y. MUSTER: Improving protein sequence profile-profile alignments by using multiple sources of structure information. Proteins: Structure, Function, and Bioinformatics 2008;72(2):547-556.

63. Ghasemi F, Zomorodipour A, Karkhane AA, Khorramizadeh MR. In silico designing of hyper-glycosylated analogs for the human coagulation factor IX. Journal of Molecular Graphics & Modelling 2016;68:39-47.

64. Kurachi K, Davie EW. Isolation and characterization of a cDNA coding for human factor IX. Proceedings of the National Academy of Sciences of the United States of America 1982;79(21):6461-6464.

65. He L, Niemeyer B. A novel correlation for protein diffusion coefficients based on molecular weight and radius of gyration. Biotechnology Progress 2003;19(2):544-548.

66. Gupta SV. Consolidation of various viscosity values.In: Gupta SV, editor. Viscometry for Liquids: Calibration of Viscometers. 1st ed. Cham, Switzerland: Springer International Publishing; 2014. p. 221-224.

67. Fluxion Biosciences I. Viscosity: understanding effects of viscosity in the BioFlux system. 2009;1038-01.

68. Österberg R, Sjöberg B, Österberg P, Stenflo J. Conformational change of human prothrombin induced by calcium ions: an X-ray scattering study. Biochemistry 1980;19(10):2283-2286.

69. Vanderslice NC. Pharmacokinetic characterization of procoagulation proteins. Unpublished, University of Nebraska-Lincoln, 2014.

70. Smilgies D, Folta-Stogniew E. Molecular weight-gyration radius relation of globular proteins: a comparison of light scattering, small-angle X-ray scattering and structure-based data. Journal of Applied Crystallography 2015;48(Pt 5):1604-1606.

71. Lundblad RL. Vitamin K-dependent proteins.Biotechnology of Plasma Proteins. 1st ed. Boca Raton, FL: CRC Press; 2013. p. 367-368.

72. Atkins P, de Paula J. Reactions in solution: diffusion.In: Atkins P, de Paula J, editors. Elements of Physical Chemistry. 5th ed. New York: W. H. Freeman and Company; 2009. p. 257-257.

73. Borowski M, Furie BC, Goldsmith GH, Furie B. Metal and phospholipid binding properties of partially carboxylated human prothrombin variants. The Journal of Biological Chemistry 1985;260(16):9258-9264.

74. Bloom JW, Mann KG. Metal ion induced conformational transitions of prothrombin and prothrombin fragment 1. Biochemistry 1978;17(21):4430-4438.

75. Nelsestuen GL, Suttie JW. Mode of action of vitamin K. Calcium binding properties of bovine prothrombin. Biochemistry 1972;11(26):4961-4964.

76. Nelsestuen GL, Resnick RM, Wei GJ, Pletcher CH, Bloomfield VA. Metal ion interactions with bovine prothrombin and prothrombin fragment 1. Stoichiometry of binding, protein self-association, and conformational change induced by a variety of metal ions. Biochemistry 1981;20(2):351-358.

77. Furie BC, Mann KG, Furie B. Substitution of lanthanide ions for calcium ions in the activation of bovine prothrombin by activated factor X. High affinity metal-binding sites of prothrombin and the derivatives of prothrombin activation. The Journal of Biological Chemistry 1976;251(11):3235-3241.

78. Karlsson M, Ekeroth J, Elwing H, Carlsson U. Reduction of irreversible protein adsorption on solid surfaces by protein engineering for increased stability. Journal of Biological Chemistry 2005;280(27):25558-25564.

79. Wild D, Kusnezow W. 3.3 Separation systems.In: Wild D, John R, editors. The immunoassay handbook: theory and applications of ligand binding, ELISA and related techniques. 4th ed. Oxford: Elsevier; 2013. p. 289.

80. Lim TK, Bloomfield VA, Nelsestuen GL. Structure of the prothrombin- and blood clotting factor X-membrane complexes. Biochemistry 1977;16(19):4177-4181.

81. Esser P. Principles in Adsorption to Polystyrene. 2014;D19559.

82. Vadivel K, Agah S, Messer AS, Cascio D, Bajaj MS, Krishnaswamy S, et al. Structural and functional studies of γ-carboxyglutamic acid domains of factor VIIa and

activated protein C: Role of magnesium at physiological calcium. Journal of Molecular Biology 2013;425(11):1961-1981.

83. Clamp JR. Structure and function of glycoproteins.In: Putnam FW, editor. The Plasma Proteins: Strutcure, Function, and Genetic Control. 2nd ed. New York: Academic Press; 1975. p. 163-211.

84. Wang S, McDonnell EH, Sedor FA, Toffaletti JG. pH effects on measurements of ionized calcium and ionized magnesium in blood. Archives of Pathology & Laboratory Medicine 2002;126(8):947-950.

85. Sunnerhagen M, Forsén S, Hoffrén AM, Drakenberg T, Teleman O, Stenflo J. Structure of the Ca^{2+}-free Gla domain sheds light on membrane binding of blood coagulation proteins. Nature Structural Biology 1995;2(6):504-509.

86. Stenflo J, Suttie JW. Vitamin K-dependent formation of gamma-carboxyglutamic acid. Annual Review of Biochemistry 1977;46:157-172.

87. Gajsiewicz JM, Nuzzio KM, Rienstra CM, Morrissey JH. Tissue factor residues that modulate magnesium-dependent rate enhancements of the tissue factor/factor VIIa complex. Biochemistry 2015;54(30):4665-4671.

88. de Courcy B, Pedersen LG, Parisel O, Gresh N, Silvi B, Pilmé J, et al. Understanding selectivity of hard and soft metal cations within biological systems using the subvalence concept. I. Application to blood coagulation: direct cation-protein electronic effects vs. indirect interactions through water networks. Journal of Chemical Theory and Computation 2010;6(4):1048-1063.

89. Natishan PM, O'Grady WE. Chloride ion interactions with oxide-covered aluminum leading to pitting corrosion: A review. Journal of the Electrochemical Society 2014;161(9):C421-C432.

90. Mann KG, Nesheim ME, Tracy PB, Hibbard LS, Bloom JW. Assembly of the prothrombinase complex. Biophysical Journal 1982;37(1):106-107.

91. Borowski M, Furie BC, Bauminger S, Furie B. Prothrombin requires two sequential metal-dependent conformational transitions to bind phospholipid. Conformation-specific antibodies directed against the phospholipid-binding site on prothrombin. Journal of Biological Chemistry 1986;261(32):14969-14975.

92. How to maintain the performance of your MS system. 3rd Nordic MS Symposium Jurmala: Waters; 2012.

93. Waters. Data for the calculation of the molecular masses of glycopeptides, glycoproteins and oligosaccharides for use in mass spectrometry. 2003;720000537EN.

94. Bo N, Horne MKI, Gralnick HR. The carbohydrate of human thrombin: Structural analysis of glycoprotein oligosaccharides by mass spectrometry. Archives of Biochemistry and Biophysics 1983;224(1):127-133.

95. Liu T, Qian W, Gritsenko MA, Camp DG, Monroe ME, Moore RJ, et al. Human plasma N-glycoproteome analysis by immunoaffinity subtraction, hydrazide chemistry, and mass spectrometry. Journal of Proteome Research 2005;4(6):2070-2080.

96. Lanchantin GF, Hart DW, Friedmann JA, Saavedra NV, Mehl JW. Amino acid composition of human plasma prothrombin. The Journal of Biological Chemistry 1968;243(20):5479-5485.

97. Kisiel W, Hanahan DJ. Purification and characterization of human factor II. Biochimica et Biophysica Acta 1973;304(1):103-113.

98. Wu AH, Gerona R, Armenian P, French D, Petrie M, Lynch KL. Role of liquid chromatography–high-resolution mass spectrometry (LC-HR/MS) in clinical toxicology. Clinical Toxicology 2012;50(8):733-742.

99. Goding JW. Analysis of antigens recognized by monoclonal antibodies.Monoclonal Antibodies: Principles and Practice. 3rd ed. London; San Diego: Academic Press; 1996. p. 234-326.

100. Herrmann SH, Chow CM, Mescher MF. Proteolytic modifications of the carboxyl-terminal region of H-2Kk. The Journal of Biological Chemistry 1982;257(23):14181-14186.

Chapter 9

1. Stroeve P, Ileri N. Biotechnical and other applications of nanoporous membranes. Trends in Biotechnology 2011;29(6):259-266.

2. Platschek B, Keilbach A, Bein T. Mesoporous structures confined in anodic alumina membranes. Advanced Materials 2011;23(21):2395-2412.

3. Kumeria T, Kurkuri MD, Diener KR, Parkinson L, Losic D. Label-free reflectometric interference microchip biosensor based on nanoporous alumina for detection of circulating tumour cells. Biosensors and Bioelectronics 2012;35(1):167-173.

4. Shi W, Shen Y, Ge D, Xue M, Cao H, Huang S, et al. Functionalized anodic aluminum oxide (AAO) membranes for affinity protein separation. Journal of Membrane Science 2008;325(2):801-808.

5. Fu J, Mao P, Han J. Artificial molecular sieves and filters: A new paradigm for biomolecule separation. Trends in Biotechnology 2008;26(6):311-320.

6. Manzano M, Vallet-Regi M. New developments in ordered mesoporous materials for drug delivery. Journal of Materials Chemistry 2010;20(27):5593-5604.

7. Brüggemann D. Nanoporous aluminium oxide membranes as cell interfaces. Journal of Nanomaterials 2013;2013:1-18.

8. La Flamme K,E., Popat KC, Leoni L, Markiewicz E, LaTempa TJ, Roman BB, et al. Biocompatibility of nanoporous alumina membranes for immunoisolation. Biomaterials 2007;28(16):2638-2645.

9. Aramesh M, Cervenka J. Surface modification of porous anodic alumina for medical and biological applications.In: Seifalian A, de Mel A, Kalaskar DM, editors. Nanomedicine. 1st ed. VIC, AU: One Central Press; 2014. p. 439-467.

10. Karlsson M, Johansson A, Tang L, Boman M. Nanoporous aluminum oxide affects neutrophil behaviour. Microscopy Research and Technique 2004;63(5):259-265.

11. Lim JY, Donahue HJ. Cell sensing and response to micro- and nanostructured surfaces produced by chemical and topographic patterning. Tissue Engineering 2007;13(8):1879-1891.

12. Martínez E, Engel E, Planell JA, Samitier J. Effects of artificial micro- and nano-structured surfaces on cell behaviour. Annals of Anatomy 2009;191(1):126-135.

13. Flemming RG, Murphy CJ, Abrams GA, Goodman SL, Nealey PF. Effects of synthetic micro- and nano-structured surfaces on cell behavior. Biomaterials 1999;20(6):573-588.

14. Schmitt GL, Pietrzyk DJ. Liquid chromatographic separation of inorganic anions on an alumina column. Analytical Chemistry 1985;52(12):2247-2253.

15. Wang J, Zhang Y, Feng C, Li J, Li G. Adsorption capacity for phosphorus comparison among activated alumina, silica sand and anthracite coal. Journal of Water Resource and Protection 2009;1(4):260-264.

16. Hyndman D, Burrell R, Lever G, Flynn TG. Protein immobilization to alumina supports: I. Characterization of alumina-organophosphate ligand interactions and use in the attachment of papain. Biotechnology and Bioengineering 1992;40(11):1319-1327.

17. Hyndman D, Burrell R, Lever G, and Flynn G. Protein immobilization to alumina supports: II. Papain immobilization to alumina via organophosphate linkers. Biotechnology and Bioengineering 1992;40(11):1328-1336.

18. Del Nero M, Galindo C, Barillon R, Halter E, Madé B. Surface reactivity of α-Al2O3 and mechanisms of phosphate sorption: In situ ATR-FTIR spectroscopy and ζ potential studies. Journal of Colloid and Interface Science 2010;342(2):437-444.

19. Goldberg S, Sposito G. On the mechanism of specific phosphate adsorption by hydroxylated mineral surfaces: A review. Communications in Soil Science and Plant Analysis 1985;16(8):801-821.

20. Rajan SSS. Adsorption of selecnite, phosphate and sulphate on hydrous alumina. Journal of Soil Science 1979;30(4):709-718.

21. Rajan SSS, Perrott KW, Saunders WMH. Identification of phosphate-reactive sites of hydrous alumina from proton consumption during phosphate adsorption at constant pH values. J Soil Sci 1974;25(4):438-447.

22. Popat KC, Mor G, Grimes CA, Desai TA. Surface modification of nanoporous alumina surfaces with poly(ethylene glycol). Langmuir 2004;20(19):8035-8041.

23. Lee SW, Shang H, Haasch RT, Petrova V, Lee GU. Transport and functional behaviour of poly(ethylene glycol)-modified nanoporous alumina membranes. Nanotechnology 2005;16(8):1335-41.

24. Kasprzyk-Hordern B. Chemistry of alumina, reactions in aqueous solution and its application in water treatment. Adv Colloid Interface Sci 2004;110(1):19-48.

25. Thurman RB, Gerba CP. Characterization of the effect of aluminum metal on poliovirus. Journal of Industrial Microbiology 1988;3(1):33-38.

26. Murray JP, Laband SJ. Degradation of poliovirus by adsorption on inorganic surfaces. Applied and Environmental Microbiology 1979;37(3):480-486.

27. Wittayanukulluk A, Jiang D, Regnier FE, Hem SL. Effect of microenvironment pH of aluminum hydroxide adjuvant on the chemical stability of adsorbed antigen. Vaccine 2004;22(9):1172-1176.

28. Clapp T, Siebert P, Chen D, Jones Braun L. Vaccines with aluminum-containing adjuvants: Optimizing vaccine efficacy and thermal stability. Journal of Pharmaceutical Sciences 2011;100(2):388-401.

29. Tang L, Eaton JW. Natural responses to unnatural materials: A molecular mechanism for foreign body reactions. Molecular Medicine 1999;5(6):351-358.

30. Anderson JM. Chapter 4 Mechanisms of inflammation and infection with implanted devices. Cardiovascular Pathology 1993;2(3):33-41.

31. Tang L. Molecular mechanism of biomaterial-mediated phagocyte responses.In: Wise DL, Gresser JD, Trantolo DJ, Cattaneo MV, Lewandrowski K, Yaszemski MJ, editors. Biomaterials Engineering and Devices: Human Applications. 1st ed. Totowa, NJ: Humana Press; 2000. p. 3-14.

32. Courtney JM, Lamba NMK, Sundaram S, Forbes CD. Biomaterials for blood-contacting applications. Biomaterials 1994;15(10):737-744.

33. Lim TK, Bloomfield VA, Nelsestuen GL. Structure of the prothrombin-and blood clotting factor X-membrane complexes. Biochemistry 1977;16(19):4177-4181.

34. van den Brand J, Blajiev O, Beentjes PCJ, Terryn H, de Wit, J. H. W. Interaction of anhydride and carboxylic acid compounds with aluminum oxide surfaces studied using infrared reflection absorption spectroscopy. Langmuir 2004;20(15):6308-6317.

35. Karaman ME, Antelmi DA, Pashley RM. The production of stable hydrophobic surfaces by the adsorption of hydrocarbon and fluorocarbon carboxylic acids onto alumina substrates. Colloids and Surfaces A: Physicochemical and Engineering Aspects 2001;182(1):285-298.

36. Moeremans M, Daneels G, Van Dijck A, Langanger G, De Mey J. Sensitive visualization of antigen-antibody reactions in dot and blot immune overlay assays with immunogold and immunogold/silver staining. Journal of Immunological Methods 1984;74(2):353-360.

37. Kisiel W, Hanahan DJ. Purification and characterization of human factor II. Biochimica et Biophysica Acta 1973;304(1):103-113.

38. Goldstein JI, Newbury DE, Joy DC, Lyman C, Echlin P, Lifshin E, et al. Electron beam-specimen interactions.Scanning electron microscopy and X-ray microanalysis. 3rd ed. New York, USA: Springer; 2003. p. 61-98.

39. Cooper MS, Ma MT, Sunassee K, Shaw KP, Williams JD, Paul RL, et al. Comparison of (64)Cu-complexing bifunctional chelators for radioimmunoconjugation: labeling efficiency, specific activity and in vitro/in vivo stability. Bioconjugate chemistry 2012;23(5):1029-1039.

40. Alves CM, Reis RL, Hunt JA. The competitive adsorption of human proteins onto natural-based biomaterials. Journal of the Royal Society Interface 2010;7(50):1367-1377.

41. Pradas MM, Sánchez MS, Gloria GF, Ribelles JLG. Thermodynamics and statistical mechanics of multilayer adsorption. Journal of Chemical Physics 2004;121(17):8524-8531.

42. Girods P, Dufour A, Fierro V, Rogaume Y, Rogaume C, Zoulalian A, et al. Activated carbons prepared from wood particleboard wastes: Characterisation and phenol adsorption capacities. Journal of Hazardous Materials 2009;166(1):491-501.

43. Liu Y. Is the free energy change of adsorption correctly calculated? Journal of Chemical and Engineering Data 2009;54(7):1981-1985.

44. Xia M, Li A, Zhu Z, Zhou Q, Yang W. Factors influencing antibiotics adsorption onto engineered adsorbents. Journal of Environmental Sciences 2013;25(7):1291-1299.

45. Vinu A, Murugesan V, Tangermann O, Hartmann M. Adsorption of cytochrome c on mesoporous molecular sieves: Influence of pH, pore diameter, and aluminum incorporation. Chemistry of Materials 2004;16(16):3056-3065.

46. Janshoff A, Dancil KS, Steinem C, Greiner DP, Lin VSY, Gurtner C, et al. Macroporous p-type silicon Fabry-Perot layers. Fabrication, characterization, and applications in biosensing. Journal of the American Chemical Society 1998;120(46):12108-12116.

47. Karlsson LM, Tengvall P, Lundström I, Arwin H. Penetration and loading of human serum albumin in porous silicon layers with different pore sizes and thicknesses. Journal of Colloid and Interface Science 2003;266(1):40-47.

48. Gispert MP, Serro AP, Colaço R, Saramago B. Bovine serum albumin adsorption onto 316L stainless steel and alumina: a comparative study using depletion, protein radiolabeling, quartz crystal microbalance and atomic force microscopy. Surface and Interface Analysis 2008;40(12):1529-1537.

49. Rezwan K, Meier LP, Rezwan M, Vörös J, Textor M, Gauckler LJ. Bovine serum albumin adsorption onto colloidal Al_2O_3 particles: A new model based on zeta potential and UV-Vis measurements. Langmuir 2004;20(23):10055-10061.

50. Lei C, Shin Y, Liu J, Ackerman EJ. Entrapping enzyme in a functionalized nanoporous support. Journal of the American Chemical Society 2002;124(38):11242-11243.

51. Jenney CR, Anderson JM. Adsorbed serum proteins responsible for surface dependent human macrophage behavior. Journal of Biomedical Materials Research 2000;49(4):435-447.

52. UnitProt Consortium. UniProtKB - P02768 (albu_human). 2018; Available from: http://www.uniprot.org/uniprot/P02768. [cited 03/05/2018].

53. UnitProt Consortium. UniProtKB - P00734 (thrb_human). 2017; Available from: http://www.uniprot.org/uniprot/P00734. [cited 02/04/2017].

54. Sugio S, Kashima A, Mochizuki S, Noda M, Kobayashi K. Crystal structure of human serum albumin at 2.5 Å resolution. Protein Engineering 1999;12(6):439-446.

55. Whicher SJ, Brash JL. Platelet–foreign surface interactions: Release of granule constituents from adherent platelets. Journal of Biomedical Materials Research 1978;12(2):181-201.

56. Karlsson M, Tang L. Surface morphology and adsorbed proteins affect phagocyte responses to nano-porous alumina. Journal of Materials Science: Materials in Medicine 2006;17(11):1101-1111.

57. Gessner A, Waicz R, Lieske A, Paulke B, Mäder K, Müller RH. Nanoparticles with decreasing surface hydrophobicities: Influence on plasma protein adsorption. International Journal of Pharmaceutics 2000;196(2):245-249.

58. Nakanishi K, Sakiyama T, Imamura K. On the adsorption of proteins on solid surfaces, a common but very complicated phenomenon. Journal of Bioscience and Bioengineering 2001;91(3):233-244.

59. Liu B, Cao S, Deng X, Li S, Luo R. Adsorption behavior of protein onto siloxane microspheres. Applied Surface Science 2006;252(22):7830-7836.

60. Efimova,Y.M., Haemers, S., Wierczinski, B., Norde, W., Well AAv. Stability of globular proteins in H_2O and D_2O. Biopolymers 2007;85(3):264-273.

61. Bergkvist M, Carlsson J, Oscarsson S. Surface-dependent conformations of human plasma fibronectin adsorbed to silica, mica, and hydrophobic surfaces, studied with use of Atomic Force Microscopy. Journal of Biomedical Materials Research Part A 2003;64A(2):349-356.

62. Carter DC, Ho JX. Structure of serum albumin. Advances in Protein Chemistry 1994;45:153-203.

63. Hermanson GT. Chapter 12 - Isotopic labeling techniques.In: Hermanson GT, editor. Bioconjugate Techniques. 3rd ed. Boston: Academic Press; 2013. p. 507-534.

64. Rapaport SI, Hjort PF, Patch MJ, Jeremic M. Consumption of serum factors and prothrombin during intravascular clotting in rabbits. European Journal of Haematology 1966;3(1):59-75.

65. Silverberg SA. Proteolysis of prothrombin by thrombin. Determination of kinetic parameters, and demonstration and characterization of an unusual inhibition by Ca2+ ions. The Journal of Biological Chemistry 1979;254(1):88-94.

66. Ganrot PO, Niléhn J. Prothrombin fragmentation during coagulation of whole blood and plasma. Scandinavian Journal of Clinical and Laboratory Investigation 1969;24(1):15-21.

67. Ganrot PO, Stenflo J. Prothrombin derivatives in human serum. Isolation and some properties of the non-thrombin fragments. Scandinavian Journal of Clinical and Laboratory Investigation 1970;26(2):161-168.

68. Aronson DL, Stevan L, Ball AP, Franza BRJ, Finlayson JS. Generation of the combined prothrombin activation peptide (F1-2) during the clotting of blood and plasma. The Journal of Clinical Investigation 1977;60(6):1410-1418.

69. Owen WG, Esmon CT, Jackson CM. The conversion of prothrombin to thrombin: I. Characterization of the reaction products formed during the activation of bovine prothrombin. Journal of Biological Chemistry 1974;249(2):594-605.

70. Esmon CT, Owen WG, Jackson CM. The conversion of prothrombin to thrombin: II. Differentiation between thrombin- and factor Xa-catalyzed proteolyses. The Journal of Biological Chemistry 1974;249(2):606-611.

71. Radcliffe R, Nemerson Y. Activation and control of factor VII by activated factor X and thrombin. Isolation and characterization of a single chain form of factor VII. Journal of Biological Chemistry 1975;250(2):388-395.

72. Esmon CT, Owen WG, Jackson CM. The conversion of prothrombin to thrombin: V. The activation of prothrombin by factor Xa in the presence of phospholipid. The Journal of Biological Chemistry 1974;249(24):7798-7807.

73. Ware AG, Seegers WH. Studies on prothrombin; purification, inactivation with thrombin, and activation with thromboplastin and calcium. The Journal of Biological Chemistry 1948;174(2):565-575.

74. Sandström T, Stenberg M, Nygren H. Visual detection of organic monomolecular films by interference colors. Applied Optics 1985;24(4):472-479.

75. Vroman L, Adams AL. Identification of rapid changes at plasma–solid interfaces. Journal of Biomedical Materials Research 1969;3(1):43-67.

76. Pacheco B. Cytodiagnostics (personal communication). 2015.

77. Xia N, Castner DG. Preserving the structure of adsorbed protein films for time-of-flight secondary ion mass spectrometry analysis. Journal of Biomedical Materials Research Part A 2003;67A(1):179-190.

78. Hayat MA. Fixation for electron microscopy. New York: Academic Press; 1981.

Chapter 10

1. Foote J, Eisen HN. Kinetic and affinity limits on antibodies produced during immune responses. Proceedings of the National Academy of Sciences of the United States of America 1995;92(5):1254-1256.

2. Reverberi R, Reverberi L. Factors affecting the antigen-antibody reaction. Blood Transfusion 2007;5(4):227-240.

3. Hill S, Mitchell J, Burnett D, Stockley R. IgG subclasses in the serum and sputum from patients with bronchiectasis. Thorax 1998;53(6):463-468.

4. Burry RW. Antibodies.Immunocytochemistry: A Practical Guide for Biomedical Research. 1st ed. New York: Springer; 2010. p. 7-16.

5. Invitrogen Corp. Immunoassay guide. 2017;COL31747 0717.

6. Bio-Rad Laboratories I. ELISA basics guide. 2017;29251V1.2017.

7. Demeule B, Shire SJ, Liu J. A therapeutic antibody and its antigen form different complexes in serum than in phosphate-buffered saline: A study by analytical ultracentrifugation. Analytical Biochemistry 2009;388(2):279-287.

8. Oda M, Uchiyama S, Noda M, Nishi Y, Koga M, Mayanagi K, et al. Effects of antibody affinity and antigen valence on molecular forms of immune complexes. Molecular Immunology 2009;47:357-364.

9. Oda M, Azuma T. Reevaluation of stoichiometry and affinity/avidity in interactions between anti-hapten antibodies and mono- or multi-valent antigens. Molecular Immunology 2000;37(18):1111-1122.

10. Drake AW, Tang ML, Papalia GA, Landes G, Haak-Frendscho M, Klakamp SL. Biacore surface matrix effects on the binding kinetics and affinity of an antigen/antibody complex. Analytical Biochemistry 2012;429(1):58-69.

11. Armstrong B. Antigen–antibody reactions. ISBT Science Series 2008;3(2):21-32.

12. Rolih SD. Enhancement techniques for antigen-antibody interactions. Laboratory Medicine 1986;17(4):203-206.

13. Xiao Y, Isaacs SN. Enzyme-linked immunosorbent assay (ELISA) and blocking with bovine serum albumin (BSA)—not all BSAs are alike. Journal of Immunological Methods 2012;384(1):148-151.

14. Finn TE, Nunez AC, Sunde M, Easterbrook-Smith S. Serum albumin prevents protein aggregation and amyloid formation and retains chaperone-like activity in the presence of physiological ligands. The Journal of Biological Chemistry 2012;287(25):21530-21540.

15. Jeyachandran YL, Mielczarski JA, Mielczarski E, Rai B. Efficiency of blocking of non-specific interaction of different proteins by BSA adsorbed on hydrophobic and hydrophilic surfaces. Journal of Colloid and Interface Science 2010;341(1):136-142.

16. Ortiz D, Yannatos I, Nath A. Comparing antibody-antigen binding in serum versus buffer with fluorescence correlation spectroscopy. Biophysical Journal 2017;112(3):150a-151a.

17. Burrell RE, Naylor AG, Rosenfeld AM, inventors. Alcan International Ltd, assignee. Thin film diagnostic device. US patent 5,124,172. 1992 Jun. 23.

18. Lim TK, Bloomfield VA, Nelsestuen GL. Structure of the prothrombin-and blood clotting factor X-membrane complexes. Biochemistry 1977;16(19):4177-4181.

19. Tan YH, Liu M, Nolting B, Go JG, Gervay-Hague J, Liu G. A nanoengineering approach for investigation and regulation of protein immobilization. ACS Nano 2008;2(11):2374-2384.

20. Lee JF, Stovall GM, Ellington AD. Aptamer therapeutics advance. Current Opinion in Chemical Biology 2006;10(3):282-289.

21. Mollison PL, Engelfriet CP, Contreras M. Mollison's blood transfusion in clinical medicine. 10th ed. Malden, MA: Blackwell Science Ltd.; 1997.

22. Lai H, Horng Y, Yeh P, Wang J, Shu C, Lu C, et al. The assessment of host and bacterial proteins in sputum from active pulmonary tuberculosis. J Microbiol 2016;54(11):761-767.

23. Lippok S, Seidel SAI, Duhr S, Uhland K, Holthoff H, Jenne D, et al. Direct detection of antibody concentration and affinity in human serum using microscale thermophoresis. Analytical Chemistry 2012;84(8):3523-3530.

Appendix 1 – SOPs

1.1 Piranha Cleaning SOP

Piranha cleaning 2015-04-01

Location: Aisle 2 (Wetdeck 2B)

Primary Trainer: Stephanie Bozic
587.879.1515
sbozic@ualberta.ca

Secondary Trainer: Scott Munro
587.879.1517
smunro@ualberta.ca

OVERVIEW

This document outlines the process for preparing a piranha bath (3:1 H_2SO_4:H_2O_2) used for removing organics and metallic contaminants from substrates. Cold piranha (<40 °C) is also used to clean chrome photomasks. Most surfaces are hydroxylated during piranha cleaning, becoming strongly hydrophilic.

SAFETY PRECAUTIONS

> **N.B. Organics (acetone, isopropyl alcohol, photoresist, polymer films, etc.) should not be placed in a piranha bath or on the piranha wet deck. Contact between piranha and a large volume of organic contaminants will cause a violent reaction and a substantial explosion.**

While not carcinogenic, the chemicals used in piranha cleaning are dangerous; care must therefore be taken to avoid physical contact with the cleaning solutions and their fumes. Please refer to the nanoFAB MSDS binder if you have any concerns using these chemicals.

Sulphuric acid, H_2SO_4 (96%) A highly corrosive, strong mineral acid which is clear, colourless to slightly yellow, viscous, and pungent. Sulphuric acid causes severe burns on contact. The harmful vapour and mist can cause burns to eyes, skin, and respiratory tract.

Hydrogen Peroxide, H_2O_2 (30%) A strong oxidizer and corrosive clear liquid. It can cause burns to skin, eyes, and respiratory tract.

Acid gear must be worn when preparing the piranha bath:

Chemical apron

Chemical-resistant gloves

Face shield

Important safety notes:

- **Mixing the chemicals for a piranha bath causes an exothermic reaction: the solution can self-heat up to 120 °C. Due to the high temperature, the bath should never be agitated.**
- **NEVER use plastic labware—use glass only.**
- **NEVER put piranha solution in a closed container: gas generation and the resulting over pressurisation can lead to an explosion.**
- **Piranha solution also explodes if the peroxide concentration exceeds 50%. Consequently, the hydrogen peroxide must always be added to the sulphuric acid, NEVER vice versa.**

NO CHEMICALS ARE TO BE REMOVED FROM THE WET DECK IN OPEN CONTAINERS.

Before bringing any new materials into the nanoFAB for processing, it is necessary to fill out a new chemical import form (www.nanofab.ualberta.ca/user-information/user-forms/chemical-import-form/).

OPERATING PROCEDURE

1. Transfer substrates to a Teflon carrier (boat or basket, depending upon substrate size). Blue polypropylene locking tweezers may also be used to hold individual chips.
2. Choose a glass container for the bath which will fit the carrier. Label the container with the bath name ("piranha"), the user name, the date, and the time.
3. Determine the volume of solution required to immerse the substrates completely. This can be done "by eye" or more quantitatively by measuring with a beaker.
4. Calculate the amounts of sulphuric acid and hydrogen peroxide yielding the necessary final volume, using a volumetric H_2SO_4:H_2O_2 ratio of 3:1.

The table to the right lists volumes for typical 3:1 piranha baths. When choosing the final volume, it is worth noting that the vigour of the reaction depends on the surface-to-volume ratio of the solution (e.g., 400 mL of piranha in a large beaker may not bubble as violently as 400 mL in a small beaker).

Final volume (mL)	H_2SO_4 volume (mL)	H_2O_2 volume (mL)
400	300	100
600	450	150
800	600	200
1000	750	250
1200	900	300
1600	1200	400
2000	1500	500

5. Select two beakers for measuring sulphuric acid and hydrogen peroxide and mark the correct volume on each beaker. Place the measuring beakers and bath container on the wet deck.
6. Check the condition of a pair of chemical-resistant gloves by inspecting for dark spots or other evidence of chemical spills, then filling them with nitrogen using the nitrogen gun to check for leaks. If gloves are not in good condition, discard and obtain a new pair. New gloves may be obtained from the shelf in the sulphuric acid cabinet (Aisle 2); label with the size and date.
7. Don the acid gear: apron, face shield, and gloves.
8. Slowly pour the required amount of sulphuric acid into the marked beaker. Transfer this amount into the bath container labeled piranha and place the empty beaker into dump rinser.
9. Slowly pour the required amount of hydrogen peroxide into the second marked beaker. Transfer this amount into the bath already containing the sulphuric acid. Place the empty beaker into the dump rinser and start the 5× rinsing cycle (press **STOP** → **START**).
10. Carefully place the Teflon carrier of substrates into the piranha bath. There may be a vigorous reaction evident by "bubbling and spitting". If holding chips with blue tweezers, thread a Teflon rod through the tweezer handles and place the rod across the top of the bath beaker, such that the chips are below the piranha surface.
11. Start a timer for 15 minutes. After 15 minutes the piranha will have cooled such that the reaction is no longer vigorous enough to etch effectively.
12. Wash the chemical bottles on the outside with DI water and pat dry with a cleanroom wipe. Place the bottles back in the appropriate storage cabinets. If you empty a chemical bottle, rinse the inside 3× with DI water, wash the outside, pat dry, cross out the bottle label with a Sharpie marker, write "washed bottle" on the outside, and place in the washed bottle storage bin opposite the gowning room door.
13. Rinse the chemical-resistant gloves with DI water and dry with a cleanroom wipe. Remove acid gear and place back on the appropriate racks.
14. Once the rinse cycle is finished, press **OPEN** to drain the dump rinser, remove the beakers, and place them on the drying rack. Wipe off measuring marks with a cleanroom wipe moistened with acetone or IPA.
15. When the piranha clean has finished, don the acid gear again and slowly remove the carrier from the piranha bath, allowing excess liquid to drip back into the bath.
16. Transfer the carrier carefully into the dump rinser and start the 5× rinsing cycle. If using chips with blue tweezers, hold them over the dump rinser and spray copiously with DI water.
17. Push the piranha bath vessel to the back of the wet deck; nanoFAB staff will aspirate the piranha once cool.
18. Spray the wet deck with DI water to rinse any drips of piranha.
19. Rinse the chemical-resistant gloves with DI water and dry with a cleanroom wipe. Remove acid gear and place back on the appropriate racks.

20. Once the dump rinser cycle has finished, dry substrates with nitrogen gun or use the spin rinse dryer (if wafers are in a boat).

    Wipe the front of the wet deck with a cleanroom wipe to ensure there are no water droplets.

TROUBLESHOOTING

If you encounter any unexpected errors or require assistance, please contact the primary or secondary trainer listed above. If they are not available, please contact any nanoFAB staff member for assistance.

APPROVAL

Qualified Trainer: Stephanie Bozic

Group Leader – Fabrication: Aaron Hryciw

1.2 *Bob Sputtering System SOP*

BOB SPUTTERING TOOL

August 06 2014

Location: 10K PVD area
Primary Trainer: Les Schowalter (587-879-1516), les.schowalter@ualberta.ca)
Secondary Trainer:

OVERVIEW
A planar magnetron sputter system with three sources. The gun/substrate configuration is designed for sequential sputtering. The third source can be used for magnetic materials.

SAFETY PRECAUTIONS
When using the hoist to close the system take care that your fingers are not between the chamber lid and body. Some materials are not compatible with a vacuum system; if you aren't sure of your material please see the primary trainer.

If you are bringing any new materials into the NanoFab for use in your process, it is necessary to fill out a chemical import form (available on our website, http://www.nanofab.ualberta.ca) and supply an MSDS data sheet to Stephanie Bozic.

OPERATING INSTRUCTIONS

Opening & Loading

1.0 Press "**emis**" on the multi gauge controller to turn off the ion gauge then press "**channel**" until TC1 is shown and nothing on the bottom right.
2.0 Turn the Baratron valve clockwise until closed.
3.0 Close the cryopump valve clockwise until closed; there should be a solid click sound when closed. Also note the cryopump temperature, if it's not below 20K please inform nanoFAB staff.
4.0 Flip the chamber vent switch up. When the pressure readout is at 760 Torr the chamber should be at atmosphere and the chamber vent switch must be closed.
5.0 Lift the lever on the back of the chamber lid.
6.0 Press the up button on the hoist and raise the top of the chamber until the substrate holder is clear of the main chamber, and then move the chamber top away.
7.0 Please put gloves on for the next steps.
8.0 Check the inside of the chamber for flaking and other debris; vacuum as required.
9.0 If the glass view port is coated with metal, pull out and replace glass. Please use IPA to clean all six sides of glass before installing.
10.0 Change targets as required, check to see if the proper target is in the chamber or in the correct container. Sputtering the wrong material may set your project back.
11.0 Make sure the dark space shield has adequate spacing. Most targets are ¼" thick and the dark space shield shouldn't be on any notch, Targets such as Au and Pt are thinner and should go onto the smallest notch. Check spacing with the voltmeter, you should have an open circuit.
12.0 Close the shutters. Remove any particles around the main o-ring using a cleanroom wipe and IPA.
13.0 Load your substrate(s) and move the top over the chamber; move the lever down and press the lower button on the hoist. Make sure you hold onto the top section as it wants to move to the right. When the top meets the chamber stop pressing the lower button, it can't lower any further!

Pump down

1.0 Open the chamber roughing valve about one full turn and observe if the chamber pressure is dropping. If the pressure doesn't change, check to see if the lid is properly seated onto the chamber. If pressure still doesn't drop close roughing valve and find nano**FAB** staff to look into the issue.
2.0 Rough to about 350 Torr then open the roughing valve all the way then close about a half turn. Rough out to $3.0X10^{-1}$ (about five minutes depending on which roughing pump is used.) then close roughing valve.
3.0 Slowly open the cryo valve all the way by turning counterclockwise.
4.0 Open the Baratron valve by turning it counterclockwise.
5.0: Press "**channel**" on the multi gauge controller until BA1 is shown in the lower right of the display, then press "**emis**".
6.0 Pumpdown takes about one hour to reach the low -6 Torr.
7.0 Write your deposition parameters in the logbook, and put the sputter system in use sign up.

Deposition

1. Press "**emis**" on the multi gauge to turn off the filament, then press "**channel**" until aux1 is shown in the lower section of the display.
2.0 Pull and lift the power switch on the MKS controller, then lift switch 1 for Ar gas, close the cryo gate valve about four turns until the Multi gauge controller reads $7X10^{-3}$ Torr.
3.0 Put target selector switch to the desired target. Switch on the power on the back of the MDX 500 power supply; adjust the power setting required for the material you are depositing. Remember the power supply should only be used in power mode.
4.0 Set substrate rotation to the desired speed, three to four is normal. Press the rotation switch.
5.0 Set a timer for the deposition time plus preconditioning. Target conditioning is usually three minutes except for Pt and Au which is one minute.
6.0 Press start on the power supply to condition the target. Look in the chamber to make sure the shutter is closed.
7.0 After the target conditioning step is over gently open the shutter and deposit for the desired time. Remember to write the voltage in the logbook. Press stop on the power supply when the desired time is reached.
8.0 Close the shutter and repeat steps three to six if another metal is required.
9.0 After the deposition is completed, turn off MDX 500 power supply (switch at the back).
10.0 Stop substrate rotation.
11.0 Turn target selector switch to off.
12.0 Turn off Argon switch, and MKS master power.
13.0 Press "**channel"** on the multi gauge controller until TC1 is shown and nothing else in the lower right section of the display.
14.0 Close the Baratron valve.
15.0 Close the cryo gate valve.
16.0 Flick the chamber vent switch to put a few Torr of N_2 in the chamber then wait five minutes before venting.
17.0 After venting, open chamber using the same instructions as opening and loading starting at step #5. Put gloves on after moving the chamber top, remove substrate(s) and inspect chamber for flaking. If flaking is discovered please vacuum.
18.0 If you used a Pt target, please remove it from the system.
19.0 Follow steps from pumpdown section. Please note that you don't have to start with slow pump down.

TROUBLESHOOTING
If you can't get a plasma do the following:
Close the cryo gate valve to the point of causing resistance.
Change power setting to 50 watts.

If you still can't get a plasma find the trainer for the tool or other nanoFAB staff to look into the issue.

If you encounter an unexpected error or require assistance please contact the primary or secondary trainer listed above. Should they not be available, please contact any staff member for assistance.

APPROVAL

Qualified Trainer: Les Schowalter
Training Coordinator: Stephanie Bozic

1.3 Floyd Sputtering System SOP

Sputtering System #3 (Floyd)

2017-07-06

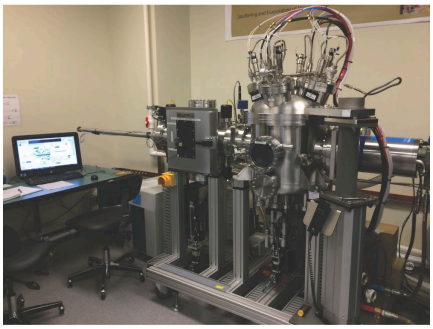

Location: 10k Deposition Area

Primary Trainer: Les Schowalter
587.879.1516
les.schowalter@ualberta.ca

Secondary Trainer: Aaron Hryciw
780.940.7938
ahryciw@ualberta.ca

OVERVIEW

Sputtering System #3 (Floyd) is an automated planar DC magnetron sputtering system with four sputter guns. The system load lock contains six shelves, each of which can accommodate substrates from small pieces up to 150 mm diameter wafers, in a sputter-down configuration. The transfer of shelves to/from the process chamber, as well as the deposition itself, is computer controlled. The system is also equipped with a power supply for RF etchback, primarily used for resist descum prior to deposition for lift-off.

SAFETY PRECAUTIONS

Do not put any pressure on the load lock door: this can put it out of alignment, compromising the load lock chamber vacuum.

Before bringing any new materials into the nanoFAB for processing, it is necessary to fill out a new chemical import request on LMACS.

OPERATING PROCEDURE

1. On LMACS, login to tool *Sputtering System #3 (Floyd)*; Location: *10k Deposition Area*.
2. The system control software, eKLipse, should be running. If not, start it by clicking the eKLipse icon on the desktop.

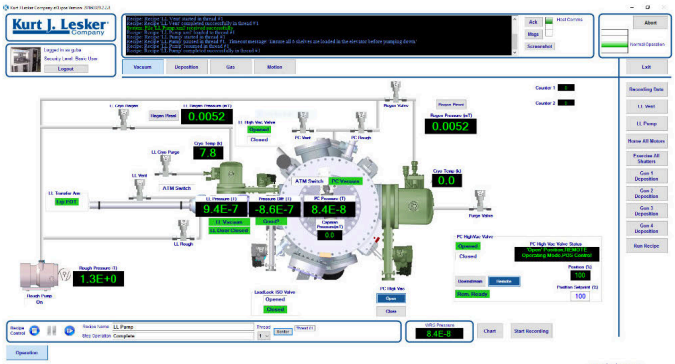

3. Login to eKLipse: click the **Login** button in the upper-left corner and enter your username and password. All users receive their own unique login information once signed off on Floyd.
4. Click **LL Vent** on the right side of the screen. Wait for venting to finish: the Recipe Name field of the *RecipeMonitor* window should read LL Vent Recipe Complete, and the load lock atmosphere indicator should be green: ATM Switch.
5. Open the load lock door and load your specimens.
   - If you only require one shelf, place specimen(s) on the top shelf (Shelf 6); in this case, it is not necessary to remove the shelf or shelf stack from the load lock.
   - If you require more than one shelf, remove the six-shelf stack and place it on a cleanroom wipe on the table. Load each individual shelf with your samples. It is important that the top shelf has notches cut out of the left and right sides, and that all shelves have their flat edges aligned to the right side of the stack (see following image). Ensure each shelf is securely seated on its three pins: failure to do this will cause a loading failure and possible damage to the loading arm. Return the six-shelf stack to the load lock, fitting it securely to the three pins in the load lock.

     N.B. Ensure that the shelf stack is full (i.e., has six shelves loaded) and that the top shelf has the appropriate notches before continuing.

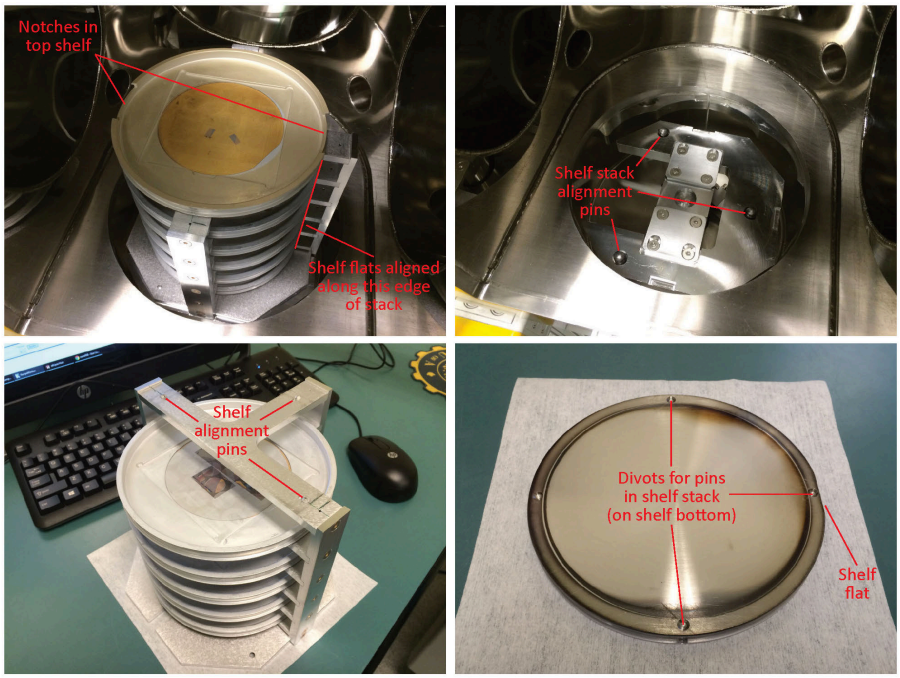

6. Click **LL Pump** to start pumping down the load lock.
7. Once the **LL Pump** recipe completes, exercise the gun shutters: click **Exercise All Shutters**. Repeat as necessary to ensure all shutters open and close smoothly and quickly.
8. Wait until the load lock pressure drops below 5e-6 Torr; this may be a few minutes after the **LL Pump** recipe completes.
9. Load the desired shelf into the process chamber: click **Run Recipe** to open the *RecipeSelector* window, and select the appropriate "S[N] to PC" recipe, where [N] is the number of the shelf you wish to load. Remember that the shelves are numbered from 6 to 1, top to bottom. Click the **Run Recipe** button in the *RecipeSelector* window to start the shelf transfer.
10. After the shelf load recipe is finished, you may run a deposition or RF etchback process. To deposit a film, click the appropriate **Gun [N] Deposition**, where [N] is the gun containing the material you wish to deposit (e.g., **Gun 4 Deposition** to deposit Al); the current gun configuration is posted on the wall above the computer monitor. In the resulting *Parameter Passing Recipe* window, adjust the parameters in the *Value* column as required. The default parameters usually do not need to be changed, except for deposition time and possibly burn-in time. The default burn-in time of 30 s

is generally sufficient unless a lot of material (different from the material you wish to sputter) has been deposited immediately before (consult the logbook to verify); in this case, a burn-in time of 60 s is recommended. Next, enter your required deposition time in seconds; a table of deposition rates for different materials and powers is posted on the power supply rack. Click **Continue Load**.

N.B. It is also possible to run process recipes by clicking the **Run Recipe** button and choosing from the list in the *RecipeSelector* window. The four **Gun [N] Deposition** recipes can be run this way, as well as **Cr/Au Deposition** (a shortcut to deposit two common films back to back) and **RF Etchback**.

11. After the recipe is complete, repeat Step 9 to perform further deposition/etchback processes on the loaded shelf, if required.
12. Unload the shelf from the process chamber: click **Run Recipe** to open the *RecipeSelector* window, and select the appropriate "PC to S[N]" recipe. Click the **Run Recipe** button in the RecipeSelector window to start the shelf transfer back to the load lock.
13. After the shelf unload recipe is complete, repeat Steps 8–11 to process additional shelves, if required.
14. Vent the load lock by clicking the **LL Vent** button.
15. When the recipe is complete you can safely open the door and remove the shelf stack and/or remove your specimens from the shelves. Return all shelves to the shelf stack (ensuring that each one is properly seated on its three pins in the shelf stack), and return the shelf stack to the load lock (properly seated on the three load lock pins).
16. Click **LL Pump**.
17. Logout from eKLipse: click the **Logout** button in the upper-left corner.
18. Logout from tool *Sputtering System #3 (Floyd)*; on LMACS.

TROUBLESHOOTING

If there are any problems or questions regarding use of the tool, do not hesitate to contact the primary or secondary trainers. If a process must be stopped, press the **Abort** button in the Recipe Monitor.

APPROVAL

Qualified Trainer: Les Schowalter

Fabrication Group Manager: Aaron Hryciw

Version history
Les Schowalter, 2016-11-08 (*Floyd SOP.docx*)

1.4 NAIT Sputtering System SOP

---

1. Purpose

This document provides instructions on how to operate the SPUTTER-02 DC Magnetron Sputter System for producing metal coatings using the targets mounted in the system. This document details the operation of SPUTTER-02 under normal operating conditions, which involve wafer loading via a load-lock. This SOP does not include the procedure associated with venting and pumping the entire chamber.

2. Safety

- Use of compressed gases (Nitrogen and Argon)
- Electrical hazards associated with high voltage power supply
- Potential for metallic dust and particulate from chamber opening
- Noise exposure associated with equipment operating in the area
- Use of pneumatics and pressurized gases
- Potential for being struck by falling objects, specifically the chamber dome
- Sharps hazard associated with using wafers or sharp substrates
- Potential pinch points associated with the wafer carrier, load lock door, or intervac door

If safe to do so, alert a nanotechnology staff member immediately about any safety hazards or concerns.

3. Materials

- Silicon wafers or substrates
- Wafer tweezers
- Nitrile Gloves
- Lab jackets
- SPUTTER-02 Logbook

4. Equipment

N/A

5. Procedure

This procedure will introduce you to the procedure for pumping down the system. Refer to Figure 1 for vacuum, vent, carrier, and load lock controls.

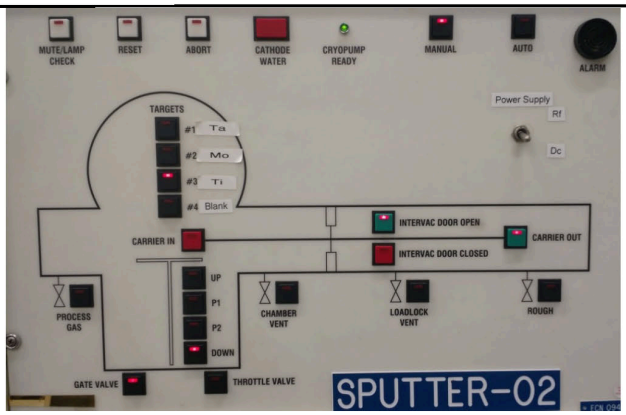

Fig 1 – Main Control Panel on SPUTTER-02

1. Write down relevant information in the SPUTTER-02 Logbook as it becomes available.
2. Ensure that the Intervac Door is closed (Fig. 1). If it is not closed, close the Intervac Door by pressing "INTERVAC DOOR CLOSED".
3. Ensure that the 307 Vacuum Gauge Controller is on, as shown in Fig. 2. If it is not on, push the "ON" button. Also, check that IG1 light is lit. If not, press IG1 to turn on Ion Gauge.
4. Ensure that the Nitrogen and Argon valves are open in the gowning area, on the wall behind SPUTTER-01, and on the manifold to the left of the dome chamber.
5. Vent the load-lock by pressing "LOADLOCK VENT" (Fig. 1) and wait for the door to open a crack.
6. Place substrate(s) on a platen (note – if you are concerned about dust, cover the sample with a large petri dish lid while transferring from the flow hood to the load lock).
7. Open the load lock door. Slide the armature out, and mount the sample platen on the armature.
8. Close load lock door.
9. Turn off the ion gauge by pressing "IG1" on the 307 Vacuum Gauge Controller
10. Rough the load-lock by pressing "ROUGH" (Fig. 1). Note that you must push the door closed to meet the interlock. Once the crossover pressure in the load lock is reached, the roughing pump will automatically turn off. The pressures can be monitored on the 307 Vacuum Gauge Controller.

Fig. 2 – 307 Granville-Phillips Vacuum Gauge Controller

11. Open the Intervac Door by pressing “INTERVAC DOOR OPEN” (Fig. 1).
12. Turn the ion gauge back on by pressing “IG1” on the 307 Vacuum Gauge Controller (Fig. 2).
13. Ensure that the “DOWN” button on the main panel (Fig. 1) is lit up.
14. Select the appropriate target for your process. Note that the most up-to-date target materials are labeled on the main control panel as shown under “TARGETS” in Fig. 1
15. Press “CARRIER IN” (Fig. 1) to move the platen to the process chamber.
16. Press “UP” (Fig. 1) to pick up the platen in the process chamber.
17. Once the light has stopped flashing, press “CARRIER OUT” (Fig. 1) to remove the armature from the process chamber.
18. Close the Intervac Door by pressing “INTERVAC DOOR CLOSED” (Fig. 1).
19. Move the substrate platen to position “P1” or “P2” (Fig. 1), depending on your process.
20. Wait until the chamber pressure reaches drops to 2×10^{-6} Torr or lower, as displayed on the ion gauge on the 307 Vacuum Gauge Controller (Fig. 2).
21. Turn on the Gas Flow for argon (labelled “Ar”, Channel 2) on the MFC controller (MKS Type 247), as shown in Fig. 3.

Fig. 3 – MKS Type 247 Mass Flow Controller

22. Turn off the Ion Gauge by pressing “IG1” (Fig. 2) on the 307 Vacuum Gauge Controller.
23. Press the “THROTTLE VALVE” button (Fig. 1). This partially closes the gate valve so the cryo pump doesn’t work so hard and we don’t need as much Argon flow.
24. Press the “PROCESS GAS” button (Fig. 1). This introduces argon into the chamber.
25. Observe the chamber pressure: it should read approximately 10 mTorr on the Type 250 Baratron Gauge Controller (Fig. 4).
    - Note the pressure may appear high initially, but should decrease and stabilize after approximately 1 minute.
    - If the chamber pressure does not stabilize to 10 mTorr (to within 0.1 mTorr), manually adjust the throttle valve below the workspace in front of the chamber, or ask your instructor to change the set point on the MKS Type 247 MFC (Fig. 3).
26. Turn on the chiller to the right of SPUTTER-02 (ensure that it has enough water; if not, top it up with demineralized water).
27. Turn the key 180° so that the MDX Power Supply display no longer shows “OFF”, as shown in Fig. 5.

Fig. 4 – Baratron Gauge Controller

Fig. 5 – MDX Magnetron Drive Controller

28. Hold the "OFF" button under the "OUTPUT" heading on the MDX (Fig. 5) until the light on the button stops flashing.
29. Check the power setting of the MDX Magnetron Drive Controller; it should be set to 0.5 kW. This is done by holding "LEVEL", and pressing "SET PT". If it is not set to 0.5 kW, and adjust as follows:
    - Hold "LEVEL" button
    - Turn the "MODIFY" knob to adjust the power setting (note – the knob adjusts by 0.05 kW increments, for greater precision push in the knob and turn)
30. Consult the chart on the system that lists deposition rates for the various materials.
31. From the chart, determine the deposition time required to achieve the desired film thickness, and set a countdown timer appropriately.
32. Press the "ON" button on the MDX (Fig. 5) and start the timer.
33. Ensure that the plasma is lit in the chamber.

34. Once desired sputter duration has been reached, turn off the MDX power supply by pressing "OFF" (under "OUTPUT"), then turning the key to the off position (Fig. 5).
35. Press "THROTTLE VALVE" button (Fig. 1) to stop the process gas.
36. Turn off the flow of argon on the MKS Type 247 MFC controller. Note that off position is in the middle of the three-way switch (Fig. 3).
37. Move the platen to the "UP" position (Fig. 1).
38. Open the Intervac Door by pressing "INTERVAC DOOR OPEN" (Fig. 1).
39. Press "CARRIER IN" to bring the wafer carrier armature into the process chamber.
40. Press "DOWN" (Fig. 1) to lower the platen onto the armature. Wait until the light stops blinking before moving on to the next step.
41. Press "CARRIER OUT" (Fig. 1). This should retrieve the platen from the process chamber.
42. Close the Intervac Door by pressing "INTERVAC DOOR CLOSED" (Fig. 1).
43. Vent the Load Lock by pressing "LOADLOCK VENT" (Fig. 1).
44. Remove the platen from the armature, and slide the armature back into the load lock.
45. Close the load lock door, and rough out the load lock by pressing "ROUGH" (Fig. 1).
46. Turn off the chiller.
47. Turn on the ion gauge by pressing "IG1" on the 307 Vacuum Gauge Controller (Fig. 2).
48. Close all Nitrogen and Argon valves in the chase and by SPUTTER-01.

6. Documentation

- Hazard Assessment for using SPUTTER-02, found in the Nano network drive
- Table fastened to SPUTTER-02 indicating deposition rates of various target materials.

7. Document Approval

	Name (Printed)	Signature	Date
Author	James Gospodyn		Sept. 22, 2017
Nanotechnology Staff Member	Keith Oldford		Sept. 22, 2017
Chair	James Gospodyn		Sept. 22, 2017

8. Revisions

Revision	Date	Responsible Person	Description of Change
0	Jun. 18, 2015	James Gospodyn	Original Release
1	Jan. 8, 2016	James Gospodyn	Clarification of a few steps; added missed step to close load lock door after sample loaded; addition of steps to turn off/on the ion gauge before opening load lock door after load lock roughed.

2	Mar. 28, 2016	James Gospodyn	Added steps so that the user moves platen to P1 or P2 position for process.
3	Oct. 12, 2016	James Gospodyn	Removed "open load lock door" step at the end; load lock door should remain closed to prevent accidental venting to cryo. Modified step 2 to ensure that the Intervac Door is closed.
4	Mar. 10, 2017	James Gospodyn	Removal of any reference to the use of Kapton Tape
5	Sept. 22, 2017	James Gospodyn	Clarified two steps; Added reference to the Baratron for the deposition pressure; Added steps to check power and pressure settings.

1.5 *Spectrophotometer SOP*

Spectrophotometer – Hitachi U-3900H

April 10, 2017

Location: W6-040 Characterization Lab
Primary Trainer: Nancy Zhang (780-289-1707, nzhang@ualberta.ca)

OVERVIEW
The Hitachi U-3900H Spectrophotometer is a dual beam spectrophotometer with a wavelength range of 185-850nm. Transmission, absorbtion and reflectance measurements can be performed. Available modules include transmission/absorbtion, as well as 5 degree and 45 degree reflection modules.

SAFETY PRECAUTIONS
Normal laboratory practices apply; gloves should be worn when handling any samples or optics (mirrors, windows).

Take care not to spill liquids onto the spectrophotometer, and immediately clean up any spills with cleanroom wipes. Damage to the optics and electronics can result if liquids are spilled and run inside the instrument.

This equipment contains a power supply that delivers hazardous voltages, and operates in the UV region. Do not operate if any panels are missing.

If you are bringing any new materials into the NanoFab for use in your process, it is necessary to fill out a chemical import form (available on our website, http://www.nanofab.ualberta.ca) and supply an MSDS data sheet to Stephanie Bozic.

PROCESS COMPONENTS OR FEATURES
Before starting, ensure the proper modules are installed for your intended use.

OPERATING INSTRUCTIONS

1. Samples should be clean and ready for measurement. Liquid samples should be contained in spectroscopic cells designed for the cell holder. Users are required to provide their own cuvettes for analysis.

2. Turn on the U-3900H system power by turning on the switch located at the lower left hand side of the optical unit.

3. Open the **UV Solutions 3.0** program on the desktop to access the scanning window. The system will automatically initialize.

4. Once initialized, a method may be opened and modified as required. Click the **Method** icon to view the method settings. The default scan settings and parameters are loaded, and can be edited as required by selecting the appropriate tab in the method window. The scanning parameters can be modified as required, and are located in the **Instrument** tab.

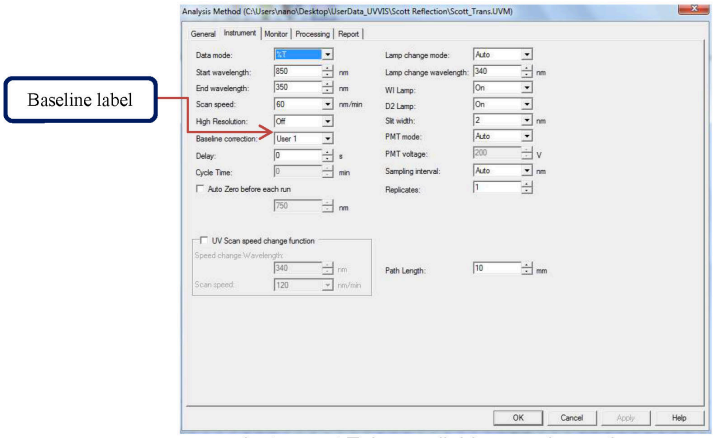

Instrument Tab – available scanning options

- **General tab** – Measurement type, typically set to Wavelength Scan. Other options are Time scan and Photometry. Methods can be saved and loaded while in this tab. Use Sample Table is also selected in this tab. By default it is on, but samples can be scanned without using the sample table.

- **Instrument tab** – Scan settings can be customized as required.
    - Data Mode in either %T, A or %R. Energy scans (E) are available, but are more suited for troubleshooting.
    - Wavelength start and end points (scans from high to low, in 0.5nm intervals).
    - Scan speeds vary from 1.5nm/min - 2400nm/min.
    - High Resolution – On will use all measured data values, Off will smooth the data using the Savitsky-Golay method.
    - Baseline correction selection; remember which option is selected as it must match the actual baseline file.
    - Delay (s) can provide a time delay before starting the scan, in the case further stabilization is required.
    - Cycle time is active when the Replicates option is set to 2 or more, and refers to the time between the start of one measurement and the start of the next measurement.
    - Auto Zero before each run; should remain unchecked in most cases.
    - UV scan speed allows users to adjust the scanning speed while in the UV region. Check this box if required. The Speed change Wavelength and Speed will become active; enter a wavelength and time as required.
    - Lamp change mode should remain in Auto
    - Lamp change wavelength; default is 340nm, may be adjusted if this specific wavelength is critical.
    - WI and D2 lamps should both be on, but can be turned off if the scan range is outside of one of the lamps usable range (WI 850nm-340nm, D2 340nm-190nm).
    - Slit width (2mm), PMT mode (Auto), and PMT voltage (200V) should not be adjusted unless absolutely necessary.

Save the method if required using a unique filename (do not save over the default scan method). Click **OK** to continue.

5. Access the sample table by clicking the **Sample** icon. Select a location for the data to be saved by clicking **Browse**, and selecting a proper location. Edit the **File Name** as required. Fill out the sample table as required, first by entering the number of samples to be scanned. Once done, click **OK**.

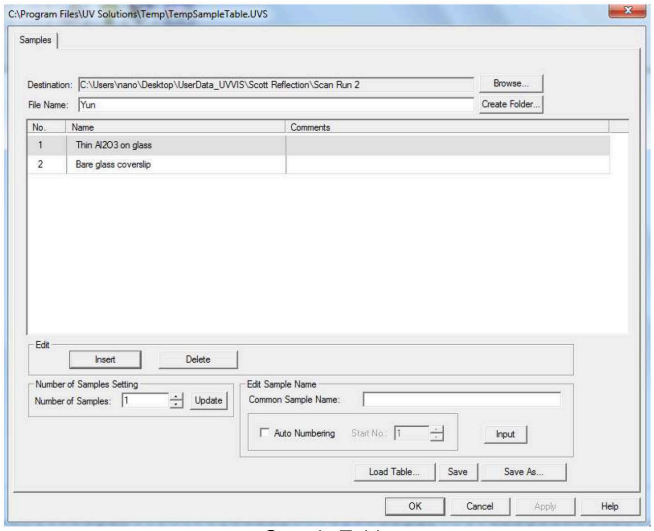

Sample Table

6. Before any samples are scanned, a baseline should be run to correct for the background. Begin by selecting the **Baseline** icon. A window indicating the baseline file to be used will pop up. Ensure that the file name matches the file selected in the Method. Remove all samples from the scanning compartment, and click **OK**.

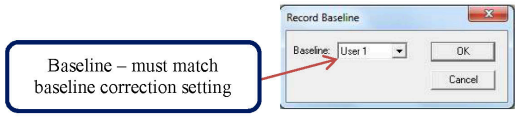

7. Once the baseline is complete, sample analysis may begin. Place a sample in the beam path using the provided clips. If reflection scans are being performed, ensure the mirrors are rotated and positioned as required.

8. Click the **Measure** icon. Ensure the sample has been loaded, select the appropriate option in the scan window when prompted (Scan or Skip), and press **OK**. The scan will begin, and should plot in real time. The scan may be stopped at any time by pressing the Stop button.

9. If multiple samples are being scanned and are entered in the sample table, the scan will continue automatically in order. Users will be prompted to load the next sample when the system is ready.

10. When all samples in the sample table have been run, the raw data will be saved automatically, in a .UDS format. It is advisable to convert the data into a different format, typically in ASCII. Data may be converted using the UV solutions software. Begin by selecting **File → Files Conversion**. Select the file(s) to be converted, Edit the destination, and select output file type. Click **OK** to continue.

11. Once all scanning, analysis, and conversion are done, close the software program. Transfer data as required. Shut down windows when complete.

12. Turn off the system power switch.

Accessories
In addition to the standard transmission module, there is a 5 degree and a 45 degree reflection module available. The reflection modules use the same detector, but the transmission sample holder must be removed. The holder is held in place by a single screw; loosen and remove the holder, then place the reflection modules on the alignment pins.

For baseline collection, insert the reflectance mirror to front baseline position, and turn the "light path switch" to "baseline → detection". For sample measurement, insert the reflectance mirror to back measurement position, and switch the light path to align "measurement → detection".

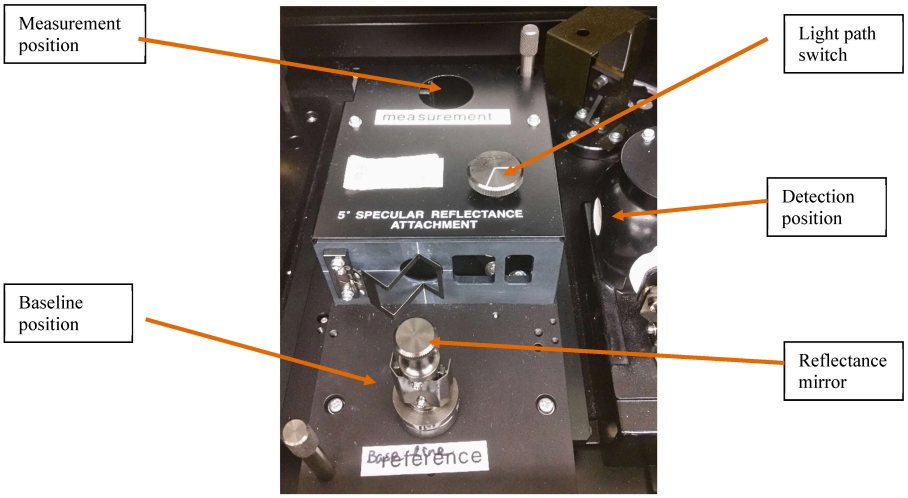

TROUBLESHOOTING

If you encounter an unexpected error or require assistance please contact the primary or secondary trainer listed. Should they not be available, please contact any staff member for assistance.

APPROVAL

Qualified Trainer: Nancy Zhang

Appendix 2 – Alpha Step IQ Profilometer SOP

The purpose of this section was to outline a standard operating procedure (SOP) for consistent thickness measurements of deposited thin films with the Alpha Step IQ (ASIQ) profilometer (KLA-Tencor, Milpitas, CA). Controlled deposition of thin layers is fundamental to research in nanotechnology and specifically the development of this multilayer device. Reproducibility and film uniformity of 5% or less is a necessity for this work.

Initial thicknesses measurements collected using various scan methods and data review processes resulted in large discrepancies. Through the evaluation of these techniques an SOP was generated to ensure accurate, and more importantly, consistent thickness measurements were achieved during tantalum and aluminum deposition. Thin pieces of Kapton tape, ~2 mm by 1 cm, were placed on a minimum of four locations of the wafer prior to sputtering and removed upon completion. This creates valley profiles and provides thicknesses of the deposited thin film when measured. Analysis of thin film thickness using the ASIQ profilometer is a multistep process outlined below:

1) Check calibration of ASIQ with Zygo calibration sample
2) Input Scan Parameters
    - Scan length: 3000μm, 1 time
    - Scan Speed: 50μm/s
    - Sampling Rate: 50 Hz
    - Sensor Range: 550μm/32.8 pm
    - Adjustment: Valley Bias
    - Analysis: Step Height Analysis
    - Contact Speed: 3
    - Required Radius: 5.0μm
    - Scan Direction: Right
3) Collect Scan
    - Place sample on the stage under the probe tip
    - Adjust the sensor by double clicking the down arrow beside the image in the top right corner of the screen

- Rotate the stage and use x and y knobs on the left side of the stage to position the sample for a scan while referencing the image in the top right
- Ensure a minimum of 500 µm on each side of the valley for accurate levelling prior to measurement of step height
- Select the *start* button

4) Form Removal
    - Data Review > Operators and Studies Tabs > Remove Form (if Data Review function enabled) OR select *Form removing* positioned along the left margin

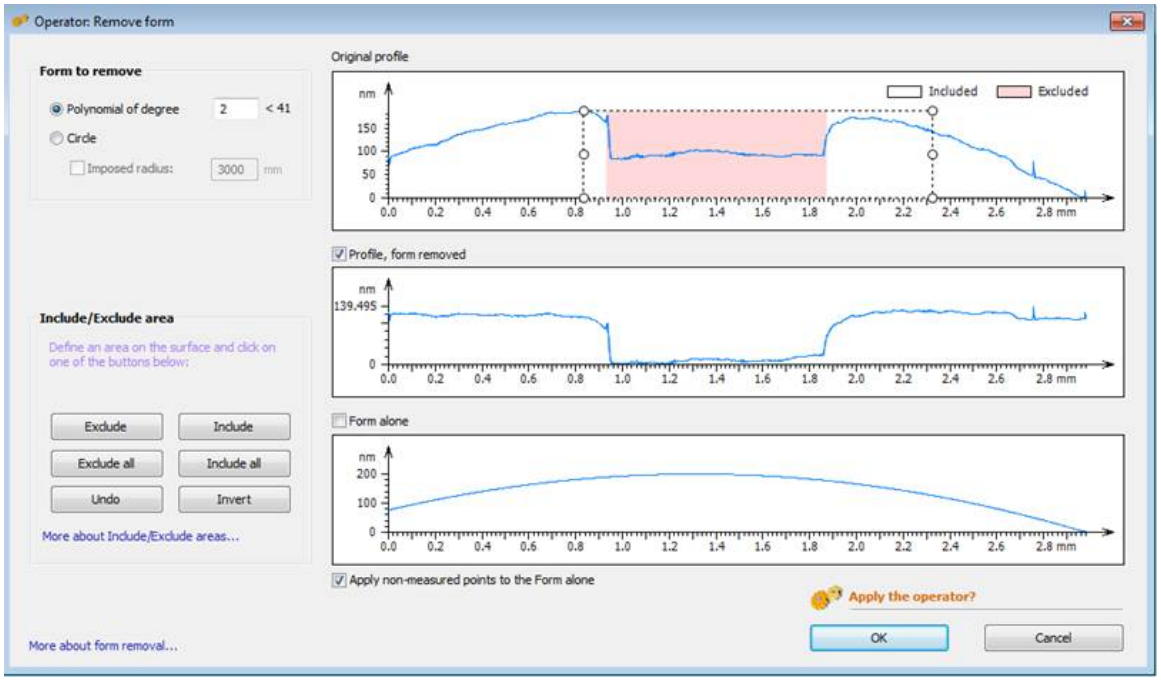

- Exclude lower area by highlighting on the original profile and hitting *Exclude* to generate the form removed profile
- Form to remove: Polynomial of degree = 2
- Profile, form removed and Apply non-measured points to the Form alone should both be checked
- Finish by clicking the *OK* button in the bottom right

5) Levelling
    - Data Review > Operators and Studies Tabs > Level (if Data Review function enabled) OR select *Levelling* button just above the *Form removing* button

- Levelling method: Least squares line
- Exclude the valley portion of the profile when levelling by highlighting this region and selecting *Exclude*, and finish by selecting *OK*

6) Thickness Measurement
    - Right click on the scanned profile in the bottom right corner of the screen and select *Automatic method* or *Iso method* to allow the thickness to be measured more consistently as cursors are placed automatically
    - Generates maximum thickness, mean thickness, and width values

Inconsistencies upward of 50 nm were found within one scan region and subsequent to testing have been attributed to error in the analysis process. Bowing is a natural occurrence during the use of profilometers hence, reinforcing the importance of form removal and levelling functions to correct for this prior to obtaining step height measurements. Without form removal the zones measuring film thickness are extremely dependent on the placement and width as the upper profiles are sloped, meaning small position changes can generate vast thickness changes. Automatic placement and width of zone methods versus manual methods give higher accuracy and will be used for future measurements. Either the *Automatic method* or *Iso method* can be used to generate mean thicknesses. Furthermore, scans will be conducted across the entire valley to ensure maximum accuracy of the profile when compensating with form removal and levelling software applications. For addition information on this tool please refer to the ASIQ3 User Manual.

Appendix 3 – XPS Spectra

Representative low resolution XPS spectra for each surface are shown below for unanodized devices and devices prepared with anodic potentials of 5 or 8 V. These spectra were used to measure phosphorous and nitrogen content, among other elements of interest. XPS spectra were collected from as prepared surfaces, surfaces exposed to prothrombin solutions, and surfaces exposed to prothrombin and anti-prothrombin solutions.

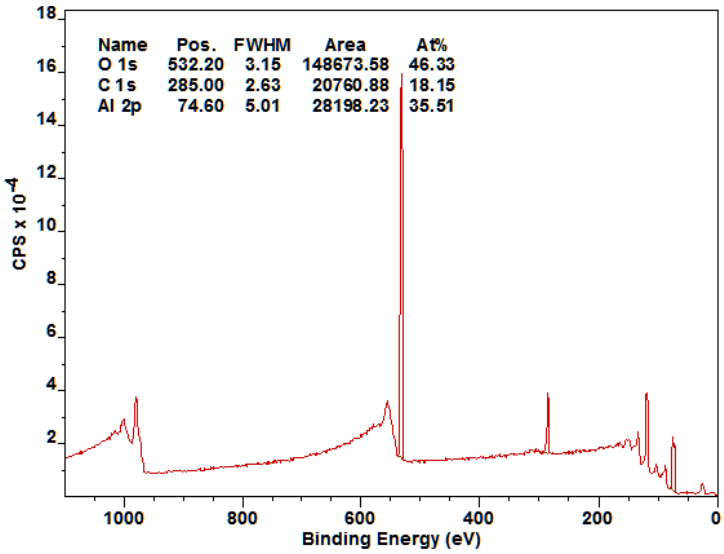

Figure A3.1. Low resolution spectra of an unanodized aluminum surface.

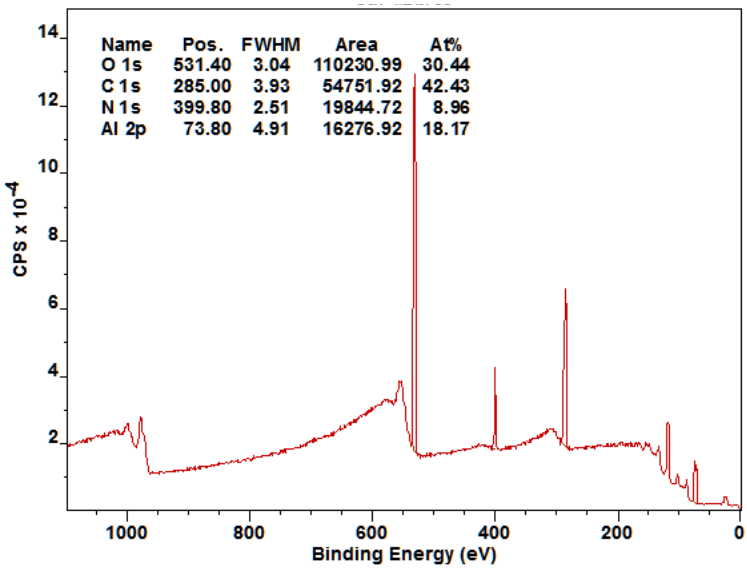

Figure A3.2. Unanodized aluminum surface exposed to prothrombin.

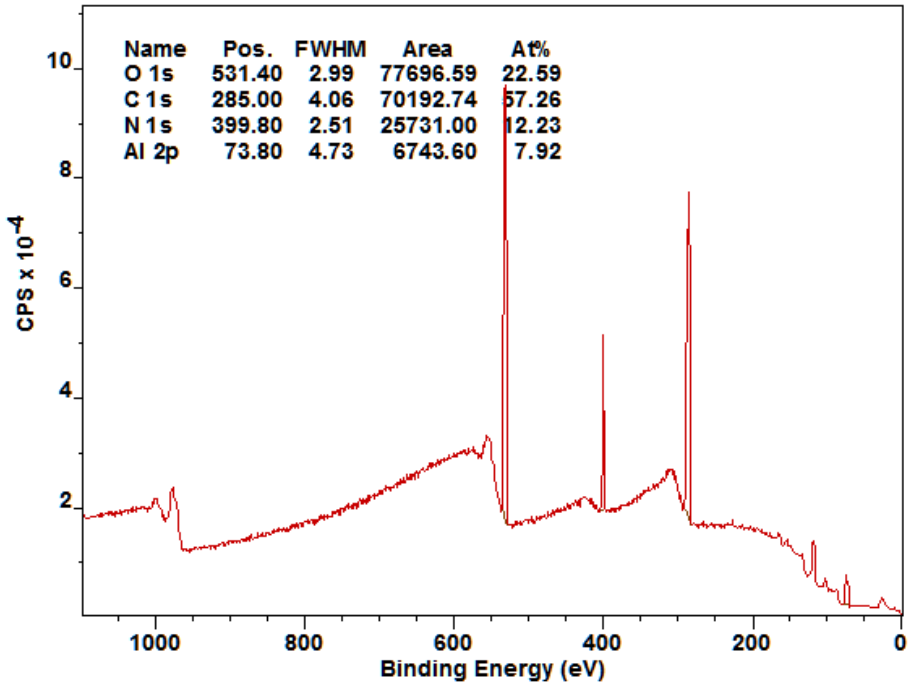

Figure A3.3. Unanodized aluminum surface exposed to prothrombin and anti-prothrombin solutions.

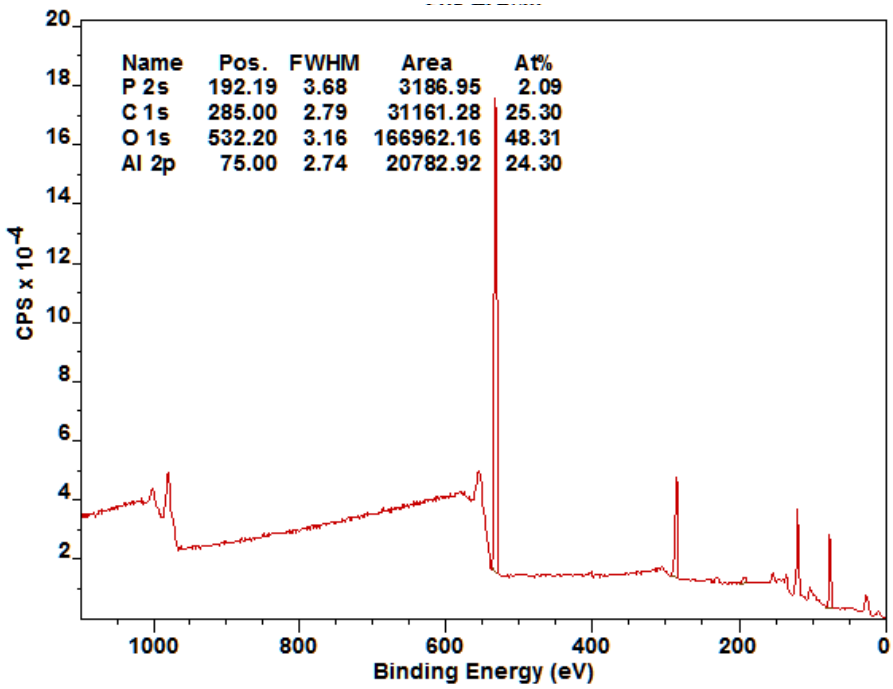

Figure A3.4. As prepared surface created with an applied anodic potential of 5 V.

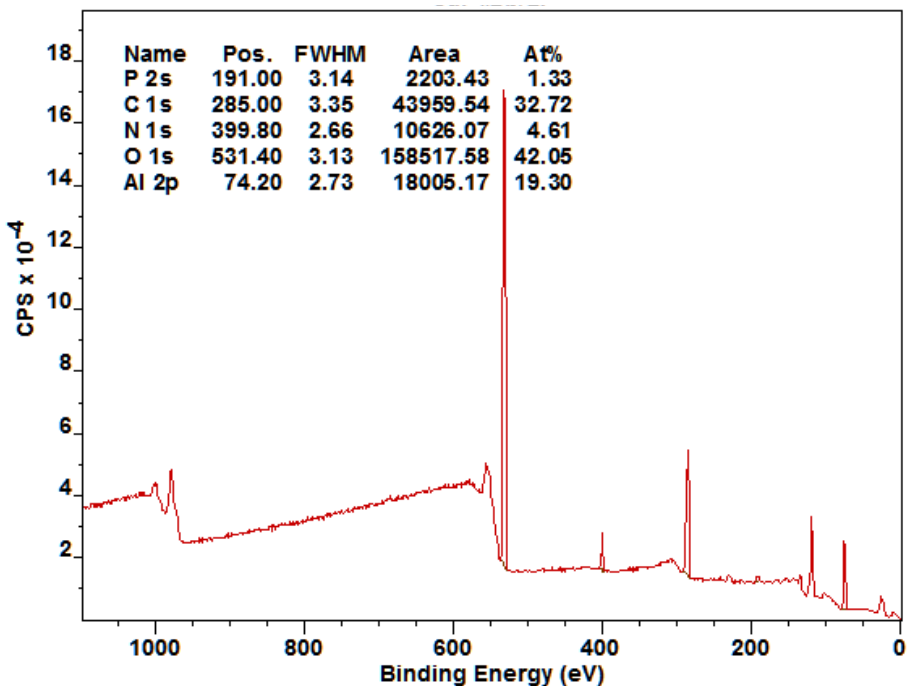

Figure A3.5. Surface exposed to prothrombin solution created with an applied anodic potential of 5 V.

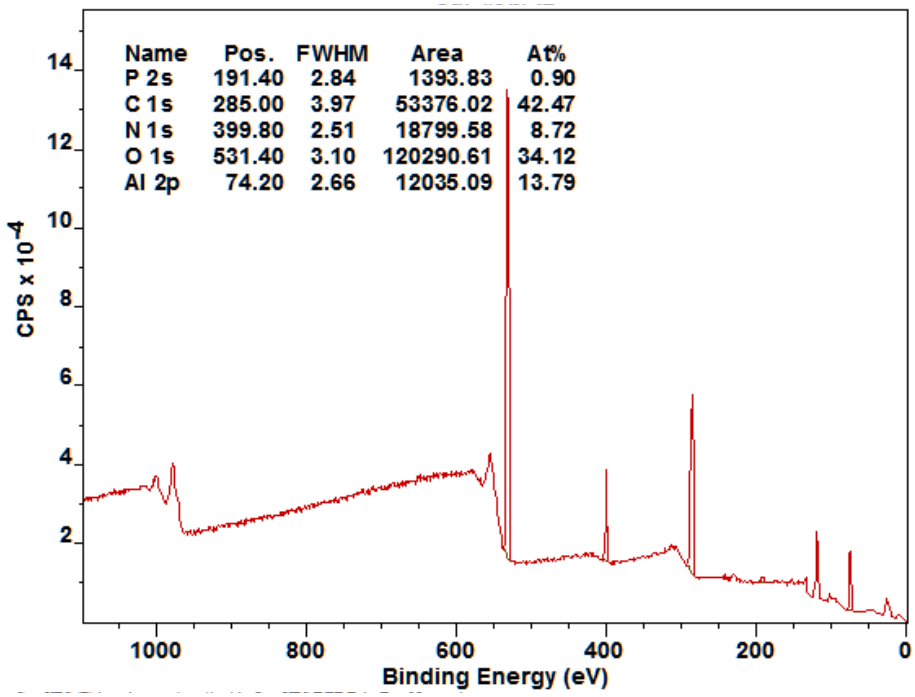

Figure A3.6. Surface exposed to prothrombin and anti-prothrombin solutions created with an applied anodic potential of 5 V.

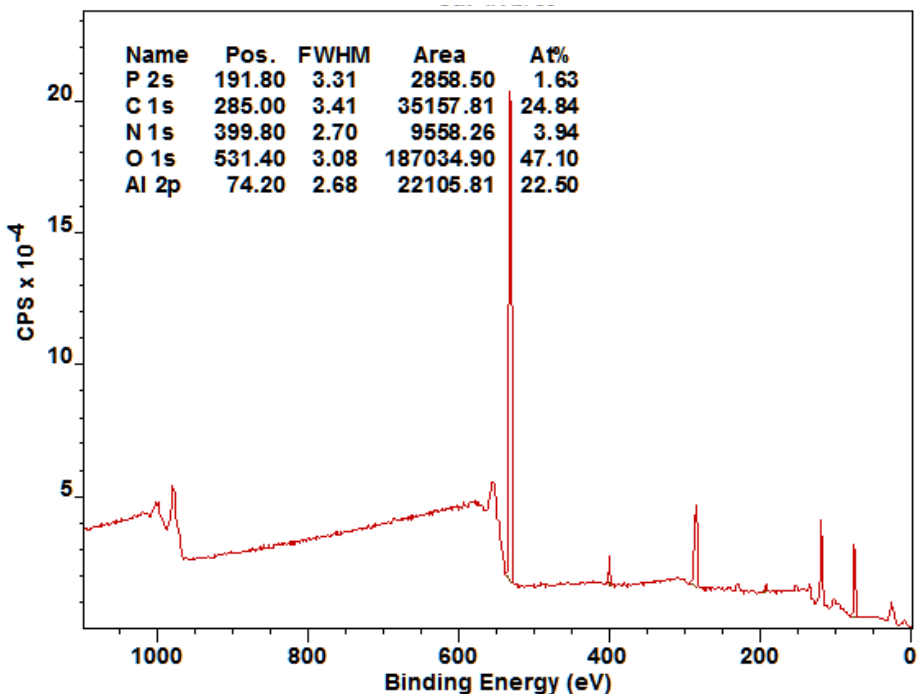

Figure A3.7. As prepared surface created with an applied anodic potential of 8 V.

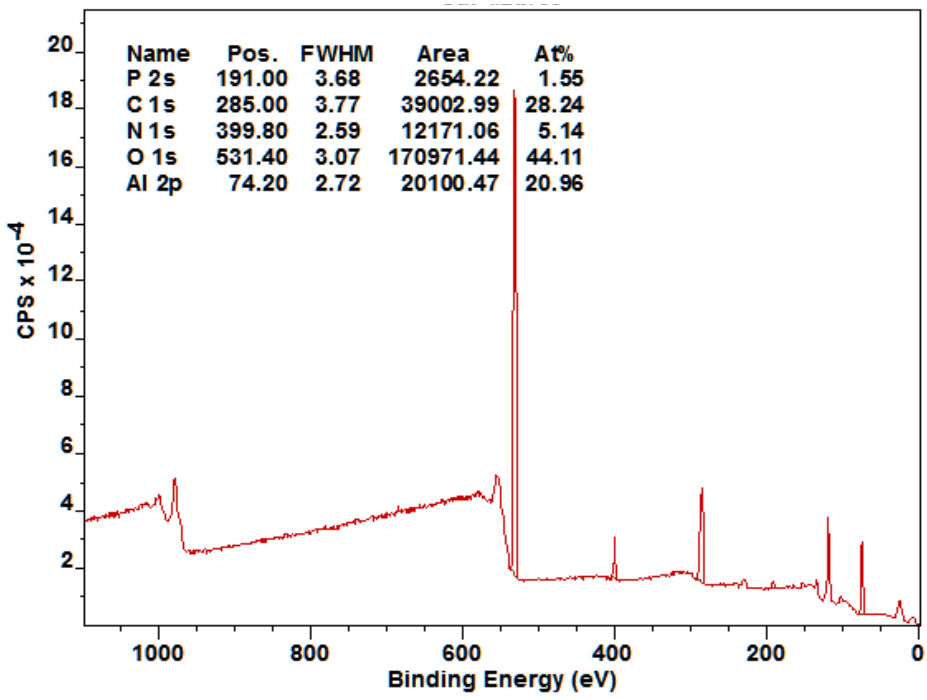

Figure A3.8. Surface exposed to prothrombin solution created with an applied anodic potential of 8 V.

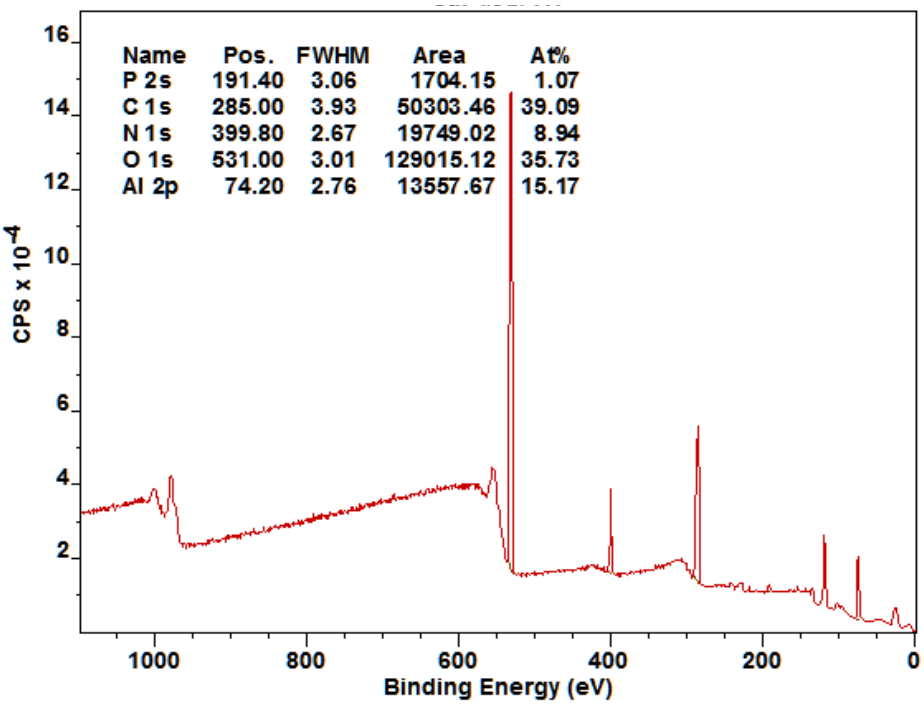

Figure A3.9. Surfaces exposed to prothrombin and anti-prothrombin solutions created with an applied anodic potential of 8 V.